ERCOFTAC Series

Maria Vittoria Salvetti
Vincenzo Armenio
Jochen Fröhlich
Bernard J. Geurts
Hans Kuerten *Editors*

Direct and Large-Eddy Simulation XI

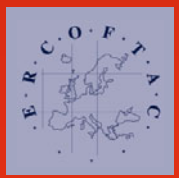

Springer

ERCOFTAC Series

Volume 25

Aims and Scope of the Series

ERCOFTAC (European Research Community on Flow, Turbulence and Combustion) was founded as an international association with scientific objectives in 1988. ERCOFTAC strongly promotes joint efforts of European research institutes and industries that are active in the field of flow, turbulence and combustion, in order to enhance the exchange of technical and scientific information on fundamental and applied research and design. Each year, ERCOFTAC organizes several meetings in the form of workshops, conferences and summerschools, where ERCOFTAC members and other researchers meet and exchange information.

The ERCOFTAC Series will publish the proceedings of ERCOFTAC meetings, which cover all aspects of fluid mechanics. The series will comprise proceedings of conferences and workshops, and of textbooks presenting the material taught at summerschools.

The series covers the entire domain of fluid mechanics, which includes physical modelling, computational fluid dynamics including grid generation and turbulence modelling, measuring-techniques, flow visualization as applied to industrial flows, aerodynamics, combustion, geophysical and environmental flows, hydraulics, multiphase flows, non-Newtonian flows, astrophysical flows, laminar, turbulent and transitional flows.

More information about this series at http://www.springer.com/series/5934

Maria Vittoria Salvetti · Vincenzo Armenio
Jochen Fröhlich · Bernard J. Geurts
Hans Kuerten
Editors

Direct and Large-Eddy Simulation XI

Springer

Editors
Maria Vittoria Salvetti
Dipartimento di Ingegneria
Civile e Industriale
Università di Pisa
Pisa, Italy

Vincenzo Armenio
Dipartimento di Ingegneria
Civile e Ambientale
Università degli studi di Trieste
Trieste, Italy

Jochen Fröhlich
Institut für Strömungsmechanik
Technische Universität Dresden
Dresden, Germany

Bernard J. Geurts
Faculty of Electrical Engineering,
Mathematics and Computer Science,
Multiscale Modeling and Simulation
University of Twente
Enschede, The Netherlands

Hans Kuerten
Department of Mechanical Engineering
Eindhoven University of Technology
Eindhoven, The Netherlands

ISSN 1382-4309 ISSN 2215-1826 (electronic)
ERCOFTAC Series
ISBN 978-3-030-04914-0 ISBN 978-3-030-04915-7 (eBook)
https://doi.org/10.1007/978-3-030-04915-7

Library of Congress Control Number: 2018962385

This Springer imprint is published by the registered company Springer Nature Switzerland AG
The registered company address is: Gewerbestrasse 11, 6330 Cham, Switzerland

Committees

Organizing Committee

V. Armenio, University of Trieste, Italy
J. Fröhlich, TU Dresden, Germany
B. J. Geurts, University of Twente, The Netherlands
H. Kuerten, TU Eindhoven, The Netherlands
M.-V. Salvetti, University of Pisa, Italy

Scientific Committee

B. J. Boersma, TU Delft, The Netherlands
D. Borello, University of Rome, Italy
M. Breuer, Helmut-Schmidt-University, Hamburg, Germany
W. P. Breugem, TU Delft, The Netherlands
L. Davidson, Chalmers University of Technology, Sweden
M. De Marchis, Kore University, Italy
S. Elghobashi, University of California, Irvine, USA
R. Friedrich, TU Munich, Germany
K. Fukagata, Keio University, Japan
M. García-Villalba, Universidad Carlos III de Madrid, Spain
W. P. Jones, Imperial College, London, Great Britain
T. Kempe, TU Dresden, Germany
L. Kleiser, ETH Zurich, Switzerland
E. Lamballais, PPRIME Poitiers, France
C. Marchioli, University of Udine, Italy
M. Meldi, PPRIME Poitiers, France
J. Meyers, University Leuven, Belgium
U. Piomelli, Queens University, Kingston, Canada

M.-V. Salvetti, University of Pisa, Italy
S. Sarkar, University of California, San Diego, USA
W. Schröder, RWTH Aachen, Germany
J. Sesterhenn, TU Berlin, Germany
S. Sherwin, Imperial College London, Great Britain
D. Thévenin, Universität Magdeburg, Germany
A. Tomboulides, Aristotle University of Thessaloniki, Greece
F. Toschi, TU Eindhoven, The Netherlands
M. Uhlmann, Karlsruhe Institute of Technology, Germany
L. Vervisch, Coria, Rouen, France

Preface

The DLES Workshop series, which started in 1994, focuses on modern techniques to simulate turbulent flows based on the partial or full resolution of the instantaneous turbulent flow structures, as Direct Numerical Simulation (DNS), Large-Eddy Simulation (LES), or hybrid models based on a combination of LES and RANS approaches.

With the growing capacities of modern computers, these approaches have been gaining more and more interest over the years. Significant progress has been made in computational techniques as well as in subgrid scale (SGS) modeling. In parallel, these approaches are applied to more and more complex flow problems and configurations, both in academic and industrial contexts, and they will undoubtedly be further enhanced and applied in the future. Nonetheless, open problems and challenges still remain. The increasing complexity of the simulated problems and the use of turbulence resolving approaches in an engineering context require the development of numerical methods being accurate but at the same time able to deal with complex geometries and/or with physical phenomena interacting with turbulence, e.g., particle/droplet dispersion, combustion, or heat transfer. At the same time, physical models must be developed, improved, and validated for the increasing complexity and variety of applications. Validation is indeed a crucial issue for LES and hybrid simulations, since different sources of errors may be present (numerics, boundary conditions, closure models) and these errors may interact in a complicated way. Moreover, systematic sensitivity studies to computational or modeling parameters are difficult to be carried out because of the large cost of each single simulation. On the other hand, the availability of more and more DNS data sets provides a detailed and accurate reference to validate the other approaches and to guide in the development of physical models.

The goal of the workshop series is to establish a state-of-the-art of DNS, LES, and related techniques for the computation and modeling of turbulent and transitional flows and to provide an opportunity for discussions about recent advances and applications.

The 11th edition of the bi-annual Workshop series on Direct and Large-Eddy Simulation (DLES11) was held in Pisa, Italy on May 29–31, 2017. A record number of 140 participants from 17 different countries attended this 3-day workshop. The majority of participants was from academia and research institutes, but several companies were also represented. Eight keynote lectures were given by experts in different scientific fields: extreme scale direct numerical simulations of turbulent combustion (Jacqueline Chen, Sandia National Laboratories, USA), modulation and control of jets and flames (Arthur Tyliszczak, University of Czestochowa, Poland), ocean modeling and idealized DNS applied to rotating and stratified flows (Beth Wingate, University of Exeter, UK), direct numerical simulations of fluid–structure interaction in biological flows (Marco De Tullio, Politecnico di Bari, Italy), simulation and control of wind farms by means of large-eddy simulation (Johan Meyers, Katholieke Universiteit Leuven, Belgium), new insight on how roughness affects the dynamics of turbulence (Ugo Piomelli, Queen's University, Kingston, Canada), applications of DNS and LES to multiphase flows of industrial interest (Djamel Lakehal, ASCOMP, Switzerland), and direct numerical simulations of particulate flows (Markus Uhlmann, Karlsruhe Institute of Technology, Germany).

Next to the invited lectures, 114 oral and poster presentations were selected by a Scientific Committee of 28 experts. This volume contains most of the contributed papers, which were submitted and further reviewed for publication. They cover advances in computational techniques, SGS modeling, boundary conditions, post-processing and data analysis, and applications in several fields, namely, multiphase and reactive flows, convection and heat transfer, compressible flows, aerodynamics of airfoils and wings, bluff-body and separated flows, internal flows and wall turbulence, and other complex flows.

The organization of DLES11 and the preparation of these proceedings would not have been possible without the help of many. Funding from ERCOFTAC (SIG1) enabled the participation of Ph.D. students to DLES11 to be supported. J. M. Burgerscentrum and University of Pisa are also gratefully acknowledged for their support. Finally, thanks go to the members of the Scientific Committee for their help in reviewing the submitted abstracts and the contributions to the proceedings.

Pisa, Italy
March 2018

Maria Vittoria Salvetti
Vincenzo Armenio
Jochen Fröhlich
Bernard J. Geurts
Hans Kuerten

Contents

Part I
Numerical Methods

Adaptive Direct Numerical Simulation with Spatially-Anisotropic Wavelet-Based Refinement

G. De Stefano, E. Brown-Dymkoski and O. V. Vasilyev

1 Methodology

In the wavelet-based adaptive multi-resolution approach to the numerical simulation of turbulent flows, the separation between resolved energetic structures and unresolved flow motions is achieved through the application of a wavelet thresholding filter. For very small threshold values, the effect of residual motions upon the resolved flow dynamics can be completely neglected, which leads to the adaptive Wavelet-based Direct Numerical Simulation (W-DNS) approach. The method allows for the direct solution of the organized flow motions, which consist of both large-scale and small-scale coherent structures with non-negligible energy, e.g. [6, 8].

Due to the ability to identify and efficiently represent energetic dynamically important turbulent eddies, the method has been proven reliable and effective for the simulation of unsteady external flows [7, 9]. However, when dealing with flow around obstacles, one of the main challenges of the traditional W-DNS approach is the requirement of high spatial grid resolution in both the near-wall and the wake regions. Furthermore, when the presence of the obstacle is mimicked by means of the volume-penalization technique, e.g. [5, 12], for the accurate estimation of the wall stresses, and thus the aerodynamic loads, the thin boundary layer inside of

G. De Stefano (✉)
Dipartimento di Ingegneria, Università della Campania, 81031 Aversa, Italy
e-mail: giuliano.destefano@unicampania.it

E. Brown-Dymkoski
Department of Mechanical Engineering, University of Colorado,
Boulder, CO 80309, USA
e-mail: ericbrownd@gmail.com

O. V. Vasilyev
Adaptive Wavelet Technologies, Superior, CO 80027, USA
e-mail: oleg.v.vasilyev@gmail.com

O. V. Vasilyev
Skolkovo Institute of Science and Technology, Moscow 143026, Russia

M. V. Salvetti et al. (eds.), *Direct and Large-Eddy Simulation XI*,
ERCOFTAC Series 25, https://doi.org/10.1007/978-3-030-04915-7_1

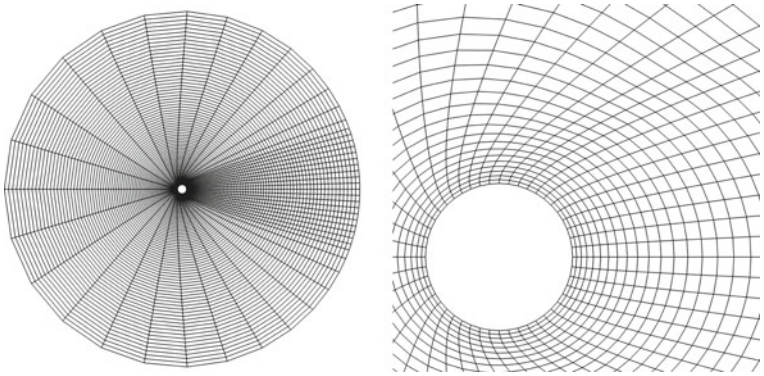

Fig. 1 Example of spatially non-adaptive anisotropic two-dimensional mesh: (left) global and (right) close-up views of the near wake zone

the porous region representing the obstacle also needs to be accurately resolved. The isotropic mesh refinement, which is characteristic of classical wavelet-based methods, results in the simultaneous grid refinement in all directions, irrespective of the actual requirement, even in situations where just one particular direction is involved. This represents a strong constraint of realizability and limits the application of W-DNS to moderate Reynolds number flows. In this study, a novel approach that overcomes this limitation is exploited.

The new W-DNS methodology is developed by making use of the adaptive wavelet transform on curvilinear grids recently introduced in [3]. The traditional wavelet methods suffer from the "curse of anisotropy," due to the isotropic wavelet refinement procedure and the inability to deal with mesh elements with spatially varying aspect ratio and orientation. The new approach utilizes a spatially anisotropic wavelet-based refinement, which takes advantage of coordinate mapping between the physical space, where the curvilinear numerical mesh is defined, and the computational space, where the adaptive rectilinear wavelet collocation grid is used. The new approach permits to construct dynamically adaptive body-fitted meshes, thus avoiding the use of the volume penalization technique. The anisotropic wavelet-based mesh refinement has been recently employed also to develop adaptive unsteady Reynolds-averaged turbulence models of external flows [4].

2 Numerical Experiments

In this work, the flow around a circular cylinder is considered as a prototype for wall-bounded external flows. The curvilinear approach makes it possible to construct stretched body-fitted O-meshes, differently from [2], where the same flow was simulated by exploiting uniform rectilinear meshes in conjunction with a volume penalization approach. Moreover, the introduction of a suitable mapping between computational and physical spaces allows for a particular arrangement of the grid

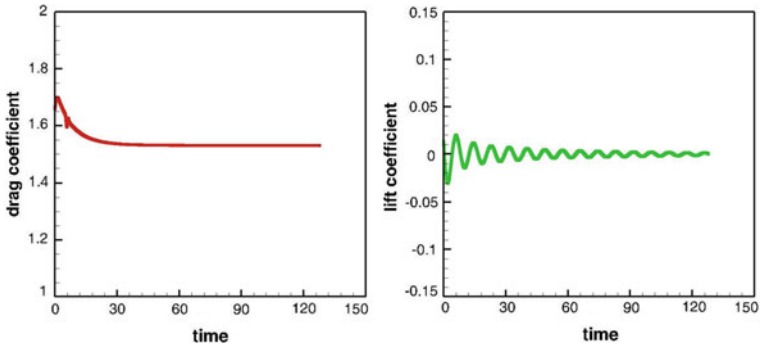

Fig. 2 Two-dimensional cylinder flow at $Re_D = 40$: time histories of (left) the drag and (right) the lift force coefficients

points that permits a more efficient representation of both the wall and the wake regions. In the current work, a more favorable mesh anisotropy is imposed using the wake envelope mapping proposed in [1]. For example, a non-adaptive spatially anisotropic two-dimensional mesh is illustrated in Fig. 1, along with the close-up view of the grid in the near wake region.

The newly proposed W-DNS method is demonstrated for both the laminar steady separated two-dimensional flow at a low Reynolds number, which is $Re_D = 40$, and the three-dimensional turbulent flow at a sub-critical Reynolds number, which is $Re_D = 1000$, where the Reynolds number is based on the cylinder diameter D. For the low Reynolds number simulation, five levels of resolution are used to simulate the vortex shedding flow, which corresponds to employing five nested wavelet collocation grids in the computational space ($J = 5$). Based on previous experience, the wavelet thresholding level is prescribed at the value of $\varepsilon = 5 \times 10^{-4}$.

Looking at the aerodynamic loads on the cylinder, the time histories of the drag and the lift force coefficients are reported in Fig. 2. After the transient period, during which the regular shedding flow develops starting from initial conditions, the drag coefficient achieves the constant value of $C_D = 1.52$, which is very close to the reference value of 1.51 provided in [11]. As to the lift coefficient, predictably, it tends towards zero, with oscillations of decreasing amplitude. The present method allows for the exact enforcement of the no-slip condition at the body surface, whereas, with the volume penalization approach, the same condition could be only approximated. In that case, the inexact nature of the wall boundary condition manifested itself in higher resolution requirement to compensate for the velocity slip error at the body surface [2]. Due to the adaptivity of the method, the number of retained wavelets, and thus the computational cost, nearly follow the flow evolution. After the initial increase caused by the evolution of the wake region, the number of grid points remains practically constant for fully developed flow.

The key characteristic of the proposed W-DNS method stands in the possibility to effectively control the accuracy of the numerical solution. On the one hand, the spatial resolution can be increased by adding further levels of resolution. On the

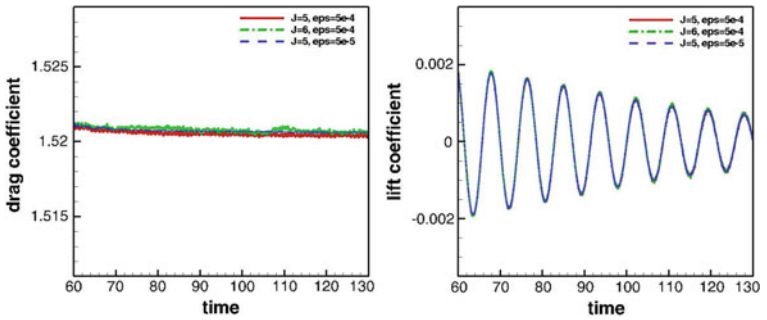

Fig. 3 Two-dimensional cylinder flow at $Re_D = 40$: time histories of (left) the drag and (right) the lift coefficients for three different resolutions that are ($J = 5$; $\varepsilon = 5 \times 10^{-4}$) (solid line), ($J = 6$; $\varepsilon = 5 \times 10^{-4}$) (dash-dotted line) and ($J = 5$; $\varepsilon = 5 \times 10^{-5}$) (dashed line)

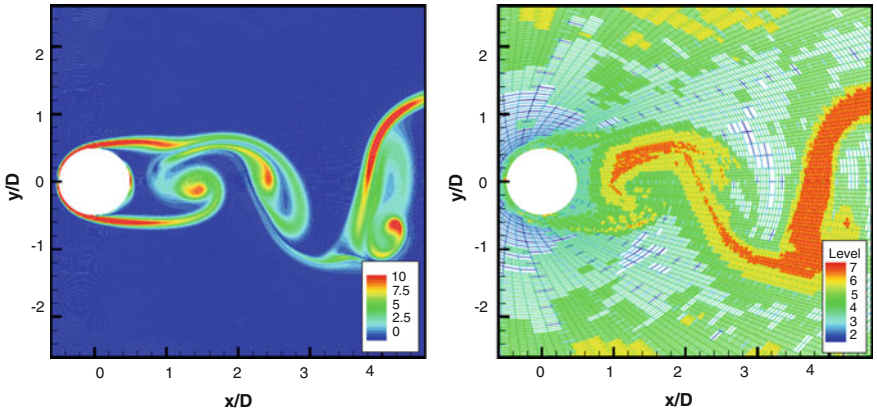

Fig. 4 Three-dimensional cylinder flow at $Re_D = 1000$: (left) instantaneous vorticity contours and (right) adaptive mesh in the mid plane, colored by the level of resolution

other hand, for a given number of wavelet collocation grids, the thresholding level can be properly reduced. In this work, two additional simulations are carried out, starting form the previous baseline solution at the non-dimensional time $tU/D = 60$, where U stands for the freestream velocity, by either using a further level of resolution ($J = 6$) or choosing a lower wavelet threshold that is $\varepsilon = 5 \times 10^{-5}$. The time histories of the drag and the lift force coefficients for three different simulations with different resolutions are reported in Fig. 3. While the use of an extra level of resolution, without changing ε, results in a more noisy solution, the use of a lower threshold undoubtedly results in a more accurate solution. This demonstrates that the direct numerical solution is actually achieved for a sufficiently low level of thresholding.

The present method has been developed for the accurate and efficient simulation of wall-bounded turbulent flows. Some preliminary experiments for the unsteady

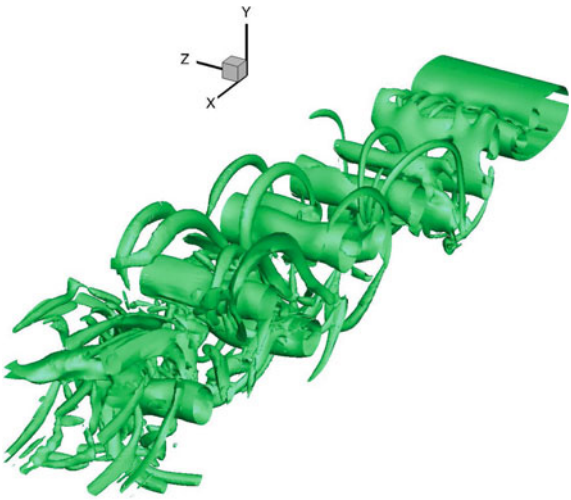

Fig. 5 Three-dimensional cylinder flow at $Re_D = 1000$: main vortical structures in the near wake of the cylinder identified by the iso-surfaces of Q

three-dimensional W-DNS solution of the turbulent flow past a circular cylinder are conducted for the sub-critical flow regime, where the boundary layer exhibits laminar separation and the transition to turbulence occurs in the shear layers developing on the cylinder side, e.g. [10]. The calculation is performed at $Re_D = 1000$, by using seven nested rectilinear wavelet collocation grids in the computational space. The associated anisotropic O-meshes in the physical space are constructed following the same approach of the previous two-dimensional solution in the cross-section planes, while no mapping is used in the third spanwise homogeneous direction, where uniform grid spacing is used. The adaptive method provides a non-uniform spatial resolution, which is actually varying in time following the dynamic evolution of the turbulent flow structures in the three spatial dimensions. This is illustrated in Fig. 4, where the contours of the vorticity magnitude and the numerical mesh, colored by the level of resolution, in the mid-plane, are reported at a given time instant. The anisotropic refinement results in a more efficient representation of the flow field at the wall region, which, in turn, translates into the decrease of the number of active wavelet collocation points and, ultimately, into the reduction of the computational cost. In fact, the use of anisotropically stretched mesh elements close to the surface reduces the number of wavelet levels that are actually needed to resolve the local flow structures. In particular, the maximum level of resolution ($J = 7$) is only involved in very limited zones, compared to excessively high resolution requirement in the near-wall region for the volume penalization approach [3]. Finally, in order to demonstrate how the complex three-dimensional vortex structures in the wake behind the cylinder are well represented by the W-DNS solution, the instantaneous iso-surfaces of the second invariant of the velocity gradient tensor, $Q = 0.4U^2/D^2$, are shown in Fig. 5.

Acknowledgements This work was supported by the Russian Science Foundation (Project 16-11-10350). This support is gratefully acknowledged. Authors are also thankful for the computing time

on the Janus supercomputer, which was supported by the US National Science Foundation (award number CNS-0821794) and the University of Colorado Boulder. The Janus supercomputer was a joint effort of the University of Colorado Boulder, the University of Colorado Denver and the US National Center for Atmospheric Research.

References

1. Beaudan, P., Moin, P.: Numerical experiments on the flow past a circular cylinder at sub-critical Reynolds number, Mech Eng Dept, Stanford University, No. TF-62 (1994)
2. Brown-Dymkoski, E., Kasimov, N., Vasilyev, O.V.: A characteristic based volume penalization method for general evolution problems applied to compressible viscous flows. J. Comput. Phys. **262**, 344–357 (2014)
3. Brown-Dymkoski, E., Vasilyev, O.V.: Adaptive-anisotropic wavelet collocation method on general curvilinear coordinate systems. J. Comput. Phys. **333**, 414–426 (2017)
4. De Stefano, G., Brown-Dymkoski, E., Vasilyev, O.V.: Wavelet-based adaptive unsteady Reynolds-averaged turbulence modelling of external flows. J. Fluid Mech. **837**, 765–787 (2018)
5. De Stefano, G., Nejadmalayeri, A., Vasilyev, O.V.: Wall-resolved wavelet-based adaptive large-eddy simulation of bluff-body flows with variable thresholding. J. Fluid Mech. **788**, 303–336 (2016)
6. De Stefano, G., Vasilyev, O.V.: A fully adaptive wavelet-based approach to homogeneous turbulence simulation. J. Fluid Mech. **695**, 149–172 (2012)
7. De Stefano, G., Vasilyev, O.V.: Wavelet-based adaptive simulations of three-dimensional flow past a square cylinder. J. Fluid Mech. **748**, 433–456 (2014)
8. Goldstein, D.E., Vasilyev, O.V., Kevlahan, N.K.-R.: CVS and SCALES simulation of 3D isotropic turbulence. J. Turbul. **6**, 1–20 (2005)
9. Kevlahan, N.K.-R., Vasilyev, O.V.: An adaptive wavelet collocation method for fluid-structure interaction at high Reynolds numbers. SIAM J. Sci. Comput. **26**, 1894–1915 (2005)
10. Naito, H., Fukagata, K.: Numerical simulation of flow around a circular cylinder having porous surface. Phys. Fluids **24**, 117102 (2012)
11. Sen, S., Mittal, S., Biswas, G.: Steady separated flow past a circular cylinder at low Reynolds numbers. J. Fluid Mech. **620**, 89–119 (2009)
12. Vasilyev, O.V., Kevlahan, N.K.-R.: Hybrid wavelet collocation-Brinkman Penalization method for complex geometry flows. Int. J. Num. Methods Fluids **40**, 531–538 (2002)

Towards Adaptive Mesh Refinement for the Spectral Element Solver Nek5000

N. Offermans, A. Peplinski, O. Marin, P. F. Fischer and P. Schlatter

1 Introduction

When performing computational fluid dynamics (CFD) simulations of complex flows, the a priori knowledge of the flow physics and the location of the dominant flow features are usually unknown. For this reason, the development of adaptive remeshing techniques is crucial for large-scale computational problems. Some work has been made recently to provide Nek5000 with adaptive mesh refinement (AMR) capabilities in order to facilitate the generation of the grid and push forward the limit in terms of problem size and complexity [10]. Nek5000 is an open-source, highly scalable and portable code based on the spectral element method (SEM) [4], which offers minimal dissipation and dispersion, high accuracy and exponential convergence. It is aimed at solving direct and large-eddy simulations of turbulent incompressible or low Mach-number flows with heat transfer and species transport. The approach chosen for adapting the mesh is the h-refinement method, where elements are split locally, which requires the relaxation of the conforming grid constraint currently

N. Offermans (✉) · A. Peplinski · P. Schlatter
Linné FLOW Centre, KTH Mechanics, Royal Institute of Technology, Stockholm, Sweden
e-mail: nof@mech.kth.se

A. Peplinski
e-mail: adam@mech.kth.se

P. Schlatter
e-mail: pschlatt@mech.kth.se

O. Marin
Mathematics and Computer Science Division, Argonne National Laboratory, Lemont, IL, USA
e-mail: oanam@mcs.anl.gov

P. F. Fischer
Siebel Center for Computer Science, University of Illinois, Urbana-Champaign, Champaign, IL, USA
e-mail: fischerp@illinois.edu

M. V. Salvetti et al. (eds.), *Direct and Large-Eddy Simulation XI*,
ERCOFTAC Series 25, https://doi.org/10.1007/978-3-030-04915-7_2

imposed by Nek5000. Other challenges include the implementation of an efficient management of the grid as refinement is applied, the development of tools to localize the critical flow regions via error estimators and the extension of the current preconditioning strategy to non-conforming grids. In this paper, we present a new procedure to setup an algebraic multigrid solver used as part of the preconditioner for the pressure equation.

2 Pressure Preconditioning in Nek5000

2.1 Coarse Grid Solver

The major source of stiffness when solving the Navier–Stokes equations comes from the pressure equation, which requires an efficient preconditioning strategy. The method chosen for Nek5000 is additive Schwarz [2] and the preconditioner can be expressed as $M_0^{-1} = R_0^T A_0^{-1} R_0 + \sum_{k=1}^{K} R_k^T A_k^{-1} R_k$, where K is the number of spectral elements and R_k and R_0 are restrictions operators. This preconditioner can be seen as the sum of the global coarse grid operator (A_0) and local subdomain operators (A_k). The present work focuses on the solution of the coarse grid operator, A_0, a finite element Laplacian matrix. The so-called "coarse grid" denotes the spectral-element grid, where the inner collocation points are not taken into account. Two choices are available in Nek5000 to solve this problem: using a sparse basis projection method, called XXT [11] or an algebraic multigrid (AMG) method, which is more efficient for massively parallel large simulations (more than 10,000 cores and 100,000 elements) [3]. As usual with AMG methods, a setup step is required for the matrix A_0, which will define the necessary data for solving the problem: a coarsening operation and the definition of the interpolation and smoother operators. In the particular case of Nek5000, the AMG solver performs a single V-cycle, and a fixed number of Chebyshev iterations, computed during the setup, is applied during the smoothing part. This method has the advantage to avoid inner products, thus reducing communication. More information about the theoretical background for the setup can be found in Ref. [7]. While the AMG solver is highly scalable and efficient, the setup phase is currently performed by a serial Matlab code, which can take up to a few hours for the largest current cases on a modern desktop computer. This bottleneck is an obstacle to the use of AMR, where the grid, and thus the operator A_0, is modified regularly, every time requiring a new setup computation. For that reason, an alternative method has been investigated to replace the Matlab setup.

Table 1 Summary of the cases used for testing the Hypre setup. The name of the case, number of spectral elements, polynomial order and total number of degrees of freedom for each velocity component are indicated

Case name	Num. of el.	Pol. order	D.O.F.
Jet in crossflow [9]	47,960	7	16,461,424
Straight pipe [1]	853,632	7	293,870,304
NACA4412 [5]	1,847,664	11	1,847,664,000

2.2 Use of Hypre for the AMG Setup

As an alternative way of performing the setup, the Hypre library for linear algebra is used [6]. Specifically, only the time consuming coarsening and interpolation operations are performed with Hypre, while the computation of the smoother remains unchanged in order to keep the good performance of the AMG solver. The use of Hypre offers the possibility to choose among various algorithms for coarsening and interpolation. For the current tests, we chose the Ruge–Stuben algorithm for the coarsening and the so-called "classical" modified technique for the interpolation. The setup is currently performed by a serial, external C code. The main goal with this new setup is to demonstrate two points: the use of the Hypre library reduces significantly the setup time but does not impact the solver time.

3 Validation of the Hypre Setup

In this section, we experiment with the new setup code on several real test cases. In particular, we verify that the Hypre setup is faster than the Matlab one, while the computational time is not affected. We also show the advantage of AMG over XXT for large parallel simulations.

The test cases considered are the simulations of a jet in a crossflow [9], of a turbulent straight pipe ($Re_\tau = 550$) [1] and of the flow around a NACA4412 airfoil ($Re = 400{,}000$) [5]. Some basic information about the cases is summarized in Table 1. All cases are physically relevant, three-dimensional, flagship simulations. The cases of the straight pipe and the NACA4412 are both obtained by extrusion of a 2D grid and are chosen for their large number of elements. The wing case also has elements with large aspect ratios, which makes it more challenging. The grid of the jet in a crossflow is smaller but is chosen because it is not built by extrusion of a 2D grid. Moreover, the complexity of the grid at the junction between the pipe and the channel makes it an interesting case.

Table 2 Comparison between the timings of the Matlab and Hypre codes for the AMG setup

	Time (s.)	I/O	Computation	Total
Jet in crossflow	Matlab	1.17	97.47	**98.64**
	Hypre	0.4	2.02	**2.42**
Straight pipe	Matlab	26.49	2205	**2231**
	Hypre	32.75	44.4	**77.15**
NACA4412	Matlab	93.98	3662	**3756**
	Hypre	90.4	91.7	**182.1**

3.1 Timing of the AMG Setup

The timings for the setup are reported in Table 2 for the Matlab and the Hypre setups. The total setup time is split between I/O time (reading and writing the setup data) and computational time (coarsening and computation of the interpolation operator and smoother at each level). All setups are performed a single time on the same desktop machine (CPU: Intel Core I7 990 Extreme, RAM: 24gb), in serial.

In all cases, the computational and total times for the setup are reduced by more than one order of magnitude. The timings for I/O remain similar on the other hand. Overall, numerical experiments clearly show that Hypre can be used to drastically reduce the setup time, up to levels that can be used for AMR simulations. In addition, so far only the serial version of Hypre has been used; upon inclusion of the setup phase into the main code, even the parallel capabilities will be employed, which might lead to additional reduction of the setup time.

3.2 Timing of the Simulation

The mean total wall clock time per time step during the simulation is presented in Figs. 1 and 2 for the jet in crossflow and the straight pipe, respectively. A straight line showing linear strong scaling is also plot as an indication. Similarly, the time for the coarse grid solver and the total computational time are shown, per time step, in Fig. 3a, b for the NACA4412 airfoil. For all cases, the reported times correspond to averages over 20 time steps and exclude I/O. Each simulation has been run, once, on Beskow, a Cray XC40 supercomputer (1676 nodes, 32 cores per node) based at The Royal Institute of Technology in Stockholm. For the jet in crossflow and the pipe, several number of cores have been considered and the plots show the strong scaling of the code. The NACA4412 simulation has been run on 16,384 cores only.

The results for the jet in crossflow, illustrated in Fig. 1, show that the Hypre setup does not affect the time to solution, as both setups lead to very similar results in terms of computational time. Regarding the comparison between AMG and XXT, the simulation of the jet in crossflow is too small to see a consistent difference between

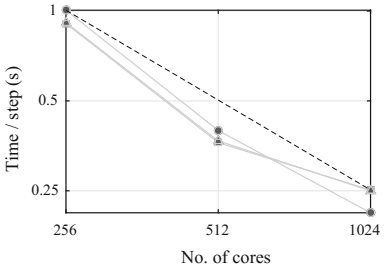

Fig. 1 Jet in crossflow - Total computational time using XXT (circles), AMG with the Matlab setup (squares) and AMG with the Hypre setup (triangles). Dashed line shows linear strong scaling

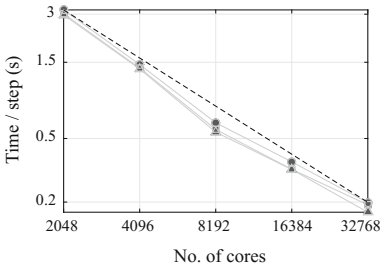

Fig. 2 Straight pipe ($Re_\tau = 550$) - Total computational time using XXT (circles), AMG with the Matlab setup (squares) and AMG with the Hypre setup (triangles). Dashed line shows linear strong scaling

both coarse grid solvers, as can be seen by the fact that the best performing method depends on the number of processes.

It is observed again in Fig. 2 that both the Hypre and the Matlab setups perform similarly well in the case of the simulation of a turbulent straight pipe. Given the larger size of the case, it also appears that the use of XXT for preconditioning the pressure equation is systematically slower compared to AMG. This difference is a only a few percents but occurs at all numbers of cores considered.

Furthermore, Fig. 3a, b show once more that either setup method can be used without affecting significantly the solver time. The slightly higher time for the coarse grid solver may be partly attributed to a higher number of Chebyshev iterations when using Hypre compared to Matlab (33 vs. 26). Other factors that might explain the difference are the algorithms used for coarsening and interpolation. Both figures also illustrate that the use of AMG should be preferred over XXT for large simulations. In the case of the wing, the gain in coarse grid solver time is about 70%, which translates into a reduction of the total computational time by about 10%.

Finally, we show the effect of the setup method on the number of pressure iterations, i.e. the number of iterations of the iterative solver (GMRES in this case) required to drive the L_2-norm of the residual of the divergence equation to some tolerance (10^{-7} in this case), at the start of the simulation of the straight pipe in Fig. 4.

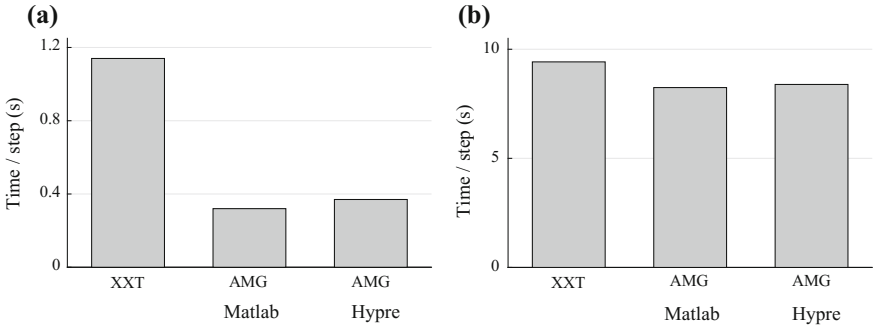

Fig. 3 **a** NACA4412 airfoil - Coarse grid solver time using XXT, AMG with the Matlab setup and AMG with the Hypre setup. **b** NACA4412 airfoil - Total computational time using XXT, AMG with the Matlab setup and AMG with the Hypre setup

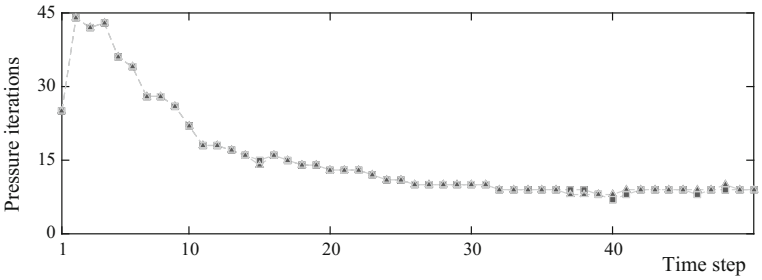

Fig. 4 Comparison of the number of pressure iterations for the AMG setups in the case of the turbulent straight pipe ($Re_\tau = 550$) using Matlab (squares) and Hypre (triangles)

Both plots collapse most of the time, showing once more that both setup methods are equivalent. Similar results have been observed for the two other cases.

4 Conclusion and Outlook

The present work shows numerical results for speeding up the pressure preconditioner with the eventual goal of using adaptive mesh refinement (AMR) with Nek5000 [10].

First, with the help of Hypre, the setup time was reduced by more than one order of magnitude compared to the Matlab code. This improvement will benefit the users of Nek5000 and should facilitate the use of the AMG solver within the framework of AMR. It has been shown that the use of AMG instead of XXT for solving the coarse grid problem in Nek5000 significantly improves the time to solution for large cases (typically more than 100,000 elements on more than 10,000 cores) [8].

Finally, it was shown that replacing the coarsening and interpolation operations of the original Matlab code for the setup by the Hypre routines, while keeping the same strategy for the smoother, does not affect significantly the total solver.

In the future, the setup code using Hypre will be parallelized and included inside Nek5000 such that no interruption in the workflow of a simulation is required. As the result of the AMG setup in Hypre is dependent on the number of parallel processes used, the effect of parallelization on the quality of the coarsening and interpolation operations will also be studied.

References

1. El Khoury, G.K., Schlatter, P., Noorani, A., Fischer, P.F., Brethouwer, G., Johansson, A.: Direct numerical simulation of turbulent pipe flow at moderately high Reynolds numbers. Flow Turbul. Combust. **91**(3), 475–495 (2013)
2. Fischer, P.F.: An overlapping Schwarz method for spectral element solution of the incompressible Navier–Stokes equations. J. Comput. Phys. (1997)
3. Fischer, P.F., Lottes J., Pointer D., Siegel A.: Petascale algorithms for reactor hydrodynamics. J. Phys.: Conf. Ser. **125**(1), 012076 (2008)
4. Fischer, P.F., Lottes, J., Kerkemeier, S.: http://nek5000.mcs.anl.gov
5. Hosseini, S.M., Vinuesa, R., Schlatter, P., Hanifi, A., Henningson, D.: Direct numerical simulation of the flow around a wing section at moderate Reynolds number. Int. J. Heat Fluid Flow **61**, 117–128 (2016)
6. Hypre, high performance preconditioners: User's Manual. Center for Applied Scientific Computing Lawrence Livermore National Laboratory
7. Lottes, J.: Towards Robust Algebraic Multigrid Methods for Nonsymmetric Problems. Springer Theses, Berlin (2017)
8. Offermans, N. et al.: On the Strong Scaling of the Spectral Element Solver Nek5000 on Petascale Systems. Proceedings of the EASC 2016, Stockholm, Sweden, 5:1–5:10
9. Peplinski, A., Schlatter, P., Henningson, D.: Investigations of stability and transition of a jet in crossflow Using DNS. In: Theofilis, V., Soria, J. (eds.) Proceedings of the International Conference on Instability and Control of Massively Separated Flows, pp. 7–18 . Springer, Berlin (2015)
10. Peplinski, A., Fischer, P.F., Schlatter, P.: Parallel performance of h-type adaptive mesh refinement for Nek5000. In: Proceedings of the Exascale Applications and Software Conference 2016. Stockholm, Sweden
11. Tufo, H.M., Fischer, P.F.: Fast parallel direct solvers for coarse grid problems. J. Parallel Distrib. Comput. **61**(2), 151–177 (2001)

Discrete Conservation of Helicity in Numerical Simulations of Incompressible Turbulent Flows

D. Vallefuoco, F. Capuano and G. Coppola

1 Introduction

Helicity is the scalar product between velocity and vorticity and, just like energy, its integral is an inviscid invariant of the 3D incompressible Navier–Stokes equations,

$$\frac{\partial u_i}{\partial t} + \mathcal{N}_i(u) = -\frac{\partial p}{\partial x_i} + \frac{1}{\mathrm{Re}} \frac{\partial^2 u_i}{\partial x_j \partial x_j}, \qquad \frac{\partial u_i}{\partial x_i} = 0 \,, \tag{1}$$

where $\mathcal{N}_i(u)$ is the non-linear convective term and Re is the Reynolds number.

Since its relatively recent discovery [8], helicity has been found to play an important role in both laminar and turbulent flows [7]. A significant research effort has been carried out over the last years to develop numerical algorithms that preserve invariants also in a discrete sense, with the aim of obtaining stable computations and physically relevant solutions. Particular attention has been paid to the development of energy-preserving numerical methods, that have ultimately allowed stable long-time integrations and realistic representations of the energy cascade [1]. On the other side, invariance of helicity has been very seldom considered in the derivation of numerical methods, despite recent developments showing the physical importance of helicity cascade [3]. Notable exceptions include the works by Lui and Wang [6], for axisymmetric flows, and by Rebholz and coworkers (see, e.g., [9]), in the framework of finite-element methods.

D. Vallefuoco
LMFA, École Centrale de Lyon, UMR 5509 CNRS, Écully, France
e-mail: donato.vallefuoco@ec-lyon.fr

F. Capuano (✉) · G. Coppola
University of Naples Federico II, Naples, Italy
e-mail: francesco.capuano@unina.it

G. Coppola
e-mail: gcoppola@unina.it

M. V. Salvetti et al. (eds.), *Direct and Large-Eddy Simulation XI*,
ERCOFTAC Series 25, https://doi.org/10.1007/978-3-030-04915-7_3

The aim of the present work is to investigate the discrete helicity conservation properties in physical-space finite-difference or finite-volume methods. Particularly, the conservation properties of the various discretized forms of the nonlinear term $\mathcal{N}_i$ are discussed. Time advancement is also taken into consideration in the analysis.

2 Discrete Helicity Balance

A semi-discretized version of Eq. (1) can be expressed as

$$\mathbf{S}\frac{\mathrm{d}\mathbf{u}}{\mathrm{d}t} + \mathbf{C}(\mathbf{u})\mathbf{u} = -\mathbf{S}\mathbf{G}\mathbf{p} + \frac{1}{\mathrm{Re}}\mathbf{L}\mathbf{u}\,, \qquad \mathbf{M}\mathbf{u} = \mathbf{0}\,, \tag{2}$$

where $\mathbf{u}$ is the discrete velocity vector containing the three components on the three-dimensional mesh, $\mathbf{u} = \left[\mathbf{u}_x\ \mathbf{u}_y\ \mathbf{u}_z\right]^T$, $\mathbf{S}$ is a diagonal matrix containing the metrics of the mesh, and the operators $\mathbf{C}$, $\mathbf{L}$, $\mathbf{G}$, $\mathbf{M}$ are suitably defined discrete approximations of the corresponding convective, laplacian, gradient and divergence terms respectively (see [1] for further details). A general colocated mesh is considered here (i.e., variables are all arranged in the same points); periodic boundary conditions are also assumed hereinafter.

We aim to derive a discrete evolution equation for helicity, defined as

$$h = \mathbf{u}^T\mathbf{S}\mathbf{w}\,, \tag{3}$$

where $\mathbf{w} = \mathbf{S}^{-1}\mathbf{R}\mathbf{u}$ is the vorticity. The curl operator $\mathbf{R}$ is defined as

$$\mathbf{R} = \begin{bmatrix} & -\mathbf{D}_z & \mathbf{D}_y \\ \mathbf{D}_z & & -\mathbf{D}_x \\ -\mathbf{D}_y & \mathbf{D}_x & \end{bmatrix}\,, \tag{4}$$

where the matrices $\mathbf{D}$ are the difference operators along the three directions and are supposed to be skew-symmetric. This property is a discrete analogous of the summation-by-parts rule and is satisfied by any central-differencing scheme, both explicit and compact [1]. Note that $\mathbf{R}$ is a skew-symmetric block matrix constituted by skew-symmetric blocks, and is thus symmetric, $\mathbf{R}^T = \mathbf{R}$.

The fully discrete evolution equation for helicity can be derived by further assuming a time-integration method. Here, a generic $s-$stage Runge–Kutta method is considered. After proper manipulation, one has

$$\frac{\Delta h}{\Delta t} = \frac{2}{\mathrm{Re}}\sum_i^s b_i\mathbf{u}_i^T\mathbf{R}\mathbf{S}^{-1}\mathbf{L}\mathbf{u}_i - 2\sum_i^s b_i\mathbf{u}_i^T\mathbf{R}\mathbf{S}^{-1}\mathbf{C}\left(\mathbf{u}_i\right)\mathbf{u}_i - \Delta t\sum_{i,j}^s g_{ij}\mathbf{f}_i^T\mathbf{S}^{-1}\mathbf{R}\mathbf{S}^{-1}\mathbf{f}_j, \tag{5}$$

where a_{ij} and b_i are the Runge–Kutta coefficients, $g_{ij} = b_i a_{ij} + b_j a_{ji} - b_i b_j$, and $\mathbf{f}_i = -\mathbf{C}\left(\mathbf{u}_i\right)\mathbf{u}_i + \mathbf{L}\mathbf{u}_i/\mathrm{Re}$. The three terms appearing in the right-hand side of Eq. (5)

are respectively the contribution of the discretized (physical) viscous dissipation, the spatial error term due to convection, and the temporal error. No pressure term arises as long as $\mathbf{RG} = 0$. For a simulation to be physically relevant, the last two terms should vanish, so that helicity preservation is correctly recovered for $\mathrm{Re} \to \infty$.

Concerning the spatial term, the conservation properties depend on the formulation adopted for the convective term. In the continuous case, the nonlinear term $\mathcal{N}_i$ can be written in several analytically equivalent forms (skew-symmetric, divergence, rotational, among others) which instead behave differently when discretized due to violation of the product rule. The property $\mathbf{C}^T = -\mathbf{C}$, that is sufficient to provide discrete conservation of energy [1], does not guarantee helicity preservation alone. However, if the rotational form is employed, $\mathbf{C}^{\mathrm{rot}} = -\mathbf{V}(\mathbf{u})\mathbf{R}$, with $\mathbf{V}(\mathbf{u})$ a skew-symmetric matrix expressing vector product with $\mathbf{u}$, both energy and helicity are spatially preserved. All the other commonly used forms of convection contribute spuriously to the energy and helicity balance.

The temporal error vanishes for *symplectic* (implicit) integrators, which provide $b_i a_{ij} + b_j a_{ji} - b_i b_j = 0$. Indeed, these methods are known to preserve all quadratic invariants of a conservative system. Any explicit method gives an error term in both the energy and helicity discrete evolution equations [2].

By collecting the outcome of this section with known literature results [1], the conservation properties (also including global momentum and energy) of several NS algorithms are reported in Table 1. Note that the rotational form, coupled to a symplectic integrator, fully conserves momentum, energy and helicity.

3 Numerical Results

We are interested here in the effect of the different possible formulations of the nonlinear term on the helical dynamics. Simulating an inviscid system allows to eliminate the numerical error related to the viscous term in Eq. (5). Therefore, in order to isolate the errors related to the formulation of the convective term (and possibly to the time-advancing scheme) from the truncation error, we choose to use a pseudo-spectral method with no de-aliasing. In particular, we solve the spherically truncated Euler equations, i.e. the system obtained by truncating the periodic Euler equations in Fourier space at a wavenumber $|\mathbf{k}| = k_{\max}$. In the absence of numerical errors, this truncated system also preserves energy and helicity. We analyze the statistically stationary state (*absolute* or statistical equilibrium), for which the exact spectra of both energy and helicity are available [5],

$$E(k) = \frac{4\pi}{\alpha} \frac{k^2}{1 - \left(\frac{\beta}{\alpha}\right)^2 k^2}, \qquad H(k) = \frac{8\pi\beta}{\alpha^2} \frac{k^4}{1 - \left(\frac{\beta}{\alpha}\right)^2 k^2}, \tag{6}$$

where α and β are constants that depend on the energy and helicity content. The statistical equilibrium is governed by a single non-dimensional parameter, e.g. the

Table 1 Conservation properties of 3D Navier–Stokes discretizations on a colocated grid. + conservative a priori, ∘ conservative *if and only if* continuity is discretely satisfied, × non conservative

#	Algorithms space	Time	Momentum space	Time	Energy space	Time	Helicity space	Time
1	Rot.	Symp.	∘	+	∘	+	+	+
2	Rot.	Expl.	∘	+	∘	×	+	×
3	Skew	Symp.	∘	+	∘	+	×	+
4	Skew	Expl.	∘	+	∘	×	×	×
5	Div.	Expl.	+	+	×	×	×	×

relative helicity $H_{\text{rel}} = K_h/(2k_{\max}K_e)$, where K_e and K_h are the mean energy and helicity, respectively. In the non-helical case, i.e. $H_{\text{rel}} = \beta = 0$, the helicity spectrum vanishes and the energy spectrum becomes simply

$$E(k) = \frac{4\pi}{\alpha}k^2. \tag{7}$$

In the performed simulations $k_{\max} = 42$ and the initial condition is the sum of two Arnold–Beltrami–Childress (ABC) flows [4], yielding $H_{\text{rel}} = 0.687$. The various algorithms listed in Table 1 are tested; the explicit method is a third-order RK scheme (RK3), while the symplectic one is the Gauss midpoint method.

Time evolutions of global energy and helicity are reported in Fig. 1. Algorithm 1 is fully conservative and indeed is found to preserve energy and helicity in time up to machine precision. The rotational and skew-symmetric forms in conjunction with explicit Runge–Kutta schemes (Algorithms 2 and 4) are found to slightly dissipate energy in time, with Algorithm 2 being more dissipative than Algorithm 4. This is attributed to the accumulation of energy at the smallest scales due to the larger aliasing errors of the rotational form. On the other hand, the skew-symmetric form is found to completely dissipate the initial helicity content in few turnover times. It is interesting to note that Algorithm 2, which employs the rotational form and an explicit RK3, is slightly helicity-productive.

Energy and helicity spectra are reported in Fig. 2. The fully conservative computation matches very closely the exact solution, while Algorithm 2 is slightly dissipative due to the temporal dissipation of the RK3. Importantly, the computation employing Algorithm 4 drives the system towards the non-helical equilibrium solution, i.e. the relative helicity vanishes and $E(k)$ is proportional to k^2, see Eq. (7). Finally, the solution computed through Algorithm 5 diverges due to violation of energy conservation.

We also tested the classical second-order staggered scheme (not shown here) and observed that it dissipates helicity similarly to the collocated skew-symmetric form.

The effects of discrete helicity conservation will be further characterized and quantified via direct numerical simulations of high-Reynolds number turbulence.

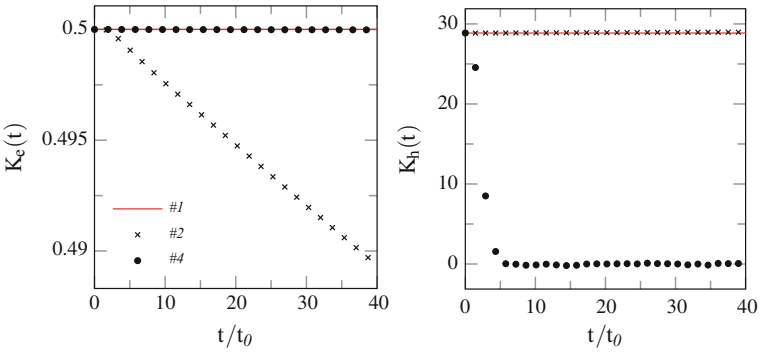

Fig. 1 Time evolution of global energy and helicity for spherically truncated Euler dynamics using the algorithms listed in Table 1; $t_0 = K_e^{-1/2} k_{\max}^{-1}$ is the system characteristic time scale

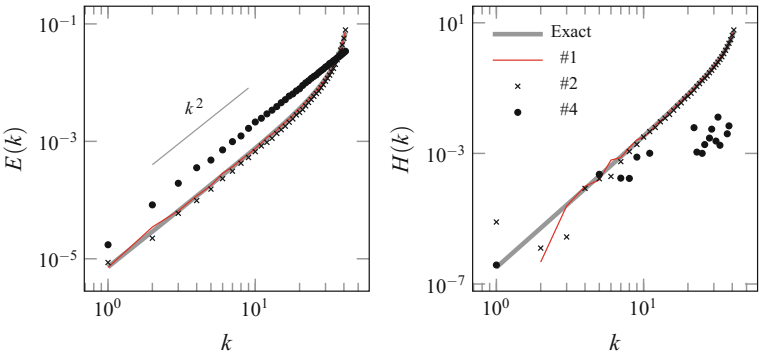

Fig. 2 Energy and helicity spectra in spherically truncated Euler dynamics for the algorithms listed in Table 1. The exact solution is reported in Eq. (6)

References

1. Capuano, F., Coppola, G., Balarac, G., de Luca, L.: Energy preserving turbulent simulations at a reduced computational cost. J. Comput. Phys. **298**, 480–494 (2015)
2. Capuano, F., Coppola, G., Ràndez, L., de Luca, L.: Explicit Runge–Kutta schemes for incompressible flow with improved energy-conservation properties. J. Comput. Phys. **328**, 86–94 (2017)
3. Chen, Q., Chen, S., Eyink, G.L.: The joint cascade of energy and helicity in three-dimensional turbulence. Phys. Fluids **15**(2), 361–374 (2003)
4. Childress S., Gilbert A.D.: Stretch, Twist, Fold: The Fast Dynamo. Springer, Berlin **37** (1995)
5. Kraichnan, R.H.: Helical turbulence and absolute equilibrium. J. Fluid Mech. **59**(4), 745–752 (1973)
6. Lui, J., Wang, W.: Energy and helicity preserving schemes for hydro- and magnetohydrodynamics flows with symmetry. J. Comput. Phys. **200**, 833 (2004)
7. Moffatt, H.K., Tsinober, A.: Helicity in laminar and turbulent flow. Ann. Rev. Fluid Mech. **24**, 281–312 (1992)

8. Moreau, J.J.: Constantes d'un îlot tourbillonnaire en fluide parfait barotrope. C.R. Acad. Sci. Paris **252**, 2810–2812 (1961)
9. Rebholz, L.G.: An energy- and helicity-conserving finite element scheme for the Navier–Stokes equations. SIAM J. Numer. Anal. **45**(4), 1622–1638 (2007)

A Massively Parallel, Direction-Splitting Solver for DNS in Complex Geometries

F. Auteri, M. D. de Tullio, J.-L. Guermond, D. Montagnani and P. D. Konghar

1 Introduction

The Direct Numerical Simulation of turbulent flows (DNS) has proved itself, over the years, an extremely valuable tool to investigate the fundamental properties of turbulence, often rivalling experiments by virtue of its accuracy and of the insight it offers to the investigator [15].

While DNS has been restricted to very simple geometries for quite a long time—the plane channel is still the most investigated one, see [12] and the references therein—the increasing availability of high performance computers allowed the application of this valuable tool to more general geometries. Among the various numerical approaches adopted to reach this goal, of particular interest are spectral elements [7], well suited to deal with complex geometries by construction, and finite differences. The latter can be applied to complex geometries either using boundary fitted grids, that usually require sophisticated, multi-block grid generators [3], or using an immersed boundary approach [14]. This technique has two notable advantages:

F. Auteri (✉) · D. Montagnani
Dipartimento di Scienze e Tecnologie Aerospaziali, Politecnico di Milano, Milan, Italy
e-mail: franco.auteri@polimi.it

D. Montagnani
e-mail: davide.montagnani@polimi.it

M. D. de Tullio
Dipartimento di Meccanica, Matematica e Management, Politecnico di Bari, Bari, Italy
e-mail: m.detullio@poliba.it

J.-L. Guermond
Department of Mathematics, Texas A&M University, College Station, TX, USA
e-mail: guermond@math.tamu.edu

P. D. Konghar
DICCA, Università degli Studi di Genova, Genova, Italy
e-mail: peyman.davvalo.khongar@edu.unige.it

M. V. Salvetti et al. (eds.), *Direct and Large-Eddy Simulation XI*,
ERCOFTAC Series 25, https://doi.org/10.1007/978-3-030-04915-7_4

it requires very simple, inexpensive Cartesian grids; it allows the treatment of very complicated geometries while maintaining a relatively simple algorithmic structure.

The simple algorithmic structure of immersed boundary codes is the key for their success in the DNS of turbulence in complex geometries [5]. In fact, exploiting the full power of recent supercomputers, which are necessary to support DNS of flows at a relatively high Reynolds number, is by itself a challenge. Porting complicated algorithms on massively parallel computers, or even on hybrid architectures, fully exploiting GPUs and many-core CPUs, can be very expensive. In this respect, Cartesian-grid finite differences can offer a distinct advantage.

Despite the fact that several techniques have been developed to increase the performance of finite-difference solvers, for instance multigrid and fast Poisson solvers [13, 16], DNS is such a demanding application that the quest for faster algorithms never ends. Quite recently, Guermond and Minev [9, 10] proposed a new class of direction-splitting, fractional step algorithms whose computational complexity scales linearly with the number of grid points. A *quasi*-optimal version of this method based on Chebyshev polynomials has also been developed [1]. This class of solvers has also two distinct advantages: it can be parallelised with ease to scale on thousands of processors, since the communication overload grows as the cubic root of the number of processors, and it has the potential to fully exploit hybrid architectures, since the large part of the computing time is spent solving tridiagonal linear systems.

In this work, we show that the aforementioned fractional-step method can be effectively coupled with the treatment of immersed boundaries to obtain a very fast, scalable and flexible solver for the DNS of turbulent flows in complex geometries.

2 The Numerical Approach

The equations to be solved are the incompressible Navier–Stokes equations,

$$\frac{\partial \mathbf{u}}{\partial t} + (\mathbf{u}\cdot\nabla)\mathbf{u} - \nu\nabla^2\mathbf{u} + \nabla p = \mathbf{f}(\mathbf{r},t), \qquad \nabla\cdot\mathbf{u} = 0, \tag{1}$$

supplemented by Dirichlet or Neumann boundary conditions. Here $\mathbf{f}(\mathbf{r},t)$ represents a volume-force field, e.g. the gravity-force field, and p is the pressure rescaled by the density. A second order Crank–Nicolson scheme with explicit treatment of the nonlinear term is employed for time discretization,

$$\begin{cases} \frac{\mathbf{u}^{k+1}-\mathbf{u}^k}{\Delta t} - \frac{\nu}{2}\nabla^2(\mathbf{u}^{k+1}+\mathbf{u}^k) = \mathbf{f}^{k+1/2} - (\mathbf{u}_\star^{k+1/2}\cdot\nabla)\mathbf{u}_\star^{k+1/2}, -\nabla p_\star^{k+1/2}, \\ \nabla\cdot\mathbf{u}^{k+1} = 0, \end{cases} \tag{2}$$

where $p_\star^{k+1/2} = p^{k-1/2} + \phi^{k-1/2}$ represents the pressure predictor and $\mathbf{u}_\star^{k+1/2} = (3\mathbf{u}^k - \mathbf{u}^{k-1})/2$.

The discretised Navier–Stokes equations are then advanced in time according to the fully split fractional step pressure-correction algorithm proposed in [9, 10].

According to the algorithm, the velocity can be obtained by solving the following sequence of 1D equations

$$\frac{\mathbf{w}^{k+1}-\mathbf{u}^k}{\Delta t} - \frac{\nu}{2}\partial_{xx}(\mathbf{w}^{k+1}-\mathbf{u}^k) = \mathbf{f}^{k+1/2} + \nu\nabla^2\mathbf{u}^k - (\mathbf{u}_\star^{k+1/2}\cdot\nabla)\mathbf{u}_\star^{k+1/2} - \nabla p_\star^{k+1/2}, \tag{3}$$

$$\frac{\mathbf{v}^{k+1}-\mathbf{w}^{k+1}}{\Delta t} - \frac{\nu}{2}\partial_{yy}(\mathbf{v}^{k+1}-\mathbf{u}^k) = 0, \tag{4}$$

$$\frac{\mathbf{u}^{k+1}-\mathbf{v}^{k+1}}{\Delta t} - \frac{\nu}{2}\partial_{zz}(\mathbf{u}^{k+1}-\mathbf{u}^k) = 0, \tag{5}$$

where $\mathbf{w}^{k+1}$ and $\mathbf{v}^{k+1}$ denote auxiliary variables representing the intermediate solution of the direction-splitting algorithm, while $\mathbf{u}^{k+1}$ is the intermediate velocity.

Once the velocity field has been updated, the pressure field is updated in two steps. First, the following cascade of 1D Neumann elliptic problems is solved

$$\begin{cases} \big(1-\partial_{xx}\big)\psi = -\frac{1}{\Delta t}\nabla\cdot\mathbf{u}^{k+1}, & \partial_x\psi|_{\xi=\pm1} = 0, \\ \big(1-\partial_{yy}\big)\varphi = \psi, & \partial_y\varphi|_{\eta=\pm1} = 0, \\ \big(1-\partial_{zz}\big)\phi^{k+1/2} = \varphi, & \partial_z\phi^{k+1/2}|_{\zeta=\pm1} = 0 \end{cases} \tag{6}$$

to compute the auxiliary variable $\phi^{k+1/2}$; then, the pressure is updated by applying the explicit relation

$$p^{k+1/2} = p^{k-1/2} + \phi^{k+1/2} - \chi\,\frac{\nu}{2}\,\nabla\cdot(\mathbf{u}^{k+1}+\mathbf{u}^k). \tag{7}$$

The algorithm is stable for $0 \le \chi \le 1$ [9, 10]. This process preserves the ellipticity of the pressure Poisson equation, since the split operator is also elliptic.

The elliptic problems are all discretised by standard, second-order finite differences in all the directions, this allows nonperiodic boundary conditions to be imposed easily and it makes the parallelisation of the code easier.

A sponge region is employed in the outlet region together with homogeneous Neumann conditions to avoid the reflection of pressure perturbations [4].

Solid boundaries that are present within the computational domain are treated by means of a discrete-forcing immersed boundary technique, based on a moving least-square approximation to reconstruct the solution in the vicinity of the immersed surface [6]. The body surface is discretised into triangular elements (Lagrangian mesh), whose centroids act as Lagrangian markers. The forcing required to impose the interfacial boundary condition is first computed on the markers lying on the immersed surface, and then transferred to the fixed Eulerian mesh. A moving–least–square (MLS) approach is adopted to build a transfer function around each Lagrangian marker, which is used to exchange information between the Eulerian and Lagrangian meshes. To this purpose, a support domain is built, centred around each Lagrangian marker, which includes N_e Eulerian grid nodes closer than a threshold value in each Cartesian direction. Here, $N_e = 7$ Eulerian nodes are considered in three dimensions. The reconstruction procedure consists in the following steps:

1. Compute the intermediate ith velocity component in all the Eulerian grid points, $\hat{\mathbf{u}}_i$;
2. Using the MLS approach, compute the velocity components at each Lagrangian grid point, approximated in the support domain as:

$$\hat{U}_i(\mathbf{x}) = \sum_{k=1}^{N_e} \phi_k^l(\mathbf{x})\, \hat{\mathbf{u}}_i^k \,, \tag{8}$$

   where k indicates the Eulerian point in the support domain and ϕ_k^l are the shape-function values for marker point l, calculated as in [6];
3. Calculate the volume force component F_i at all Lagrangian grid points:

$$F_i = \frac{V_i^b - \hat{U}_i}{\Delta t} \,, \tag{9}$$

   where V_i^b is the velocity component on the marker to be imposed as a boundary condition.
4. Transfer back F_i to the k Eulerian grid points associated with each Lagrangian grid point, using the same shape functions employed in the interpolation procedure, properly scaled by imposing that the total force acting on the fluid is not changed by the transfer;
5. Correct the intermediate velocity so as to impose the correct boundary conditions on the immersed body.

3 Results

The scalability of the code has been tested on an IBM NeXtScale Linux Infiniband cluster, with 512 nodes and two 8-core Intel Haswell 2.40 GHz processors per node. The results of a weak scalability analysis are reported in Fig. 1. For ideal scalability, the elapsed time would be constant. The timing results reported in the figure show that the communication overhead grows as the cubic root of the number of processors.

The code has been first validated comparing the lift coefficients on the two cylinders in a reference flow, obtaining a difference with the reference solution less than 2%, and then it has been used to investigate the properties of the flow past two side-by-side cylinders for a Reynolds number and non-dimensional distance between the cylinders (g) just beyond the neutral curve associated with the steady asymmetric baseflow [2]. For values of the aforementioned parameters near the instability threshold, reaching the steady final state requires very long transients that are hardly affordable with a standard immersed boundary code [8]. In Fig. 2 we report the evolution towards the periodic limit cycle of the drag coefficients starting from a steady, symmetric base flow. As can be appreciated from the figure, a very long transient is necessary to attain the final limit cycle, which bifurcates from the steady asymmetric

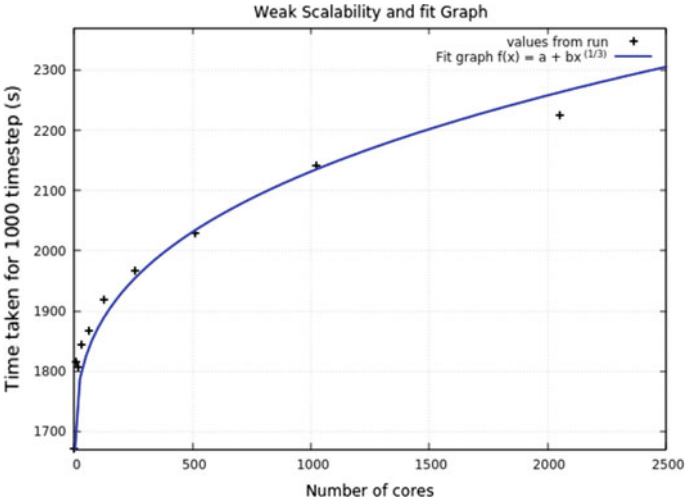

Fig. 1 Weak scalability test: elapsed time for 10^3 time steps and 10^6 points per node on an IBM NeXtScale Linux Infiniband cluster. Solid line: least-square fitting with $a = 1645$ and $b = 49$

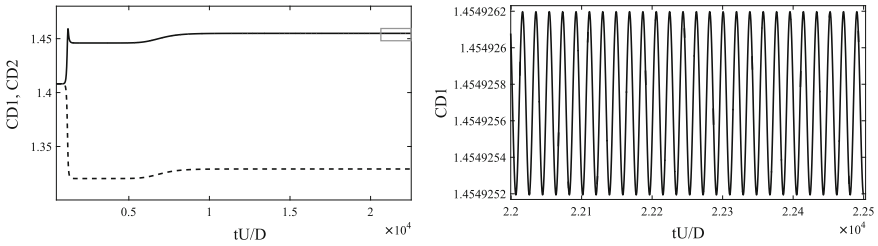

Fig. 2 Long time simulation of the flow past two side-by-side cylinders for $\mathrm{Re} = 68$ and $g = 0.57$. Left: time history of the drag coefficients on the two cylinders. Right: Zoom corresponding to the small rectangle in the left panel to highlight the asymptotic limit cycle

flow. In fact the flow first approaches the steady, asymmetric base flow, a saddle fixed point according to dynamical system terminology, this first transient being quite long. Then the flow evolves towards the final limit cycle, whose amplitude is quite small owing to the proximity to the neutral curve. The simulation is very time consuming since a very long domain is necessary to obtain results independent from the domain size, as shown by the linear stability analysis. In this case the domain is a rectangle 950 cylinder diameters long and 100 cylinder diameters wide with 1028608 grid points. The simulation has been run for 4.5×10^6 time steps with a time step $\Delta t = 0.005$.

To test the 3D version of the code, the steady flow around a rotating sphere has been simulated for two different rotation rates, $\omega^* = \omega R/U = 0.5$ and $\omega^* = \omega R/U = 0.6$. The computational domain is a box of size $15D \times 15D \times 45D$ and a nonuniform grid of $200 \times 200 \times 400$ points has been used, as reported in Fig. 3.

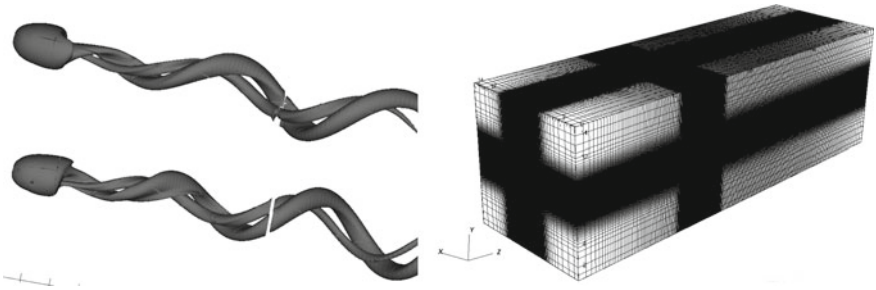

Fig. 3 Steady flow past a rotating sphere for two different rotation rates and Re = 300: $\omega^* = 0.5$ (left, top) and $\omega^* = 0.6$ (left, bottom). Employed mesh (right)

The results, reported in Fig. 3, agree very well with the reference results reported in [11].

In all the presented test cases, a vanishing volume force **f** was assumed.

References

1. Auteri, F.: A quasi-optimal spectral method for turbulent flows in non-periodic geometries. In: Talamelli, A., Oberlack, M., Peinke, J. (eds.) Progress in Turbulence V. Springer Proceedings in Physics, vol. 149. Springer, Dordrecht (2014)
2. Carini, M., Giannetti, F., Auteri, F.: First instability and structural sensitivity of the flow past two side-by-side cylinders. J. Fluid Mech. **749**, 627–648 (2014)
3. Castagna, J., Yao, Y.: Multi-block high order DNS code development for jet in turbulent cross-flow simulation. J. Algorithms Comput. Technol. **6**, 593–622 (2012)
4. Chevalier, M., Schlatter, P., Lundbladh, A., Henningson, D.S.: SIMSON: a pseudo-spectral solver for incompressible boundary layer flows. Technical Report, TRITA-MEK 2007:07. KTH Mechanics
5. de Tullio, M., Cristallo, A., Balaras, E., Verzicco, R.: Direct numerical simulation of the pulsatile flow through an aortic bileaflet mechanical heart valve. J. Fluid Mech. **622**, 259–290 (2009)
6. de Tullio, M.D., Pascazio, G.: A moving-least-squares immersed boundary method for simulating the fluid-structure interaction of elastic bodies with arbitrary thickness. J. Comput. Phys. **325**, 201–225 (2016)
7. Fischer, P.F.: An overlapping Schwarz method for spectral element solution of the incompressible Navier–Stokes equations. J. Comput. Phys. **133**, 84–101 (1997)
8. Giannetti, F., Luchini, P.: Structural sensitivity of the first instability of the cylinder wake. J. Fluid Mech. **581**, 167–197 (2007)
9. Guermond, J.-L., Minev, P.D.: A new class of fractional step techniques for the incompressible Navier–Stokes equations using direction splitting. C. R. Acad. Sci. Paris Ser. I **348**, 581–585 (2010)
10. Guermond, J.-L., Minev, P.D.: A new class of massively parallel direction splitting for the incompressible Navier-Stokes equations. Comput. Methods Appl. Mech. Eng. **200**, 2083–2093 (2011)
11. Kim, D., Choi, H.: Laminar flow past a sphere rotating in the streamwise direction. J. Fluid Mech. **461**, 365–386 (2002)

12. Lee, M., Moser, R.D.: Direct numerical simulation of turbulent channel flow up to $\mathrm{Re}_\tau \approx 5200$. J. Fluid Mech. **774**, 395–415 (2015)
13. Liu, C., Liu, Z.: High order finite difference and multigrid methods for spatially evolving instability in a planar channel. J. Comput. Phys. **106**, 92–100 (1993)
14. Mittal, R., Iaccarino, G.: Immersed boundary methods. Ann. Rev. Fluid Mech. **37**, 239–261 (2005)
15. Moin, P., Mahesh, K.: Direct numerical simulation: a tool in turbulence research. Ann. Rev. Fluid Mech. **30**, 539–578 (1998)
16. Simens, M.P., Jimenez, J., Hoyas, S., Mizuno, Y.: A high-resolution code for turbulent boundary layers. J. Comput. Phys. **228**, 4218–4231 (2009)

An Analysis of Time-Integration Errors in Large-Eddy Simulation of Incompressible Turbulent Flows

F. Capuano, E. M. De Angelis, G. Coppola and L. de Luca

1 Introduction

There is widespread theoretical and numerical evidence that Large-Eddy Simulation (LES) of turbulent flows has to be performed using high-order accurate numerical schemes. Much of the research has so far focused on the spatial discretization, coming to the conclusion that: (1) higher-order methods (≥ 2) are preferred, to ensure that the magnitude of the truncation error does not overwhelm the subgrid-scale model contribution, and (2) non-dissipative (centered) schemes should be employed, so that the energy cascade mechanism is not artificially contaminated [2, 3].

This work is concerned with time-integration errors. Although the above reasonings can be similarly applied to the time-advancement method, errors in time are usually considered to be negligible, provided that (at least) second-order methods are employed and the time step is kept lower than the smallest time scale of the flow. As a consequence, a systematic analysis of time-integration errors has been seldom carried out in literature. Choi and Moin [5] investigated the effects of using large time steps in a turbulent channel flow, and found that excessively large time increments led to relaminarization or inaccurate turbulence statistics. Verstappen et al. [8] compared several explicit schemes for the numerical simulation of a driven-cavity flow, and found no significant differences in the results. They also concluded that the time step is generally determined by stability and not by accuracy.

F. Capuano (✉) · E. M. De Angelis · G. Coppola · L. de Luca
Department of Industrial Engineering, University of Naples Federico II, Naples, Italy
e-mail: francesco.capuano@unina.it

E. M. De Angelis
e-mail: enricomaria.deangelis@unina.it

G. Coppola
e-mail: gcoppola@unina.it

L. de Luca
e-mail: deluca@unina.it

M. V. Salvetti et al. (eds.), *Direct and Large-Eddy Simulation XI*,
ERCOFTAC Series 25, https://doi.org/10.1007/978-3-030-04915-7_5

The aim of this work is to carry out systematic tests to investigate time-integration errors in LES of a canonical turbulent flow at time steps close to the ones dictated by the stability constraint of the temporal scheme. Building on the basis of a recent paper by the authors [4], the discrete energy evolution equation is considered, and the contribution of the temporal error is compared to the physical and subgrid-scale model dissipation rates. The analysis is carried out for general Runge–Kutta schemes, although it can be extended to other methods (e.g., multi-step).

2 Theoretical Framework

2.1 Discretization of Navier–Stokes Equations

The filtered incompressible Navier–Stokes (N–S) equations read:

$$\frac{\partial \overline{u}_i}{\partial t} = -\mathscr{C}_i(\overline{u}) - \frac{\partial \overline{p}}{\partial x_i} + \frac{1}{\mathrm{Re}} \frac{\partial^2 \overline{u}_i}{\partial x_j \partial x_j} - \mathscr{R}_i\left(u, \overline{u}\right), \qquad \frac{\partial \overline{u}_i}{\partial x_i} = 0 , \tag{1}$$

where $\mathscr{C}_i(\overline{u})$ is the non-linear convective term, Re is the Reynolds number and $\mathscr{R}_i = \overline{\mathscr{C}_i(u)} - \mathscr{C}_i(\overline{u})$ is the subfilter-scale term. A discretization in space leads to the semi-discrete version of the filtered N-S equations, which can be expressed as:

$$\frac{\mathrm{d}\overline{\mathbf{u}}}{\mathrm{d}t} = -\mathbf{C}(\overline{\mathbf{u}})\overline{\mathbf{u}} - \mathbf{G}\overline{\mathbf{p}} + \frac{1}{\mathrm{Re}}\mathbf{L}\overline{\mathbf{u}} - \mathbf{r}(\overline{\mathbf{u}}) , \qquad \mathbf{M}\overline{\mathbf{u}} = \mathbf{0} , \tag{2}$$

where $\overline{\mathbf{u}}$ is the filtered discrete velocity vector containing the three components on the three-dimensional mesh and the operators $\mathbf{C}$, $\mathbf{L}$, $\mathbf{G}$, $\mathbf{M}$, $\mathbf{r}$ are suitably defined discrete approximations of the corresponding convective, Laplacian, gradient, divergence and subfilter-scale terms respectively. For this last term a further model assumption has been implicitly made in order to express $\mathbf{r}$ as a function of $\overline{\mathbf{u}}$ only.

From Eq. (2) an evolution equation for the kinetic energy of the filtered field can be derived. For uniform meshes it reads:

$$\frac{\mathrm{d}\overline{E}}{\mathrm{d}t} = -\overline{\mathbf{u}}^T\mathbf{C}(\overline{\mathbf{u}})\overline{\mathbf{u}} - \overline{\mathbf{u}}^T\mathbf{G}\mathbf{p} + \frac{1}{\mathrm{Re}}\overline{\mathbf{u}}^T\mathbf{L}\overline{\mathbf{u}} - \overline{\mathbf{u}}^T\mathbf{r}\left(\overline{\mathbf{u}}\right) , \tag{3}$$

where $\overline{E} = \overline{\mathbf{u}}^T\overline{\mathbf{u}}/2$. A similar equation can be derived for the case of nonuniform mesh by considering the relevant scalar product. In Eq. (3) the pressure term vanishes if the divergence free constraint is satisfied (and assuming that $\mathbf{M}^T = -\mathbf{G}$ holds), while the convective term vanishes only if a skew-symmetric operator $\mathbf{C}$ is adopted. Thus, an energy-conserving spatial discretization leads to a semi-discrete energy balance which is a close counterpart of the continuous energy budget.

Due to the incompressibility constraint, the system in Eq. (2) is an index-2 Differential Algebraic system. By introducing a projector operator $\mathbf{P}$ it can be formally recast as the system of ODE $\dot{\overline{\mathbf{u}}} = \widetilde{\mathbf{F}}(\overline{\mathbf{u}})$, where $\widetilde{\mathbf{F}} = \mathbf{PF}$ and $\mathbf{F}(\mathbf{u}) = -\mathbf{C}(\mathbf{u})\,\mathbf{u} + \frac{1}{\mathrm{Re}}\mathbf{L}\mathbf{u} - \mathbf{r}(\mathbf{u})$, with $\mathbf{P} = \mathbf{I} - \mathbf{G}\mathscr{L}^{-1}\mathbf{M}$ and $\mathscr{L} = \mathbf{MG}$. Time integration is now straightforward. Here, a $s-$stage Runge–Kutta method is considered [1]:

$$\overline{\mathbf{u}}^{n+1} = \overline{\mathbf{u}}^{n} + \Delta t \sum_{i=1}^{s} b_i \widetilde{\mathbf{F}}(\overline{\mathbf{u}}_i)\ , \tag{4}$$

$$\overline{\mathbf{u}}_i = \overline{\mathbf{u}}_n + \Delta t \sum_{j=1}^{s} a_{ij} \widetilde{\mathbf{F}}(\overline{\mathbf{u}}_j)\ . \tag{5}$$

The pressure at each RK sub-step is evaluated by solving a Poisson equation [2].

2.2 Evaluation of Temporal Errors

In general, Eqs. (4)–(5) introduce aliasing errors [6] (due to discrete evaluation of products) as well as dispersive and diffusive errors (coming from both spatial and temporal discretizations). This work is primarily concerned with diffusive errors, which are believed to be the most critical in LES. Indeed, in recent years energy conservation has been considered a priority over the formal order of accuracy of the method. In this work, spatially energy-conserving methods are assumed and the attention is focused on temporal errors.

The diffusive temporal error can be evaluated by deriving an expression for the variation of the kinetic energy of the filtered field introduced by Eqs. (4)–(5). The fully discrete evolution equation can be obtained in closed form by taking the inner product between $\overline{\mathbf{u}}^{n+1}$ and itself. After some basic manipulation [4], one has

$$\frac{\Delta \overline{E}}{\Delta t} = \frac{1}{\mathrm{Re}} \sum_i b_i \overline{\mathbf{u}}_i^T \mathbf{L} \overline{\mathbf{u}}_i - \sum_i b_i \overline{\mathbf{u}}_i^T \mathbf{r}(\overline{\mathbf{u}}_i) - \frac{\Delta t}{2} \sum_{i,j=1}^{s} g_{ij} \widetilde{\mathbf{F}}_i^T \widetilde{\mathbf{F}}_j, \tag{6}$$

where $\Delta \overline{E} = \overline{E}^{n+1} - \overline{E}^{n}$ and $g_{ij} = b_i a_{ij} + b_j a_{ji} - b_i b_j$.

The first two terms in the r.h.s. of Eq. (6) are, in order, the time-discrete counterparts of the viscous (physical) dissipation rate ε^{ν}, and of the subfilter-scale contribution ε^{SGS}. The last term is a purely temporal error, which will be denoted as ε^{RK}. In a LES simulation, it would be desirable to have the filtered energy balance to be modified only by the viscous dissipation and the subfilter-scale terms. Currently available methods to reduce the magnitude of the temporal error, on equal time step, include using symplectic (implicit) or pseudo-symplectic (explicit) methods, which are able to eliminate the error entirely, or to reduce it to $\mathscr{O}(\Delta t^q)$ respectively [4].

The aim of this work is to evaluate the magnitude of the temporal error term with respect to the viscous and subfilter-scale contributions for a canonical turbulent flow, for various RK methods and as a function of proper non-dimensional parameters.

3 Results

The three-dimensional Taylor–Green vortex is here investigated to assess the impact of temporal errors. The problem is entirely governed by the Reynolds number, which is chosen to assume the values $\mathrm{Re} = 1600$ and $\mathrm{Re} = 3000$. Estimates of the Kolmogorov length- and time-scale can be obtained by well-known relations [7]. The flow is well resolved with 256^3 grid points. Here, a large-eddy simulation is carried out using 64^3 points, and a dynamic Smagorinsky model is adopted. The Navier–Stokes equations are solved using a second- or fourth-order centred method with the convective term cast in skew-symmetric form, so that the spatial scheme is energy conserving. The Runge–Kutta schemes here investigated belong both to classical methods and to more recently investigated pseudo-symplectic explicit schemes. More specifically, five RK schemes are employed: the third- and fourth-order classical RK schemes (denoted as RK3 and RK4 respectively) and the four-, five- and six-stage explicit pseudo-symplectic schemes studied in [4], denoted respectively as 3p5q, 3p6q and 4p7q (refer to [4] for details). In Figs. 1 and 2 the results of a preliminary calculation without any model (i.e. by dropping the subfilter-scale term in Eq. (2)) obtained by employing fourth-order spatial discretization and for $\mathrm{CFL} = 1$ are reported. The normalized temporal numerical dissipation $\varepsilon^{RK}/\varepsilon^{\nu}$ is plotted as a function of time for various RK schemes at $\mathrm{Re} = 1600$ and $\mathrm{Re} = 3000$. These plots show that a significative numerical dissipation is produced by classical RK3 and RK4 schemes, as compared to the physical viscous contribution, while pseudo-symplectic schemes are effective in reducing this production to negligible values. These conclusions are also supported by the ratio of the effective to nominal Reynolds number, reported on the right y-axis, where the effective Reynold number is defined to take into account the sum of physical and numerical viscosity (see [4] for further details). In Fig. 3 the same calculation is performed in conjunction with the application of the dynamic Smagorinsky model for the $\mathrm{Re} = 1600$ case. In this simulation the spatial discretization is obtained with second-order schemes and the CFL number is set to 0.5. The numerical dissipation is in this case normalized with the sum of the physical viscous dissipation and the subfilter-scale contribution. The results confirm that classical RK schemes can provide a significative spurious contribution to energy dissipation, while pseudo-symplectic schemes are able to reduce this contribution to values below 0.1%.

A more systematic comparison among the various methods is reported in Fig. 4 and in Fig. 5, where the ratio $\varepsilon^{RK}/(\varepsilon^{\nu} + \varepsilon^{SGS})$, evaluated at the point of transition to turbulence, is shown as a function of the time step adopted, starting from the maximum Δt allowed from stability criteria. An inspection of Figs. 4 and 5 suggests that higher-order methods might be more efficient than lower-order ones. In Fig. 4 two

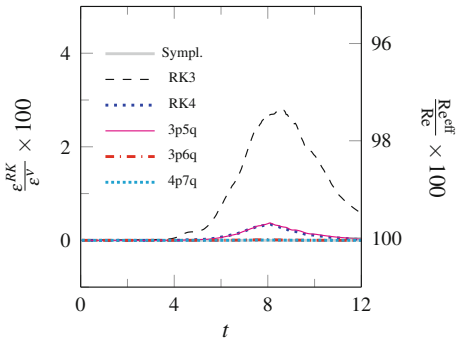

Fig. 1 Normalized temporal numerical dissipation ε^{RK} as a function of time for various RK schemes for the TGV test case at $\mathrm{Re} = 1600$

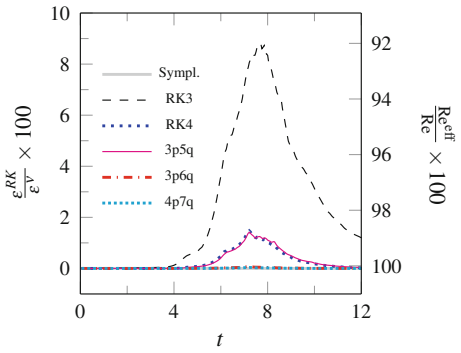

Fig. 2 Normalized temporal numerical dissipation ε^{RK} as a function of time for various RK schemes for the TGV test case at $\mathrm{Re} = 3000$

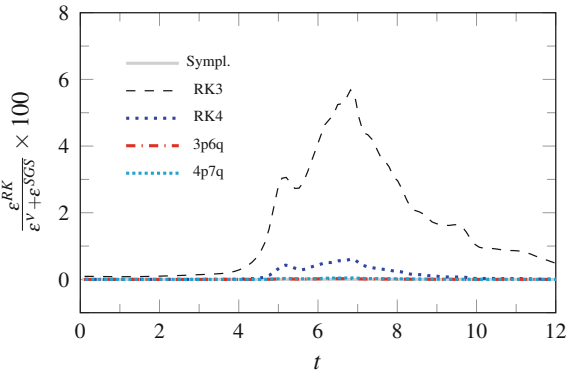

Fig. 3 Normalized temporal numerical dissipation ε^{RK} as a function of time for various RK schemes for a LES simulation with the dynamic Smagorinsky model of the TGV test case at $\mathrm{Re} = 1600$

thresholds have been fixed: $\left|\frac{\varepsilon^{RK}}{(\varepsilon^{\nu}+\varepsilon^{SGS})}\right| < 0.1\%$, to keep low numerical dissipation levels, and $\Delta t/\tau_{\eta} < 0.5$ for proper temporal resolution, where τ_{η} is the Kolmogorov time scale. The pseudo-symplectic methods 3p6q and 4p7q fall within the operative area at higher time steps. In Fig. 5 the same results are plotted by evaluating a cost function, which is defined as the number of total r.h.s. evaluations required to reach a given error level at the transition point. This second plot confirms that pseudo-

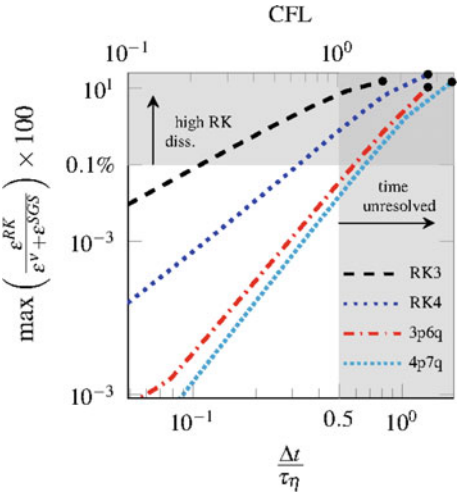

Fig. 4 Maximum normalized dissipation as a function of time step. LES of TGV test case at Re = 1600

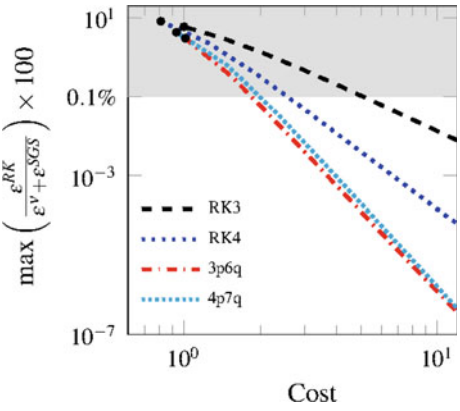

Fig. 5 Maximum normalized dissipation as a function of the number of function evaluations. LES of TGV test case at Re = 1600

symplectic schemes are more efficient than classical RK schemes, and suggest that the 3p6q scheme should be more cost effective than the more accurate 4p7q scheme.

In Fig. 6 the variation of the maximum temporal dissipation produced by the different schemes with the Reynolds number is reported. The plot shows that the relative importance of the spurious dissipation increases as the Reynolds number is increased. This is particularly true for the RK3 scheme, while RK4 and pseudo-symplectic schemes are able to keep lower level of dissipation uniformly in the range investigated.

In conclusion, temporal dissipation errors have been analyzed for standard and pseudo-symplectic Runge–Kutta methods in large-eddy simulations of the Taylor–Green vortex flow. At time steps close to the ones dictated by the linear stability constraint (but lower than the Kolmogorov time scale), standard RK methods are found to introduce significant numerical dissipation, as compared to the contributions

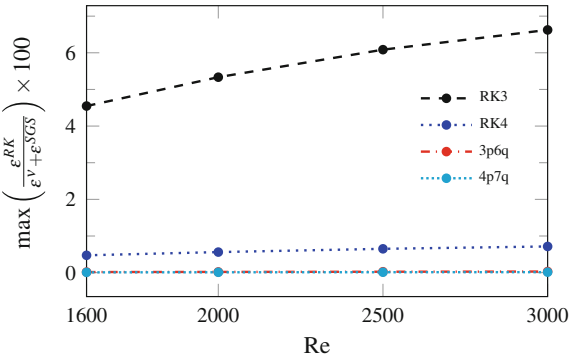

Fig. 6 Variation of maximum temporal dissipation with Reynolds number. LES of TGV test case with second-order spatial discretization on a 64^3 grid. CFL = 0.5

of the physical and modeling terms. Pseudo-symplectic schemes, and particularly the 3p6q method, are found to be more efficient than standard RK methods in providing the same error levels with a lower number of r.h.s. evaluations.

References

1. Capuano, F., Coppola, G., de Luca, L.: An efficient time advancing strategy for energy-preserving simulations. J. Comput. Phys. **295**, 209–229 (2015)
2. Capuano, F., Coppola, G., Balarac, G., de Luca, L.: Energy preserving simulations at a reduced computational cost. J. Comput. Phys. **298**, 480–494 (2015)
3. Capuano, F., Coppola, G., de Luca, L.: Low-cost energy-preserving RK schemes for turbulent simulations. In: Peinke, J., Kampers, G., Oberlack, M., Wacawczyk, M., Talamelli, A. (eds.) Progress in Turbulence VI. Springer Proceedings in Physics, vol 165, Springer, Cham (2016)
4. Capuano, F., Coppola, G., Rández, L., de Luca, L.: Explicit Runge-Kutta schemes for incompressible flow with improved energy-conservation properties. J. Comput. Phys. **328**, 86–94 (2017)
5. Choi, H., Moin, P.: Effects of the computational time step on numerical solutions of turbulent flow. J. Comput. Phys **113**, 1–4 (1993)
6. Kravchenko, A.G., Moin, P.: On the effect of numerical errors in large-eddy simulations of turbulent flows. J. Comput. Phys. **131**, 310–322 (1997)
7. Pope, S.B.: Turbulent Flows. Cambridge University Press, Cambridge (2000)
8. Verstappen, R., Wissink, J.G., Veldman, A.E.P.: Direct numerical simulation of driven cavity flows. Appl. Sci. Res. **51**, 377–381 (1993)

Evaluation of the Spectral Element Dynamic Model for LES on Unstructured, Deformed Meshes

G. Lodato and J. B. Chapelier

Discontinuous finite element methods (DFEM) such as the discontinuous Galerkin (DG) [1] or the spectral difference (SD) [7, 9, 21] methods show a strong potential for the direct numerical simulation (DNS) and large-eddy simulation (LES) of turbulent flows on realistic geometries. These methods are characterized by a rather peculiar mix of features, such as their high-orders of accuracy, the ability to handle unstructured meshes, curved boundary elements and the compactness of the stencil, which allows for optimal parallelism. The extremely low level of numerical dissipation which can be achieved when high-orders are selected, and the consequent significant increase in resolving power, make DFEM particularly well suited for LES. Nonetheless, recent studies on the SD and DG methods have highlighted the need of an explicit sub-grid scale (SGS) model in order to obtain physical results when performing LES [2, 4]. Being the order of accuracy a user-selected—potentially adaptable via p-refinement techniques—parameter, the question arises of designing SGS models which can detect and adapt to the level of numerical dissipation. The semi-local nature of DFEM, which provides a spectral representation of the solution in each of the discretization cells, offers many possibilities in terms of turbulence modeling. In particular, the modal decomposition of the signal in each cell allows to evaluate local spectra which can then be used for various modeling approaches.

Based on the above considerations, the Spectral Element Dynamic Model (hereafter referred to as SEDM) was recently developed [3]. Thanks to the adoption of a

G. Lodato (✉)
Department of Energy and Propulsion, Normandie Université,
INSA et Université de Rouen, CNRS CORIA UMR6614, Rouen, France
e-mail: guido.lodato@insa-rouen.fr

J. B. Chapelier
Department of Mechanical Engineering, Purdue University,
West Lafayette, IN, USA
e-mail: jchapeli@purdue.edu

M. V. Salvetti et al. (eds.), *Direct and Large-Eddy Simulation XI*,
ERCOFTAC Series 25, https://doi.org/10.1007/978-3-030-04915-7_6

modal *turbulence sensor*, which detects the level of local resolution of the flow, the SEDM has the ability to *dynamically* adapt the SGS viscosity according to the numerical dissipation of the scheme. The model blends ingredients from existing dynamic turbulence models and modal detection techniques, in order to provide an accurate, robust and easy-to-implement LES methodology for DFEM. The SEDM has been extensively validated over canonical test cases on structured Cartesian meshes. In view of applications to more realistic geometries, the performances of the SEDM are here assessed on selected *academic* test cases which involve the use of unstructured and deformed meshes and some level of additional physical complexity (e.g., curved boundaries, detached flows).

1 Methodology

The compressible low-pass Favre filtered Navier–Stokes equations for the evolution of the density ρ, momentum $\rho\mathbf{u}$ and total energy ρE (internal + kinetic) of an ideal gas are considered in the present study. According to the LES formalism [8, 17], these equations are augmented by a flux $\mathbf{f}_{\text{sgs}}$ which characterizes the interaction between sub-grid and resolved scales. Using the eddy-viscosity assumption, $\mathbf{f}_{\text{sgs}}$ is:

$$\mathbf{f}_{\text{sgs}} = \begin{pmatrix} \mathbf{0} \\ 2\overline{\rho}\nu_{\text{sgs}}\widetilde{\mathsf{A}} \\ \lambda_{\text{sgs}}\nabla\widetilde{\vartheta} \end{pmatrix}, \quad \text{with} \quad \lambda_{\text{sgs}} = \frac{\overline{\rho}\nu_{\text{sgs}}C_p}{Pr_{\text{sgs}}}, \tag{1}$$

where $\widetilde{\mathsf{A}}$ is the deviator of the strain rate tensor computed on the resolved velocity gradient, $\widetilde{\vartheta}$ is the filtered macro-temperature [8, 13], $Pr_{\text{sgs}} = 0.5$ is the SGS Prandtl number [5], C_p the heat capacity at constant pressure and ν_{sgs} the SGS eddy-viscosity. The relevant transport equations are discretized on hexahedral elements using the SD methodology [7, 9, 19, 21].

The eddy-viscosity in Eq. (1) is approximated using the SEDM, for which, full details can be found in [3]. One of the main features of the SEDM is its ability to *detect* under-resolution at the cell level and *adapt* the intensity of the SGS dissipation accordingly. The relevant expression of the eddy-viscosity within the jth element is

$$\nu_{\text{sgs}}^{j} = C_{\text{SEDM}}^2 f(\sigma_j, \sigma_{\text{th}}, \kappa)\Delta_j\sqrt{k_j}, \quad j = 1, \ldots, N_{\text{el}}, \tag{2}$$

where k_j is the mean turbulent kinetic energy in the element and $\Delta_j \sim \sqrt[3]{V_j}/p$ the relevant cutoff length, with V_j the element volume. A continuous spatial variation of ν_{sgs} is recovered by computing the mean values of the viscosity at the element vertices. The eddy viscosity is then made piece-wise linear within each element.

The main ingredient of the SEDM is its turbulence sensor $f(\sigma_j, \sigma_{\text{th}}, \kappa)$, which is able to discriminate between (well-resolved) laminar and (under-resolved) turbulent regions. Starting from the fundamental assumption in LES that small scales

are expected to have a rather *universal* character, and from the hypothesis that the turbulence is spectrally self-similar in the inertial range—in which the energy spectrum verifies $E(k) \propto k^{-5/3}$ in the Fourier space, for high Reynolds number isotropic turbulence—the evaluation of the spectral energy decay (in each element) provides a powerful indication of the presence of well- or under-resolved turbulence. The one-dimensional energy spectrum in each element is obtained by computing the modes of the velocity components corresponding to the hierarchical Legendre polynomial basis. The modal energy decay rate is evaluated by assuming that the energy spectrum follows a power decay law with exponent σ_j. High values of $|\sigma_j|$ characterize a fast decay of energy in the cell (well-resolved regions in which the small-scale energy is low), whereas low values correspond to under-resolved regions with highly-energetic small-scales and the possible presence of high-frequency numerical oscillations. Hence, using the measured modal decay exponent σ_j, the turbulence sensor guarantees a smooth transition of ν_{sgs} between the well- and under-resolved regions of the flow, and locally triggers the SGS viscosity such as to complement the numerical dissipation where necessary. In a sense, phenomena of error cancellation between the scheme and the LES model are not possible, as the SEDM is *numerical-dissipation-aware*. The retroactive loop established by the sensor between the flow and the eddy-viscosity provides the dynamic behavior of the SEDM. Thanks to this

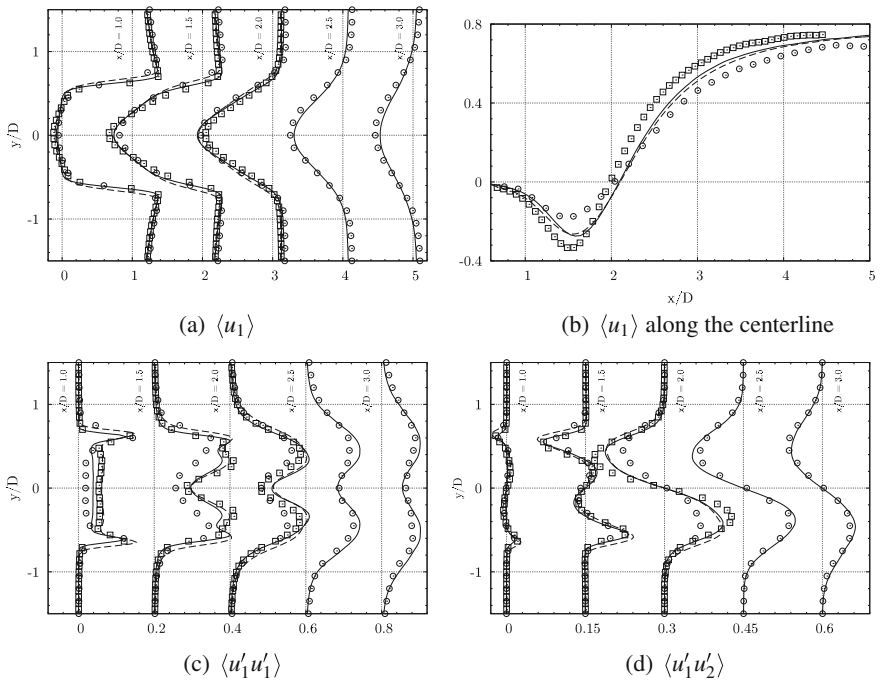

(a) $\langle u_1 \rangle$ (b) $\langle u_1 \rangle$ along the centerline

(c) $\langle u_1' u_1' \rangle$ (d) $\langle u_1' u_2' \rangle$

Fig. 1 Circular cylinder at $Re_D = 2\,580$: solid lines, present LES; dashed lines, reference LES at $Re_D = 3\,900$ [15]; circles, experiments [6]; squares, experiments at $Re_D = 3\,900$ [15]

dynamic behavior, the model parameters $C_{\text{SEDM}} = 0.23$, $\sigma_{\text{th}} = 1.6$ and $\kappa = 0.3$—which were calibrated from a priori DNS of isotropic turbulence [3]—show a rather weak problem-dependency. To further prove this particularly desirable property, the same values of these parameters are retained in the present study.

2 Results

Large-eddy simulations are performed using the SD code with the SEDM. Results are reported on three configurations for which the computational grids are fully unstructured, the relevant hexahedral elements being characterized by some level of distortion. The computations are a circular cylinder in cross-flow at Reynolds 2 580 (6th-order, 4.0×10^6 degrees of freedom, or DoF), a square cylinder in cross-flow at Reynolds 22 400 (4th-order, 2.3×10^6 DoF), and a channel with periodic constrictions at Reynolds 10 595 (5th-order, 9.0×10^6 DoF). The Mach number has been set at 0.3 for the three simulations. Details of the computational meshes can be found in [10–12].

The relevant results are reported in Figs. 1, 2 and 3, where selected (resolved) statistical quantities are plotted against experimental measurements or reference LES

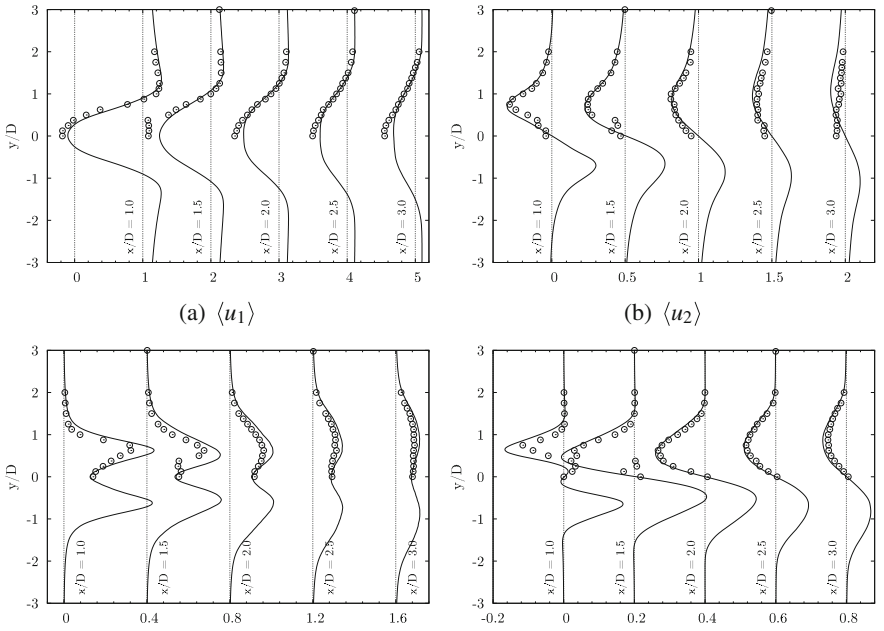

Fig. 2 Square cylinder at $Re_D = 22\,400$: lines, LES; symbols, experiments [14]

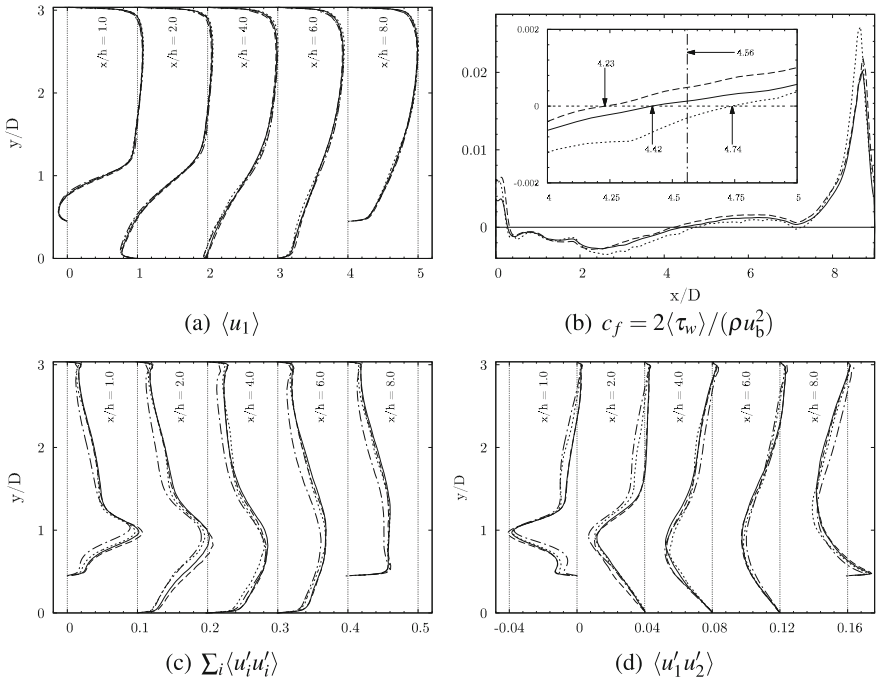

Fig. 3 Channel with periodic constrictions at $Re_h = 10\,595$: solid line, SEDM with Roe flux [16]; dashed line, SEDM with AUFS flux [18]; dotted line, WALE Similarity Model [11, 13]; dash-dotted line, DSM [20]

[6, 11, 14, 15, 20]. Mean profiles and Reynolds stresses are well captured in all the configurations. For the circular and square cylinder tests, the right shedding frequency is captured, with Strouhal numbers of 0.219 and 0.135, respectively. Regarding the circular cylinder, in particular, the recirculation length is accurately reproduced (see Fig. 1b), and the results are in better agreement with the PIV measurement and LES results in [15] for a $Re_D = 3\,900$ test case. Although no major impact is expected due to the different Reynolds number, additional tests at $Re_D = 3\,900$ are advisable. Concerning the channel with periodic constrictions, the skin friction coefficient at the lower boundary is in good agreement with the reference LES and the reattachment length—a parameter which is extremely sensitive to overall dissipation—is slightly underestimated. For this test case, different interface fluxes (with different levels of numerical diffusion) have been tested [16, 18]. Here, despite the SEDM reacts to the different amounts of numerical diffusion by producing different levels of SGS viscosity (not shown), first- and second-order statistics collapse on each other and good agreement with reference results is observed. This confirms the ability of the model to properly compensate for different levels of numerical dissipation.

3 Conclusions

In view of applications to complex geometries, the behavior and the performances of the Spectral Element Dynamic Model for LES using DFEM have been assessed in the case that unstructured hexahedral meshes are adopted. The original development and validation of the model having been done on structured Cartesian meshes, and the relevant modal resolution sensor being formalized assuming direction-splitting in computational space, the present study aimed at highlighting potential issues in the case that the physical elements' axis are non-orthogonal. Different configurations have been addressed, namely, circular and square cylinders in cross-flow and a channel with periodic constrictions, with mesh topologies spanning from body-fitted to fully unstructured element distributions.

The statistical results, in good agreement with the experimental measurements and reference computations reported in the available literature, confirm the accuracy of the proposed model without any need of a priori tuning, which also confirms the rather weak problem-dependency of the relevant parameters. The use of different orders of accuracy and different numerical fluxes in the present tests, these two aspects being intimately connected to the amount of numerical dissipation of the scheme, confirms the ability of the model to *detect* and *compensate* numerical diffusion in order to provide the right amount of SGS dissipation overall.

Acknowledgements The use of the SD solver originally developed by Antony Jameson's group at Stanford University, and joint financial support from the *Agence Nationale de la Recherche* (ANR) and *Fondation de Recherche pour l'Aéronautique et l'Espace* (FRAE) under Grant No. ANR-14-CE05-0029 are gratefully acknowledged. This work was granted access to the HPC resources of IDRIS-CNRS under the allocation i2015-2a7361. The Haute Normandie Computing center CRIANN is also acknowledged.

References

1. Cockburn, B., Karniadakis, G., Shu, C. (eds.): Discontinuous Galerkin Methods: Theory, Computation, and Applications. Lecture Notes in Computational Science and Engineering, vol. 11. Springer, Berlin (2000)
2. Chapelier, J.B., De La Llave Plata, M., Lamballais, E.: Comput. Meth. Appl. Mech. Eng. **307**, 275–299 (2016)
3. Chapelier, J.B., Lodato, G.: J. Comput. Phys. **321**, 279–302 (2016)
4. Chapelier, J.B., Lodato, G., Jameson, A.: Comput. Fluids **139**, 261–280 (2016)
5. Erlebacher, G., Hussaini, M., Speziale, C., Zang, T.: J. Fluid Mech. **238**, 155–185 (1992)
6. Konstantinidis, E., Balabani, S., Yianneskis, M.: Exp. Fluids **39**(1), 38–47 (2005)
7. Kopriva, D., Kolias, J.: J. Comput. Phys. **125**(1), 244–261 (1996)
8. Lesieur M., Métais O., Comte P.: Large-Eddy Simulations of Turbulence. Cambridge University Press, Cambridge (2005)
9. Liu, Y., Vinokur, M., Wang, Z.: J. Comput. Phys. **216**(2), 780–801 (2006)
10. Lodato G., Castonguay P., Jameson A.: AIAA P, 2012-2963: 1–12. In: 42nd AIAA Fluid Dynamics Conference and Exhibit, New Orleans, LA, 25–28 Jun 2012
11. Lodato, G., Castonguay, P., Jameson, A.: Flow Turbul. Combust. **92**(1–2), 579–606 (2014)

12. Lodato G., Rossi R.: AIAA P, 2013-3100: 1–17. In: 43rd Fluid Dynamics Conference, San Diego, CA, 24–27 Jun 2013
13. Lodato, G., Vervisch, L., Domingo, P.: Phys. Fluids **21**(3), 035102 (2009)
14. Lyn, D., Rodi, W.: J. Fluid Mech. **267**, 353–376 (1994)
15. Parnaudeau, P., Carlier, J., Heitz, D., Lamballais, E.: Phys. Fluids **20**, 085101 (2008)
16. Roe, P.: J. Comput. Phys. **43**, 357–372 (1981)
17. Sagaut, P.: Large Eddy Simulation for Incompressible Flows: An Introduction, 2nd edn. Springer, Berlin (2001)
18. Sun, M., Takayama, K.: J. Comput. Phys. **189**(1), 305–329 (2003)
19. Sun, Y., Wang, Z., Liu, Y.: Commun. Comput. Phys. **2**(2), 310–333 (2007)
20. Temmerman, L., Leschziner, M., Mellen, C., Fröhlich, J.: Int. J. Heat Fluid Fl. **24**(2), 157–180 (2003)
21. Wang, Z., Liu, Y., May, G., Jameson, A.: J. Sci. Comput. **32**(1), 45–71 (2007)

A Discontinuous Galerkin Variational Multiscale Approach to LES of Turbulent Flows

M. de la Llave Plata, E. Lamballais and V. Couaillier

1 Introduction and Numerical Method

In recent work [1] we have developed a variational multiscale simulation (VMS) approach based on a modal discontinuous Galerkin (DG) method. The separation of scales is achieved in each element via projection onto the discontinuous modal space. In [1], the DG-VMS technique was applied to the Taylor–Green vortex (TGV) flow at $Re = 3\,000$ demonstrating the potential of this approach to perform LES.

In this paper, we investigate the behaviour of the DG-VMS technique for two higher-Reynolds-number configurations, the TGV at $Re = 20\,000$ and the flow past a circular cylinder at $Re = 3\,900$ and $20\,000$, which constitutes a more complex configuration, involving real boundary conditions and flow separation. The no-model as well as the standard LES approaches are also considered and confronted to DG-VMS. For our model-based LES simulations two methods are employed: standard LES based on either the Smagorinsky model, referred to as DG-Smag, or the WALE model, denoted by DG-Wale, and the DG-VMS approach in combination with a Smagorinsky eddy viscosity to model the effect of the unresolved scales on the small-scale resolved field. The results from the DG simulations are assessed by detailed comparisons against reference data from DNS and experiment. The effect of the numerical flux function on the different terms involved in the kinetic energy (k.e.) balance equation is also studied in the case of the TGV configuration.

M. de la Llave Plata (✉) · V. Couaillier
ONERA, 92322 Châtillon, France
e-mail: marta.de_la_llave_plata@onera.fr

V. Couaillier
e-mail: vincent.couaillier@onera.fr

E. Lamballais
Institute PPRIME, Université de Poitiers, Chasseneuil-du-Poitou, France
e-mail: eric.lamballais@univ-poitiers.fr

M. V. Salvetti et al. (eds.), *Direct and Large-Eddy Simulation XI*,
ERCOFTAC Series 25, https://doi.org/10.1007/978-3-030-04915-7_7

The simulation results presented here have been performed using the compressible DG solver *Aghora* developed at ONERA [1, 2]. The DG discretization is based on a modal approach, and over-integration is performed for de-aliasing purposes. As regards the numerical flux used in the discretisation of the convective terms the Roe and local Lax–Friedrichs (LLF) fluxes are employed in this work. We also use a modified version of the LLF flux, hereafter called αLLF, in which a parameter $\alpha = 0.1$ scales its upwind component, thus allowing us to reduce the numerical dissipation introduced by the scheme. The time integration is performed using an explicit third-order accurate Runge–Kutta method.

2 Taylor–Green Vortex Problem at $Re = 20\,000$

In this section, LES simulations of the TGV at $Re = 20\,000$ and $M = 0.1$ are carried out and compared to filtered DNS data. The reference DNS data have been generated using a 6th-order FD code on a grid composed of 3458^3 nodes [3]. These data are filtered following a procedure similar to the one described in [1].

A very coarse grid composed of 28^3 hexahedral elements is used in the LES. The degree of the polynomial basis is set to $p = 8$ which leads to 9th-order accuracy in space. The number of degrees of freedom (DOFs) in the LES is thus 252^3, which corresponds to approximately $1/14^3$ of the number of DOFs of the reference DNS.

We monitor the quantities involved in the balance of the volume-averaged k.e. E. For a DNS, this energy balance is simply given by $-\frac{dE}{dt} = \varepsilon + \varepsilon_c$, in which $-\frac{dE}{dt}$ is the k.e. dissipation, $\varepsilon = 2\frac{\mu}{\rho_0 V}\int_V \mathbf{S} : \mathbf{S}\, dV$ is the viscous dissipation, and $\varepsilon_c = -\frac{1}{\rho_0 V}\int_V p\nabla \cdot \mathbf{u}\, dV$ is the dissipation due to compressibility effects. Here, $\mathbf{S}$ denotes the rate-of-strain tensor, μ the molecular viscosity, ρ_0 the volume-averaged density, and p the static pressure.

In an LES, however, the energy balance involves an additional term, ε_{sgs}, which is called the subgrid-scale (SGS) dissipation, leading to $-\frac{dE}{dt} = \varepsilon_{ls} + \varepsilon_{sgs} + \varepsilon_c$. The term ε_{ls} is computed using the full resolved LES field in the expression for ε provided above, and is now called the large-scale (LS) dissipation. As regards ε_{sgs}, there does not exist, in the general case, an explicit expression for this term, and in a posteriori computations it is simply obtained as $\varepsilon_{sgs} = -\frac{dE}{dt} - \varepsilon_{ls} - \varepsilon_c$. If the Mach number is low, ε_c is expected to be negligible. We will see however that, due to under-resolution and other numerical errors, this term can actually take on very important values.

Figure 1 compares the evolution of ε_{ls}, ε_{sgs}, and ε_c, respectively, for the three different approaches considered. The LLF flux is employed in these simulations. It is straightforward to see from Fig. 1 that the no-model DG exhibits an under-dissipative behaviour, with a peak of LS dissipation which is largely above that of the reference, and the lowest level of SGS dissipation, well below the reference. The opposite behaviour is observed for the DG-Smag simulation which presents the lowest level of LS dissipation. Overall, we see that the DG-VMS solution appears to provide the closest results to the reference with an evolution of LS dissipation almost on top of

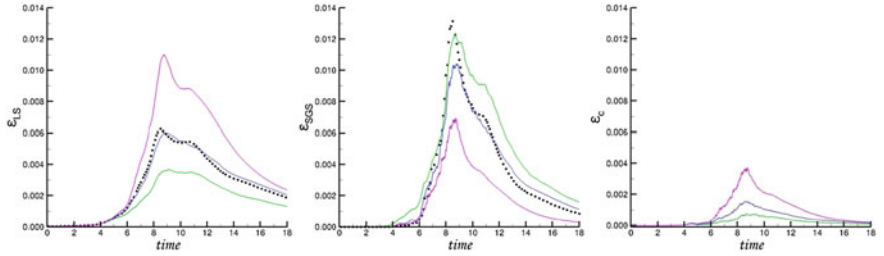

Fig. 1 From left to right, evolution of ε_{ls}, ε_{sgs}, and ε_c for TGV at $Re = 20\,000$. Filtered DNS: •, no-model DG: —, DG-VMS: —, DG-Smag: —

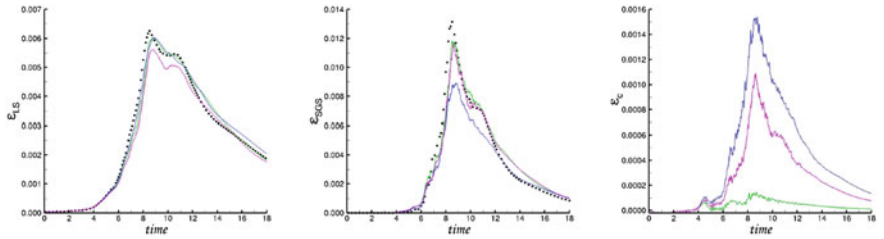

Fig. 2 From left to right, evolution of ε_{ls}, ε_{sgs}, and ε_c for DG-VMS of the TGV at $Re = 20\,000$. Filtered DNS: •, LLF flux: —, αLLF flux: —, Roe flux: —

the reference. The evolution of SGS dissipation, in between the no-model DG and the DG-Smag solutions, is however far from the reference data. If we now examine the evolution of ε_c, we notice that, contrary to what we would expect, the dissipation due to pressure dilatation is far from being negligible. The levels of ε_c tend to be reduced with the introduction of SGS viscosity, the DG-Smag simulation presenting the lowest values, while for the no-model DG ε_c is even larger than ε_{sgs} near the peak. Further investigation into the behaviour of ε_c using different discretisations (not shown here for brevity) results in the following observations: the levels of ε_c are reduced when the number of DOFs is increased, when the polynomial order p is increased (at equal number of DOFs), and when the SGS dissipation is increased. These observations suggest that, in the context of this low-Mach-number flow, a non-negligible value of ε_c is clearly linked to under-resolution, and thus somehow to the jumps in the DG solution, which lead to excessive numerical dissipation via the flux upwinding term.

In a quest to get rid of these *spurious compressibility effects* we have studied the effect of the numerical flux on the solution. Recent research [4] has actually shown the strong influence that the numerical flux employed can have on the accuracy of no-model DG simulations of the Euler equations. In Fig. 2 we therefore compare three simulations using different fluxes: the standard LLF, the αLLF (with $\alpha = 0.1$), and the Roe flux. Only the DG-VMS approach is shown in this figure. The DG-Smag approach yielded similar trends to the DG-VMS, while the no-model DG simulations

crashed when the αLLF or the Roe flux were considered. By looking at the evolution of ε_c shown in Fig. 2 we readily see that this term is linked to a numerical dissipation mainly introduced by the numerical flux at this low Mach number. Note that, for clarity, the y-axis scale in the plot of ε_c has been stretched by a factor of about 10 with respect to the other graphs. The better performance displayed by the Roe flux with respect to the LLF scheme was pointed out in [4]. In terms of agreement of the three dissipation components ε_{ls}, ε_{sgs}, and ε_c with the filtered DNS, the use of the αLLF flux is found here to provide the best results over the whole course of the simulation.

Finally, we would like to highlight the importance of examining each of the terms involved in the balance equation, rather than focusing on the analysis of an isolated quantity such as the k.e. dissipation, or even the enstrophy alone. Indeed, we have seen from this study that a successful LES simulation is one that is able to yield accurate results for ε_{ls}, ε_{sgs}, and ε_c, separately.

3 Flow Past a Circular Cylinder at $Re = 3\,900$ and $20\,000$

In this section, we consider the flow past a circular cylinder at Reynolds numbers, $Re = 3\,900$ and $20\,000$ based on the cylinder diameter D, and the freestream velocity U_c. Periodicity of the flow is assumed in the spanwise direction, and an isothermal no-slip boundary condition is imposed on the cylinder wall. The freestream Mach number is set to $M = 0.2$. A fourth-order hexahedral O-type grid composed of 20 736 elements is considered in a computational domain with radial and spanwise extension of $25D$ and πD, respectively. The mesh resolution at the wall is $\Delta r = 0.05D$. The polynomial degree is set to $p = 4$, which leads to fifth-order accuracy in space, and an effective resolution at the wall of $\Delta r/p + 1 = 0.01D$. The number of DOFs of the problem is 2.59 million (Mdofs).

For the lowest Re, three different approaches are considered: no-model DG, DG-Wale, and DG-VMS. For $Re = 20\,000$ only the DG-Smag and the DG-VMS approaches yielded stable simulations and their outcome is reported here.

Following the conclusions drawn from the previous section, the αLLF flux is used in the case of model-based LES, whereas the Roe flux is used in the no-model simulation. For the sake of comparison, Table 1 compiles, together with the present DG results, a number of simulation results from the literature for the two Reynolds numbers considered, as well as the PIV experimental results of Parnaudeau et al. [5] at $Re = 3\,900$. As regards the lower Re, we observe that overall the results from the no-model and the DG-VMS simulations are the closest to the experimental data. We know from previous studies [5] that the length of the recirculation bubble L_r is one of the most sensitive quantities, as can be seen from the significant scatter in the values reported in Table 1. We see that the no-model DG approach leads to the lowest value of $L_r/D = 1.42$, while the use of DG-Wale leads to the largest $L_r/D = 1.69$, closer to the value of Lysenko et al. [6]. Finally, the value of $L_r/D = 1.47$ from DG-VMS appears close to that of the experimental data and the values reported in

Table 1 Simulation results for the flow past a circular cylinder at $Re = 3\,900$ and $20\,000$

$Re = 3\,900$									
Simulation	Mach	Model	Mdofs	T_{vs}	C_d	Cl_{rms}	St	$\frac{L_r}{D}$	$-\frac{U_{min}}{U_c}$
Parnaudeau et al. [5]	–	(Exp. PIV)	–	–	–	–	0.208	1.51	0.34
Wornom et al. [7]	0.1	VMS-Wale	1.80	30	0.99	0.11	0.210	1.45	–
Lysenko et al. [6]	0.2	TKE	5.76	150	0.97	0.09	0.209	1.67	0.27
DG-P4 WALE	0.2	Wale	2.59	100	0.96	0.09	0.209	1.69	0.31
DG-P4 VMS4	0.2	VMS-Smag	2.59	150	0.99	0.16	0.206	1.47	0.30
DG-P4 no-model	0.2	–	2.59	150	1.00	0.15	0.209	1.42	0.30
$Re = 20\,000$									
Wornom et al. [7]	0.1	VMS-Wale	1.80	30	1.27	0.60	0.19	0.80	–
Lysenko et al. [8]	0.2	TKE	5.76	75	1.39	0.73	0.17	0.59	0.18
Lysenko et al. [8]	0.2	TKE	12.4	75	1.36	0.70	0.19	0.57	0.16
DG-P4 SMAG	0.2	Smag	2.59	40	1.09	0.30	0.21	1.05	0.29
DG-P4 VMS2	0.2	VMS-Smag.	2.59	40	1.38	0.62	0.19	0.69	0.20

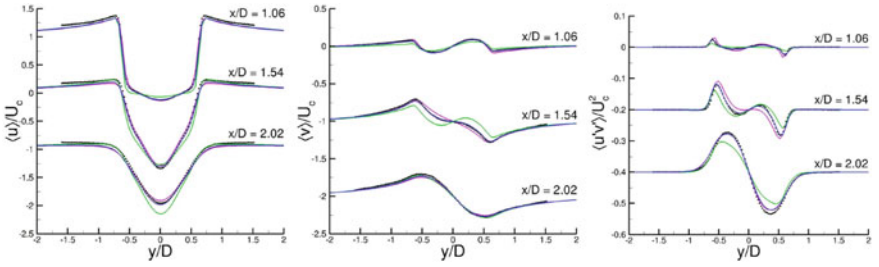

Fig. 3 Flow past a circular cylinder at $Re = 3\,900$. Wake statistics at $x/D = 1.06,\ 1.54$, and 2.02. • : PIV [5], —: no-model DG, —: DG-VMS, —: DG-Wale

[7]. Nevertheless, our values of root-mean-square of the lift coefficient $C_{l,rms}$ are higher and those of the Strouhal number S_t lower than those reported in [7], which might be interpreted as the result of a lower amount of numerical dissipation in the DG simulation. The values of the drag coefficient C_d from the DG simulations are in line with those reported in the literature.

To examine in more detail the performance of the different approaches considered we have also compared the wake statistics with the reference PIV data reported in [5]. The outcome from this comparison can be seen in Fig. 3. A quick look at these figures, and in particular at the plot of $\langle u'v' \rangle / U_c^2$, shows that the DG-Wale exhibits the most significant discrepancies with the experimental data. Despite the fact that the no-model DG simulation clearly outperforms the standard LES approach, it is the DG-VMS simulation that yields the best agreement with the experimental data. These observations are corroborated by the results at the higher $Re = 20\,000$. Indeed, despite the large scatter found in the data compiled in Table 1, it is fair to state that

overall, the DG-VMS results are in line with the reference data from the literature, whereas the DG-Smag approach leads to an over-estimation of L_r and St.

4 Conclusions

The performance of the DG-VMS approach to LES has been assessed in two high-Reynolds-number configurations by detailed comparison with reference data from DNS and experiment. The DG-VMS results have also been contrasted to those from the no-model DG and the standard LES approaches. It appears from this research that the use of the DG-VMS approach in combination with a low dissipative numerical flux leads to the best match with the reference data for the two configurations considered. We have also highlighted the lack of robustness of the no-model DG approach for under-resolved simulations when the Reynolds number is high, as well as the over dissipative character of the standard approach to LES. Finally, a methodology has been proposed for the detailed evaluation of LES simulations on the TGV configuration in the context of very coarse discretisations.

Acknowledgements This research is partly funded by the European H2020 TILDA project. This work was performed using HPC resources from GENCI (Grants 2016-c20162a7622 and 2017-A0022A10129). We thank F. Naddei for his help with generating the cylinder meshes.

References

1. Chapelier, J.B., de la Llave Plata, M., Lamballais, E.: Development of a multiscale LES model in the context of a modal DG method. Comput. Method Appl. Mech. Eng. **307**, 275–299 (2016)
2. de la Llave Plata M., Couaillier V., le Pape M.C.: On the use of a high-order DG method for DNS and LES of wall-bounded turbulence. Comput. Fluids (2017). https://doi.org/10.1016/j.compfluid.2017.05.013
3. Dairay, T., Lamballais, E., Laizet, S., Vassilicos, J.C.: Numerical dissipation vs. subgrid-scale modelling for LES. J. Comput. Phys. **337**, 252–274 (2017)
4. Moura, R.C., Mengaldo, G., Peiró, J., Sherwin, S.J.: On the eddy-resolving capability of high-order DG approaches to implicit LES/under-resolved DNS of Euler turbulence. J. Comput. Phys. **330**, 615–623 (2017)
5. Parnaudeau, P., Carlier, J., Heitz, D., Lamballais, E.: Experimental and numerical studies of the flow over a circular cylinder at Reynolds number 3900. Phys. Fluids **20**(8), 085101 (2008)
6. Lysenko, D.A., Ertesvåg, I.S., Rian, K.E.: LES of the flow over a circular cylinder at Reynolds number 3900 using the OpenFOAM toolbox. Flow Turbul. Combust. **89**(4), 491–518 (2012)
7. Wornom, S., Ouvrard, H., Salvetti, M.V., et al.: Variational multiscale LES of the flow past a circular cylinder: Reynolds number effects. Comput. Fluids **47**(1), 44–50 (2011)
8. Lysenko, D.A., Ertesvåg, I.S., Rian, K.E.: LES of the flow over a circular cylinder at Reynolds number 2×10^4. Flow Turbul. Combust. **92**(3), 673–698 (2014)

Implicit LES Approaches via Discontinuous Galerkin Methods at Very Large Reynolds

R. C. Moura, J. Peiró and S. J. Sherwin

1 Introduction

We consider the suitability of implicit large-eddy simulation (iLES) approaches via discontinuous Galerkin (DG) schemes. These are model-free eddy-resolving approaches which solve the governing equations in unfiltered form and rely on numerical stabilization techniques to account for the missing scales. In DG, upwind dissipation from the Riemann solver provides the baseline mechanism for regularization. DG-based iLES approaches are currently under rapid dissemination due to their success in predicting complex transitional and turbulent flows at moderate Reynolds numbers [1–4]. However, at higher Reynolds number, accuracy and stability issues can arise due to the highly under-resolved character of the computations and the suppression of stabilizing viscous effects.

As iLES approaches rely on numerical stabilization techniques in lieu of subgrid-scale models, the assessment of built-in dissipation is of key importance in understanding why and how to use these methods at high Reynolds numbers. In spite of that, fundamental studies along those lines have only appeared recently [5–8] and still need wider dissemination. These are discussed in the present work along with new results, covering the effects of polynomial order, Riemann solver and dealiasing techniques on resolution power, solution quality and robustness in the limit of vanishing viscosity.

R. C. Moura (✉) · J. Peiró · S. J. Sherwin
Imperial College, London, UK
e-mail: r.moura@imperial.ac.uk

J. Peiró
e-mail: j.peiro@imperial.ac.uk

S. J. Sherwin
e-mail: s.sherwin@imperial.ac.uk

M. V. Salvetti et al. (eds.), *Direct and Large-Eddy Simulation XI*,
ERCOFTAC Series 25, https://doi.org/10.1007/978-3-030-04915-7_8

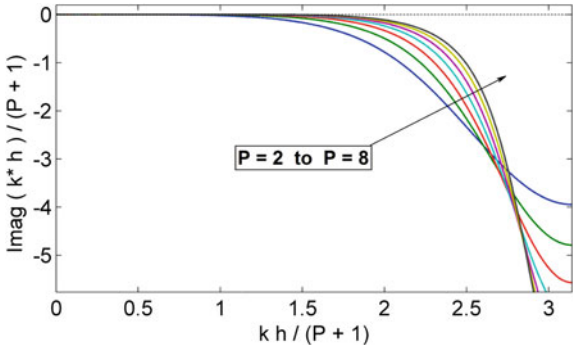

Fig. 1 DG's dissipation for linear advection (with standard upwinding) versus normalised wavenumber $kh/(p+1)$, with h being the mesh spacing and p the polynomial order

2 Rationale and Resolution Power

Dispersion-diffusion analysis has revealed that DG's dissipation in wavenumber space becomes sharper as the scheme's polynomial order p is increased, as shown in Fig. 1, which is based on 1D linear advection with standard upwinding [6]. In the same work, Burgers turbulence simulations confirmed these dissipation characteristics in a nonlinear setting and motivated a measure of spectral resolution power based on the extent of the wavenumber region where dissipation is negligible (less than 1% of wave damping per DOF crossed). This became a criterion named 'the 1% rule' whereby one estimates the wavenumber $k_{1\%}$ beyond which dissipation becomes significant, given the DOF length h/m, where h is the mesh spacing and $m = p + 1$ is the number of polynomial modes per element, cf. Fig. 1. This criterion indicated the wavenumber where a numerically-induced dissipation range begins to take place in the energy spectrum of (Burgers turbulence) simulations.

The 1% rule was subsequently adapted for 3D energy spectra in the context of Euler turbulence [7], which mimics Navier-Stokes turbulence at high Reynolds number. As the behaviour in Fig. 1 holds for inviscid turbulence, it seems legitimate to compare DG-iLES to a direct numerical approach where hyperviscosity is used to truncate the energy spectrum. If this truncation is placed well within the inertial range, one can expect the large scales to be faithfully represented. This is currently perhaps the main rationale for DG-based iLES.

As can be anticipated from Fig. 1, higher order discretisations provide superior resolution power (larger $k_{1\%}$) per DOF employed. This has been in fact confirmed in simulations [2] and suggests one should use the largest order possible. However, as p is increased, dissipation becomes increasingly sharp (in wavenumber space) and induces a spurious accumulation of energy at the small scales [6, 7]. This is seen as an 'energy bump' in the energy spectra of solutions obtained with very high orders and will be discussed further in the next section. Therefore, use of moderately high orders is advised (e.g. sixth order).

3 Robustness and TGV Instabilities

Reference [7] considered a comprehensive set of test cases of the inviscid Taylor-Green vortex (TGV) problem, spanning different polynomial orders ($m = 4$–8) and Riemann solvers (Roe and Lax–Friedrichs in particular). Here we complement these test cases with low-order ones ($m = 2$ and 3) and discuss aspects of solution quality and robustness. The inviscid TGV can be extremely demanding in terms of numerical stability due to the formation of very thin shear layers which, if not adequately resolved, may feature spurious oscillations and cause numerical divergence. Not surprisingly, high-order test cases can easily crash if polynomial dealiasing is not employed to start with. Hence, all test cases relied on consistent/over-integration of the nonlinear terms, so as to reduce polynomial aliasing errors to a minimum. Even so, some of the test cases diverged during the transitional phase of the flow, prior to the dissipation peak.

All computations have been conducted on equispaced grids of n_{el} cubic elements. Higher-order cases, namely, $m = 6$ to 8 for Lax–Friedrichs and $m = 7$ and 8 for Roe, were prone to numerical divergence. Moreover, Roe-based cases showed superior robustness and diverged less often. As explained in detail in [7], it is believed that discretisations with sharper dissipation (in Fourier space) induce the formation of energy bumps and promote spurious oscillations at the small scales, thus favouring TGV instabilities. This energy bump consists of a spurious pile-up of small-scale energy which takes place prior to the dissipation range of turbulent spectra, cf. Fig. 2 (bottom plot). Pre-dissipative bumps are caused by the bottleneck phenomenon [9, 10] and are intensified by a sharper spectral dissipation [11, 12].

We stress that the Lax–Friedrichs flux yields a much sharper dissipation than that shown in Fig. 1 due to its over-upwind bias for the momentum equations (the convective eigenvalue being replaced by the acoustic one), see [8]. The other Riemann solvers tested matched the behaviour of either Roe or Lax-Friedrichs, see Fig. 2. The vertical dashed lines delimit the wavenumber region were numerical dissipation is expected to begin, as estimated from dispersion-diffusion analysis [7]. The lack of robustness observed at higher orders revealed that standard DG schemes, even with consistent/over-integration, might require additional stabilisation for under-resolved turbulence computations at very large Reynolds numbers.

A recently developed DG discretisation based on the skew-symmetric form of the governing equations proved capable of stabilizing inviscid TGV cases even at much higher orders [13]. This scheme is currently being analysed with regards to solution quality, but preliminary results indicate that high-order solutions have accuracy very similar to that provided by standard DG with consistent/over-integration. If this is confirmed for the TGV and other types of flows, the proposed scheme will aggregate significant advantages for DG-iLES.

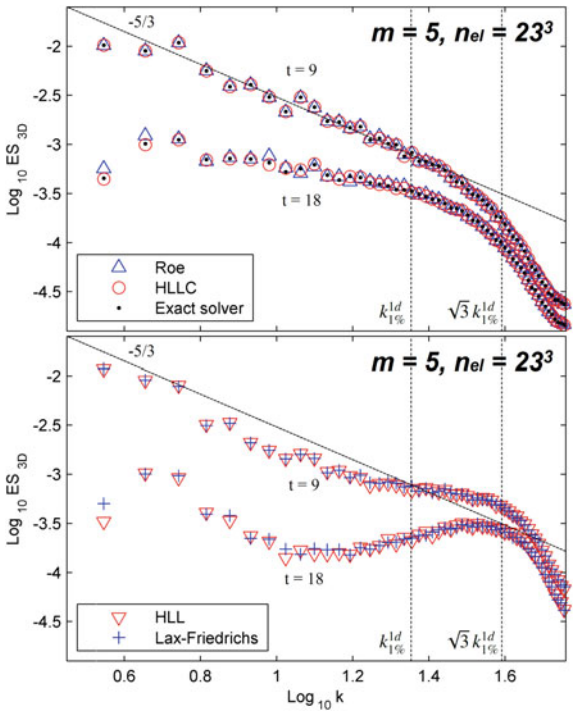

Fig. 2 Energy spectra of the inviscid TGV flow at $t = 9$ (dissipation peak) and $t = 18$ for various Riemann solvers. Results obtained for $m = 5, n_{el} = 23^3$

4 Analysis of Solution Quality

Figure 2 indicates that "complete" solvers, such as Roe's, yield better solution quality, considering their compliance to Kolmogorov's $-5/3$ slope, which is expected near the peak dissipation ($t \approx 9$). Visual inspection of flow structures via the Q-criterion, see Fig. 3, also suggests that Roe-based solutions are "cleaner" than those obtained with Lax-Friedrichs. This is not surprising, since the over-energetic scales at the energy bump are poorly-resolved and thus strongly contaminated by dispersion errors.

Further insight into flow topology can be obtained through the so-called QR diagrams [14], cf. Fig. 4. These are derived from the Q and R invariants of the velocity gradient tensor $A_{ij} = \partial u_i / \partial x_j$, where $Q = -A_{ij}A_{ji}/2$ and $R = -A_{ij}A_{jk}A_{ki}/3$, Einstein's notation being assumed. As shown in Fig. 4, QR diagrams consist of joint PDFs of the normalised values $Q/\langle S_{ij}S_{ij}\rangle$ and $R/\langle S_{ij}S_{ij}\rangle^{3/2}$. Note that averaging $\langle\cdot\rangle$ is performed over the whole domain and $S_{ij} = (A_{ij} + A_{ji})/2$.

The teardrop-like profile of Roe-based solutions at moderately high order shown in Fig. 4 (upper-right corner) agrees very well with the canonical shape expected from well-resolved turbulent flows [15]. When Lax–Friedrichs is used instead, this same case yields a more symmetrical QR profile (upper-left corner), suggesting the presence of random (dispersive) turbulent features probably caused by the energy

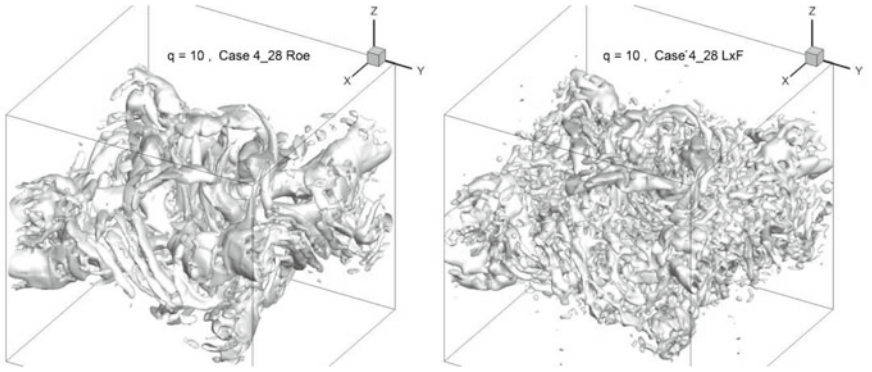

Fig. 3 Isosurfaces of the Q-criterion comparing simulations based on Roe (left) and Lax–Friedrichs (right). Results based on test case $m = 4$, $n_{el} = 28^3$ at $t = 7$

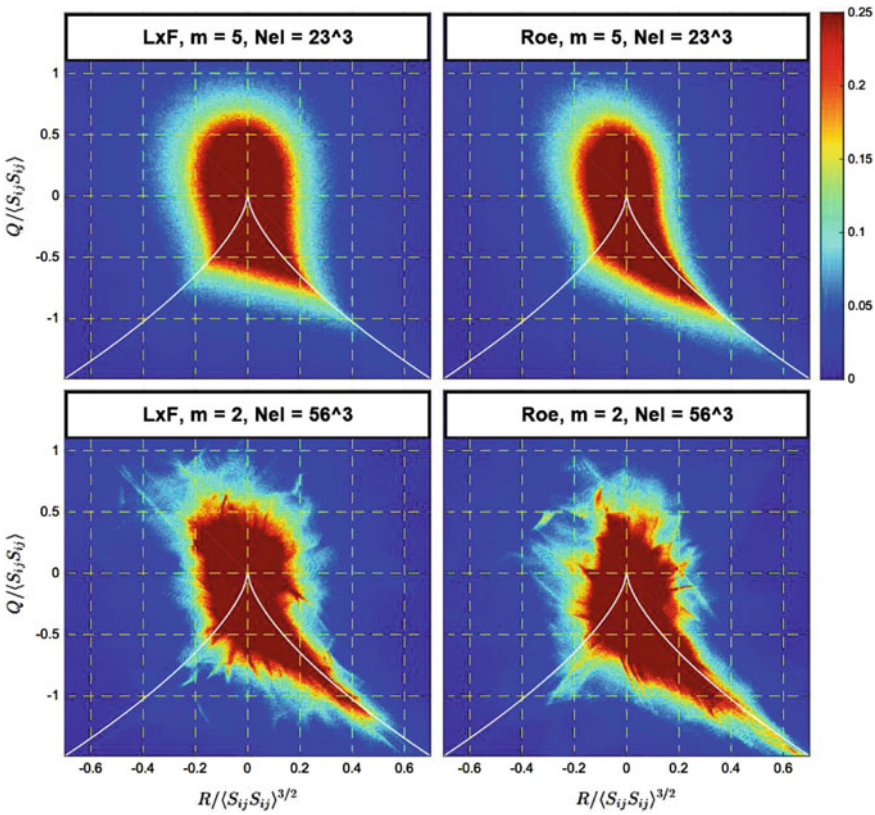

Fig. 4 QR diagrams of same-DOF solutions at $t = 9$ for Lax–Friedrichs (left) and Roe (right)

bump. Lower-order cases ($m = 2$ and 3) of the same DOFs (on finer grids) provided results of inferior quality, i.e. with smaller inertial range and noisier QR diagrams. The latter are exemplified in Fig. 4 (bottom). While these still retain the correct profile shape (overall), their quality is clearly inferior to that obtained at moderately high orders for the same number of DOFs.

5 Concluding Remarks

The results discussed support the suitability of high-order DG-based implicit LES approaches for the simulation of free turbulence at high Reynolds numbers, although conscientious usage is advised. Dealiasing techniques should be employed, use of extremely high orders is not encouraged and 'complete' Riemann solvers are to be preferred. Further analysis is needed to assess how well upwind dissipation alone is able to yield the correct behaviour for the decay phase of the TGV flow. Preliminary results (not discussed here) indicate that a certain percentage of viscous dissipation might be required to that end.

Acknowledgements RCM would like to acknowledge funding under the Brazilian Science without Borders scheme. JP and SJS acknowledge support from the Engineering and Physical Sciences Research Council (EPSRC) under grant EP/L000407/1. SJS additionally acknowledges support as Royal Academy of Engineering Research Chair under grant 10145/86.

References

1. Uranga, A., Persson, P.O., Drela, M., Peraire, J.: Implicit large eddy simulation of transition to turbulence at low Reynolds numbers using a Discontinuous Galerkin method. Int. J. Numer. Meth. Eng. **87**(1–5), 232–261 (2011)
2. Gassner, G.J., Beck, A.D.: On the accuracy of high-order discretizations for underresolved turbulence simulations. Theor. Comp. Fluid Dyn. **27**(3–4), 221–237 (2013)
3. Beck, A.D., Bolemann, T, Flad, D., Frank, H., Gassner, G.J., Hindenlang, F., Munz, C.D.: High-order discontinuous Galerkin spectral element methods for transitional and turbulent flow simulations. Int. J. Numer. Methods Fluids **76**(8), 522–548 (2014)
4. Wiart, C.C., Hillewaert, K., Bricteux, L., Winckelmans, G.: Implicit LES of free and wall-bounded turbulent flows based on the discontinuous Galerkin/symmetric interior penalty method. Int. J. Numer. Methods. Fluids **78**, 335–354 (2015)
5. Moura, R.C., Sherwin, S.J., Peiró, J.: Modified equation analysis for the discontinuous Galerkin formulation. Spectral and High Order Methods for PDEs – ICOSAHOM 2014. Springer, Cham (2015)
6. Moura, R.C., Sherwin, S.J., Peiró, J.: Linear dispersion-diffusion analysis and its application to under-resolved turbulence simulations using discontinuous Galerkin spectral/*hp* methods. J. Comput. Phys. **298**, 695–710 (2015)
7. Moura, R.C., Mengaldo, G., Peiró, J., Sherwin, S.J.: On the eddy-resolving capability of high-order discontinuous Galerkin approaches to implicit LES/under-resolved DNS of Euler turbulence. J. Comput, Phys (2016)

8. Moura, R.C., Mengaldo, G., Peiró, J., Sherwin, S.J.: An LES setting for DG-based implicit LES with insights on dissipation and robustness. Spectral and High Order Methods for PDEs – ICOSAHOM 2016. Springer, Cham (2017)
9. Falkovich, G.: Bottleneck phenomenon in developed turbulence. Phys. Fluids **6**(4), 1411 (1994)
10. Coantic, M., Lasserre, J.: On pre-dissipative 'bumps' and a Reynolds-number-dependent spectral parameterization of turbulence. Eur. J. Mech. B **18**(6), 1027–1047 (1999)
11. Lamorgese, A.G., Caughey, D.A., Pope, S.B.: Direct numerical simulation of homogeneous turbulence with hyperviscosity. Phys. Fluids **17**(1), 015106 (2005)
12. Frisch, U., Kurien, S., Pandit, R., Pauls, W., Ray, S.S., Wirth, A., Zhu, J.Z.: Hyperviscosity, Galerkin truncation, and bottlenecks in turbulence. Phys. Rev. Lett. **101**(14), 144501 (2008)
13. Gassner, G.J., Winters, A.R., Kopriva, D.A.: Split form nodal discontinuous Galerkin schemes with summation-by-parts property for the compressible Euler equations. J. Comput. Phys. **327**, 39–66 (2016)
14. Chong, M.S., Perry, A.E., Cantwell, B.J.: A general classification of three-dimensional flow fields. Phys. Fluids A **2**(5), 765–777 (1990)
15. Laizet, S., Nedić, J., Vassilicos, C.: Influence of the spatial resolution on fine-scale features in DNS of turbulence generated by a single square grid. Int. J. Comput. Fluid D. **29**(3–5), 286–302 (2015)

Implicit LES of a Turbulent Channel Flow with High-Order Discontinuous Galerkin and Finite Volume Discretization

M. Bergmann, C. Morsbach and M. Franke

1 Introduction

Owing to the permanently growing computational resources and the known predictive deficiencies of unsteady Reynolds averaged Navier–Stokes (URANS) simulations, scale-resolving methods, i.e. direct numerical simulations (DNS) and large eddy simulations (LES), become affordable methods to further study the unsteady phenomena of complex flows. To resolve all or most of the scales of turbulent flows, high grid resolutions and highly accurate spatial discretization schemes are required. In this regard, the discontinuous Galerkin (DG) finite element method has become a widely used method as it combines the flexibility of state-of-the-art finite volume methods (FVM) with an arbitrary order of accuracy and, nevertheless, local data and algorithmic structures.

Several authors have highlighted the dispersion and dissipation properties of the DG method, cf. [6, 10]. It has been shown that dissipation errors of the DG discretization only affect higher wave numbers, leaving low and medium wave numbers unaffected. In the context of scale-resolving simulations, this inherent property of the method leads to a dissipation of the smallest scales and is comparable to a sub-grid scale model. Therefore, the DG method may be well suited to the implicit LES (ILES) approach [4].

M. Bergmann (✉) · C. Morsbach · M. Franke
Institute of Propulsion Technology, German Aerospace Center (DLR),
Linder Höhe, 51147 Cologne, Germany
e-mail: Michael.Bergmann@dlr.de

C. Morsbach
e-mail: Christian.Morsbach@dlr.de

M. V. Salvetti et al. (eds.), *Direct and Large-Eddy Simulation XI*,
ERCOFTAC Series 25, https://doi.org/10.1007/978-3-030-04915-7_9

If the polynomial approximation order is increased, the range of affected wave numbers decreases and the dissipation error of the highest wave number grows. Therefore, it is desirable to choose a high polynomial order of the DG discretization. In the context of high-order polynomial approximations, the collocation discontinuous Galerkin spectral element method (DGSEM) is an efficient alternative to the standard nodal or modal DG approaches [3, 5].

In this paper, we investigate and compare the suitability of DGSEM and FVM for an ILES of a turbulent channel flow. Both investigated spatial discretization schemes are integrated into DLR's in-house solver for turbomachinery flows TRACE, which is developed at DLR's Institute of Propulsion Technology, c.f. [2].

2 Numerical Methods

2.1 Discontinuous Galerkin Spectral Element Method

The DG discretization of the compressible Navier–Stokes equations is based on the weak formulation. The solution is approximated as piecewise polynomial functions, which are not continuous across the element interfaces. As a consequence of the non-unique definition, an approximate Riemann solver is used in the surface integrals. In this work, we apply Roe's numerical flux function for the convective part and the Bassi-Rebay 2 method for the diffusive terms, cf. [1]. The integrals are computed using Gaussian quadrature formulae.

In the DGSEM, proposed by *Kopriva* [9], we apply tensor-product nodal Lagrange polynomials as basis functions with Legendre-Gauss (LG) points as interpolation nodes, which are also used as the quadrature nodes. Utilizing this collocation and the property of Lagrange polynomials, i.e. $l_i(x_j) = \delta_{ij}$, where x_j are the LG nodes, many numerical operations can be omitted and the scheme becomes highly efficient (see [3] for further details). The downside of the efficiency is the fixed precision of integration, which is only exact for polynomials of degree $p \leq 2M + 1$, where M denotes the number of Gauss points.

2.2 Finite Volume Method

We used a FVM with a 2nd order accurate mid-point approximation of the flux integrals. Roe's flux difference splitting method is applied with a constant blending factor ϕ for the upwind term. A blending factor of $\phi = 1$ leads to the standard Roe's numerical flux, as it is used for all DG simulations, and $\phi = 0$ results in a central flux. The reconstruction of the states is performed with a 3rd order accurate MUSCL scheme without limiter function, cf. [7]. The derivatives for the viscous fluxes are approximated by central differences. The time integration is performed using a 3rd

order accurate explicit Runge–Kutta method with a constant time step for both the DG and FV simulations. The maximal, stable time step was estimated through numerical experiments for each mesh resolution. The maximum CFL number, based on the acoustic eigenvalues, is typically about 1.

3 Implicit LES of a Channel Flow at $Re_\tau = 395$

Both spatial discretization schemes are investigated for the ILES of a fully developed turbulent channel flow. The flow is considered to be periodic in both the stream- (x) and spanwise (z) directions. A constant body force source term in the streamwise momentum equation is used to enforce the Reynolds number based on the friction velocity of $Re_\tau = \delta u_\tau / \nu = 395$, where δ is half of the channel height. The ILES results are compared with the incompressible reference DNS results of *Iwamoto* et al. [8]. In order to minimize the compressibility effects in our simulations, the Mach number is set to $Ma = 0.1$. Furthermore, a computational domain of $2\pi\delta \times 2\delta \times \pi\delta$ is chosen for all simulations and the same grid stretching in the normal wall direction is applied for FVM and DGSEM. Note that the usage of geometrically linear elements, i.e. no inner element stretching, in combination with the location of the LG nodes does not lead to same spacing between the degrees of freedom (DOF), see Fig. 1. Moreover, when comparing both methods, the number of DOF in the wall-normal as well as in wall-parallel directions are equal for FVM and DGSEM.

The flow is initialized with a superposition of a RANS solution and synthetic turbulence, proposed by *Shur* et al. [11], to create the turbulent velocity fluctuations. Starting from this point, a transient phase of 20 eddy turnover times ETT $= tu_\tau/\delta$ is simulated to reach a converged state, i.e. linear profile of the total shear stress, and, following that, another 20 ETT to average the flow variables. In Table 1, the effictive mesh spacings for all simulations are listed.

Figure 2 shows the average streamwise velocity profiles and the velocity fluctuations for both discretization schemes with the same order of accuracy and number of DOF. Comparing DGSEM and FVM using the Roe's numerical flux (*red* and *blue* line), both results show large differences to the DNS reference data and overestimate the mean velocity and streamwise velocity fluctuations dramatically. It seems that the naive low-order application is not sufficient for the ILES on the given mesh as

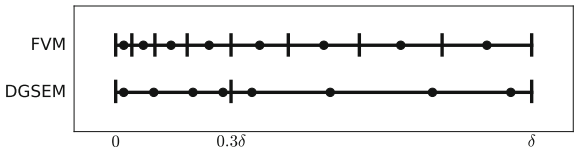

Fig. 1 One-dimensional distribution of DOF with grid stretching. The DOF are visualized as black dots and the element vertices are shown as vertical black lines. The one-dimensional FV grid with cell centered DOF is shown at the top and DGSEM with $p = 3$ and LG nodes at the bottom

Table 1 Effecitve mesh spacing for all presented simulations. The effective mesh spacing is equal to $hu_\tau/\nu(p+1)$, where p is the polynomial approximation order, which is 0 for FV simulations. h is the cell size in x and z direction for Δx^+ and Δz^+, respectively. In case of the wall normal direction Δy^+, h is the distance from the first solution point to the wall

Figures	Method	Order of accuracy	DOF			Mesh spacing		
			n_x	n_y	n_z	Δx^+	Δy^+	Δz^+
Figure 2	FV	2nd	96	64	96	25.69	0.53	12.84
Figures 2, 3	DG	2nd	96	64	96	24.86	0.47	12.43
Figure 3	DG	3rd	90	72	90	27.59	0.38	13.80
Figure 3	DG	4th	96	64	96	25.66	0.37	12.83
Figure 3	DG	5th	100	80	100	25.09	0.26	12.54
Figure 4	FV	2nd	128	96	128	19.21	0.34	9.60
Figure 4	DG	4th	128	96	128	19.41	0.23	9.91

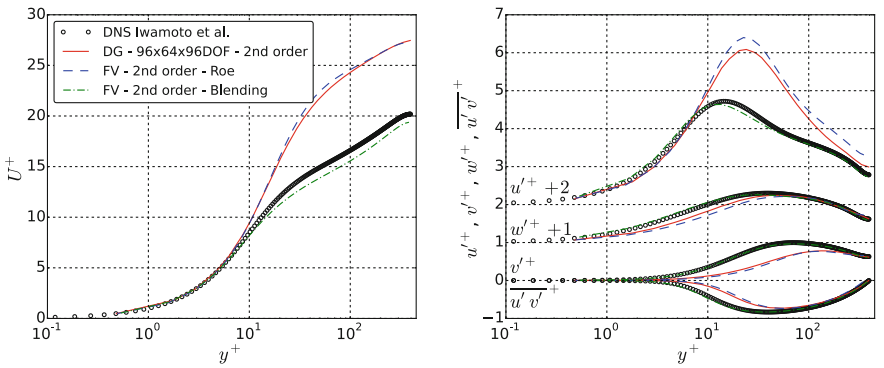

Fig. 2 ILES of a turbulent channel flow at $Re_\tau = 395$. Mean streamwise velocity profiles U^+ *(left)* and RMS turbulent velocities u'^+, v'^+, w'^+ and shear stress $\overline{u'v'}$ *(right)* of the 2nd order accurate DGSEM (*red solid*), FVM using the standard Roe flux (*blue dashed*) and FVM using a fraction of Roe's flux, i.e. $\phi = 10^{-3}$,(*green dash dotted*) on a mesh with $96 \times 68 \times 96$ DOF compared with the DNS results of *Iwamoto* et al. [8]

both schemes are too dissipative. However, it can be noted that both schemes lead to similar results when the same numerical properties are applied. In order to reduce the dissipation of the FV scheme, we decrease the impact of the Roe damping term by setting the blending factor to $\phi = 10^{-3}$ (*green* line). Thus, the mean velocity profiles as well as the velocity fluctuations are in a significantly better accordance with the reference profiles. In fact, the fluctuations in the y and z directions and the shear stress of the blended FVM match the reference solution almost perfectly.

A way to improve the dissipation properties of the DG scheme is to increase the polynomial approximation order, see Fig. 3. The number of DOF are nearly constant for all approximation orders. Using the 3rd order accurate DGSEM improves the results significantly in comparison to the 2nd order scheme. Still similar trends are

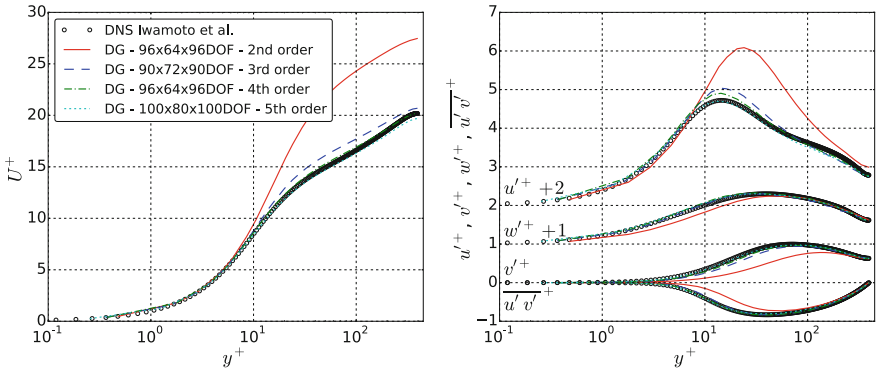

Fig. 3 ILES of a turbulent channel flow at $Re_\tau = 395$. Mean streamwise velocity profiles U^+ *(left)* and RMS turbulent velocities u'^+, v'^+, w'^+ and shear stress $\overline{u'v'}$ *(right)* with DGSEM and various polynomial approximation orders compared to the DNS results of *Iwamoto* et al. [8]

present, including an over-prediction of the streamwise mean velocity and velocity fluctuations. When we further increase the approximation order, the average velocity profile matches the DNS results nearly perfectly. The largest deviations are noticeable in the streamwise velocity fluctuations with an overestimation in the buffer layer and no visible curvature in the log layer ($y^+ \approx 105$). When applying a 5th order accurate scheme, the peak of streamwise RMS velocity is in a perfect agreement with the DNS. On the other hand, the mean velocity profile of the 4th order accurate DGSEM is closer to the DNS results than the 5th order. It seems that the slight overestimation of the streamwise velocity fluctuations leads to a shift of the mean velocity and, therefore, to a better match of the average velocity profiles.

In Fig. 4, the results of the 2nd order accurate FVM with a blending factor of $\phi = 10^{-3}$ and the 4th order accurate DGSEM on a finer mesh with $128 \times 96 \times 128$ DOF are shown. It can be observed that the higher-order DGSEM results are overall closer to DNS reference profiles than the FVM results. Especially, the peak of RMS streamwise turbulent velocity and the mean velocity around $y^+ \approx 120$ are underestimated by the FV scheme, whereas the DGSEM profiles are in nearly perfect agreement with the reference data. The only deviations are visible in the log layer ($y^+ \approx 105$) of the streamwise velocity fluctuations profiles, which is on the other hand well captured by the FV scheme. Although the cost per timestep of the 4th order DG scheme was lower than the 2nd order FV scheme with the same number of DOF, the overall runtime was about 1.3 times greater, which can be attributed to a stricter time step limit.

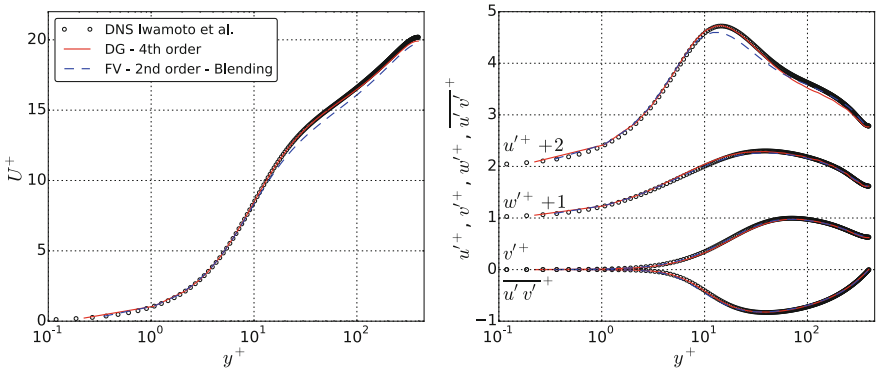

Fig. 4 ILES of a turbulent channel flow at $Re_\tau = 395$. Mean streamwise velocity profiles U^+ *(left)* and RMS turbulent velocities u'^+, v'^+, w'^+ and shear stress $\overline{u'v'}$ *(right)* of the 2nd order accurate FVM using a fraction of Roe's numerical flux and the 4th order accurate DGSEM on a mesh with $128 \times 96 \times 128$ DOF compared with DNS of *Iwamoto* et al. [8]

4 Conclusions

In this work, we have investigated the implicit LES of a fully developed turbulent channel flow using low-order FVM and higher-order DGSEM, which are both integrated into the CFD solver TRACE. We have demonstrated that the results of both schemes are very similar when applying the same numerical properties, i.e. same accuracy order, same numerical flux and same DOF. Increasing the polynomial approximation order of DGSEM and using only a fraction of Roe's numerical flux in the context of the FVM can significantly improve the results on a coarse mesh in comparison to a lower-order naive approach. Overall, a 4th order DGSEM shows advantages over a 2nd order FVM on the same grid. In the future, we plan to extend our studies to higher Reynolds number flows and further investigate the potential of over-integration and entropy-stable formulations in the context of the DGSEM.

References

1. Bassi, F., Rebay, S.: A high order discontinuous Galerkin method for compressible turbulent flows. In: Cockburn, B.R., Karniadakis, G.E., Shu, C.W. (eds.) Discontinuous Galerkin Methods: Theory. Computation and Applications, p. 7788. Springer, Berlin (2000)
2. Becker, K., Heitkamp, K., Kügeler, E.: Recent progress in a hybrid-grid CFD solver for turbomachinery flows. In: Proceedings 5th ECCOMAS (2010)
3. Bergmann, M., et al.: A comparison of various nodal discontinuous Galerkin methods for the 3d Euler equations. In: Proceedings 8th ECCOMAS, pp. 7956–7966 (2016)
4. Carton de Wiart, C. et al.: Implicit LES of free and wall-bounded turbulent flows based on the discontinuous Galerkin/symmetric interior penalty method. Int. J. Num. Meth. Fluids **78**, 335–354 (2015)

5. Gassner, G., Kopriva, D.A.: On the quadrature and weak form choices in collocation type discontinuous Galerkin spectral element methods. J. Sci. Comput. **44**, 136–155 (2010)
6. Gassner, G., Kopriva, D.A.: A comparison of the Dispersion and Dissipation errors of Gauss and Gauss-Lobatto discontinuous Galerkin spectral element methods. SIAM J. Sci. Comput. **33**, 2560–2579 (2011)
7. Hirsch, C.: Numerical Computation of Internal and External Flows: Computational Methods for Inviscid and Viscous Flows. Wiley, New York (1990)
8. Iwamoto, K., Suzuki, Y., Kasagi, N.: Database of fully developed channel flow. THTLAB Internal Report No ILR-0201
9. Kopriva, D.A.: Implementing Spectral Methods for Partial Differential Equations. Springer Publishing Company, New York (2009)
10. Moura, R.C., et al.: On the eddy-resolving capability of high-order discontinuous Galerkin approaches to implicit LES/under-resolved DNS of Euler turbulence. J. Comput. Phys. **330**, 615–623 (2017)
11. Shur, M.L., et al.: Synthetic turbulence generators for RANS-LES interfaces in zonal simulations of aerodynamic and aeroacoustic problems. Flow Turbul. Combust. **93**, 63–92 (2014)

An Implicit Discontinuous Galerkin Method with Reduced Memory Footprint for the Simulation of Turbulent Flows

A. Crivellini, M. Franciolini and A. Nigro

1 Introduction

In recent years the increasing availability of High Performance Computing (HPC) resources strongly promoted Large Eddy Simulation (LES) as a viable approach to the simulation of those moderate Reynolds flow conditions where Reynolds-averaged Navier–Stokes (RANS) formulation fails, e.g. massively separated flows. In particular, the practice of an implicit LES (ILES) based on the Discontinuous Galerkin (DG) method showed to be very promising due to the favourable dispersion and dissipation properties [1]. The high potential of DG approximations for the under-resolved simulation of turbulent flows has already been demonstrated in literature and research on this topic is growing fast [2, 6]. However, how to integrate in the most efficient way the semidiscrete set of NS equations exploiting at best such large computational facilities is an active research topic. A growing interest in using high-order implicit time integration schemes has born mainly to overcome the strict stability limits of explicit methods which significantly decrease for high order of polynomial approximation. Nevertheless, implicit schemes require to solve large non-linear/linear systems of equations, which may become prohibitive for massively computations due to the high memory demand. The present paper attempts to overcome such limitations by introducing a memory saving and computationally efficient strategy to solve the system of equations in the context of high-order DG discretizations. The numerical framework relies on Runge–Kutta schemes of the Rosenbrock type, which require

A. Crivellini (✉) · M. Franciolini
Universita' Politecnica delle Marche, Via Brecce Bianche 12, Ancona, Italy
e-mail: a.crivellini@univpm.it

M. Franciolini
e-mail: m.franciolini@pm.univpm.it

A. Nigro
Libera Universita' di Bolzano, Piazza Universita' 5, Bolzano, Italy
e-mail: alessandra.nigro@unibz.it

M. V. Salvetti et al. (eds.), *Direct and Large-Eddy Simulation XI*,
ERCOFTAC Series 25, https://doi.org/10.1007/978-3-030-04915-7_10

the solution of linear systems within each stage. We propose here a matrix-free implementation of the generalized minimal residual method (GMRES) linear solver. Such implementation enjoys more flexibility than standard matrix-based methods since the Jacobian is employed only to build the preconditioner operator, which can also be assembled using an approximation of the iteration matrix. While for non-stiff problems the use of a cheap and memory saving element-wise block Jacobi (EWBJ) can be an effective choice, the efficiency of such operator is typically insufficient for stiff systems (e.g. stretched elements, low Mach flows or large time step). The present work overcomes such limitation by combining EWBJ preconditioners with multigrid operators. The effectiveness of the solution strategy is here assessed on two test cases: the first one is the two-dimensional laminar incompressible flow over a cylinder at $Re = 200$, while the second involves the solution of the transitional incompressible turbulent flow on the T3L configuration at $Re = 3450$ using different levels of free-stream turbulence. Preliminary results show that the proposed strategy reduces the memory footprint and the computational time.

2 Matrix-Free Implicit Time Integration

The Incompressible Navier–Stokes equations are discretized as in [3]. The artificial compressibility flux approach is employed for the convective numerical fluxes, and the BR2 scheme is used for the diffusive terms. The time integration of the semidiscrete system of equations, performed by means of linearly implicit four-stage, order-three ROSI2PW scheme [5] can be compactly written as

$$\mathbf{U}^{n+1} = \mathbf{U}^n + \sum_{j=1}^{s} m_j \Delta \mathbf{U}_j, \tag{1}$$

$$\left(\frac{\widetilde{\mathbf{M}}}{\gamma \Delta t} + \mathbf{J} \right) \Delta \mathbf{U}_i = -\mathbf{R} \left(\mathbf{U}^n + \sum_{j=1}^{i-1} a_{ij} \Delta \mathbf{U}_j \right) - \frac{\widetilde{\mathbf{M}}}{\Delta t} \sum_{j=1}^{i-1} c_{ij} \Delta \mathbf{U}_j, \tag{2}$$

with $i = 1, \ldots, s$, where s is the number of stages and $\gamma, m_j, a_{ij}, c_{ij}$ are the coefficients of the scheme. Here, $\mathbf{U} = [p \; u_i]^T$ is the vector of degrees of freedom, $\mathbf{R}$ is the residuals vector, $\mathbf{J} = \partial \mathbf{R}(\mathbf{U}^n)/\partial \mathbf{U}$ is the Jacobian matrix and $\widetilde{\mathbf{M}}$ is a modified mass matrix equal to the identity matrix due to the choice of orthonormal basis functions apart from the entries corresponding to the pressure DoFs, which are zero. The matrix-vector product required by the GMRES algorithm is approximated, in a matrix-free fashion, by a double evaluation of the residuals vector

$$\mathbf{A} \Delta \mathbf{U}_i = \left(\frac{\widetilde{\mathbf{M}}}{\gamma \Delta t} + \mathbf{J} \right) \Delta \mathbf{U}_i \simeq \frac{\widetilde{\mathbf{M}}}{\gamma \Delta t} \Delta \mathbf{U}_i + \left(\frac{\mathbf{R}(\mathbf{U}^n + h \Delta \mathbf{U}_i) - \mathbf{R}(\mathbf{U}^n)}{h} \right); \tag{3}$$

which avoids the storage of the Jacobian to compute the time step.

3 GMRES Preconditioners

For practical applications the linear system should be always preconditioned. Standard approaches, such as the ILU(0) in serial computations or the block-Joacobi (BJ) and the Additive Schwartz method (AS) in parallel, use the iteration matrix $\mathbf{A}$ to compute the preconditioner. Those approaches still need the evaluation and the storage of one matrix, even in the matrix-free framework, which is CPU and memory consuming. In fact, $\mathbf{A}$ is a block structured matrix, whose computational effort for its evaluation scales as $N_e(N_f+1)(d+1)^2k^{3d}$, and the memory footprint scales as $N_e(N_f+1)(d+1)^2k^{2d}$, where N_e is the number of mesh elements, N_f the number of element faces, d is the space dimension and k is the polynomial approximation.

A valuable alternative, able to significantly reduce these computational requests, employs an element-wise block-Jacobi (EWBJ) preconditioner obtained neglecting the off-diagonal blocks of the Jacobian. Despite the EWBJ is a less effective preconditioner, which means that the number of GMRES iterations required to converge increases, the overall computational efficiency can raise for non-stiff problems since, in a matrix-free framework, only the diagonal portion of the full Jacobian matrix is computed. Moreover, the off-diagonal blocks in each row of $\mathbf{J}$, equal to the number of faces of one element, are not stored, and therefore the EWBJ preconditioner requires less memory. For example, using hexahedral elements, its memory footprint is only $1/7$ of those employed by a standard ILU(0) approach. In other words coupling the matrix-free and the EWBJ approaches it is possible to save about 93% of the memory used by the ILU(0)-MB algorithm to store the iteration matrix and its preconditioner operator [3].

For highly stretched space discretizations this approach becomes ineffective since the number of linear iterations raises excessively. To solve this issue we propose a new class of memory saving preconditioning operators. The idea is to couple a p-Multigrid (pMG) preconditioner, which in the DG context is known to be quite efficient, to a flexible GMRES (FGMRES) matrix-free solution algorithm. In our implementation all the smoothers consist of preconditioned solutions on coarse levels, obtained using the restriction of $\mathbf{A}$, namely $\mathbf{A}_i$, to a lower order polynomial approximation, i. Note that, in a modal DG framework, all the restriction and prolongation operators can be performed easily by manipulating directly the DoFs. According to the above mentioned scaling, the size of $\mathbf{A}_i$ can be quite small for $i \ll k$. For instance, within a three-dimensional case, when $k = 6$ and $i = 1$ $\mathbf{A}_i$ is 440 times smaller with respect to the original $\mathbf{A}$ matrix, while with $i = 2$ is about 70 times smaller. In addition, if the EWBJ algorithm is adopted as fine level smoother, it is possible to obtain a still effective and memory saving solution strategy using few multigrid levels with low order smoothers, even with very high order polynomials.

Table 1 Laminar flow over a two-dimensional circular cylinder at $Re = 200$. Results obtained in serial computations on an AMD Opteron CPU

	ILU(0)-MB	ILU(0)-MF	EWBJ-MF	pMG-MF
CPU ratio	1	2.8	12	1.9
Memory ratio	1	0.65	0.97	0.24
GMRES	120	110	543	6.2

4 Results

The new solution strategies have been tested by solving two problems. In both the cases we used a 6th order polynomial approximation of the solution and three multigrid levels, built on 1st and 2nd order coarse smoothers. The first test case is a two-dimensional laminar flow over a cylinder at $Re = 200$. The computational domain, characterized by 4710 curved and anisotropic mesh elements with a severe refinement on the wake region, resulted in a very stiff space discretization. Moreover, the time-step used is equal to 1/20 of the shedding period, which further increases the ill-conditioning of the linear system. Table 1 reports the computational performance, in terms of relative CPU-Time, allocated memory for the linear solver, and average number of GMRES iterations per stage, for different solution strategies and preconditioners in serial computations. Note that the CPU-Time and the memory saving are related to the corresponding ILU(0)-MB approach. It can be seen that in such two-dimensional test case the matrix-free solver penalizes the CPU-Time by a factor of 2.8 with respect to the corresponding matrix-based case. This quite large value is due to the fact that a single residual computation is more expensive than performing a matrix-vector product, particularly for a grid consisting of curved elements (second-order piecewise polynomial representation of the faces) as in the current case. Nevertheless, it should be noted that the procedure saves the 35% of memory. While the pure EWBJ preconditioner is not enough efficient for such stiff problem (a huge increase in CPU-Time and GMRES iterations can be noted, as well as a similar memory to the ILU(0)-MB due to the very high number of Krylov subspaces allocated), the situation changes if it is employed within a pMG context. Here the EWBJ-MF is employed only on the finest level smoother. The results show that, while reducing the 76% of memory footprint, this procedure improves also the efficiency from the CPU-Time point of view respect to the ILU(0)-MF strategy, and reduces considerably the number of GMRES iterations.

The second test case is an ILES of the transitional flow on a flat plate with semi-circular leading edge. This test case, named T3L, is part of the ERCOFTAC test case suite and it is characterized by a diameter-based Reynolds number $Re = 3450$. The solution exhibits a leading edge laminar separation bubble and, downstream the transition, an attached turbulent boundary layer. The simulations were performed in parallel using 540 cores and a grid consisting of 38320 elements clustered at the wall and near the reattachment region. Table 2 reports the computational performances

Table 2 Transitional flow over a rounded leading edge flat plate at $Re = 3450$. Results obtained on 540 Intel Xeon CPUs

	BJ-MB	BJ-MF	EWBJ-MF	pMG-MF	pMG-MF L3
CPU ratio	1	0.95	1.01	0.47	0.31
Memory ratio	1	0.6	0.28	0.15	0.15
GMRES	115	115	229	3	3

obtained similarly to that of the previous test case. Here the reference is the BJ-MB, which employs the ILU(0) preconditioner within each domain partition. In this case we used the integration formulas for straight faces, being the number of curved elements small (second order representation) and located only close to the leading edge, where the boundary layer is still laminar. Thus, switching from the matrix-based to the matrix-free solver using the BJ preconditioner, we observed that the computational efficiency is more or less the same. Also in this case, the EWBJ preconditioner is poorly performing from the CPU-Time point of view, although reduces the memory requirements of about the 72%. Differently, when it is employed as fine level smoother on a multigrid preconditioner, the code saves the 85% of memory and requires the 0.47 of the baseline computational time. Note that, in addition, a very small number of Krylov subspaces are required for the iterative process. Note that the pMG is used only for preconditioning purposes, and therefore it is possible to freeze it for some time steps (three in this case) to further reduce the CPU time to the 0.31 of the reference, see Table 2.

From a physical point of view, we solved the T3L problem with different free-stream turbulence (Tu) intensities. The Tu was synthetically injected in the flow field through a properly defined random forcing, in consistency to what has been done in [4]. The bubble length, which has been evaluated on the time and spanwise averaged flow fields, was found to be very sensitive to the turbulence levels. In particular, increasing the Tu from 0 to 0.2 and 5.6% the bubble length reduces from $x/d = 3.9$ to 2.69 and 1.08, respectively (see Fig. 1). We point out that, in the $Tu = 0.2\%$ case, the value $x/d = 2.69$ is in a better agreement to the experimental data, equal to $x/d = 2.75$, if compared to other literature values. The Fig. 2 reports a visualization of the obtained instantaneous flow-fields. For the low turbulence intensity case it is possible to identify the quasi two-dimensional Kelvin–Helmholtz instabilities taking place in the shear-layer above the separation bubble and the appearance of hairpin vortices after the flow reattachment. With the highest turbulence level, streaky like structures stream-wise oriented are visible close to the leading edge, while the Kelvin–Helmholtz instability stage is bypassed anticipating the reattachment and the formation of the hairpin vortices.

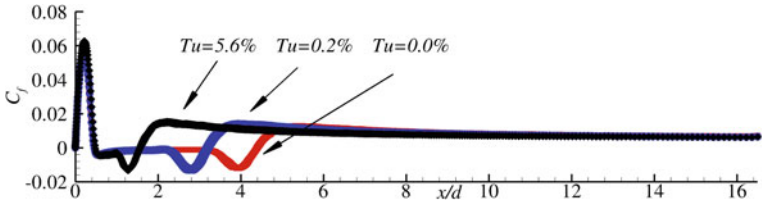

Fig. 1 Skin friction coefficient for the solution obtained using different free stream turbulence intensities

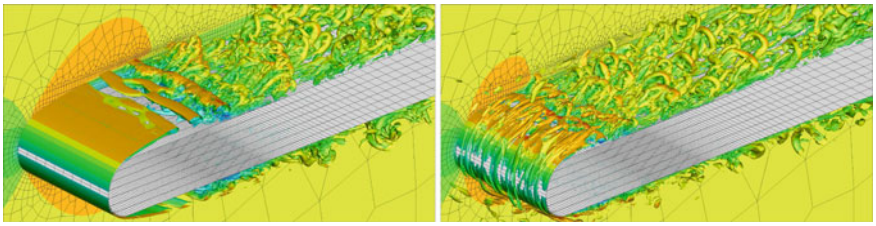

Fig. 2 $\lambda_2 = -1.5$ iso-contour, for two different Turbulence Intensities (Tu) – 0.2% (left) and 5.0% (right) – coloured by the streamwise velocity magnitude

5 Conclusions

An implicit in time DG solver with a low memory requirement has been here proposed. The approach relies on the use of a matrix-free FGMRES solver coupled with a pMG preconditioner. The computational efficiency, as well as the solution quality for a quite complex test case demonstrate that the approach is very well suited for the DNS/ILES using unstructured highly stretched meshes.

References

1. Bassi, F., Botti, L., Colombo, A., Crivellini, A., Ghidoni, A., Massa, F.: On the development of an implicit high-order Discontinuous Galerkin method for DNS and implicit LES of turbulent flows. Eur. J. Mech. B-Fluid Part 2 **55**, 367–379 (2016)
2. Chapelier, J.-B., de la Llave Plata, M., Renac, F., Lamballais, E.: Evaluation of a high-order discontinuous Galerkin method for the DNS of turbulent flows. Comput. Fluids **95**, 210–226 (2014)
3. Franciolini, M., Crivellini, A., Nigro, A.: On the efficiency of a matrix-free linearly implicit time integration strategy for high-order Discontinuous Galerkin solutions of incompressible turbulent flows. Comput. Fluids **159**, 276–294 (2017)
4. Langari, M., Yang, Z.: Numerical study of the primary instability in a separated boundary layer transition under elevated free-stream turbulence. Phys. Fluids **25**, 74–106 (2013)
5. Rang, J., Angermann, L.: New Rosenbrock methods of order 3 for PDAEs of index 2. In: Proceedings of Equadiff-11 2005, pp. 385–394 (2007)
6. de Wiart, C.C., Hillewaert, K., Bricteux, L., Winckelmans, G.: Implicit LES of free and wall-bounded turbulent flows based on the discontinuous Galerkin/symmetric interior penalty method. Int. J. Numer. Methods Fluids **78**, 335–354 (2015)

On the Development of an Implicit High-Order Discontinuous Galerkin Solver for a Hybrid RANS-LES Model

F. Bassi, L. Botti, A. Colombo, A. Ghidoni, F. Massa and G. Noventa

1 Introduction

Recent years have seen an ever-increasing interest in turbulence models able to go beyond the limited predictive capability of the Reynolds-averaged Navier–Stokes (RANS) formulation. In the range of moderate Reynolds numbers, availability of large HPC resources now allows to employ Large Eddy Simulation (LES) also in complex flow applications. In this context, the practice of an implicit LES (ILES) based on the Discontinuous Galerkin (DG) method showed to be very promising due to the good dispersion and dissipation properties of DG methods. However, to date, characteristic Reynolds numbers of many industrial applications are too large for a fully resolved LES. For these applications the use of a hybrid RANS-LES model or a wall modelled LES approach seems mandatory. In hybrid RANS-LES models the RANS equations are active close to solid walls, where LES would be

F. Bassi · L. Botti · A. Colombo (✉) · F. Massa
Dipartimento di Ingegneria e Scienze Applicate, Università degli Studi di Bergamo, Dalmine, (BG), Italy
e-mail: alessandro.colombo@unibg.it

F. Bassi
e-mail: francesco.bassi@unibg.it

L. Botti
e-mail: lorenzo.botti@unibg.it

F. Massa
e-mail: francescocarlo.massa@unibg.it

A. Ghidoni · G. Noventa
Dipartimento di Ingegneria Meccanica e Industriale, Università degli Studi di Brescia, Brescia, Italy
e-mail: antonio.ghidoni@unibs.it

G. Noventa
e-mail: gianmaria.noventa@unibs.it

M. V. Salvetti et al. (eds.), *Direct and Large-Eddy Simulation XI*,
ERCOFTAC Series 25, https://doi.org/10.1007/978-3-030-04915-7_11

prohibitively costly, while LES is used in regions of separated flow where larger eddies can be resolved. Among the hybrid approaches available in the literature, we chose the eXtra-Large Eddy Simulation (X-LES) [1, 2] for three attractive features: (i) independence from the wall distance; (ii) use in LES mode of a clearly defined subgrid-scale (SGS) model [3]; (iii) use of the k-ω turbulence model integrated to the wall.

2 Implementation and Discretization of the X-LES Model

In this section we review some details of the proposed X-LES model implementation and DG discretization [2]. For the sake of compactness we only report the governing equations for the turbulent kinetic energy k and the logarithm of the specific dissipation rate $\widetilde{\omega}$

$$\frac{\partial}{\partial t}(\rho k) + \frac{\partial}{\partial x_j}\left(\rho u_j k\right) = \frac{\partial}{\partial x_j}\left[\left(\mu + \sigma^* \bar{\mu}_t\right)\frac{\partial k}{\partial x_j}\right] + P_k - D_k, \tag{1}$$

$$\frac{\partial}{\partial t}(\rho \widetilde{\omega}) + \frac{\partial}{\partial x_j}\left(\rho u_j \widetilde{\omega}\right) = \frac{\partial}{\partial x_j}\left[\left(\mu + \sigma \bar{\mu}_t\right)\frac{\partial \widetilde{\omega}}{\partial x_j}\right] + \left(\mu + \sigma \bar{\mu}_t\right)\frac{\partial \widetilde{\omega}}{\partial x_k}\frac{\partial \widetilde{\omega}}{\partial x_k} + P_\omega - D_\omega + C_D, \tag{2}$$

where the production, destruction and cross diffusion terms are

$$P_k = \tau_{ij}\frac{\partial u_i}{\partial x_j}, \quad P_\omega = \alpha\left[\alpha^* \frac{\rho}{e^{\widetilde{\omega}_r}}\left(S_{ij} - \frac{1}{3}\frac{\partial u_k}{\partial x_k}\delta_{ij}\right) - \frac{2}{3}\rho\delta_{ij}\right]\frac{\partial u_i}{\partial x_j}, \tag{3}$$

$$D_k = \beta^* \rho \bar{k}\hat{\omega}, \quad D_\omega = \beta\rho e^{\widetilde{\omega}_r}, \quad C_D = \sigma_d \frac{\rho}{e^{\widetilde{\omega}_r}}\max\left(\frac{\partial k}{\partial x_k}\frac{\partial \widetilde{\omega}}{\partial x_k}, 0\right), \tag{4}$$

and

$$\bar{\mu}_t = \alpha^* \frac{\rho \bar{k}}{\hat{\omega}}, \quad \bar{k} = \max\left(0, k\right). \tag{5}$$

In our implementation, being k limited to zero, X-LES actually switches between three different flow models, i.e., ILES, LES with a well defined explicit SGS model [3] and RANS closed by the k-ω model. The automatic switching among the models is obtained through the definition of a "composite" specific dissipation rate

$$\hat{\omega} = \max\left(e^{\widetilde{\omega}_r}, \frac{\sqrt{\bar{k}}}{C_1 \Delta}\right), \tag{6}$$

where Δ is the SGS filter width and $C_1 = 0.05$. Although in the literature the filter width parameter is often related to the local mesh spacing, here we set Δ to a constant value over the whole computational grid.

The variable $\widetilde{\omega}_r$ in the source terms of Eqs. 3 and 4, and in the "composite" specific dissipation rate definition in Eq. 6, indicates that $\widetilde{\omega}$ must fulfill a suitably defined "realizability" condition, which sets a lower bound on $\widetilde{\omega}$. This constraint ensures that X-LES, regardless of being in RANS or LES mode, predicts positive normal turbulent stresses and satisfies the Schwarz inequality for shear stresses

$$\overline{\rho u_i'^2} \geq 0, \quad i = 1, 2, 3; \qquad \left(\overline{\rho u_i' u_j'}\right)^2 \leq \overline{\rho u_i'^2}\,\overline{\rho u_j'^2}, \quad i, j = 1, 2, 3, \quad i \neq j, \tag{7}$$

where u_i' indicates the fluctuating part of the ith component of the velocity and the overline symbol the temporal average operator.

Being in X-LES both the Reynolds and the subgrid stress tensor modelled according to the Boussinesq hypothesis, an overall "realizability" condition can be enforced through the definition of a suitably modified specific dissipation rate. In fact, after some algebra, Eqs. 7 can be written in terms of modelled stresses as

$$\frac{e^{\widetilde{\omega}}}{\alpha^*} - 3\left(S_{ii} - \frac{1}{3}\frac{\partial u_k}{\partial x_k}\right) \geq 0, \quad i = 1, 2, 3, \tag{8}$$

$$\begin{aligned} &\left(\frac{e^{\widetilde{\omega}}}{\alpha^*}\right)^2 - 3\left(S_{ii} + S_{jj} - \frac{1}{3}\frac{\partial u_k}{\partial x_k}\right)\frac{e^{\widetilde{\omega}}}{\alpha^*} \\ &+ 9\left[\left(S_{ii} - \frac{1}{3}\frac{\partial u_k}{\partial x_k}\right)\left(S_{jj} - \frac{1}{3}\frac{\partial u_k}{\partial x_k}\right) - S_{ij}^2\right] \geq 0, \quad i, j = 1, 2, 3, \quad i \neq j. \end{aligned} \tag{9}$$

Let us denote with a the maximum value of the unknown $e^{\widetilde{\omega}}/\alpha^*$ that fulfills the inequalities Eqs. 8 and 9. The lower bound $\widetilde{\omega}_{r0}$ that guarantees realizable stresses is then given by

$$\frac{e^{\widetilde{\omega}_{r0}}}{\alpha^*} = a. \tag{10}$$

Since in this work the underlaying turbulence model is the high-Reynolds version of k-ω, α^* is constant and the solution of Eq. 10 is trivial. The "realizability" constraint can be finally enforced as

$$\widetilde{\omega}_r = \max\left(\widetilde{\omega}, \widetilde{\omega}_{r0}\right). \tag{11}$$

X-LES equations are here discretized in space according to the DG method, see [2] for details. The complete governing system can be written in compact form as

$$\mathbf{P}\left(\mathbf{w}\right)\frac{\partial \mathbf{w}}{\partial t} + \nabla \cdot \mathbf{F}_{\mathrm{c}}\left(\mathbf{w}\right) + \nabla \cdot \mathbf{F}_{\mathrm{v}}\left(\mathbf{w}, \nabla \mathbf{w}\right) + \mathbf{s}\left(\mathbf{w}, \nabla \mathbf{w}\right) = \mathbf{0}, \tag{12}$$

where $\mathbf{w}$ is the unknown solution vector of the m variables, the tensors $\mathbf{F}_c$ and $\mathbf{F}_v$ are the convective and viscous flux functions, $\mathbf{s}$ is the vector of source terms. In this work we rely on the set of variables $\mathbf{w} = [\widetilde{p}, \widetilde{T}, u_i, k, \widetilde{\omega}]^T$, where $\widetilde{p} = \log(p)$ and $\widetilde{T} = \log(T)$. In practice we substitute (p, T) with $e^{\widetilde{p}}, e^{\widetilde{T}}$ in the governing equations, and use the polynomial approximation of the working variables $\widetilde{p}$ and $\widetilde{T}$ instead of p and T directly. This trick ensured, by design, the positivity of the thermodynamic unknowns at a discrete level, adding robustness to high-order simulations of transonic flows. The matrix $\mathbf{P}(\mathbf{w})$ is the transformation matrix that takes into account of the change of variables from the conservative set $\mathbf{w}_c = [\rho, \rho E, \rho u_i, \rho k, \rho\widetilde{\omega}]^T$ to the set $\mathbf{w}$.

The system of Eq. 12 is discretized in space firstly multiplying by an arbitrary smooth test function and then integrating by parts, thus obtaining its weak form. The solution and the test function are then replaced with a finite element approximation and a discrete test function both belonging to the set $\mathbf{V}_h := [\mathbb{P}^k_d(\mathscr{T}_h)]^m$, where $\mathbb{P}^k_d(\mathscr{T}_h) := \{v_h \in L^2(\Omega) \mid v_{h|K} \in \mathbb{P}^k_d(K),\ \forall K \in \mathscr{T}_h\}$ is the discrete polynomial space in physical coordinates. $\mathbb{P}^k_d(K)$ denotes the restriction of the polynomial functions of $d = 3$ variables and total degree k to the element K belonging to the triangulation $\mathscr{T}_h = \{K\}$, consisting of a set of non-overlapping elements, built on an approximation Ω_h of the computational domain Ω. A set of hierarchical and orthonormal basis functions for the space $\mathbb{P}^k_d(K)$ is computed following the approach of Bassi et al. [4].

Being the functional approximation discontinuous, the flux functions are not uniquely defined over the mesh faces, and thus a numerical flux vector is suitably defined both for the convective and viscous part of the equations. The former relies on the van Leer flux vector splitting method as modified by Hänel et al. [5]. The latter employs the BR2 scheme, proposed in Bassi et al. [6].

By assembling together all the elemental contributions a system of ordinary differential equations governing the evolution in time of the discrete solution is obtained. The accurate high-order time integration is performed by means of the multi-stage linearly implicit (Rosenbrock-type) Runge–Kutta schemes. Such schemes require the solution of a linear system at each stage, while the Jacobian matrix needs to be assembled only once per time step. An extended review of several Rosenbrock schemes as well as their coefficients is reported in [7].

3 Numerical Experiments

In this section we present preliminary results obtained with X-LES in the computation of the transonic turbulent flow through the NASA Rotor 37. These results are compared with the RANS simulations to assess the predicting capabilities of the two different approaches. This test case has been thoroughly investigated both numerically and experimentally, e.g. [8–10].

We performed all the computations up to $\mathbb{P}^2$ solution on a grid of 160512 20-node hexahedral elements (quadratic edges), created by agglomerating a structured linear mesh. The height of elements adjacent to the solid wall corresponds to $y^+ \approx 7$. The

governing equations were formulated in the non-inertial reference frame, see [10], setting the rotational speed equal to $\omega = [1800\text{rad/s}, 0, 0]^T$. We prescribed adiabatic wall boundary conditions on the blade, the hub and the tip surfaces. The total pressure and temperature, the flow angle $\alpha_1 = 0°$ and the turbulence intensity $Tu_1 = 3\%$ were set at the inlet, while the static pressure was imposed at the outlet. For the RANS computations we relied on the DG implementation proposed in [10, 11], performing the implicit time integration to the steady state by means of the linearized backward Euler scheme coupled with a pseudo-transient continuation strategy to evolve the CFL number. X-LES computations were initialized with the RANS fields, advancing the solution in time with the linearly-implicit third-order three-stages ROS3P Rosenbrock scheme [7, 12]. The X-LES filter width was set equal to $\Delta = 5 \times 10^{-5}$.

Figures 1 and 2 compare the RANS and instantaneous X-LES solutions in terms of pressure contours and skin friction lines on the blade. The unsteady nature of X-LES can be clearly appreciated together with the remarkably different distribution of separation lines with respect to the RANS result. In Figs. 3 and 4 the pitch-wise mass averaged $p_{0,2}/p_{0,1}$ and $T_{0,2}/T_{0,1}$ radial distributions for the RANS and X-LES computations are compared with the experimental data at 98% of the choked mass flow. X-LES results are averaged over 46800 time-steps, corresponding to 13 convective time units, defined as $t_c = c/(a\, M_{r,tip})$, where c is the chord at midspan, $M_{r,tip}$ the relative tip Mach number at the inlet, and a the speed of sound at the

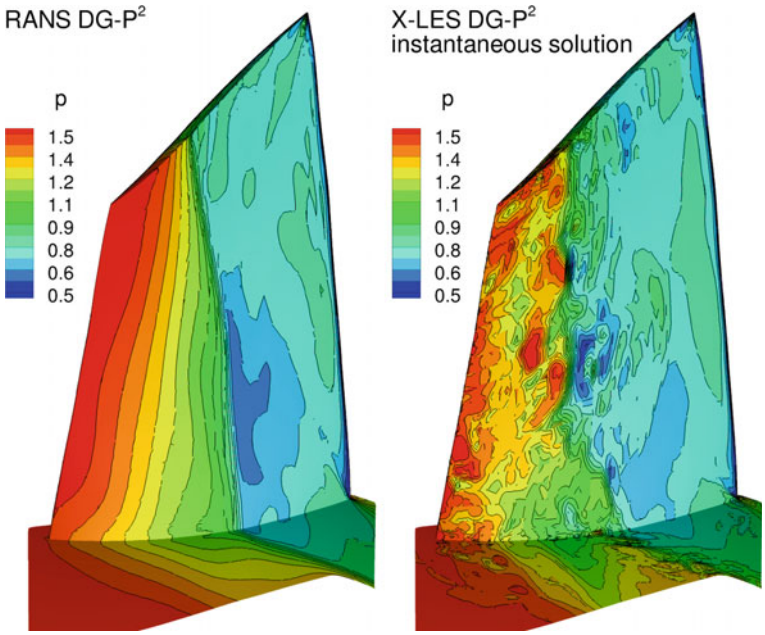

Fig. 1 Pressure contours, $\mathbb{P}^2$ solutions

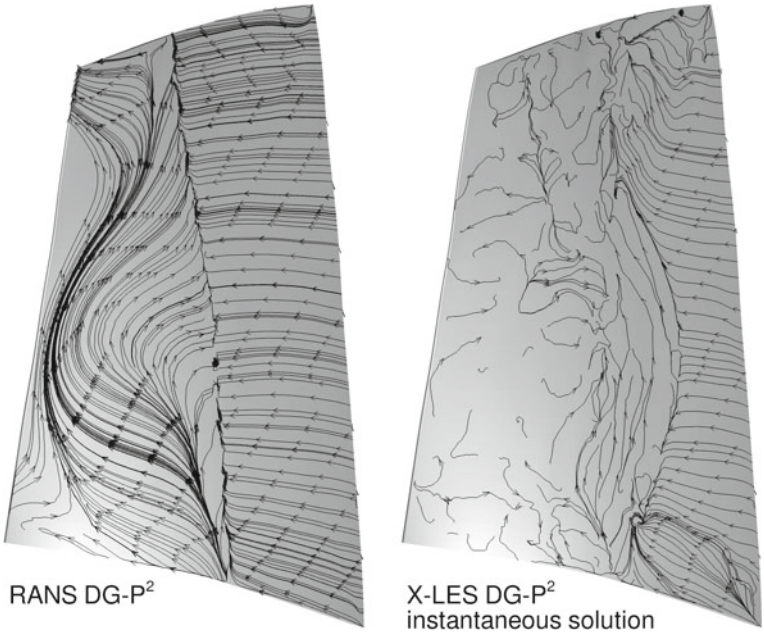

Fig. 2 Skin friction lines, $\mathbb{P}^2$ solutions

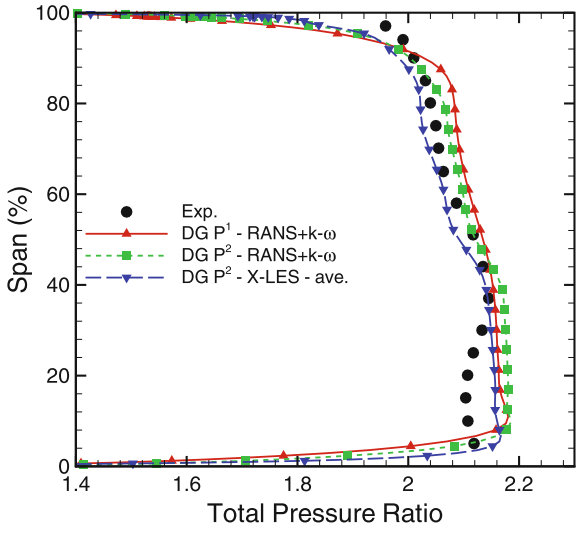

Fig. 3 Pitch-wise total pressure ratio $p_{0,2}/p_{0,1}$, $\mathbb{P}^{1\to 2}$ solutions

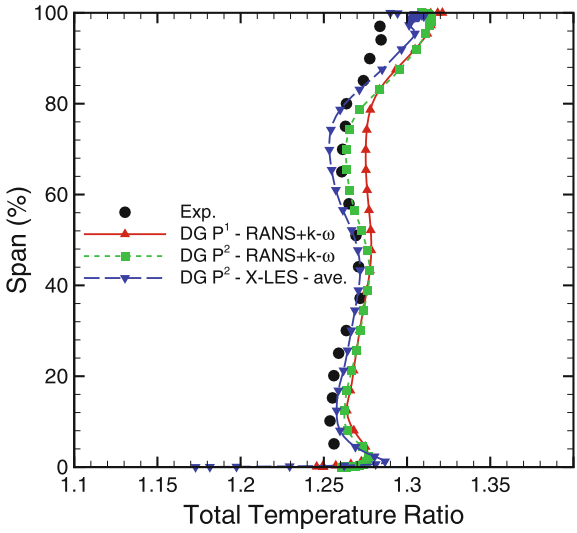

Fig. 4 Pitch-wise total temperature ratio $T_{0,2}/T_{0,1}$, $\mathbb{P}^{1\to 2}$ solutions

inlet. The pressure ratio distribution is better predicted by X-LES starting from 40% of the span, while up to 40% both models, i.e. RANS and X-LES, are not able to capture the total pressure deficiency. The total temperature distribution is better predicted by X-LES everywhere with the exception of the zone near 60% of the span, where it is slightly underestimated. At hub and tip regions some discrepancies with respect to experimental measurements occur, even if less pronounced for the X-LES; however similar behaviours are also observed for other numerical results reported in the literature.

4 Conclusion

A high-order DG method coupled with an implicit time integration strategy for the high-fidelity simulation of turbulent flows was presented. The X-LES hybrid approach was chosen, being considered appealing for many industrial applications characterized by high Reynolds numbers. X-LES proved to be robust and able to correctly deal with separated flows, also improving the predicting capabilities over RANS model.

Future work will be addressed to further investigate the filter width influence on results accuracy, to move towards very-large scale parallel computations (ten-of-thousands cores), and to include in our X-LES implementation some recently proposed improvements to the model [13].

Acknowledgements The results reported in this paper have been achieved using the PRACE Research Infrastructure resource MARCONI-KNL based at CINECA, Casalecchio di Reno, Italy, within the Project "Discontinuous Galerkin method for the X-LES of TRAnsonic flows" (DGX-TRA).

References

1. Kok, J.C., Dol, H.S., Oskam, B., van der Ven, H.: Extra-large eddy simulation of massively separated flows. AIAA Paper 2004–264 (2004)
2. Bassi, F., Botti, L., Colombo, A., Crivellini, A., Ghidoni, A., Nigro, A., Rebay, S.: Time Integration in the Discontinuous Galerkin Code MIGALE - Unsteady Problems. In: Kroll, N., Hirsch, C., Bassi, F., Johnston, C., Hillewaert, K. (eds.) IDIHOM: Industrialization of High-Order Methods - A Top-Down Approach. Notes on Numerical Fluid Mechanics and Multidisciplinary Design, vol. 128, pp. 205–230. Springer International Publishing, Berlin (2015)
3. Yoshizawa, A.: Statistical theory for compressible turbulent shear flows, with the application to subgrid modelling. Phys. Fluids **29**, 2152–2160 (1986)
4. Bassi, F., Botti, L., Colombo, A., Di Pietro, D., Tesini, P.: On the flexibility of agglomeration based physical space discontinuous Galerkin discretizations. J. Comput. Phys. **231**(1), 45–65 (2012). https://doi.org/10.1016/j.jcp.2011.08.018
5. Hänel, D., Schwane, R., Seider, G.: On the accuracy of upwind schemes for the solution of the Navier–Stokes equations, AIAA Paper 87-1105 CP. In: AIAA, Proceedings of the AIAA 8th Computational Fluid Dynamics Conference (1987)
6. Bassi, F., Rebay, S., Mariotti, G., Pedinotti, S., Savini, M.: A high-order accurate discontinuous finite element method for inviscid and viscous turbomachinery flows. In: Decuypere, R., Dibelius, G. (eds.) 2nd European Conference on Turbomachinery Fluid Dynamics and Thermodynamics, pp. 99–108. Technologisch Instituut, Antwerpen, Belgium (1997)
7. Bassi, F., Botti, L., Colombo, A., Ghidoni, A., Massa, F.: Linearly implicit Rosenbrock-type Runge–Kutta schemes applied to the discontinuous Galerkin solution of compressible and incompressible unsteady flows. Comput. Fluids **118**, 305–320 (2015)
8. Dunham, J.: CFD validation for propulsion system components. Technical Report AR-355. AGARD (1994)
9. Denton, J.D.: Lessons from Rotor 37. J. Thermal Sci. **6**, 1–13 (1997)
10. Bassi, F., Botti, L., Colombo, A., Crivellini, A., Franchina, N., Ghidoni, A.: Assessment of a high-order accurate Discontinuous Galerkin method for turbomachinery flows. Int. J. Comput. Fluid Dyn. **30**, 307–328 (2016). https://doi.org/10.1080/10618562.2016.1198783
11. Bassi, F., Crivellini, A., Rebay, S., Savini, M.: Discontinuous Galerkin solution of the Reynolds-Averaged Navier–Stokes and k-ω turbulence model equations. Comput. Fluids **34**, 507–540 (2005)
12. Lang, J., Verwer, J.: ROS3P–An accurate third-order Rosenbrock solver designed for parabolic problems. BIT **41**, 731–738 (2001)
13. Kok, J.C.: A stochastic backscatter model for grey-area mitigation in detached eddy simulations. Flow, Turbul. Combust. (2017). https://doi.org/10.1007/s10494-017-9809-y

Assessment of High-Order Discontinuous Galerkin Methods for LES of Transonic Flows

J. S. Cagnone, Z. Zeren, A. Châtel, M. Rasquin, K. Hillewaert and L. Bricteux

1 Introduction

This paper concerns implicit large eddy simulation (ILES) of turbulent flows of industrial interest using high order discontinuous Galerkin method (DGM). DGM has a high potential for industrial applications using ILES. As dissipation is only active on very small scale features, the method mimics a subgrid scale model, while its high accuracy ensures that large scale dynamics are not contaminated by dispersive/dissipative errors. Previously DGM/ILES has been assessed on many low Mach number canonical test cases (e.g. Carton et al. [3]). This paper recapitulates recent validation on transonic benchmarks (Hillewaert et al. [6]) and proceeds to the application on the LS89 cascade, a well-known turbomachinery benchmark.

J. S. Cagnone · Z. Zeren (✉) · M. Rasquin · K. Hillewaert
Cenaero, Rue des Frères Wright, 29, 6041 Gosselies, Belgium
e-mail: zafer.zeren@cenaero.be

J. S. Cagnone
e-mail: jean-sebastien.cagnone@cenaero.be

M. Rasquin
e-mail: michel.rasquin@cenaero.be

K. Hillewaert
e-mail: koen.hillewaert@cenaero.be

A. Châtel · L. Bricteux
Université de Mons (UMONS), Rue du Joncquois 53, 7000 Mons, Belgium
e-mail: adrien.chatel@umons.ac.be

L. Bricteux
e-mail: laurent.bricteux@umons.ac.be

M. V. Salvetti et al. (eds.), *Direct and Large-Eddy Simulation XI*,
ERCOFTAC Series 25, https://doi.org/10.1007/978-3-030-04915-7_12

2 Computational Framework

The discontinuous Galerkin method [4] is a Galerkin finite element method. Its interpolants are polynomials of arbitrary order p on each of the elements in the mesh, but are not required to be continuous across the interfaces between elements.

Due to the solution discontinuities, DG method faces the appearance of the convective and diffusive flux contributions for the element interfaces that couple the solutions between the elements. The Roe approximate Riemann solver is used for the convective and the symmetric interior penalty (Arnold et al. [1]) for the diffusive part. The method provides $O(h^{p+1})$ accuracy and good dispersion/dissipation properties on unstructured, low quality meshes. Combining this with good scalability performances provides the necessary properties for fast and reliable LES of complex industrial geometries. The shock capturing method (SCM) of Persson and Peraire [9] is used for this study due to the transonic flow regime. An artificial viscosity decreasing with polynomial degree is activated by a resolution indicator that measures the energy contained in the pth mode of the polynomial expansion in each element.

3 Compressible Homogeneous Isotropic Turbulence

Following Johnsen [7], the first validation test case concerns a compressible homogeneous isotropic decaying turbulent flow in a periodic box. The Reynolds number based on the Taylor length scale is $Re_\lambda = 100$. The grid includes (64^3) DOF and different interpolation orders ($p = 3, 4, 5$) were investigated.

To complete the reference work, a fine resolution DNS, was also performed with a (384^3) resolution using fifth order elements. The simulations were run with and without a shock capturing method in order to investigate its impact on the stability.

The flow is initialized with an incompressible synthetic turbulent flow field following Rogallo [10]. This induces a violent transient phase due to acoustic imbalance in the initial incompressible turbulent flow field and the large turbulent Mach number ($M_t = 0.6$), resulting in the formation of high intensity shocks. We propose to use the energy dissipation (W) budget

$$\underbrace{-\frac{d}{dt}\left(\frac{1}{2}\int_V \rho\,\mathbf{u}\cdot\mathbf{u}\,dV\right)}_{W} = \underbrace{\int_V \left(2\mu\mathbf{S}:\mathbf{S} - \lambda(\nabla\cdot\mathbf{u})^2\right)\,dV}_{W_d} - \underbrace{\int_V p\,\nabla.u\,dV}_{W_c}. \quad (1)$$

as an error indicator. For a periodic control volume V, there is no net flux of energy in or out of the volume, and the balance of W only consists of viscous dissipation W_d and compression work W_c. Here p, ρ, $\mathbf{u}$ and $\mathbf{S}$ represent respectively pressure, density, velocity and strain rate tensor, while μ and λ represent dynamic viscosity coefficients. Eq. 1 will not be exactly satisfied due to discretization errors and shock capturing. The imbalance between the right and the left hand sides of Eq. 1 will be a quality

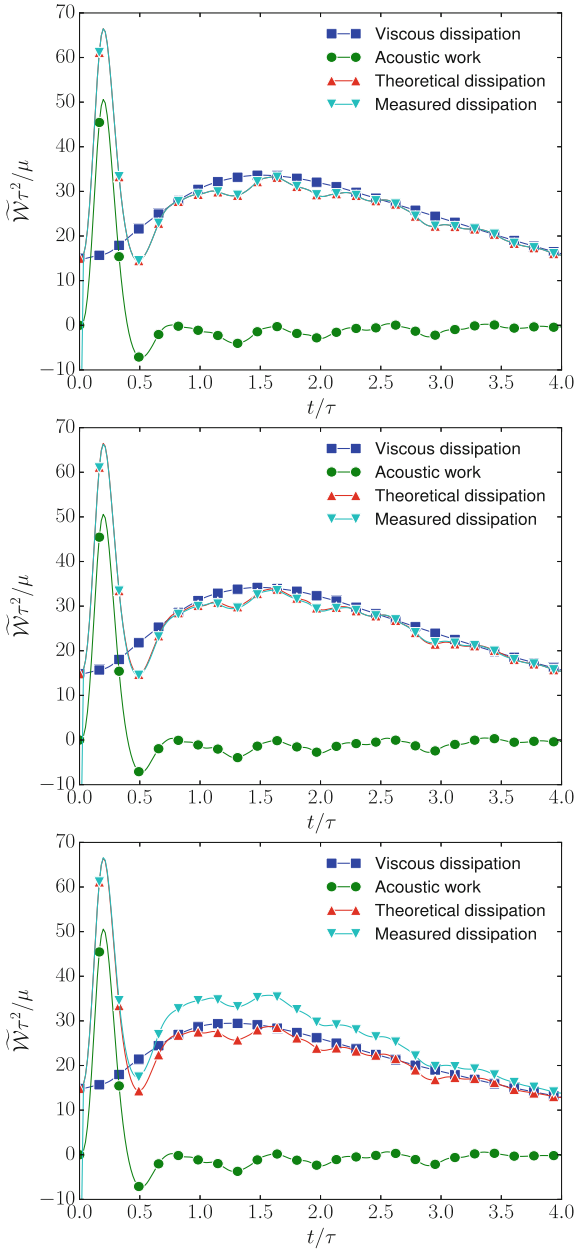

Fig. 1 Dissipation balances for the compressible HIT, top: $p = 4\ 384^3$ DNS, middle: $p = 5\ 64^3$ LES, bottom: $p = 5\ 64^3$ LES using SCM

indicator of the simulation. The results are presented in Fig. 1. For both computations without SCM, the difference between the left hand side W and the right hand side $W_d - W_c$ of Eq. 1 is very small, both at so-called DNS (384) and LES (64) resolution. It is worth mentioning that the DG solver was not consistently stable during these simulations and often crashed around $t/\tau = 0.6 - 0.7$ for $p = 3, 4$ without SCM. The inclusion of SCM stabilized the simulations, however resulted in loss of precision (see the bottom plot of Fig. 1). The so-called LES resolution (64) is in fact still close to DNS. As the difference is attributable to the SCM, it is clear that improvements are required for transonic turbulence levels. These conditions are not, however, readily encountered in free stream flows: for transonic flows, the turbulence intensity would correspond to about 50%.

4 Homogeneous Isotropic Turbulence Passing Through a Shock

The second test case consists in a high Mach number freestream with superposed turbulent flow passing through a stabilized shock. The inflow Mach number is $M_{in} = 1.5$ as in the reference DNS of Larsson and Lele [8]. The size of the computational domain is $[4\pi \times 2\pi \times 2\pi]$, where periodic boundary conditions are applied in the y and z directions and x is the streamwise direction. Three simulations were performed using a coarse (192×64^2) and a fine mesh (384×128^2) clustered around the shock.

The inlet turbulence is extracted from a precursor simulation of incompressible homogeneous isotropic turbulence, initialized with $Re_\lambda = 140$. It was then evolved in time to a Reynolds value of 40 and was blended following the procedure of Xiong et al. [12] in order to obtain a larger flow realization. The fluctuations were then continuously superposed on the main inflow condition. The outlet static pressure was adjusted in order to fix the position of the shock following Larsson [8].

The turbulence intensities are shown in Fig. 2 for two different grid resolutions and compared to the reference data. The intensities initially decrease approaching the shock and sharply increase through it. They then continue to decay downstream. The relatively large fluctuations for the streamwise component is most likely due to the unsteady shock position which intensifies the fluctuations. The monotonically decaying behavior persist but the anisotropy of the turbulent structures, acquired through the shock, keeps its strength until the domain outlet. The present simulations correctly reproduce the reference results, even if resolution-dependent differences were observed. By varying the baseline artificial viscosity for the fine mesh, it is shown that the effect of the SCM is minor. As the SCM is only active around the shock location it does not affect fundamentally the physics of the turbulence for this much more prevalent flow regime.

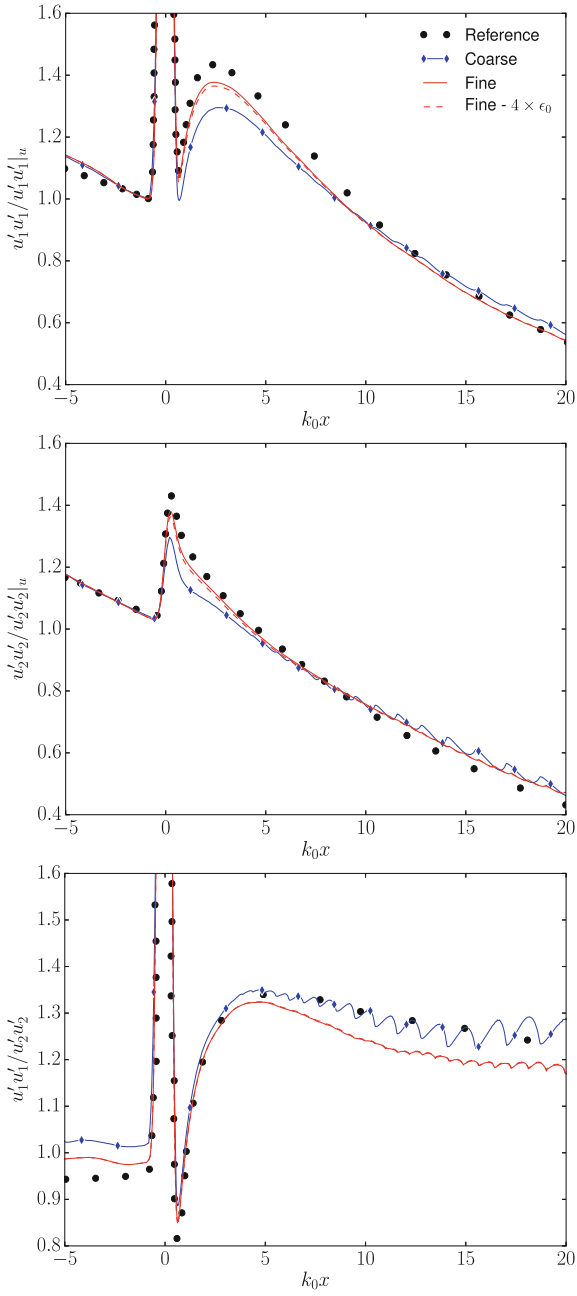

Fig. 2 Evolution of velocity correlations for the shock/turbulence interaction case. $M_{in} = 1.5$

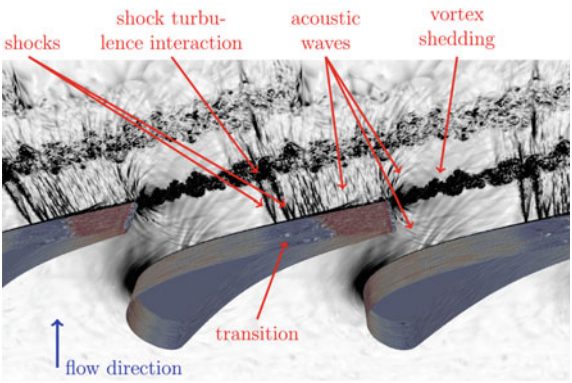

Fig. 3 LS89 transonic stator blade geometry and flow features

5 Flow Around a Transonic Turbine Stator Blade

The transonic flow around a high pressure turbine blade cascade LS89 (Arts. [2]) is simulated. A $2D$ quadrilateral mesh is extruded in the spanwise direction leading to 1.56×10^6 elements and 100×10^6 degrees of freedom using $p = 3$. The mesh is refined close to the walls resulting in equivalent normal $\Delta y^+ \approx 1$ and tangential resolutions $\Delta t^+ \approx 11$. A subsonic turbulent inflow superposed on a uniform inlet velocity of 60 m/s is imposed at the inlet. Two inlet turbulence generation methods were considered. The first one uses a precursor simulation similar to the previous test cases and the second one relies on the analytical method proposed by Davidson [5]. The subsonic flow at the inlet becomes transonic at blade suction side where the Mach number increases up to around 1.2. Resulting complex unsteady shock system can be seen in Fig. 3.

The isentropic Mach number and heat transfer coefficient are presented in Fig. 4 compared to the experimental measurements for the inlet turbulence intensity of $TI = 6\%$. The agreement is satisfactory for the isentropic Mach number for both inflow generation methods. The heat transfer coefficient curve requires more comments. Experimental results for both $TI = 4\%$ and $TI = 6\%$ are included in the figure for the discussion. Focusing on these experimental measurements, there is a significant effect of the inlet flow turbulence on the heat transfer coefficient, especially on the suction side from $S/c = 0.5$ onwards. None of the inflow methods are able to capture correctly the leading edge behavior, although there is an important improvement with the precursor method. Both methods seem to reproduce the results with $TI = 4\%$, although 6% was imposed at the inlet. Only the method of Davidson is able to correctly predict the maximum heat transfer for $S/c > 1$. We foresee a grid refinement study to capture the bypass transition on suction side, which is known to provide the enhance the heat transfer, instead of increasing the turbulence at the inlet to better match with experiments [11].

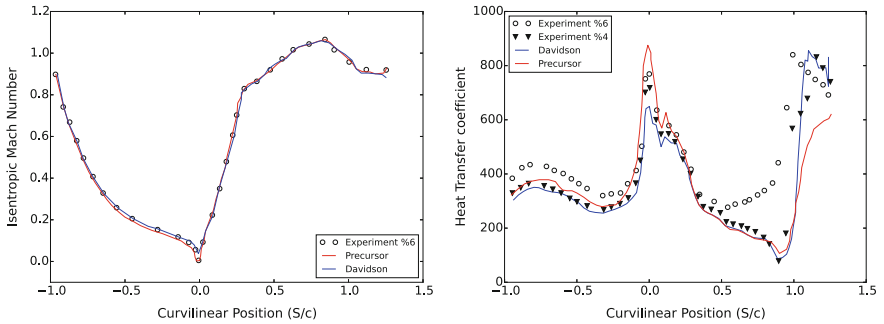

Fig. 4 Left: Isentropic Mach number; Right: Heat transfer coefficient on the blade surface. S: Curvilinear coordinate on the blade; c: the chord

6 Conclusion and Perspectives

We conclude based on the test cases that the DGM has good prediction capabilities for transonic flows. For applications with a limited turbulent Mach number where shocks are not caused by high level of turbulent fluctuations, the SCM seems to perform well. Larger Reynolds numbers are required in order to be more conclusive on the subject. No discernible solver instability were observed during the LS89 turbine blade case, which confirms the applicability of the current SCM for transonic applications in turbomachinery. Current results seem to indicate that a good match with experiments can be obtained without tuning the inlet turbulence level, leading to truly predictive simulations.

Acknowledgements The present research benefited from computational resources made available on the Tier-1 supercomputer of the Fédération Wallonie-Bruxelles, infrastructure funded by the Walloon Region under the grant agreement n°1117545.

References

1. Arnold, D., Brezzi, F., Cockburn, B., Marini, L.: Unified analysis of discontinuous Galerkin methods for elliptic problems. SIAM J. Numer. Anal. **39**, 1749–1779 (2002)
2. Arts, T., Lambert de Rouvroit, M.: Aero-thermal performance of a two-dimensional highly loaded transonic turbine nozzle guide vane : a test case for inviscid and viscous flow computations. J. Turbomach. **114**, 147–154 (1992)
3. Carton de Wiart, C., Hillewaert, K., Bricteux, L., Winckelmans, G.: Implicit LES of free and wall-bounded turbulent flows based on the discontinuous Galerkin/symmetric interior penalty method. Numer. Methods Fluids **78**, 335–354 (2015)
4. Cockburn, B., Karniadakis, G.E., Shu, C.-W.: The development of discontinuous Galerkin methods. In: Cockburn, B., Karniadakis, G.E., Shu, C.-W. (eds.) Discontinuous Galerkin Methods: Theory, Computation and Applications. Volume 11 of Lecture Notes in Computer Science and Engineering, pp. 350. Springer, Berlin (2000)

5. Davidson, L.: Using isotropic synthetic fluctuations as inlet boundary conditions for unsteady simulations. Adv. Appl. Fluid Mech. **1**(1), 2007, 1–35 (2006)
6. Hillewaert, K., Cagnone, J.S., Murman, S., Garai, A., Lv, Y., Ihme, M.: Assessment of high-order DG methods for LES of free-stream transonic turbulence. In: Proceedings of CTR Summer Program, pp. 363–372. Stanford University (2016)
7. Johnsen, E., Larsson, J., Bhagatwala, A.V., Cabot, W.H., Moin, P., Olson, B.J., Rawat, P.S., Shankar, S.K., Sjgreen, B., Yee, H., Zhong, X., Lele, S.K.: Assessment of high-resolution methods for numerical simulations of compressible turbulence with shock waves. J. Comput. Phys. **229**, 1213–1237 (2010)
8. Larsson, J., Lele, S.K.: Direct numerical simulation of canonical shock/turbulence interaction. Phys. Fluids **21**, 126101 (2009)
9. Persson, P., Peraire, J.: Sub-cell shock capturing for discontinuous Galerkin methods. In: 44th AIAA Aerospace Sciences Meeting and Exhibit, pp. 112. Reno, Nevada (2006)
10. Rogallo, R.: Numerical experiments in homogeneous turbulence. NASA TM-81315 (1981)
11. Segui, L., Gicquel, L., Duchaine, F., de Laborderie, J.: LES of the LS89 cascade: influence of inflow turbulence on the flow predictions. In: Proceedings of 12th European Conference on Turbomachinery Fluid dynamics and Thermodynamics ETC12. Stockholm, Sweden, 3–7 April (2017)
12. Xiong, Z., Nagarajan, S., Lele, S.K.: Simple method for generating inflow turbulence. AIAA J. **42**, 2164–2166 (2004)

Efficient Pressure-Correction Method for Interfacial Tracking Appropriate for the Immersed Boundary Method

C. Frantzis and D. G. E. Grigoriadis

1 Introduction

Solving the Navier–Stokes equations to simulate incompressible two-fluid flows with interfaces, is still a developing scientific field. One of the main challenges, is the reduction of the computational cost which is still significantly higher when compared to single-fluid problems. This is mainly due to the variable coefficients Poisson equation arising from the projection method to impose mass conservation. Recently, [1, 2] proposed a new pressure correction method to transform the variable coefficients Poisson equation into a constant coefficients one. Among other advantages, such a transformation allows the use of efficient and robust Fast Direct Solvers (FDS) to solve the Poisson equation. As a result, the pressure solution could be achieved 20-60 times faster when compared to classical iterative multigrid solvers, such as those implemented in HYPRE library.

In the present study, a pressure correction formulation that is based on FDS and is appropriate for the Immersed Boundary (IB) method of two-fluid flow problems is proposed. The resulting constant coefficients Poisson equation was solved using FISHPAK. The proposed formulation has been compared with the original one [2] for density ratios up to 1000, showing very good agreement. In addition, it does not add any extra complexity or cost; on the contrary, it extends the capabilities of the constant coefficients approach and the IB method even further.

C. Frantzis (✉) · D. G. E. Grigoriadis
Department of Mechanical and Manufacturing Engineering,
University of Cyprus, Nicosia, Cyprus
e-mail: frantzis.charalambos@ucy.ac.cy

D. G. E. Grigoriadis
e-mail: grigoria@ucy.ac.cy

M. V. Salvetti et al. (eds.), *Direct and Large-Eddy Simulation XI*,
ERCOFTAC Series 25, https://doi.org/10.1007/978-3-030-04915-7_13

The results presented in this study are generated using the conservative Level-Set method [3] to track the position of the interface. The proposed methodology could also be used along with different interface tracking approaches such as VoF or phase-field methods.

2 Mathematical Formulation and Numerical Methods

Governing Equations

In the absence of surface tension effects, the two-phase incompressible viscous flow for immiscible fluids is described by the Navier–Stokes equations, which in their non-dimensional form read,

$$\nabla \cdot \mathbf{u} = 0 \tag{1}$$

$$\frac{\partial \mathbf{u}}{\partial t} = -\frac{\nabla P}{\rho} + \frac{1}{\rho Re}\nabla \left[\mu \left(\nabla \mathbf{u} + (\nabla \mathbf{u})\right)\right] + \frac{1}{Fr}\mathbf{a} - \mathbf{u}\nabla \cdot \mathbf{u} \tag{2}$$

where Re and Fr are the Reynolds and Froude number, respectively. P represents the total pressure, $\mathbf{u}$ is the velocity vector field and $\mathbf{a}$ is the acceleration vector. The non-dimensional density and viscosity are denoted as ρ and μ respectively.

Fractional Step Technique for Interfacial Problems

The fractional step method is one of the most popular techniques to numerically solve the Navier–Stokes (NS) equations. In this method, a provisional velocity field $\mathbf{u}^*$ is first computed from Eq. (2) which is not solenoidal, i.e. it does not satisfy mass-continuity since $\nabla \cdot \mathbf{u}^* \neq 0$. Mass conservation is then imposed by solving a Poisson equation for the pressure at each time step. For single fluid-flow problems the derived Poisson equation can easily be solved because it involves constant coefficients in time. Following this approach for the case of two-fluid flow problems with density gradients, the derived Poisson equation becomes,

$$\nabla \cdot \left(\frac{\nabla P^{n+1}}{\rho}\right) = \nabla \cdot \mathbf{u}^* \tag{3}$$

In this case the discretised form of (3) leads to a mathematical problem with variable coefficients in time, due to density variations. To overcome this complexity, [1] proposed to split the variable coefficients operator into two parts according to,

$$\frac{\nabla P^{n+1}}{\rho^{n+1}} \longrightarrow \frac{\nabla P^{n+1}}{\rho_o} + \left(\frac{1}{\rho^{n+1}} - \frac{1}{\rho_o}\right)\nabla \hat{P} \tag{4}$$

where ρ_o is the density of the lighter fluid and $\hat{P}$ is an approximation of P^{n+1}. Using this formulation, Eq. (3) leads to a constant coefficients Poisson equation of the form,

$$\nabla^2 P^{n+1} = \nabla \cdot \left[\left(1 - \frac{\rho_o}{\rho^{n+1}} \right) \nabla \hat{P} \right] + \frac{\rho_o}{\Delta t} \nabla \cdot \mathbf{u}^* \tag{5}$$

Proper Pressure Correction for the IB Method

The formulation of Eq. (5) has been proposed in [1, 2] for problems without internal obstructions. In the present study, we propose an approach to extend the formulation in order to be consistent with the IB method. In doing so, flows with interfaces can be simulated efficiently in the presence of obstacles, which may even deform or move.

FDS is a very efficient and popular choice for the solution of the Poisson equation with constant coefficients. When combined with the IB method, FDS solvers generate a solution for all the nodes within a rectangular domain, meaning that the pressure is also solved inside the solid phase of immersed obstacles. Looking at Eq. (5), or (3), an appropriate RHS or density field should be set for the solid nodes respectively, in order to satisfy the proper BC on the IB solid interface. More sophisticated IB forms [4, 5] have been proposed, that modify the LHS of the Poisson for the fluid nodes close to the IB solid interface, in order to solve the pressure only in the fluid phase. However, such a modification automatically excludes the use of FDS for the solution of the pressure Poisson equation.

To overcome this restriction, we propose a new pressure correction formulation. Instead of solving an equation for the overall pressure P^{n+1}, we formulate a pressure correction scheme based on a pressure difference δP^{n+1}, defined as $P^{n+1} = P^n + \delta P^{n+1}$. Combined with Eq. (5), one can derive a constant coefficients Poisson equation for the pressure difference,

$$\nabla^2 \delta P^{n+1} = \nabla \cdot \left[\left(1 - \frac{\rho_o}{\rho^{n+1}} \right) \nabla \hat{P} \right] + \frac{\rho_o}{\Delta t} \nabla \cdot \mathbf{u}^* - \nabla^2 P^n \tag{6}$$

which is now appropriate for FDS and the IB method. Using the above formulation, we can set the RHS of Eq. (6) equal to zero for all the solid nodes, which is valid regardless of the unknown density field ρ^{n+1} inside the solid body.

Contrary to the VBF method [5] and the ghost cell approach [4], the LHS of the pressure Poisson equation that we solve in Eq. (6) is not modified at all. However, when the RHS of Eq. (6) is calculated, we explicitly set it equal to zero if it refers to a solid node. As a result, the Poisson equation for the pressure difference in Eq. (6) reduces to a Laplace equation inside the solid. Moreover, the pressure gradient terms, that appear in the RHS of Eq. (6) and the correction step of the fractional step method, are modified at the locations where a solid pressure node is required for the calculation. In that sense, we indirectly satisfy the proper boundary condition for the pressure on the IB solid interface.

Discretisation Schemes

The equations are discretised with central differences on Cartesian staggered grids. The momentum field of Eq. (2) is advanced in time using a fully explicit 2nd order Adams-Bashforth scheme. The spatial discretisation of the convective terms is performed either with a 2nd order central or a 5th order WENO scheme. The LS

advection equation is discretised in space using the WENO scheme, while for the re-initialisation equation a 2nd order upwind scheme is used. Time advancement for both the LS advection and re-initialisation is performed with a 3rd order TVD Runge–Kutta scheme.

3 Validations and Results

The proposed formulation was first validated without the use of the IB for low and high density ratios. The results given by the three different formulations of Eqs. (3), (5), (6) have been compared using the same LU-based solver. Afterwards, the coupling of the FDS, the IB method and the proposed formulation is examined by comparing the results given by Eq. (3) on a boundary conforming grid. Very small time steps Δt were used ($CFL < 0.01$) in order to eliminate temporal errors.

Rayleigh–Taylor Instability

The vertical position of the front of the rising and falling fluids as a function of time are shown in Fig. 1 and they are compared against previous studies by [6, 7] in Fig. 2. Our results are in absolute agreement with each other, while they are in very good agreement with other numerical studies as well.

Run-up of a Solitary Wave

Figure 4 shows the wave run-up A_{run-up} as a function of the solitary wave height A_c defined in Fig. 3. The results given by each formulation are exactly the same and also in very good agreement with other studies [8–10].

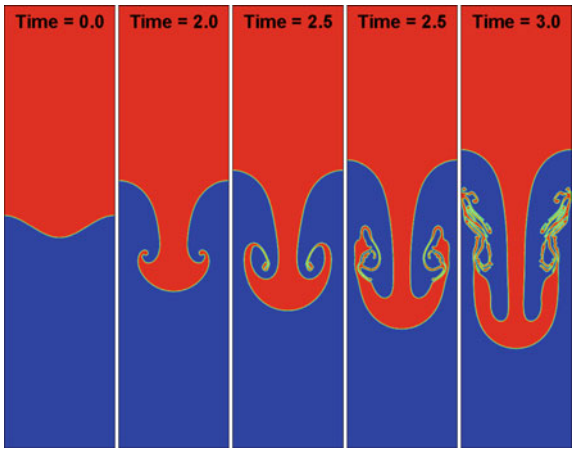

Fig. 1 Interface profile at different time instants

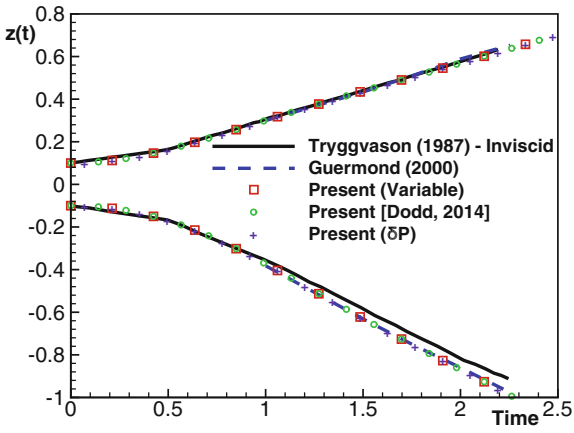

Fig. 2 Comparison for the temporal evolution of the highest (top line) and lowest (lower line) location of the interface

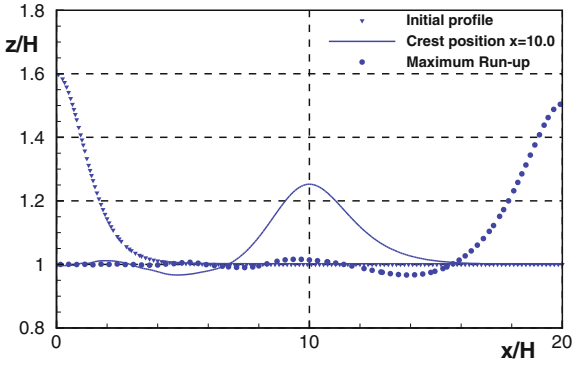

Fig. 3 Run-up of a solitary wave schematic diagram

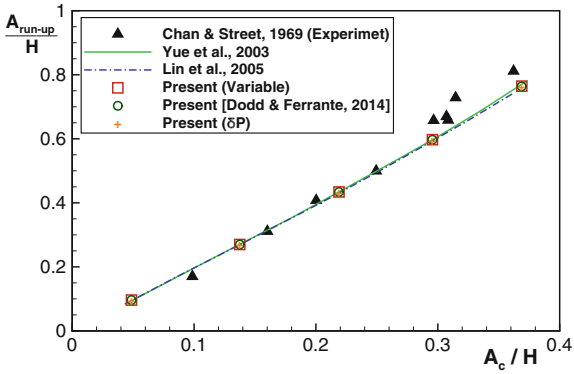

Fig. 4 Run-up of the solitary wave as a function of the wave height

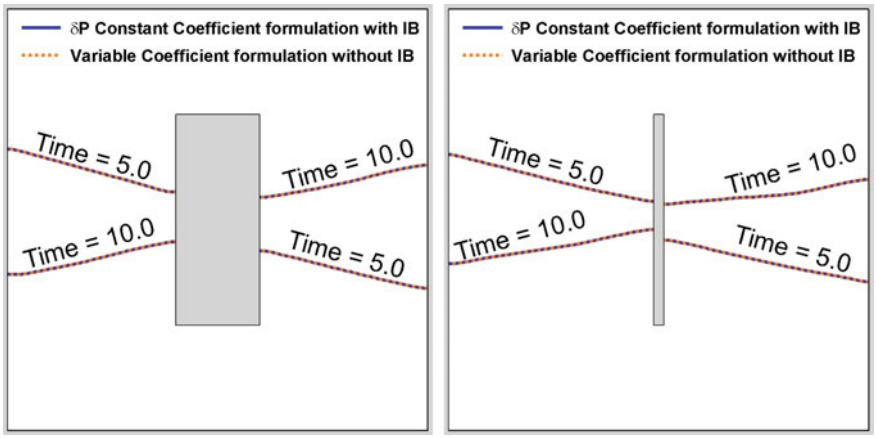

Fig. 5 Profile of the free-surface at different time instants and different baffle widths. $W_{baffle} = 0.4$ (left) and 0.05 (right)

Sloshing in a 2D-Baffled Tank (FDS/IB Coupling Validation)

Figure 5 presents the profile of the interface in two different time instants for the case of a thick and a thin baffle. The computed results are exactly the same using either the variable coefficients approach on a boundary conforming grid or the constant coefficients approach of Eq. (6) with the IB method and a FDS.

Computational Efficiency

The efficiency of the proposed methodology can be demonstrated by comparing the required CPU time of LU-based and the proposed FDS-based solvers. An $OpenMP$ implementation was tested on a computational node with 48 cores for a 3D sloshing case. Table 1 shows the time required by each approach and the speed-up of the proposed formulation. The first line refers to the LU-solution of Eq. (3) and the second line to the LU-solution of Eq. (5). The third line refers to the proposed FDS (with FFT along y direction), to solve either Eq. (5) or (6).

An enormous speed-up occurs for the proposed approach when comparing with the first one, due to the inversion of the matrix that is required at every time step by the first approach. Keeping the formulation the same, the speed-up of the FDS over the LU-direct solver is still considerably large.

Moreover, the memory requirements of each solver were examined. The RAM required by the LU direct solver increases exponentially with the grid nodes, while it increases almost linearly for the FDS. For considerably large problems the RAM required by the proposed FDS formulation is more than 100 times less than the memory required by an LU-based direct solver.

Table 1 Execution time for a 3D-sloshing test case using ($320 \times 48 \times 264$) computing cells

		Poisson (sec/itr)	NS (sec/itr)	Poisson/NS (%)
1	VC-LU	$5.259e+2$	$5.261+2$	99.96
2	CC-LU	$1.130e+1$	$1.170e+1$	96.58
3	CC-1DFFT	$1.492e-1$	$5.507e-1$	27.10

4 Conclusions

We have developed a robust and efficient pressure-correction scheme which solves a constant coefficients Poisson equation for two-fluid problems. This formulation allows the use of FDS while it is also appropriate for the use of the IB method, satisfying the pressure BC indirectly on the IB solid interface.

We verified that the proposed methodology has the same accuracy as the conventional variable coefficients approach. The proposed formulation maintains all the advantages of a FDS pressure solution concerning the computational efficiency, as they were presented in [2]. Moreover, it offers the additional capability of using the IB method, allowing the simulation of two-fluid flows around obstacles with complex geometries which can also deform or move.

The proposed methodology allows the simulation of interfacial tracking problems with immersed obstacles for considerably larger problems (several million nodes) on smaller computers, even on laptops.

Acknowledgements The research leading to these results has received funding from the People Programme (Marie Curie Actions) of the European Union's Seventh Framework Programme FP7/2007-2013/ under REA grant agreement n^o 607394-SEDITRANS.

References

1. Dong, S., Shen, J.: A time-stepping scheme involving constant coefficient matrices for phase-field simulations of two-phase incompressible flows with large density ratios. J. Comput. Phys. **231**(17), 5788–5804 (2012)
2. Dodd, M.S., Ferrante, A.: A fast pressure-correction method for incompressible two-fluid flows. J. Comput. Phys. **273**, 416–434 (2014)
3. Sussman, M., Fatemi, E., Smereka, P., Osher, S.: An improved level set method for incompressible two-phase flows. Comput. Fluids **27**(5), 663–680 (1998)
4. Berthelsen, P.A., Faltinsen, O.M.: A local directional ghost cell approach for incompressible viscous flow problems with irregular boundaries. J. Comput. Phys. **227**(9), 4354–4397 (2008)
5. Liu, D., Lin, P.: Three-dimensional liquid sloshing in a tank with baffles. Ocean Eng. **36**(2), 202–212 (2009)
6. Tryggvason, G.: Numerical simulations of the Rayleigh-Taylor instability. J. Comput. Phys. **75**(2), 253–282 (1988)
7. Guermond, J.L., Quartapelle, L.: A projection FEM for variable density incompressible flows. J. Comput. Phys. **165**(1), 167–188 (2002)

8. Chan, R.K.C., Street, R.L.: A computer study of finite-amplitude water waves. J. Comput. Phys. **6**(1), 68–94 (1970)
9. Lin, C.L., Lee, H., Lee, T., Weber, L.J.: A level set characteristic Galerkin finite element method for free surface flows. Int. J. Numer. Method Fluids **49**(5), 521–547 (2005)
10. Yue, W., Lin, C.L., Patel, V.C.: Numerical simulation of unsteady multidimensional free surface motions by level set method. Int. J. Numer. Method Fluid **42**(8), 853–884 (2003)

Part II
LES Modeling

On the Eddy Viscosity Associated with the Subgrid Stresses

A. Cimarelli, A. Abbà and M. Germano

1 Introduction

Thanks to its simplicity and robustness, the models based on the eddy viscosity concept represent the most common procedure to introduce the effect of the unresolved scales in the equations of motion for the Large Eddy Simulation (LES) approach. Indeed, the subgrid scale (sgs) viscosity approach allows from an energetic point of view to respect the dissipative nature of turbulence.

Starting from the pioneering proposal of Smagorinsky [18], a large number of modifications have been proposed in literature in order to account for relevant physical phenomena that can not be adequately reproduced by the original model. Between them, a significant improvement has been done by the contribution of Germano et al. [13] in which the dynamic procedure allows the subgrid model to better adapt to the local structure of the flow and to transitional conditions.

Besides, all the models based on a scalar subgrid viscosity are developed in the Kolmogorov hypothesis of isotropicity of the small turbulent scales. Instead it is well known that not only the large turbulent structures are not isotropic, but also the unresolved turbulent ones [6]. To overcome this limit several proposals can be found in literature. On the one hand anisotropic grid and filters can be used to reproduce the

A. Cimarelli (✉)
Dipartimento di Ingegneria Industriale e Scienze Matematiche,
Università Politecnica delle Marche, Ancona, Italy
e-mail: a.cimarelli@staff.univpm.it

A. Abbà
Department of Aerospace Science and Technology,
Politecnico di Milano, Milan, Italy
e-mail: antonella.abba@polimi.it

M. Germano
Department of Civil and Environmental Engineering,
Duke University, Durham, NC, USA
e-mail: mg234@duke.edu

M. V. Salvetti et al. (eds.), *Direct and Large-Eddy Simulation XI*,
ERCOFTAC Series 25, https://doi.org/10.1007/978-3-030-04915-7_14

anisotropy of the flow structures. The definition of the characteristic length Δ of the filter is still an open question when anisotropic filters are used or when the Navier–Stokes equations are implicitly filtered using strongly anisotropic unstructured grids, although several attempts have been done to solve this ambiguity [3, 4, 8, 16, 17].

Moreover, the eddy viscosity models are based on the proportionality between the subgrid stress tensor components and the strain rate tensor of the filtered velocity field, but it has been demonstrated that the sgs stress tensor is not usually aligned with the resolved strain rate one [1]. Some tensorial eddy viscosity models are proposed in literature with the aim to solve this contradiction [2, 5, 9, 14]. In this work we further exploit the subgrid viscosity approach by analysing an alternative formulation which leads to a tensorial eddy viscosity and takes into account the shape and the size of the applied filter.

2 Theoretical Framework

The flow equations in a LES approach are obtained by applying a filter to the Navier–Stokes equations. In the present work we will focus on the filter in space operator, applied to the incompressible flow equations, assuming that the scale of the filter in time is directly related to the characteristic length of the filter in space and the filtered velocity. A filter in space extracts the large scales velocity vector components $\overline{u}_i$ as follow [15]:

$$\overline{u}_i(\mathbf{x}) = \int G(\mathbf{x}, \boldsymbol{\xi}) u_i(\boldsymbol{\xi}) d\boldsymbol{\xi}, \qquad (i = 1, 3) \tag{1}$$

where G denotes the filter kernel with characteristic length Δ and

$$\int_{\Omega} G(\mathbf{x}, \boldsymbol{\xi}) d\boldsymbol{\xi} = 1.$$

By assuming commutativity with spatial derivatives, the filtering of the convective terms of the Navier–Stokes equations leads to the unknown subgrid stress tensor $\tau(u_i, u_j)$, defined as [12]

$$\tau(u_i, u_j) = \overline{u_i u_j} - \bar{u}_i \bar{u}_j \ , \tag{2}$$

which needs to be modeled. This subgrid stresses can be usefully expressed by the equivalent relation

$$\tau(u_i, u_j) = \frac{1}{2} \iint G(\mathbf{x}, \boldsymbol{\xi}) G(\mathbf{x}, \boldsymbol{\eta}) [u_i(\boldsymbol{\xi}) - u_i(\boldsymbol{\eta})][u_j(\boldsymbol{\xi}) - u_j(\boldsymbol{\eta})] d\boldsymbol{\xi} d\boldsymbol{\eta}. \tag{3}$$

Let us now introduce the following velocity decomposition

$$u_i = \bar{u}_i + \upsilon_i \ , \tag{4}$$

where υ_i represents the subgrid scale fluctuations. Applying this decomposition to the subgrid flux (2) [11] it is easy to verify that

$$\tau(u_i, u_j) = \frac{1}{2}\left(\tau(\bar{u}_i, u_j) + \tau(\upsilon_i, u_j) + \tau(u_i, \bar{u}_j) + \tau(u_i, \upsilon_j)\right) \tag{5}$$

where

$$\begin{aligned} \tau(\bar{u}_i, u_j) &= \overline{\bar{u}_i u_j} - \bar{\bar{u}}_i \bar{u}_j \\ \tau(\upsilon_i, u_j) &= \overline{\upsilon_i u_j} - \bar{\upsilon}_i \bar{u}_j . \end{aligned} \tag{6}$$

We remark that this decomposition is Galilean invariant since it is composed by Galilean invariant terms [10]. Similarly to (3) we can apply the filter operator (1) to the previous mentioned subgrid contributions [12]

$$\begin{aligned} \tau(\bar{u}_i, u_j) &= \frac{1}{2}\iint G(\mathbf{x}, \boldsymbol{\xi}) G(\mathbf{x}, \boldsymbol{\eta})[\bar{u}_i(\boldsymbol{\xi}) - \bar{u}_i(\boldsymbol{\eta})][u_j(\boldsymbol{\xi}) - u_j(\boldsymbol{\eta})] d\boldsymbol{\xi} d\boldsymbol{\eta} \\ \tau(\upsilon_i, u_j) &= \frac{1}{2}\iint G(\mathbf{x}, \boldsymbol{\xi}) G(\mathbf{x}, \boldsymbol{\eta})[\upsilon_i(\boldsymbol{\xi}) - \upsilon_i(\boldsymbol{\eta})][u_j(\boldsymbol{\xi}) - u_j(\boldsymbol{\eta})] d\boldsymbol{\xi} d\boldsymbol{\eta} \ . \end{aligned} \tag{7}$$

By assuming that the filtered value $\bar{u}_i$ is sufficiently smooth at the LES scale, we can make use of the Taylor expansion approximations

$$\bar{u}_i(\boldsymbol{\xi}) \approx \bar{u}_i(\mathbf{x}) + (\xi_h - x_h)\partial_h \bar{u}_i(\mathbf{x}) \tag{8}$$

neglecting higher orders terms. We remark that the Taylor expansion is formally justified only for filtered quantities. The same expansion cannot be applied to subgrid quantities that are rapidly varying at the LES scale of resolution. Introducing, expansion (8) in Eq. (7), we get

$$\begin{aligned} \tau(\bar{u}_i, u_j) &= \frac{1}{2}\iint G(\mathbf{x}, \boldsymbol{\xi}) G(\mathbf{x}, \boldsymbol{\eta})(\xi_h - \eta_h)\partial_h \bar{u}_i(\mathbf{x})[u_j(\boldsymbol{\xi}) - u_j(\boldsymbol{\eta})] d\boldsymbol{\xi} d\boldsymbol{\eta} \\ &= -\nu_{hj}\partial_h \bar{u}_i \end{aligned} \tag{9}$$

where the eddy viscosity tensor ν_{hj}

$$\nu_{hj} = -\tau(x_h, u_j) \tag{10}$$

defined as

$$\tau(x_h, u_j) = \frac{1}{2}\iint G(\mathbf{x}, \boldsymbol{\xi}) G(\mathbf{x}, \boldsymbol{\eta})(\xi_h - \eta_h)[u_j(\boldsymbol{\xi}) - u_j(\boldsymbol{\eta})] d\boldsymbol{\xi} d\boldsymbol{\eta} \tag{11}$$

has been introduced. The eddy viscosity tensor ν_{hj} only depends on the turbulent velocity field u_j and on the filter G. As such it is peculiar of the given turbulent velocity field, and the study of this quantity should be of some interest by itself. In particular its variations with the filter shape and length Δ, and near the boundaries could be interesting for modeling.

We would like to observe that a similar procedure can be applied to the subgrid fluxes $\tau(f, u_i) = \overline{f u_i} - \bar{f}\bar{u}_i$ of a transported scalar f. It easy to verify that the proposed approach leads to the relation

$$\tau(f, u_i) = \nu_{hi}\partial_h \bar{f} \tag{12}$$

where the eddy viscosity ν_{hi} depends on the convective velocity field and has no relation with the transported scalar f.

The expression (11) highlights the relevance of taking into account how the velocity field is distributed within the filter scales. If an implicit filter is used and the operator coincides with a projection onto the discrete solution space, the eddy viscosity (11) depends on the structure function of the velocity of grid element size. Moreover a tensorial viscosity should be an important contribution to subgrid models in order to take into account the anisotropy of the flow. Actually if we now make the approximation

$$\tau(u_i, u_j) = \frac{1}{2}\left(\tau(\bar{u}_i, u_j) + \tau(u_i, \bar{u}_j)\right) \tag{13}$$

where we introduce the eddy viscosity tensor, we get

$$\tau(u_i, u_j) = -\frac{1}{2}\left(\nu_{hj}\partial_h \bar{u}_i + \nu_{ki}\partial_k \bar{u}_j\right). \tag{14}$$

In the relation (14) a coefficient to be determined using the dynamic procedure, or an additional Smagorinsky like term, can be added to take in account the terms discarded by the approximation (13).

3 Comparison with the Gradient Model

In more traditional approaches, the Leonard decomposition for the subgrid stresses

$$\tau(u_i, u_j) = \tau(\bar{u}_i, \bar{u}_j) + \tau(\bar{u}_i, \upsilon_j) + \tau(\upsilon_i, \bar{u}_j) + \tau(\upsilon_i, \upsilon_j) \tag{15}$$

is used. Here

$$\tau(\bar{u}_i, \bar{u}_j) = \frac{1}{2}\iint G(\mathbf{x}, \boldsymbol{\xi})G(\mathbf{x}, \boldsymbol{\eta})[\bar{u}_i(\boldsymbol{\xi}) - \bar{u}_i(\boldsymbol{\eta})][\bar{u}_j(\boldsymbol{\xi}) - \bar{u}_j(\boldsymbol{\eta})]d\boldsymbol{\xi}d\boldsymbol{\eta} \tag{16}$$

are the so called Leonard stresses $\tau(\bar{u}_i, \bar{u}_j) = \overline{\bar{u}_i \bar{u}_j} - \bar{\bar{u}}_i \bar{\bar{u}}_j$. Introducing the Taylor expansion for the filtered velocity in Eq. (16) we get

$$\tau(\bar{u}_i, \bar{u}_j) = \frac{1}{2} \iint G(\mathbf{x}, \boldsymbol{\xi}) G(\mathbf{x}, \boldsymbol{\eta}) (\xi_h - \eta_h)(\xi_k - \eta_k) \partial_h \bar{u}_i(\mathbf{x}) \partial_k \bar{u}_j(\mathbf{x}) d\boldsymbol{\xi} d\boldsymbol{\eta}. \quad (17)$$

If we now make the following similarity approximation

$$\tau(u_i, u_j) \approx \tau(\bar{u}_i, \bar{u}_j) \quad (18)$$

we recover the so called gradient model for the subgrid stresses [7],

$$\tau(u_i, u_j) \approx \tau(x_h, x_k) \partial_h \bar{u}_i \partial_k \bar{u}_j \quad (19)$$

where

$$\tau(x_h, x_k) = \frac{1}{2} \iint G(\mathbf{x}, \boldsymbol{\xi}) G(\mathbf{x}, \boldsymbol{\eta}) (\xi_h - \eta_h)(\xi_k - \eta_k) d\boldsymbol{\xi} d\boldsymbol{\eta} \quad (20)$$

is a tensor a priori known and depending on the geometrical properties of the filter. We would highlight that similar procedure has been applied by Clark et al. [7] and Vreman et al. [19, 20] to obtain different versions of the original gradient model.

We remark that introducing the Taylor expansion for the velocity in Eq. (11) we get

$$\tau(x_h, u_j) = \frac{1}{2} \iint G(\mathbf{x}, \boldsymbol{\xi}) G(\mathbf{x}, \boldsymbol{\eta}) (\xi_h - \eta_h)(\xi_k - \eta_k) \partial_k \bar{u}_j d\boldsymbol{\xi} d\boldsymbol{\eta} \quad (21)$$

from which the gradient model can be again recovered. It is finally interesting to remark that the tensor $\tau(x_h, x_k)$ can be actually understood as generalized definition of filter length that can be computed in every type of computational grids thus solving the ambiguity of the determination of the filter length Δ in non-Cartesian computational grids.

4 Concluding Remarks

In the present work a particular subgrid stress decomposition is considered, which leads to a tensorial subgrid viscosity tensor. This approach highlights that the subgrid viscosity is a peculiar property of the filtered velocity field. Moreover this tensorial formulation of the subgrid viscosity overcomes the limit of the isotropicity assumption related to the eddy viscosity models and it should constitute a useful element for subgrid models suitable for numerical simulations using unstructured grids.

References

1. Abbà, A., Cercignani, C., Valdettaro, L.: Analysis of subgrid scale models. Comput. Math. Appl. **46**, 521–535 (2003)
2. Abbà, A., Bonaventura, L., Nini, M., Restelli, M.: Dynamic models for large eddy simulation of compressible flows with a high order DG method. Comput. Fluids **122**, 209–222 (2015). https://doi.org/10.1016/j.compfluid.2015.08.021
3. Abbà, A., Campaniello, D., Nini, M.: Filter size definition in anisotropic subgrid models for large eddy simulation on irregular grids. J. Turbul. **18**(6), 589–610 (2017). https://doi.org/10.1080/14685248.2017.1312001
4. Bardina, J., Ferziger, J., Reynolds, W.: Improved subgrid scale models for large eddy simulation. AIAA Paper 801357 (1980)
5. Carati, D., Cabot, W.: Anisotropic eddy viscosity models. In: Proceedings of the Summer Program - Center for Turbulence Research, pp. 249–259 (1996)
6. Cimarelli, A., De Angelis, E.: Anisotropic dynamics and subgrid energy transfer in wall-turbulence. Phys. Fluids **24**, 015102 (2012)
7. Clark, R.A., Ferziger, J.H., Reynolds, W.C.: Evaluation of subgrid-scale models using an accurately simulated turbulent flow. J. Fluid Mech. **91**, 1–16 (1979)
8. Colosqui, C., Oberai, A.: Generalized Smagorinsky model in physical space. Comput. Fluids **37**, 207217 (2008)
9. Gallerano, F., Napoli, E.: A dynamic subgrid-scale tensorial eddy viscosity model. Contin. Mech. Thermodyn. **11**, 114 (1999)
10. Germano, M.: A proposal for a redefinition of the turbulent stresses in the filtered Navier-Stokes equations. Phys. Fluids **29**, 2323–2324 (1986)
11. Germano, M.: Turbulence: the filtering approach. J. Fluid Mech. **238**, 325–336 (1992)
12. Germano, M.: A direct relation between the filtered subgrid stress and the second order structure function. Phys. Fluids **19**, 038102 (2007)
13. Germano, M., Piomelli, U., Moin, P., Cabot, W.H.: A dynamic subgrid-scale eddy viscosity model. Phys. Fluids A **3**, 1760–1765 (1991)
14. Horiuty, K.: A proper velocity scale for modelling subgrid-scale eddy viscosities in large eddy simulation. Phys. Fluids A **5**(1), 146–157 (1993)
15. Leonard, A.: Energy cascade in large-eddy simulations of turbulent fluid flows. Adv. Geophys. **18**, 237–248 (1974)
16. Piomelli, U., Amirreza, R., Geurts, B.J.: A grid-independent length scale for large-eddy simulations. J. Fluid Mech. **766**, 499–527 (2015)
17. Scotti, A., Meneveau, C., Lilly, D.: Generalized Smagorinsky model for anisotropic grids. Phys. Fluids **5**(9), 23062308 (1993)
18. Smagorinsky, J.: General circulation experiments with the primitive equations. Mon. Weather Rev. **91**(3), 99–164 (1963)
19. Vreman, B., Geurts, B., Kuerten, H: Subgrid-modelling in LES of compressible flows. In: Proceedings of the First ERFOCTAC Workshop on Direct and Large Eddy Simulation. Guildford (1994)
20. Vreman, B., Geurts, B., Kuerten, H.: Large-eddy simulation of the temporal mixing layer using the Clark model. Theoret. Comput. Fluid Dyn. **8**, 309–324 (1996)

Implicit/Explicit Spectral Viscosity and Large-Scale SGS Effects

E. Lamballais, T. Dairay, S. Laizet and J. C. Vassilicos

1 Introduction

Subgrid-scale (SGS) modelling based on regularization has become a popular approach for Large Eddy Simulation (LES). When the regularization is driven by the numerical error or by an extra discrete operator like a filter, it is usual to refer to implicit LES in the sense that the discretization provides an artificial dissipation interpreted as a substitute of SGS modelling. Typically, it is expected that this artificial dissipation is inactive at very large scales thanks to the numerical convergence of the associated discretization. This assumption of large-scale dynamics virtually free from any artificial dissipation can even be intentionally extended on a wide range of scales through an optimal design of the associated discrete schemes. This idea can also be recovered in explicit SGS models with for instance the concept of Spectral Vanishing Viscosity (SVV) [1] and the Variational Multiscale (VMS) methods [2].

The goal of this study is to assess this inviscid assumption at very large scales for a flow at high Reynolds number while using DNS results to estimate the exact energy transfers from large to SGS. These transfers are investigated in the challenging situation of a flow subjected to a complete transition up to a fully developed turbulent state. The corresponding benchmark is the Taylor–Green vortex problem at $Re = 20{,}000$. In a previous work [3], using an implicit SVV associated to the differentiation errors of the viscous term, we have shown that very accurate results can be obtained by LES at $Re = 10{,}000$ with a reduction of the number of degrees of freedom (DOF) of 8^3 by reference to DNS. In this study, we want to investigate the ability of this type of SGS modelling (without any direct influence on large

E. Lamballais (✉) · T. Dairay
Incompressible Turbulence and Control Group, Pprime Institute,
CNRS-Univ-Poitiers-ISAE/ENSMA, Poitiers, France
e-mail: eric.lamballais@univ-poitiers.fr

S. Laizet · J. C. Vassilicos
Turbulence, Mixing and Flow Control Group, Department of Aeronautics, Imperial College London, London, UK

M. V. Salvetti et al. (eds.), *Direct and Large-Eddy Simulation XI*,
ERCOFTAC Series 25, https://doi.org/10.1007/978-3-030-04915-7_15

scales) at higher Reynolds number and with a stronger reduction of DOF. Note that both Reynolds numbers $Re = (10{,}000; 20{,}000)$ correspond to fully turbulent conditions as suggested by the value of their counterparts based on the Taylor microscale $Re_\lambda \approx (200; 300)$ obtained after the complete turbulence breakdown at $t \approx 13$.

2 A Priori Analysis from DNS Results

The DNS of reference as well as the LES are performed using the sixth-order flow solver "Incompact3d" which is kinetic energy conserving in the discrete and inviscid sense (up to the time advancement error). For the present high Reynolds number case $Re = 20{,}000$, 3456^3 mesh nodes are required for a computational domain of $(2\pi)^3$ but using some symmetries of the problem, the number of DOF is actually divided by 8. Here, the goal is to carry out counterpart LES where the number of DOF and computational cost are reduced by 16^3 and 16^4 respectively leading to a cutoff wavenumber of $k_c = 108$ for the LES mesh against 1728 for the DNS one.

Following our conclusions in a previous work, the targeted LES solution is defined using a progressive spatial filter as illustrated in Fig. 1-left where raw and filtered DNS energy spectra are compared. The filter is obtained by solving the Lin equation using a simplified spectral Pao-like closure while taking the implicit SGS dissipation into account [3]. An important remark is that this filter is applied once in each spatial direction and not in all directions as it would be for an isotropic filter. This 1D definition of the filter is believed to be more significant by reference to the actual anisotropy of the LES mesh. Using this specific filter applied on the DNS data, the time evolution of the supergrid scale kinetic energy $\bar{E}_k$ can be computed a priori with its associated total dissipation $\bar{\varepsilon} = -d\bar{E}_k/dt$. Then, it is easy to estimate the viscous large-scale dissipation ε_{LS} and its complementary SGS part ε_{SGS} such as $\bar{\varepsilon} = \varepsilon_{LS} + \varepsilon_{SGS}$. These dissipations as well as the full DNS dissipation are presented in Fig. 1-right where it can be seen that this benchmark is very challenging with SGS dissipation ε_{SGS} up to 90% of the total dissipation $\bar{\varepsilon}$, this unequal distribution giving a major role to the SGS model.

To have a more detailed view of the kinetic energy transfer, a scale by scale analysis of the SGS dissipation can be done starting from the large-scale Lin equation decomposed as

$$\left(\frac{\partial}{\partial t} + 2\nu k^2\right)\bar{E}(k,t) = \bar{T}(k,t) + T_{SGS}(k,t) \tag{1}$$

where $\bar{E}(k,t)$ is the kinetic energy of the filtered solution, $\bar{T}(k,t)$ the transfer term involving only the filtered solution (i.e. explicitly computed in LES) and $T_{SGS}(k,t)$ the remaining term that describes transfers between the supergrid and subgrid scales. In this formalism expressed in the Fourier space, $T_{SGS}(k,t)$ is simply the spectral density of ε_{SGS} that leads to the introduction of the spectral eddy viscosity

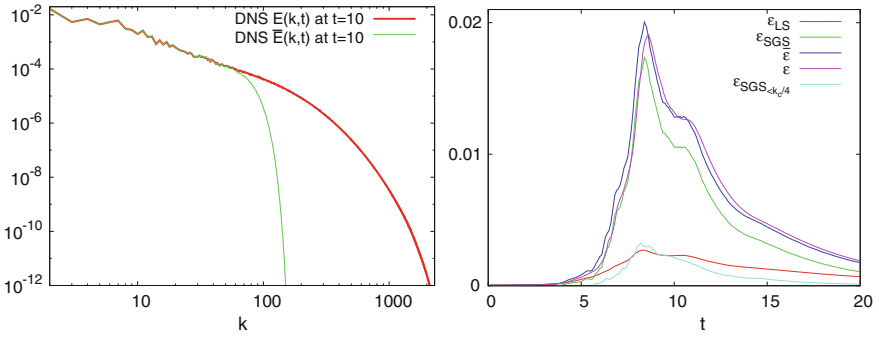

Fig. 1 Left: raw and filtered DNS energy spectra. Right: time evolution of the viscous large-scale, SGS, SGS for $k < k_c/4$, filtered DNS and full DNS dissipations (ε_{LS}, ε_{SGS}, $\varepsilon_{SGS_{<k_c/4}}$, $\bar{\varepsilon}$, ε)

$$\nu_t(k,t) = -\frac{T_{SGS}(k,t)}{2k^2\bar{E}(k,t)}\,. \tag{2}$$

Using the DNS data and following the procedure of [4] adapted in the present context, $\nu_t(k,t)$ is estimated from 200 snapshots distributed throughout the calculation.

Figure 2-left presents 5 samples of $\nu_t(k,t)$ with a normalization based on the molecular viscosity ν. This figure clearly exhibits the dominant transfers close to k_c meaning that the "hyperviscous feature" is observed for this benchmark, especially in the early transition. Figure 2-left also reveals that more distant triad interactions result in high values of $\nu_t(k,t)$ at small k, not only during the transition (for instance at $t = 10$) but also until the end of the simulation where a fully developed non-equilibrium turbulence is observed. Then, at least qualitatively, the "plateau-cusp" profile of the spectral eddy viscosity, as predicted by two-point closure theories at high Reynolds numbers [5–7], is well recovered in the present a priori analysis.

In Fig. 2-right, the average value $\nu_{t_{<k_c/4}}$ of $\nu_t(k,t)$ for $2 < k < k_c/4$ (as an estimation of the "plateau" value) and its cutoff value $\nu_{t_{=k_c}}$ at $k = k_c$ are plotted throughout the simulation. The values of $\nu_{t_{=k_c}}$ are found to be very high in the early transition but exhibit a global decrease as the turbulence develops. More importantly, the significance of direct effect of SGS on the large scale dynamics is confirmed during the turbulence breakdown (with $\nu_{t_{<k_c/4}}$ that can be more than 4 times larger than ν) but also when the turbulence is fully developed where $\nu_{t_{<k_c/4}}$ is still of the same order as ν. This observation is against the lack of any direct dissipative effect at large scales in the SGS modelling as it is assumed in implicit LES, SVV or VMS.

It could be thought that despite the high values of $\nu_t(k,t)$ for $k < k_c/4$, the corresponding fraction of SGS dissipation

$$\varepsilon_{SGS_{<k_c/4}} = 2\int_0^{k_c/4} \nu_t(k,t)k^2\bar{E}(k,t)\,dk \tag{3}$$

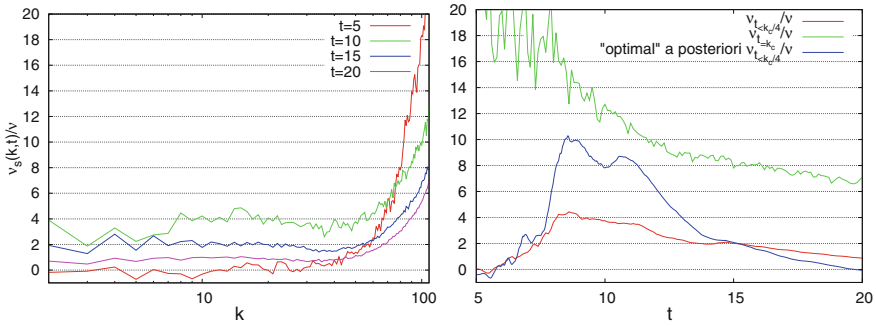

Fig. 2 Left: spectral eddy viscosity $\nu_t(k,t)$ at $t = 5$, 10, 15 and 20. Right: time evolution of the average $\nu_{t_{<k_c/4}}$ and cutoff $\nu_{t_{=k_c}}$ values of $\nu_t(k,t)$

is negligible. In Fig. 1-right, it can be seen that this quantity can actually be about 20% of the full SGS dissipation ε_{SGS} during the turbulence breakdown while remaining about 10% until the end of the calculation. In the next section, it will be examined whether this significant contribution can be ignored in practical LES.

3 A posteriori Analysis of LES Results

The same flow configuration is investigated by LES (i) without any SGS modelling; (ii) with the standard/dynamic Smagorinsky model and (iii) with our implicit SVV [3]. Figure 3 presents the time evolution of the total dissipation $\bar{\varepsilon}$ obtained for the different LES. The very unrealistic behaviour observed for the no-model case confirms the major role of the SGS modelling for the present high Reynolds number case where the LES are based on a coarse mesh by comparison to DNS. The strong overestimation of $\bar{\varepsilon}$ without SGS model corresponds to an almost complete thermalization of the flow due to the development of small-scale spurious oscillations during the transition, as it can be clearly observed by visualization and spectral analysis (not shown for conciseness). The standard and dynamic Smagorinsky models are found to lead to a partial thermalization resulting in an overdissipative behaviour in the early transition. The resulting damping of small-scale spurious oscillations has, in a second stage, a feedback effect with an underestimation of $\bar{\varepsilon}$.

The use of implicit SVV prevents any thermalization with a good prediction of $\bar{\varepsilon}$ in the early transition. However, the excellent agreement obtained in [3] at $Re = 10{,}000$ with a less coarse mesh is not recovered for the present more demanding benchmark. In particular, the peak of dissipation cannot be captured (underestimation of $\bar{\varepsilon}$) and as a subsequent feedback effect, a spurious secondary peak (overestimation of $\bar{\varepsilon}$) can be clearly observed. A similar spurious secondary peak can be observed for the enstrophy ζ (see Fig. 4-right).

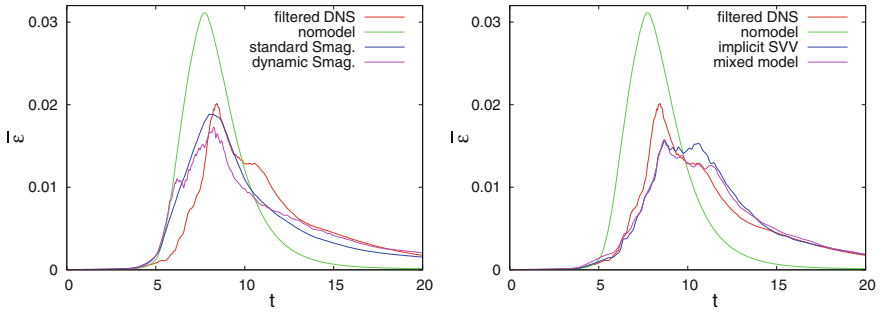

Fig. 3 Time evolution of the total dissipation $\bar{\varepsilon}$ predicted by LES

For the implicit SVV, the main discrepancy can be attributed to the poor reproduction of the main peak of $\bar{\varepsilon}$ that has the potential to spoil the flow any time thereafter. Even a very strong increase of the implicit SVV near k_c is unable to capture this peak (not shown for conciseness). A spectral analysis shows that the kinetic energy is overestimated at large scales during this particular moment, especially in the range $10 < k < k_c/2$, as illustrated in Fig. 4-left. This overestimation is interpreted as the consequence of the quasi-inviscid cascade at large scales. For this type of LES, free from distant triad interaction modelling, the overestimation of $\bar{E}(k,t)$ in the range $10 < k < k_c/2$ can be interpreted as a bottleneck effect. This interpretation is consistent with the a priori analysis presented in previous section. This view can even be supported quantitatively by observing that the main peak of dissipation is underestimated by about 22%. Because the implicit SVV is essentially inactive for $k < k_c/4$, this behaviour may be related to the a priori ratio $\varepsilon_{SGS_{<k_c/4}}/\varepsilon_{SGS} \approx 20\%$ reported in the previous section.

To restore the peak, an idea could be to combine an explicit model with our implicit SVV with the hope that the former can boost the total dissipation during the transition while the latter can avoid the unrealistic partial thermalization. This kind of mixed model approach has been tried with the standard Smagorinsky (see Fig. 3-right) but without any improvement for the prediction of the main peak of $\bar{\varepsilon}$. However, it is worth noting that this mixed model can remove the spurious secondary peak.

Another attempt was to modify our implicit model to allow non-vanishing spectral viscosity while adjusting its "plateau" value in order to follow precisely the time evolution of $\bar{\varepsilon}$. Such LES can be considered as "optimal" in terms of ability to predict the filtered kinetic energy $\bar{E}_k$. The time evolution of the resulting plateau value is presented in Fig. 2-right. Even if significantly higher levels of eddy viscosity are required by comparison with the a priori estimation of $\nu_{t_{<k_c/4}}$, it confirms the ability of a direct influence of the SGS model on very large scales to ensure the correct energy dissipation. However, this "optimal" approach (that is only a test case in the sense that it requires to know the expected time evolution of $\bar{E}_k$) is found to underestimate

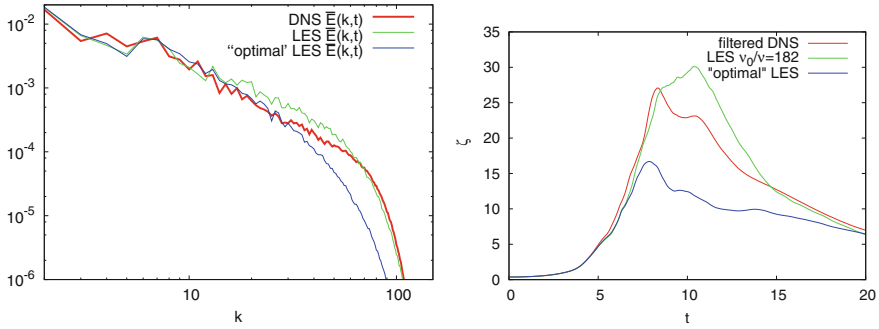

Fig. 4 Left: energy spectra $\bar{E}(k,t)$ at $t = 10$. Right: time evolution of the enstrophy ζ

$\bar{E}(k,t)$ at small scales (see Fig. 4-left) with a resulting strong underestimation of enstrophy (see Fig. 4-right).

4 Conclusion

In order to investigate the scale-selective influence of SGS on the large scale dynamics, DNS and LES are performed for the Taylor–Green vortex problem. An a priori analysis confirms the interest of the hyperviscous feature at small scale as used in implicit LES, SVV and VMS. However, the assumption of zero SGS dissipation at very large scales is found unrealistic for the high Reynolds number and coarse LES mesh considered. A posteriori analysis shows that SGS modelling based on the assumption of an inviscid cascade leads to a bottleneck effect on the kinetic energy spectrum with a significant underprediction of the total SGS dissipation. The simple addition of a constant eddy viscosity, even targeted to be optimal in terms of SGS dissipation, is unable to give realistic results. To allow accurate predictions by LES, a specific closure that incorporates both the hyperviscous feature (i.e. regularisation) and the expected SGS dissipation at large scales has to be developed.

Acknowledgements This work was granted access to the HPC resources of TGCC under the allocation 2014/2015/2016-2a0912 made by GENCI.

References

1. Maday, Y., Tadmor, E.: Analysis of the spectral vanishing viscosity method for periodic conservation laws. SIAM J. Numer. Anal. **26**(4), 854–870 (1989)
2. Hughes, T., Jansen, L.M.K.: Large eddy simulation and the variational multiscale method. Comput. Vis. Sci. **3**(1), 47–59 (2000)

3. Dairay, T., Lamballais, E., Laizet, S., Vassilicos, J.C.: Numerical dissipation vs. subgrid-scale modelling for large eddy simulation. J. Comp. Phys. **337**, 252–274 (2017)
4. Domaradzki, J.A., Liu, W., Brachet, M.E.: An analysis of subgridscale interactions in numerically simulated isotropic turbulence. Phys. Fluids A **5**(7), 1747 (1993)
5. Kraichnan, R.H.: Eddy viscosity in two and three dimensions. J. Atmos. Sci. **33**, 1521–1536 (1976)
6. Chollet, J.P., Lesieur, M.: Parameterization of small scales of the three-dimensional isotropic turbulence utilizing spectral closures. J. Atmos. Sci. **38**, 2747–2757 (1981)
7. Lesieur, M.: Turbulence in Fluids, 4th edn. Springer, Berlin (2008)

Realizable Dynamic Large Eddy Simulation

R. Mokhtarpoor, S. Heinz and M. K. Stoellinger

1 Introduction

A very attractive feature of large eddy simulation (LES) is the possibility to apply the dynamic subgrid scale model calculation developed by Germano et al. [1]. This is a method for the calculation of model parameters as functions of time and space as the simulation progresses. It avoids empirical treatment of model parameters such as damping or wall modeling near the wall boundaries. On the other hand, dynamic LES models usually suffer from instabilities. The mechanism of instability of dynamic sub-grid scale (SGS) models has not yet been fully clarified. Several methods are in use for the stabilization of dynamic SGS models. The most popular methods are clipping of model parameters and their space averaging in homogeneous directions. These stabilization techniques are often difficult or even impossible to apply. In real flows, there are no homogeneous directions in space. It is also difficult to find appropriate clipping values for dynamic LES parameters, which can depend on the type of flow, Reynolds number and grid resolution.

The first step to avoid instability would be developing a physically consistent SGS model. The application of the realizability principle is extremely useful for the design of consistent dynamic LES models [2]. A dynamic SGS model based on a realizable stochastic model for turbulent velocities [2, 3] was proposed. By applying this realizable model for different flows we found that the model was always stable

R. Mokhtarpoor · S. Heinz (✉)
Department of Mathematics, University of Wyoming, 1000 E. Univ. Ave., Laramie, WY 82071, USA
e-mail: heinz@uwyo.edu

R. Mokhtarpoor
e-mail: rmokhtar@uwyo.edu

M. K. Stoellinger
Department of Mechanical Engineering, University of Wyoming, 1000 E. Univ. Ave., Laramie, WY 82071, USA
e-mail: mstoell@uwyo.edu

M. V. Salvetti et al. (eds.), *Direct and Large-Eddy Simulation XI*,
ERCOFTAC Series 25, https://doi.org/10.1007/978-3-030-04915-7_16

for turbulent channel flow [4] and the turbulent Ekman layer [5]. But with respect to periodic hill flow simulations it was almost always but not always stable. We also found that a dynamic LES model based on a realizable stochastic model does not necessarily ensure the realizability of SGS stress tensor. In this paper we introduce a method for the stabilization of any SGS model that applies the Boussinesq hypothesis for the eddy viscosity. By examining the structure of the SGS stress tensor we derive a condition for the realizability of the SGS stress tensor.

The paper is organized as following. In Sect. 2, we will consider the realizability of an LES model based on two approaches: realizability with respect to the underlying probability density function (PDF), which is also called filter density function (FDF), and realizability of the SGS stress tensor. We show the derivation of the condition for the realizability of the SGS stress tensor. In Sect. 3, we describe the flow considered for testing our method. The results are presented in Sect. 4.

2 A Realizable LES Model

The concept of realizability expresses the need that an acceptable turbulence model must describe a velocity field that is physically possible or realizable [6]. There are several ways to actually apply this constraint. One way is to derive LES equations from an appropriate realizable stochastic velocity model. This will be referred to as PDF-realizability. Heinz proposed a dynamic LES model based on a realizable stochastic model for turbulent velocities [2–4, 7–10]. This model implies the exact but unclosed filtered Navier–Stokes equations.

The second way is to relate realizability constraints to the structure of the SGS stress tensor. This will be referred to as stress-realizability. It is known that the realizability constraints can be related to the property of the SGS stress tensor to be a positive semi-definite matrix [11]. The SGS stress tensor τ_{ij} is a positive semi-definite matrix if it satisfies

$$\tau_{ij} \geq 0 \qquad for \qquad i = j, \tag{1}$$

$$\tau_{ij}^2 \leq \tau_{ii}\tau_{jj} \qquad for \qquad i \neq j, \tag{2}$$

$$det(\tau_{ij}) \geq 0. \tag{3}$$

By using the Boussinesq eddy viscosity assumption $\tau_{ij} = 2/3k\delta_{ij} - 2\nu_t\tilde{S}_{ij}$, the resulting three realizability conditions can be written

$$k \geq 0, \tag{4}$$

$$|\nu_t^*| \leq 1, \tag{5}$$

$$\nu_t^{*2}\left\{1+\frac{2\sqrt{2}}{3}s\nu_t^*\right\}\leq\frac{1}{3}. \tag{6}$$

Here, the nondimensional variables ν_t^* and s are defined by

$$\nu_t^*=\frac{\sqrt{3}}{2}\frac{\nu_t|\widetilde{S}|}{k},\quad s=\frac{3^{3/2}det(\widetilde{S}_{ij})}{(\widetilde{S}_{mn}\widetilde{S}_{mn})^{3/2}}. \tag{7}$$

A relevant property of s follows from linear algebra. Using Hadamard's inequality we conclude that $|s|\leq 1$. The use of a ν_t^* realizability criterion that is independent of s simplifies the use of this approach significantly. This can be accomplished by the constraint that ν_t^* varies between the allowed values at $s=-1$ and $s=1$, this means $|\nu_t^*|\leq 23/48$. To summarize, given that $k\geq 0$ the condition to ensure that the sub-grid scale (SGS) stress tensor τ_{ij} is a positive semi-definite matrix is to ensure that $|\nu_t^*|\leq 23/48$, which satisfies both Eqs. (5) and (6).

Now, we apply the stress realizability condition to the PDF-realizable LES model proposed by Heinz, which will be referred to as linear dynamic model with k-equation (LDMK) [2]. This model uses the expression $\nu_t=C_S k^{1/2}\Delta$ for the eddy viscosity, where C_S is obtained via

$$C_S=-\frac{L_{ij}^d M_{ji}}{M_{kl}M_{lk}}. \tag{8}$$

Here, L_{ij}^d refers to the deviatoric Leonard stress $L_{ij}=\overline{\widetilde{U}_i\widetilde{U}_j}-\overline{\widetilde{U}_i}\,\overline{\widetilde{U}_j}$ (the overbar refers to the test filter operation), and M_{ij} is given by

$$M_{ij}=2\Delta^T\sqrt{k^T}\,\overline{\widetilde{S}}_{ij}, \tag{9}$$

which involves the test-filter SGS kinetic energy $k^T=L_{nn}/2$ and filter width $\Delta^T=2\Delta$ on the test-filter level.

According to the realizability condition $|\nu_t^*|\leq 23/48$ derived, we find the C_S realizability condition for the LDMK to be given by

$$|C_S|\leq\frac{23}{24\sqrt{3}}\frac{k^{1/2}}{\Delta|\widetilde{S}|}. \tag{10}$$

3 The Flow Considered

For testing our stabilization method we apply the new realizable LDMK model to a separated flow over two-dimensional hills. This flow configuration encompasses a variety of relevant flow features such as separation, recirculation, and natural reattachment. Figure 1 shows the computational domain applied in our simulations. The size

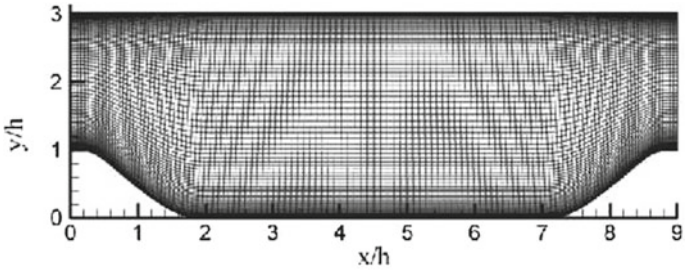

Fig. 1 Computational domain of two-dimensional hill flow simulations

of the computational domain is $L_x = 9h$, $L_y = 3.035h$, and $L_z = 4.5h$ in streamwise (x), wall normal (y), and spanwise (z) directions, respectively, where h is the height of the hill. The Reynolds number $Re = U_b h/\nu$ is $Re = 37{,}000$ based on the hill height and bulk velocity above the hill crest. At the bottom and top, the channel is constrained by solid walls. No-slip and impermeability boundary conditions are used at these walls. Periodic boundary conditions are employed in streamwise and spanwise directions. In a recently published paper [12] we investigated the same flow using pure LES and also unified RANS-LES models. We also studied grid effects for both models for grids ranging from 60 K to 20 M cells. In the present study, our aim is to analyze the stability of dynamic models by investigating the effect of different parameters. Therefore, we will use the same grid for all of our studies. From our previous studies we found that the grid of $N_x \times N_y \times N_z = 128 \times 80 \times 48$ with 500 K cells is a well appropriate mesh for the present study. Computations are initialized by a uniform bulk velocity U_b except in cases in which we wanted to calculate correlation functions (we used stationary solutions to calculate correlation functions).

4 Stability and Realizability

Although our original SGS model LDMK [2] was based on a realizable stochastic model for turbulent velocities, it does not necessarily ensure the realizability of the stress tensor. We found that our PDF-realizable LES model was computationally stable for turbulent channel flow [3] and turbulent Ekman layer [5] simulations. However, in periodic hill flow simulations [12] it turned out that PDF-realizable model simulations were almost always but not always stable. This fact is shown in Fig. 2 which shows the time histories of C_s and realizability bounds for two probe points for 30 flow-through times (FTT). The location of the probe point P1 is in the shear layer at the top of the first hill, and P2 is downstream of P1 in the middle of the two hills. The red and blue circles in Fig. 2 indicate the times at which C_s values hit the upper and lower realizabilty bounds, respectively. At P1, we found that over

Table 1 Stability of the LDMK and its extended bound versions depending on Δt

Simulation	$\Delta t = 0.001$	$\Delta t = 0.002$	$\Delta t = 0.004$	$\Delta t = 0.008$	$\Delta t = 0.01$
$LDMK$	Stable	Stable	Stable	Stable	Stable
$LDMK - 1.2B$	Stable	Stable	Unstable	Unstable	Unstable
$LDMK - 1.5B$	Unstable	Unstable	Unstable	Unstable	Unstable
$LDMK - 2B$	Unstable	Unstable	Unstable	Unstable	Unstable

30 FTT (corresponding to 150,000 iterations) on average 2% of C_s values hit the upper (positive) realizability bound and about the same number of C_s values hit the lower (negative) realizability bound. With respect to the probe point P2, we observed corresponding hittings in about 0.4% of cases (again, the lower and upper bounds had about the same hitting rates).

First, this shows that the PDF-realizable LDMK model, which is not combined with the realizability bounds Eq. (10), is almost always realizable, but it is not strictly always realizable, which may promote instability. Second, these results do also indicate that the stress-realizable LDMK (the LDMK combined with the use of the realizability bounds Eq. (10)) is stable. It should be noted that the realizability of the LDMK model was also studied in the entire flow field (not shown here), and we came to the same conclusions. We also considered the effect of the simulation time step Δt on the realizability of the model. We found that an increasing simulation time step increases the fluctuations of C_s values such that the probability of hitting the bounds increase as well.

To study the effectiveness of the realizability bounds on the stability of the dynamic model we applied bounds that are 1.2, 1.5, and 2 times bigger than the regular bounds Eq. (10). We refer to these models as LDMK-1.2B, LDMK-1.5B and LDMK-2B,

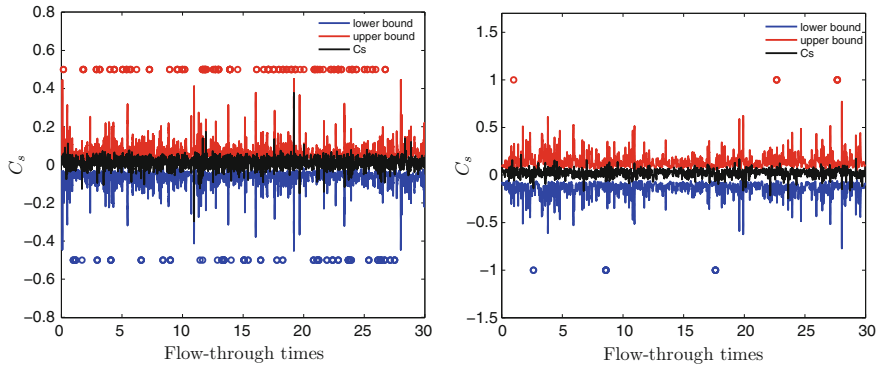

Fig. 2 Time histories of C_s and its realizability bounds in LDMK simulations for the last 30 flow-through times at two different probe points P1 (left) and P2 (right). The red and blue circles indicate the times at which C_s values hit the upper and lower realizabilty bounds, respectively. The time step is $\Delta t = 0.002$

respectively. Table 1 summarizes the stability analysis results for the LDMK and its extended bound versions. We called a model stable when it does not become unstable for 100 FTT. We see that the LDMK is strongly stable for a wide range of time steps $\Delta t = 10^{-3}$–10^{-2}, which corresponds to CFL numbers ranging between 0.1–0.8. But the LDMK-1.2B is only stable for $\Delta t = (0.001, 0.002)$, and the LDMK-1.5B and LDMK-2B are unstable even for small CFL numbers (small Δt). First, it can be concluded that the use of realizability bounds makes the LDMK model fully realizable, and second, a model that is not stress-realizable can become unstable. It seems that realizability is a required and sufficient condition for stability.

5 Conclusions

A PDF-realizable LES model has significant advantages compared to non-realizable LES models. In particular, it has been shown for several flows that a PDF-realizable models enabled stable simulations without any model parameter clipping or averaging. But for complex flows, a PDF-realizable model can suffer from instability. On the other hand, we found that consistency with underlying stochastic model equations does not necessarily ensure the realizability of the SGS stress tensor. Therefore, we derived a condition for the realizability of the SGS stress tensor which makes the LES model fully realizable. Stability analysis performed for a high Reynolds number separated flow shows that the new fully realizable LES model (the LDMK) is always stable for a wide range of CFL numbers. It is found that strict realizability (PDF-realizability and stress-realizability) ensures the stability of the model. A model that is not stress-realizable can become unstable.

Acknowledgements The authors would like to acknowledge support through NASA's NRA research opportunities in aeronautics program (Grant No. NNX12AJ71A) and support from the National Science Foundation (DMS-CDS&E-MSS, Grant No. 1622488). We are very thankful for computational resources provided by the Wyoming Advanced Research Computing Center [13] and the Wyoming-NCAR Alliance [14].

References

1. Germano, M., Piomelli, U., Moin, P., Cabot, W.H.: A dynamic sub grid-scale eddy viscosity model. Phys. Fluids A **3**, 1760–1765 (1991)
2. Heinz, S.: Realizability of dynamic subgrid-scale stress models via stochastic analysis. Monte Carlo Methods Appl. **14**, 311–329 (2008)
3. Heinz, S., Gopalan, H.: Realizable versus non-realizable dynamic subgrid-scale stress models. Phys. Fluids **24**, 115105 (2012)
4. Gopalan, H., Heinz, S., Stoellinger, M.: A unified RANS-LES model: computational development, accuracy and cost. J. Comput. Phys. **249**, 249–274 (2013)
5. Kazemi, E., Heinz, S.: Dynamic large eddy simulations of the Ekman layer based on stochastic analysis. Int. J. Nonlinear Sci. Numer. Simul. **17**, 77–98 (2016)

6. Girimaji, S.S.: A new perspective on realizability of turbulence models. J. Fluid Mech. **512**, 191–210 (2004)
7. Heinz, S.: On Fokker-Planck equations for turbulent reacting flows. Part 2. Filter density function for large eddy simulation. Flow Turbul. Combust. **70**, 153–181 (2003)
8. Heinz, S.: Statistical Mechanics of Turbulent Flows. Springer, Berlin (2003)
9. Heinz, S.: A dynamic nonlinear subgrid-scale stress model. Phys. Fluids **17**, 099101 (2005)
10. Heinz, S.: Unified turbulence models for LES and RANS, FDF and PDF simulations. Theor. Comput. Fluid Dyn. **21**, 99–118 (2007)
11. Vreman, B., Geurts, B., Kuerten, H.: Realizability conditions for the turbulent stress tensor in large-eddy simulation. J. Fluid Mech. **278**, 351–362 (1994)
12. Mokhtarpoor, R.S., Heinz, S., Stoellinger, M.: Dynamic unified RANS-LES simulations of high Reynolds number separated flows. Phys. Fluids **28**, 095101 (2016)
13. Advanced Research Computing Center. Mount Moran: IBM System X cluster. Laramie, WY: University of Wyoming, http://n2t.net/ark:/85786/m4159c. Accessed 25 June 2017
14. Computational and Information Systems Laboratory. Yellowstone: IBM iDataPlex System (Wyoming-NCAR Alliance). Boulder, CO: National Center for Atmospheric Research, http://n2t.net/ark:/85065/d7wd3xhc. Accessed 25 June 2017

The Dynamic Smagorinsky Model in 512^3 Pseudo-Spectral LES of Decaying Homogeneous Isotropic Turbulence at Very High Re_λ

O. Thiry, G. Winckelmans and M. Duponcheel

1 Introduction

We consider the large-eddy simulation (LES) of turbulent flows, in the classical view where no regular explicit filtering is added to the truncation/projection due to the LES grid. The truncation of the complete field u_i (experimental or from direct numerical simulation, DNS) to the much coarser LES grid corresponds to the incomplete LES field and is noted $\overline{u}_i$. Assuming perfect numerics, the "effective subgrid-scales (SGS) stress" is then obtained as $\overline{\sigma}_{ij}^{\text{SGS}} = \overline{\overline{u}_i \overline{u}_j} - \overline{u_i u_j}$: i.e., the product of LES quantities minus the product of complete quantities, and further truncated to the LES grid. The divergence of that stress (i.e., the "effective SGS force") represents the effect of the removed scales on the LES scales. As there is no information beyond the LES grid cutoff, the SGS stress (or the SGS force) can only be modeled.

The Smagorinsky model [8] is one of the oldest ones used to parameterize, in a simple way, the effect of the deviatoric part of the SGS stress tensor on the scales captured by the LES grid. It reads:

$$\overline{\tau}_{ij}^{\text{SGS}} \overset{\text{model}}{=} 2\,\nu^{\text{SGS}} \overline{S}_{ij} \ ,$$

where $\overline{S}_{ij}$ is the strain rate tensor of the LES field and $\nu^{\text{SGS}} = C_S\,\Delta^2\,|\overline{S}|$ is the "effective SGS viscosity" (with $|\overline{S}| \overset{\text{def}}{=} \sqrt{2\overline{S}_{kl}\overline{S}_{kl}}$ the characteristic inverse time scale and Δ the characteristic size of the local grid). The value $C_S \simeq (0.3)^3 = 0.027$ is obtained

O. Thiry · G. Winckelmans (✉) · M. Duponcheel
Institute of Mechanics, Material and Civil Engineering (iMMC), Université catholique de Louvain (UCL), 1348 Louvain-la-Neuve, Belgium
e-mail: gregoire.winckelmans@uclouvain.be

O. Thiry
e-mail: olivierthiry1@gmail.com

M. Duponcheel
e-mail: matthieu.duponcheel@uclouvain.be

M. V. Salvetti et al. (eds.), *Direct and Large-Eddy Simulation XI*,
ERCOFTAC Series 25, https://doi.org/10.1007/978-3-030-04915-7_17

from an a priori analysis when assuming decaying homogeneous isotropic turbulence (DHIT) at high Re_λ, LES on a uniform grid (hence $\Delta = h$) with cutoff well within the inertial range, and a Kolmogorov constant $C_K \simeq 1.6$, see [5] (and [6] for a complete analysis).

Based on the assumed similarity of the SGS stress at two levels (the LES grid level, and a coarser "test level" obtained by additional projection of the LES field onto a coarser grid), a dynamic procedure was then further proposed that allows to obtain the optimal value of the C_S coefficient of the model [4]. Good success was obtained with that "dynamic version of the Smagorinsky model" (DSM) by comparing LES results to DNS results (hence necessarily at moderately high Re): first in DHIT, next in turbulent channel flow, and then on more complex flows.

In DHIT, the least-square error minimization used in the dynamic procedure can be volume averaged, and the obtained C_S is then solely a function of time. The Smagorinsky model is also only "weakly non linear" in DHIT, because the LES field $|\overline{S}|$ is quite uniform: the expected spectral behavior is thus that of an quasi-linear SGS viscosity model.

When using classical numerical methods (finite differences, finite volumes, etc.), there are dispersion errors; even for methods without numerical dissipation (i.e., with energy conserving discretization of the convective term). When using a de-aliased pseudo-spectral method, as here, there are neither dispersion errors nor diffusion errors (except the small numerical diffusion caused by the time integrator). Such a method can, of course, only be used for flows with homogeneous directions such as DHIT; yet, such study is instructive as it allows to investigate how the SGS model really performs when using an "essentially perfect" numerical method.

The spectral behavior of various SGS models (Smagorinsky model, filtered Smagorinsky model, filtered structure function model, multiscale models that solely act on the high wavenumbers part of the LES field, linear high order hyper-viscosity model) in DHIT was already studied in [2]: at moderate Re_λ (and then compared to a reference DNS); and then at very high Re_λ (not even defined, as LES run without molecular viscosity) and using large LES grids (128^3 and 256^3). A de-aliased pseudo-spectral method (energy conserving in the absence of molecular or SGS viscosity [3]) was used as the reference. Then a hybrid (i.e., Eulerian–lagrangian) "vortex particle-mesh" (also called "vortex-in-cell") method was also used: it solves the Navier–Stokes equations in the vorticity-velocity formulation, also has good properties (negligible numerical dispersion and dissipation) and also can be used for LES (using SGS models expressed in vorticity form). Those simulations were all done using the static approach: the coefficient of each model was calibrated so as to provide the desired global dissipation: that of the truncated DNS for the former case; that obtained using the Smagorinsky model with $C_S = 0.027$ for the latter case.

2 Present Investigation: Set Up and Results

In the present investigation, we revisit the Smagorinsky model with the de-aliased pseudo-spectral code, but using instead the dynamic procedure to determine C_S: thus the "dynamic Smagorinsky model" (DSM). We consider DHIT at very high Re_λ, and we use an even larger LES grid (512^3) than in [2]. The fundamental question is then: how does the DSM perform in such DHIT, relatively to the state of knowledge and theory?

The computational box is L^3 with $L = 2\pi$. The 1-D grid cutoff wavenumber is thus $k_c = \frac{\pi}{h} = 256$. When integrating in time the LES equations, we do not apply a spherical truncation after each time step to the modes with $k^2 = k_x^2 + k_y^2 + k_z^2 \geq k_c^2$. The test filter used in the dynamic procedure corresponds to a sharp Fourier cutoff of the modes with $\frac{k_c}{2} \leq |k_x|, |k_y|, |k_z| \leq k_c$. We also do not apply a spherical truncation when applying the test filter: the dynamic procedure is thus fully self-consistent as the cutoff test filter is similar to the cutoff filter corresponding to the LES grid.

We start from a theoretical energy spectrum, using random phases for the spectral modes. It then takes an initial transient (not shown) to reach LES of DHIT at statistical equilibrium. The time $t = 0$ is here a time when such a statistical equilibrium has been reached. We then measure global quantities at that time: the turbulent kinetic energy E_0 ($\simeq$0.689), the characteristic global velocity $U_0 = \sqrt{E_0}$ ($\simeq$0.830), the energy dissipation rate $\varepsilon_0 = -\frac{dE}{dt}\big|_0$ ($\simeq$0.752), the characteristic global length scale $\mathscr{L}_0 = \frac{U_0^3}{\varepsilon_0}$ ($\simeq$0.760), and the characteristic global time scale $t_0 = \frac{\mathscr{L}_0}{U_0}$ ($\simeq$0.915); those are used to make plots dimensionless. The Taylor micro-scale Reynolds number is defined as usual: $Re_\lambda = \sqrt{\frac{20}{3}\frac{E^2}{\varepsilon\nu}}$. As can be seen in Fig. 1, it is very high. The obtained statistical equilibrium is thus here also maintained for very long times (times much longer than the present LES), so long as the molecular viscosity remains negligible relatively to the SGS viscosity. As expected, the dynamically obtained C_S is very stable, and it slowly decreases in time. The obtained value is of the order of $C_s \simeq 0.0115$: less than half the value predicted by the simplified, a priori, theoretical analysis (that value is not an error: the predicted C_S at one time was cross-checked using two implementations, and codes, of the dynamic procedure run on the same LES field).

We also recall that, in DHIT, the energy E decays like t^{-n}; and hence the dissipation rate ε decays like $t^{-(n+1)}$. Values of n between 1.15 and 1.45 are reported in the literature; the study by [7] suggesting that the good quality data are consistent with $n \simeq 1.3$. One then also obtains that $\frac{1}{n} = \frac{d}{dt}\left(\frac{E}{\varepsilon}\right)$; which is here also used to measure the "effective n exponent" (noted n_e) of the present DSM LES. We here obtain that $n_e \simeq 1.5$, see Fig. 2 (the variations are due to computing the instantaneous derivative of $\frac{E}{\varepsilon}$, where $\varepsilon = -\frac{dE}{dt}$ is also computed instantaneously; they should not be taken as an "experimental range" of our LES). For comparison, the studies in [2], using static SGS models, gave $n_e \simeq 1.49$ for the Smagorinsky model (thus very close to the value obtained here using the DSM), $n_e \simeq 1.45$ for the structure function model, and $n_e \simeq 1.38$ for the regularized variational multiscale (RVM) model. As the exper-

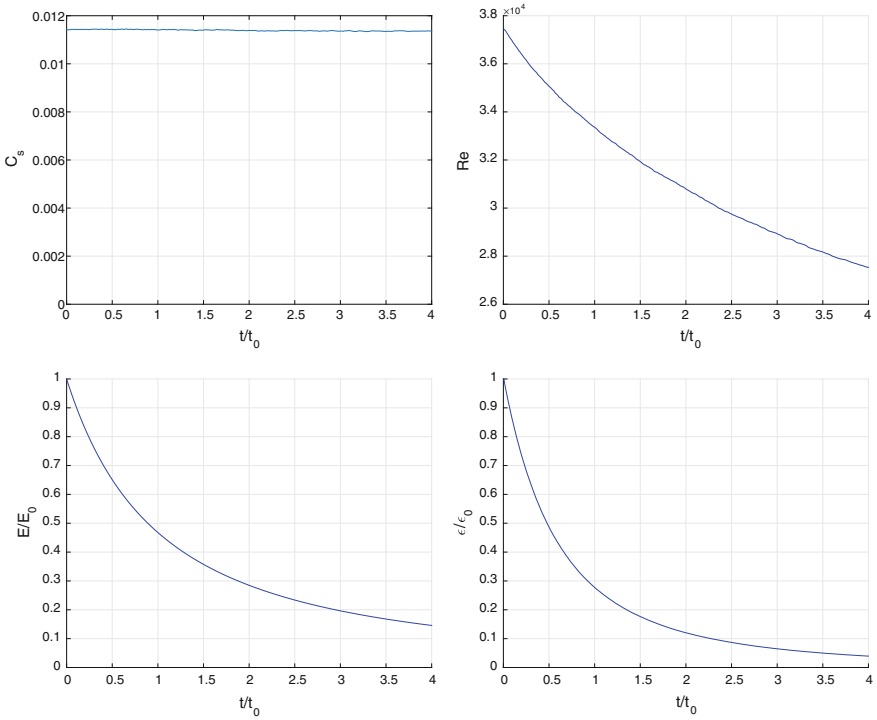

Fig. 1 Evolution of the dynamic coefficient C_S, of the Taylor micro-scale Reynolds number Re_λ, of the energy E (relatively to E_0) and of the energy dissipation rate ε (relatively to ε_0)

imental data used to measure n were at moderately high Re_λ, an interesting question arises as to a possibly higher value of n for DHIT at very high Re_λ.

The next investigation concerns the spectra. The energy spectra, made dimensionless using $E(k_c, t)$, collapse very well over the range $k \simeq 20$ to $k_c = 256$. So do the compensated energy spectra. We, of course, do not expect to recover a fully inertial $k^{-5/3}$ range all the way to the highest wavenumbers, as such behavior can only correspond to zero dissipation. The obtained spectra are however quite remarkable, see Fig. 2: we obtain an inertial behavior over a wide range of wavenumbers: from $k_{i,1} \simeq 30$ to $k_{i,2} \simeq 180$ ($\simeq 0.70\, k_c$). Even the rest of the spectrum, from $k_{i,2}$ all the way to k_c, is still quite good, as it does not depart much from the inertial range. To anyone experienced in LES, this additional "pseudo-inertial" behavior is quite remarkable (and, to our knowledge, not seen before in such LES of DHIT); it is also quite encouraging for the use of the DSM in LES of more complex flows.

The SGS model dissipation spectra are then also provided in Fig. 2, and with linear scale axes (the molecular viscosity dissipation spectrum, $\varepsilon^\nu(k, t) = 2\nu\, k^2\, E(k, t)$, is here relatively very small as the SGS dissipation overwhelms the molecular one). When made dimensionless using $L\, \varepsilon(t)$, those spectra are seen to collapse very well, over all wavenumbers. We have thus obtained the effective dissipation spectrum of

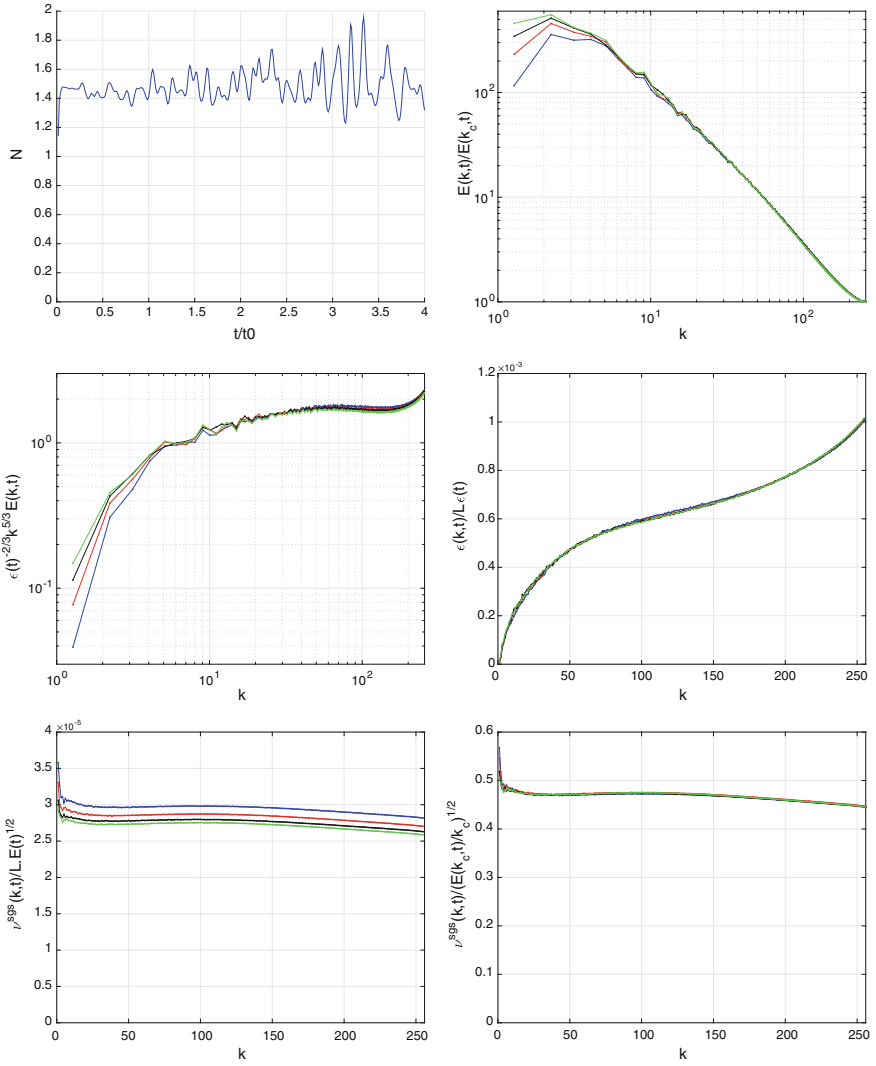

Fig. 2 Evolution of the effective n exponent. Dimensionless energy spectra, compensated energy spectra, SGS dissipation spectra, and effective spectral SGS viscosity (using two normalizations) at $t/t0 = 0, 4/3, 8/3$ and 4 (for the SGS viscosity normalized using $L\sqrt{E}$, $t/t_0 = 0$ corresponds to the top curve and $t/t_0 = 4$ to the bottom one)

such "DSM fluid in DHIT at very high Re_λ and run on a large LES grid". From that result, we can further compute the "effective spectral SGS viscosity" defined as $\varepsilon^{\text{SGS}}(k,t) \stackrel{\text{def}}{=} 2\,\nu^{\text{SGS}}(k,t)\,k^2\,E(k,t)$: see Fig. 2, also with linear scale axes. When made dimensionless using $\sqrt{\frac{E(k_c,t)}{k_c}}$, as also done in [1], the collapse is very good; whereas

it is clearly not that good when using $L\sqrt{E(t)}$. We also clearly observe the quasi-uniform value of the spectral SGS viscosity over all wavenumbers; confirming the quasi-linear behavior of the Smagorinsky model in such DHIT (i.e., re-running the LES using a uniform SGS viscosity would lead to very similar results). Finally, we stress that such DSM LES is basically "under-resolved with respect to its own dynamic SGS viscosity". Indeed, if we compute the "velocity gradient mesh Reynolds number" based on that SGS viscosity, we obtain $Re_h^{\text{SGS}} = \frac{|\bar{S}|h^2}{\nu^{\text{SGS}}} = \frac{1}{C_s} \simeq 87$: this is too high for properly resolving such SGS viscosity effects on such grid. This also explains why the end of the spectrum does not plunge down more at the highest wavenumbers; here, it instead sort of prolongates the inertial range into a pseudo-inertial range all the way to k_c.

3 Conclusion

The DSM has been investigated in pseudo-spectral LES of decaying HIT (DHIT) at very high Re_λ and using a large 512^3 LES grid. The asymptotic behavior has been reached, and the effective SGS dissipation spectrum has been obtained. The derived spectral SGS viscosity was confirmed to be essentially uniform over all wavenumbers; confirming the quasi-linear behavior of the DSM in LES of DHIT. Moreover, the obtained SGS viscosity value is such that the mesh Reynolds number based on it is too high to properly resolve the SGS viscosity effects on the LES grid; this leads to an energy spectrum where the true inertial range (here ending at $\simeq 0.70\,k_c$) is prolongated by a sort of "pseudo-inertial" range all the way to k_c.

References

1. Cholet, J.-P., Lesieur, M.: Parameterization of small scales of three-dimensional isotropic turbulence utilizing spectral closures. J. Atmos. Sci. **38**, 2747 (1981)
2. Cocle, R., Bricteux, L., Winckelmans, G.: Scale dependence and asymptotic very high Reynolds number spectral behavior of multiscale models. Phys. Fluids **21**, 085101 (2009)
3. Duponcheel, M., Orlandi, P., Winckelmans, G.: Time-reversibility of the Euler equations as a benchmark for energy conserving schemes. J. Comput. Phys. **227**(19), 8736–8752 (2008)
4. Germano, M., Piomelli, U., Moin, P., Cabot, W.H.: A dynamic subgrid-scale eddy-viscosity model. Phys. Fluids A **3**(7), 1760–1765 (1991)
5. Lilly, D.K.: On the application of the eddy viscosity concept in the inertial sub-range of turbulence. NACAR Manuscript 123, Boulder, CO (1966)
6. Meneveau, C., Lund, T.S.: The dynamic Smagorinsky model and scale-dependent coefficients in the viscous range of turbulence. Phys. Fluids **9**(12), 3932–3934 (1997)
7. Mohamed, M.S., LaRue, J.C.: The decay power law in grid-generated turbulence. J. Fluid Mech. **219**, 195 (1990)
8. Smagorinsky, J.: General circulation experiments with the primitive equations. Mon. Weather. Rev. **93**, 99–165 (1963)

Nonlinear Subgrid-Scale Models for Large-Eddy Simulation of Rotating Turbulent Flows

M. H. Silvis and R. Verstappen

1 Introduction

We consider large-eddy simulation of incompressible rotating turbulent flows. In large-eddy simulation one seeks to predict the large-scale behavior of turbulent flows without resolving all the relevant flow details. This is commonly done by supplementing the Navier–Stokes equations with an additional forcing term, a subgrid-scale model, aimed at representing the unresolved flow physics.

Rotating turbulent flows form a challenging test case for large-eddy simulation due to the presence of the Coriolis force. The Coriolis force conserves the total kinetic energy, while also redistributing it. More specifically, the Coriolis force transports kinetic energy from small to large scales of motion, leading to the formation of large-scale anisotropic structures [7]. Many subgrid-scale models for large-eddy simulation are, however, (primarily) designed to parametrize the dissipative nature of turbulent flows, ignoring transport processes.

We therefore consider a subgrid-scale model consisting of two terms. The first term is of eddy viscosity type. It is linear in the rate-of-strain tensor and it is used to represent the dissipative behavior of turbulent flows. The second term is nonlinear in the local velocity gradient and is aimed at parametrizing nondissipative processes, such as those due to rotation. We study the behavior of this nonlinear subgrid-scale model in large-eddy simulations of a spanwise-rotating plane-channel flow.

The structure of this paper is as follows. The nonlinear subgrid-scale model for large-eddy simulation is introduced in Sect. 2. Then, Sect. 3 describes the details of spanwise-rotating plane-channel flows, of which we perform large-eddy simulations in Sect. 4. Finally, conclusions are drawn in Sect. 5.

M. H. Silvis (✉) · R. Verstappen
University of Groningen, Nijenborgh 9, 9747 AG Groningen, The Netherlands
e-mail: m.h.silvis@rug.nl

R. Verstappen
e-mail: r.w.c.p.verstappen@rug.nl

M. V. Salvetti et al. (eds.), *Direct and Large-Eddy Simulation XI*,
ERCOFTAC Series 25, https://doi.org/10.1007/978-3-030-04915-7_18

2 Nonlinear Subgrid-Scale Models

Large-eddy simulations of incompressible rotating turbulent flows can be described by

$$\frac{\partial u_i}{\partial x_i} = 0, \quad \frac{\partial u_i}{\partial t} + \frac{\partial}{\partial x_j}(u_i u_j) = -\frac{1}{\rho}\frac{\partial p}{\partial x_i} + 2\nu\frac{\partial}{\partial x_j}S_{ij} - 2\varepsilon_{ijk}\Omega_j u_k - \frac{\partial}{\partial x_j}\tau_{ij}^{\text{mod}}. \tag{1}$$

Here, u_i indicates the x_i-component of the large-scale velocity field, while p represents the modified large-scale pressure, including the centrifugal force. The density and kinematic viscosity are labeled ρ and ν, respectively. The rate-of-strain and rate-of-rotation tensors of the large-scale velocity field are defined according to

$$S_{ij} = \frac{1}{2}\left(\frac{\partial u_i}{\partial x_j} + \frac{\partial u_j}{\partial x_i}\right), \qquad \Omega_{ij} = \frac{1}{2}\left(\frac{\partial u_i}{\partial x_j} - \frac{\partial u_j}{\partial x_i}\right), \tag{2}$$

while Ω_i represents the rotation rate of the frame of reference about the x_i-axis. Without loss of generality we will assume that the axis of rotation is the x_3-axis, i.e., $\Omega_i = \delta_{i3}\Omega_3$. The Einstein summation convention is assumed for repeated indices. Note that we consider large-eddy simulation without explicit filtering. Hence, no bars or tildes indicating a filtering operation appear in the above equations.

We model the deviatoric part of the subgrid-scale stress tensor with the following nonlinear model,

$$\tau^{\text{mod,dev}} = -2\nu_e S + \mu_e(S\Omega - \Omega S). \tag{3}$$

The first term on the right-hand side of (3), the usual eddy viscosity term, is used to parametrize dissipative processes in turbulent flows. The second term, that is nonlinear in the velocity gradient, is added because it is perpendicular to the rate-of-strain tensor. Therefore, it does not directly contribute to the subgrid dissipation and it represents energy transport. As this term contains the rate-of-rotation tensor, it has "a particular potential for [the simulation of] rotating flows" [4].

We propose to define the eddy viscosity, ν_e, and the transport coefficient, μ_e, by

$$\nu_e = (C_\nu\delta)^2\frac{1}{2}|S|f_{\text{VS}}^3, \tag{4}$$

$$\mu_e = C_\mu\delta^2\frac{1}{4}f_{\text{VS}}^4. \tag{5}$$

Here, C_ν and C_μ are the model constants, δ represents the subgrid characteristic length scale and the magnitude of the rate of strain is defined as $|S| = \sqrt{\text{tr}(S^2)}$. The nondimensionalized vortex stretching magnitude,

$$f_{\text{VS}} = \frac{|S\boldsymbol{\omega}|}{|S||\boldsymbol{\omega}|}, \tag{6}$$

is used to enforce the proper near-wall scaling behavior of the modeled stresses and to make sure that the model vanishes in two-component flows [6]. The vorticity vector is given by $\omega_i = -\varepsilon_{ijk}\Omega_{jk}$.

3 Spanwise-Rotating Plane-Channel Flow

To study the vortex-stretching-based nonlinear subgrid-scale model of (3) we consider large-eddy simulations of a spanwise-rotating plane-channel flow. Such a flow can be characterized using the friction Reynolds and rotation numbers,

$$Re_\tau = \frac{u_\tau d}{\nu}, \qquad Ro^+ = \frac{2\Omega_3 d}{u_\tau}, \tag{7}$$

where u_τ is the friction velocity and d represents the channel half-width.

The rotation number, Ro^+, determines the behavior of a spanwise-rotating plane-channel flow. For small rotation numbers the flow is mostly turbulent, although a (small) laminar region may appear close to one of the walls. As the rotation number increases, the laminar flow portion grows, until, for significant rotation numbers, the flow fully laminarizes. The mean velocity profile of a spanwise-rotating plane-channel flow exhibits a characteristic linear slope (proportional to Ro^+) corresponding to the unstable (turbulent) part of the flow, while a parabolic profile emerges on the stable (laminar) side. Laminarization is further characterized by the decay of the Reynolds stresses. Refer to the work by Grundestam et al. [3] for more information about spanwise-rotating plane-channel flows.

4 Numerical Results

We studied the vortex-stretching-based nonlinear subgrid-scale model of (3) by performing direct and large-eddy simulations of a spanwise-rotating plane-channel flow with $Re_\tau \approx 395$ and a moderate rotation number, $Ro^+ = 100$. These simulations were performed using an incompressible Navier–Stokes solver employing a kinetic-energy-conserving spatial discretization of finite-volume type [9]. As such, the kinetic energy in the simulations was by construction conserved by convection, by the Coriolis force and by the nonlinear term of the subgrid-scale model.

The flow domain in the simulations had dimensions $2\pi d \times 2d \times \pi d$ and was taken periodic in the streamwise (x_1) and spanwise (x_3) directions. The large-eddy and direct numerical simulations were, respectively, performed on 32^3 and $128 \times 256 \times 128$ grids that were stretched in the wall-normal direction.

The large-eddy simulations made use of the vortex-stretching-based eddy viscosity model ((3) with $C_\mu = 0$) and the vortex-stretching-based nonlinear subgrid-scale model of ((3) with $C_\mu \neq 0$). The value of the eddy viscosity constant was estimated

to be $C_v \approx 0.59$ by requiring that the average dissipation due to the model matches the average dissipation of the Smagorinsky model [6]. The value of the transport coefficient of the nonlinear model, C_μ, was subsequently tuned to obtain the best prediction of the Reynolds stresses. As is commonly done, the subgrid characteristic length scale was defined using the local grid size, $\delta = (\Delta x_1 \Delta x_2 \Delta x_3)^{1/3}$ [2]. Refer to the literature for an overview of alternative (flow-dependent) definitions of this length scale [5, 8]. Results from direct numerical simulations and from large-eddy simulations without a subgrid-scale model serve as reference data.

Figure 1 shows the mean velocity profile, and the behavior of the Reynolds shear stress and spanwise Reynolds stress as obtained from the simulations. Since we consider traceless subgrid-scale models, only the deviatoric (anisotropic) part of the Reynolds stresses is considered. These results are further compensated by the average contribution from the subgrid-scale model [10].

The typical features of the flow in a spanwise-rotating plane-channel are clearly visible: the mean velocity profile exhibits a linear slope on the unstable side of the channel, while the Reynolds shear stress attains small values on the stable side. Contrary to what could be expected, the stresses do not exactly vanish on the stable side of the channel, which is most likely due to the occurrence of turbulent bursts [1].

The large-eddy simulations with the vortex-stretching-based subgrid-scale models slightly improve the prediction of the peak height and slope of the mean velocity profile when compared to the no-model result. Corresponding behavior can be observed in the Reynolds shear stress. These results indicate that the vortex-stretching-based eddy viscosity and nonlinear subgrid-scale models behave well.

The added value of these subgrid-scale models becomes clear when considering the deviatoric part of the streamwise Reynolds stress. Large-eddy simulations without a subgrid-scale model fail to predict that quantity, supporting the conclusion that subgrid-scale modeling is indeed justified, even at low friction Reynolds numbers [5]. Large-eddy simulations with the vortex-stretching-based eddy viscosity model provide a reasonable prediction of the streamwise Reynolds stress. This prediction is improved when including the nonlinear model term, as can most clearly be seen on the unstable side of the channel ($0 \leq x_2/d \leq 1$). Similar conclusions can be drawn for the deviatoric part of the wall-normal and spanwise Reynolds stresses (not shown). Thus, the addition of the nonlinear term to an eddy viscosity model leads to an improved prediction of the Reynolds stress anisotropy, while maintaining a reasonable prediction of the mean velocity profile and the Reynolds shear stress.

5 Conclusions

We focused on the construction of subgrid-scale models for large-eddy simulation of rotating turbulent flows. Rotating turbulent flows are characterized by the presence of the conservative Coriolis force. These flows form a challenging test case for large-eddy simulations using eddy viscosity models, as these subgrid-scale models are mainly aimed at capturing the dissipative behavior of turbulent flows. We therefore

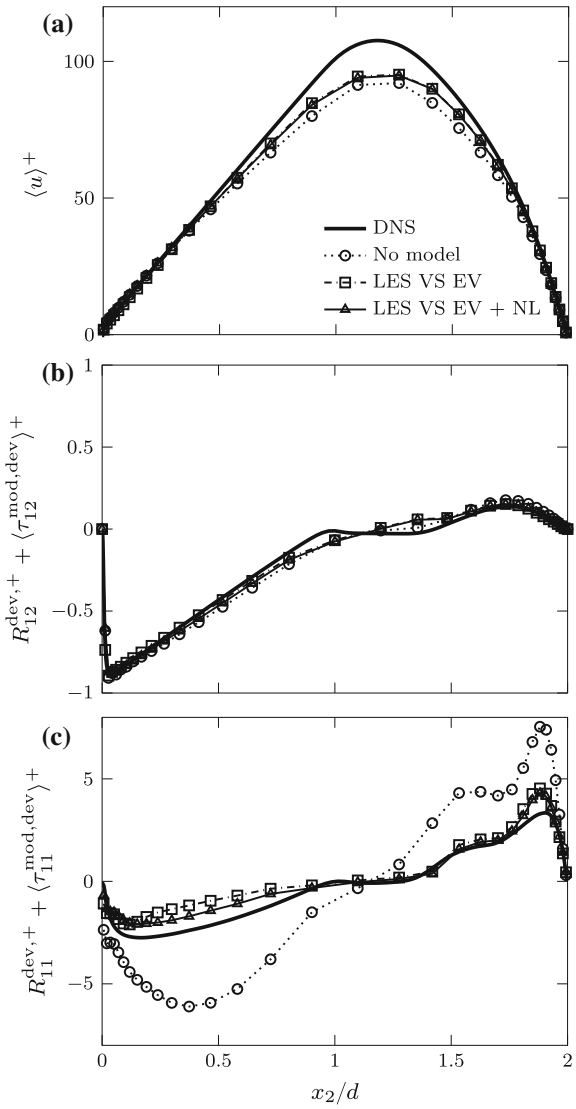

Fig. 1 **a** Mean velocity profile, **b** Reynolds shear stress compensated by the model contribution and **c** deviatoric part of the streamwise Reynolds stress compensated by the model contribution, as obtained from large-eddy simulations (LES) of a spanwise-rotating plane-channel flow at $Re_\tau \approx 395$ and $Ro^+ = 100$ on a 32^3 grid. Simulations were performed without a subgrid-scale model (*dotted line, circles*), with the vortex-stretching-based eddy viscosity (VS EV) model ((3) with $C_\nu \approx 0.59$ and $C_\mu = 0$) (*dashed line, squares*), and with the vortex-stretching-based nonlinear (VS EV + NL) subgrid-scale model ((3) with $C_\nu \approx 0.59$ and $C_\mu = 5$) (*solid line, triangles*). Results from direct numerical simulations (DNS) on a $128 \times 256 \times 128$ grid are shown as reference (*thick solid line*). The quantities on the vertical axis are nondimensionalized using the friction velocity

proposed a new subgrid-scale model that, in addition to a dissipative eddy viscosity term, contains a nondissipative nonlinear term. This subgrid-scale model was successfully tested in large-eddy simulations of a spanwise-rotating plane-channel flow. In particular, we showed how the addition of the nonlinear model term leads to an improved prediction of the Reynolds stress anisotropy. These findings confirm the potential of a nondissipative nonlinear model term for large-eddy simulation of rotating turbulent flows.

Acknowledgements Part of this research was conducted during the Center for Turbulence Research (CTR) Summer Program 2016 at Stanford University. The authors thank the CTR for its hospitality and financial support. This work is part of the research programme Free Competition in the Physical Sciences with project number 613.001.212, which is financed by the Netherlands Organisation for Scientific Research (NWO).

References

1. Brethouwer, G.: Statistics and structure of spanwise rotating turbulent channel flow at moderate Reynolds numbers. J. Fluid Mech. **828**, 424–458 (2017). https://doi.org/10.1017/jfm.2017.526
2. Deardorff, J.W.: Numerical study of three-dimensional turbulent channel flow at large Reynolds numbers. J. Fluid Mech. **41**, 453–480 (1970). https://doi.org/10.1017/S0022112070000691
3. Grundestam, O., Wallin, S., Johansson, A.V.: Direct numerical simulations of rotating turbulent channel flow. J. Fluid Mech. **598**, 177–199 (2008). https://doi.org/10.1017/S0022112007000122
4. Marstorp, L., Brethouwer, G., Grundestam, O., Johansson, A.V.: Explicit algebraic subgrid stress models with application to rotating channel flow. J. Fluid Mech. **639**, 403–432 (2009). https://doi.org/10.1017/S0022112009991054
5. Silvis, M.H., Trias, F.X., Abkar, M., Bae, H.J., Lozano-Durán, A., Verstappen, R.W.C.P.: Exploring nonlinear subgrid-scale models and new characteristic length scales for large-eddy simulation. In: Proceedings of the Summer Program, pp. 265–274. Center for Turbulence Research, Stanford University (2016)
6. Silvis, M.H., Remmerswaal, R.A., Verstappen, R.: Physical consistency of subgrid-scale models for large-eddy simulation of incompressible turbulent flows. Phys. Fluids **29**, 015105 (2017). https://doi.org/10.1063/1.4974093
7. Thiele, M., Müller, W.-C.: Structure and decay of rotating homogeneous turbulence. J. Fluid Mech. **637**, 425–442 (2009). https://doi.org/10.1017/S002211200999067X
8. Trias, F.X., Gorobets, A., Silvis, M.H., Verstappen, R., Oliva, A.: A new subgrid characteristic length for turbulence simulations on anisotropic grids. Phys. Fluids **29**, 115109 (2017). https://doi.org/10.1063/1.5012546
9. Verstappen, R.W.C.P., Veldman, A.E.P.: Symmetry-preserving discretization of turbulent flow. J. Comput. Phys. **187**, 343–368 (2003). https://doi.org/10.1016/S0021-9991(03)00126-8
10. Winckelmans, G.S., Jeanmart, H., Carati, D.: On the comparison of turbulence intensities from large-eddy simulation with those from experiment or direct numerical simulation. Phys. Fluids **14**, 1809–1811 (2002). https://doi.org/10.1063/1.1466824

A New Subgrid Characteristic Length for LES

F. X. Trias, A. Gorobets and A. Oliva

1 Introduction

Large-eddy simulation (LES) equations result from applying a spatial commutative filter, with filter length Δ, to the Navier–Stokes equations

$$\partial_t \overline{\boldsymbol{u}} + (\overline{\boldsymbol{u}} \cdot \nabla)\,\overline{\boldsymbol{u}} = \nu \nabla^2 \overline{\boldsymbol{u}} - \nabla \overline{p} - \nabla \cdot \tau(\overline{\boldsymbol{u}}), \quad \nabla \cdot \overline{\boldsymbol{u}} = 0, \tag{1}$$

where $\overline{\boldsymbol{u}}$ is the filtered velocity and $\tau(\overline{\boldsymbol{u}})$ is the subgrid stress (SGS) tensor and aims to approximate the effect of the under-resolved scales, i.e. $\tau(\overline{\boldsymbol{u}}) \approx \overline{\boldsymbol{u} \otimes \boldsymbol{u}} - \overline{\boldsymbol{u}} \otimes \overline{\boldsymbol{u}}$. Most of the difficulties in LES are associated with the presence of walls where SGS activity tends to vanish. Therefore, apart from many other relevant properties, LES models should properly capture this feature [1]. Numerically, this implies an accurate resolution of the near-wall region which results on a high computational cost at high Reynolds numbers. Accurate estimations of these costs, including the temporal scales, are given in the next section. They lead to the conclusion that, in the near future, the feasibility of wall-resolved LES (WRLES) at high-Reynolds numbers should rely on substantial cost reductions in the viscous wall region. This may be achieved by decreasing the number of grid points using high-order schemes or/and using larger time-steps (implicit-explicit time-integration?). Furthermore, it is

F. X. Trias (✉) · A. Gorobets · A. Oliva
Heat and Mass Transfer Technological Center, Technical University of Catalonia, C/Colom 11, 08222 Terrassa, Spain
e-mail: xavi@cttc.upc.edu

A. Gorobets
e-mail: andrey@cttc.upc.edu; cherepock@gmail.com

A. Oliva
e-mail: oliva@cttc.upc.edu

A. Gorobets
Keldysh Institute of Applied Mathematics, 4A, Miusskaya Sq., Moscow 125047, Russia

M. V. Salvetti et al. (eds.), *Direct and Large-Eddy Simulation XI*,
ERCOFTAC Series 25, https://doi.org/10.1007/978-3-030-04915-7_19

also concluded that the mesh anisotropy increases with the Reynolds numbers. This represents an additional challenge for WRLES. In this context, a novel definition of subgrid characteristic length, Δ, is proposed with the aim to answer the following research question: *can we find a simple and robust definition of Δ that minimizes the effect of mesh anisotropies on the performance of SGS models?*

2 Wall-Resolved LES: Computational Costs and Mesh Anisotropies

In his 1979 pioneering paper, Chapman [2] estimated the number of grid points for an LES of turbulent boundary layers with and without wall modeling as

$$N_{wm} \sim Re_{L_x}^{2/5} \quad \text{and} \quad N_{wr} \sim Re_{L_x}^{9/5}, \tag{2}$$

respectively, where $Re_{L_x} = UL_x/\nu$ is the Reynolds number based on the free-stream velocity, U, and the flat plate length in the streamwise direction, L_x. To reach these scalings, Chapman used the following skin friction correlation

$$c_f = 0.045 Re_\delta^{-1/4}, \tag{3}$$

where $Re_\delta = U\delta/\nu$ is the Reynolds number based on the boundary layer thickness, $\delta(x)$, and assumed a seventh-power velocity distribution law, i.e. $u \sim y^{1/7}$. The latter leads to an exact relation between the momentum thickness, θ, and δ given by $\theta = 7\delta/72$. Then, using Eq. (3) and $c_f = 2d\theta/dx$ leads to

$$\frac{\delta}{x} = 0.37 Re_x^{-1/5} \quad \text{and} \quad c_f = 0.0577 Re_x^{-1/5}, \tag{4}$$

where $Re_x = Ux/\nu$ is the Reynolds number based on the streamwise distance from the leading edge, x. From these equations it is relatively easy to show the scaling given by Chapman in Eq. (2). Recently, Choi and Moin [3] gave new estimations based on a more accurate skin friction correlation for high Reynolds numbers ($10^6 \leq Re_x \leq 10^9$) given by

$$c_f = 0.020 Re_\delta^{-1/6}. \tag{5}$$

In this case, the analysis leads to

$$N_{wm} \sim Re_{L_x} \quad \text{and} \quad N_{wr} \sim Re_{L_x}^{13/7}. \tag{6}$$

These findings are extensively used to emphasize the prohibitive costs of LES without wall-modeling and the necessity, in the foreseeable future, of wall-modeling techniques for applications at high Reynolds numbers. However, under some assumptions, these scalings are only valid for a range of Re_x; moreover, they do not

include the costs associated with temporal scales which eventually can be even more restrictive due to the inherent difficulty (impossibility?) to parallelize LES equations in time. These two issues are addressed in the next paragraphs. Let us consider a general power-law for the skin friction coefficient

$$c_f = aRe_\delta^\beta. \tag{7}$$

Then, following the above explained reasonings it leads to

$$\frac{\delta}{x} = bRe_x^\alpha \quad \text{and} \quad c_f = 7b/36(\alpha+1)Re_x^\alpha, \tag{8}$$

where $b = (36a(1-\beta)/7)^{1/(1-\beta)}$ and $\alpha = \beta/(1-\beta)$. Notice that with $a = 0.045$ and $\beta = -1/4$ it leads to the Chapman's scalings given in Eqs. (4). Following the same reasonings as in Ref. [3] the number of grid points in the outer layer and the viscous wall region can be estimated as follows

$$N^{out} = n_x n_y n_z \left(\frac{1}{b^2(1+2\alpha)}\right) \frac{L_z}{L_x} Re_{L_x}^{-2\alpha} \left(\left(\frac{Re_{L_x}}{Re_{x_0}}\right)^{1+2\alpha} - 1\right), \tag{9}$$

$$N^{vis} = \frac{n_y^w}{\Delta x_w^+ \Delta z_w^+} \frac{7b}{72} \frac{L_z}{L_x} Re_{L_x}^{2+\alpha} \left(1 - \left(\frac{Re_{x_0}}{Re_{L_x}}\right)^{1+\alpha}\right), \tag{10}$$

where $n_x n_y n_z$ is the number of grid points to resolve the cubic volume $\delta^3(x)$ in the outer layer (typically in the range $10^3 - 10^4$ [3]), L_z is the spanwise length and x_0 is the initial streamwise location where the skin friction correlation (8) holds. Then, Δx_w^+, Δz_w^+ and n_y^w are respectively the grid resolutions (in wall units) and the number of grid points in the wall-normal direction in the viscous wall region, i.e. $0 \leq y^+ \lesssim l_y^+ \approx 100$. Typical values for WRLES lead to $n_y^w/(\Delta x_w^+ \Delta z_w^+) \sim 0.01$ [3]. This analysis can be extended giving estimations of the number of time-steps for the outer layer and the viscous wall region

$$N_t^{out} = \frac{N_{TU} n_x}{bC_{conv}} Re_{L_x} Re_{x_0}^{-(1+\alpha)}; \quad N_t^{vis} = \max(N_{t_{diff}}^{vis}, N_{t_{conv}}^{vis}), \tag{11}$$

where

$$N_{t_{diff}}^{vis} = \frac{N_{TU}}{C_{diff}} \frac{7b}{72} \frac{\alpha+1}{(\Delta y_w^+)^2} Re_{L_x} Re_{x_0}^\alpha; \quad N_{t_{conv}}^{vis} = \frac{N_{TU}}{C_{conv}} \sqrt{\frac{7b}{72} \frac{\alpha+1}{(\Delta x_w^+)^2}} Re_{L_x} Re_{x_0}^{\alpha/2}, \tag{12}$$

where N_{TU} is the number of time-units, L_x/U, to be computed; C_{conv} and C_{diff} are the convective and diffusive constants in the CFL condition. In summary, combining Eqs. (9)–(11) leads to the following costs for LES with and without wall-modeling:

$$N_t^{wm} N_{wm} \sim Re_{L_x}^2 \quad \text{and} \quad N_t^{wr} N_{wr} \sim Re_{L_x}^{3+\alpha}. \tag{13}$$

Nowadays, this represents the main limitation of (wall-resolved) LES. On the other hand, it is also possible to give estimations of the mesh anisotropy, i.e. $\Delta x/\Delta y$, in the boundary layer. Namely, in the viscous sublayer, $\max(\Delta x/\Delta y) = \Delta x_w^+/\Delta y_w^+ \approx 50 - 100$ is not expected to change with the Reynolds number. However, in the overlap region ($y^+ \gtrsim 50$, $y/\delta < 0.1$) where control volumes of the viscous wall region and the outer layer ($y^+ \gtrsim 50$) must be smoothly connected, the grid anisotropy can be estimated as

$$\left(\frac{\Delta x}{\Delta y}\right)_{overlap} \approx \frac{(\Delta x)_{out}}{(\Delta y)_{vis}} = \frac{\delta}{n_x}\frac{n_y^w}{l_y}, \tag{14}$$

where l_y is the size of the viscous wall region, i.e. $l_y^+ = u_\tau l_y/\nu \approx 50 - 100$. Recalling the definition of the skin friction coefficient, $c_f = \tau_w/(\rho U^2/2)$, and using the relation given in Eq. (8), an expression in terms of Re_x can be obtained

$$\left(\frac{\Delta x}{\Delta y}\right)_{overlap} \approx \frac{1}{\sqrt{2}}\frac{n_y^w}{n_x}\frac{b}{l_y^+}\sqrt{\frac{7b}{36}(\alpha+1)}\,Re_x^{1+3\alpha/2}. \tag{15}$$

Therefore, for any value of $\alpha > -2/3$ the mesh anisotropy, $\Delta x/\Delta y$, tends to grow with Re_x. Taking typical values for $n_x = 10$, $n_y^w = 20$ and $l_y^+ = 100$, and using, respectively, the skin friction coefficient correlations used by Chapman [2], i.e. $\alpha = -1/5$ and $b = 0.37$, and Choi and Moin [3], i.e. $\alpha = -1/7$ and $b = 0.17$, it simplifies

$$\left(\frac{\Delta x}{\Delta y}\right)_{overlap}^{Chapman} \approx 0.00125 Re_x^{7/10}; \quad \left(\frac{\Delta x}{\Delta y}\right)_{overlap}^{Choi\&Moin} \approx 4.047 \times 10^{-4} Re_x^{11/14}. \tag{16}$$

Just as examples, this leads to mesh anisotropies of 19.9 and 20.96 at $Re_x = 10^6$, and 99.7 and 127.97 at $Re_x = 10^7$. Therefore, numerical techniques that behave robustly in such meshes are of great interest. In this context, a new definition of the subgrid characteristic length in presented and tested in the next section.

3 A New Definition of the Subgrid Characteristic Length

Because of its inherent simplicity and robustness, the eddy-viscosity assumption, $\tau(\overline{\boldsymbol{u}}) \approx -2\nu_e S(\overline{\boldsymbol{u}})$, is by far the most used closure model for LES equations (1). Then, the eddy-viscosity, ν_e, is usually modeled as follows

$$\nu_e = (C_m \Delta)^2 D_m(\overline{\boldsymbol{u}}). \tag{17}$$

In the last decades most of the research has focused on either the calculation of the model constant, C_m (e.g. the dynamic modeling approach), or the development of

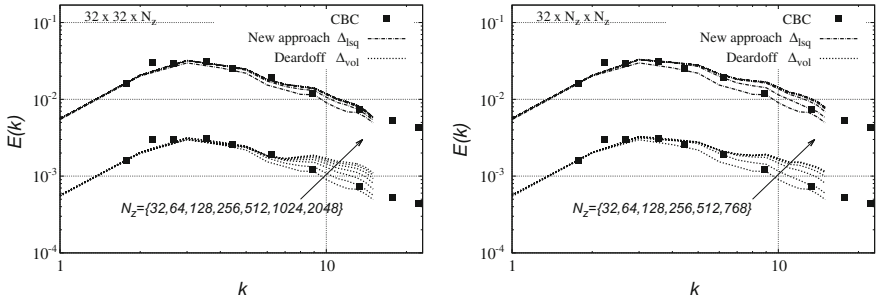

Fig. 1 Energy spectra for decaying isotropic turbulence corresponding to the experiment of Comte-Bellot and Corrsin [10]. Results obtained with the new definition Δ_{lsq} proposed in Eq. (18) are compared with the classical definition proposed by Deardorff given in Eq. (20). For clarity, latter results are shifted one decade down

more appropriate model operators $D_m(\overline{\boldsymbol{u}})$ (e.g. WALE [4], Vreman's [5], Verstappen's [6], σ-model [7], S3PQR [1],…). Surprisingly, little attention has been paid on the computation of the subgrid characteristic length, Δ, which is also a key element of any eddy-viscosity model. Despite the fact that in some situations it may provide very inaccurate results, three and a half decades later, the approach proposed by Deardorff [8], i.e., the cube root of the cell volume (see Eq. 20), is by far the most widely used to computed the subgrid characteristic length, Δ. Its inherent simplicity and applicability to unstructured meshes is probably a very good explanation for that. With the aim to overcome the limitations of the Deardorff definition, the following definition is proposed [9]

$$\Delta_{\text{lsq}} = \sqrt{\frac{\mathsf{G}_\Delta \mathsf{G}_\Delta^T : \mathsf{G}\mathsf{G}^T}{\mathsf{G}\mathsf{G}^T : \mathsf{G}\mathsf{G}^T}}, \tag{18}$$

where $\mathsf{G} \equiv \nabla\overline{\boldsymbol{u}}$, $\mathsf{G}_\Delta \equiv \mathsf{G}\Delta$ and $\Delta \equiv \text{diag}(\Delta x, \Delta y, \Delta z)$ (for a Cartesian grid). This definition of Δ fulfills a set of desirable properties. Namely, it is locally defined and well bounded, $\Delta x \leq \Delta_{\text{lsq}} \leq \Delta z$ (assuming that $\Delta x \leq \Delta y \leq \Delta z$). Moreover, it is sensitive to flow orientation and applicable to unstructured meshes (by simply replacing the tensor by the Jacobian of the mapping from the physical to the computational space). This definition (18) is obtained minimizing (in a least-squares sense) the difference between the leading terms of the Taylor series of the SGS tensor, $\tau(\overline{\boldsymbol{u}})$, for an isotropic and an anisotropic filters lengths; namely,

$$\tau(\overline{\boldsymbol{u}}) = \frac{\Delta^2}{12}\mathsf{G}\mathsf{G}^T + \mathscr{O}(\Delta^4); \quad \tau(\overline{\boldsymbol{u}}) = \frac{1}{12}\mathsf{G}_\Delta \mathsf{G}_\Delta^T + \mathscr{O}(\Delta^4). \tag{19}$$

Results displayed in Fig. 1 correspond to the classical experimental results obtained by Comte-Bellot and Corrsin [10]. LES results have been obtained using the Smagorinsky model, for a set of (artificially) stretched meshes. Regarding the

spatial discretization of the eddy-viscosity models, the approach proposed in Ref. [11] has been used. Results for pancake-like meshes with $32 \times 32 \times N_z$ and $N_z = \{32, 64, 128, 256, 512, 1024, 2048\}$ are displayed in Fig. 1 (top): for increasing values of N_z the results obtained using the Deardorff definition, given in

$$\Delta_{\text{vol}} = (\Delta x \Delta y \Delta z)^{1/3}, \tag{20}$$

diverge. This is because the value of Δ tends to vanish and, therefore, the subgrid-scale models switch off. This is not the case for the definition of Δ proposed in this work. Instead, results rapidly converge for increasing values of N_z. A similar behavior is observed in Fig. 1 (bottom) for pencil-like meshes with $32 \times N_z \times N_z$ and $N_z = \{32, 64, 128, 256, 512, 768\}$. Therefore, the proposed definition of the subgrid characteristic length, Δ_{lsq}, seems to minimize the effect of mesh anisotropies on the performance of subgrid-scale models.

4 Concluding Remarks

Estimations of the computational costs for LES with and without wall modeling were originally given by Chapman [2], and more recently, by Choi and Moin [3]. Here, these estimations have been extended by the general power-law of the skin friction coefficient given in Eq. (7), including the temporal scales. Furthermore, it has been found that the mesh anisotropy in the overlap region increases with the Reynolds number (see Eq. 15). This represents an additional challenge for LES. In this context, a novel definition of subgrid characteristic length, Δ, is proposed with the aim to answer the following research question: *can we find a simple and robust definition of Δ that minimizes the effect of mesh anisotropies on the performance of SGS models?* In this regard, we consider the novel definition of Δ_{lsq} proposed in Eq. (18) as a very good candidate. Results for decaying isotropic turbulence show that the proposed definition of Δ seems to minimize the effect of mesh anisotropies on the performance of subgrid scale models.

Acknowledgements This work has been financially supported by the *Ministerio de Economía y Competitividad*, Spain (ENE2017-88697-R), and a *Ramón y Cajal* postdoctoral contract (RYC-2012-11996). Calculations have been performed on the IBM MareNostrum supercomputer at the Barcelona Supercomputing Center. The authors thankfully acknowledge these institutions.

References

1. Trias, F.X., Folch, D., Gorobets, A., Oliva, A.: Building proper invariants for eddy-viscosity subgrid-scale models. Phys. Fluids **27**(6), 065103 (2015)
2. Chapman, D.R.: Computational aerodynamics development and outlook. AIAA J. **17**(12), 1293–1313 (1979)

3. Choi, H., Moin, P.: Grid-point requirements for large eddy simulation: chapman's estimates revisited. Phys. Fluids **24**(1), 011702 (2012)
4. Nicoud, F., Ducros, F.: Subgrid-scale stress modelling based on the square of the velocity gradient tensor. Flow Turbul. Combust. **62**(3), 183–200 (1999)
5. Vreman, A.W.: An eddy-viscosity subgrid-scale model for turbulent shear flow: algebraic theory and applications. Phys. Fluids **16**(10), 3670–3681 (2004)
6. Verstappen, R.: When does eddy viscosity damp subfilter scales sufficiently? J. Sci. Comput. **49**(1), 94–110 (2011)
7. Nicoud, F., Toda, H.B., Cabrit, O., Bose, S., Lee, J.: Using singular values to build a subgrid-scale model for large eddy simulations. Phys. Fluids **23**(8), 085106 (2011)
8. Deardorff, J.W.: Numerical study of three-dimensional turbulent channel flow at large Reynolds numbers. J. Fluid Mech. **41**, 453–480 (1970)
9. Trias, F.X., Gorobets, A., Silvis, M.H., Verstappen, R.W.C.P., Oliva, A.: A new subgrid characteristic length for turbulence simulations on anisotropic grids. Phys. Fluids **29**(11), 115109 (2017)
10. Comte-Bellot, G., Corrsin, S.: Simple Eulerian time correlation of full- and narrow-band velocity signals in grid-generated, isotropic turbulence. J. Fluid Mech. **48**, 273–337 (1971)
11. Trias, F.X., Gorobets, A., Oliva, A.: A simple approach to discretize the viscous term with spatially varying (eddy-)viscosity. J. Comput. Phys. **253**, 405–417 (2013)

On the Richardson Extrapolation of the Reynolds Stress with the Systematic Grid and Model Variation Method

M. Klein, G. Scovazzi and M. Germano

1 Introduction

The error assessment, and more generally the Uncertainty Quantification, of a Large Eddy Simulation is a difficult topic that presently is extensively explored. Apart the error-landscape approach [1], that requires a large number of simulations as well as a reference DNS, two are mainly the practical approaches to this problem, the first based on stochastic projections, and the second based on the Richardson extrapolation. The first approach addresses the sensitivity of LES to grid resolution and subgrid scale modeling by using a small number of LES simulations. They are considered as input random variables with a given probability distribution, and the propagation of the uncertainty through the computational model is quantified by using the generalized Polynomial Chaos (gPC) approach. This technique can be applied in two different ways: the intrusive approach is based on inserting the gPC decomposition of all stochastic quantities directly into the Navier-Stokes equations [2], while in the non intrusive approach the errors are directly projected over the orthogonal basis spanning the random space, without any modification of the deterministic solver [3].

The Richardson extrapolation [4], or the deferred approach to the limit [5], is based on the intuitive and appealing idea that if we combine two or more different simulations at different grid resolution, we could eliminate leading order error terms in an assumed error expansion. Its application to computational fluid dynamics has

M. Klein (✉)
Fakultät für Luft-und Raumfahrttechnik, Universität der Bundeswehr Muenchen,
Werner-Heisenberg-Weg 39, 85577 Neubiberg, Germany
e-mail: markus.klein@unibw.de

G. Scovazzi · M. Germano
Department of Civil and Environmental Engineering, Duke University,
Durham, NC 27708, USA
e-mail: guglielmo.scovazzi@duke.edu

M. Germano
e-mail: massimo.germano@duke.edu

M. V. Salvetti et al. (eds.), *Direct and Large-Eddy Simulation XI*,
ERCOFTAC Series 25, https://doi.org/10.1007/978-3-030-04915-7_20

been pioneered by Roache [6] and can be applied both as a postprocessing technique and an error estimator. Its extension to LES presents some specific problems [7], due to the interaction of the discretization error with the subgrid scale model contribution. Another important peculiarity of the application of the Richardson extrapolation to LES is due to the chaotic nature of the numerical results. They are averaged in time, and the extrapolation is usually applied to the statistical mean extracted by postprocessing procedures.

The quantities that are usually extrapolated, both in order to improve the computational results and to estimate the related errors, are the long time averages of the velocity components and the Reynolds stresses. The application of the Richardson extrapolation to the mean velocities is straightforward, but its extension to the Reynolds stresses is not so simple. First of all we have to distinguish in the reconstruction of the statistical Reynolds stresses starting from a LES database, two distinct contributions: the resolved part, directly given by the filtered velocity components, and the subgrid scale contribution, in some cases explicitly provided by the subgrid model. The trace of the Reynolds stresses is two times the turbulent kinetic energy, a very important quantity both from the practical point of view and as an indicator of the quality of LES [7].

In order to estimate the discretization error and the subgrid scale model uncertainty in a large eddy simulation, a Systematic Grid and Model Variation has been recently proposed by Klein [7]. As in the case of the error-landscape approach, and the non intrusive stochastic method, it requires some different simulations at different grid length and modeling constants but their number is limited to three. As such this method seems more practical when the complexity of the case requires too much time for an extended multisimulation as required by different UQ methods. In this paper we will explore in more detail the fundamentals of this approach, in particular as regards the extrapolation of the Reynolds stresses.

2 The Operational Systematic Grid and Model Variation Method

The key idea of the Richardson extrapolation [4] is to consider a numerical calculation, provided by a numerical code, as an analytic function, possibly very complex, of some parameters introduced by the discretization, typically the grid length. We remark an interesting analogy with the key idea that sixty years later is applied by Leonard [8] to the formalization of the Large Eddy Simulation. In this last case we assume that an under-resolved numerical computation can be formally represented as a convolution in the physical space operated by an analytic, possibly very complex, explicit filter. In both cases, at the very beginning of two capital advancements of the applied research, we have a similar attitude. In this paper we would like to connect these two approaches. Ideally we will interpret the Richardson extrapolation operationally, as a defiltering procedure that should provide the best that can be extracted

by a multigrid large eddy estimation. In a sense we try to couple the Leonard filtering and the Richardson extrapolation in a joint filtering-defiltering approach.

In order to be more precise as regards the operational procedure proposed, we will apply here the new method to a particular Richardson extrapolation recently proposed by Klein [7] in order to estimate the discretization error and the subgrid scale model uncertainty in a Large Eddy Simulation, the Systematic Grid and Model Variation method. Let us indicate with $\mathscr{F}_1$, $\mathscr{F}_2$ and $\mathscr{F}_3$ three filtering operators associated to three large eddy simulations at different grid resolution and modeling factor, and let us indicate with $\mathscr{I}$ the identity operator. The operational interpretation of the SGMV method can be written as

$$\mathscr{I} = c_1\mathscr{F}_1 + c_2\mathscr{F}_2 + c_3\mathscr{F}_3 \tag{1}$$

where

$$c_1 + c_2 + c_3 = 1 \tag{2}$$

and in a sense should represent the approximate deconvolution operated by the Richardson extrapolation to the three LES simulations. We will further assume that this relation can also be applied to Reynolds stresses. Following this idea and using $\mathscr{F}_i = \langle\cdot\rangle_i$ we can write

$$\begin{aligned} u_i &= c_1\langle u_i\rangle_1 + c_2\langle u_i\rangle_2 + c_3\langle u_i\rangle_3 \\ u_iu_j &= c_1\langle u_iu_j\rangle_1 + c_2\langle u_iu_j\rangle_2 + c_3\langle u_iu_j\rangle_3 \end{aligned} \tag{3}$$

and we finally obtain

$$\begin{aligned} R_{ij} &= c_1R_{1,ij} + c_2R_{2,ij} + c_3R_{3,ij} \\ &+ c_1\overline{\tau_{1,ij}} + c_2\overline{\tau_{2,ij}} + c_3\overline{\tau_{3,ij}} \\ &+ c_1c_2\left(\overline{\langle u_i\rangle_1} - \overline{\langle u_i\rangle_2}\right)\left(\overline{\langle u_j\rangle_1} - \overline{\langle u_j\rangle_2}\right) \\ &+ c_2c_3\left(\overline{\langle u_i\rangle_2} - \overline{\langle u_i\rangle_3}\right)\left(\overline{\langle u_j\rangle_2} - \overline{\langle u_j\rangle_3}\right) \\ &+ c_3c_1\left(\overline{\langle u_i\rangle_3} - \overline{\langle u_i\rangle_1}\right)\left(\overline{\langle u_j\rangle_3} - \overline{\langle u_j\rangle_1}\right) \end{aligned} \tag{4}$$

where R_{ij} is the extrapolated Reynolds stress

$$R_{ij} = \overline{u_iu_j} - \overline{u}_i\overline{u}_j \tag{5}$$

$R_{\alpha,ij}$, $\tau_{\alpha,ij}$ are the resolved Reynolds stresses and the subgrid stresses associated to the three LES simulations

$$\begin{aligned} R_{\alpha,ij} &= \overline{\langle u_i\rangle_\alpha\langle u_j\rangle_\alpha} - \overline{\langle u_i\rangle_\alpha}\ \overline{\langle u_j\rangle_\alpha} \\ \tau_{\alpha,ij} &= \langle u_iu_j\rangle_\alpha - \langle u_i\rangle_\alpha\langle u_j\rangle_\alpha \qquad , \qquad \alpha = 1,2,3 \end{aligned} \tag{6}$$

and where the overline stands for the statistical average. We see that three different contributions concur to the reconstruction of the Reynolds stresses. The first T_{res} is due to the resolved stresses at the three different simulations, the second T_{sgs} is due to the averaged subgrid stresses, null in the case of a no-model LES, and finally we have some new terms T_{diff} that depend explicitly on the differences between the statistical mean values of the velocity components in the three different simulations. The first term is the usual one, while the second and the third terms are relatively new, and their importance should be verified in specific tests.

It seems to be worth remarking that the above formalism covers the LES error assessment of the full Reynolds stress tensor in a systematic manner. The formula for turbulent kinetic energy can be derived straightforward from Eq. 4. Furthermore the method is not limited to a three grid study as discussed here. It could as well be applied to a two (or more) grid study like the concept proposed in [10]. For clarity, it is briefly mentioned that the Systematic Grid and Model Variation approach has been suggested in the context of LES using implicit filtering. For an implicit LES (i.e. without an explicit sgs model) the classical Richardson extrapolation, i.e. a two-grid study would be more suitable.

3 Extrapolation of the Reynolds Stress in the LES of a Plane Jet. Preliminary Results

The method outlined above has been tested for a plane turbulent jet. The configuration is identical to the setup described in [9] except that here Re = 10000 and consequently a higher resolution is required. Three simulations form the basis of the extrapolation approach in this work: a standard LES solution, a LES solution with a grid coarsened by a factor of two in each direction and a LES solution with a doubled Smagorinsky parameter. It is assumed that numerical and modelling error scale as $n = 2$ respectively $m = 4/3$. The coefficients c_1, c_2, c_3 have been calculated based on the suggestion in [7].

Earlier studies on LES error assessment have mostly been focused on turbulent kinetic energy [10] or mean velocities [7]. Hence, it will be interesting to analyse the possibility of estimating the shear stress error in the LES of a plane jet i.e. the component R_{13} in the present setup. The shear stress vanishes at the centerline of the jet. Figures 1, 2 and 3 therefore shows lateral plots of the quantities under consideration at two different axial positions. The quantity $R_{DNS,13} - R_{1,13}$ refers to the difference between DNS and standard LES solution, whereas $T_{res} - R_{1,13}$ refers to the estimated error in shear stress prediction based on resolved quantities. Transition and breakup of plane jets are very sensitive to resolution and model viscosity. As a result of this, the breakup point in the three simulations is shifted to some extent, resulting in different jet widths at the same axial location (see Fig. 1). Nevertheless the magnitude of the shear stress error is captured qualitatively well. The extrapolated subgrid contribution T_{sgs} and the term based on differences of resolved quantities

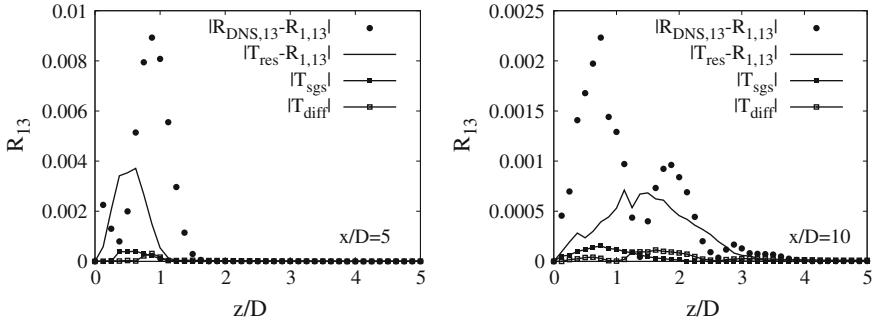

Fig. 1 Absolute error in shear stress prediction for a plane turbulent jet at two different axial locations $x/D = 5$, $x/D = 10$. $R_{DNS,13} - R_{1,13}$ refers to the difference between DNS and standard LES solution. $T_{res} - R_{1,13}$ refers to the estimated error in shear stress prediction based on extrapolated resolved quantities using the SGMV three grid study. T_{sgs}, T_{diff} are the extrapolated new terms shown in Eq. (4)

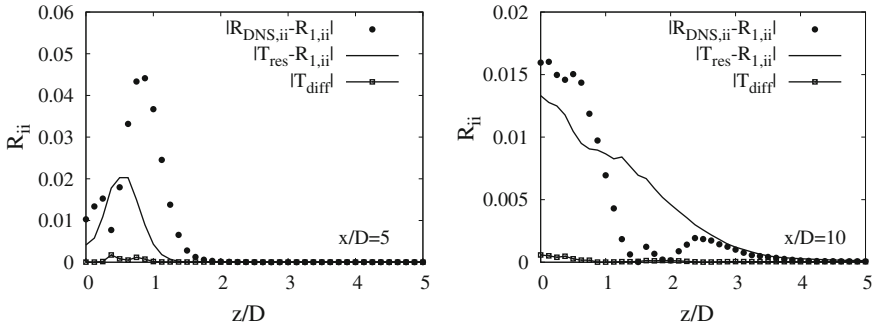

Fig. 2 Absolute error when predicting the trace of the Reynolds stresses for a plane turbulent jet at two different axial locations $x/D = 5, x/D = 10$. $R_{DNS,ii} - R_{1,ii}$ refers to the difference between DNS and standard LES solution. $T_{res} - R_{1,ii}$ refers to the estimated error in shear stress prediction based on extrapolated resolved quantities using the SGMV three grid study. T_{diff} is the extrapolated new term shown in Eq. (4). Note that the trace of the modelled sgs contribution T_{sgs} is zero

T_{diff} are relatively small for this configuration. For completeness the trace of the Reynolds stresses is shown in Figs. 2 and 3. Results from Fig. 2 are based on a three grid study whereas results from Fig. 3 are based on a two grid study assuming the scaling exponents $n = m = 2$. The behavior observed in Figs. 2, 3 is qualitatively similar to Fig. 1. However, it is worth noting that under the assumption that the contribution T_{sgs} can be represented by the model actually used in the simulations the trace of this term vanishes in the context of the Smagorinsky model and is therefore not shown in Figs. 2, 3. Future research has to show if these new terms will help to improve the error assessment for other configurations.

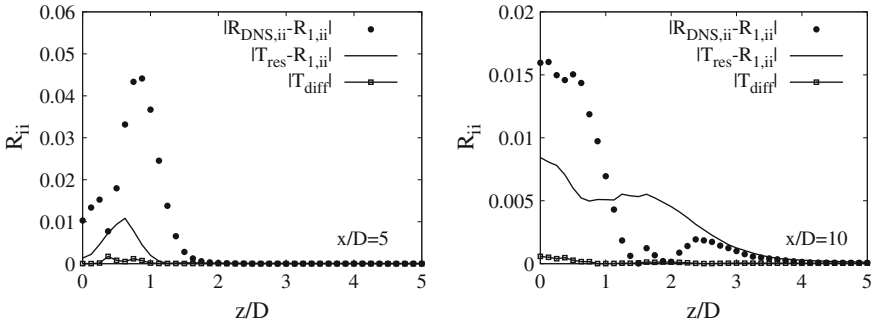

Fig. 3 Absolute error when predicting the trace of the Reynolds stresses for a plane turbulent jet at two different axial locations $x/D = 5, x/D = 10$. $R_{DNS,ii} - R_{1,ii}$ refers to the difference between DNS and standard LES solution. $T_{res} - R_{1,ii}$ refers to the estimated error in shear stress prediction based on extrapolated resolved quantities using a two grid study. T_{diff} is the extrapolated new term shown in Eq. (4). Note that the trace of the modelled sgs contribution T_{sgs} is zero

4 Conclusions

A new operational Richardson extrapolation applied to the SGMV method in order to reconstruct the Reynolds stress associated to three LES simulations is proposed. The main difference with the standard reconstruction consists in two new terms, and their importance is tested in the case of a plane turbulent jet. Preliminary results show that in this case their contribution is small but reasonable. The extrapolation of the resolved shear stress works qualitatively well. Different Reynolds numbers and different turbulent flows will be examined in the future.

References

1. Klein, M., Meyers, J., Geurts, B.J.: Assessment of LES quality measures using the error landscape. In: Meyers, J., et al. (eds.) Quality and Reliability of Large-Eddy Simulations, pp. 131–142. Springer, Berlin (2008)
2. Knio, O.M., Le Maître, O.P.: Uncertainty propagation in CFD using polynomial chaos decomposition. Fluid Dyn. Res. **38**, 616–640 (2006)
3. Meldi, M., Salvetti, M.V., Sagaut, P.: Quantification of errors in large-eddy simulations of a spatially evolving mixing layer using polynomial chaos. Phys. Fluids **24**, 035101–035125 (2012)
4. Richardson, L.F.: The Approximate Arithmetical Solution by finite differences of physical problems involving differential equations, with an application to the stresses In a Masonry dam. Philos. Trans. R. Soc. Lond. Ser. A **210**, 307–357 (1910)
5. Richardson, L.F., Gaunt, J.A.: The deferred approach to the limit. Philos. Trans. R. Soc. Lond. Ser. A **226**, 299–361 (1927)
6. Roache, P.: Quantification of uncertainty in computational fluid dynamics. Annu. Rev. Fluid. Mech. **29**, 123–160 (1997)

7. Klein, M.: An attempt to assess the quality of large eddy simulations in the context of implicit filtering. Flow Turbul. Combust. **75**, 131–147 (2005)
8. Leonard, A.: Energy cascade in Large-Eddy simulations of turbulent fluid flows. Adv. Geophys. **18A**, 237–248 (1974)
9. Klein, M., Sadiki, A., Janicka, J.: Investigation of the influence of the Reynolds number on a plane jet using direct numerical simulation. Int. J. Heat Fluid Flow **24**(6), 785–794 (2003)
10. Celik, I., Cehreli, Z., Yavuz, I.: Index of resolution quality for large eddy simulations. ASME J. Fluids Eng. **127**(5), 949–958 (2005)

Spatial Filtering for Reduced Order Modeling

L. C. Berselli, D. Wells, X. Xie and T. Iliescu

1 Introduction

Spatial filtering has been central in the development of large eddy simulation reduced order models (LES-ROMs) [9, 11, 12] and regularized reduced order models (Reg-ROMs) [4, 7, 10] for efficient and relatively accurate numerical simulation of convection-dominated fluid flows. In this paper, we perform a numerical investigation of spatial filtering. To this end, we consider one of the simplest Reg-ROMs, the Leray ROM (L-ROM) [4, 7, 10], which uses ROM spatial filtering to smooth the flow variables and decrease the amount of energy aliased to the lower index ROM basis functions. We also propose a new form of ROM differential filter [7, 10] and use it as a spatial filter for the L-ROM. We investigate the performance of this new form of ROM differential filter in the numerical simulation of a flow past a circular cylinder at a Reynolds number $Re = 760$.

L. C. Berselli (✉)
Dipartimento di Matematica, Università di Pisa, Pisa, Italy
e-mail: luigi.carlo.berselli@unipi.it

D. Wells
Department of Mathematics, University of North Carolina at Chapel Hill, Chapel Hill, NC, USA
e-mail: drwells@email.unc.edu

X. Xie
Computational and Applied Mathematics Group, Oak Ridge National Laboratory, Oak Ridge, TN, USA
e-mail: xiex@ornl.gov

T. Iliescu
Department of Mathematics, Virginia Tech, Blacksburg, VA, USA
e-mail: iliescu@vt.edu

M. V. Salvetti et al. (eds.), *Direct and Large-Eddy Simulation XI*,
ERCOFTAC Series 25, https://doi.org/10.1007/978-3-030-04915-7_21

2 Reduced Order Modeling

For the Navier–Stokes equations (NSE), the standard reduced order model (ROM) is constructed as follows: (i) choose modes $\{\boldsymbol{\varphi}_1, \ldots, \boldsymbol{\varphi}_d\}$, which represent the recurrent spatial structures of the given flow; (ii) choose the dominant modes $\{\boldsymbol{\varphi}_1, \ldots, \boldsymbol{\varphi}_r\}, r \leq d$, as basis functions for the ROM; (iii) use a Galerkin truncation $\mathbf{u}_r = \sum_{j=1}^{r} a_j \boldsymbol{\varphi}_j$; (iv) replace $\mathbf{u}$ with $\mathbf{u}_r$ in the NSE; (iii) use a Galerkin projection of NSE($\mathbf{u}_r$) onto the ROM space $X^r := \text{span}\{\boldsymbol{\varphi}_1, \ldots, \boldsymbol{\varphi}_r\}$ to obtain a low-dimensional dynamical system, which represents the ROM:

$$\dot{\mathbf{a}} = A\,\mathbf{a} + \mathbf{a}^\top B\,\mathbf{a}\,, \tag{1}$$

where $\mathbf{a}$ is the vector of unknown ROM coefficients and A, B are ROM operators; (iv) in an offline stage, compute the ROM operators; and (v) in an online stage, repeatedly use the ROM (for various parameter settings and/or longer time intervals).

3 ROM Differential Filter

The ROM differential filter is based on the classic Helmholtz filter that has been used to great success in LES for turbulent flows [3]. For a given velocity field $\mathbf{u}_r \in X^r$, the filtered flow field $\mathscr{F}(\mathbf{u}_r) \in X^f$, where X^f is a yet to be specified space of filtered ROM functions, is defined as the solution to the Helmholtz problem

$$\text{Find } \mathscr{F}(\mathbf{u}_r) \in X^f \text{ such that } \big((I - \delta^2 \Delta)\mathscr{F}(\mathbf{u}_r), \mathbf{v}\big) = (\mathbf{u}_r, \mathbf{v}), \text{ for all } \mathbf{v} \in X^f, \tag{2}$$

where δ is the radius of the ROM differential filter and Δ is the Laplacian. We consider two different versions for the choice of the range of the ROM differential filter X^f:

The FE Version. This version corresponds to $X^f = X^h$, where X^h is the finite element (FE) space: we seek the FE representation of $\mathscr{F}(\mathbf{u})$ and work in the full discrete space when calculating the filtered ROM vectors. The FE representation of $\mathscr{F}(\mathbf{u})$ suffices in applications because we use it to assemble the components of the ROM before time evolution: put another way, since filtering is a linear procedure, it only has to be done once and not in every ROM time step, e.g., for FE mass and stiffness matrices M and S we have that, modulo boundary condition terms,

$$a_j(M + \delta^2 S)\mathscr{F}\left(\boldsymbol{\varphi}_j\right) = a_j M \boldsymbol{\varphi}_j \Rightarrow (M + \delta^2 S)\sum_{j=1}^{r} a_j \mathscr{F}(\boldsymbol{\varphi}_j) = M \sum_{j=1}^{r} a_j \boldsymbol{\varphi}_j. \tag{3}$$

Hence, applying the differential filter to each proper orthogonal decomposition (POD) basis vector $\boldsymbol{\varphi}_j$, results in $\mathscr{F}(\boldsymbol{\varphi}_j) \notin X^r$. Due to the properties of the differ-

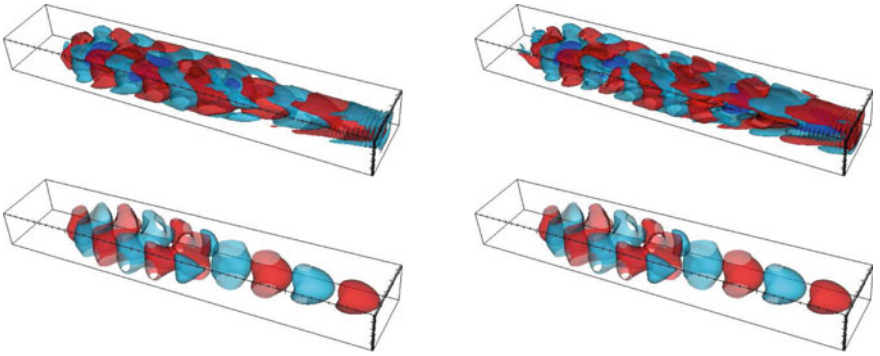

Fig. 1 Contour plots of y velocity of the first and fifth POD vectors from a 3D flow past a cylinder computation. We use the FE version of the ROM differential filter with $\delta = 0.5$. The unfiltered POD vectors are on top and the filtered are on the bottom. The choice $\delta = 0.5$ is too large for practical purposes, but demonstrates that filtering both removes kinetic energy (the isosurface s are smaller) and enlarges the scales of motion (e.g., the first POD vector goes from twelve structures to just nine)

ential filter (see Fig. 1), these new ROM functions will correspond to longer length scales and contain less energy.

The ROM Version. Alternatively, we can pick $X^f = X^r$, i.e., the ROM differential filter simply corresponds to an $r \times r$ Helmholtz problem.

$$(M_r + \delta^2 S_r)\mathscr{F}(\mathbf{a}) = M_r \mathbf{a}\,, \tag{4}$$

where M_r and S_r and the ROM mass and stiffness matrices, respectively, and $\mathbf{a}$ and $\mathscr{F}(\mathbf{a})$ are the POD coefficient vectors of $\boldsymbol{\varphi}_j$ and $\mathscr{F}(\boldsymbol{\varphi}_j)$, respectively. Here, unlike in the FE version, the range of the Helmholtz filter is X^r, so filtered solutions retain the weakly divergence free property.

Properties. Both versions of the ROM differential filter (2) share several appealing properties [2]. They act as spatial filters, since they eliminate the small scales (i.e., high frequencies) from the input. Indeed, the ROM differential filter (2) uses an elliptic operator to smooth the input variable. They also have a low computational overhead. For efficiency, the algorithmic complexity of any additional filters should be dominated by the $\mathscr{O}(r^3)$ cost in evaluating the nonlinearity. The ROM version is equivalent to solving an $r \times r$ linear system; since the matrix only depends on the POD basis, it may be factorized and repeatedly solved for a cost of $\mathscr{O}(r^2)$, which is also dominated by the cost of the nonlinearity. The FE version requires solving large FE linear systems, but these linear systems are solved in the offline stage; thus, the online computational cost of the FE version is negligible. Finally, we emphasize that the ROM differential filter uses an *explicit* length scale δ to filter the ROM solution vector. This is contrast to other types of spatial filtering, e.g., the ROM projection, which do not employ an explicit length scale.

4 Leray ROM

Jean Leray attempted to solve the NSEs in his landmark 1934 paper [6]. He was able to prove the existence of solutions for the modified problem

$$\mathbf{w}_t = \frac{1}{Re}\Delta\mathbf{w} - \mathscr{F}(\mathbf{w})\cdot\nabla\mathbf{w} - \nabla p, \tag{5}$$

where $\nabla\cdot\mathbf{w} = 0$, and $\mathscr{F}(\mathbf{w})$ is a convolution with a compact support mollifier with filter radius δ, or

$$\mathscr{F}(\mathbf{w}) = g_\delta \star \mathbf{w}. \tag{6}$$

For additional discussion on the properties of different filters see [2, 5, 8]. We approximate the convolution with the differential filter

$$\mathscr{F}(\mathbf{w}) = (\delta^2\Delta + 1)^{-1}\mathbf{w}. \tag{7}$$

In turbulence modeling, Leray's model is the basis for a class of stabilization methods called the Leray-α regularization models [5]. Leray's key observation was that the nonlinear term is the most problematic as it serves to transfer energy from resolved to unresolved scales.

The Leray model has been recently extended to the ROM setting [7, 10]. The resulting *Leray-ROM (L-ROM)* can be written as

$$(\mathbf{w}_r)_t = \frac{1}{Re}\Delta\mathbf{w}_r - \mathscr{F}(\mathbf{w}_r)\cdot\nabla\mathbf{w}_r - \nabla p, \tag{8}$$

which is the same as the Galerkin ROM up to the filtering of the advective term in the nonlinearity.

5 Numerical Results

We consider the flow past a cylinder problem with parabolic Dirichlet inflow conditions, no-slip boundary conditions on the walls of the domain, and zero tangential flow at the outflow. We compute snapshots by running the `deal.II` [1] step-35 tutorial program for $t \in [0, 500]$. We use a kinematic viscosity value of $1/100$, a circular cylinder with diameter of 1, and parabolic inflow boundary conditions with a maximum velocity of 7.6; this results in a Reynolds number $Re = 760$. We calibrate the filter radius δ by choosing a value for δ that gives the L-ROM the same mean kinetic energy as the original numerical simulation. Calibrating the ROM to this filter radius also improves accuracy in some structural properties: this amount of filtering removes enough kinetic energy that the phase portrait connecting the coefficients in

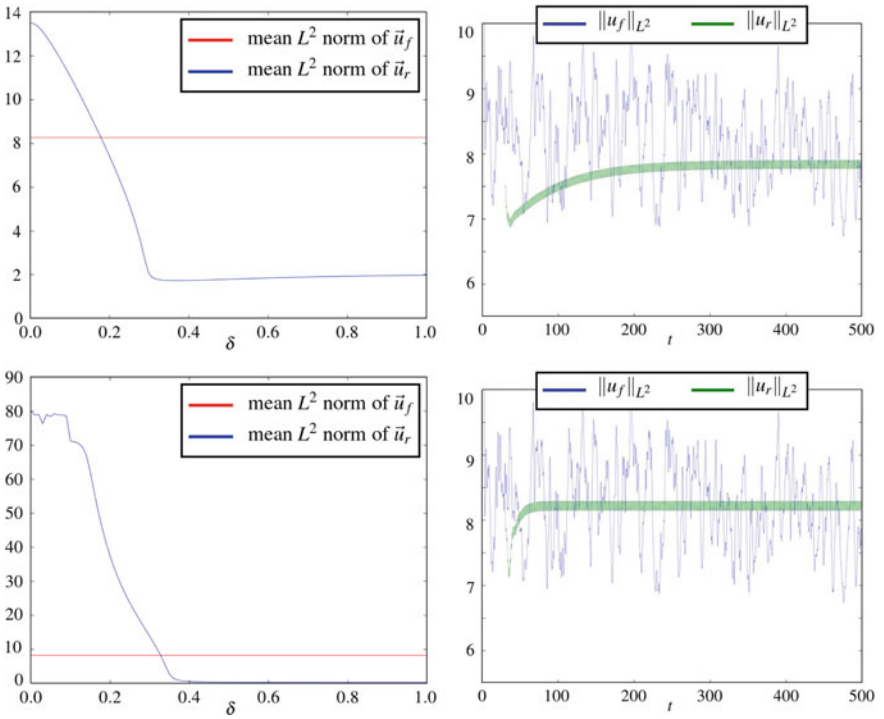

Fig. 2 3D flow past a cylinder, L-ROM (green) and DNS (blue). Mean (left column) and time evolution (right column) of the L^2 norm of the solution; $r = 6$ (top row) and $r = 20$ (bottom row). The time evolution of the L^2 norm of the solution (right column) is plotted for the optimal mean L^2 norm of the solution (left column): $\delta = 0.33$ for $r = 6$ (top row) and $\delta = 0.18$ for $r = 20$ (bottom row)

the ROM on the first and second POD basis functions are close to the values obtained by projecting the snapshots onto the POD basis over the same time interval.

Figure 2 displays the time evolution of the L^2 norm of the solutions of the L-ROM and DNS for $r = 6$ and $r = 20$. Figure 2 shows that, for the optimal δ value, the L-ROM-DF accurately reproduces the average, but not the amplitude of the time evolution of the L^2 norm of the DNS results for both $r = 6$ and $r = 20$. Figure 3 displays the phase portraits for the first and second POD coefficients of the L-ROM-DF and POD projection of DNS data for $r = 6$ and $r = 20$. Figure 3 shows that, for the optimal δ value, the L-ROM-DF yields moderately accurate results for $r = 6$ and accurate results for $r = 20$.

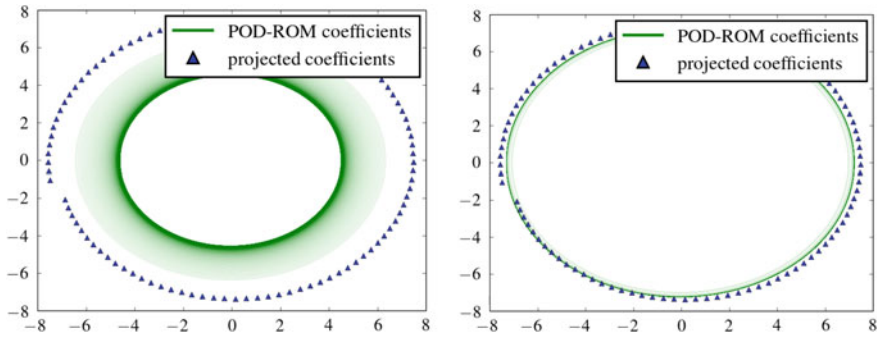

Fig. 3 3D flow past a cylinder, L-ROM-DF with optimal δ value (green) and POD projection of DNS data (blue). Phase portraits for a_1 and a_2; $r = 6$ (left) and $r = 20$ (right)

6 Conclusions

In this paper, we proposed a new type of ROM differential filter. We used this new filter with the L-ROM, which is one of the simplest Reg-ROMs. We tested this filter/ROM combination in the numerical simulation of a flow past a circular cylinder at Reynolds number $Re = 760$ for $r = 6$ and $r = 20$. The new type of ROM differential filter yielded encouraging numerical results, which were comparable to those for the standard type of ROM differential filter and better than those for the ROM projection [10]. We emphasize that a major advantage of the new type of ROM differential filter over the standard ROM differential filter is its low computational overhead. Indeed, since the filtering operation in the new type of ROM differential filter is performed at a FE level (as opposed to the ROM level, as it is generally done), the new filter is applied to each ROM basis function in the offline stage. In the online stage, the computational overhead of the new type of ROM differential filter is practically zero, since it simply amounts to using the filtered ROM basis functions computed and stored in the offline stage.

The first results for the new type of ROM differential filter are encouraging. We plan to perform a thorough investigation of the new filter, including a comparison with the standard form of the ROM differential filter and the ROM projection, in the numerical simulation of realistic flows [10, 12].

References

1. Bangerth, W., Davydov, D., Heister, T., Heltai, L., Kanschat, G., Kronbichler, M., Maier, M., Turcksin, B., Wells, D.: The `deal.ii` Library, Version 8.4. J. Numer. Math. **24**, 135–141 (2016)
2. Berselli, L.C., Iliescu, T., Layton, W.J.: Mathematics of Large Eddy Simulation of Turbulent Flows. Scientific Computation. Springer, Berlin (2006)
3. Germano, M.: Differential filters of elliptic type. Phys. Fluids **29**, 1757–1758 (1986)

4. Iliescu, T., Liu, H., Xie, X.: Regularized reduced order models for a stochastic Burgers equation. Int. J. Numer. Anal. Mod. **15**, 594–607 (2018)
5. Layton, W.J., Rebholz, L.G.: Approximate Deconvolution Models of Turbulence. Lecture Notes in Mathematics, vol. 2042. Springer, Berlin (2012)
6. Leray, J.: Sur le mouvement d'un liquide visqueux emplissant l'espace. Acta Math. **63**, 193–248 (1934)
7. Sabetghadam, F., Jafarpour, A.: α regularization of the POD-Galerkin dynamical systems of the Kuramoto–Sivashinsky equation. Appl. Math. Comput. **218**, 6012–6026 (2012)
8. Sagaut, P.: Large Eddy Simulation for Incompressible Flows. Scientific Computation. Springer, Berlin (2006)
9. Wang, Z., Akhtar, I., Borggaard, J., Iliescu, T.: Proper orthogonal decomposition closure models for turbulent flows: a numerical comparison. Comput. Methods Appl. Mech. Eng. **237–240**, 10–26 (2012)
10. Wells, D., Wang, Z., Xie, X., Iliescu, T.: An evolve-then-filter regularized reduced order model for convection-dominated flows. Int. J. Numer. Meth. Fluids **84**, 598–615 (2017)
11. Xie, X., Mohebujjaman, M., Rebholz, L.G., Iliescu, T.: Data-driven filtered reduced order modeling of fluid flows. SIAM J. Sci. Comput. **40**, B834–B857 (2018)
12. Xie, X., Wells, D., Wang, Z., Iliescu, T.: Approximate deconvolution reduced order modeling. Comput. Methods Appl. Mech. Eng. **313**, 512–534 (2017)

A RANS Assisted LES Approach

A. Abbà, M. Germano and M. Nini

1 Introduction

In the particular approach herein proposed, RANS and LES are combined in order to achieve a detailed description of turbulent flows without incurring in infeasible computational effort. This model is based on the hybrid filter approach proposed by Germano [5]. One of the most interesting point of this approach, is that the equations obtained by filtering Navier–Stokes equations, already include terms which are able to represent the interactions between RANS and LES regions. Therefore no further artificial terms are needed to allow the appropriate energy and momentum transfer between RANS and LES. This approach has already been tested [3, 8, 10] showing promising results.

The present proposal is quite different from a traditional hybrid RANS/LES approach. The main novelty preliminary presented in [7] and herein completely developed is represented by the reconstruction of Reynolds stress tensor, which avoid dependencies from the choice of RANS model and, potentially, could give significant benefits in terms of computational cost. Numerical simulations have been performed using a variational approach with a Discontinuous Galerkin (DG) space discretization, which allows high accuracy and parallelization efficiency [1, 9].

A. Abbà (✉) · M. Nini
Department of Aerospace Science and Technology,
Politecnico di Milano, Milan, Italy
e-mail: antonella.abba@polimi.it

M. Nini
e-mail: michele.nini@polimi.it

M. Germano
Department of Civil and Environmental Engineering,
Duke University, Durham, NC, USA
e-mail: mg234@duke.edu

M. V. Salvetti et al. (eds.), *Direct and Large-Eddy Simulation XI*,
ERCOFTAC Series 25, https://doi.org/10.1007/978-3-030-04915-7_22

2 Model Description

We apply Germano's hybrid filter [5] defined as:

$$\mathscr{H} = k\mathscr{F} + (1-k)\mathscr{E} \tag{1}$$

to the Navier–Stokes equations. In Eq. (1) $\mathscr{F}$ and $\mathscr{E}$ represent respectively the LES filter and the statistical operator (i.e. RANS operator) while k is a blending factor which can vary between 1, resulting in a pure LES, to 0 yielding a pure RANS. We observe that the hybrid filter does not commute with space and time derivative. Although in the following this hybrid filter will be applied to the compressible Navier-Stokes equations, the model will be used at low Mach number such that the effect of the density variations can be neglected. The extension of the model to full compressible flow will be object of future works.

Applying the filter to the convective term of the momentum equation and using the definition for the generalized central moment of second order [4], we arrive at

$$\tau_{ij}^{\mathscr{H}} = k\tau^{\mathscr{F}}(u_i, u_j) + (1-k)\tau^{\mathscr{E}}(u_i, u_j) + \mathscr{G}(u_i, u_j), \tag{2}$$

where $\tau^{\mathscr{F}}(u_i, u_j)$ is the LES stress, $\tau^{\mathscr{E}}(u_i, u_j)$ is the RANS stress and

$$\mathscr{G}(u_i, u_j) = k(1-k)(\langle u_i\rangle_{\mathscr{F}} - \langle u_i\rangle_{\mathscr{E}})(\langle u_j\rangle_{\mathscr{F}} - \langle u_j\rangle_{\mathscr{E}}) \tag{3}$$

represents the Germano term, an additional stress peculiar of the hybrid filter approach [8]. The filtered velocity $\langle u\rangle_{\mathscr{F}}$ can be obtained from

$$\langle u_i\rangle_{\mathscr{F}} = \frac{\langle u_i\rangle_{\mathscr{H}} - (1-k)\langle u_i\rangle_{\mathscr{E}}}{k}, \tag{4}$$

and introducing Eq. (4) in Eq. (2) we get

$$\tau_{ij}^{\mathscr{H}} = k\tau^{\mathscr{F}}(u_i, u_j) + (1-k)\tau^{\mathscr{E}}(u_i, u_j) + \frac{1-k}{k}(\langle u_i\rangle_{\mathscr{H}} - \langle u_i\rangle_{\mathscr{E}})(\langle u_j\rangle_{\mathscr{H}} - \langle u_j\rangle_{\mathscr{E}}) \tag{5}$$

It is worth noting that Eq. (5) can be closed by means of two arbitrary RANS and LES models for $\tau^{\mathscr{F}}(u_i, u_j)$ and $\tau^{\mathscr{E}}(u_i, u_j)$ respectively. In this work we have used the anisotropic model for LES presented in [2] where the equivalent filter length is determined dynamically. Concerning the RANS stress, it is here reconstructed from the hybrid and LES stress tensor, as we discuss in the next paragraph.

2.1 RANS Reconstruction

Applying the properties of the hybrid filter to the tensor $\tau^{\mathscr{E}}(u_i, u_j)$ we get

$$\tau^{\mathscr{E}}(u_i, u_j) = \langle \tau^{\mathscr{H}}(u_i, u_j) \rangle_{\mathscr{E}} + \tau^{\mathscr{E}}(\langle u_i \rangle_{\mathscr{H}}, \langle u_j \rangle_{\mathscr{H}}) \tag{6}$$

where the latter term represents the resolved turbulent stresses

$$\tau^{\mathscr{E}}(\langle u_i \rangle_{\mathscr{H}}, \langle u_j \rangle_{\mathscr{H}}) = \langle (\langle u_i \rangle_{\mathscr{H}} - \langle u_i \rangle_{\mathscr{E}})(\langle u_j \rangle_{\mathscr{H}} - \langle u_j \rangle_{\mathscr{E}}) \rangle_{\mathscr{E}}. \tag{7}$$

Substituting the hybrid stress tensor definition (5) in Eq. (6) and using relation (7), the Reynolds stress tensor becomes:

$$\tau^{\mathscr{E}}(u_i, u_j) = \langle \tau^{\mathscr{F}}(u_i, u_j) \rangle_{\mathscr{E}} + \frac{1}{k^2} \tau^{\mathscr{E}}(\langle u_i \rangle_{\mathscr{H}}, \langle u_j \rangle_{\mathscr{H}}). \tag{8}$$

A drawback of this procedure is represented by the presence of term $\frac{1}{k^2}$ in Eq. (8), which leads to an ill conditioned problem for low values of k. In fact, although a lower limit for k must be set also in the traditional approach (i.e. using an explicit RANS model), the square terms k^2 at the denominator leads to a greater value for this limit.

3 Constant Blending Factor

First of all three different values of blending factor k, constant in all the domain, have been tested, $k = 0.5, 0.75$ and $k = 1.0$, to simulate the turbulent channel flow at Ma = 0.2 at two different skin friction Reynolds numbers: $Re_\tau = 180$ and 395. The results are compared to data obtained by the incompressible DNS [6]. The computational domain size, in dimensionless units, is $2\pi \times 2 \times 4/3\pi$. The structured mesh used is composed by $6 \times 12 \times 10$ hexahedra, each ones divided into 6 tetrahedral elements and 4th order polynomial degree is used. The resolution parameters are reported in Table 1. The mean velocity profiles are shown in Fig. 1. Although the results obtained are quite similar, the hybrid method with $k = 0.75$ gives better results for $Re_\tau = 180$, whereas for $Re_\tau = 395$ the better results are the ones obtained with $k = 0.5$. This trend is confirmed also by the shear stress profiles in Fig. 2. The blending factor strongly impacts on the amount of the resolved and modelled quantities. As shown by Fig. 2 for the shear stress and by Fig. 3 for the turbulent kinetic energy, the resolved part is the most important in pure LES, for $k = 0.75$ the resolved part decreases while the modelled one increases and finally, for $k = 0.5$, the magnitude of two contributions is inverted. Therefore, at least theoretically, the blending factor permits a direct control of the resolved kinetic energy.

Table 1 Grid and simulations parameters for constant blending factor

	Re_b	Δ_x^+	Δ_z+	$\Delta_{y_{min}}^+/\Delta_{y_{max}}^+$
$Re_\tau = 180$	2800	31.68	12.8	0.65/11.52
$Re_\tau = 395$	6880	69.5	28.1	1.4/25.28

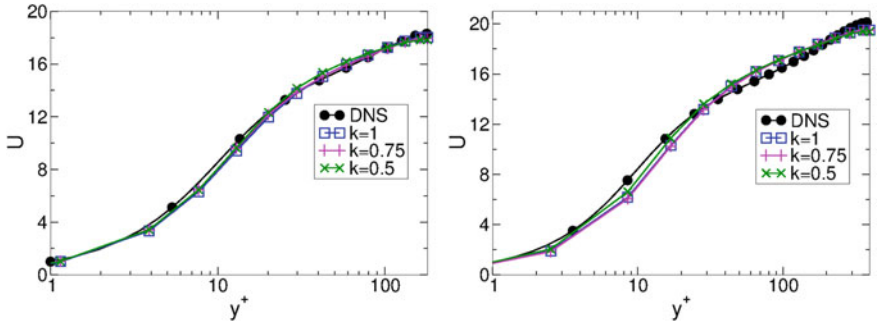

Fig. 1 Mean velocity profiles in wall units. Left: $Re_\tau = 180$; right: $Re_\tau = 395$

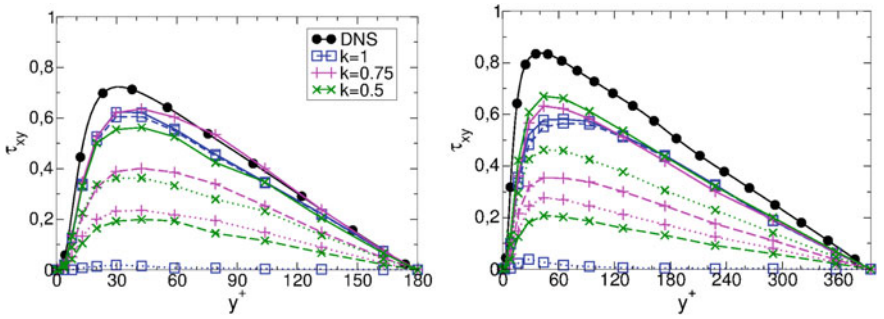

Fig. 2 Turbulent shear stress. Dotted: modelled; dashed: resolved; continuous: total. Left: $Re_\tau = 180$; right: $Re_\tau = 395$

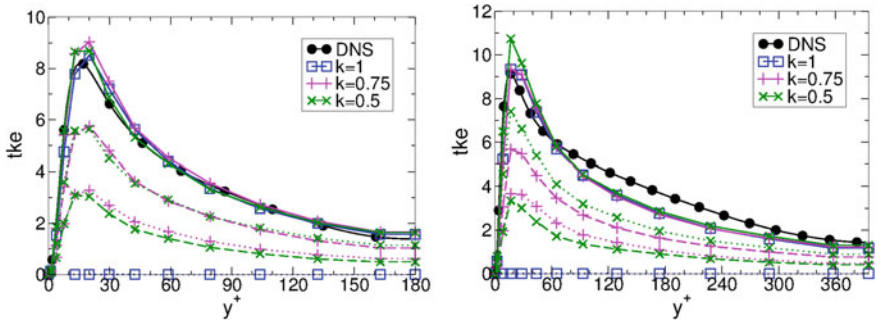

Fig. 3 Turbulent kinetic energy. Dotted line: modelled; dashed line: resolved; continuous: total. Left: $Re_\tau = 180$; right: $Re_\tau = 395$

Table 2 Grid and simulations parameters for the channel flow at $Re_\tau = 590$

	grid A		grid B
	$p = 4$	$p = 2$	$p = 4$
Elements	3840	3840	12960
Degrees of freedom	134400	38400	453600
Δ_x^+	78	118	52
Δ_z+	39	59	26
$\Delta_{y_{min}}^+$	1.78	2.71	1.19

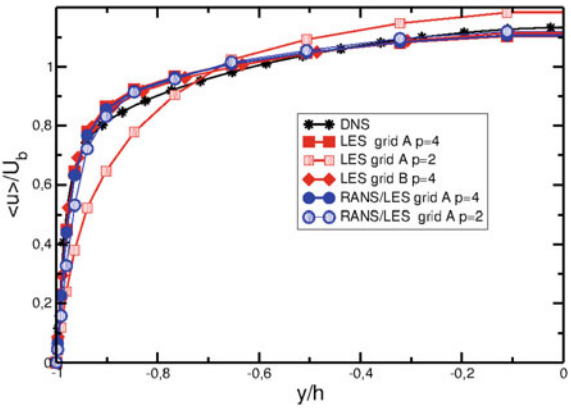

Fig. 4 Mean velocity profiles in the channel flow at $Re_\tau = 590$ using variable blending factor

4 Variable Blending Factor

Simulations of the channel flow at the higher Reynolds number $Re_\tau = 590$ have been made to the aim of investigate the behaviour of a variable blending factor using different space resolutions. The parameters of the grids, the polynomial order p and the corresponding space resolutions used in the simulations are reported in Table 2. The blending factor is determined as the ratio between the turbulent kinetic energy $tke(j), 0 \leq j \leq p/2$, corresponding to the lower polynomial degrees and larger resolved scales, and the total one

$$k = \frac{< \sum_{j=0}^{p/2} tke(j) >}{< \sum_{j=0}^{p} tke(j) >}.$$

Here $< \cdot >$ represents average over the element and in time, so a piecewise constant blending factor results and commutation terms are avoided. The blending factor results varying in the ranges $0.45-0.66$ and $0.47-0.75$ for the grid A respectively with second- and fourth-order polynomial. The mean velocity profiles, the shear stress and the turbulent kinetic energy profiles reported in Figs. 4 and 5 demonstrate

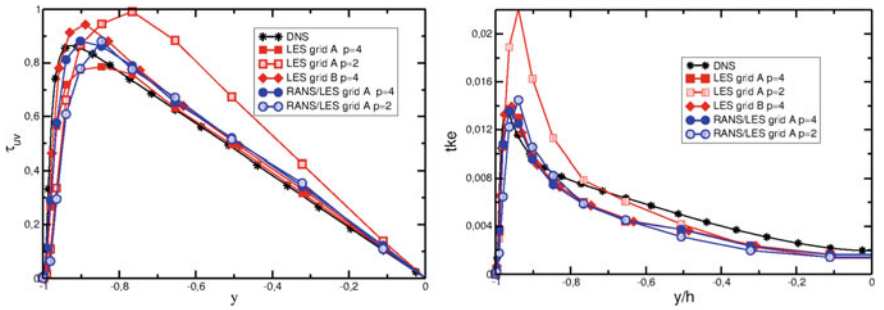

Fig. 5 Mean shear stress (left) and turbulent kinetic energy (right) profiles in the channel flow at $Re_\tau = 590$ using variable blending factor

the improvement when the RANS/LES approach is applied. Actually we can see that when a very low resolution is used with the RANS assisted model, the correct mean profiles are restored while a pure LES gives a completely non-physical solution.

5 Conclusions

We have studied and tested a RANS reconstruction technique for Germano's hybrid filter approach. Different tests for the simulation of channel flow using constant or variable blending factor, have demonstrated the advantages in using this approach with low resolution in space, allowing saving of computational resource. Moreover the results highlighted the importance of the blending factor to control the ratio between resolved and modelled turbulent kinetic energy.

Acknowledgements The presented numerical results have been obtained with the computational resources provided by CINECA (Italy) and NIIF (Hungary), respectively within the high performance computing projects ISCRA-C LES-DiG and DECI-11 HyDiG.

References

1. Abbà, A., Bonaventura, L., Nini, M., Restelli, M.: Dynamic models for large eddy simulation of compressible flows with a high order DG method. Comp. Fluids **122**, 209–222 (2015)
2. Abbà, A., Campaniello, D., Nini, M.: Filter size definition in anisotropic subgrid models for large eddy simulation on irregular grids. J. Turbul. **18**(6), 589–610 (2017)
3. Bhushan, S., Walters, D.K.: A dynamic hybrid Reynolds-averaged Navier Stokes-large eddy simulation modelling framework. Phys. Fluids **24** (2012)
4. Germano, M.: Turbulence: the filtering approach. J. Fluid Mech. **238**, 325–336 (1992)
5. Germano, M.: Properties of the hybrid RANS/LES filter. Theor. Comput. Fluid Dyn. **17**(4), 225–231 (2004)

6. Moser, R.D., Kim, J., Mansour, N.N.: Direct numerical simulation of turbulent channel flow up to $Re_\tau = 590$. Phys. Fluids **11**, 943–945 (1999)
7. Nini, M., Abbà, A., Germano, M., Restelli, M.: Analysis of a hybrid RANS/LES model using RANS reconstruction. Progress in Turbulence VI Proceedings of the iTi 2014–Conference on Turbulence. Springer Proceedings in Physics, vol. 165, pp. 299–303. Springer International Publishing, Switzerland (2016)
8. Rajamani, B., Kim, J.: A hybrid-filter approach to turbulence simulation. Flow Turbul. Combust. **85**, 421–441 (2010)
9. Restelli M. et al.: FEMilaro, a finite element toolbox effective substances. https://bitbucket.org/mrestelli/femilaro/wiki/Home
10. Sànchez-Rocha, M., Menon, S.: An order-of-magnitude approximation for the hybrid terms in the compressible hybrid RANS/LES governing equations. J. Turbul. **12**(16), 1–22 (2011)

Part III
Pre-processing, Post-processing and Data Analysis

Analysis of a Synthetic Turbulence Generation Method for Periodic Configurations

C. Morsbach and M. Franke

1 Introduction

With increasingly available computational resources, scale-resolving simulations begin to become affordable for industrially relevant flows. While full Large Eddy Simulations (LES) may still be out of reach, the combination of Reynolds-Averaged Navier–Stokes (RANS) and LES methods is a promising approach. Both LES and zonal RANS-LES methods require the prescription of resolved velocity fluctuations at the inflow or the RANS-LES interfaces. Especially in turbomachinery applications, due to upstream blade rows or the combustor, the inflow is highly turbulent and the prediction of phenomena such as transition depends crucially on the correct representation of turbulent scales. To save computational resources, the solution is usually assumed to be periodic in one or two directions. One assumption is spanwise periodicity when blade profiles are computed. Specifically in a turbomachinery application, it is often reasonable to compute only the flow around a fraction of the blades and apply rotational periodicity to model the full wheel.

A method to obtain realistic velocity fluctuations is a precursor simulation, from which the turbulent flow field is extracted and prescribed at the inflow of the actual simulation. Since this is not feasible for general industrial applications, various methods have been devised to generate resolved velocity fluctuations from statistical quantities, such as the Reynolds stress tensor and the turbulent length scale [6]. Keating et al. [2] review the performance of different approaches of prescribing a proper turbulence field in plane channel flow. We implemented the synthetic turbulence generation method recently suggested by Shur et al. [4] in DLR's flow solver for turbomachinery applications TRACE [1]. The method is based on a Fourier reconstruction of the fluctuating velocity field using wave number vectors with uniformly distributed random directions.

C. Morsbach (✉) · M. Franke
Numerical Methods, Institute of Propulsion Technology,
German Aerospace Center (DLR), Cologne, Germany
e-mail: christian.morsbach@dlr.de

M. V. Salvetti et al. (eds.), *Direct and Large-Eddy Simulation XI*,
ERCOFTAC Series 25, https://doi.org/10.1007/978-3-030-04915-7_23

By definition, turbulence generated by Shur's method is not periodic in a given direction. This leads to a violation of continuity at periodic boundaries of the computational domain and can, in turn, result in abnormal turbulence statistics downstream. Motivated by this deficiency, we propose a simple correction which restores periodicity. We will evaluate the performance of the correction with respect to statistical properties of turbulence such as Reynolds stresses, two-point correlations and energy spectra.

2 Synthetic Turbulence Generator and Periodic Correction

The synthetic turbulence generator is implemented as described in Shur et al. [4] Only the parts of the formulation which are important to understand the deficiency and proposed correction are stated here. For all details of the approach, the reader is referred to the original publication. The velocity fluctuations $\mathbf{v}'$ at the location $\mathbf{r}$ and time t are given by

$$\mathbf{v}'(\mathbf{r},t) = 2\sqrt{\frac{3}{2}}\sum_{n=1}^{N}\sqrt{q^n}\left[\sigma^n \cos\left(k^n\mathbf{d}^n\cdot\mathbf{r}'(\mathbf{r},t)+\phi^n\right)\right]. \tag{1}$$

The wave numbers k^n and amplitudes $\sqrt{q^n}$ are determined from a modified von-Karman spectrum. The vectors $\mathbf{d}^n$ are uniformly distributed over a unit sphere. For the condition of vanishing divergence, $\sigma^n \perp \mathbf{d}^n$ is required and σ^n is computed to be in the plane perpendicular to the respective $\mathbf{d}^n$ and rotated by a uniformly distributed angle in the interval $[0, 2\pi)$. Finally, uniformly distributed random phases ϕ^n are selected. The spatiotemporal variation is determined by

$$\mathbf{r}'(\mathbf{r},t) = \begin{pmatrix} \frac{k_e}{k^n}(x - U_0 t) \\ y \\ z \end{pmatrix} \tag{2}$$

with the wave number k_e of the most energetic eddies and the mean velocity U_0.

For the velocity signal to be periodic in a domain with lengths L_i, the relations

$$k^n d_i^n L_i = 2\pi m_i^n, \quad i \in \{y, z\} \tag{3}$$

with integer numbers $m_i^n \in \mathbb{Z}$ need to be fulfilled for every combination of wave number k^n and random unit vector $\mathbf{d}^n$. In the original formulation of the method, this is generally not the case. Therefore, we propose a simple algorithm for each k^n to ensure these conditions:

1. Find the largest m_y^n for which $d_y^n < 1$
2. Find the largest m_z^n for which $\sqrt{(d_y^n)^2 + (d_z^n)^2} < 1$

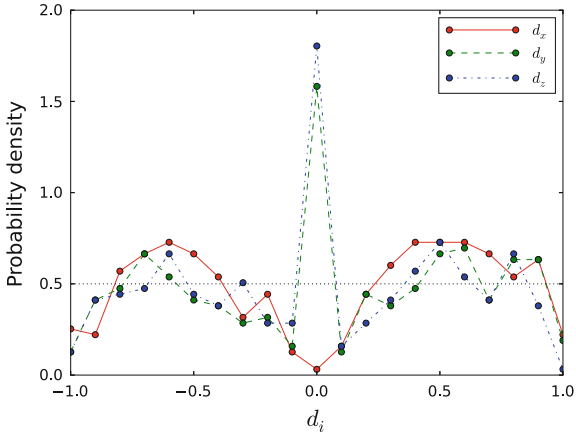

Fig. 1 Probability density function for components of $\mathbf{d}^n$ after application of periodic correction in y- and z-direction. The dotted line indicates the expected value for uniformly distributed random vectors on a sphere

3. Rescale $d_i^n = \frac{2\pi m_i^n}{k^n L_i}$ for $i \in \{y, z\}$
4. Recompute $d_x = 1 - \sqrt{(d_y^n)^2 + (d_z^n)^2}$

In other words, the $k_i^n d_i^n L_i$ are rounded to the closest multiple of 2π with the restriction of the resulting vector being possible to scale to a length of 1. For the wave number vectors $k^n\mathbf{d}^n$ this means that their y- and z-components are multiples of the minimum wavenumber corresponding to the domain size.

Figure 1 shows the effect of this algorithm on the distribution of random vectors in terms of a probability density function (PDF) for each component of the vectors $\mathbf{d}^n$. For random vectors uniformly distributed on a sphere, the expected PDF would be a constant value of 0.5 as indicated by the dotted line. Both y- and z-components show a peak at zero with a resulting depletion of the x-component. This is a result of the proposed rounding strategy for small wave numbers k^n.

3 Analysis of Generated Turbulence

Spatially decaying homogeneous isotropic turbulence was computed to test the inflow boundary condition. The domain size is given in multiples of the turbulent length scale L_T as $8\pi \times 2\pi \times 2\pi$ on a mesh of $128 \times 32 \times 32$ cells. At the inlet, the velocity fluctuations obtained from the synthetic turbulence generator are superimposed on the constant bulk velocity U_0. At the outlet, a constant static pressure is specified using a non-reflecting boundary condition.

The filtered Navier–Stokes equations are discretised using a second-order accurate finite volume scheme applying MUSCL reconstruction with $\kappa = 1/3$ [7]. A fraction of 10^{-3} of Roe's numerical flux [3] is added to a central flux to avoid odd-even decoupling. Time integration is performed using a third order accurate explicit

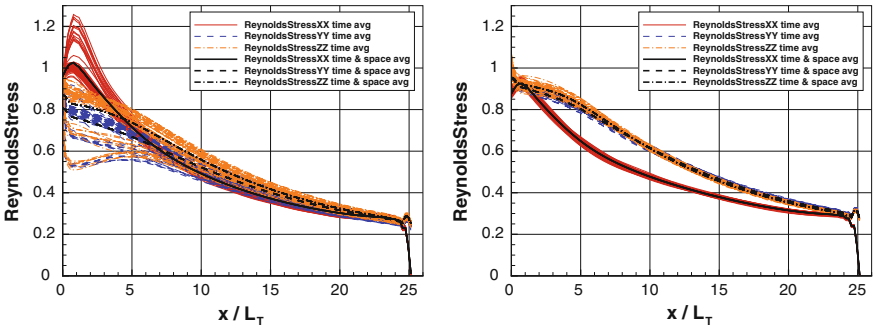

Fig. 2 Temporally and both temporally and spatially averaged decay of Reynolds stress tensor components for the original formulation (*left*) and periodic correction (*right*)

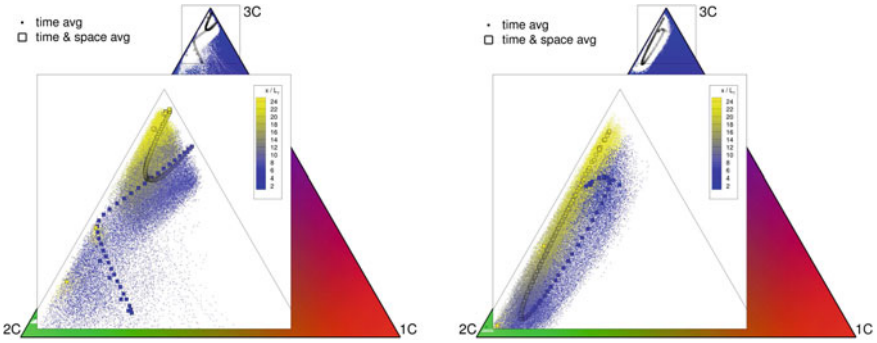

Fig. 3 Temporally and both temporally and spatially averaged decay of Reynolds stress anisotropy invariants for the original formulation (*left*) and periodic correction (*right*)

Runge–Kutta method. The subgrid stresses are computed by a classic Smagorinsky model [5].

In the following, we will compare the development of the Reynolds stress tensor, its anisotropy invariants as well as two-point correlations and energy spectra. First insights into the deficiency of the original method in a periodic configuration can be gained from Fig. 2 (*left*). The thin lines represent the variation in temporal averages while the thick lines are temporally and spatially averaged. It can be observed that even in the temporal average, a spatial variation remains. The extreme values for the Reynolds stresses can be located at the periodic boundaries of the domain. If the periodic correction is applied, these spatial variations vanish and the temporal average at all locations converges to the spatial average. Furthermore, the spatial average of the y- and z-fluctuating velocities do not show the spurious drop below the reference value of 1 as in the original formulation. Figure 3 confirms these observations in terms of the turbulence anisotropy. The axial development within the barycentric map is colour-coded from blue at the inlet to yellow at the outlet. After a short distance

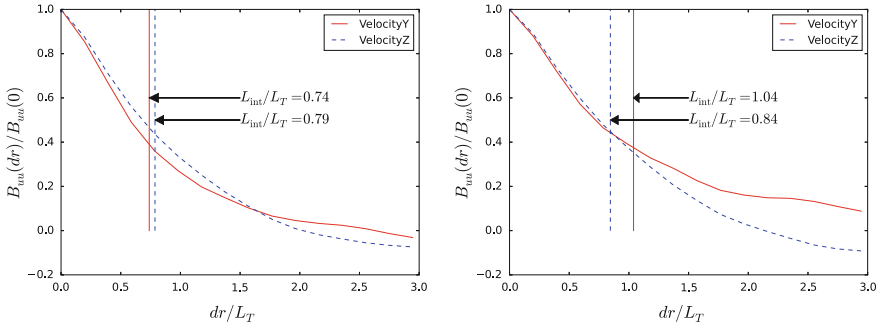

Fig. 4 Two-point correlations for y- and z-velocity components at $x/L_T = 1.5$ downstream of the inlet for the original formulation (*left*) and periodic correction (*right*)

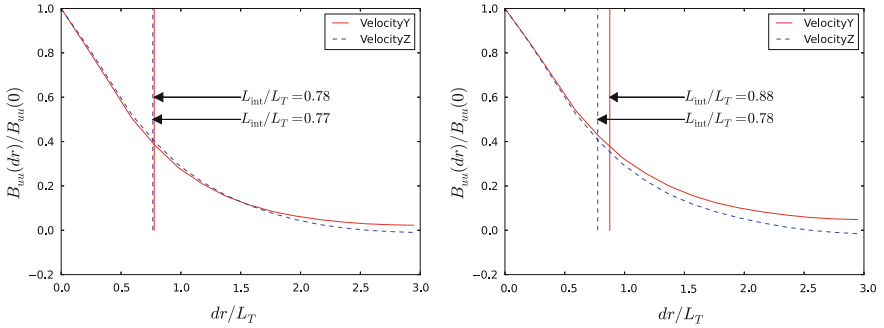

Fig. 5 Two-point correlations for y- and z-velocity components at $x/L_T = 14$ downstream of the inlet for the original formulation (*left*) and periodic correction (*right*)

of adaptation, the generated turbulence follows a return-to-isotropy path. With the correction, the scatter is greatly reduced.

Two-point correlations were gathered at various distances downstream of the inlet in both homogeneous directions. Figure 4 shows them at an axial position $x/L_T = 1.5$. In the original formulation (*left*), the length scales for y- and z-components of the velocity are nearly equal. The chosen algorithm clearly affects the length scale for the y-component of the velocity (*right*) whose two-point correlation does not reach 0. Downstream, at $x/L_T = 14$, this effect has already mixed out and both formulations show only very subtle differences in Fig. 5. From the two-point correlations at the latter station, one-dimensional energy spectra were computed by taking the Fourier transform. Figure 6 shows that the periodic correction does not negatively affect the energy spectra.

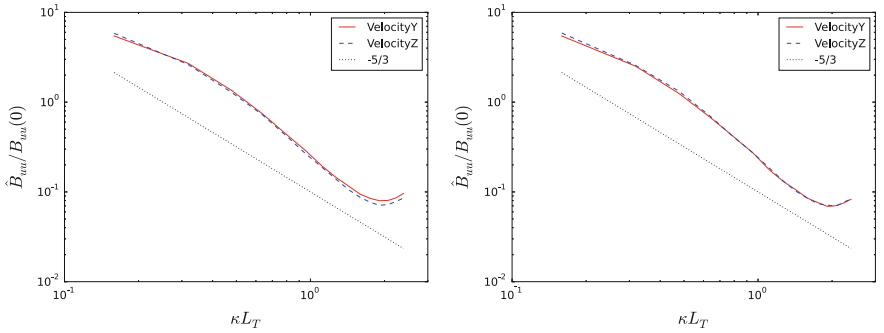

Fig. 6 Energy spectra for y- and z-velocity components at $x/L_T = 14$ downstream of the inlet for the original formulation (*left*) and periodic correction (*right*)

4 Conclusion

We investigated the performance of a method to generate synthetic turbulence in the case of spatially decaying homogeneous isotropic turbulence. As this method showed spurious effects at the periodic domain boundaries, we suggested an approach to ensure periodicity. This approach eliminates the spatial variation of the temporal average. Analysis of the turbulence anisotropy as well as two-point statistics has shown that properties of the original method are preserved in the far field.

References

1. Becker, K., Heitkamp, K., Kügeler, E.K.: Recent progress in a hybrid-grid CFD solver for turbomachinery flows. In: V European Conference on Computational Fluid Dynamics ECCOMAS CFD 2010, Lisbon, Portugal (2010)
2. Keating, A., Piomelli, U., Balaras, E., Kaltenbach, H.-J.: A priori and a posteriori tests of inflow conditions for large-eddy simulation. Phys. Fluids **16**(12), 4696–4712 (2004)
3. Roe, P.L.: Approximate Riemann solvers, parameter vectors, and difference schemes. J. Comput. Phys. **43**(2), 357–372 (1981)
4. Shur, M.L., Spalart, P.R., Strelets, M.K., Travin, A.K.: Synthetic turbulence generators for RANS-LES interfaces in zonal simulations of aerodynamic and aeroacoustic problems. Flow Turbul. Combus. **93**(1), 63–92 (2014)
5. Smagorinsky, J.: General circulation experiments with the primitive equations. Mon. Weather. Rev. **91**, 99–164 (1963)
6. Tabor, G., Baba-Ahmadi, M.: Inlet conditions for large eddy simulation: a review. Comput. Fluids **39**(4), 553–567 (2010)
7. van Leer, B.: Towards the ultimate conservative difference scheme. V. A second-order sequel to Godunov's method. J. Comput. Phys. **32**(1), 101–136 (1979)

The Effect of Lossy Data Compression in Computational Fluid Dynamics Applications: Resilience and Data Postprocessing

E. Otero, R. Vinuesa, P. Schlatter, O. Marin, A. Siegel and E. Laure

1 Introduction

The field of computational fluid dynamics (CFD) is data intensive, particularly for high-fidelity simulations. Direct and large-eddy simulations (DNS and LES), which are framed in this high-fidelity regime, require to capture a wide range of flow scales, a fact that leads to a high number of degrees of freedom. Besides the computational bottleneck, brought by the size of the problem, a slightly overlooked issue is the manipulation of the data. High amounts of disk space and also the slow speed of I/O (input/output) impose limitations on large-scale simulations. Typically the computational requirements for proper resolution of the flow structures are far higher than those of post-processing. To mitigate such shortcomings we employ a lossy data compression procedure, and track the reduction that occurs for various levels of truncation of the data set. The Discrete Chebyshev Transform (DCT) has been used in the image compression community [1], as well as in CFD [7]. In the present work we assess the use of the DCT in situations such as data post-processing, vortex identification, as well as simulation restart from compressed data fields. In the com-

E. Otero (✉) · R. Vinuesa · P. Schlatter
Linné FLOW Centre, KTH Mechanics and Swedish e-Science Research Centre (SeRC), Stockholm, Sweden
e-mail: otero@mech.kth.se

R. Vinuesa
e-mail: rvinuesa@mech.kth.se

P. Schlatter
e-mail: pschlatt@mech.kth.se

O. Marin · A. Siegel
MCS, Argonne National Laboratory, Lemont, IL, USA
e-mail: oanam@mcs.anl.gov

E. Laure
Center for High Performance Computing, KTH, Stockholm, Sweden
e-mail: erwinl@pdc.kth.se

M. V. Salvetti et al. (eds.), *Direct and Large-Eddy Simulation XI*,
ERCOFTAC Series 25, https://doi.org/10.1007/978-3-030-04915-7_24

pression algorithm under consideration [5], the data is truncated using an a priori error estimator, thus allowing total control over the permissible error. Note that this is an improvement with respect to previous compression algorithms. Here we illustrate the ability of the data compression algorithm to compress the data at very large scales and on complex grids, with a very good approximation of the total error.

2 Error Controlled Lossy Data Compression

The lossy data compression used in the present work relies on applying orthogonal transforms (DCT, or Discrete Legendre Transform (DLT)) to reference elements stemming from a discretization on hexahedral elements. This can be performed on either finite difference/volume discretizations, but preferably on discretizations based on variational formulations, since in this case the reference elements are universal for the simulation and a single orthogonal transform has to be computed. In this case the computation over a reference hypercube differs from the computation over a distorted curvilinear hypercube only via a mapping.

Consider the entire domain Ω as consisting of elements Ω_e, as in Fig. 1a, such that $\Omega = \cup_e \Omega_e$. A local elemental restriction of the global velocity field $\mathbf{u}$ is $\mathbf{u}_e = \mathbf{u}|_{\Omega_e}$. On a general curvilinear mesh, the L_2 norm of the global velocity field $||\mathbf{u}||$ has to be weighted by $V = \int_\Omega d\Omega$, the volume of the domain. Given the decomposition of the entire mesh in hexahedral elements e, we have $\mathbf{u}|_{\Omega_e} = \mathbf{u}_e$. Then we can write the global L_2 norm as a sum of local norms as: $||\mathbf{u}||^2_{L_2} = \sum_e ||\mathbf{u}_e||^2_{L_2}$. Straightforward algebra yields $||\mathbf{u}|| \leq \varepsilon \rightarrow ||\mathbf{u}_e|| \leq \varepsilon$. Presume now that we apply, blockwise, the orthogonal transform T to a signal u yielding $w = Tu$, where T is an $N \times N$ matrix and w is an array in spectral space corresponding to the array u in physical space. At the element level we can note that $||\mathbf{u}||_2 = \sqrt{\mathbf{u}^T\mathbf{u}} = \sqrt{(T\mathbf{u})^T T\mathbf{u}}$, where $T\mathbf{u} = \mathbf{w}$ is the signal transformed in DCT space. It is therefore natural to perform the truncation in spectral space, based on the error we intend to commit in real space. In the context of the present work, the data compression is used in a spectral-element code, Nek5000 [3], where the partial differential equations (PDEs) are discretized over a spectral-element grid of hexahedral elements (Fig. 1a). The PDEs are further discretized over

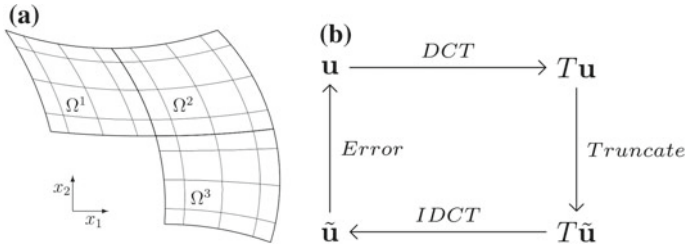

Fig. 1 **a** Spectral-element mesh. **b** Schematic view of the algorithm for data compression

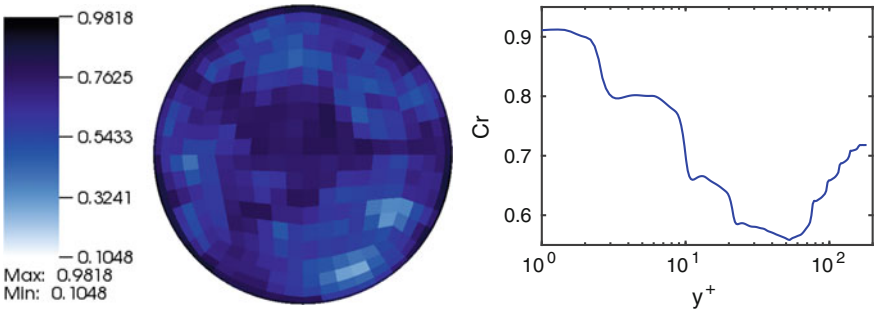

Fig. 2 (Left) Compression ratio distribution per element on the pipe-flow case described in Sect. 3. (Right) Compression ratio profile averaged in time, streamwise and azimuthal directions with respect to the wall-normal distance in inner scaling

each element using a spectral quadrature. In the context of Nek5000, the quadrature is based on Gauss–Lobatto–Legendre (GLL) points, however it might as well have been Chebyshev (GLC) points.

The truncation procedure is the core of the whole algorithm, sketched in Fig. 1b, and is the main novelty of our method. In fact our DCT truncation is defined in terms of mode amplitude instead of mode frequency, as it is the case when performing simple downsampling. Therefore, our method truncates data in an adaptive way by setting to zero the weak modes with less contribution to the flow. More precisely, the algorithm is applied on each spectral element, and the truncation is carried out with respect to an error threshold adapted to the element volume. Then, the compression ratio Cr for that element is computed as the number of entries set to zero over the total number of grid points. The larger the compression ratio is, the smaller the files size is. In this work we define the overall compression ratio as the arithmetic average over all the elements. Finally, the error estimator allows to control the error incurred through the truncation. Figure 2 illustrates the behavior of the DCT truncation with respect to the flow properties and using an error threshold of 10^{-4}. It can be observed that higher compression ratios are present in regions of low turbulent fluctuations, as it is the case in the viscous sublayer. The corresponding averaged compression ratio is of 68%.

3 Results

We investigate the effect of the data compression on different post-processing methods used to characterize the flow, and in various test cases. The first case is the turbulent flow through a smooth circular pipe at a friction Reynolds number $Re_\tau = 180$ [2], and we use 205 instantaneous velocity fields from a fully-resolved DNS [2]. In the second case, we use instantaneous velocity fields from a well-resolved LES of the turbulent flow around a NACA4412 wing section at a Reynolds number based

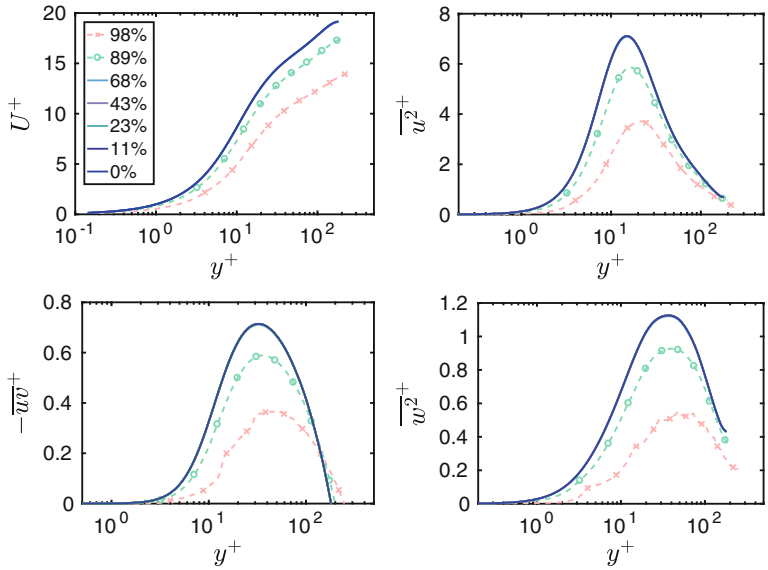

Fig. 3 Turbulence statistics for the pipe case at $Re_\tau = 180$, obtained from fields with different levels of compression

on inflow velocity and chord length of $Re_c = 100{,}000$ [9]. Finally, we also consider results from the jet in cross-flow (JCF) [6]. This case was chosen due to its sensitivity to initial conditions, and we select a stable configuration [6] with a polynomial order of $N = 7$ and a velocity ratio of $R = 0.63$ defined as $R = V/U_\infty$ where V and U_∞ are the peak jet velocity and the free-stream velocity, respectively.

3.1 Turbulence Statistics

In Fig. 3 we analyze the effect of various compression ratios on the turbulence statistics in the pipe case. The statistics were computed based on the original flow fields (with 0% compression ratio), and based on the compressed instantaneous fields. In particular, we show inner-scaled mean streamwise velocity U^+, the streamwise and azimuthal velocity fluctuations $\overline{u^2}^+$ and $\overline{w^2}^+$, and the Reynolds shear stress $-\overline{uv}^+$. This figure shows that up to a compression ratio of around 70%, corresponding to an error of 10^{-4}, the turbulence statistics are in very good agreement with the ones obtained without any compression. Note that the significant deviations in the largest compression ratios are mainly caused by changes in the friction velocity.

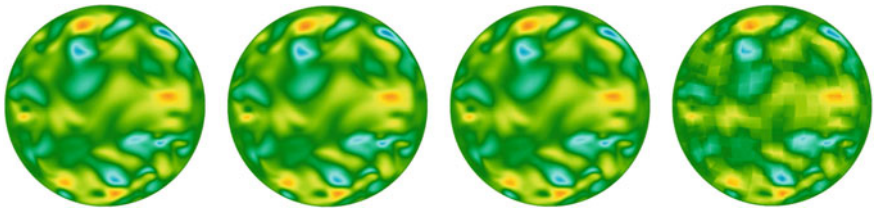

Fig. 4 Instantaneous in-plane horizontal velocity in the pipe, for compression ratios of (from left to right) 0, 68, 89 and 98%

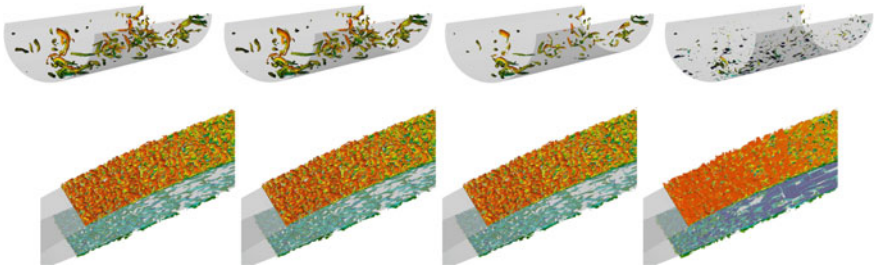

Fig. 5 Vortical structures identified with the λ_2 criterion [4] in the turbulent flow (top) through the pipe and (bottom) around the wing section. The compression ratios under consideration are (from left to right) 0, 68, 89 and 98%. The isovalues of λ_2 are fixed in viscous units to -0.01 and -9×10^{-4} for the pipe and the wing, respectively

3.2 Flow Visualization and Vortex Identification

In Fig. 4 we show the instantaneous in-plane horizontal velocity in a Cartesian frame of reference in the pipe for a number of compression ratios ranging from 0% to the maximum, i.e., 98%. It can be observed that, for simple visualization purposes, a compression ratio of around 90% is acceptable. Higher compression ratios show significant discontinuities across element boundaries, as observed in the case with $Cr = 98\%$. The impact of compression on the vortical structures in the turbulent flow through the pipe, and around the wing section, is studied in Fig. 5. In that case, a compression ratio of 89% shows deviations with respect to the case without compression. However, a lower Cr of 68% still shows good agreement with the original structures. Note that, since the isovalues used to define the structures are defined in viscous scaling, part of the observed effect is due to the modified u_τ as a result of the compression. Furthermore, it would be possible to achieve even higher Cr values in fully-resolved DNS cases, such as the one reported in Ref. [8].

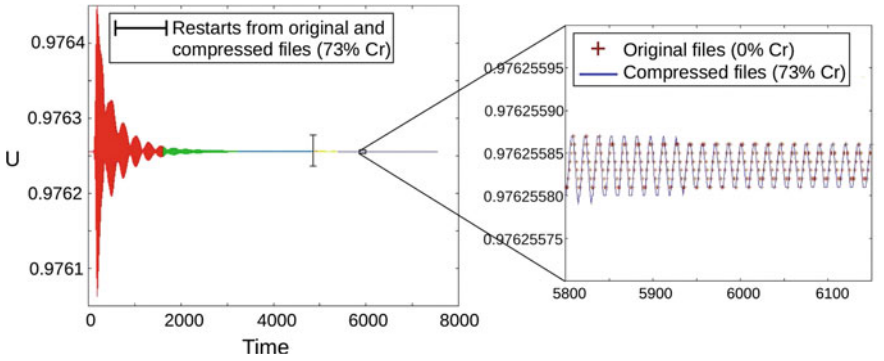

Fig. 6 Restart procedure on the JCF case. (Left) Time evolution of the streamwise velocity for different restart points, from fields without and with compression. (Right) Comparison of a restart from a field without compression and a restart using compressed files with 73% compression ratio

3.3 Resilience

Finally, we analyze the impact of data compression on the simulation restart using the jet in cross-flow case. Figure 6 (left) shows the evolution in time of the streamwise velocity U for different restart points, from fields without and with compression for comparison. As indicated in this figure, we perform a restart at around 5,000 convective time units from the beginning of the simulation, using files with 73% compression ratio. In Fig. 6 (right) it can be observed that the impact of restarting from compressed files is negligible. This implies that in less sensitive cases, such as turbulent simulations, highly compressed files could potentially be used for restart, which would give large benefits in terms of checkpointing, and resilience in large-scale simulations.

4 Conclusions

In the present work we propose a lossy data compression algorithm, with which we have obtained high levels of acceptable compression ratios for the turbulent pipe and the wing cases. It was possible to truncate up to 70 and 90% of the data for statistics computation and visualization purposes, respectively. Our DCT truncation has shown to remove data in an adaptive way depending on the flow properties in the domain. Moreover, we have observed that the data compression could be also applied for a restart procedure in simulations of transition, which are typically highly sensitive to the initial conditions. Hence, our method highly compresses the data, while preserving the most relevant flow physics with a control on the error incurred.

Acknowledgements Financial support from the Stiftelsen för strategisk forskning (SSF) and the Swedish e-Science Research Centre (SeRC) via the SESSI project is acknowledged. The computations were performed on resources provided by the Swedish National Infrastructure for Computing (SNIC).

References

1. Ahmed, N., Natarajan, T., Rao, K.R.: Discrete cosine transform. IEEE Trans. Comput. **C–23**, 90–93 (1974)
2. El Khoury, G.K., Schlatter, P., Noorani, A., Fischer, P.F., Brethouwer, G., Johansson, A.V.: Direct numerical simulation of turbulent pipe flow at moderately high Reynolds numbers. Flow Turbul. Combust. **91**, 475–495 (2013)
3. Fischer, P.F., Lottes, J.W., Kerkemeier, S.G.: Nek5000: open source spectral element CFD solver (2008). https://nek5000.mcs.anl.gov
4. Jeong, J., Hussain, F.: On the identification of a vortex. J. Fluid Mech. **285**, 69–94 (1995)
5. Marin, O., Schanen, M., Fischer, P.F.: Large-scale lossy data compression based on an a priori error estimator in a spectral element code. In: ANL/MCS-P6024-0616 (2016)
6. Peplinski, A., Vinuesa, R., Offermans, N., Schlatter, P.: ExaFLOW use cases for Nek5000: incompressible jet in cross-flow and flow around a NACA4412 wing section. In: H2020 FETHPC-1-2014 D3.1
7. Schmalzl, J.: Using standard image compression algorithms to store data from computational fluid dynamics. Comput. Geosci. **29**, 1021–1031 (2003)
8. Vinuesa, R., Hosseini, S. M., Hanifi, A., Henningson, D.S., Schlatter, P.: Pressure-gradient turbulent boundary layers developing around a wing section. Flow Turbul. Combust. **99**, 613–641 (2017)
9. Vinuesa, R., Schlatter, P.: Skin-friction control of the flow around a wing section through uniform blowing. In: Proceedings of European Drag Reduction and Flow Control Meeting (EDRFCM) (2017)

Augmented Prediction of Turbulent Flows via Sequential Estimators

M. Meldi and A. Poux

1 Introduction

Among the numerous research aspects in the analysis of complex flow configurations of industrial interest, the accurate prediction of turbulent flows is one of the ultimate open challenges. Investigation via classical tools, such as experiments and numerical simulation, is difficult because of fundamental drawbacks which can not be completely excluded. Experiments provide a local description of flow dynamics via measurements sampled by sensors. A complete reconstruction of the flow behavior in the whole physical domain is problematic because of the non-linear, strongly inertial behavior of turbulence. While reduced-order models, such as POD [4], have been extensively used for this purpose, they usually provide an incomplete reconstruction of turbulent flows for the aforementioned reasons.

While CFD can provide flow characteristics on large physical domains, it is affected by errors/epistemic uncertainties. The boundary conditions/turbulence modeling [7, 8] can not exactly reproduce the fine perturbations and inhomogeneity of the real flow, which are unknown a priori but are responsible for the emergence of turbulent regimes. This bias, which stems from uncertainties of a completely different nature, is among the reasons why the comparison of experiments and numerical results is a difficult task even for the classical case of grid turbulence decay [1].

New methodological approaches coming from Estimation Theory (ET) [9] and Data Assimilation (DA) are nowadays used to obtain an optimal state estimation of flow configurations, accounting for the level of uncertainty/stochasticity in multiple sources of information. These techniques, which are usually referred to as estimators, are used to integrate experimental/numerical data and they have the potential to eliminate the bias which can not be identified in the two methods alone.

M. Meldi (✉) · A. Poux
Institut Pprime, Department of Fluid Flow, Heat Transfer and Combustion,
CNRS - ENSMA - Universit'e de Poitiers, UPR 3346, SP2MI - Teleport,
211 Bd. Marie et Pierre Curie, B.P. 30179, 86962 Futuroscope Chasseneuil Cedex, France
e-mail: marcello.meldi@ensma.fr

M. V. Salvetti et al. (eds.), *Direct and Large-Eddy Simulation XI*,
ERCOFTAC Series 25, https://doi.org/10.1007/978-3-030-04915-7_25

A new reduced order technique for sequential state estimation via Data Assimilation is here proposed. This method can naturally integrate sampled data (*observation*) obtained via experimental sampling or numerical databases in CFD solvers.

2 Methodological and Numerical Ingredients

The method exploits features of the segregated solvers implemented in commercial CFD software in order to obtain sequential state estimation via Kalman filter [3, 5, 10]. An optimized (*augmented*) prediction is achieved accounting for the information by a *model* and by available *observation*, which are characterized by a different level of confidence. The sequential time advancement goes through two steps:

1. A *prediction* step, where the model is used to advance in time the physical state
2. An *update* step, where available observation is integrated in the model prediction to obtain the *augmented* state estimation.

This algorithm is reminiscent of CFD solvers for incompressible flows, such as the PISO algorithm [2]. In this case, the resolving algorithm is defined as follows:

1. A *predictor* step, where the momentum equation is resolved to obtain a first estimation of the velocity field $\mathbf{U}$
2. An *corrector* step, where a pressure equation resolution/velocity correction is iteratively performed until the velocity field complies with both the momentum equation and the zero-divergence condition.

The similarity between the two algorithms has been exploited in order to integrate the sequential Kalman filter in the PISO algorithm of a finite volume solver [5]:

$$\hat{\mathbf{U}} = \mathbf{U} + K\ (\mathbf{z} - H\,\mathbf{U}) = \frac{\Phi(\mathbf{U})}{a_P} - \frac{\nabla p}{a_P} + F \tag{1}$$

$$\nabla \cdot \left(\frac{\nabla p}{a_P}\right)_f = \sum_f S \times \left(\frac{\Phi(\mathbf{U})}{a_P} + F\right)_f \tag{2}$$

$$\mathbf{U} = \frac{\Phi(\mathbf{U})}{a_P} - \frac{\nabla p}{a_P} \tag{3}$$

where p is the pressure, $\mathbf{z}$ is available local observation and $\hat{\mathbf{U}}$ is the augmented state estimation for the velocity field. ∇ and $\nabla\cdot$ represent the gradient operator and the divergence operator, respectively. The subscript f indicates face values of the quantities investigated. The resulting *augmented prediction* naturally exhibits a zero-divergence condition and the confidence in the observation and in the model is controlled via the Kalman gain matrix K. In the present analysis, a reduced order *observer* is employed, which filters all the off-diagonal elements of K.

3 Application: Turbulent Spatially Evolving Mixing Layer

The numerical method introduced in Sect. 2 is applied to the analysis of the spatially evolving mixing layer test case [6] for $Re_\Delta = (U_1 - U_2)\Delta/2\nu = 100$. Δ is the vorticity thickness at the inlet and it is a measure of the transition between the two asymptotic regimes characterized by the asymptotic velocities U_1 and U_2. The streamwise direction x indicates the asymptotic trajectory of the flow. The velocity gradient is observed in the normal direction y. Finally z is the spanwise direction. The Kalman observer, which will be referred to as DA-LES, will integrate:

- *Model*: a Smagorinsky LES numerical simulation, which will be performed on the whole physical domain $[x \times y \times z] \in [0, 20 \times -9, 6 \times -3, 3]$. The physical domain is normalized over the characteristic instability length $\Lambda = 15.4\Delta$.
- *Observation*: data sampled from a high resolution DNS, which is performed using the same physical domain and boundary conditions of the LES previously introduced. The observation is not provided in the whole physical domain, but it is limited to the rectangular windows $[y \times z] \in [-0.0012, 0.0012 \times -3, 3]$ for the streamwise stations $x = 6, 10, 14$ (see highlighted regions in Fig. 1a).

This analysis is justified by the physical features of this test case. In fact, a progressive transition from a laminar unsteady state towards turbulence is observed for $x > 10\Lambda$ moving downstream from the inlet. While the DNS accurately captures this transition, the Smagorinsky LES simulation introduces an unwanted eddy viscosity effect upstream, which affects the global prediction. Thus, the Kalman observer is employed to improve the characteristics of the LES simulation via integration of DNS data. The numerical results obtained are compared with a classical LES simulation, carried out with the same set up, and with DNS data taken from the same simulation which has been sampled to provide the *observation*. Numerical details are given in Table 1. Mesh spacing is constant in the x and z directions. In the y direction $\Delta y = const.$ for $y \in [-1, 1]$ and it follows a geometric progression outside.

First, the instantaneous streamwise velocity U_x sampled in a plane normal to the spanwise direction are shown in Fig. 1a (DNS), b (LES), c (DA-LES). The comparison between the DNS and the LES results show that the latter fails in providing a precise physical prediction of the flow, and the shear region appears to be larger in size. On the other hand, the streamwise velocity contours for the DA-LES simulation appear to be more physical in the whole domain, and in particular downstream with respect to the very first assimilation window. While information is propagated upstream, the beneficial effects of the state estimation are in this case reduced by the proximity of the inlet boundary condition for $x \in [0, 6]$. In addition, the isocontours for the simulation DA-LES appear to be continuous. This aspect highlights the good performance of the Kalman observer, which exploits the Poisson equation for smooth diffusion of the local information integrated.

A significant improvement in state estimation via observer is obtained as well in the prediction of statistical quantities. In Fig. 2a, the time averaged streamwise velocity $\overline{U_x}$ is shown at the streamwise section $x = 15$. Averages are performed

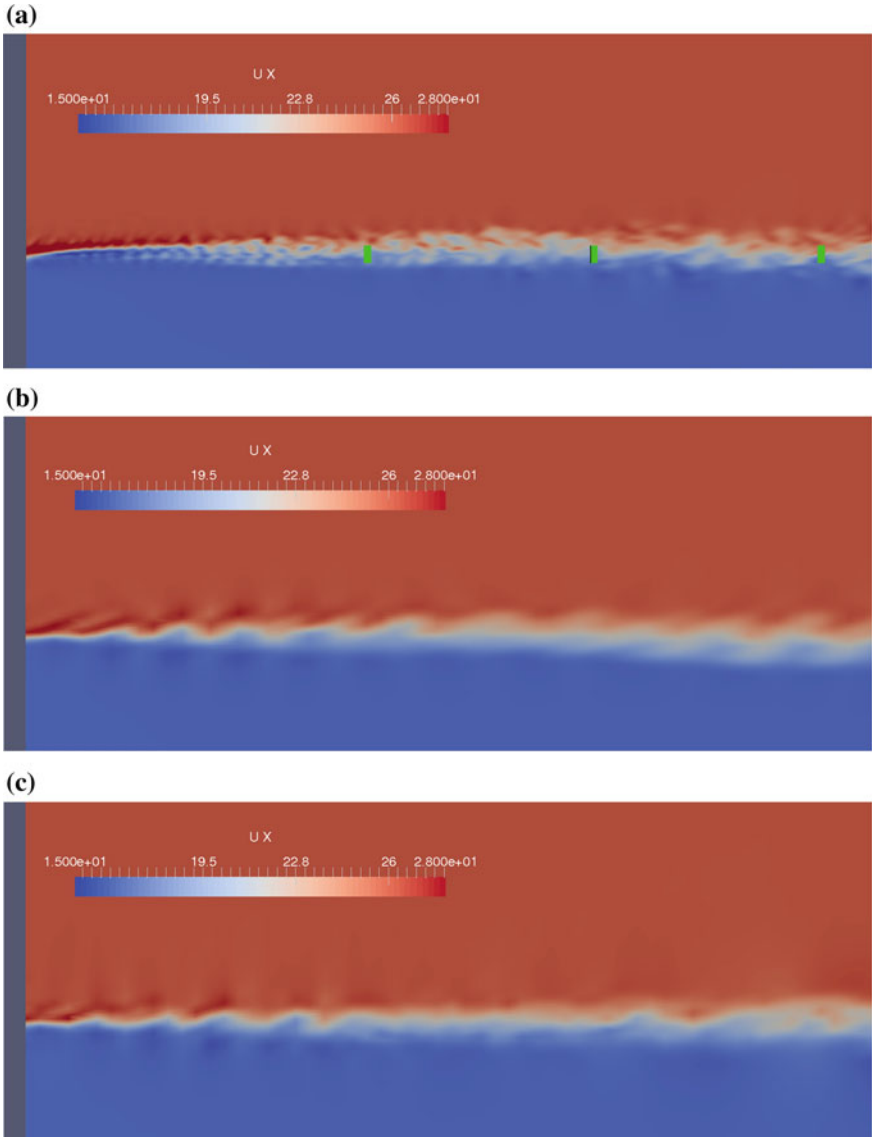

Fig. 1 **a** Isocontours of the instantaneous streamwise velocity U_x. DNS data. The x axis is aligned with the horizontal direction. **b** Isocontours of the instantaneous streamwise velocity U_x. LES data. The x axis is aligned with the horizontal direction. **c** Isocontours of the instantaneous streamwise velocity U_x. DA-LES data. The x axis is aligned with the horizontal direction

Table 1 Numerical details of the meshes used for the simulations. The value of Δy provided represents the resolution in the range $y \in [-1, 1]$ in Λ units. η is the bulk flow Kolmogorov scale

Simulation	Δx	Δy	Δz	Nr. elem.
DNS	5.86η	2.93η	3.5η	10^7
LES	23.44η	5.86η	14η	$3.4 \cdot 10^5$
DA-LES	23.44η	5.86η	14η	$3.4 \cdot 10^5$

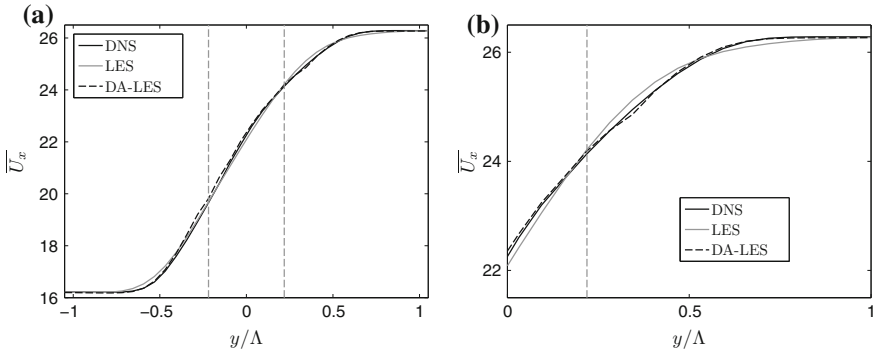

Fig. 2 **a** Spanwise time averaged $\overline{U_x}$ profiles sampled at the station $x = 15\Lambda$. **b** Zoom (upper region) of the velocity profiles $\overline{U_x}$

in the spanwise direction as well. The comparison between the three numerical simulations, which is magnified in Fig. 2b, indicates that the Kalman observer is significantly closer to the DNS prediction than to the pure LES simulation, which has been used as *model*. This augmented prediction is improved as well outside of the assimilation region. In addition, this gain has been obtained introducing data in a very limited region, which is around 0.3% of the whole physical domain investigated.

At last, the streamwise evolution of the mean momentum thickness

$$\overline{\Theta}(x) = \int_{-9\Lambda}^{6\Lambda} (U_2 - \overline{U_x}(x))(\overline{U_x}(x) - U_1)dy \tag{4}$$

is investigated. Results of the streamwise evolution of $\overline{\Theta}$ are reported in Fig. 3. The LES prediction is qualitatively similar to the DNS result, but it is shifted to higher values. This result stems from the unwanted eddy viscosity contribution of the Smagorinsky model upstream, which is carried in the turbulent region. This result is as well tied with previous discussion about the thickness of the shear region observed in the instantaneous velocity isocontours. On the other hand, the prediction from DA-LES is roughly in the middle between the LES and the DNS. This result has been obtained without any active modification of the subgrid scale model. Thus,

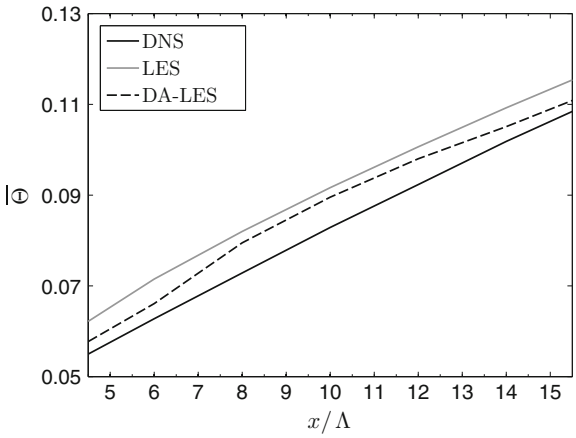

Fig. 3 Streamwise evolution of the momentum thickness $\overline{\Theta}$

an open question to be investigated is to what extent this state estimation can be employed to actively improve the features of turbulence/subgrid scale models, as well as any other parametric characteristic describing the numerical set-up.

4 Conclusions

In the present work, a reduced order Kalman filter observer for state estimation of turbulent flows has been introduced. Its capabilities have been validated with the analysis of the spatially evolving mixing layer test case. The observer produces a smooth, physical flow condition via integration of different sources of information. Even if the observation region is limited, the propagation of information via Poisson equation appears to be efficient and the flow prediction is definitely more accurate. In addition, the increase in computational resources compared to the model is very limited (of the order of 15%). This class of models deserves further analysis for testing their efficiency when integrated in active control strategies. The research work has been developed employing computational resources within the framework of the project A0012A07590 nr gen7590 DARI-GENCI.

References

1. Davidson, P.A.: Turbulence. An Introduction for Scientists and Engineers. Oxford University Press, Oxford (2004)
2. Issa, R.I.: Solution of the implicitly discretized fluid flow equations by operator-splitting. J. Comput. Phys. **62**, 40–65 (1986)
3. Kalman, R.E.: A new approach to linear filtering and prediction problems. J. Basic Eng. **82**, 35–45 (1960)

4. Lumley, J.: Stochastic Tools in Turbulence. Academic Press, New York (1970)
5. Meldi, M., Poux, A.: A reduced order Kalman Filter model for sequential data assimilation of turbulent flows. J. Comput. Phys. (2017). https://doi.org/10.1016/j.jcp.2017.06.042
6. Meldi, M., Salvetti, M.V., Sagaut, P.: Quantification of errors in large-eddy simulations of a spatially evolving mixing layer using polynomial chaos. Phys. Fluids **24**, 035101 (2012)
7. Pope, S.: Turbulent Flows. Cambridge University Press, Cambridge (2000)
8. Sagaut, P.: Large-Eddy Simulation for Incompressible Flows. An Introduction, 3rd edn. Springer, Berlin (2005)
9. Simon, D.: Optimal State Estimation: Kalman, H Infinity, and Nonlinear Approaches. Wiley, New York (2006)
10. Suzuki, T.: Reduced-order Kalman-filtered hybrid simulation combining particle tracking velocimetry and direct numerical simulation. J. Fluid Mech. **709**, 249–288 (2012)

Part IV
Multiphase and Reactive Flows

High Performance CFD/DEM Approach in Complex Geometries on Unstructured Meshes

Y. Dufresne, G. Lartigue, V. Moureau, E. Masi and O. Simonin

1 Introduction

Over the years, attention has been drawn to Computational Fluid Dynamics (CFD) as a necessary tool to get a better understanding of Fluidized Bed Reactors (FBR) dynamics and to avoid time-consuming and costly experiments on pilot-scale reactors. In industry, FBR typically consists of ten up to a few tens meter high cylinders also containing more complex parts and gathering several hundred billion particles (see [8] for a complete review on FBR modeling). In such complex geometries, unstructured meshes are easier to build and locally refine, but often shunned because of the extra coding effort required. Moreover, the employ of thousands of processors is often essential to ensure sufficient memory and performance of the code. In this context, the Discrete Element Method (DEM) introduced by Alder and Wainwright [1] is a promising meso-scale approach to perform simulations of industrial scale FBR that has already proven to be a valuable tool for a few tens centimeter high systems studies [8]. This paper aims at suggesting a numerical methodology compatible with the DEM approach to move towards large scale simulations involving complex

Y. Dufresne (✉) · G. Lartigue · V. Moureau
CORIA, CNRS UMR6614 Université et INSA de Rouen,
Saint-Etienne du Rouvray, France
e-mail: yann.dufresne@coria.fr

G. Lartigue
e-mail: ghislain.lartigue@coria.fr

V. Moureau
e-mail: vincent.moureau@coria.fr

E. Masi · O. Simonin
IMFT, CNRS UMR5502 INP et Université de Toulouse, Toulouse, France
e-mail: enrica.masi@imft.fr

O. Simonin
e-mail: olivier.simonin@imft.fr

M. V. Salvetti et al. (eds.), *Direct and Large-Eddy Simulation XI*,
ERCOFTAC Series 25, https://doi.org/10.1007/978-3-030-04915-7_26

geometries on unstructured meshes. Recently, in the framework of the MORE4LESS project funded by the French National Research Agency and coordinated by IFP-EN, this methodology has been applied in the finite-volume code YALES2, a Large-Eddy Simulation and Direct Numerical Simulation solver based on unstructured meshes [7], in the case of a semi-industrial scale FBR involving natural gas conversion [4].

2 DEM: A Challenging Cost

DEM computations can yield local information at the grid spacing scale as each particle is individually described, despite only being represented by their center of mass. To simulate dense particle-laden flows where multiple and simultaneous contacts between particles and walls can occur, it is often associated with a soft sphere model [3]. Here the contacts are accounted by inserting a collision force in Newton's second law of motion followed for the time advancement of spherical particles:

$$m_p \frac{d\mathbf{u}_p}{dt} = \mathbf{F}_D + \mathbf{F}_G + \mathbf{F}_C \quad \text{and} \quad \frac{d\mathbf{x}_p}{dt} = \mathbf{u}_p, \tag{1}$$

where m_p, $\mathbf{u}_p$, and $\mathbf{x}_p$ are the particle mass, velocity, and position, $\mathbf{F}_D$ is the drag force, $\mathbf{F}_G$ is the gravity force, and $\mathbf{F}_C$ is the collision force. The modeling of these forces is beyond the scope of the presented work.

The total collision force $\mathbf{F}_C$ acting on particle a is computed as the sum of all forces $\mathbf{f}^{col}_{b\to a}$ exerted by the N_p other particles and N_w walls in contact.

$$\mathbf{F}_C = \sum_{b=1}^{N_p+N_w} \mathbf{f}^{col}_{b\to a}. \tag{2}$$

When dealing with computational domain decomposition it is then clear that among the N_p other particles, some don't belong to the same processor as the particle a though physically colliding with it, revealing the need for an efficient parallel algorithm for collisions. Furthermore, in complex geometries the N_w walls can actually be made of several concave or convex entities that have to be individually treated for collision. This twofold aim will be discussed in Sects. 3 and 4.

3 Algorithm for Non-planar Boundaries Collisions in DEM

Industrial systems often contain non-planar boundaries, such as cylindrical parts or more complex elements, which require special treatment. Several options have been proposed by different authors to address this problem. Among them, the more commonly used is the one of the glued particles to approximate geometric surface and

thus treat particle-wall interactions the same way as particle-particle interactions [6]. However, this method requires further effort concerning particle configuration of the geometry, and suffers from a lack of accuracy, especially in the vicinity of convex parts. Interesting work has been carried out to circumvent these drawbacks in a more robust and accurate manner, but without dealing with parallelism [5]. Here is thus proposed an algorithm for detecting the interaction between a spherical particle and an arbitrarily complex geometric surface and mesh in the framework of the DEM and consistent with massive parallelism.

This algorithm relies on the fact that a particle can collide with only three geometrical entities; either a vertex, or an edge, or a face, or with any combination of these objects simultaneously. It is based on the existence of a unique Voronoi regions decomposition of those surface geometrical entities. The Voronoi region of an entity is defined as the part of the domain where any point is closer to that entity than to any other (see Fig. 1). Voronoi regions are defined by the oriented normals to each of its faces (apart from the one opposite to the entity), i.e.:

1. A vertex Voronoi region is defined by surface normals corresponding to the unit direction vectors carried by each edge connected to that vertex.
2. An edge Voronoi region is defined by four surface normals. Two are given by the unit direction vector carried by this edge (but oriented oppositely), and the two others correspond to unit vectors carried by each one of the connected faces and orthogonal to this edge (see Fig. 1).
3. A face Voronoi region is defined by surface normals given by the unit vectors orthogonal to each one of the bounding edges and belonging to the face plane.

The belonging of a particle to a specific Voronoi region is then given by the following condition if the surface normals are oriented outwards:

$$\text{particle} \in \text{Voronoi region if} \quad \forall i \in [1; N_{norm}] \quad \mathbf{n_{S,i}}.\mathbf{P_{C,i}} \leq 0, \tag{3}$$

where N_{norm} is the number of surface normals $\mathbf{n_{S,i}}$ of this Voronoi region, and $\mathbf{P_{C,i}}$ different vectors oriented towards the particle center, as presented in Fig. 1 for the example of a convex edge. To avoid wasteful calculation, this test is discarded as soon as one dot product is found positive.

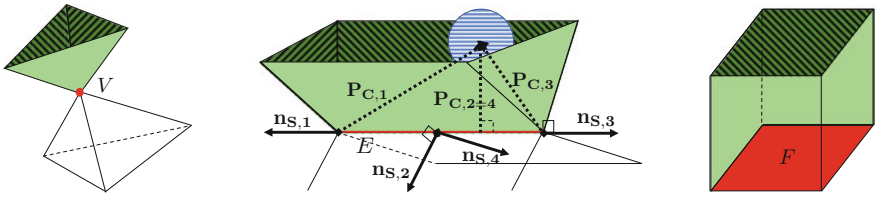

Fig. 1 In green, Voronoi regions of a convex: vertex (left), edge (center), and face (right). The case of the edge is explicited, with a particle approaching: the four unit surface normals $\mathbf{n_{S,i}}$ are oriented outwards. $\mathbf{P_{C,i}}$ vectors are oriented towards the particle center

The nearest non-planar boundaries to a particle are not straightforwardly obtained, and a priori, Voronoi belonging tests have to be performed for each particle and for each vertex, edge and face of all boundaries. To slash this brute-force cost, preliminary operations are performed:

1. Layers of mesh elements (usually two) near boundaries are flagged at the beginning of the simulation, so that the first test of the algorithm consists in discarding the particles that are not located in flagged elements (see Fig. 2).
2. Boundary Face Groups (BFG) are created as groups of adjacent faces, and their bounding spheres are defined using a center and a radius. The second step of the algorithm is thus to discard particles that don't overlap at least one BFG bounding sphere (see Fig. 3).
3. Bounding spheres are also stored for each boundary face at the beginning of the simulation. At that point of the algorithm, the remaining particles are close to one BFG at least. The third preliminary step consists in selecting faces whose bounding sphere is overlapping the particle.

The complete algorithm is represented in Fig. 4. Note that all distance checking in that algorithm use comparison of squared distance to avoid costly square roots calculations.

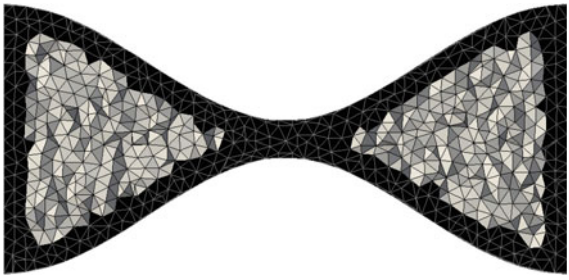

Fig. 2 Cut of an hourglass unstructured mesh. Only particles located in black cells are accounted for boundary collisions

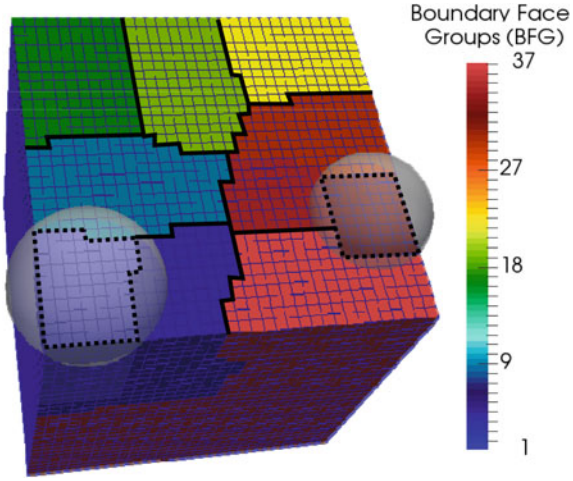

Fig. 3 Boundary Face Groups (BFG) on one processor domain on Cartesian mesh with two bounding spheres represented

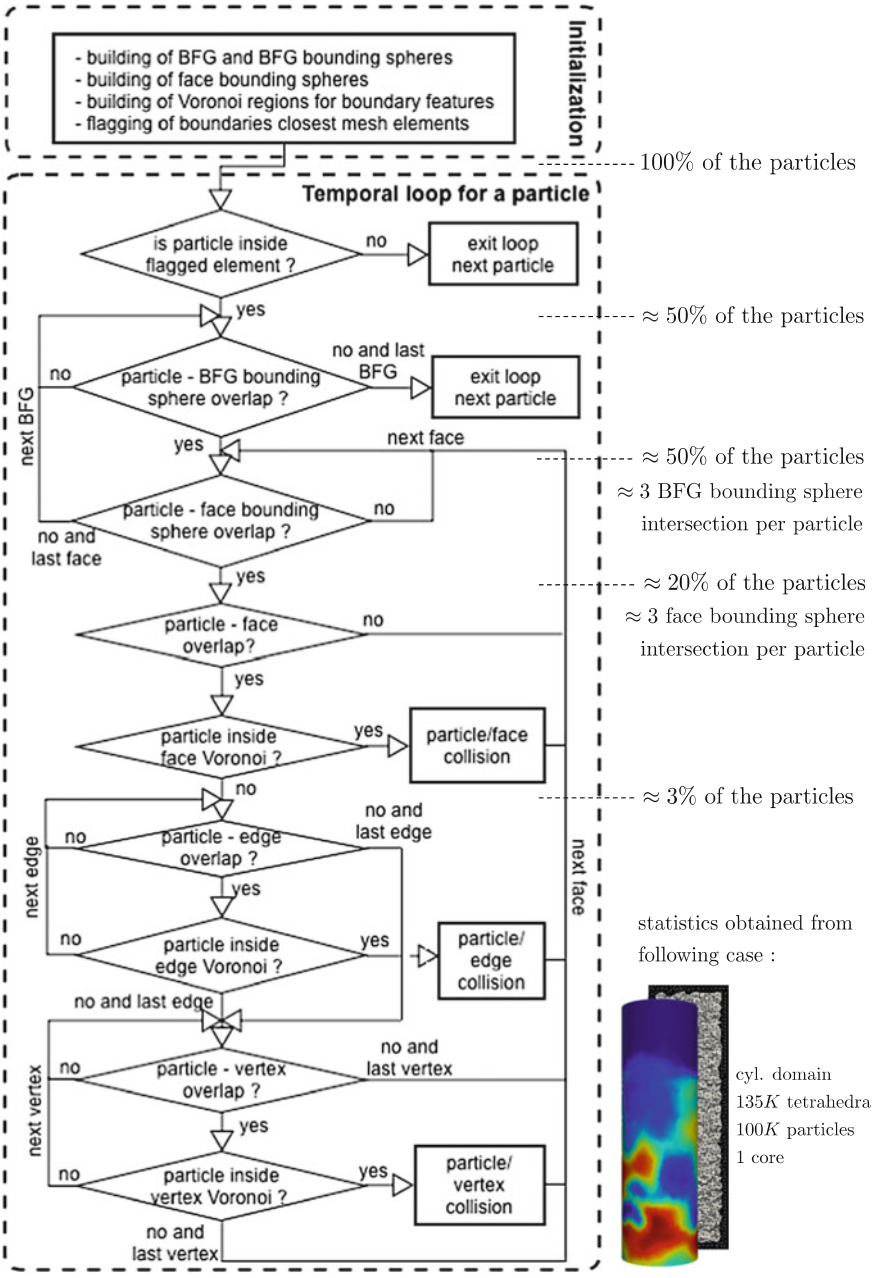

Fig. 4 Algorithm for the management of non-planar boundaries. The initialization part is performed once by run. The temporal loop part is performed by each particle at each particle time step. On the right, statistics show that 80% of the particles are discarded by preliminary tests

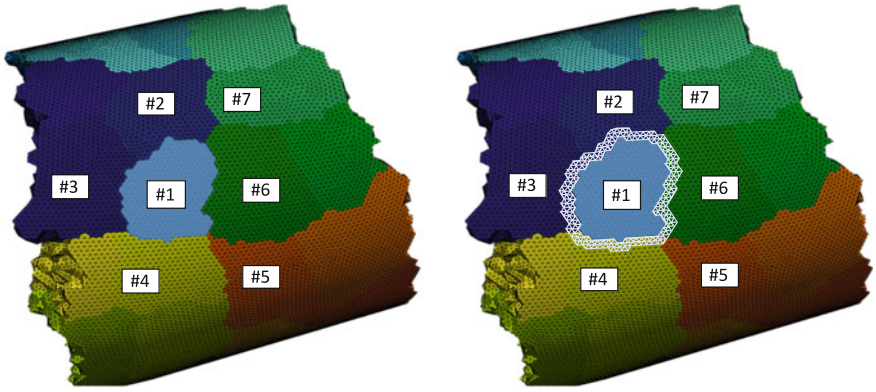

Fig. 5 Unstructured mesh partitioning of a cylindrical domain part. On the right, the cell halo (white) of processor ranked 1 is defined by two layers of neighboring processors' cells

4 Algorithm for Parallelism Management

In order to simulate systems of which size has to tend towards the one of industrial scale ones, a proper management of massive parallelism is an obvious step. To this end, an efficient algorithm using message passing interface (MPI) based on ghost particles [2] that has been optimized for unstructured meshes is presented.

At the beginning of the simulation, a cell halo is defined around each processor domain, containing layers of cells belonging to neighboring processors (see Fig. 5). This operation allows to store for each processor an exhaustive and symmetric list of the closest processors and the corresponding closest mesh elements. All parallel communications occurring during the run are based on this list: particles located in a cell halo are first copied in a particle group to send. Only necessary data for collision force computing are copied, i.e. velocities (translational and rotational), position, diameter and mass. To shrink the number of exchanges between processors, a packing method is employed to group all these data in one array that is next sent using non-blocking MPI sending procedure. Reception of the packed data is done by using MPI probes to detect which pack is ready to be received, so that waiting is minimized for MPI receive operations as well. All the received packed data are finally unpacked in "ghost" particle groups that can be treated locally for collision. Communications have to be performed each time particles are advanced in time. It should be highlighted that here particles don't need to be sent back to their former processor because only local particles' momentum are updated.

The weak scaling of the DEM/CFD solver is plotted on Fig. 6, exhibiting a good behavior on up to 4096 cores and 820 million particles.

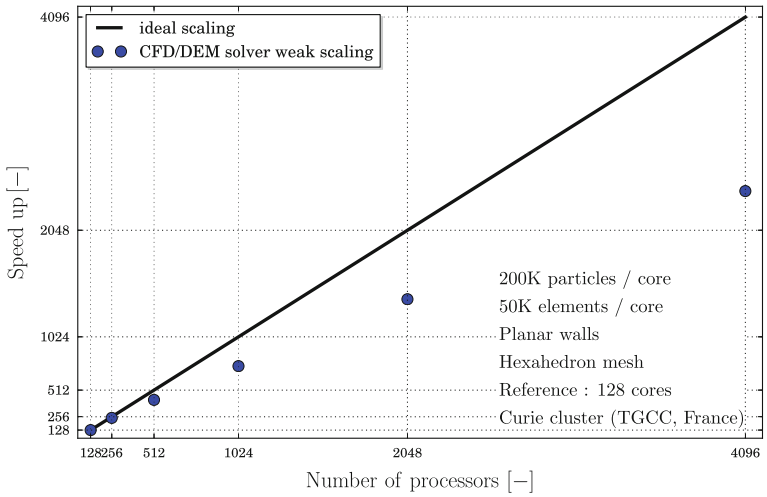

Fig. 6 Weak scaling of DEM/CFD solver

References

1. Alder, B.J., Wainwright, T.E.: Phase transition for a hard-sphere system. J. Chem. Phys. **27**, 1208 (1957)
2. Capecelatro, J., Desjardins, O.: An Euler-Lagrange strategy for simulating particle-laden flows. J. Comput. Physics. **238**, 1–31 (2013)
3. Cundall, P.A., Strack, O.D.L.: A discrete numerical model for granular assemblies. Géotech **29**, 47 (1979)
4. Dufresne, Y. et al.: Simulation of a reactive fluidized bed reactor using CFD/DEM. Technical report of the Cent. for Turbul. Res. (2016)
5. Junwei, S., Zhaolin, G., Xiao, Y.X.: Discrete element simulation of particle flow in arbitrarily complex geometries. Chem. Eng. Sci. **66**, 6069–6088 (2011)
6. Kodam, M., et al.: Force model considerations for glued-sphere discrete element method simulations. Chem. Eng. Sci. **64**, 3466–3475 (2009)
7. Moureau, V., Domingo, P., Vervisch, L.: Design of a massively parallel CFD code for complex geometries. C. R. méc. **339**, 141–148 (2011)
8. Van Der Hoef, M.A., et al.: Multiscale modeling of gas-fluidized beds. Adv. Chem. Eng. J. **31**, 65–149 (2006)

Direct Numerical Simulation of Spherical Bubbles in a Downward Turbulent Channel Flow

C. Santarelli and J. Fröhlich

1 Introduction

Downward bubbly flows occur when the direction of the fluid velocity is opposite to the direction of the rise velocity of the bubbles. This type of flow represents an important element of several industrial processes such as drilling [8] and reactions in chemical plants [4]. Many differences arise between upward and downward flows and one basic, yet dominant issue is the transfer of energy between the fluid and the bubbles. In upward flows the buoyancy force is oriented in the same direction as the force induced on the bubbles by the fluid [14]. In downward configurations, instead, the rise velocity of the bubbles must overcome the fluid-induced force on the bubbles themselves, yielding physical phenomena which are quite different from the corresponding ones in upward flows. Mainly experimental investigations, e.g. [2, 15] and recently [1], were carried out to address such issues, while numerical studies are limited in number [6, 7], despite providing valuable insight into the complex phenomena involved. The goal of the present work is to investigate the influence of the direction of the fluid velocity on different flow features by means of numerical simulations. To this end, two Direct Numerical Simulations (DNS) of an upward and a downward configuration, only differing by the direction of the fluid velocity, will be compared to address the physics of such flows.

2 Numerical Method

The simulations reported here were performed with an Eulerian-Lagrangian method where the Navier–Stokes equations for an incompressible fluid are solved on a fixed,

C. Santarelli · J. Fröhlich (✉)
Institute of Fluid Mechanics, Technische Universität Dresden, Dresden, Germany
e-mail: jochen.froehlich@tu-dresden.de

M. V. Salvetti et al. (eds.), *Direct and Large-Eddy Simulation XI*,
ERCOFTAC Series 25, https://doi.org/10.1007/978-3-030-04915-7_27

equidistant Cartesian grid and the bubbles are accounted for by means of an Immersed Boundary Method (IBM), as described in [3]. The original method was improved in [13] to account for light objects, such as bubbles and light spheres, introducing a numerical virtual mass force in the bubble equations of motion. Bubble-bubble and bubble-wall collisions were represented by a collision model, which is based on a repulsive force proportional to the distance between the surfaces. The numerical method was extensively validated [3, 12, 13] and previously employed for very similar problems [9, 10]

3 Configuration

The configuration investigated is the same for the two simulations presented here and features a vertical channel between two parallel walls, with periodic conditions in the streamwise (x) and spanwise (z) direction and a no-slip condition at the solid walls, $y/H = 0$ and $y/H = 1$, with y the wall-normal direction. The extensions of the computational domain are $4.43H \times H \times 2.21H$ in x-, y- and z-direction, respectively, discretised with $1024 \times 232 \times 512$ mesh points. For all simulations the fluid Reynolds number is equal to 5263, based on the bulk velocity U_b, the wall distance H and the fluid viscosity ν. The bulk velocity is kept constant by an instantaneously adjusted volume force.

The composition of the swarms is equal in the two cases, featuring 2880 bubbles of density ρ_p, with $\rho_p/\rho = 0.001$ where ρ is the fluid density, and diameter $d_p = 0.052H$, so that the total void fraction is 2.14%. Contaminated fluid is considered justifying a no-slip condition at the bubble surface. The Archimedes number $Ar = |\rho_p - \rho| g d_p^3/(\rho\nu^2)$ is 38171 and the mean bubble Reynolds number, obtained by averaging over all bubbles in the flow field and in time, is Re_p =221 for the downward case and Re_p =235 for the upward case.

The gravity force is oriented in the negative x-direction, so that bubbles tend to rise in the positive x-direction. This motion is counteracted by the mean fluid velocity oriented downwards, so that this case is labelled *SmManyDo* here. An instantaneous flow visualisation of an arbitrary instant in time is provided in Fig. 1. The case *SmManyDo* is compared with an upward bubbly flow labelled *SmMany* which features exactly the same parameters as the downward case apart from the direction of fluid velocity, pointing in positive x-direction. This case was extensively investigated in [9, 11]. The volume force required to drive the flow is 18% larger in the downward case.

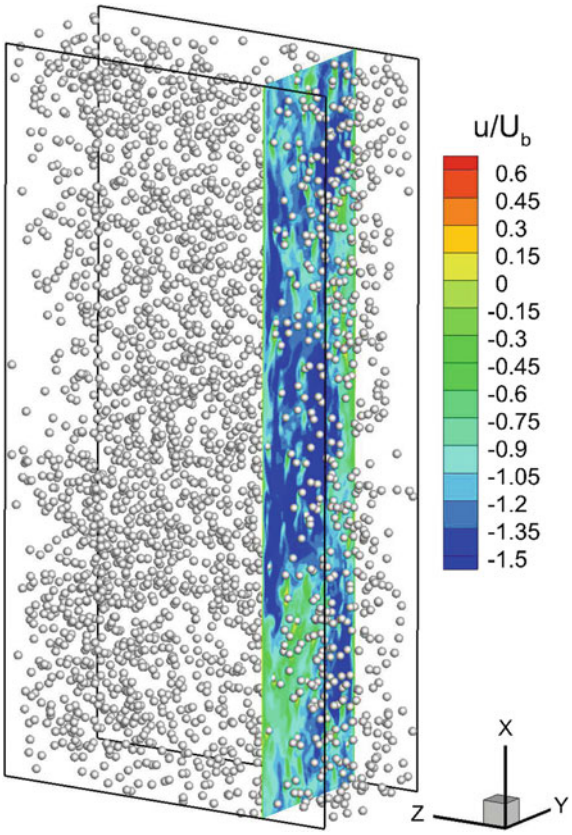

Fig. 1 Computational domain and instantaneous flow in the case *SmManyDo*. The contour plot in the x-y plane shows the instantaneous streamwise velocity component. Bubble positions and fluid velocity are shown for an arbitrary instant in time

4 Results

4.1 Fluid Phase

Fluid statistics were collected only for the domain cells completely filled with the liquid and averaged over the two periodic directions and in time over a duration of $T_{stat} \approx 500H/U_b$. As shown in Fig. 2, left, the presence of the bubbles modifies the mean velocity profile substantially in the case *SmManyDo*. In the core region the velocity profile is flatter due to the presence of bubbles in this region (see Sect. 4.2 below). This feature was observed also in other downward flows [5, 15]. On the other hand, the mean fluid velocity profile is almost not influenced by the presence of the bubbles in the upward configuration.

For the downward configuration, the components of the Reynolds stress tensor are substantially increased with respect to both the unladen flow and the upward configuration, confirming that for the chosen parameter range bubbles enhance the

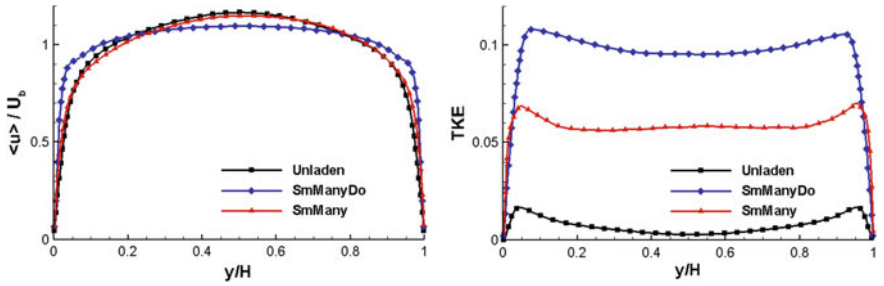

Fig. 2 Averaged streamwise fluid velocity (left) and TKE (right): comparison between case *SmMany*, case *SmManyDo* and case *Unladen*. For case *SmManyDo*, the velocity is inverted in sign

liquid turbulence, as reported, e.g., in [2, 5]. This feature is represented here by means of the turbulent kinetic energy (TKE), displayed in Fig. 2, right. It is also backed by the analysis of the individual contributions to the budget of the TKE (not shown here).

4.2 Disperse Phase

Figure 3 shows bubble-related statistics collected over the two periodic directions and over a duration T_{stat}. The mean void fraction distribution $\langle\phi\rangle$ for the case *SmManyDo* is presented in Fig. 3, right. It exhibits two peaks near the walls and an almost uniform value in the core region, similar to the case *SmMany*, Fig. 3, left. For the downward case, as well as for the upward case, it can be demonstrated that such profiles result from the contributions of the shear-induced lift force due to the gradient of the mean fluid velocity and the turbophoresis, which represents the tendency of particles and bubbles to acquire a drift velocity in the direction of decreasing turbulence intensity [9]. The influence the bubble collisions, instead, is negligible due to the very low number of such events, around 3.1 and 2.2 collision events for each instantaneous flow considered for case *SmManyDo* and *SmMany*, respectively.

In the downward configuration, the mean rise velocity of the bubbles is slightly positive close to the walls and then smoothly decreases towards the centre region. Here, the value is $\langle u_p \rangle / U_b \approx 0.3$ showing that for the chosen parameter range on average the bubbles do not rise in the channel but are rather pushed down by the fluid. The relative velocity, defined as the difference between the averaged bubble velocity and the averaged fluid velocity, is almost uniform across the channel and is similar, both in shape and magnitude, to the one of the case *SmMany*, as expected due to the same buoyancy force and the very similar fluid-induced drag force in the two configurations.

The fluctuations of the three components of the bubble velocity are reported in Fig. 4 for the two cases addressed. The fluctuations are higher for the downward case

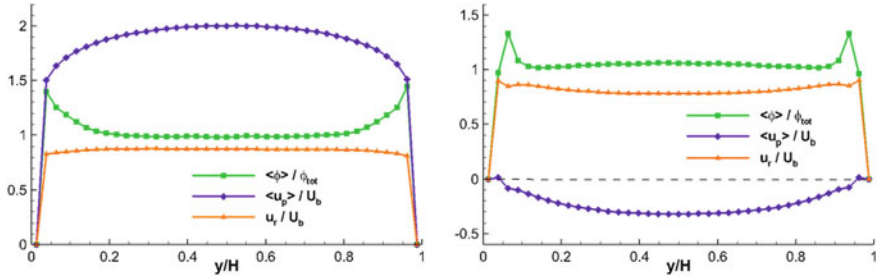

Fig. 3 Mean void fraction distribution, streamwise bubble velocity and relative velocity for case *SmMany* (left) and case *SmManyDo* (right)

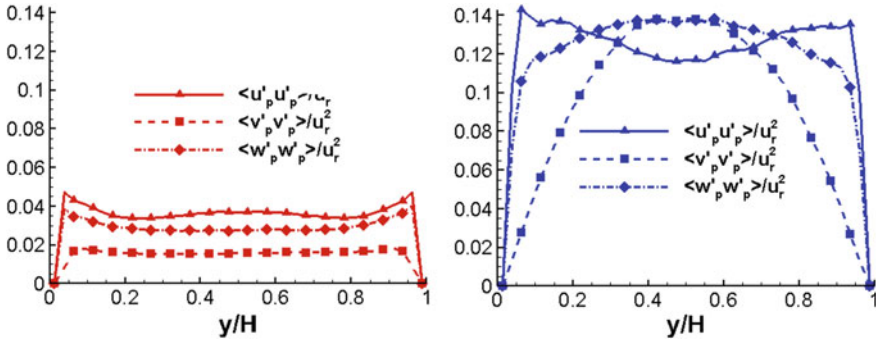

Fig. 4 Bubble velocity fluctuations for case *SmMany* (left) and case *SmManyDo* (right)

and this is due to the higher turbulence level in the flow, as already mentioned when the TKE was addressed. The maxima of the streamwise fluctuations are located very close to the maxima of the mean void fraction distribution (Fig. 3) and the streamwise fluctuations of the fluid velocity (not shown here). With respect to the upward case, the different shape of the wall-normal and spanwise fluctuations for the case *SmManyDo* is due to the presence of large-scale flow structures induced by the bubbles in the flow. They have a pronounced spanwise component and, hence, strongly influence the bubble trajectories. These structures are not observed in the upward configuration and will be further investigated in a forthcoming publication.

Acknowledgements The present work was partially funded by the German Federal Ministry of Education and Research, Project 01071513, and by the Helmholtz Alliance LIMTECH, Project A5. Computing time was provided by the Leibniz Supercomputing Centre in Munich.

References

1. Besagni, G., Inzoli, F.: Comprehensive experimental investigation of counter-current bubble column hydrodynamics: holdup, flow regime transition, bubble size distributions and local flow properties. Chem. Eng. Sci. **146**, 159–290 (2016)
2. Kashinsky, O.N., Lobanov, P.D., Randin, V.V.: The influence of a small gas addition to the structure of gas-liquid downward flow in a tube. J. Eng. Thermophys. **231**, 120–125 (2008)
3. Kempe, T., Fröhlich, J.: An improved immersed boundary method with direct forcing for the simulation of particle laden flow. J. Comput. Phys. **231**, 3663–3684 (2012)
4. Kunii, D., Levenspiel, O. and Brenner, H.: Bubbling fluidized beds. In: Fluidization Engineering, pp. 137–164. Butterworth-Heinemann Series in Chemical Engineering, Boston (2013)
5. Lelouvetel, J., Tanaka, T., Sato, Y., Hishida, K.: Transport mechanisms of the turbulent energy cascade in upward/downward bubbly flows. J. Fluid Mech. **741**, 514–542 (2014)
6. Lu, J., Tryggvason, G.: Effect of bubble size in turbulent bubbly downflow in a vertical channel. Chem. Eng. Sci. **62**, 3008–3018 (2007)
7. Lu, J., Tryggvason, G.: Effect of bubble deformability in turbulent bubbly upflow in a vertical channel. Phys. Fluids **20**, 040701 (2008)
8. Rehm, B., Schubert, J., Haghshenas, A., Paknejad, A.S. Hughes, J.: The why and basic principles of managed well-bore pressure. In: Managed Pressure Drilling, pp. 1–38. Gulf Publishing Company, Houston (2008)
9. Santarelli, C., Fröhlich, J.: Direct numerical simulations of spherical bubbles in vertical turbulent channel flow. Int. J. Multiph. Flow **75**, 174–193 (2015)
10. Santarelli, C., Fröhlich, J.: Direct numerical simulations of spherical bubbles in vertical turbulent channel flow. Influence of bubbly size and bidispersity. Int. J. Multiph. Flow **81**, 27–45 (2016)
11. Santarelli, C., Roussel, J., Fröhlich, J.: Budget analysis of the turbulent kinetic energy for bubbly flow in a vertical channel. Chem. Eng. Sci. **141**, 46–62 (2016)
12. Schwarz, S., Fröhlich, J.: Numerical study of single bubble motion in liquid metal exposed to a longitudinal magnetic field. Int. J. Multiph. Flow **62**, 134–151 (2014)
13. Schwarz, S., Kempe, T., Fröhlich, J.: A temporal discretization scheme to compute the motion of light particles in viscous flows by an immersed boundary method. J. Comput. Phys. **281**, 519–613 (2015)
14. Sommerfeld, M.: Bubbly Flows: Analysis, Modelling and Calculation. Springer Science & Business Media, Berlin (2012)
15. Sun, X., Paranjape, S., Kim, S., Goda, H., Ishii, M., Kelly, J.M.: Local liquid velocity in vertical air-water downward flow. J. Fluids Eng. **126**(4), 539–545 (2004)

DNS of Thermocapillary Migration of Deformable Droplets

N. Balcázar, O. Antepara, J. Rigola and A. Oliva

1 Introduction

A nonuniform distribution of temperature field on a fluid-fluid interface leads to surface tension gradients, which induce shear stresses that produce the motion of a drop in the direction of the temperature gradient. This phenomenon is known as thermocapillary flow or Marangoni migration. In addition to its importance from a fundamental point of view, thermocapillary flows play an important role in micro gravity environments [1] and micro-devices [2].

Experimental research of these flows has inherent difficulties. However, the development of high-performance computing in combination with Direct Numerical Simulation (DNS) of the Navier–Stokes equations open the possibility to perform controlled numerical experiments, providing a good way to non-invasive measure of droplet flows, although computationally expensive. Multiple methods have been developed for DNS of bubbly (or droplet) flows [3–8], all of them based on the so-called one fluid formulation. In the present work a novel multiple marker level-set method introduced in [9] and extended in [3] to non-isothermal two-phase flows with variable surface tension, is employed for DNS of thermocapillary migration of deformable droplets. Thus, using the conservative level-set approach [4, 6], accumu-

N. Balcázar (✉) · O. Antepara
Termo Fluids S.L., Terrassa, Spain
e-mail: nestor@termofluids.com; nestor@cttc.upc.edu; nestorbalcazar@yahoo.es

O. Antepara
e-mail: oscar@termofluids.com; oscar@cttc.upc.edu

N. Balcázar · O. Antepara · J. Rigola · A. Oliva
Heat and Mass Transfer Technological Center (CTTC),
Technical University of Catalonia (UPC), Barcelona, Spain
e-mail: quim@cttc.upc.edu

A. Oliva
e-mail: cttc@cttc.upc.edu

M. V. Salvetti et al. (eds.), *Direct and Large-Eddy Simulation XI*,
ERCOFTAC Series 25, https://doi.org/10.1007/978-3-030-04915-7_28

lation of mass conservation error inherent to standard level-set methods is avoided. Furthermore, the multiple marker methodology [3, 9] prevents the numerical and potentially unphysical coalescence of the fluid interfaces, taking into account the collision of the droplets, while their volumes are kept constant throughout the simulation [10].

2 Mathematical Model and Numerical Methods

The mathematical formulation has been introduced in our previous work [3], and here is presented for the sake of completeness. The Navier–Stokes equations for the dispersed fluid in Ω_d and continuous fluid in Ω_c are written using the so-called one-fluid formulation, in a global domain $\Omega = \Omega_d \cup \Omega_c$ [3]:

$$\frac{\partial(\rho \mathbf{v})}{\partial t} + \nabla \cdot (\rho \mathbf{v}\mathbf{v}) = -\nabla p + \nabla \cdot \mu \left(\nabla \mathbf{v} + (\nabla \mathbf{v})^T\right) + \rho \mathbf{g} + \mathbf{f}_\sigma(T)\delta_\Gamma, \qquad \nabla \cdot \mathbf{v} = 0 \tag{1}$$

where $\mathbf{v}$ is the fluid velocity, p is the pressure field, ρ is the fluid density, μ is the dynamic viscosity, defined as $\rho = \rho_d H_d + \rho_c(1 - H_d)$ and $\mu = \mu_d H_d + \mu_c(1 - H_d)$, H_d is the Heaviside step function that is one in Ω_d and zero elsewhere, subscripts d and c are used for the dispersed and continuous fluids respectively, $\mathbf{g}$ is the gravitational acceleration, $\mathbf{f}_\sigma$ is the surface tension force, and δ_Γ is the Dirac delta function concentrated at the interface. Furthermore, an energy equation is introduced in order to compute the temperature field (T):

$$\frac{\partial T}{\partial t} + \nabla \cdot (\mathbf{v}T) = \frac{1}{\rho c_p} \nabla \cdot (\lambda \nabla T) \tag{2}$$

where c_p is the heat capacity and λ is the thermal conductivity, defined as $\lambda = \lambda_d H_d + \lambda_c(1 - H_d)$, and $c_p = c_{p,d} H_d + c_{p,c}(1 - H_d)$. A multiple marker level-set method introduced in [4, 9] is used for interface capturing. The ith droplet interface is the 0.5 iso-surface of a level-set function ϕ_i [4], where $i = 1, ..., n_d$ and n_d is the total number of droplets. Since the velocity field is solenoidal, the ith interface transport equation is written in conservative form [3]. Furthermore, a re-initialization equation is solved for steady state, in order to keep a sharp and constant level-set profile [4]:

$$\frac{\partial \phi_i}{\partial t} + \nabla \cdot \phi_i \mathbf{v} = 0, \qquad \frac{\partial \phi_i}{\partial \tau} + \nabla \cdot \phi_i(1 - \phi_i)\mathbf{n}_i = \nabla \cdot \varepsilon \nabla \phi_i \tag{3}$$

Normal vectors $\mathbf{n}_i$ and curvature κ_i at the interface, are computed as $\mathbf{n}_i(\phi_i) = \nabla\phi_i / \|\nabla\phi_i\|$ and $\kappa_i(\phi_i) = -\nabla \cdot \mathbf{n}_i$. The capillary and Marangoni forces [3] are introduced in the context of the continuous surface force model [11], extended to the multiple markers methodology with variable surface tension in [3]:

$$\mathbf{f}_\sigma \delta_\Gamma = \sum_{i=1}^{n_d} (\sigma(T)\kappa_i(\phi_i)\mathbf{n}_i - \nabla\sigma(T) + \mathbf{n}_i(\mathbf{n}_i \cdot \nabla)\sigma(T)) \, ||\nabla\phi_i|| \tag{4}$$

The fluid properties are regularized by employing a global level-set function for the dispersed phase [9], $H_d = \phi_d$, with $\phi_d = max\{\phi_1, ..., \phi_{n_d-1}, \phi_{n_d}\}$, computing the fluid properties as described in [3]. The mathematical model is discretized using the finite-volume method on a collocated unstructured grid as reported in [3, 4].

3 Numerical Experiments

Validations and verifications of the unstructured multiphase solver used in this work are reported in [4, 9, 10, 12, 13]. Additional validations and verifications are reported in [3] for thermocapillary flows, including the Marangoni migration of $3D$ single and multiple droplets. Thus, this work can be considered as a further step in the understanding of the thermocapillary motion of multiple deformable droplets. Thermocapillary flows ($\mathbf{g} = 0$), are characterized by the thermal conductivity ratio $\eta_\lambda = \lambda_d/\lambda_c$, heat capacity ratio $\eta_{c_p} = c_{p,d}/c_{p,c}$, viscosity ratio $\eta_\mu = \mu_c/\mu_d$, density ratio $\eta_\rho = \rho_c/\rho_d$, Marangoni number $Ma = U_r L_r \rho_c c_{p,c}/\lambda_c$, Capillary number $Ca = U_r \mu_c/\sigma_0$, and Reynolds number $Re = U_r L_r \rho_c/\mu_c$, with $U_r = (\partial\sigma/\partial T)||\nabla T_\infty||(d/2)/\mu_c$, $L_r = d$, dimensionless time $t^* = 2tU_r/d$, dimensionless migration velocity $V_i^* = (\mathbf{e}_y \cdot \mathbf{v}_i)/U_r$, and $\mathbf{v}_i = \int_\Omega \mathbf{v}\phi / \int_\Omega \phi dV$. Material property ratios are 2, unless otherwise stated.

First, a set of two-dimensional experiments is performed. The size of the domain Ω is $(L_x, L_y) = (6d, 12d)$, where d is the initial droplet diameter. No-slip boundary conditions are used at the top and bottom boundaries, whereas Ω is periodic in the $x\text{-}direction$, with $\mathbf{g} = \mathbf{0}$. A linear temperature profile is imposed at the initial time, with a higher temperature at the top boundary, and lower temperature at the bottom boundary. A uniform cartesian mesh with 480×720 cells is employed ($h = d/40$). In the beginning, 18 droplets are distributed randomly in 3 layers of 6 droplets. Figure 1 shows the time evolution of the migration velocity for each droplet, including the effect of Ma, Ca, Re, and bi-dispersion of droplet size. Figures 2 and 3 depict instantaneous snapshots of the droplet distributions, the vorticity, and the Isotherms. Finally, Fig. 4 illustrates the effect of the convective numerical scheme [3, 4] used to discretize the momentum equation and energy equation.

Second, the thermocapillary interaction of 18 droplets is investigated in a $3D$ domain. Ω is a rectangular channel of section $6d \times 6d$ on the plane $x - z$, and length $12d$ on the y-axis. A uniform cartesian mesh of $240 \times 240 \times 480$ cells ($h = d/40$) is employed, distributed in 1536 CPU-cores. No-slip boundary condition is used at the adiabatic lateral walls (x and z directions), a constant temperature is fixed at the top (T_t) and bottom boundaries (T_b), with $T_t > T_b$. At the initial time, 18 droplets are distributed randomly in two layers of 9 droplets, similarly to the arrangement used in [3], for $Re = 40$, $Ma = 60$, $Ca = 0.0416\bar{6}$ with physical property ratios 2.

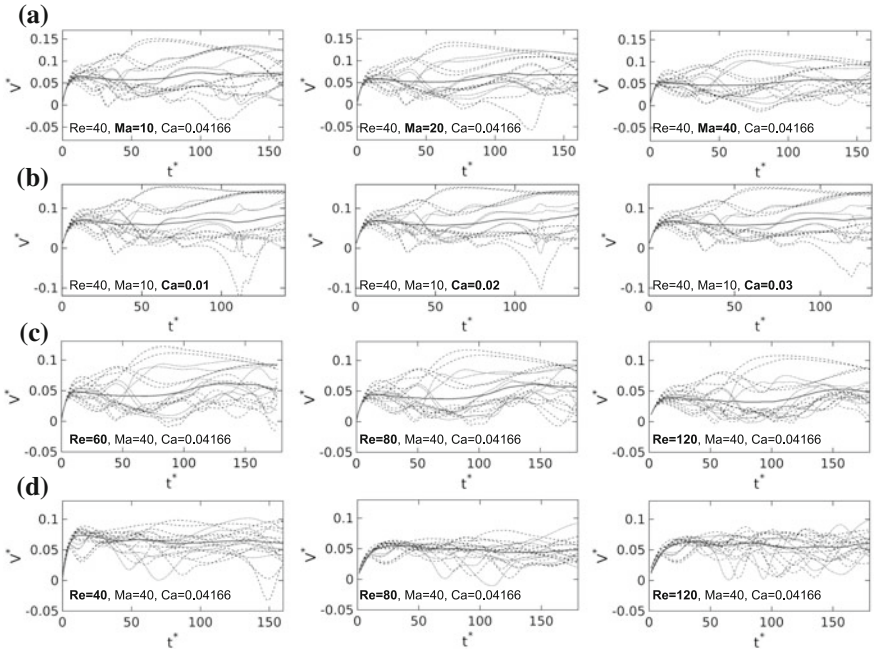

Fig. 1 18 droplets. **a** Effect of Ma. **b** Effect of Ca. **c** Effect of Re. **d** Effect of Re for a bi-dispersed system, with bi-dispersed ratio 0.625. Continuous line for the average velocity. Discontinuous line for each droplet velocity

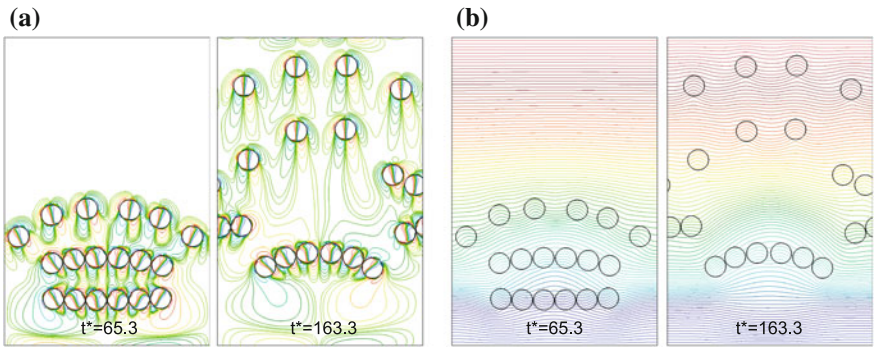

Fig. 2 18 droplets with diameter d, $Re = 40$, $Ma = 10$, $Ca = 0.03$, material property ratios are 2. **a** Vorticity $\mathbf{e}_z \cdot (\nabla \times \mathbf{v})$. **b** Isotherms

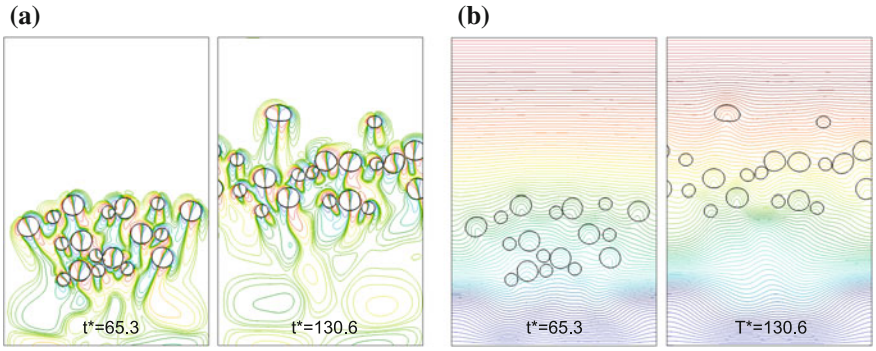

Fig. 3 9 droplets with diameter d, and 9 droplets with diameter $0.625d$, $Re = 40$, $Ma = 10$, $Ca = 0.0416\bar{6}$, material property ratios are 2. **a** Vorticity $\mathbf{e}_z \cdot (\nabla \times \mathbf{v})$. **b** Isotherms

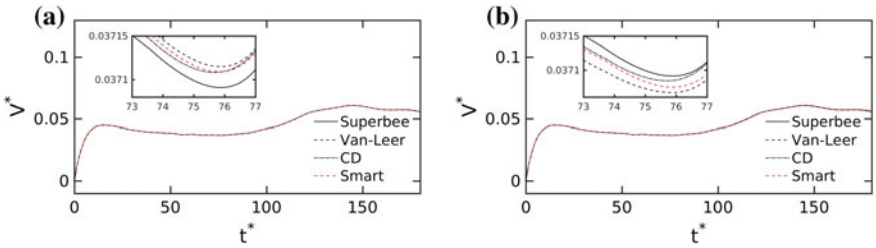

Fig. 4 Effect of convective scheme, flux limiters [3, 4]. Average velocity of 18 droplets, $Re = 80$, $Ma = 40$, $Ca = 0.0416\bar{6}$, material property ratios are 2. **a** Energy equation. **b** Momentum equation

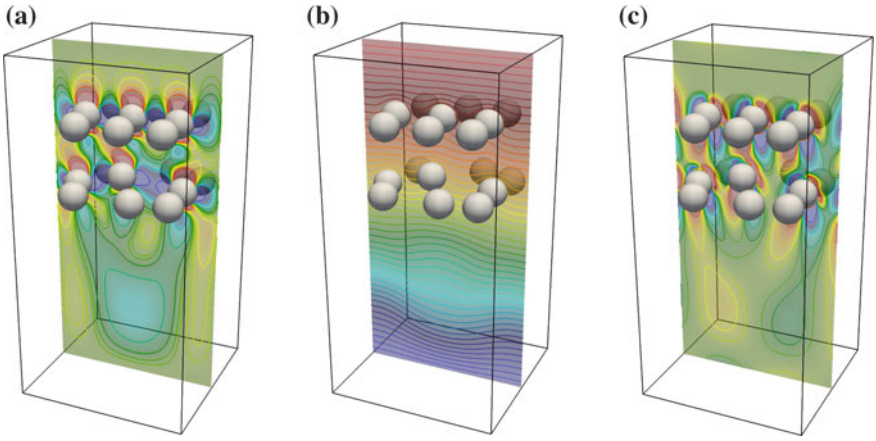

Fig. 5 18 droplets with diameter d, $Re = 40$, $Ma = 60$, $Ca = 0.0416\bar{6}$, material property ratios are 2, $t^* = 111$. **a** Velocity $\mathbf{e}_y \cdot \mathbf{v}$. **b** Isotherms. **c** Vorticity $\mathbf{e}_z \cdot (\nabla \times \mathbf{v})$

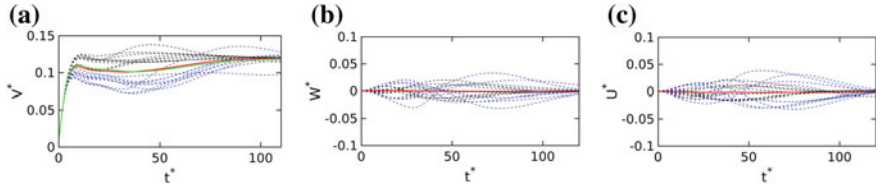

Fig. 6 18 droplets with diameter d, $Re = 40$, $Ma = 60$, $Ca = 0.0416\bar{6}$, material property ratios are 2. First layer of 9 droplets (blue lines), second layer of 9 droplets (black lines), average (red line). Average migration velocity of a second initial condition (green line). $U^* = \mathbf{e}_x \cdot \mathbf{v}_i / U_r$, $V^* = \mathbf{e}_y \cdot \mathbf{v}_i / U_r$, $W^* = \mathbf{e}_z \cdot \mathbf{v}_i / U_r$, $\mathbf{v}_i$ is the droplet velocity

Figure 5 shows the migration velocity $\mathbf{e}_y \cdot \mathbf{v}$, temperature and vorticity $\mathbf{e}_z \cdot (\nabla \times \mathbf{v})$ on the plane $x - y$ of the channel. Furthermore, the time evolution of the ith droplet migration velocity (V^*) is depicted in Fig. 6. This figure also indicates slight sensitivity of the average migration velocity for a different initial droplet distribution. A separation of the two droplet layers is observed, consistently with our previous results [3]. Figure 6 also shows that lateral velocities (U^*, W^*) of the droplets present oscillations, although the average velocity tends to zero.

4 Conclusions

DNS of thermocapillary-driven motion of droplet clouds has been performed using a multiple marker level-set method introduced in our previous works [3, 9], including the effect of Ma, Re and Ca and bi-dispersion of the droplet size, in both $2D$ and $3D$ domains. A repulsion effect arises from the interaction of two-droplets in vertical alignment which induces the formation of horizontal layers. These interactions lead to the random motion of the droplets, however the average velocity of the droplet cloud tend to a quasi-steady state.

Acknowledgements This work has been financially supported by MINECO (ENE2015-70672-P), and by Termo Fluids S.L., Spain. Néstor Balcázar acknowledges financial support of the *Programa Torres Quevedo* MINECO (PTQ-14-07186), Spain. Oscar Antepara acknowledges financial support of MINECO (DI-14-06886), and *Secretaria d' Universitats i Recerca del Departament d'Economia i Coneixement de la Generalitat de Catalunya* (2015DI-68), Spain. Three-dimensional simulations were carried out using computer time awarded by PRACE 14th Call (project 2014112666) on the supercomputer MareNostrum IV based in Barcelona, Spain.

References

1. Subramanian, R.S., Balasubramaniam, R.: The Motion of Bubbles and Drops in Reduced Gravity. Cambridge University Press, Cambridge (2001)
2. Darhuber, A.A., Troian, S.M.: Principles of microfluidic actuation by modulation of surface stresses. Annu. Rev. Fluid Mech. **37**, 425–455 (2005)
3. Balcázar, N., Rigola, J., Castro, J., Oliva, A.: A level-set model for thermocapillary motion of deformable fluid particles. Int. J. Heat Fluid Flow **62, Part B**, 324–343 (2016)
4. Balcázar, N., Jofre, L., Lehmkhul, O., Castro, J., Rigola, J.: A finite-volume/level-set method for simulating two-phase flows on unstructured grids. Int. J. Multiph. Flow **64**, 55–72 (2014)
5. Coyajee, E., Boersma, J.B.: Numerical simulation of drop impact on a liquid-liquid interface with a multiple marker front-capturing method. J. Comp. Phys. **228**, 4444–4467 (2009)
6. Olsson, E., Kreiss, G.: A conservative level set method for two phase flow. J. Comput. Phys. **210**, 225–246 (2005)
7. Sussman, M., Smereka, P., Osher, S.: A level set approach for computing solutions to incompressible two-phase flow. J. Comput. Phys. **144**, 146–159 (1994)
8. Tryggvason, G., Bunner, B., Esmaeeli, A., Juric, D., Al-Rawahi, N., Tauber, W., Han, J., Nas, S., Jan, Y.-J.: A front-tracking method for the computations of multiphase flow. J. Comput. Phys. **169**, 708–759 (2001)
9. Balcázar, N., Lehmkhul, O., Rigola, J., Oliva, A.: A multiple marker level-set method for simulation of deformable fluid particles. Int. J. Multiph. Flow **74**, 125–142 (2015)
10. Balcázar, N., Castro, J., Rigola, J., Oliva, A.: DNS of the wall effect on the motion of bubble swarms. Procedia Comput. Sci. **108**, 2008–2017 (2017)
11. Brackbill, J.U., Kothe, D.B., Zemach, C.: A continuum method for modeling surface tension. J. Comput. Phys. **100**, 335–354 (1992)
12. Balcázar, N., Lehmkhul, O., Jofre, L., Rigola, J., Oliva, A.: A coupled volume-of-fluid/level-set method for simulation of two-phase flows on unstructured meshes. Comput. Fluids **124**, 12–29 (2016)
13. Balcázar, N., Lemhkuhl, O., Jofre, L., Oliva, A.: Level-set simulations of buoyancy-driven motion of single and multiple bubbles. Int. J. Heat Fluid Flow **56**, 91–107 (2015)

The Motion of Settling Particles in Isotropic Turbulence: Filtering Impact and Kinematic Simulations as Subfilter Model

J. Pozorski and B. Rosa

1 Introduction

Turbulent two-phase flows with small particles are quite common in environmental and industrial contexts. The dispersed phase is involved in a range of phenomena, including preferential concentration, collisions/agglomeration, and wall deposition. In computations of practical flow cases, beyond relatively low Reynolds numbers and simple geometries, DNS reveals to be overly expensive, even in the point-particle approximation with the one-way momentum coupling. Therefore, LES has gained more and more interest over the years. When feasible, the LES becomes particularly well suited for situations where the solution of instantaneous eddy structures is crucial for the prediction of the particulate phase. The subgrid scales (SGS) may have an impact on the motion of particles, especially those of lower inertia. This issue is called here the SGS particle dispersion. Several classes of models have been proposed to account for the effect, as reviewed in [6], but the issue remains open.

Here, we use the DNS, spectrally-filtered DNS, and LES of forced isotropic turbulence to study the effect of filtering on the dynamics of point-particles under gravity, motivated by the physics of cloud droplets. The effects of gravity imply changes in the radial distribution function and particle relative velocity [7] as well as an increase (usually) of the mean settling velocity due to preferential sweeping [9, 12]. In no-gravity cases, the filtering of the fluid velocity, performed in spectral space, has already been shown to have a non-trivial impact on these quantities [1]. In the present contribution, building on [10], we further examine the impact of filtering on the dispersed phase. Another aim is to use the resulting data for model validation and to test the closures based on the kinematic simulations of subfilter turbulence.

J. Pozorski (✉)
Institute of Fluid Flow Machinery (IMP PAN), Gdańsk, Poland
e-mail: jp@imp.gda.pl

B. Rosa
Institute of Meteorology and Water anagement – National Research Institute (IMGW-PIB), Warsaw, Poland
e-mail: Bogdan.Rosa@imgw.pl

M. V. Salvetti et al. (eds.), *Direct and Large-Eddy Simulation XI*,
ERCOFTAC Series 25, https://doi.org/10.1007/978-3-030-04915-7_29

2 DNS and LES with Particle Tracking, Impact of Filtering

The carrier phase is described by the incompressible Navier–Stokes equations written in the rotational form. The DNS of homogeneous isotropic turbulence are performed on a 256^3 grid, resulting in the Taylor-based Reynolds number $Re_\lambda = 107$ for most simulations. An efficient, massively parallel flow solver is used, as described in [8] and references therein. The LES are run on a coarser grid of 64^3 points ($N = 64$). The filtered velocity in the spectral space, $\hat{\bar{\mathbf{U}}}(\mathbf{k}, t)$, is solved from

$$\left\{ \frac{\partial}{\partial t} + [\nu + \nu_e(k|k_c)]k^2 \right\} \hat{\bar{\mathbf{U}}}(\mathbf{k}, t) = \mathbf{P}(\mathbf{k}) F(\bar{\mathbf{U}} \times \bar{\boldsymbol{\omega}}) + \hat{\mathbf{f}}(\mathbf{k}, t) \tag{1}$$

where $\mathbf{P}$ is the projection tensor, F denotes the Fourier transformation, and k_c is the maximum wavenumber resolved in the simulation; here, the cutoff is set to $k_c = int(N/2 - 1.5) = 30$. Then, $\bar{\mathbf{U}}$ and $\bar{\boldsymbol{\omega}}$ are respectively the filtered velocity and vorticity in physical space. In LES runs, the subgrid term is closed with the Chollet-Lesieur expression for the spectral eddy viscosity $\nu_e = \nu_e(k|k_c)$, see [10]. Both in the DNS and LES, a stochastic forcing term, $\hat{\mathbf{f}}(\mathbf{k}, t)$, is applied at large wavenumbers.

Heavy ($\rho_p/\rho \gg 1$), point-particles are tracked in the flow:

$$\begin{aligned} \frac{d\mathbf{x}_p(t)}{dt} &= \mathbf{V}_p(t) \\ \frac{d\mathbf{V}_p(t)}{dt} &= \frac{\mathbf{U}(\mathbf{x}_p(t), t) - \mathbf{V}_p(t)}{\tau_p} + \mathbf{g} \end{aligned} \tag{2}$$

where only the Stokes drag and gravity forces are retained; $\tau_p = (\rho_p/\rho) d_p^2/(18\nu)$ is the particle momentum relaxation time. In the DNS, the fluid velocity seen by the particles is computed as $\mathbf{U}^*(t) = \mathbf{U}(\mathbf{x}_p(t), t)$; in the LES, $\bar{\mathbf{U}}$ is taken instead.

The control parameters for particle motion are the Stokes number St and the Froude number Fr (or the velocity ratio S_V), expressed with the Kolmogorov time τ_k and velocity v_k, and the terminal settling velocity in still fluid $V_T = \tau_p g$:

$$St = \frac{\tau_p}{\tau_k}, \quad Fr = St\, S_V^2, \quad S_V = V_T/v_k\ . \tag{3}$$

The filtering of the fluid velocity has been performed in spectral space to allow for a precise assessment of the small-scale impact on the inertial particles, representing cloud droplets. Apart from the changes in the average settling velocity, due to preferential sweeping, there occurs a direction-dependent reduction of the r.m.s. particle velocity, see Fig. 1a. These quantities have not been considered in a comprehensive study on filtering effects for particle systems in turbulence [3]. Then, we have computed some collision-related statistics: the radial distribution function (RDF) of the particles at contact and the radial relative velocity (RRV). We have found that both RDF and RRV get reduced upon filtering for smaller-inertia droplets [10]. The effect

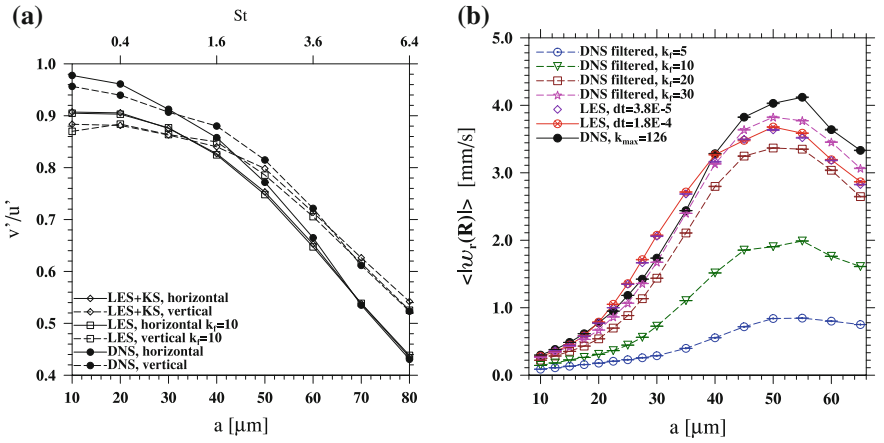

Fig. 1 Effect of filtering on particle statistics: **a** the rms of the respective particle velocity v' component (horizontal or vertical) as a function of the Stokes number or particle size; DNS and LES studies with gravity (u' is the rms fluid velocity); **b** radial relative velocity of nearly-touching cloud droplets in presence of gravity: DNS, filtered DNS (for several k_f) and LES (at two Δt)

is observed both in a priori and a posteriori LES. The radial relative velocity w_r is defined in terms of the relative velocity $\mathbf{w}$ between two droplets with the separation vector $\mathbf{r}$ as $w_r(\mathbf{r}) = \mathbf{w} \cdot \mathbf{r}/|\mathbf{r}|$. The methodology for computing w_r is similar to that described in [8]. The average value of RRV, $\langle |w_r| \rangle (2a)$, is shown in Fig. 1b for a monodisperse system of nearly touching particles as a function of their radii a for DNS, filtered DNS and LES runs. The RRV generally increases with particle radius, corresponding to a weakening correlation of velocities of two particles coming to contact. For the largest particle radii considered, the gravity effect prevails and the RRV starts to decrease. The effect of a priori filtering on w_r is readily noticed; also, in the LES the relative radial velocity is reduced. We note that the LES study, with some surplus energy close to the spectrum cutoff, slightly overpredicts the RRV for medium-inertia particles w.r.t. the DNS data.

3 Kinematic Simulation as Subfilter Model

When modelling the SGS particle dispersion, so-called functional and structural approaches may be distinguished. The functional approaches aim at retrieving only some 'integral' features of subfilter turbulence. In particular, stochastic models of particle dispersion, such as Lagrangian, one-point diffusion-type closures for the subfilter fluid velocity, belong to this category, see [6]. This is analogous to single-phase turbulence closures in LES where the impact of subfilter scales on the resolved ones is modelled with an additional viscosity.

The structural-type approaches to subfilter particle dispersion in LES aim at mimicking the residual scales themselves (see [6] and references therein for more details). Essentially, (a part of) the subfilter velocity field is reconstructed in a simplified manner at a low computational overhead. The clear advantage of these approaches is the account, at least in part, for the spatial correlation of the SGS fluid veloc-

ity field. Thus, unlike the one-point stochastic diffusion models, they allow for an approximate retrieval of two-point particle statistics at the subfilter scale, such as relative small-scale velocity and particle segregation patterns. These quantities are crucial for particle collision rates and short-time relative dispersion. The structural approaches include the approximate deconvolution (ADM) of the large-scale fluid velocity field, the fractal interpolation, and the so-called kinematic simulations (KS) based on Fourier modes. ADM is mathematically elegant, yet it retrieves only a part of the non-resolved velocity field, of wavenumbers close to the cutoff flows was proposed [5].

The KS [2], meant here to represent the small-scale velocity field, have recently been used with some success to estimate the particle collision rates in isotropic turbulence [7, 11], and to estimate the particle deposition in wall-bounded turbulence for the aerosol drug inhalation [4]. Therefore, we have decided to test the suitability of KS as a structural model for subfilter particle dispersion under gravity. In KS [7], the incompressible velocity field is constructed as a sum of $N_k \times M$ separate random modes $\mathbf{k}_{nm}$ with frequencies (or inverse time scales) ω_n

$$\mathbf{u}_{\mathrm{KS}}(\mathbf{x},t) = \sum_{n=1}^{N_k} \sum_{m=1}^{M} \left[\mathbf{A}_{nm} \times \hat{\mathbf{k}}_{nm} \cos(\mathbf{k}_{nm} \cdot \mathbf{x} + \omega_n t) + \mathbf{B}_{nm} \times \hat{\mathbf{k}}_{nm} \sin(\mathbf{k}_{nm} \cdot \mathbf{x} + \omega_n t) \right] \tag{4}$$

where $\hat{\mathbf{k}}_{nm} = \mathbf{k}_{nm}/k_n$ and $k_n = |\mathbf{k}_{nm}|$, $n = 1, 2, \ldots, N_k$, are prescribed wavevector magnitudes, or inverse length scales. The values of k_n are chosen as a geometric series. For given n, the modes $\mathbf{k}_{nm}$, $m = 1, 2, \ldots, M$ differ by orientation on a spherical shell of radius k_n. The random coefficients $\mathbf{A}_{nm}$ and $\mathbf{B}_{nm}$ are chosen to satisfy the incompressibility constraint $\nabla \cdot \mathbf{u}_{\mathrm{KS}} = 0$. Also, the magnitude of the cross-products, $|\mathbf{A}_{nm} \times \hat{\mathbf{k}}_{nm}|^2 = |\mathbf{B}_{nm} \times \hat{\mathbf{k}}_{nm}|^2 = E(k_n)\Delta k_n/M$, should yield the pre-defined energy spectrum of the flow beyond the LES cut-off wavenumber. It is most often taken as spectrum in the inertial range, $E(k) \sim k^{-5/3}$, since it is assumed that the eddy structures of that size are universal, i.e. independent (or weakly dependent) on the detailed way of turbulence generation in the range of large scales.

The magnitudes of the modes are taken from the Gaussian (or normal) probability distribution with zero-mean and the variance equal to the energy of particular mode:

$$\mathbf{A}_{nm} \in \mathcal{N}(0, \sigma_n), \quad \mathbf{B}_{nm} \in \mathcal{N}(0, \sigma_n) \tag{5}$$

where $\sigma_n^2 = E(k_n)\Delta k_n/M$. The KS field may vary in time, if frequencies ω_n of the modes are set non-zero. Most often:

$$\omega_n \sim \sqrt{k_n^3 E(k_n)} \quad \text{or} \quad \omega_n \sim u_{\mathrm{rms}} k_n \ . \tag{6}$$

We have computed particle trajectories in the frozen DNS field, $\mathbf{U} = \mathbf{U}(\mathbf{x}_p(t), t_0)$, rather than $\mathbf{U}(\mathbf{x}_p(t), t)$ in Eq. (2), and next in the frozen LES field $\mathbf{U} = \bar{\mathbf{U}}(\mathbf{x}_p(t), t_0)$. As seen in Fig. 2a, the average particle settling velocity $\langle V_S \rangle$ in such frozen fields is reduced w.r.t. the true DNS or LES results. Regarding the particle velocity variance,

results are shown in Fig. 1a. Here, some improvement is noticed for mid-inertia particles upon the addition of KS as a subfilter model to a priori LES. Yet, this is still not sufficient to retrieve the r.m.s. levels known from DNS.

Next, we have put forward an alternative way to make the KS field time-dependent. Rather than taking non-zero frequencies of the modes, we have prescribed a variability of the magnitudes, $\mathbf{A}_{nm}$ and $\mathbf{B}_{nm}$. To make them constant on the average, yet varying on a suitable time-scale, we have proposed the Ornstein-Uhlenbeck model for the magnitudes. The time-discrete formulae have the form:

$$\begin{aligned}\mathbf{A}_{nm}(t+\Delta t) &= r_n \mathbf{A}_{nm}(t) + \sigma_n \sqrt{1-r_n^2}\,\boldsymbol{\xi}_A \\ \mathbf{B}_{nm}(t+\Delta t) &= r_n \mathbf{B}_{nm}(t) + \sigma_n \sqrt{1-r_n^2}\,\boldsymbol{\xi}_B \end{aligned} \tag{7}$$

where $r_n = \exp(-\omega_n \Delta t)$ and the independent random vectors $\boldsymbol{\xi}_A, \xi_B \in \mathcal{N}(0, 1)$.

We have implemented the KS in the code described above and used for particle tracking, Eq. (2), as $\mathbf{U}^*(t) = \bar{\mathbf{U}}(\mathbf{x}_p, t) + \mathbf{u}_{\mathrm{KS}}(\mathbf{x}_p, t)$. We have studied the effect of the KS parameters (N_k, M and ω_n) on the mean settling velocity of particles; yet, no clear-cut conclusion has appeared so far. In the test runs of particle tracking in a frozen KS field, meant to reconstruct the whole DNS spectrum, an increase in the average settling velocity $\langle V_S \rangle$ w.r.t. the value of V_T is noticed, see Fig. 2b. However, the results for $\langle V_S \rangle$ found from the LES with a KS-based SGS model, both steady and unsteady, also the one expressed by Eqs. (4) and (7), are not much different from those obtained using just the LES (with no KS on top of it, not shown here). A possible reason may be the inability of KS to mimic correctly the sweeping mechanism in turbulence where small-scale eddies are advected by the large ones.

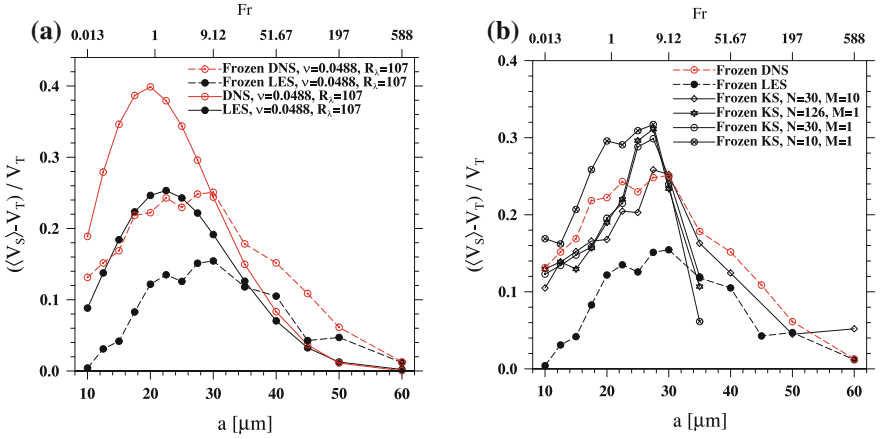

Fig. 2 The difference between the average particle settling velocity $\langle V_S \rangle$ and terminal velocity V_T versus the particle radius or Froude number. **a** DNS and LES, true and frozen, **b** frozen KS results

4 Concluding Remarks

We have considered the effect of filtering of the carrier fluid velocity on particle dynamics in forced isotropic turbulence. We have shown that the mean settling velocity gets further reduced when the frozen DNS or LES fields are taken. Next, as a candidate for particle subfilter model, we have applied kinematic simulations in the inertial range, to complement the LES of the flow. No significant enhancement of the particle settling velocity was observed in the variants tested: steady KS, the time-varying vector magnitudes or frequencies of modes. In our opinion, several aspects of KS as a closure for the SGS particle dispersion still need a more careful scrutiny, including the unsteady formulation as well as the possibility to mimic the effect of sweeping the small scales of KS by the resolved eddies. We hope that this work, together with an earlier detailed study [10], will be helpful to further improve the models of the subfilter scales impact on the dispersed phase subject to gravity.

Acknowledgements The work was supported by the National Science Centre (NCN, Poland), project 2011/03/B/ST8/05677 and ICM (Warsaw University), grants G56-25 and G49-15.

References

1. Fede, P., Simonin, O.: Numerical study of the subgrid turbulence effects on the statistics of heavy colliding particles. Phys. Fluids **17**, art. 045103 (2006)
2. Fung, J.C., Hunt, J.C., Malik, N.A., Perkins, R.J.: Kinematic simulations of homogenous turbulence by unsteady random Fourier models. J. Fluid Mech. **236**, 281–318 (1992)
3. Jin, G., He, G.-W., Wang, L.-P.: Large-eddy simulation of turbulent collision of heavy particles in isotropic turbulence. Phys. Fluids **22**, art. 055106 (2010)
4. Khan, M.A.I., Luo, X.Y., Nicolleau, F.C.G.A., Tucker, P.G., Lo Iacono, G.: Effects of LES sub-grid flow structure on particle deposition in a plane channel with a ribbed wall. Int. J. Numer. Methods Biomed. Eng. **26**, 999–1015 (2010)
5. Michałek, W.R., Kuerten, J.G.M., Liew, R., Zeegers, C.H., Pozorski, J., Geurts, B.J.: A hybrid deconvolution stochastic model for LES of particle-laden flow. Phys. Fluids **25**, art. 123202 (2013)
6. Pozorski, J.: Models of turbulent flows and particle dynamics. In: Minier, J.-P., Pozorski, J. (eds.) Particles in Wall-Bounded Turbulent Flows, pp. 97–150. Springer, Berlin (2017)
7. Ray, B., Collins, L.R.: A subgrid model for clustering of high-inertia particles in large-eddy simulations of turbulence. J. Turbul. **15**, 366–385 (2014)
8. Rosa, B., Parishani, H., Ayala, O., Wang, L.-P., Grabowski, W.W.: Kinematic and dynamic collision statistics of cloud droplets from high-resolution simulations. New J. Phys. **15**, art. 045032 (2013)
9. Rosa, B., Parishani, H., Ayala, O., Wang, L.-P.: Settling velocity of small inertial particles in homogeneous isotropic turbulence from high-resolution DNS. Int. J. Multiph. Flow **83**, 217–231 (2016)
10. Rosa, B., Pozorski, J.: Impact of subgrid fluid turbulence on inertial particles subject to gravity. J. Turbul. **18**, 634–652 (2017)
11. Voßkuhle, M., Pumir, A., Lévêque, E., Wilkinson, M.: Collision rate for suspensions at large Stokes numbers - comparing N-S and synthetic turbulence. J. Turbul. **16**, 15–25 (2015)
12. Wang, L.-P., Maxey, M.R.: Settling velocity and concentration distribution of heavy particles in homogeneous isotropic turbulence. J. Fluid Mech. **256**, 26–68 (1993)

Evaporation Dynamics in Dilute Turbulent Jet Sprays

F. Dalla Barba and F. Picano

1 Introduction

Evaporation of dispersed droplets within a turbulent flow is of crucial importance in several applications [1]. A typical example consists in designing innovative internal combustion engines, capable to increase combustion efficiency and reduce pollutants emission levels. These goals are directly related to the accurate control of the vaporization process which, in turns, affects the mixing homogeneity. In particular, turbulent sprays are complex multiphase flows in which liquid evaporating droplets are dispersed within a turbulent gaseous phase. The evaporation process occurs via mass, momentum and energy exchanges between the two phases causing the spray dynamics to be a challenging modeling task due to the presence of unsteady, multiscale and multiphase processes. An improved comprehension of this phenomenon will enhance model accuracy for applications. E.g. in these cases, sub-grid models in the framework of Large Eddy Simulation (LES) have been used to describe the jet spray evaporation and combustion at high Reynolds numbers [2, 3]. Direct Numerical Simulation (DNS) has the capability to reproduce all details of the jet spray evaporation solving the flow dynamics at any length scale and giving the possibility to directly account droplet small-scale clustering and mixing. Despite its intrinsic limitation to low Reynolds number conditions, DNS can provide significant informations to improve existing models. Following this way, the present study aims to investigate the details of the vaporization process in a turbulent jet spray considering non-reacting dilute conditions and the point-droplet approximation. The jet configu-

F. Dalla Barba (✉) · F. Picano
Department of Industrial Engineering, University of Padova,
Via Venezia 1, Padova, Italy
e-mail: federico.dallabarba@unipd.it

F. Picano
e-mail: francesco.picano@unipd.it

M. V. Salvetti et al. (eds.), *Direct and Large-Eddy Simulation XI*,
ERCOFTAC Series 25, https://doi.org/10.1007/978-3-030-04915-7_30

ration allows to consider the effect of the entrainment of dry air on the process which, to the best of authors knowledge, has never been studied using DNS.

2 Numerical Approach

In order to reproduce the spray vaporization dynamics an hybrid Eulerian/Lagrangian DNS approach is adopted and a full coupling between the two phases is considered. The governing equations for the Eulerian gas phase and for the Lagrangian dispersed phase are consistent with those of previous studies in the field (see e.g. [4–6]):

$$\frac{\partial \rho}{\partial t} + \nabla \cdot (\rho \mathbf{u}) = S_m \tag{1}$$

$$\frac{\partial}{\partial t}(\rho Y_v) + \nabla \cdot (\rho Y_v \mathbf{u}) = \nabla \cdot (\rho \mathscr{D} \nabla Y_v) + S_m \tag{2}$$

$$\frac{\partial}{\partial t}(\rho \mathbf{u}) + \nabla \cdot (\rho \mathbf{u} \otimes \mathbf{u}) = \nabla \cdot \tau - \nabla P + \mathbf{S}_p \tag{3}$$

$$\nabla \cdot \mathbf{u} = \frac{\gamma - 1}{\gamma} \frac{1}{p_0} \left(\nabla \cdot (k \nabla T) + S_e - L_v^0 S_m \right) \tag{4}$$

$$p_0 = \rho \, R_m T \tag{5}$$

$$\frac{d\mathbf{u}_d}{dt} = \frac{f}{\tau_d}(\mathbf{u} - \mathbf{u}_d), \quad f = 1 + 0.15 Re_d^{0.687} \tag{6}$$

$$\frac{dm_d}{dt} = -\frac{1}{3} \frac{m_d}{\tau_d} \frac{Sh}{Sc} H_m, \quad H_m = \ln \left(1 + \frac{1 - Y_v}{1 - Y_{v,s}} \right) \tag{7}$$

$$\frac{dT_d}{dt} = \frac{1}{3\tau_d} \left(\frac{Nu}{Pr} \frac{c_{p,g}}{c_l} (T - T_d) - \frac{Sh}{Sc} \frac{L_v}{c_l} H_m \right), \tag{8}$$

where Y_v is the vapour mass fraction, D the vapour binary diffusion coefficient, k the gaseous phase thermal conductivity, R_m the specific gas constant of the gaseous mixture, $c_{p,g}$ and c_l the specific heat of the gaseous and liquid phases, L_v^0 the latent heat of vaporization evaluated at the reference temperature $T_0 = 0K$. τ_d is the droplet relaxation time, Sh, Sc, Nu and Pr the Sherwood, Schmidt, Nusselt and Prandtl numbers. The right-hand side terms S_m , $\mathbf{S_p}$, and S_e describe the exchange of mass, momentum and energy between the two phases, respectively. An Eulerian algorithm directly evolves the gaseous phase dynamics solving a Low-Mach number asymptotic formulation of the Navier-Stokes equations (1)–(5) on a cylindrical domain, see e.g. Dalla Barba and Picano [7] and references therein for validation and tests. A Lagrangian solver evolves the droplet mass, momentum and temperature laws (6)–(8). A third order, low-storage Runge-Kutta scheme is adopted for the time integration of all the equations. A convective outflow condition is adopted together with a traction-free condition at the side boundary. The inflow velocity condition (Dirichlet) is provided by a cross sectional slice of a turbulent pipe flow companion DNS.

The present study reproduces the vaporization of liquid acetone droplets dispersed within a turbulent air/acetone vapour jet. The flow rate of the gas is kept constant fixing a bulk Reynolds number $Re = 2U_0R/\nu = 6000$, with U_0 the bulk velocity, R the inlet radius and ν the kinematic viscosity. The cylindrical domain extends for $2\pi \times 22\,R \times 70R$ in the azimuthal, θ, radial, r and axial, z, directions. The domain has been discretized by $N_\theta \times N_r \times N_z = 128 \times 225 \times 640$ points using a non-equispaced mesh in the radial and axial direction. The mesh has been stretched in order to resolve a few Kolmogorov scales in the downstream evolution. The acetone mass flow rate is set to $\Phi_m = \dot{M}_a/\dot{M}_g = 0.23$, with $\dot{M}_a = \dot{M}_l + \dot{M}_v$ the sum of liquid and gaseous acetone mass flow rates and $\dot{M}_g$ the gaseous one. Liquid acetone monodisperse droplets with diameter $d_{d,0} = 12\mu$m are injected at the inflow section within a saturated vapour carrier phase. The bulk liquid volume fraction prescribed at inlet ($\Phi_v = 8\ 10^{-5}$) is assumed to be small enough such that the effect of droplet collisions and coalescence is negligible. The inflow temperature is set to $T_0 = 275K$ both for droplets and gas.

3 Results and Discussions

Figure 1 shows how droplets are non-evenly distributed within the jet spray. A high droplet density can be observed in the jet core where droplets are preferentially confined in clusters surrounded by highly saturated vapour zones. The outer part of the jet is instead depleted of droplets even if vapour is still present. This behavior is caused by the high saturation level in the spray core that reduces the droplet vapor-

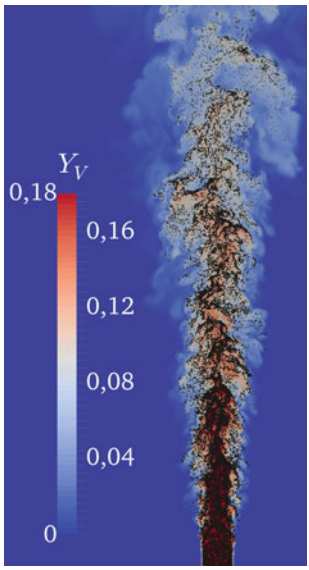

Fig. 1 Axial-radial slice of the spray. Contours represent the vapour mass fraction, Y_v. Black points represent the droplets located within a distance $h/R < 0.025$ from the slice plane

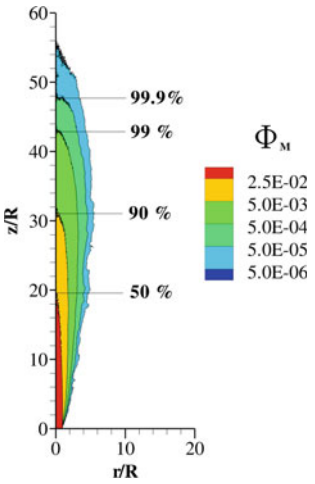

Fig. 2 Mean liquid mass fraction, Φ_m. Labels represent the axial distances from the inflow section where the 50, 90, 99 and 99.9% of the injected liquid mass has evaporated

ization rate. Conversely, in the outer shear layer acetone vapour is diluted by the dry air entrainment. Hence, droplets that can reach this region can fully evaporate. These features originate due to the finite inertia of the droplets that prevents them from following the highly convoluted turbulent structures. The deviations of droplet trajectories from local turbulent motions induce a dissipative dynamics leading to large fluctuations of the droplet concentration field originating clusters [8]. Droplet preferential segregation has been previously observed in sprays both numerically and experimentally [6, 9]. Inside these structures the vapour concentration can grow till saturation reducing or even blocking the local droplet vaporization. It is then clear how the presence of droplet clusters can strongly affect the overall vaporization process. The average liquid mass fraction distribution is provided by Fig. 2. It is possible to define a vaporization length based on the mean liquid mass fraction distribution as the distance from the jet inlet where the 99.9% of the overall injected liquid mass has evaporated. According to this definition, the vaporization process is completely terminated at $z/R \simeq 48$. The previously described spatial organization of droplet and vapour structures leads to a significant oversampling of the mean vapour concentration operated by the droplets (10–40%). In order to measure this effect it is possible to considers the unconditional mean vapour concentration, $Y_{v,u}$, and the *droplet conditional* one, $Y_{v,dc}$. This latter is defined as the average vapour mass fraction conditioned to the droplet presence at a given location. Figure 3 provides a comparison between the isolines of $Y_{v,u}$ and $Y_{v,dc}$. On average, at the same axial distance form the inflow section, the *droplet conditional* average is higher than the unconditional value. This effect is related to the strongly inhomogeneous distribution of the droplets. Within droplet clusters indeed, the local vapour concentration increases due to the high droplet density. Hence, within these features the droplets sample a mean vapour concentration level that is significantly higher then the unconditional one. In particular, in the first part of the spray downstream evolution, the

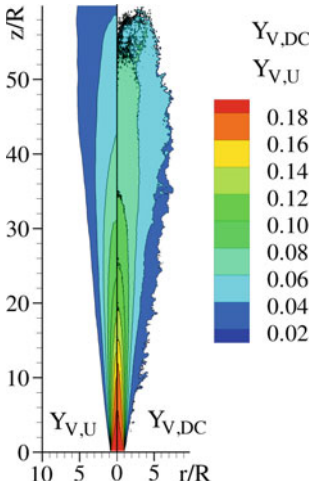

Fig. 3 Comparison between the isolines of the unconditional mean, $Y_{v,u}$, and the *droplet conditional* mean, $Y_{v,dc}$, of the vapor mass fraction field

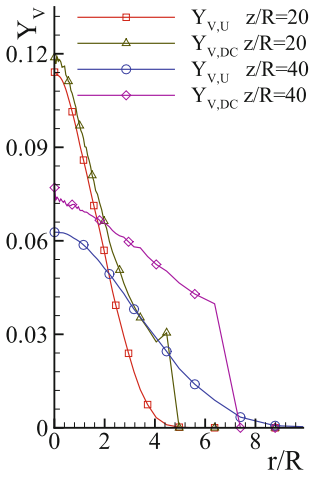

Fig. 4 Radial profiles of the unconditional and droplet conditional mean vapour concentration at $z/R = 20$ and $z/R = 40$

profile of the unconditional and *droplet conditional* statistics are similar in the spray core while differs in the jet shear layer (Fig. 4). This effect is driven by the intermittent dry air entrainment [10]. In the jet shear layer droplet-free, dry air bubbles are engulfed in the turbulent jet region thus forcing fluctuation of low vapour concentration in phase with low droplet concentration. Further downstream, the oversampling of the mean vapour concentration operated by droplets increases even in the jet core. We attribute this effect to the progressive development of small scale clustering that affect the droplet concentration even in the jet core.

The oversampling of the mean vapour concentration operated by the droplets strongly impacts on the overall vaporization length of the spray and leads to a wide polydispersity of the droplet sizes. Figure 5 provides the joint probability density

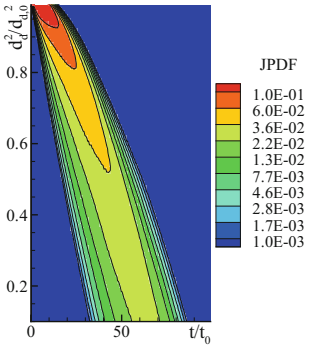

Fig. 5 Joint probability density function of the non-dimensional droplet square diameter, $d_d^2/d_{d,0}^2$, and flight time, t/t_0

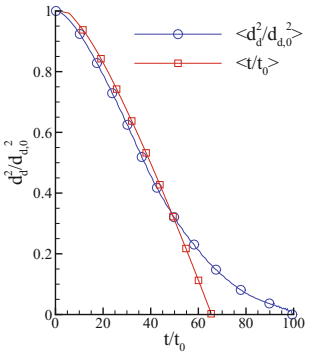

Fig. 6 Mean droplet square diameter, $\langle d_d^2/d_{d,0}^2 \rangle$, versus non-dimensional droplet flight time (circles). Mean droplet flight time, $\langle t/t_0 \rangle$, versus droplet square diameter (squares)

function of the droplet square diameter, $d_d^2/d_{d,0}^2$, and flight time, t/t_0 ($t_0 = R/U_0$). It should be remarked that, after a given interval of time from the injection, the sizes of the droplets are spread over a wide range. This extreme polydispersity together with the strong inhomogeneity affect the possibility of simply predicting the spray vaporization length. The d-2 law provides a valuable analytical tool in order to estimate the evolution of the droplet square diameter if uniform environmental conditions subsists in terms of the vapour concentration, $d_d^2/d_{d,0}^2 = 1 - k\, t/t_0$, with k the evaporation rate constant. Figure 6 provides the mean droplet square diameter, $\langle d_d^2/d_{d,0}^2 \rangle$, as a function of the droplet flight time and the mean droplet flight time, $\langle t/t_0 \rangle$, as a function of the droplet square diameter. It should be noted that no linear behavior is found for both the evolution of the mean square diameter and flight time. In addition the statistics differ one from the other. We attribute this effect to the wide polydispersity of the droplets sizes. Indeed, the time-based average is capable to capture the whole events within the time interval, $50 < t/t_0 < 100$ leading to the end-tail of the mean flight time curve. Conversely, the same occurs for the diameter-based average in a narrow range around $d_d^2/d_{d,0}^2 \simeq 1$ but this effect is much less evident due to the monodisperse condition prescribed at the inflow.

4 Final Remarks

A DNS of a turbulent jet spray of acetone droplets is performed considering the point-droplet approximation and accounting for mass, momentum and energy exchanges between the two phases. Unlike LES and RANS frameworks, DNS reproduces all details of evaporating droplet processes without using any turbulence closure model and stochastic models for non-resolved droplet dynamics. Hence, small-scale droplet clustering and micromixing are accessible and can be studied to improve existing models. We found a strongly inhomogeneous distribution of the evaporating droplets which is affected also by the jet entrainment process. This phenomenology strongly influences the overall vaporization length and time of the spray and leads to a significant increase of the droplet size polydispersity. We believe that existing evaporation models may be improved by accounting these phenomena.

Acknowledgements The financial support of the University of Padova Grant PRAT2015 (CPDA154914) is kindly acknowledged, as well as computer resources provided by CINECA ISCRA C project: TaStE (HP10CCB69W) and the contribution of the COST Action Flowing Matter (MP1305).

References

1. Jenny, P., Roekaerts, D., Beishuizen, N.: Modeling of turbulent dilute spray combustion. Prog. Energy Combust. Sci. **38**(6), 846–887 (2012)
2. Bini, M., Jones, W.P.: Large eddy simulation of an evaporating acetone spray. Int. J. Heat Fluid Flow **30**(3), 471–480 (2009)
3. Ukai, S., Kronenburg, A., Stein, O.T.: LES-CMC of a dilute acetone spray flame. Proc. Combust. Inst. **34**(1), 1643–1650 (2013)
4. Bukhvostova, A., Kuerten, J.G.M., Geurts, B.J.: Low Mach number algorithm for droplet-laden turbulent channel flow including phase transition. J. Comput. Phys. **295**, 420–437 (2015)
5. Mashayek, F.: Direct numerical simulations of evaporating droplet dispersion in forced low Mach number turbulence. Int. J. Heat Mass Transf. **41**, 2601–2617 (1998)
6. Miller, R.S., Bellan, J.: Direct numerical simulation of a confined three-dimensional gas mixing layer with one evaporating hydrocarbon-droplet-laden stream. J. Fluid Mech. **384**, 283–338 (1999)
7. Dalla Barba, F., Picano, F.: Clustering and entrainment effects on the evaporation of dilute droplets in a turbulent jet. Phys. Rev. Fluids **3**, 034304 (2018)
8. Toschi, F., Bodenschatz, E.: Lagrangian properties of particles in turbulence. Annu. Rev. Fluid Mech. **41**, 375–404 (2009)
9. Heinlein, J., Fritsching, U.: Droplet clustering in sprays. Exp. Fluids **40**(3), 464–472 (2006)
10. Da Silva, C.B., Hunt, J.C.R., Eames, I., Westerweel, J.: Interfacial layers between regions of different turbulence intensity. Annu. Rev. Fluid Mech. **41**, 567–590 (2014)

A Novel Turbulent Inflow Data Generation Method and its Application to the Simulation of Primary Breakup

S. Ketterl and M. Klein

1 Introduction

Direct Numerical Simulation (DNS) and Large Eddy Simulation (LES) of spatially inhomogeneous flows strongly depend on turbulent inflow boundary conditions. Turbulence has to be prescribed at the inflow boundary in order to simulate turbulence. Realistic coherent structures are required, otherwise random velocity fluctuations are immediately damped to zero due to the lack of energy in the low wave number range. There exists a wide range of different approaches to obtain turbulent boundary conditions. An overview of methods to tackle the problem has been provided by [7]. Without claiming completeness, these methods can be roughly classified in two categories. On the one hand, precursor or auxiliary simulations are used to extract turbulent boundary conditions. Realistic turbulence is provided but computational costs are often high and the control of turbulent quantities is difficult. On the other hand, turbulent inflow data can be produced by synthetic pseudo-turbulence generation methods. Computational costs are low and full control over turbulence characteristics e.g. turbulence intensity and integral length scale, is achieved. One possibility among many [7] of the synthetic inflow turbulence is the digital filter method suggested by one of the authors [2] which allows to reproduce first and second-order statistics as well as locally defined autocorrelation functions. The generated turbulence is often regarded as artificial and attested with a lack of physical information [2] since the velocity fields are not necessarily a solution to the Navier–Stokes equations. The goal of this contribution is to present a new inflow generation method

S. Ketterl (✉) · M. Klein
Fakultät für Luft- und Raumfahrttechnik, Universität der Bundeswehr München,
Werner-Heisenberg Weg 39, 85577 Neubiberg, Germany
e-mail: sebastian.ketterl@unibw.de

M. Klein
e-mail: markus.klein@unibw.de

M. V. Salvetti et al. (eds.), *Direct and Large-Eddy Simulation XI*,
ERCOFTAC Series 25, https://doi.org/10.1007/978-3-030-04915-7_31

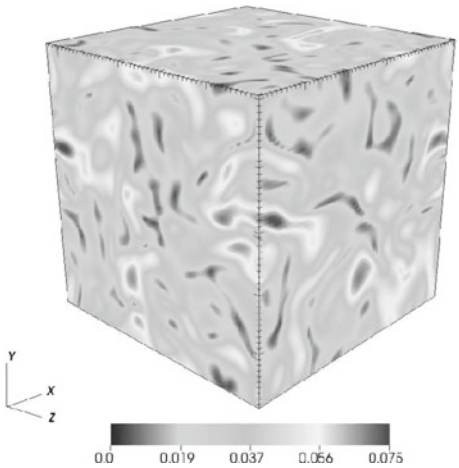

Fig. 1 Instantaneous view of the velocity magnitude of forced turbulence in the auxiliary box simulation

which aims to overcome these problems while keeping the advantages of adjustable turbulent length scales and turbulence intensity as well as reasonable computational costs.

2 New Concept of Inflow Data Generation

The new concept to generate turbulent inflow data is based on an auxiliary simulation of forced box turbulence, shown in Fig. 1. Planes of velocity fluctuations are extracted from the box turbulence, superposed to a potential mean velocity profile and prescribed as boundary condition to the application of interest. Without any driving mechanism, turbulence decays and dissipates within the auxiliary simulation. In order to maintain the global kinetic energy, turbulence is continuously excited by a driving force f_i. The turbulence excitation manifests as a source term in the momentum equation

$$\rho\left(\frac{\partial u_i}{\partial t}+\frac{\partial u_i u_j}{\partial x_j}\right)=-\frac{\partial p}{\partial x_i}+\frac{\partial}{\partial x_j}\left(\mu\left(\frac{\partial u_i}{\partial x_j}+\frac{\partial u_j}{\partial x_i}\right)\right)+f_i \tag{1}$$

where ρ and μ denote the fluid density and viscosity, u_i and p are the velocity components and the pressure. This driving force plays the essential role in the new procedure. On the one hand it allows the generation of a large time series of inflow data since turbulence decay is prevented. On the other hand it controls the integral length scale and turbulence intensity of the generated inflow data.

In contrast to Lundgren's linear forcing technique [4] in physical space, the forcing term is not chosen to be proportional to the velocity fluctuation [4] but to a high pass filtered velocity fluctuation $\overline{u'}_i^{HP}$ [1, 3]:

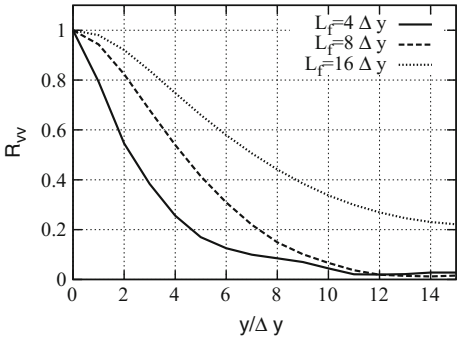

Fig. 2 Comparison of lateral autocorrelation functions depending on the filter width L_f of the spatial low pass filter G

$$f_i = A_i \, \overline{u'}_i^{HP} \tag{2}$$

The high pass filtered velocity is obtained by applying a conventional LES convolution filter with filter kernel G, e.g. a Gaussian filter

$$G(x_i) = \left(\frac{6}{\pi L_{f,i}^2} \right)^{1/2} \exp(-6\, x_i^2 / L_{f,i}^2), \tag{3}$$

to the velocity field in each time step and than subtracting it from the unfiltered velocity vector

$$\overline{u'}_i^{HP} = u'_i - \overline{u'}_i \qquad \text{with} \qquad \bar{u}_i(x) = G * u_i(x) \tag{4}$$

Other filter kernels are also possible. This band-width filtered forcing of turbulence prevents the uncontrolled growth of length scales reported in [1, 5]. The injection of energy is shifted towards small scales of turbulence. The integral length scale does not converge to a constant fraction of the domain size as for Lundren's linear forcing [5]. Instead, band-width filtered turbulence forcing allows variable integral length scales of the generated turbulent inflow boundary conditions. The filter width $L_{f,i}$ of the convolution filter defined by Eq. (3) controls the size of the integral length scale. This flexibility is demonstrated in Fig. 2 which shows the influence of the filter width L_f on the obtained autocorrelation function. The autocorrelation function grows with increasing filter widths. Hence, band-width filtered forcing allows to generate boundary fields with a desired prescribed integral length scale.

The turbulence intensity of the generated boundary data is controlled by the parameter A_i. A control mechanism of the following form

$$A_i = \max \left[0 \, , \; \frac{\overline{u'_i u'_{i,target}} - \overline{u'_i u'_i}}{\Delta t \cdot \overline{u'_i u'_{i,target}}} \right] \tag{5}$$

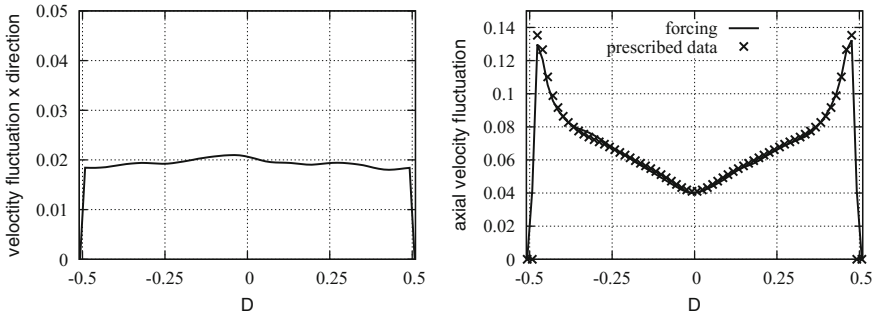

Fig. 3 Uniform (left) and spatially varying (right) turbulence intensity $\sqrt{\langle u'u' \rangle}$

regulates the forcing strength. The target function $\overline{u_i' u_{i,target}'}$ (no summation) denotes the desired prescribed specific turbulent intensity level and Δt the time step size. It should be noted, that the target turbulence intensity for the three spatial directions is not necessarily equal and can be prescribed individually. Besides the integral length scale, the desired fluctuation levels are the second of two input parameters required for the inflow data approach. The turbulence intensity can be either uniform or defined locally, i.e. $\overline{u_i' u_{i,target}'}(x)$, which allows spatially varying turbulence characteristics. If e.g. channel flow turbulence characteristics are desired, spatially varying fluctuation levels are of interest. The performance of the inflow generation method is demonstrated by prescribing DNS data of a plane channel flow. Figure 3 shows the averaged axial velocity fluctuations $\overline{u'u'}$ plotted over the channel height. The control mechanism allows to generate turbulent inflow data of uniform intensity but is also able to imitate spatially varying velocity fluctuations of a channel flow. The approach is easily adaptable to experimental data. For the application to primary breakup, the fluctuating velocity field of the simulated box turbulence is superimposed to the mean axial velocity profile prevailing in the injection nozzle, given by either an analytical function or extracted from experiments.

The generated inflow data is by construction divergence-free since it stems from the solution of the incompressible Navier–Stokes equations. It has been shown that band-width filtered forcing turbulence reveals the non-Gaussian characteristics of real turbulence [1, 6]. Hence, it is expected that the new method provides a more physical realization of inflow turbulence.

3 Application to the Simulation of Primary Breakup

The turbulent inflow data generated by the new method is applied to the simulation of primary breakup. The atomization of a liquid Diesel jet injected into stagnant air is shown in Fig. 4. The Diesel jet is characterized by a Reynolds number $Re = 5000$ and a Weber number $We = 2000$ with a viscosity and density ratio of

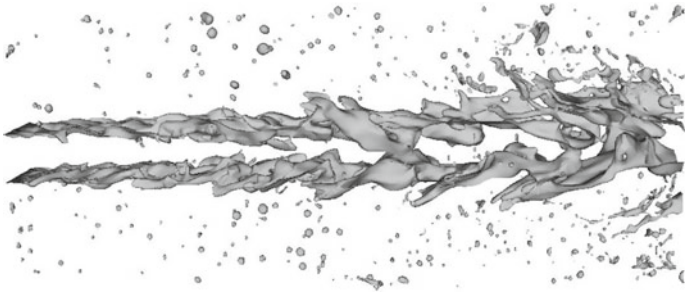

Fig. 4 Liquid isosurface of a spatially developing plane Diesel jet with the turbulent inflow data prescribed at the jet injection

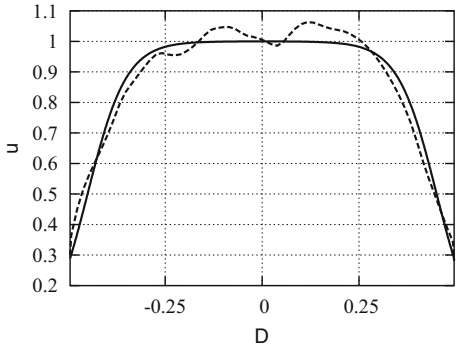

Fig. 5 Mean axial velocity (solid) and velocity profile with superposed turbulent velocity fluctuations (dashed)

$\mu_l/\mu_g = \rho_l/\rho_g = 40$. The computational domain is a rectangular box with dimension $12D \times 6D \times 2D$. The inflow nozzle is discretized with 64 control volumes but is not included in the computational domain itself. Instead, the turbulent velocity profiles are prescribed at the inflow boundary. An axial mean velocity profile in form of a hyperbolic tangent function $\bar{U} = 0.5 + 0.5 \tanh((|y| + 0.5)/2\theta)$ is superposed by turbulent velocity fluctuations extracted from the auxiliary simulation of box turbulence, see Fig. 5. A uniform turbulent intensity of 5% and a integral length scale of 1/8 D is applied. Figure 6 shows the autocorrelation functions in the three spatial direction at the inflow boundary. Integrating the autocorrelation yields an integral length scale of 8 cells which corresponds to an integral length scale of 1/8 D in the inflow nozzle. The integral length scale of the generated turbulent boundary data with the new procedure is exactly reproduced in the application to the jet simulation.

The new forcing based method is compared to results obtained with the digital filter based generation of turbulent inflow data by [2]. This comparison is carried out on velocity fluctuation statistics which are shown in Fig. 7. The axial and lateral velocity fluctuations are evaluated along the jet axis. At the inlet plane, turbulent fluctuations of 5% are observed reflecting the uniform turbulent intensity of 5% of the inflow data. For the digital filter based approach small overshoots and undershoots are visible whereas turbulence injection with the new inflow data is smoother. Further

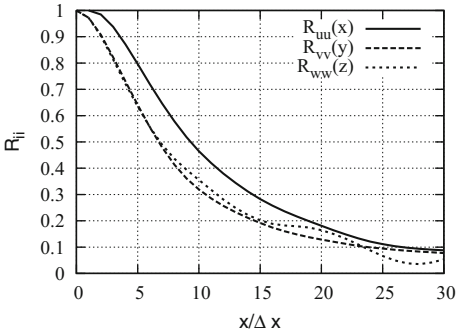

Fig. 6 Autocorrelation functions in the three spatial directions evaluated at the injection boundary at $x = 0$ of the jet simulation

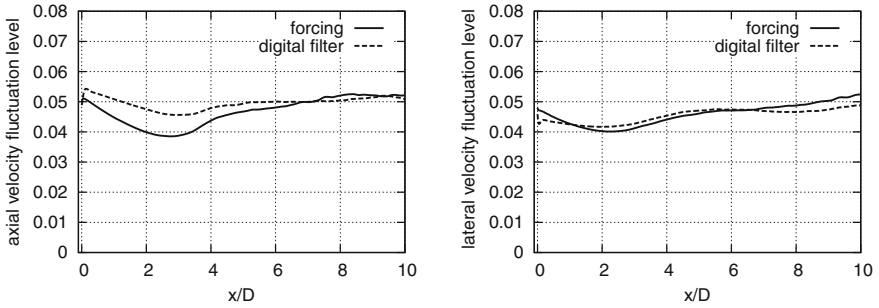

Fig. 7 Axial $\sqrt{\langle u'u' \rangle}$ and lateral $\sqrt{\langle v'v' \rangle}$ velocity fluctuations plotted over axial jet direction evaluated along the jet axis

downstream, the decrease of turbulent intensity for the new method is initially sligthly more pronounced which might be due to the fact that the spectral energy content is not the same for both methods. The influence of the different inflow data generation methods to second-order statistics is overall small. However, there might be larger differences for different flow configurations and higher-order statistics.

4 Conclusion

A new method to generate turbulent inflow data is proposed. The procedure is based on an auxiliary simulation of forced box turbulence where the turbulence forcing plays the essential role for the generation of turbulent boundary condition. The approach allows to produce turbulent boundary conditions with full control over the integral length scale and the turbulence intensity. The velocity fields are by construction divergence-free. Generated turbulence is not artificial since the turbulent velocity fields stem from a solution of the Navier–Stokes equation. The influence on

second-order statistics of the new method compared to synthetic inflow data generation method is small and has to be further examined in future studies. A possible explanation is that both methods are equally well suited for triggering turbulence transition in free shear flows. The new method might be advantageous for applications where details of the small scale physics and mixing are important, e.g. combustion.

Acknowledgements Support by the German Research Foundation (Deutsche Forschungsgemeinschaft - DFG, GS: KL1456/1-1) is gratefully acknowledged. Computer resources for this project have been provided by the Gauss Centre for Supercomputing/Leibniz Supercomputing Centre under grant: pr48no. The authors also express their gratitude to the developers of the PARIS Simulator for providing the source code.

References

1. Klein, M., Chakraborty, N., Ketterl, S.: A comparison of strategies for direct numerical simulation of turbulence chemistry interaction in generic planar turbulent premixed flames. Submitted to Flow Turbul. Combust
2. Klein, M., Sadiki, A., Janicka, J.: A digital filter based generation of inflow data for spatially developing direct numerical or large-eddy simulations. J. Comput. Phys. **186**, 652–665 (2003)
3. Klein, M., Dressler, L., Chakraborty, N., Stafford, C.: A comparison of strategies for direct numerical simulation of turbulence chemistry interaction in generic planar turbulent premixed flames. In: Proceedings of the ETMM11 (2016)
4. Lundgren T.S.: Linearly forced isotropic turbulence. Annual Research Briefs (Center for Turbulence Research), pp. 461–473 (2003)
5. Rosales, C., Meneveau, C.: Linear forcing in numerical simulations of isotropic turbulence: physical space implementations and convergence properties. Phys. Fluids **17**, 095106 (2005)
6. She, Z.S., Jackson, E., Orszag, S.A.: Scale-dependent intermittency and coherence in turbulence. J. Sci. Comput. **4**, 407–434 (1988)
7. Tabor, G.R., Baba-Ahmadi, M.H.: Inlet conditions for large eddy simulation: a review. Comput. Fluids **39**, 553–567 (2010)

Studying Transient Jet Flames by High-Resolution LES Using Premixed Flamelet Chemistry

E. Inanc, F. Proch and A. M. Kempf

1 Introduction

A transient piloted turbulent non-premixed methane jet flame approaching its blow-off limit is numerically studied by high-resolution Large-Eddy Simulations (LES). In the statistically steady jet phase, the high turbulence intensity leads to local flame extinction and re-ignition events. During the transient phase, the pulsation leads to a global flame extinction soon after the blow-off velocity is reached. The flame then re-ignites when the strain is relaxed. To model turbulent combustion with a minimum set of equations in order to reduce the computational effort, a tabulated detailed chemistry approach is tested.

The non-premixed transient piloted flame experiments reported by Wang et al. [1] are based on the original Sydney Piloted Flame L investigated by Dibble et al. [2], where the transient effects are introduced by pulsing the axial velocity of the fuel jet. The statistically steady [2] and the transient [1] non-premixed piloted flame experiments have been described extensively before, therefore the details are omitted for brevity (refer to [1] for additional information).

2 Modelling

Combustion is modelled with the Flamelet Generated Manifold (FGM) approach [3], together with the Artificially Thickened Flame (ATF) technique [4]. Flame wrinkling is considered based on the work by Charlette et al. [5]. An assumed top-hat filtered density function (FDF) for the mixture fraction Z is used to account for the sub-filter distribution of Z. The detailed formulations are omitted for brevity.

E. Inanc (✉) · F. Proch · A. M. Kempf
Chair of Fluid Dynamics, Institute for Combustion and Gasdynamics,
University of Duisburg-Essen, 47057 Duisburg, Germany
e-mail: eray.inanc@uni-due.de

M. V. Salvetti et al. (eds.), *Direct and Large-Eddy Simulation XI*,
ERCOFTAC Series 25, https://doi.org/10.1007/978-3-030-04915-7_32

The flamelets are computed with the detailed chemical mechanism GRI-3.0 [6] and a unity Lewis number assumption. The manifold of flamelet solutions is initially stored in a two-dimensional equidistant look-up table, which is then accessed in the subsequent LES calculations by the transported $\tilde{Z}$ and reaction progress variable $\tilde{Y}_p = \tilde{Y}_{CO_2} + \tilde{Y}_{CO}$, and the mixture fraction variance $\widetilde{Z''^2}$ is calculated with an analytical expression.

Two separate manifolds are created, where the first manifold (premixed FGM denoted as PFGM) uses the thermochemical data obtained from solving freely propagating flamelets with varying mixture composition, while the second manifold (non-premixed FGM denoted as NFGM) uses the data of the counter-flow diffusion flamelets with various strain rates. The strain rate contribution is included in the LES by adjusting the source term with an exponential function, taken from the work of Proch et al. [7].

The simulations are performed with the in-house LES solver PsiPhi [7, 8] in a low-Mach number formulation. The computational domain has $800 \times 200 \times 200$ equidistant grid points with $\Delta = 0.36$ mm. The inflow conditions are prescribed at all boundaries as suggested by Clayton and Jones [9], and the inflow turbulence is generated by the method by Klein [10]. Nicoud's σ-model [11] is employed to close the momentum equations. The simulation setup described above takes 5000 CPUh until 250 samples are acquired.

3 Results

In the first part, the simulation results with NFGM and PFGM methods without strain rate correction are compared with the Flame L measurements by Juddoo et al. [12] at three axial locations $x/D = 10$, 20 and 30 on the centreline. Radial profiles of the mean and root mean square (rms) axial velocity, mixture fraction and temperature are shown in Fig. 1. A good agreement is achieved for the velocity fluctuations, whilst the simulations under-predict the mean axial velocities. The mixture fraction is well predicted by the NFGM method, on the contrary the temperatures are better predicted with the PFGM method. Both the NFGM and PFGM show a good agreement for the scalars' rms values at the pilot ($0.5 < r < 1.5$) and co-flow ($1.5 < r$) sides, however, these methods slightly over-predict the scalars at the fuel side ($r < 0.5$).

The experimental radial temperature profiles imply that the flame extinction level further increases towards higher downstream locations, which is well-captured by the PFGM method. It should be noted that the flame is stabilized by a strong pilot near the nozzle so that extinction happens more likely where the pilot looses its stabilizing effect, at $x > 15D$. In the tested combustion model, the falsely predicted trend of increased extinction levels at downstream locations of the NFGM model could be explained by the abandoned scalar dissipation rate as control variable.

The conditional mean plots for the temperature, and the mass fractions of CO_2 and H_2O over the mixture fraction are presented in Fig. 2 for three different axial locations $x/D = 10$, 20 and 30 on the centreline. The temperature versus mixture fraction plots

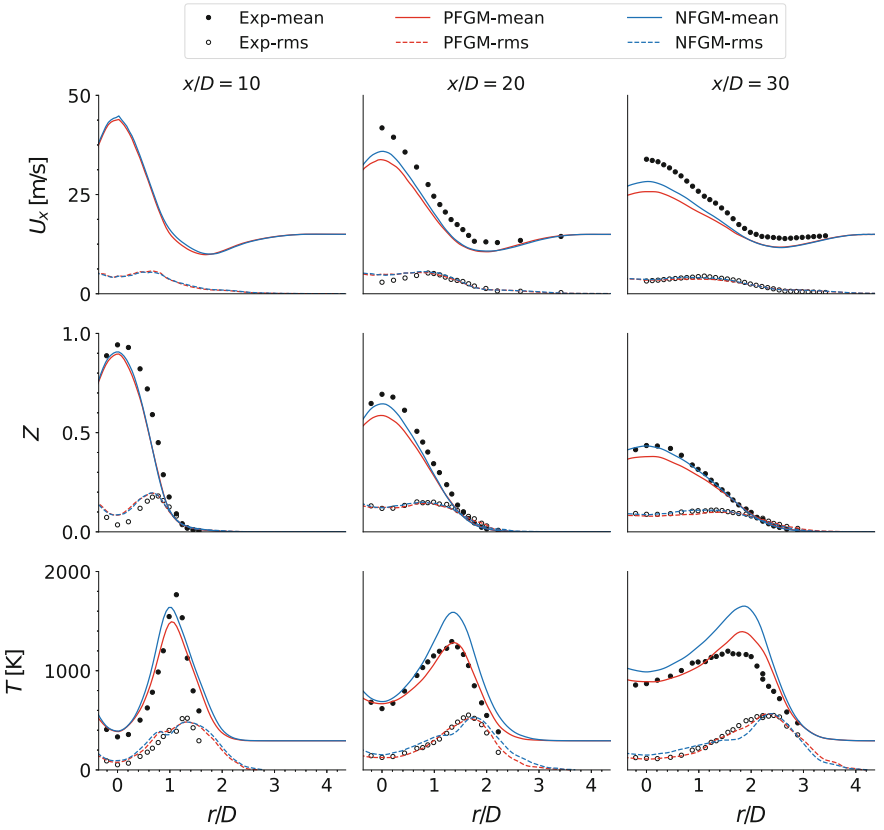

Fig. 1 Radial mean and rms profiles of axial velocity (top row), mixture fraction (middle row) and temperature

show that the local extinction level in the experiments at upstream locations is quite low, which is interpreted from the steady flamelet solution profile that is matching the experimental profile. At further downstream locations, the experimental conditional mean temperatures drop, which is a result of increasing levels of extinction towards downstream locations, which is well captured by the PFGM. On the other hand, the NFGM only shows a constant level of local flame extinction. The NFGM shows good predictions for the CO_2 mass fractions, and PFGM predicts H_2O concentrations well, where this observation is consistent with the findings of the work by Vreman et al. [13].

In the second part of this section, the Flame L simulation results with PFGM method together with the applied strain rate correction technique are presented qualitatively. The qualitative experimental results [1] are omitted for brevity. It should be noted that the strain rate effects in the transient phase of the jet is not negligible,

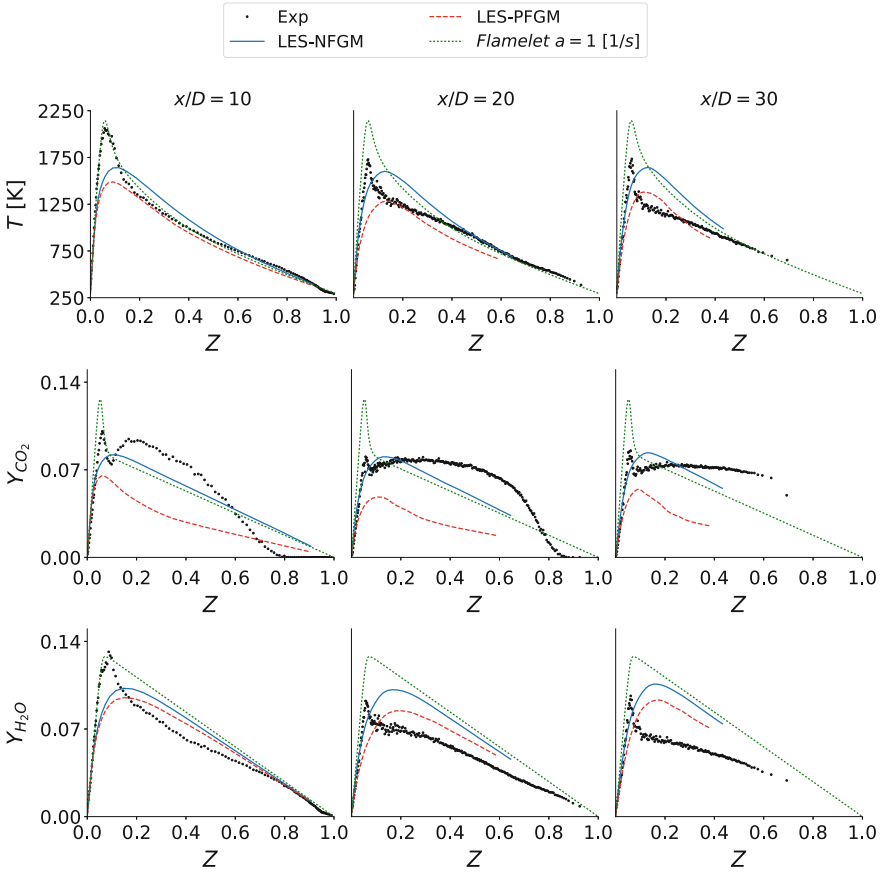

Fig. 2 Conditional mean temperatures (top row), mass fractions of CO_2 (middle row) and H_2O. A one-dimensional steady counter-flow flamelet solution with strain rate of $a = 1\,\mathrm{s}^{-1}$ is also shown to analyze the flame extinction and re-ignition events

hence the global flame quenching is fully observed if the strain correction method is applied to the simulations.

In Fig. 3, the time series of OH mass fractions are presented during a single pulsation. During the initial ramp-up phase, the pulsation interacts with the flame front (OH concentrations) after a convective time delay at downstream locations of the jet. The flame is expected to be globally quenched since the blow-off velocity of the Flame L is reached during this acceleration phase. Because of the convection time delay, the flame globally quenches at the downstream locations at the following phase when the jet is suddenly decelerated. At the last phase where the strain is relaxed, the flame re-ignites at the same location, where the initial global flame quenching happened, again with a convection time delay.

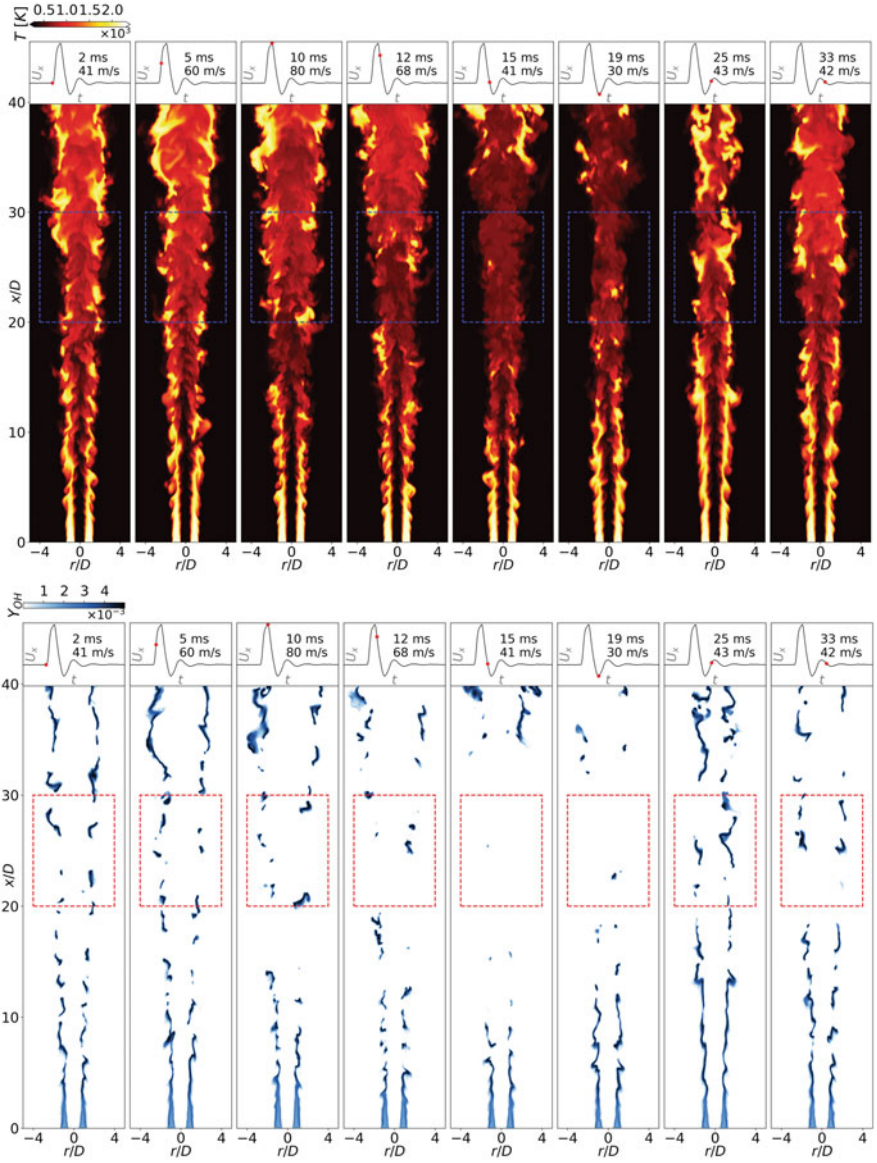

Fig. 3 Snapshots of the temperature (top row) and the OH mass fractions from the LES/PFGM simulation of the transient jet flame at different times that are indicated in the subplots. The boxes emphasize the expected location of the global flame extinction and re-ignition events

4 Conclusion

It was observed that the local flame extinction events happen more likely where the pilot loses its stabilizing effect, at $x > 15D$. The temperatures were successfully captured by the PFGM method, where the NFGM method predicted CO_2 concentrations better, which is consistent with the literature [13].

As it was shown by Vreman et al. [13], employing premixed flamelet chemistry to the turbulent flame calculations was plausible, however with aforementioned drawbacks. The fact is that the turbulent flame region consists of both premixed and non-premixed zones.

An issue was faced for the missing strain rate (or scalar dissipation rate) information in the premixed manifold, which was less of a problem in the (statistically) steady phase of the jet, where the mixture fraction fluctuations were smaller. The flame quenched globally only after the strain rate effects were included for the transient jet. Additionally, the applied ATF with flame wrinkling model in LES/PFGM resulted in additional flame thickening due to the premixed laminar flame thickness that was smaller than the non-premixed one.

The tested combustion model captured the local and global flame extinction and re-ignition events and imposed a minimal additional computational cost to the LES in spite of not having been optimized for such non-premixed cases. Hence, the modeling is well suited as a basis for further work on transient flames and development of more suitable models. Meanwhile, the flame quenching and re-ignition events in thickened flames raised questions that only flame resolved investigations could answer.

Acknowledgements The authors gratefully acknowledge the financial support by the state North Rhine-Westphalia, Germany. We thank the University of Duisburg-Essen and the Center for Computational Sciences and Simulation (CCSS) for providing time on the HPC system magnitUDE (DFG grant INST 20876/209-1 FUGG) at the Zentrum für Informations- und Mediendienste (ZIM).

References

1. Wang, H., Juddoo, M., Starner, S.H., Masri, A.R., Pope, S.B.: A novel transient turbulent jet flame for studying turbulent combustion. Proc. Combust. Inst. **34**, 1251–1259 (2013)
2. Dibble, R.W., Masri, A.R., Bilger, R.W.: The spontaneous Raman scattering technique applied to nonpremixed flames of methane. Symp. (Int.) Combust. **67**, 189–206 (1987)
3. van Oijen, J.A., de Goey, L.P.H.: Modelling of premixed laminar flames using flamelet-generated manifolds. Compos. Sci. Technol. **161**, 113–137 (2000)
4. Butler, T.D., O'rourke, P.J.: A numerical method for two dimensional unsteady reacting flows. Symp. (Int.) Combust. **16**, 1503–1515 (1977)
5. Charlette, F., Meneveau, C., Veynante, D.: A power-law flame wrinkling model for LES of premixed turbulent combustion Part I: non-dynamic formulation and initial tests. Combust. Flame **131**, 159–180 (2002)
6. Smith et al.: www.me.berkeley.edu/gri_mech (2000)
7. Proch, F., Kempf, A.M.: Numerical analysis of the Cambridge stratified flame series using artificial thickened flame LES with tabulated premixed flame chemistry. Combust. Flame **161**, 2627–2646 (2014)

8. Inanc, E., Nguyen, M.T., Kaiser, S., Kempf, A.M.: High-resolution LES of a starting jet. Comput. Fluids **140**, 435–449 (2016)
9. Clayton, D.J., Jones, W.P.: Large eddy simulation of a methane-air diffusion flame. Flow Turbul. Combust. **81**, 497–521 (2008)
10. Klein, M.: A digital filter based generation of inflow data for spatially developing direct or numerical or large eddy simulation. J. Comput. Phys. **186**, 652–665 (2003)
11. Nicoud, F., Toda, H.B., Cabrit, O., Bose, S., Lee, J.: Using singular values to build a subgrid-scale model for large eddy simulations. Phys. Fluids **23**, 085106 (2011)
12. Juddoo, M., Masri, A.R.: High-speed OH-PLIF imaging of extinction and re-ignition in non-premixed flames with various levels of oxygenation. Combust. Flame **158**, 902–914 (2011)
13. Vreman, A.W., Albrecht, B.A., Van Oijen, J.A., De Goey, L.P.H., Bastiaans, R.J.M.: Premixed and non-premixed generated manifolds in large-eddy simulation of Sandia flame D and F. Combust. Flame **153**, 394–416 (2008)

Identification of Combustion Trajectories Using t-Distributed Stochastic Neighbor Embedding (t-SNE)

E. Fooladgar and C. Duwig

1 Introduction

With increasing computational power, direct numerical and large eddy simulation (DNS and LES) of reacting flows with complex chemistry are becoming common, e.g. [1–3]. The resulting data which may occupy hundreds of gigabytes of storage, consists of millions to billions of points each of which is described by tens to hundreds of chemical species. To explore and analyze this large, high-dimensional data, conventional visualization techniques such as scatter plots, histograms and pairs plots are limited. Human visual perception is well tuned to identify patterns and trends in graphs with one or a few data variables at a time, calling for new automated identification tools.

One way to tackle the issue is employing computers to detect the main features of the data prior to visualization, for example by making use of recent dimension reduction methods originally developed for machine learning and computer vision. In these methods, the high-dimensional data is converted to a two or three dimensional embedding of the data in which nearby and distant points represent similar and dissimilar points of the original data respectively. The low-dimensional data can readily be visualized in a scatter plot or it can be used as the input for the more sophisticated visualizations and/or analysis.

One of the most promising nonlinear dimension reduction methods is t-Distributed Stochastic Neighbor Embedding (t-SNE) which has been recently introduced by Maaten and Hinton [4]. t-SNE has been employed in many fields including music analysis [5], computer aided diagnosis [6], bioinformatics [7] and electroencephalography [8]. In this paper, we explore the application of the tree-based t-SNE [9], devel-

E. Fooladgar (✉) · C. Duwig
KTH Mechanics, Linné FLOW Centre, Royal Institute of Technology, Stockholm, Sweden
e-mail: efoo@mech.kth.se

C. Duwig
e-mail: duwig@mech.kth.se

M. V. Salvetti et al. (eds.), *Direct and Large-Eddy Simulation XI*,
ERCOFTAC Series 25, https://doi.org/10.1007/978-3-030-04915-7_33

oped for large-scale data, on a dataset created from the results of an implicit LES with complex chemistry performed on a model gas turbine designed for operating in the flameless mode.

2 t-Distributed Stochastic Neighbor Embedding (t-SNE)

t-SNE is a nonparametric nonlinear dimensionality reduction method aiming to embed high-dimensional data $X = \{x_1, x_2, \ldots, x_N\}$ with $x_i \in \mathbf{R}^l$ into a s-dimensions map $Y = \{y_1, y_2, \ldots, y_N\}$ ($y_i \in \mathbf{R}^s$) where s has a typical value of 2 or 3 and is normally much smaller than l. The t-SNE algorithm starts by converting distances between original data points into Gaussian joint probabilities p_{ij} measuring the pairwise similarity between x_i and x_j using

$$p_{j|i} = \frac{\mathrm{e}\left(-d\left(x_i, x_j\right)^2 / 2\sigma_i^2\right)}{\sum_{k \neq i} \mathrm{e}\left(-d\left(x_i, x_k\right)^2 / 2\sigma_i^2\right)}, \qquad p_{i|i} = 0 \tag{1}$$

$$p_{ij} = \frac{p_{i|j} + p_{j|i}}{2N}. \tag{2}$$

Here $d\left(x_i, x_j\right)$ is a function that returns a distance between a pair of data points and σ_i is the variance of the Gaussian centered on x_i. σ_i is determined by setting the perplexity of the conditional distribution equal to a predefined perplexity u. Therefore, σ_i is adapted to the density of the data. In the low-dimensional map Y, the similarities q_{ij} between two points y_i and y_j are measured using a normalized Student-t kernel with one-degree of freedom:

$$q_{ij} = \frac{\left(1 + \| y_i - y_j \|^2\right)^{-1}}{\sum_{k \neq l} \left(1 + \| y_k - y_l \|^2\right)^{-1}}, \qquad q_{ii} = 0. \tag{3}$$

The heavy-tailed Student-t kernel allows dissimilar input points (i.e. points with large distance in the high-dimensional space) to be modeled by low-dimensional counterparts with a much larger distance in the map. This makes more space for the similar points, with small pairwise distances, to be modeled accurately in the low-dimensional embedding, leading to preserving the local data structure in the map. t-SNE determines the locations of the points y_i in the map by minimizing the Kullback–Leibler divergence between the joint distributions P and Q:

$$C(Y) = KL(P||Q) = \sum_{i \neq j} p_{ij} \log \frac{p_{ij}}{q_{ij}}. \tag{4}$$

The minimization of the objective function $C(Y)$ with respect to y_i is performed using gradient descent:

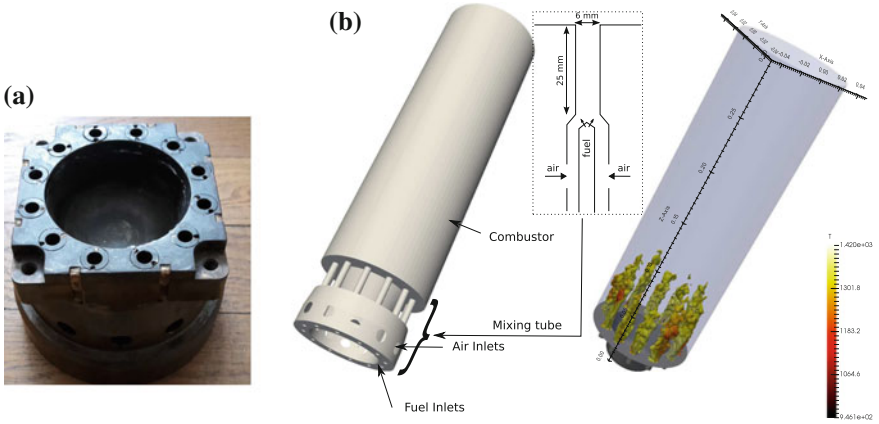

Fig. 1 **a** A real image of the burner. **b** Drawing of the burner and chamber and snapshot of the flame surfaces colored by temperature

$$\frac{\partial C}{\partial y_i} = 4 \sum_j (p_{ij} - q_{ij})(y_i - y_j) \left(1 + \| y_i - y_j \|^2\right)^{-1}, \tag{5}$$

by computing which, the solution at iteration t, Y^t, is obtained using

$$Y^t = Y^{t-1} + \eta \frac{\partial C}{\partial y_i} + \mu(t) \left(Y^{t-1} - Y^{t-2}\right), \tag{6}$$

where η indicates the learning rate and $\mu(t)$ denotes a relatively large momentum at iteration t added to speed up the optimization and to avoid poor local minima. As t-SNE scales quadratically ($\mathcal{O}[sN^2]$) with the number of data points N, it is not applicable to datasets with more than a few thousand samples. For larger datasets, computations become too slow and require substantial amount of memory. The Barnes-Hut t-SNE is developed to address this issue by first constructing a sparse approximation of the similarities between the data points using vantage-point trees and then approximating the gradient descent by computing interactions between groups of points instead of all pairs of data points. The gradient approximation is parameterized using a threshold θ trading off speed and accuracy. This results in a complexity of $\mathcal{O}[sN \log N]$ and reduces the memory requirements to only $\mathcal{O}[N]$.

3 Numerical Setup

To provide the input dataset for t-SNE, the model gas turbine studied (see Fig. 1a) by Duwig et al. [10] is simulated in the flameless mode. The model combustor consists of a plenum chamber, the flameless burner and a quartz combustion chamber, shown

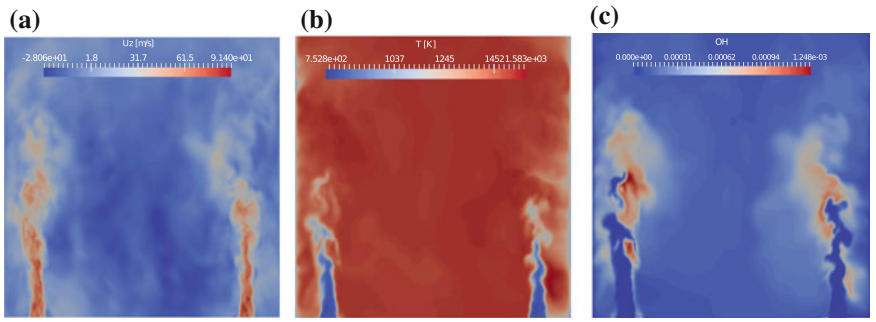

Fig. 2 **a** A snapshot of axial velocity. **b** A snapshot of temperature **c** A snapshot of OH mass fraction

in Fig. 1b, with diameter of $D = 0.1$ m and length of 0.3 m. The propane/air mixture is issued into the chamber through 12 equally spaced injectors of diameter $d = 6$ mm. The air (entering into the burner from the upstream plenum) and the fuel (coming from 12×4 fuel injection holes) are premixed within the 12 straight coaxial tube nozzles over a distance of 0.025 m before the combustion chamber.

For the numerical setup, one of the mixing tubes is simulated in isothermal condition in order to obtain the profiles of velocity, propane and temperature (and their variations with time) for the 12 chamber inlets. For the combustion chamber simulation, reactive Navier-Stokes equations are solved using large eddy simulation and Finite Rate Chemistry (FRC) approach with a 38-species skeletal mechanism [11] for chemistry description. Quasi laminar combustion model and Smagorinsky sub-grid model are employed for closing equations. A hexahedral-dominant unstructured grid with 5.8 million cells and 3 levels of refinement is used, yielding 22 cells over the diameter of each jet, d. The simulation is initialized using global equivalence ratio of $\phi = 0.35$, air temperature of 823 K and total fuel mass flow rate of 0.01 kg/s.

4 Results

Figure 2 shows the distributions of axial velocity, temperature and mass fraction of OH across an xy-plane crossing the center of two injectors and the chamber. A strong recirculation zone (RZ) induced by the injectors can be observed at the center of combustor, as seen by dark blue ($U_z \leq 0$) in Fig. 2a. RZ is the main mechanism providing rapid mixing of the burned gases and the fresh mixture needed for flameless combustion. Temperature distribution depicted in Fig. 2b reveals that the temperature jump (T/T_u) across the flame is around 1.7 which is much less than the value for conventional flames (around 6 or 7). Moreover, maximum temperature in the combustor is well below 1800K, prohibiting the formation of thermal NO_x in the flameless mode. OH mass fraction (Fig. 2c) shows a large distributed reaction

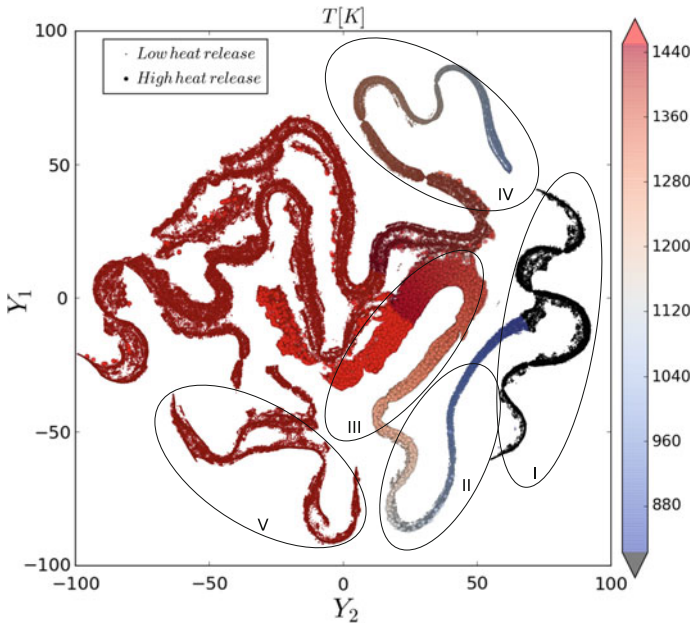

Fig. 3 t-SNE map of the LES data colored by temperature. Points with high heat release are plotted using larger markers. Regions marked with I to III show respectively unburnt mixture, preheating zones and reaction zones. Clusters marked with V and IV need more information to be distinguished. This figure also indicates the difficulty of showing more than 3 variables on a scatter plot

zone located at $z/D = 0.6$. This zone, which is created by merging jets, contains a very fuel lean, highly diluted hot mixture.

To generate the input dataset for t-SNE, the instantaneous value of all 38 species and temperature is extracted from an xy-plane (shown in Fig. 2) for 10 time step with the interval of 0.1 flow through time. This leads to an input dataset with 259,996 points (rows) and 39 dimensions or features (columns). By applying t-SNE to the normalized input dataset, an output dataset with the same number of points but with 2 dimensions is obtained. Thus, the output can be plotted using a scatter plot, called t-SNE map, in order to examine the similarity of the original data.

Figure 3 shows the t-SNE map of the LES data plotted using two components of reduced manifold, Y_1 and Y_2, colored by temperature. Points with high heat release are plotted using larger markers. Without any prior knowledge about the underlying data, t-SNE categorizes the data into distinguishable clusters (trajectories). Using temperature and heat release as labels, major features of the combustor including unburnt mixture, preheating zones and reaction zones can be intuitively marked as different clusters, as indicated by regions I to III in Fig. 3. Clusters IV and V, however, need more species information to be marked. In order to map t-SNE trajectories to the LES grid, each component of the reduced manifold is used as a band of RGB color code, $R = 0,\ G = Y_1,\ B = Y_2$, (Fig. 4a). This results in a customized colormap (t-

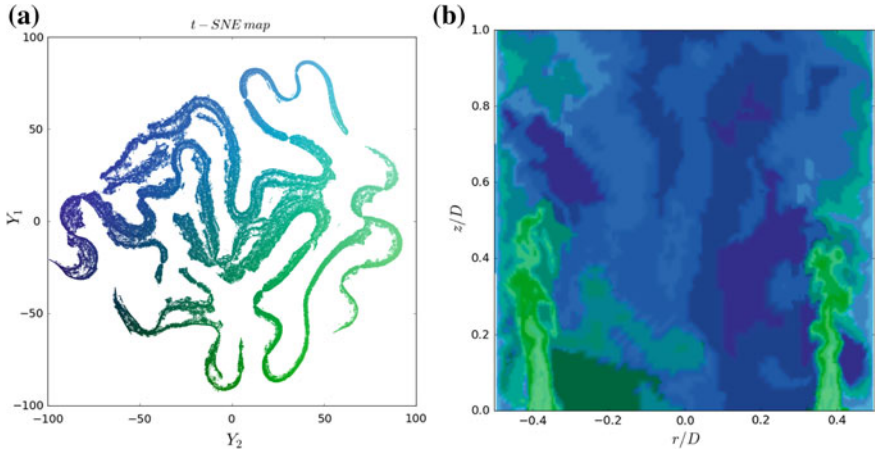

Fig. 4 **a** t-SNE map of the LES data colored with t-SNE colormap. **b** Mapping t-sne trajectories to physical space

SNE colormap) representing neighbor points with similar colors on the LES grid, see Fig. 4b. Using Figs. 3 and 4a major features of the combustor can also be identified in the physical space. Moreover, Fig. 4b depicts the contribution of all other variables on a single plot. This can be verified by tracing T and OH patterns (Figs. 2b, c) on the t-SNE contours in Fig. 4b. Hence, evolution of flame features can be monitored by plotting only t-SNE components rather than all species.

In conclusion, we report that tree-based t-SNE algorithm has a great potential to be used as a computer aided tool for visualization and analysis of the data produced by LES and DNS of combustion with detailed chemistry.

Acknowledgements The financial support of the Swedish Energy Agency (Energimyndigheten) is greatly acknowledged. The simulations were run on LUNARC and HPC2N super-computing facilities within SNIC ressource allocation.

References

1. Yoo, C.S., Luo, Z., Lu, T., Kim, H., Chen, J.H.: A DNS study of ignition characteristics of a lean iso-octane/air mixture under HCCI and SACI conditions. Proc. Combust. Inst. **34**(2), 2985–2993 (2013)
2. Duwig, C., Iudiciani, P.: Large Eddy Simulation of turbulent combustion in a stagnation point reverse flow combustor using detailed chemistry. Fuel **123**, 256–273 (2014)
3. Fooladgar, E., Chan, C.K., Nogenmyr, K.J.: An accelerated computation of combustion with finite-rate chemistry using LES and an open source library for In-Situ-Adaptive Tabulation. Comput. Fluids **146**, 42–50 (2017)
4. Maaten, L.V.D., Hinton, G.: Visualizing data using t-SNE. J. Mach. Learn. Res. **9**(Nov), 2579–2605 (2008)

5. Hamel, P., Eck, D.: Learning features from music audio with deep belief networks. In: ISMIR. Utrecht, The Netherlands, pp. 339–344 (2010)
6. Jamieson, A.R., Giger, M.L., Drukker, K., Li, H., Yuan, Y., Bhooshan, N.: Exploring nonlinear feature space dimension reduction and data representation in breast CADx with Laplacian eigenmaps and t-SNE. Med. Phys. **37**(1), 339–351 (2010)
7. Wallach, I., Lilien, R.: The protein-small-molecule database, a non-redundant structural resource for the analysis of protein-ligand binding. Bioinformatics **25**(5), 615–620 (2009)
8. Birjandtalab, J., Pouyan, M.B., Nourani, M.: Nonlinear dimension reduction for EEG-based epileptic seizure detection. In: 2016 IEEE-EMBS International Conference on Biomedical and Health Informatics (BHI). IEEE, pp. 595–598 (2016)
9. Van Der Maaten, L.: Accelerating t-SNE using tree-based algorithms. J. Mach. Learn. Res. **15**(1), 3221–3245 (2014)
10. Duwig, C., Stankovic, D., Fuchs, L., Li, G., Gutmark, E.: Experimental and numerical study of flameless combustion in a model gas turbine combustor. Combust. Sci. Technol. **180**(2), 279–295 (2007)
11. Chemical-Kinetic Mechanisms for Combustion Applications, Mechanical and Aerospace Engineering, University of California at San Diego. http://combustion.ucsd.edu

Impact of Scalar Dissipation Rate on Turbulent Spray Combustion Investigated by DNS

A. Abdelsamie and D. Thévenin

1 Introduction

Spray combustion includes a lot of physical processes that occur simultaneously, most prominently injection, atomization, dispersion, evaporation, and combustion. Therefore, it is not sufficient to rely only on experimental techniques for understanding this problem. As a complementary source of information, highly accurate numerical models can be used to perform such investigations. Using high-performance computers (HPC), even parametric studies become possible. The remaining question is, which numerical models should be used? Direct numerical simulation combined with discrete particles simulation (DNS-DPS) is recognized as one of the most accurate approaches to understand spray combustion and answer open questions [1, 2]. Even though DNS-DPS simulations do not resolve the droplet interface, they capture the relevant physics and the controlling phenomena. With this approach, impact and behavior of scalar dissipation rate during evaporation and ignition of diluted spray in turbulent reactive flows can be captured [3]. It has been observed by Abdelsamie and Thévenin (2017) that scalar dissipation rate shows non-monotonic behavior when increasing shear for spray combustion in a temporally-evolving planar jet (TEJ). Results considering TEJ have been often published [4–7], since such computations are simpler and faster than the more realistic, turbulent spray in spatially-evolving jets (SEJ). In this work, possible differences regarding the behavior of scalar dissipation rate in spray combustion using either TEJ or SEJ are investigated. It is found that the behavior is qualitatively similar but quantitatively different.

A. Abdelsamie (✉) · D. Thévenin
Laboratory of Fluid Dynamics and Technical Flows (LSS/ISUT),
University of Magdeburg "Otto von Guericke", Universitätsplatz 2,
39106 Magdeburg, Germany
e-mail: abouelmagd.abdelsamie@ovgu.de

D. Thévenin
e-mail: thevenin@ovgu.de

M. V. Salvetti et al. (eds.), *Direct and Large-Eddy Simulation XI*,
ERCOFTAC Series 25, https://doi.org/10.1007/978-3-030-04915-7_34

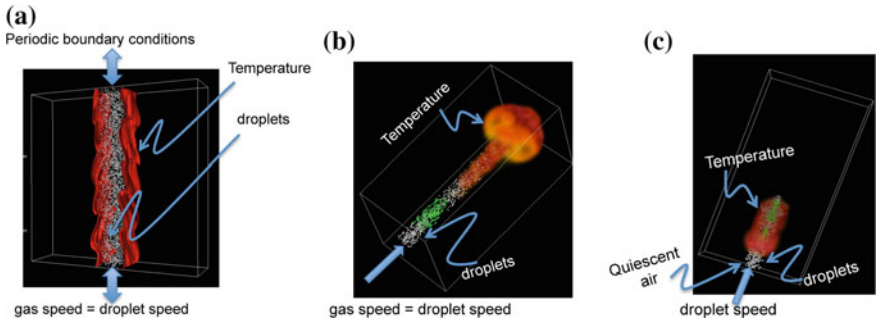

Fig. 1 Exemplary results. Left: Case A. Middle: Case B. Right: Case C. Red and green isosurface represent temperature and heptane concentration in gas, respectively. The gray spheres represent the liquid droplets (magnified)

2 Numerical Setting

Spray combustion is investigated in two main configurations: TEJ or SEJ. For spray in temporally-evolving planar jet (Case A) the domain with dimension of L_x (streamwise direction) = 5.0 mm, L_y (spanwise direction) = 5.0 mm, and L_z (crosswise direction) = 2.5 mm, is discretized over 6.3 million grid points. It is initially filled with hot air (temperature of 1600 K and pressure of 5 bar). The central jet region (width of 1 mm) moves with jet speed of 60 m/s. In this region, 6000 liquid n-heptane droplets are randomly distributed and move initially with the same speed as the surrounding air (60 m/s). The initial diameter and temperature of these liquid droplets are 10 μm and 300 K.

For SEJ two settings are considered, Cases B and C. In Case B, the domain is also filled with hot air at the same condition as Case A. Droplets with the same size and temperature as for Case A are injected with hot air (T = 1600 K) at 60 m/s as a round jet into the domain. The domain is in this case longer than for Case A in streamwise direction, in order to avoid any impact of the boundaries on the spatial evolution of spray: $L_x = 10$ mm, $L_y = 5$ mm, and $L_z = 5$ mm. It is discretized over 19 million grid points. Typical results for Cases A and B are presented in Fig. 1(left) and (middle), respectively. Case C is similar to Case B with the only difference that the droplets are injected into a quiescent flow, without simultaneous air injection, as illustrated in Fig. 1(right). As it can be observed from Fig. 1, the ignition occurs along the edges of the jet in Cases A and C, while ignition occurs at the head of the jet in Case B.

All simulations are conducted using the in-house DNS code DINO. Complete details about the code, governing equations, and validation can be found in [1, 8]. For spray combustion, the computations rely on the model of Abramzon and Sirignano [9]. Kinetic and transport terms are computed by relying on the open-source library Cantera 1.8 with a skeletal kinetic mechanism for n-heptane, which contains $N_s = 29$ species and 52 elementary reactions, as described in [10].

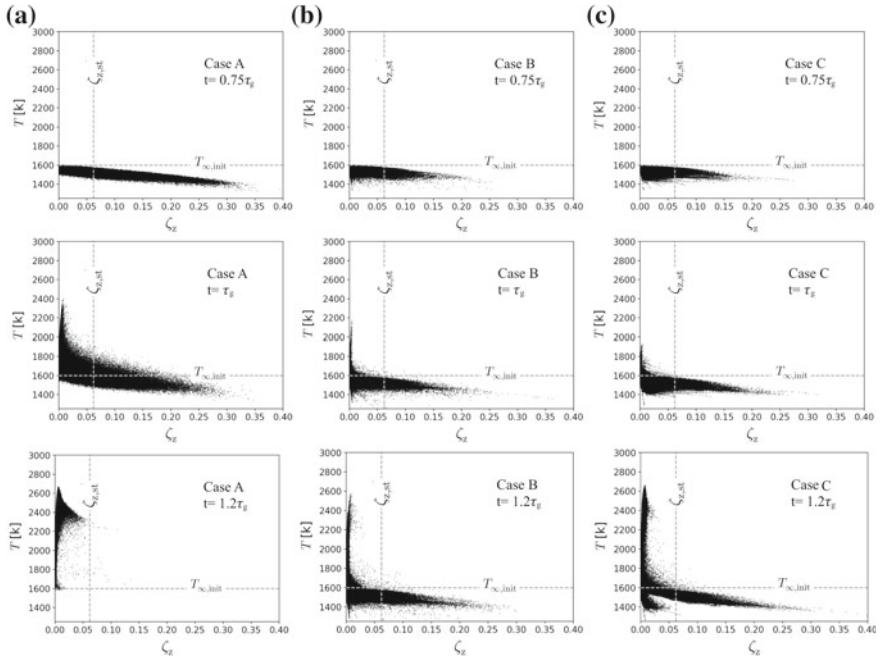

Fig. 2 Time evolution of scatter plot of temperature versus mixture fraction at three different times, $0.75\tau_g$, τ_g, and $1.2\tau_g$: Left: Case A. Middle: Case B. Right: Case C

3 Results

The results will be discussed for the three cases (A, B, and C) at three different times: $0.75\tau_g$, τ_g, and $1.2\tau_g$, where τ_g is the ignition delay time.

3.1 Temperature

Figure 2 shows the temporal evolution of the scatter plot of temperature for the three cases A, B, and C. At early time, $t = 0.75\tau_g$, the evaporation is dominating. Therefore, the gas temperature reduces compared to the initial temperature ($T_0 = 1600$ K) over a wide range of mixture fraction for all cases. In Case A, the temperature reduction exists for a wider range of mixture fraction compared to the other cases; evaporation is stronger in Case A. At time equal to ignition delay time $t = \tau_g$ (ignition being defined as the first occurrence of $T > T_0 + 400$ K), the highest temperature appears at lean condition ($\zeta_z < \zeta_{z,st}$) for all cases; ignition is always found on the lean side.

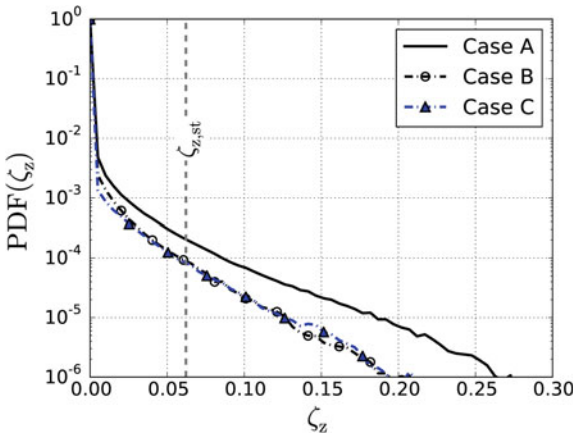

Fig. 3 Probability density function of mixture fraction at t = τ_g

At later time, $t = 1.2\tau_g$, it is observed that the maximum temperature for all cases ($T \sim 2600$ K) is found at the same mixture fraction, far in the lean range. However, the high-temperature region in Case A reaches up to stoichiometric conditions ($\zeta_z \sim \zeta_{z,st}$), which is not found for the other cases. Also, evaporation continues during and after ignition for cases B and C, which is not seen in Case A. This scenario is confirmed by the probability density function (PDF) of mixture fraction presented in Fig. 3, as well as by the scalar dissipation rate shown in the next section. It is observed from Fig. 3 that a wider range of mixture fraction can be found in Case A compared to the other cases, extending noticeably farther on the rich side. This means that evaporation is stronger and faster in Case A, leading to more n-heptane in the gas phase. Qualitatively, the trend of PDF(ζ_z) is similar for all cases.

4 Scalar Dissipation Rate

The behavior of the scalar dissipation rate χ is presented in Fig. 4. In this figure the time evolution of χ versus ζ_z is plotted for all cases. At $t = 0.75\tau_g$, χ is distributed over a wide range of ζ_z. For case A, the peak value of χ is much higher than that for the other cases, and is found at a larger value of ζ_z. Following the evaporation scenario discussed in Fig. 2, more evaporation for Case A means more mixture fraction in the gas mixture, more gradients, and hence higher and broader distributions of scalar dissipation rate. Later, at $t = \tau_g$, the scalar dissipation rate decreases for Case A, while it remains at a similar level for Cases B and C. This is attributed to the fact that fresh liquid droplets are constantly injected in SEJ (Cases B and C), which is not the case for TEJ (Case A). Finally, at $t = 1.2\tau_g$ the scalar dissipation rate vanishes for case A, because most of the evaporated fuel has been consumed, and no fresh droplets are injected.

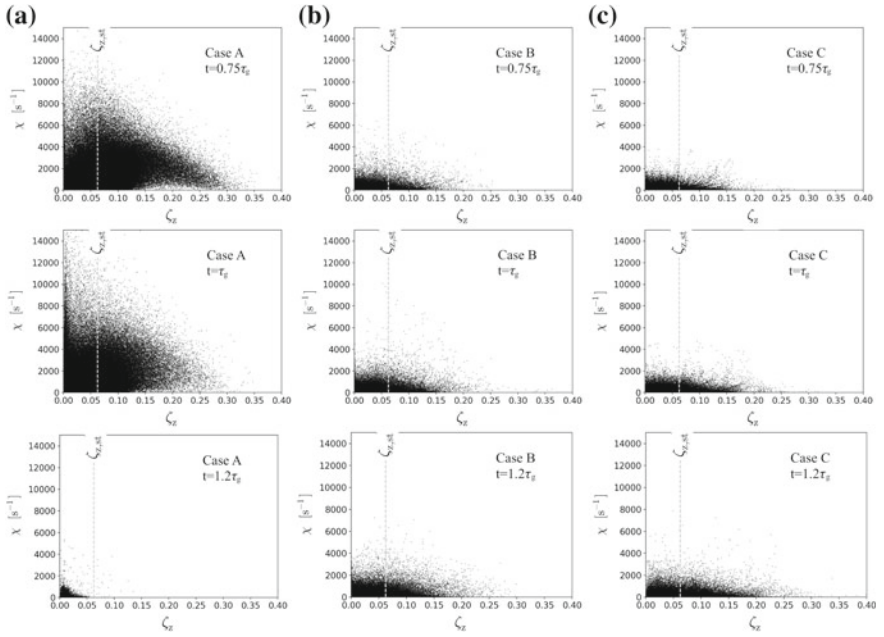

Fig. 4 Time evolution of scatter plot of scalar dissipation rate versus mixture fraction at three different times, $0.75\tau_g$, τ_g, and $1.2\tau_g$: Left: Case A. Middle: Case B. Right: Case C

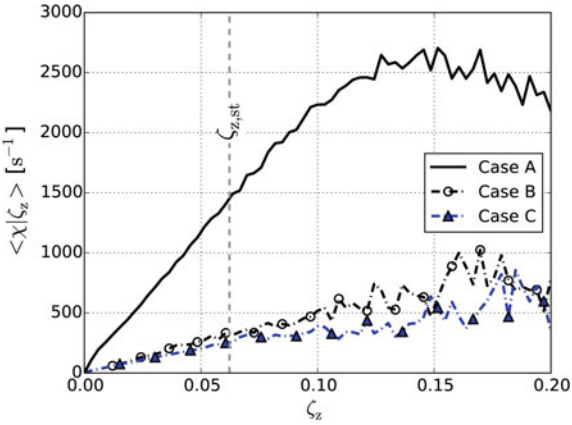

Fig. 5 Conditional mean of scalar dissipation rate versus mixture fraction at $t = \tau_g$

For a quantitative comparison between Cases A, B and C, the conditional mean of scalar dissipation rate versus mixture fraction at $t = \tau_g$ is compared in Fig. 5. It is observed that Cases B and C show nearly identical results. While Case A shows a similar trend in a qualitative manner, large quantitative deviations are observed, the mean values for Case A lying a factor 3–5 above those of Cases B and C.

4.1 Computational Efforts

Initially, TEJ has been proposed in DNS in order to reduce the computational efforts [11]. In our simulations, Case A (TEJ) consumes only 40% of the computational time needed to simulate Case B or C. Hence, parametric studies are noticeably easier with TEJ than with SEJ.

5 Summary and Conclusions

The behavior of scalar dissipation rate was compared during spray evaporation and ignition in either temporally- or spatially-evolving jets. TEJ saves about 60% of the computational time compared to SEJ. The behavior of temperature and scalar dissipation rate show a good qualitative agreement between TEJ and SEJ, but large quantitative differences. Therefore, it is recommended to use TEJ for systematic parametric studies, while individual simulations can indeed already be done using SEJ, closer to physical reality. Interestingly, Cases B and C deliver very similar correlations and statistics, though the ignition location is different (B: head of the jet; C: size of the jet). This point will be investigated further in the future, in particular for high-speed jets.

Acknowledgements The computer resources provided by the Gauss Center for Supercomputing/Leibniz Supercomputing Center Munich under grant pro84qo have been essential to obtain the DNS results presented in this work.

References

1. Abdelsamie, A., Thévenin, D.: Direct numerical simulation of spray evaporation and autoignition in a temporally-evolving jet. Proc. Combust. Inst. **36**(2), 2493–2502 (2017)
2. Réveillon, J., Pera, C., Bouali, Z.: Examples of the potential of DNS for the understanding of reactive multiphase flows. Int. J. Spray Combust. Dyn. **3**(1), 63–92 (2011)
3. Wandel, A.P.: Influence of scalar dissipation on flame success in turbulent sprays with spark ignition. Combust. Flame **161**(10), 2579–2600 (2014)
4. Wang, Y., Rutland, C.J.: Direct numerical simulation of ignition in turbulent n-heptane liquid-fuel spray jets. Combust. Flame **149**, 353–365 (2007)
5. Wandel, A.P., Chakraborty, N., Mastorakos, E.: Direct numerical simulations of turbulent flame expansion in fine sprays. Proc. Combust. Inst. **32**, 2283–2290 (2009)
6. Neophytou, A., Mastorakos, E., Cant, R.S.: The internal structure of igniting turbulent sprays as revealed by complex chemistry DNS. Combust. Flame **159**, 641–664 (2012)
7. Borghesi, G., Mastorakos, E., Cant, R.S.: Complex chemistry DNS of n-heptane spray autoignition at high pressure and intermediate temperature conditions. Combust. Flame **160**, 1254–1275 (2013)
8. Abdelsamie, A., Fru, G., Oster, T., Dietzsch, F., Janiga, J., Thévenin, D.: Towards direct numerical simulations of low-Mach number turbulent reacting and two-phase flows using immersed boundaries. Comput. Fluids **131**, 123–141 (2016)

9. Abramzon, B., Sirignano, W.A.: Droplet vaporization model for spray combustion calculations. Int. J. Heat Mass Transf. **32**(9), 1605–1618 (1989)
10. Patel, A., Kong, S.C., Reitz, R.D.: Development and validation of a reduced reaction mechanism for HCCI engine simulations. SAE Technical Paper, 2004-01-0558 (2004)
11. Hawkes, E.R., Sankaran, R., Sutherland, J.C., Chen, J.H.: Scalar mixing in direct numerical simulations of temporally evolving plane jet flames with skeletal CO/H_2 kinetics. Proc. Combust. Inst. **32**, 1633–1640 (2007)

Modeling of Convective and Conductive Conjugate Heat Transfer in a Kerosene/Air Spray Flame Used for Aeronautical Fire Resistance Tests

L. Boulet, P. Bénard, G. Lartigue, V. Moureau and S. Didorally

1 Introduction

Airworthiness standards require a fire resistance demonstration for aircraft or helicopter engines to obtain a type certificate. This demonstration relies on tests performed with prototype engines in the late stages of the development. In these tests, a propane or a kerosene standardized flame with imposed burnt gas temperature and heat flux is placed next to the engine casing during a given time. The aim of this work is to provide a better characterization of a kerosene/air certification burner in order to reach a better understanding of the thermal environment during fire tests.

To this purpose, Large-Eddy Simulation (LES) of the certification burner is carried out. Spray combustion, forced convection on walls and conduction in the solid parts of the burner are coupled to achieve a detailed description of heat transfer. To a large extent, the aim is to progress on fire test modeling so as to minimize the risks of test failure. Because convective heat transfer is dominant on systems to test, and convection and conduction are important to stabilize the flame inside the torch, radiation of burnt gases as well as radiation of the equipment are not taken into account in this first modeling step.

After introducing the geometry of the certification torch, the modeling and the Conjugate Heat Transfer (CHT) strategy for the simulations is explained. In a second part, an analysis of the flame topology and the air surrounding the torch in an CHT case is followed by a comparison of results between a CHT case and experimental data. An estimation of radiative heat transfer is finally conducted in order to quantify its influence on the heat exchange balance.

L. Boulet (✉) · P. Bénard · G. Lartigue · V. Moureau
CORIA, CNRS UMR 6614, Normandie Université, INSA and University of Rouen, 76801 Saint-Étienne-du-Rouvray, France
e-mail: lancelot.boulet@coria.fr

S. Didorally
Safran Aircraft Engines Villaroche, Rond Point René Ravaud - Réau, 77550 Moissy-Cramayel, France

M. V. Salvetti et al. (eds.), *Direct and Large-Eddy Simulation XI*,
ERCOFTAC Series 25, https://doi.org/10.1007/978-3-030-04915-7_35

2 Certification Torch Modeling

Very few detailed studies of the certification torch are available in the literature. The ISO standard [1] provides details about the flame temperature and heat flux but few geometric details such as the cone dimensions. From the simulation point-of-view, a first RANS study without CHT [2] compares the thermal behavior of a composite material during a fire stress. In this study, the torch modeling is limited to the cone.

In this paper, a high-fidelity study of the flow inside the torch is conducted in order to understand the flame dynamics and have a more precise characterization of the heat flux on the engine casing. Ultimately, these simulations will help in increasing the confidence level in the casing design before the certification tests.

The Large-Eddy Simulation approach, which resolves the large scale of the flow and models the impact of the small scales onto the large ones, is chosen as it gives access to the flame dynamics and is more accurate than RANS methods for this type of internal flow with spray combustion.

2.1 Geometry Modeling and Computation Domain

Figure 1 shows the set-up of the certification burner. It is composed of three main parts: (i) an injection line, where the air flows and the kerosene is injected, (ii) a turbulator, that allows both to generate large turbulent scales and to stabilize the flame, and (iii) a cone, guiding the burnt gases. The cone is modeled according to the ISO norm 2685 [1]. The modeling of the turbulator is based on measurements taken from the real apparatus.

Simulations are performed on unstructured grids using the parallel LES finite-volume YALES2 code [3]. The burner is placed in a computational domain that contains about 40 million tetrahedral cells with a cell size between 0.8 and 2 mm (Fig. 2, left). Due to the slimness of the cone and the fact that at least four cells

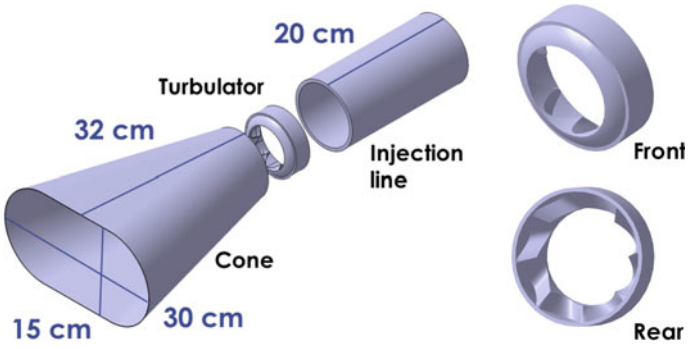

Fig. 1 Exploded-view of the certification torch (left) and turbulator (right)

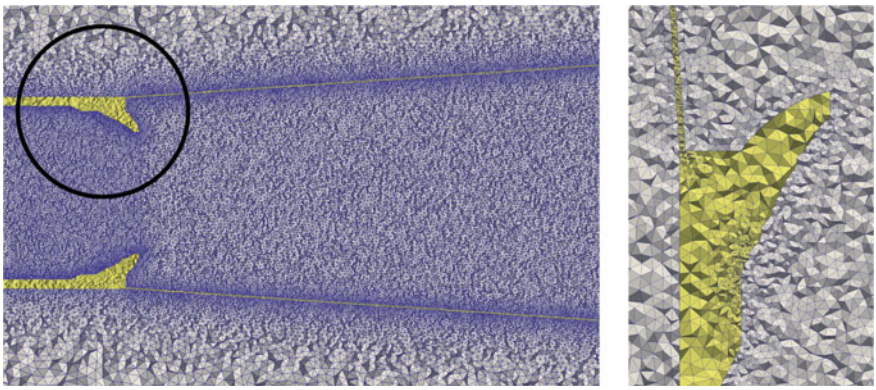

Fig. 2 Fluid and solid mesh of the torch (left) and details around the turbulator (right)

are required to capture the thermal gradient in the cone wall, the mesh of the solid consists of 140 million cells from 0.2 mm in the cone to 1 mm in the injection line (Fig. 2, right).

2.2 Models and Conjugate Heat Transfer Strategy

YALES2 solves the low-Mach number Navier–Stokes equations for the fluid phase considering combustion, buoyancy and the heat equation for conduction into the solid. The global time integration relies on a variable-density projection method [4], which enables to remove the constraints due to acoustics at low-Mach number. The full injection line and primary atomization at the injector exit are not modeled. Instead, a polydisperse spray of kerosene droplets is directly injected. The spray transport model uses a point-particle Lagrangian approach, where droplets are numerical parcels on which Newtonian mechanics can be applied. A two-way coupling approach with a single-component evaporation model, as well as a simplified swirled injector model for the atomization [5], are used. Combustion modeling relies on the dynamic Thickened Flame Model (TFLES) [6] coupled to a 2-step analytical mechanism: the BFER kerosene scheme [7]. The sub-grid turbulence model is a localized dynamic Smagorinsky model. A slip boundary condition is used on the burner walls.

The torch is surrounded by a low-speed air co-flow and parameters of the swirled air at the inlet, i.e. speed and swirling angle, are adjusted thanks to experimental data. The kerosene spray is modeled thanks to a Rosin-Rammler diameter PDF and the injection velocity is also adjusted thanks to experimental data.

To carry out CHT simulations, a parallel coupling strategy (PCS) using the OpenPALM software [8] is employed to converge to steady-state more rapidly. Dirichlet–Neumann interface conditions are used: the solid sends its temperature to the fluid

whereas the fluid sends its heat flux to the solid. In this PCS, the two solvers run simultaneously and asynchronously: each solver advance with its own timestep for a given time before exchanging data. Compared to a synchronous approach, a longer physical time can be simulated in the solid during a given fluid physical time. In the following, each solver is advanced during 1/30 of its characteristic time scale before coupling. While being efficient, this method only enables to study the converged state. The number of CPUs for each solver is adjusted to minimize idle time.

Simulations are performed on the super-computer Occigen from CINES using 1084 processors: 1024 for the fluid phase, 60 for the solid phase. This set-up allows to simulate 100 ms of physical time within 20 h of wall clock time.

3 Topology of the Flow and of the Flame in a CHT Case

Figure 3 left shows the flame topology inside the burner. The flame features large-scale wrinkling due to the shape of the turbulator. Some isolated hot spots are noticeable, which correspond to the combustion of big droplets that are able to cross the flame front. On the right hand side, the values of enthalpy source term inside the turbulator shows that the hot wall temperature helps evaporating droplets blocked inside the turbulator lobes. Moreover, an outer recirculation zone (ORZ) exists at the exit of the turbulator. In this ORZ, where burnt gases recirculate, the CHT decreases the temperature and incurs a flame lift-off, which is not present without CHT.

Figure 4 illustrates the influence of buoyancy on the flow around the torch. The air is heated at the wall and has a different behavior above and below the cone. Above, the temperature gradient induces a hot plume and below, a stable stratification is obtained due to the negative temperature gradient. The Rayleigh number Ra, associated with buoyancy-driven flow, is about 6.10^6.

This different thermal behavior leads to different wall heat losses on the cone: heat flux is more important at the upper side and represents 56% of the total. The wall heat flux on the cone can be compared to the total flux at the exit of the torch: it represents only 2% of the exit enthalpy flux.

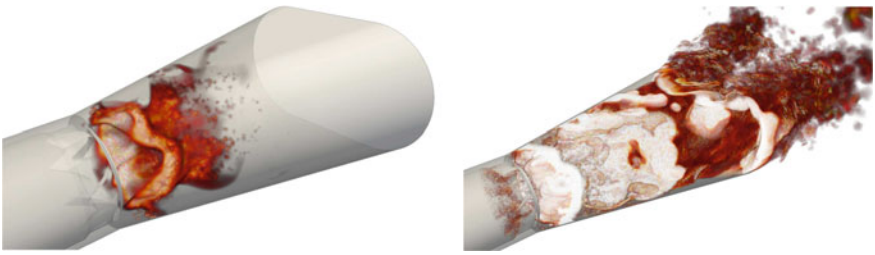

Fig. 3 Instantaneous volume rendering for high (left) and moderate values (right) of the sensible enthalpy source term $\dot{\omega}_{Hs}$. Colors go from black (low values) to white (high values) through red

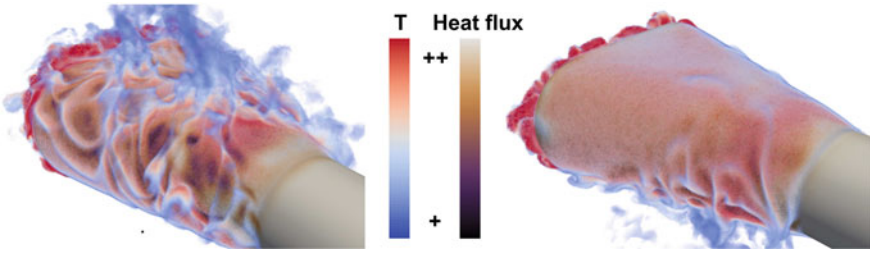

Fig. 4 Instantaneous volume rendering of the air surrounding the torch for the upper (left) and the lower side (right), heat flux is also plotted on the skin of the cone

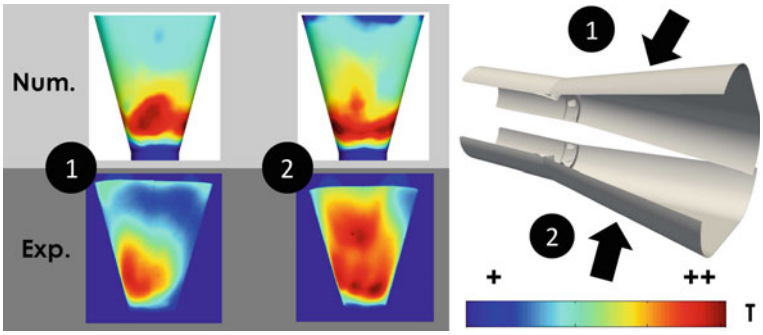

Fig. 5 Qualitative comparison of the cone temperature profile between numerical (top) and experimental (bottom) at the upper (1) and the lower (2) side of the torch

4 Temperature Distribution and Estimation of Radiative HT

The CHT computation enables to access to the temperature distribution on the torch as shown in Fig. 5 even if the lack of radiative heat loss on the solid wall in the simulation leads to unrealistically high temperature. However, a fairly good agreement between the numerical data and the experiments is obtained. At the upper side, a hot zone is observed, while in the lower part, the hot region seems to expand in the second part of the cone. This comparison is only qualitative and will have to be done again with radiative heat loss in future work.

These computations can help evaluating the radiative heat flux on the cone. An estimation of the ratio between the convective and the radiative flux can be estimated by simplifying the geometry of the cone into an equivalent cylinder. An equivalent diameter D_{eq} can be deduced keeping the same area and the same length L. Then, fluxes can be computed thanks to a Newton and a Stephan–Boltzmann law:

$$q_{conv} = (T_{cone} - T_\infty)\lambda Nu/D_{eq} \ , \quad and \quad q_{rad} = \varepsilon\sigma\pi D_{eq} L(T_{cone}^4 - T_\infty^4) \ , \qquad (1)$$

where T_∞ is the fluid temperature, ε the material emissivity, σ the Stefan–Boltzmann constant, λ the conductivity and Nu the Nusselt number. This latter can be determined thanks to a correlation [9] for $Ra < 10^{12}$.

Taking a mean experimental temperature into account reveals that the radiative flux on the torch is 88% of the total flux. So, even if convection is probably the dominant flux when considering the impingement on the engine casing, the radiative heat transfer can't be neglected to obtain a good prediction of the cone temperature and a correct stabilization of the flame into the torch.

5 Conclusion and Outlook

It has been shown that LES is a useful tool to model complex reactive flows such as those in a certification torch. In such device, all heat transfer types are important in order to have a good prediction of the flame stabilization and of the heat flux at the exit of the torch.

The future work will focus on the influence of the radiative heat transfer by coupling it with the fluid and solid simulations. The burner wall and the calorimeter heat flux and temperature will be compared to the adiabatic simulations. A mesh refinement sensitivity analysis will also be carried out in order to quantify the mesh dependency. The LES model of the burner will finally be applied to the prediction of heat transfer in an impacting flame configuration. A well instrumented metal plate placed in vicinity of the burner will be investigated as a simplified test case.

References

1. ISO 2685:1998: Aircraft - environmental conditions and test procedures for airborne equipment - resistance to fire in designated fire zones. ISO Technical report (1998)
2. Grange, N., Chetehouna, K., Gascoin, N., Senave, S.: Numerical investigation of the heat transfer in an aeronautical composite material under fire stress. Fire Saf. J. **80**, 56–63 (2016)
3. Moureau, V., Domingo, P., Vervisch, L.: Design of a massively parallel CFD code for complex geometries. C. R. Mécaniques **339**, 141–148 (2011)
4. Pierce, C.D., Moin, P.: Progress-variable approach for large eddy simulation of non-premixed turbulent combustion. J. Fluid Mech. **504**, 73–97 (2004)
5. Guedot, L.: Développement de méthodes numériques pour la caractérisation des grandes structures tourbillonnaires dans les brûleurs aéronautiques: application aux systèmes d'injection multi-points. Doctoral dissertation, Rouen, INSA (2015)
6. Charlette, F., Meneveau, C., Veynante, D.: A power-law flame wrinkling model for LES of premixed turbulent combustion Part II: d. Formulation. Comb. Fl. **131**(1), 181–197 (2002)
7. Franzelli, B., Riber, E., Sanjosé, M., Poinsot, T.: A two-step chemical scheme for keroseneair premixed flames. Comb. Fl. **157**(7), 1364–1373 (2010)
8. Duchaine, F., Jauré, S., Poitou, D., Quémerais, E., Staffelbach, G., Morel, T., Gicquel, L.: Analysis of high performance CHT with the OpenPALM coupler. Comput. Sci. Discov. **8** (2015)
9. Churchill, S.W., Chu, H.H.S.: Correlating equations for laminar and turbulent free convection from a horizontal cylinder. Int. J. Heat Mass Transf. **18**(9), 1049–1053 (1975)

Part V
Convection and Heat Transfer

Towards the Direct Numerical Simulation of a Simplified Pressurized Thermal Shock

A. Shams and E. M. J. Komen

1 Introduction

The integrity assessment of a Reactor Pressure Vessel (RPV) is considered to be an important issue for lifetime extension of nuclear reactors. A severe transient that can threaten the integrity of the RPV is the existence of a Pressurized Thermal Shock (PTS) during a Loss-of-Coolant Accident (LOCA) [1]. A PTS consists of a rapid cooling of the RPV wall under pressurized conditions that may induce the criticality of existing or postulated defects inside the vessel wall. The most severe PTS event has been identified by Emergency Core Cooling (ECC) injection during a LOCA. The injected cold water mixes with hot water present in the cold leg, and flows towards the downcomer, causing further thermal mixing and, therefore, large temperature gradients. This sudden change in temperature may induce high stresses in the RPV wall, leading to the propagation of flaws inside the vessel wall, especially in the embrittled region adjacent to the core. A proper knowledge of these loads is important for the RPV remnant lifetime assessment.

Traditional one-dimensional thermal-hydraulic system codes like RELAP-5 or CATHARE, often used in the nuclear industry, fail to reliably predict the complex three-dimensional thermal mixing phenomena in the downcomer occurring during ECC injection [1]. Hence, CFD can bring real benefits in terms of more realistic and more predictive capabilities. However, to gain trust in the application of CFD modelling for PTS, a comprehensive validation programme is necessary. In the absence of detailed experimental data for the RPV cooling during ECC injection, high fidelity DNS databases constitute a valid alternative and can serve as a reference [2, 3]. However, performing a DNS for a realistic PTS scenario is extremely expensive and not

A. Shams (✉) · E. M. J. Komen
Nuclear Research and Consultancy Group (NRG), Petten, The Netherlands
e-mail: shams@nrg.eu

E. M. J. Komen
e-mail: komen@nrg.eu

M. V. Salvetti et al. (eds.), *Direct and Large-Eddy Simulation XI*,
ERCOFTAC Series 25, https://doi.org/10.1007/978-3-030-04915-7_36

foreseeable in the near future. On the other hand, a high fidelity database of a relatively simplified PTS case can be very helpful for the scientific community. This can help in understanding the complex flow and heat transport in detail and can be used for validation of turbulence modelling approaches such as (U)-RANS and Hybrid LES/URANS models, which eventually can be applied for realistic PTS scenarios.

In this regard, at NRG, an extensive research programme has been carried out to perform a DNS of a simplified PTS case without buoyancy effects [4]. As a first step, a simplistic PTS geometry is designed and is discussed in Sect. 2. As a next step, a thorough assessment of the code NEK5000 in order to perform high quality DNS has been performed and is presented in Sect. 3. Finally, the high fidelity simulations of the simplified PTS design are performed and reported in Sect. 4. This is followed by a summary.

2 PTS Design Without Buoyancy Effects

The design of the PTS scenario without buoyancy effects has been performed via in-depth CFD analysis. In that respect, extensive RANS computations have been carried out in order to obtain an optimal PTS design, for details see [1, 2]. The PTS design consists of a square duct cold leg, down-comer, vessel wall, and barrel wall, as shown in Fig. 1. The dimensions of this PTS design are also given in Fig. 1 (Right). A simplistic planar configuration is considered for the down-comer instead of the typical curved geometry of RPV. Furthermore, the lower plenum is not considered and a pressure boundary condition is selected for the outlet. It is worth mentioning that for the DNS computations, constant flow properties are used. An additional hot water inlet (Inlet 2) has been considered at the top of the down-comer in order to obtain the characteristic cold plume cooling as observed in PTS scenarios. Namely, this additional inlet forces the flow downward in the down-comer. The inlet 2 velocity is selected as 10% of the inlet 1 bulk velocity, details are discussed in [1, 2]. A fully developed turbulent velocity profile is imposed at Inlet 1, whereas, a uniform velocity profile is chosen for Inlet 2. The inlet 1 velocity magnitude is calibrated in order to set the friction Reynolds number (Re_τ) in the square duct cold leg equal to the value of 180. Constant temperature profiles are imposed at both the inlets. Due to the constant flow properties and also the absence of thermal stratification, the ECC injected fluid at inlet 1 is considered to be fully mixed in the cold leg, upstream of the down-comer region.

Single-phase water is considered as a working fluid. This resulted in a Prandtl number (Pr) of approximately 7. However, such a high value entails that Batchelor scales are quite smaller than the Kolmogorov scales, requiring a much finer mesh resolution in order to resolve the thermal scales. Hence, the Prandtl number is scaled down to 1 by varying the water thermal properties. Effects of such a variation were thoroughly investigated, and despite of small differences, it was found that the overall topology of the thermal field remains similar [1]. Moreover, two different boundary conditions, i.e. adiabatic (iso-flux) and iso-thermal conditions, at the outer surfaces

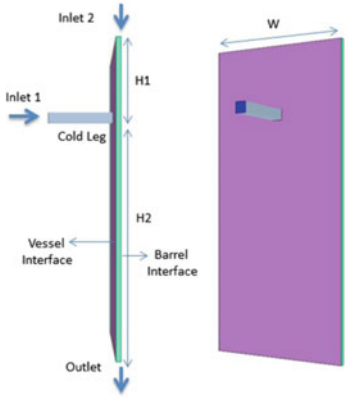

Parameters	*Description*
Inlet 1	Instead of a round pipe, a duct is considered for the inlet section. In addition, the flow parameters are calibrated to match $Re_\tau = 180$ (for details see [2])
Inlet 2	In the absence of the buoyancy effects, an artificial inlet 2 is imposed to force the inlet 1 flow towards the down-comer.
Cold Leg	The length of the cold leg is 6 times the equivalent diameter (D) of the duct.
H1	The upper height of the domain is 10D.
H2	The lower height of the down-comer is 23.3D.
W	The width of the domain is 20D.
Vessel Interface	Instead of a conjugate heat transfer, two boundary conditions are imposed (i) iso-thermal (2) iso-flux
Barrel Interface	Two boundary conditions are imposed (i) iso-thermal (2) iso-flux
Outlet	Pressure outlet

Fig. 1 Geometric design of a simplified PTS scenario without buoyancy effects (Right) list of the parameters used for the PTS design [2]

of the down-comer were studied. It is worth mentioning that, since the actual PTS is a transient scenario, steady-state RANS can only be representative of stationary flows and thermal behaviors. However, the iso-flux and iso-thermal cases are representative of different temporal stages of a transient PTS scenario. In addition, these two boundary conditions also cover the two extremes of the actual conjugate heat transfer case. Hence, these two boundary conditions are selected to replicate the PTS scenarios in the fluid-only domain of the selected PTS design. This, in turns, saves a lot of computational efforts, which is foreseen to be used for the PTS case with conjugate heat transfer case. For details regarding the PTS design, flow parameters, and the related boundary conditions, readers are referred to [1].

3 Code Assessment to Perform a True DNS

The higher order spectral element code NEK5000 has been selected as CFD tool to generate the high fidelity DNS database for the simplistic PTS without buoyancy effects. The code NEK5000 adopts a Spectral Element Method (SEM) for the spatial discretization, which is a finite element method and is coupled with a high-order weighted residual technique [5]. This consists in computing velocity in each element as Lagrange polynomials over a N-th order Gauss–Lobatto–Legendre (GLL) point's distribution. Pressure is computed on the same spatial discretization (P_N-P_N formulation) or over a $(N-2)$-th order distribution (P_N-P_{N-2} formulation) [6]. The former approach is selected in this work for the spatial discretization of the Navier–Stokes equations. NEK5000 uses a semi-implicit time-stepping method. In the formulation, the viscous terms in the Navier–Stokes equation are treated implicitly using a k-step backward differentiation formula (BDF_k) based on a truncated Taylor expansion of the solution, while the non-linear (convective) terms are treated using an explicit

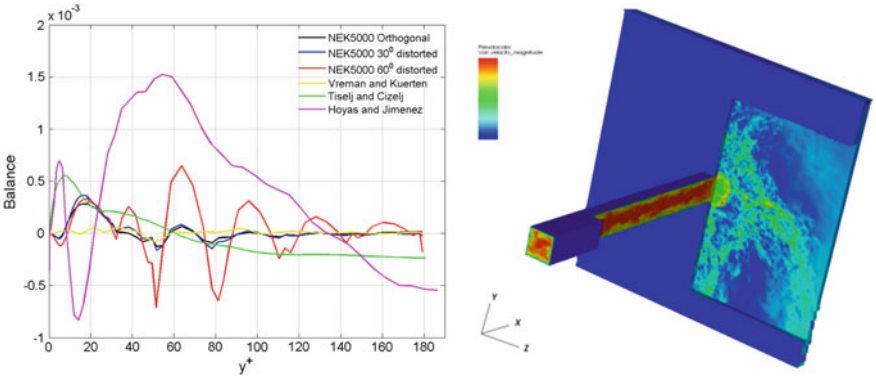

Fig. 2 (Left) Balance of the turbulent kinetic energy budget for a planar channel flow with $\mathrm{Re}_\tau = 180$. (Right) Iso-contours of velocity field in the cold leg of PTS

extrapolation scheme of order k (EXT_k). For the present study, an order of $k = 3$ is considered, which results in a $\mathrm{BDF}_3/\mathrm{EXT}_3$ time-stepping scheme which is globally third order accurate.

A thorough assessment of this code to perform high quality DNS has been performed for a well-known turbulence channel flow configuration at $\mathrm{Re}_\tau = 180$ (turbulent Reynolds number based on the wall friction velocity and half duct height). Different numerical parameters of NEK5000 have been extensively tested and their influence has been studied to obtain high quality turbulence statistics, see [2, 3]. One of the limitations of NEK5000 is that his code is able to handle only hexahedral elements (preferably orthogonal). However, application of perfectly orthogonal meshes for PTS-like geometries is not possible, and the quality of the resulting DNS could be questioned. Thus, various non-orthogonal meshes have been assessed for the selected turbulent channel flow configuration. A number of test cases are studied by distorting (shearing) the perfectly orthogonal mesh with different angles, up to 60 °. The obtained results are compared with various reference databases for mean, RMS, skewness and kurtosis of velocity and the budget for the turbulent kinetic energy. However, because of the page limitations, only the sum of the turbulent kinetic energy budgets is presented in Fig. 2 (left). This budget sum should be zero. It is clearly noticeable that the budget sum obtained by the code NEK5000 is, apart from very small statistical errors, very close to zero like in other reference databases [6–8].

4 High Fidelity Simulations of the Simplified PTS Case

Based on the aforementioned code assessment, a high quality base mesh for the simplified PTS design was generated. It consists of 0.75 million spectral elements (for details see [1, 4]). It is worth mentioning that the overall number of grid points

depends on the selected order of accuracy. For example, for N3 (i.e. third order of accuracy in space) the total mesh corresponds to 20 million grid points. Similarly, for N5 and N7, the overall mesh corresponds to 95 and 275 million grid points, respectively. Hence, a huge amount of computational power is required to perform the computations. Nevertheless, in order to achieve the eventual high quality DNS solution, this base mesh needs to run with spectral elements of fifth (N5) or seventh (N7) order of spatial accuracy [4]. Nonetheless, due to the computational constraints, a precursor Under-resolved DNS (UDNS) has been performed with N3 in order to understand the flow physics and to learn about the statistical convergence. This N3 PTS computation has been performed at Centrum Informatyczne Swierk (CIS) in Poland [9]. Due to the complex nature of the flow field, the simulation has run for 5 million core hours i.e. 208 days on 1000 processors. In this article, the results corresponding to the N3 UDNS are presented. The obtained results are analyzed both for the instantaneous velocity and temperature fields with a statistical approach. Initially, the simulation has run to achieve a fully developed turbulent flow. Subsequently, averaging was started and the statistical convergence was monitored in time. The results discussed in the article refer to a statistically converged simulation, with a normalized averaging time of about $t^+ = tu_\tau/\nu = 14000$. Because of the page limitations, a few qualitative results are presented in this article.

Figure 2 (Right) displays a zoom close to the cold leg region. It is clearly noticeable that the cold leg duct shows a fully developed turbulent flow field, which represents a well-defined inlet boundary condition. It is worth reminding that a fully developed turbulent velocity profile at inlet 1 is obtained by recycling the flow field in an extended duct upstream of the inlet 1. The length of this extended duct is 4 times the

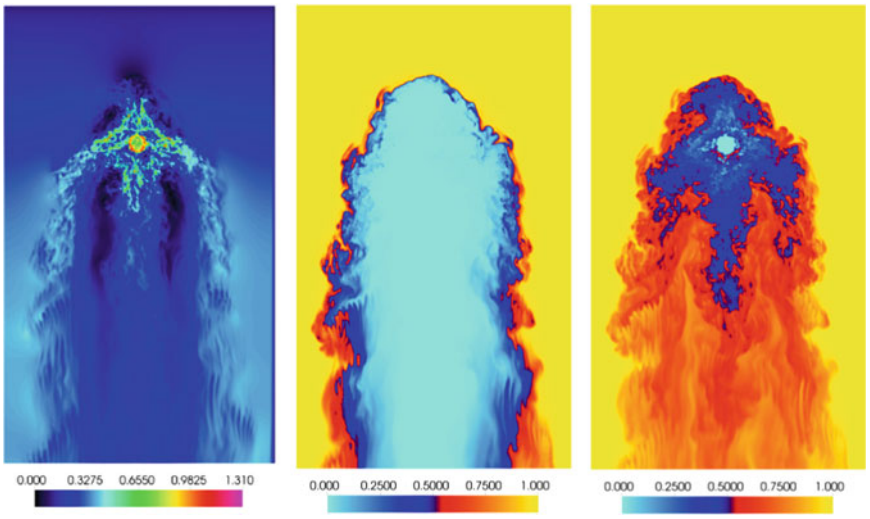

Fig. 3 Iso-contours of (Left) velocity and the temperature field along the mid cross-section corresponding to (Middle) iso-flux and (Right) iso-thermal boundary conditions

equivalent diameter of the duct [4]. This well-defined fully developed inlet boundary condition is very important for the validation phase in order to reduce the level of uncertainties. Furthermore, the flow from the cold leg hits the barrel wall and disperses in all direction, exhibiting a very complex three-dimensional flow field. To visualize it more clearly, a cross-section at the mid of the down-comer is selected to present the flow pattern appearing in this PTS design, see Fig. 3 (Left). In addition to the flow field, iso-contours of the thermal fields corresponding to two selected boundary conditions are also shown in Fig. 3. As mentioned earlier, these boundary conditions are carefully selected to represent different temporal stages of a transient PTS scenario. It is worth mentioning that this performed N3 UDNS is used as an initial condition to perform the subsequent run with N5. This N5 simulation is on-going at the CIS computing facility [9]. Although, the N5 case does still not really correspond to a true DNS, this UDNS is currently pursued, given the available computational resources. This in turns will provide a step forward to confirm the convergence towards a true DNS, from N5 to N7. In addition, it can also serve as an intermediate validation database (as discussed in [4]).

5 Summary

The aim of this research work is to generate high fidelity DNS databases for a simplified single phase PTS scenario without buoyancy effects. In this regard, an enormous effort has been put forward for the design of a simplified geometric configuration for a single phase PTS scenario without buoyancy effects. In addition, a thorough assessment of the code NEK5000 has been done in order to perform a true DNS for a PTS like scenario. Accordingly, a systemic progression towards the generation of the DNS database, for a PTS scenario without the buoyancy effects, is ongoing and will result in a successful campaign. This will provide a sort of reference database to validate low order CFD approaches, such as (U-) RANS and Hybrid (URANS/LES) methods.

Acknowledgements The work described in this paper is funded by the Dutch Ministry of Economic Affairs. The N3 UDNS computations presented in the paper are performed at Swierk Computing Centre within the framework of the EU and MSHE grant no. POIG.02.03.00-00-013/09.

References

1. Shams, A., Damiani, G., Rosa, D., Komen, E.M.J.: Nucl. Eng. Des. **300**, 282–296 (2016)
2. Damiani, G., Rosa, D., Shams, A., Komen, E.M.J., Merzari, E., Obabko, A., Fischer, P.: NURETH-16, Chicago, USA (2015)
3. Rosa, D., Shams, A., Komen, E.M.J.: CFD4NRS-6, Boston, USA (2016)
4. Shams, A., Komen, E.M.J.: International Conference on Topical Issues in Nuclear Installation Safety: Safety Demonstration of Advanced Water Cooled Nuclear Power Plants, IAEA-CN-251, Vienna, Austria (2017)

5. https://nek5000.mcs.anl.gov/
6. Tiselj, I., Cizelj, L.: D Nuclear Engineering and Design (2012)
7. Vreman, A.W., Kuerten, J.G.M.: Phys. Fluids **26**, 015102 (2014)
8. Hoyas, S., Jimenez, J.: Phys. Fluids **20**, 101511 (2008)
9. http://www.ncbj.gov.pl/pl/projekty/centrum-informatyczne-swierk/

Study of the Flow Around a Heated Cylinder in Mixed Convection Regime

S. Rolfo, K. Kopsidas, S. A. Rahman, C. Moulinec and D. R. Emerson

1 Introduction

Overhead Lines (OHL) are a key component to transmit and distribute electrical energy. The aero-thermal design of OHL is generally carried out considering the cable as a perfect heated cylinder immersed in a uniform cross flow [1]. Moreover, The design also assumes that only two regimes can occur, depending on the Reynolds number (based on the line diameter and the incoming velocity): (a) natural convection for low velocities, e.g. below a wind speed of 0.6 m/s which roughly corresponds to a Reynolds number of 850; (b) forced convection at higher Reynolds numbers. In both of these cases analytical correlations exist to compute the Nusselt number.

The flow around circular cylinders has been widely studied and a complete review can be found in [2]. The flow is laminar, bi-dimensional and steady up to a Reynolds number of 40, based on diameter and incoming velocity, and 3-D transition in the wake has been observed starting at $Re = 200$ [2].

Heat transfer has mainly been investigated experimentally and always concentrating on the forced convection regime. Experimental correlations have been widely

S. Rolfo (✉) · C. Moulinec · D. R. Emerson
Scientific Computing Department, STFC Daresbury Laboratory, Warrington, UK
e-mail: stefano.rolfo@stfc.ac.uk

C. Moulinec
e-mail: charles.moulinec@stfc.ac.uk

D. R. Emerson
e-mail: david.emerson@stfc.ac.uk

K. Kopsidas · S. A. Rahman
School of Electrical and Electronic Engineering, The University of Manchester, Manchester, UK
e-mail: k.kopsidas@manchester.ac.uk

S. A. Rahman
e-mail: shahnurriman.abdulrahman@manchester.ac.uk

M. V. Salvetti et al. (eds.), *Direct and Large-Eddy Simulation XI*,
ERCOFTAC Series 25, https://doi.org/10.1007/978-3-030-04915-7_37

developed, ranging from the very simple expression $Nu = CRe^m Pr^{1/3}$, with the coefficients C and m function of the Reynolds number, up to the more general expressions as proposed in [3] However, for moderate Reynolds numbers, the cylinder is generally operating in the mixed convection regime and aero-thermal characteristics of the flow might deviate from the assumption of simple force or natural convection. As a consequence, the focus of this work is to investigate the potential existence of large 3-D coherent structures in a flow field that conventional classification (based on the Reynolds number) will consider as laminar and bi-dimensional. The effect of the angle α between the undisturbed (or incoming) velocity U_∞ and the gravity vector $\mathbf{g}$ will be also presented.

2 Numerical Methods

The simulations have been performed using the open source CFD software *Code Saturne* [4, 5]. The Navier–Stokes–Fourier equations are discretised using a cell centred co-located finite volume approach. Velocity and pressure coupling is ensured through a prediction/correction method similar to the SIMPLEC algorithm and the Poisson equation is solved using an algebraic multigrid solver. The code handles fully unstructured grids, including polyhedral cells and embedded refinements. Second order accurate schemes are used for both time and space discretisations.

The buoyancy term in the momentum equations is evaluated using the Boussinesq approximation, which is given by $-\rho\mathbf{g} = -\rho_\infty \mathbf{g}\beta\,(T - T_W)$ with ρ being the density, ρ_∞ being the undisturbed density, β the coefficient of thermal expansion, T the fluid temperature and T_W the temperature at the cylinder surface.

3 Test Case Definition and Validation

The study under consideration is the flow around a heated cylinder characterised by a temperature T_W, a diameter D, set in a uniform flow with a velocity U_∞. The temperature T_W is such that $T_W > T_\infty$, where T_∞ is the temperature of the undisturbed incoming flow. The Reynolds number is set to $Re = U_\infty D/\nu = 150$, with ν being the kinematic viscosity and the temperature at the wall is varied to have the Richardson number $Ri = Gr/Re^2$ as $0 \leq Ri \leq 2$. The Grashof number is defined as $Gr = g\beta\,(T_W - T_\infty)\,D^3/\nu^2$. The computational domain is presented in Fig. 1, it follows a C-shape configuration and it has been meshed using a block structured approach. For validation purposes a 2-D laminar simulation of the cold flow (i.e. no heat transfer considered) has been performed at $Re = 150$. The domain used comprises of an inlet located $20D$ upstream of the cylinder, with an outlet $25D$ downstream and the top and bottom sides are $20D$ apart from the cylinder centre. This domain is made of 27,342 cells ($M01$) with 176 cells around the cylinder solid wall. For the heat transfer the domain has been enlarged moving the inlet, top and

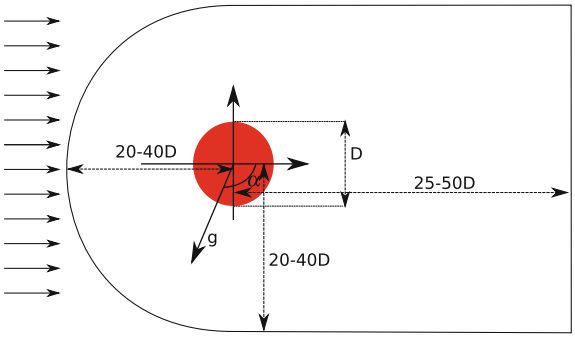

Fig. 1 Sketch of the computational domain and definition of the domain dimensions. The angle α between the undisturbed velocity U_∞ and the gravity vector **g** is negative in the clock-wise direction

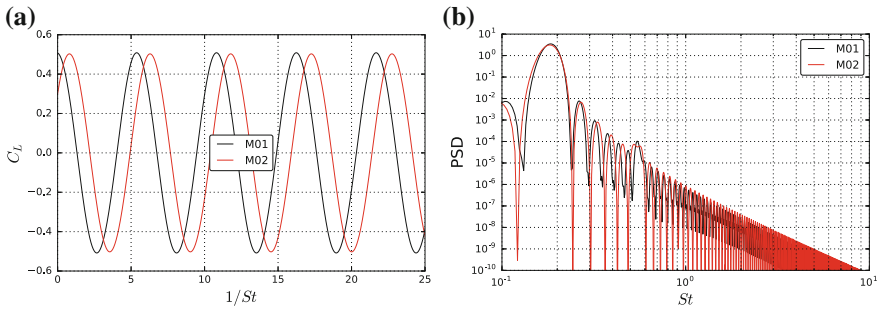

Fig. 2 **a** C_L at $Re = 150$ for forced convection $Ri = 0$ for different mesh resolution. **b** Power Spectral Density (PSD) at $Re = 150$ for forced convection $Ri = 0$ for different mesh resolution

bottom sides $40D$ apart from the cylinder and the outlet is located $50D$ downstream. The mesh has also been refined for a total number of 62,650 cells with 264 cells for the cylinder ($M02$) solid wall. This increase of the domain size and resolution has been dictated by the buoyancy effects observed in the wake of the cylinder. Comparison between the two meshes is reported in Fig. 2a for the lift coefficient time history and its spectrum (see Fig. 2b). The average coefficients, and their r.m.s.values, are in close agreement for both meshes and they are also in good agreement with the reference values. For example the Nusselt numbers given by both meshes are within 0.5% of the experimental correlation given by [3]. Results produced by the two meshes are in fairly good agreement also for higher Richardson numbers, but results on the coarser mesh show some spurious oscillations, mainly generated by the interactions between the boundaries and the wake. Therefore, all results presented in this work, and concerning mixed convection regime, have been obtained by extruding mesh $M02$. The 3-D mesh employs 128 layers in the span-wise direction for a total extrusion length of $2\pi D$, and for a total mesh size of about 8.1 million cells.

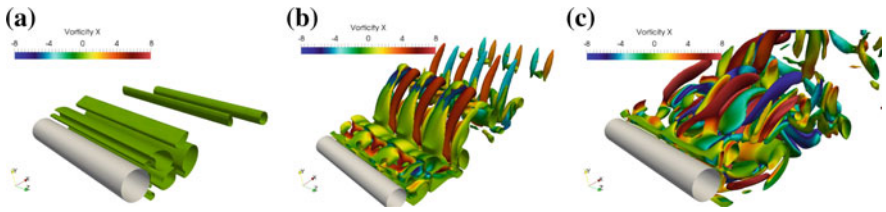

Fig. 3 **a** Q-criterion coloured by x-vorticity for $Ri = 0.5$ and $Re = 150$. **b** Q-criterion coloured by x-vorticity for $Ri = 1.0$ and $Re = 150$. **c** Q-criterion coloured by x-vorticity for $Ri = 2.0$ and $Re = 150$

4 Results

This work presents two sets of results. The first shows a comparison between bi-dimensional and full 3-D calculations up to a Richardson number equal to 2, where the flow direction and the gravity vector are kept perpendicular (i.e. $\alpha = -90°$). In the second set of results, the Richardson number is given by $Ri = 1$ and varies angle between U_∞ and $\mathbf{g}$ varies by $\pm 20°$ with respect to the perpendicular configuration (i.e. $-110 \leq \alpha \leq -70$). In all cases the Reynolds number is $Re = 150$.

Figure 3a–c show the Q-criteria at ± 10, coloured by the stream-wise vorticity, for $Ri = 0.5$, $Ri = 1.0$ and $Ri = 2.0$, respectively. For the low Richardson number the flow retains a bi-dimensional pattern. As the Richardson number increases ($Ri = 1.0$), large and coherent structures appear: the 2-D structures are forming in the wake of the cylinder, they subsequently deform into periodic manifolds that finally break into vortices with an axis pointing upwards with an angle of about 60–70°. These structures have a separation length which is about $2D$. This is in accordance with the value given by [6]. For the largest Richardson number ($Ri = 2.0$) the behaviour of the large structures becomes more chaotic and the periodic motion observed at $Ri = 1.0$ is almost lost. The addition of the buoyancy term on the mean motion is to rotate the wake anticlockwise, destroying the symmetry of the mean flow with respect to the stream-wise direction and, consequently, generating a negative lift. The heat transfer is also affected and the Nusselt number increases with the Richardson number. However, the effect of the transition to a fully 3-D flow is to impair the heat transfer (see Fig. 4a) and to plateau the increase of negative lift (Fig. 4b). More comments on heat transfer impairment will be given later in the section. The spectra of the lift coefficient for the 3-D cases shows also a gradual transition towards a more rich-of-scales flow with the increase of the Richardson number. For $Ri = 1$ the PSD still shows a banded spectrum, with the energy being present only at selected frequencies. On the other hand at $Ri = 2$, the energy content is spread continuously at all frequencies with a decay more similar to that of a turbulent flow. The effect of changing the angle α between U_∞ and $\mathbf{g}$ on the wake is shown in Fig. 5a–d for four different angles α. In the case where the horizontal component of gravity is in opposition to the flow direction, it is possible to observe a return towards a more bi-dimensional flow. This is very obvious for $\alpha = -110°$ (Fig. 5a), where

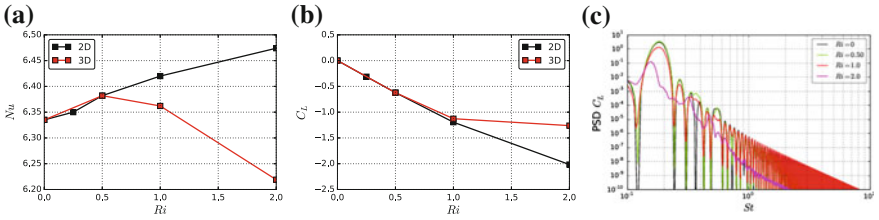

Fig. 4 **a** Nu versus Richardson number at $Re = 150$ for 2-D and 3-D calculations. **b** C_L versus Richardson number at $Re = 150$ for 2-D and 3-D calculations. **c** PSD of the lift coefficient for 3-D simulations

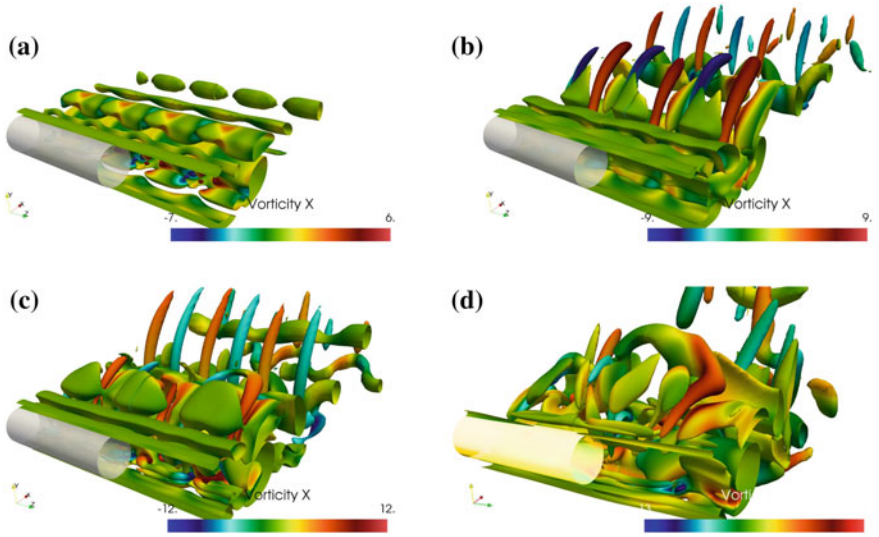

Fig. 5 **a** Q-criterion $Q = \pm 10$ coloured by x-vorticity for $Ri = 0.5$, $Re = 150$ and $\alpha = -110°$. **b** Q-criterion $Q = \pm 10$ coloured by x-vorticity for $Ri = 0.5$, $Re = 150$ and $\alpha = -95°$. **c** Q-criterion $Q = \pm 10$ coloured by x-vorticity for $Ri = 0.5$, $Re = 150$ and $\alpha = -85°$. **d** Q-criterion $Q = \pm 10$ coloured by x-vorticity for $Ri = 0.5$, $Re = 150$ and $\alpha = -70°$

the complex manifold structures return to a more simple cylindrical shape with only some cross section expansion/contraction along the span. The breakdown of these structures does not produce the very long and upwards looking vortices described previously, but rather more ellipsoidal shapes aligned with the span-wise direction. On the contrary, when the horizontal component of the gravity and the flow direction are aligned the 3-D features of the flow are enhanced. For a small positive horizontal component (see Fig. 5c) the structures leaving the cylinder tend to be fully 3-D, but the orderly pattern of the flow is still maintained with the very elongated and upwards looking structures a bit further downstream in the wake. For larger horizontal components of the gravity the flow starts to resemble the one at larger Richardson number (see Fig. 3c) with a more chaotic behaviour.

Table 1 Mean coefficients for 3-D simulations as function of the variation of the gravity angle α

Re	Gr	Ri	α	C_D	C_L	C'_L	Nu	Nu'
150	22500	1.0	−110	1.315	−1.340	0.132	6.586	0.025
150	22500	1.0	−95	1.234	−1.212	0.257	6.460	0.063
150	*22500*	*1.0*	*−90*	*1.196*	*−1.129*	*0.242*	*6.366*	*0.071*
150	22500	1.0	−85	1.159	−1.076	0.313	6.288	0.093
150	22500	1.0	−70	1.004	−0.845	0.477	5.891	0.166

The effect on the average coefficients and their r.m.s. value is detailed in Table 1. The absolute value of both drag and lift coefficients tends to increase with the increase of α (i.e. opposition between mean flow and gravity), whereas fluctuations tends to be damped. Heat transfer is also enhanced in the same configuration of flow and gravity acting in opposite directions. This might look counter-intuitive, but it shows how these long 2-D structures are effective in removing the heat from the cylinder in comparison with much smaller 3-D eddies that do not wet the hot surface as effectively. The same effect that can also be seen in Fig. 4b.

5 Conclusions

This work presents the study of flow around a circular cylinder at $Re = 150$ in mixed convection regime. Several Richardson numbers have been investigated as well as the effect of the angle between the incoming undisturbed flow and the gravity vector. As the Richardson number increases the bi-dimensional periodic flow is destroyed and 3-D coherent structures appear in the flow and progressively become more chaotic. The effect of the angle between the incoming flow and gravity depend on the sign of the horizontal component of the gravity vector: when it is negative the flow tends to become more bi-dimensional, when it is positive it is more turbulent. Heat transfer is enhanced when a more orderly bi-dimensional flow pattern is present in the wake. This shows these large structures are more efficient at extracting heat from the hot surface.

Acknowledgements The authors are grateful for financial support by the Hartree Centre and the UK Engineering and Physical Sciences Research Council (EPSRC) under grants EP/L000261/1, EP/N016602/1 and EP/K038427/1.

References

1. IEEE Standard for Calculating the Current-Temperature Relationship of Bare Overhead Conductors. In: IEEE Std 738-2012 (Revision of IEEE Std 738-2006 - Incorporates IEEE Std 738-2012 Cor 1-2013), pp. 1–72 (2013)
2. Zdravkovich, M.M.: Flow Around Circular Cylinders Volume 1: Fundamentals. Oxford University Press, Oxford (1997)
3. Churchill, S.W., Bernstein, M.: A correlating equation for forced convection from gases and liquids to a circular cylinder in crossflow. J. Heat Transf. **99**, 300–306 (1977)
4. Archambeau, F., Mechitoua, N., Sakiz, M.: Code_Saturne: a finite volume code for the computation of turbulent incompressible flows - industrial applications. Int. J. Finite **1** (2004)
5. Fournier, Y., Bonelle, J., Moulinec, C., Shang, Z., Sunderland, A., Uribe, J.: Optimizing Code_Saturne computations on petascale systems. Comput. Fluids **45**, 103–108 (2011)
6. van Steenhoven, A.A., Rindt, C.C.M.: Flow transition behind a heated cylinder. Int. J. Heat Fluid Flow **24**, 322–333 (2003)

Direct Numerical Simulation of Convective Turbulent Channel Flow of Fluid Mixtures

P. Bahavar and C. Wagner

1 Introduction

Fluid mixtures play an important role in a large variety of applications ranging from atmospheric flows to intracellular transport mechanisms. At the same time they present a significant challenge with regards to modeling and computational costs. In this work, the feasibility of treating a mixture of two fluids with different fluid properties by considering one species as the carrier fluid and treating the effect of an added trace species as a perturbative modification is explored. Towards this end, the concentration of the trace constituent is introduced as an active scalar within the flow and used as an expansion parameter analogously to the temperature in the Boussinesq approximation.

For the example of a mixture of water vapor and dry air, the effects due to the added buoyancy are investigated using direct numerical simulations (DNS) of turbulent channel flow. The limitations concerning the validity of the strict Boussinesq approximation are determined, and an extended formulation is employed to explore higher order effects which become significant towards and outside of the limits of this range.

2 Governing Equations

To describe the flow of the fluid mixture, the Navier–Stokes equations for incompressible flow are used,

P. Bahavar (✉) · C. Wagner
German Aerospace Center (DLR), Göttingen, Germany
e-mail: philipp.bahavar@dlr.de

C. Wagner
Technische Universität Ilmenau, Ilmenau, Germany

M. V. Salvetti et al. (eds.), *Direct and Large-Eddy Simulation XI*,
ERCOFTAC Series 25, https://doi.org/10.1007/978-3-030-04915-7_38

$$\nabla \cdot \mathbf{u} = 0, \tag{1}$$

$$\frac{\partial}{\partial t}\mathbf{u} + (\mathbf{u} \cdot \nabla) \cdot \mathbf{u} = -\frac{1}{\rho}\nabla p + \nu \nabla^2 \mathbf{u} - \mathbf{B}, \tag{2}$$

where $\mathbf{B}$ represents the buoyant force caused by differences in both temperature T and trace fluid concentration c, whose evolution is given by

$$\frac{\partial T}{\partial t} + \mathbf{u} \cdot \nabla T = \kappa \nabla^2 T \tag{3}$$

and

$$\frac{\partial c}{\partial t} + \mathbf{u} \cdot \nabla c = d \nabla^2 c, \tag{4}$$

respectively. Here, ν refers to the kinematic viscosity, κ the thermal diffusivity and d the mass diffusivity of the trace fluid with respect to the carrier. Calculating the expansion coefficients $\beta_\rho = \frac{1}{\rho}\partial\rho/\partial T$ and $\gamma_\rho = \frac{1}{\rho}\partial\rho/\partial c$ then yields the linearized buoyancy term [1]

$$\mathbf{B} = \left[\beta_\rho (T - T_{ref}) + \gamma_\rho (c - c_{ref})\right]\mathbf{g}. \tag{5}$$

2.1 Range of Validity and Extended Approximation

The derivation of the Boussinesq equation provided in [2] implies that the relative variation of the transport properties σ of the fluid must be small across the temperature difference ΔT characterizing the system for the strict approximation to apply. Using β_σ and γ_σ to denote the dependence of σ on T and c in the same way as the expansion coefficients used for the density, the strength of the dependence can be quantified. In practice, the conditions $\Delta T \beta_\sigma < 0.1$ and, analogously, $\Delta c \gamma_\sigma < 0.1$ are imposed as limits on the overall variation, guaranteeing that the overall error is less than 10%. If these requirements are violated for one or more fluid properties other than the density, the approximation can be recovered by explicitly including the dependence on the active scalars in the governing equations.

3 Simulation Setup

To solve the flow equations detailed above for a periodic channel geometry, DNS is performed using a finite volume approach. Fourth order central differences are employed for spatial derivatives while a second order accurate explicit leapfrog-Euler scheme is used for time integration [4]. Velocity and pressure fields are coupled via the projection method to ensure continuity. A uniform overall pressure gradient is applied to ensure steady flow with a constant volume flux. The physical domain of

$5\pi\delta \times 2\delta \times 2\pi\delta$ is resolved in an unstructured, collocated mesh with $396 \times 180 \times 316$ cells, resulting in a mesh resolution of $\Delta x^+ = 6$, $\Delta z^+ = 3$, and $\Delta y^+ = 0.2–3.7$ following a hyperbolic tangent distribution, achieving high resolution at the walls while limiting the number of cells in the bulk flow. No-slip and impermeability boundaries are imposed on the velocity at the y-normal walls. For the temperature and concentration fields, prescribed constant values are set at the walls, with the higher value at $y = -\delta$ and the lower at $y = +\delta$. Periodic boundary conditions are used in the streamwise (x) and spanwise (z) directions.

For this investigation, flows with a bulk Reynolds number of $\mathrm{Re} = u_b\delta/\nu = 2280$ and a constant temperature difference $\Delta T = 9.48$ K are considered [3]. The Prandtl number $\nu/\kappa = 0.71$ and Schmidt number $\nu/d = 0.48$ are chosen corresponding to a mixture of dry air and water vapor. Three values for the concentration difference are simulated, $\Delta c = 0,\ 0.1$, and 0.2. Gravity acts against the mean flow direction, giving rise to buoyant forces quantified by the Grashof number $\mathrm{Gr}_T = \beta_\rho g\delta^3\Delta T/\nu^2 = 1.2 \cdot 10^5$ and $\mathrm{Gr}_c = \gamma_\rho g\delta^3\Delta c/\nu^2 = 0.31 \cdot 10^5,\ 1.24 \cdot 10^5$, and $2.48 \cdot 10^5$ due to temperature and concentration, respectively.

4 Results

For a clear view on the effects of the added active scalar c, mean and root mean square values (*rms*) for both velocity and temperature are calculated by both temporal averaging as well as averaging along the homogeneous directions of the channel, denoted by $\langle\cdot\rangle$. To this end, simulations are monitored until convergence of the first statistical moments, after which averaging is restarted for the mean values and started for *rms* values. Averaging time spans are 30 viscous time units or longer in all cases.

4.1 Fluid Mixture in Strict Boussinesq Approximation

The effect of the increasing buoyant force is visible in the comparison of the mean streamwise velocity profiles shown in Fig. 1a. For better visibility, the velocity profile of channel flow without any buoyancy is subtracted from the results to isolate the effects of the added force term. Following expectations, the fluid is accelerated at the wall where buoyancy acts to aid the mean flow ($y = -1$), while at the opposing wall, the mean velocity is reduced. The effect shows intuitive scaling with increasing effective Grashof number $\mathrm{Gr} = \mathrm{Gr}_T + \mathrm{Gr}_c$ with respect to the following observations: (1) the magnitude of acceleration and deceleration increases, (2) the peaks of maximal acceleration and deceleration move towards the aiding wall, and (3) the extent of the deceleration region reaches farther across the channel center plane.

The *rms* values of the streamwise velocity component are significantly impacted by the buoyant forces as well, as seen in Fig. 1b. Interestingly, fluctuations are reduced compared to the reference shown by the dashed line at the aiding wall, where the

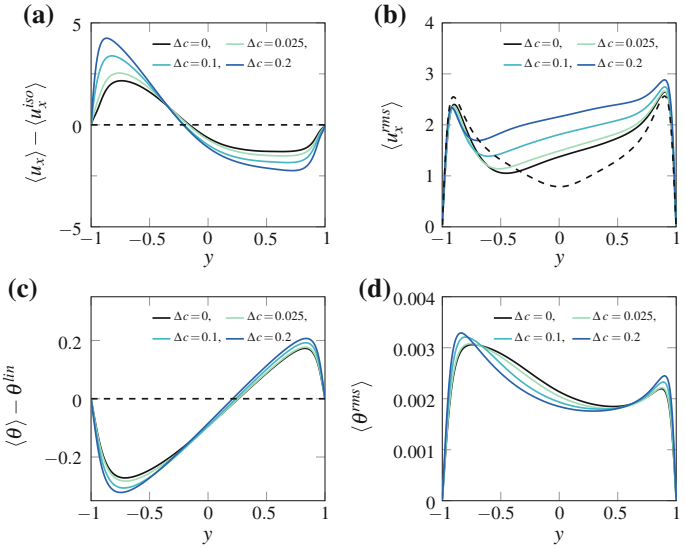

Fig. 1 First and second order statistical moments of the streamwise velocity and temperature are shown as a function of the wall-normal coordinate. **a** Mean streamwise velocity difference from an isopynic flow reference for all four buoyant configurations. **b** Streamwise velocity fluctuations. The dashed lines again represent the reference case. **c** Difference between a theoretical linear temperature curve and the observed profiles. **d** Temperature fluctuations

acceleration of the fluid and subsequent increase in Re_τ would have suggested an increase in turbulence. In contrast, $\langle u_x^{rms} \rangle$ increases as a function of Gr at the opposing wall and across a majority of the bulk region.

The mean temperature profile is illustrated in Fig. 1c by showing the deviation from a linear profile to extract the modification due to the turbulent transport in the wall-normal direction. A stronger deviation from the linear reference signifying a flattening of the profile in the bulk region coupled with increased gradients towards the walls is found as Gr increases. While there is an overall asymmetry in the temperature profile in all cases, the wall-near gradients behave completely symmetrical.

For the temperature fluctuations shown in Fig. 1d, a redistribution from the bulk towards the walls is observed. Again, the profiles exhibit an overall asymmetry, but the clear ordering of the four configurations with increasing Grashof number is preserved.

4.2 Fluid Mixture in Extended Boussinesq Approximation

It is found that for the highest concentration difference, the variation limit imposed by the strict Boussinesq approximation is violated for the thermal diffusivity, $0.2\gamma_\kappa = 0.14 > 0.1$. To address this, an additional simulation is performed using

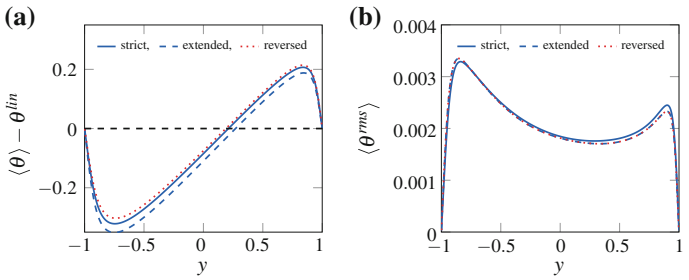

Fig. 2 Comparison between results for the strict and extended Boussinesq approximation for the highest concentration difference $\Delta c = 0.2$. **a** Difference between a theoretical linear temperature curve and the observed profiles. **b** Temperature fluctuations

$$\frac{\partial T}{\partial t} + \mathbf{u} \cdot \nabla T = \nabla(\kappa \nabla T) \simeq \kappa \nabla^2 T + \gamma_\kappa \nabla c \cdot \nabla T \tag{6}$$

instead of the simplified formulation from Eq. (3) for the evolution of the temperature field. The approximate equality corresponds to treating the variation in κ as linear with respect to changes in c.

This extended formulation qualitatively changes the temperature profile resulting in turbulent channel flow with temperature and concentration differences, as shown in Fig. 2. The additional term in the energy equation causes a preferred direction of temperature transport, resulting, in the case for a air-vapor mixture where $\gamma_\kappa < 0$, in a reduced temperature throughout the whole system. Consequently, the symmetry of the wall-near temperature gradients observed before is broken, showing a relatively steeper gradient at the aiding wall and a shallower profile at the opposing wall. Reversing the sign of γ_κ reverses the overall effect, the system temperature increases overall, and the modification of the gradients switches directions.

The temperature fluctuations presented in Fig. 2b are modified by the extended formulation as well. There is an overall decrease of the fluctuations down to the values found for the configuration with $\Delta c = 0.1$ at the peak near the opposing wall. The local increase near the aiding wall is comparatively much smaller. In contrast to the behavior of the mean temperature, this effect remains unaffected if the sign of γ_κ is changed, revealing it to be a function of the strength of the dependence instead.

5 Discussion

Using the Boussinesq approximation to describe turbulent channel flow of a fluid mixture proved successful for the mixture of water vapor and dry air considered in this investigation. The limiting factors concerning the validity of the strict approach are found to be the combination between the mismatch of the properties of the constituting fluids and the mixing ratio. Extending the approximation by taking into

account first order variations of the fluid properties (in this case, the thermal diffusivity) was shown to reveal qualitative changes in the resulting flow observables even in configurations where the violation of the applicability criteria might be considered small. For a mixture of water vapor and dry air, the limit mixing ratio evaluates to 0.147, equivalent to a dew point of 326 K, a relatively high value in the context of atmospheric flows, but very much achievable in technical applications. Considering the relatively low complexity of including variations of the fluid properties in the governing equations, the extended approach can be employed to increase the range of validity for the approximation on a case-by-case basis while still taking advantage of the majority of simplifications introduced by the Boussinesq approximation. Alternatively, the qualitative and quantitative reliability of simulation results can be increased without incurring significant computational costs by including the full dependence of the fluid properties on the active scalars with the exception of the density.

References

1. Boulama, K., Galanis, N.: Analytical solution for fully developed mixed convection between parallel vertical plates with heat and mass transfer. J. Heat Transf. (2004). https://doi.org/10.1115/1.1737774
2. Gray, D.D., Giorgini, A.: The validity of the Boussinesq approximation for liquids and gases. Int. J. Heat Mass Transf. (1976). https://doi.org/10.1016/0017-9310(76)90168-X
3. Kasagi, N., Nishimura, M.: Direct numerical simulation of combined forced and natural turbulent convection in a vertical plane channel. Int. J. Heat Mass Transf. (1994). https://doi.org/10.1016/S0142-727X(96)00148-8
4. Kath, C., Wagner, C.: Highly resolved simulations of turbulent mixed convection in a vertical plane channel. In: Dillman, A., Heller, G., Krämer, E., Wagner, C., Breitsamer, C. (eds.) New Results in Numerical and Experimental Fluid Mechanics X. Notes on Numerical Fluid Mechanics and Multidisciplinary Design, vol. 132. Springer, Cham (2016)

Momentum and Buoyancy Repartition in Turbulent Mixed Convection

T. Wetzel and C. Wagner

1 Introduction

Turbulent mixed convection is a common phenomenon in applications such as heat exchangers and climatisation in transport vehicles and buildings and was often studied in the past. Metais and Eckert [6] experimentally analyse the heat transport in a vertical pipe heated from the outside. The suppression of turbulence in vertical pipes is analysed by Bae et al. [1] by means of direct numerical simulation (DNS). Mixed convection in a vertical channel is studied in DNS by Kasagi and Nishimura [4], who report profiles of one-point statistics and budgets of the turbulent kinetic energy. They also compare asymmetrically heated turbulent channel flow with channel flow subjected to uniform wall mass injection and suction, as well as with liquid metal channel flow under the influence of a transversal magnetic field. All three flow types exhibit similar effects regarding the suppression and enhancement of turbulence near the walls and Kasagi and Nishimura state that the buoyancy does not affect the velocity fluctuations directly. In a more recent work, He, He and Seddighi [3] study the effects of generic body forces on vertical pipe flow and relate the relaminarization to a lowering of the apparent friction velocity. Wall-normal profiles of the mean streamwise velocity and the turbulent kinetic energy are presented in this paper for different Grashof numbers and demonstrate the buoyancy-induced flow asymmetry. Furthermore, budgets of the Reynolds stress tensor are analysed with regard to the repartition of turbulent stresses between the velocity components. Finally, the heat

T. Wetzel (✉) · C. Wagner
German Aerospace Center (DLR), Institute of Aerodynamics and Flow Technology, Bunsenstraße 10, 37073 Göttingen, Germany
e-mail: tim.wetzel@dlr.de

T. Wetzel · C. Wagner
Technische Universität Ilmenau Institute of Thermodynamics and Fluid Mechanics, Helmholtzring 1, 98693 Ilmenau, Germany

M. V. Salvetti et al. (eds.), *Direct and Large-Eddy Simulation XI*,
ERCOFTAC Series 25, https://doi.org/10.1007/978-3-030-04915-7_39

transport characteristics of the flow are examined with the help of a quadrant analysis of the Reynolds shear stress and the turbulent heat fluxes in order to understand how the coherent structures transport heat.

2 Computational Details

The non-dimensionalized governing Eqs. (1)–(3) are the continuity equation, the incompressible Navier–Stokes equations together with the Boussinesq approximation and the energy equation, respectively. The simulation geometry is shown in Fig. 1.

$$\frac{\partial u_i}{\partial x_i} = 0 \tag{1}$$

$$\frac{\partial u_i}{\partial t} + u_j \frac{\partial u_i}{\partial x_j} = \frac{1}{Re_b} \frac{\partial^2 u_i}{\partial x_j^2} - \frac{\partial}{\partial x_i} \left(p + \frac{\delta g x_1}{u_b^2} \right) + \frac{Gr}{Re_b^2} \theta \delta_{1i} \tag{2}$$

$$\frac{\partial \theta}{\partial t} + u_i \frac{\partial \theta}{\partial x_i} = \frac{1}{Pr \cdot Re_b} \frac{\partial^2 \theta}{\partial x_i^2} \tag{3}$$

The equations are given in tensor notation using the summation convention. The streamwise, spanwise and wall-normal velocity components are denoted by u_1, u_2, u_3. Likewise, the corresponding Cartesian coordinates are x_1, x_2, x_3. The pressure is denoted by p, the channel height with δ the gravitational acceleration by g and

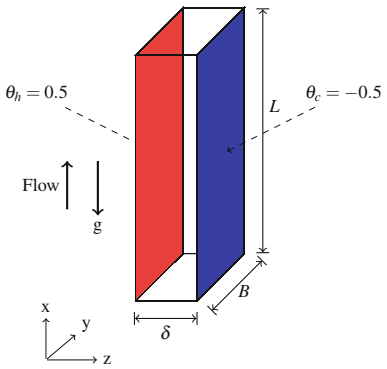

Fig. 1 Computational domain set up in the same manner as the one used in the DNS by Kasagi and Nishimura (KN) [4]. The flow is forced upwards against gravity along the differentially heated vertical walls. Periodic boundary conditions are employed in the streamwise and spanwise directions for the velocity, the temperature and the pressure fluctuations. The walls obey the no-slip and impermeability boundary conditions

the bulk velocity by u_b. δ_{ij} represents the Kronecker delta in the buoyancy term of Eq. (2). The control parameters are namely the bulk Reynolds number $Re_b = \frac{u_b \delta}{\nu} = 4328$, the Grashof number $Gr = \frac{g\beta\Delta T \delta^3}{\nu^2}$ and the Prandtl number $Pr = \frac{\nu}{\kappa} = 0.71$ with kinematic viscosity ν and thermal diffusivity κ. The Grashof number is varied from 0 over $6.4 \cdot 10^5$ to $9.6 \cdot 10^5$ and $1.6 \cdot 10^6$ in order to study its influence on the flow behaviour.

The system of Eqs. (1)–(3) is discretised on a staggered grid and solved with a finite volume method. The computations are executed on a fine wall-resolved grid in order to capture all essential flow structures and the high wall-normal gradients accordingly. The spatial interpolation and differentiation are carried out with a fourth-order accurate central difference scheme and the time stepping is realized with a second-order accurate Euler-Leapfrog scheme. The velocity pressure coupling is accomplished with Chorin's projection method and employs a direct solver for the resulting Poisson equation. This method has been adapted for Cartesian grids from the one reported by Feldmann and Wagner [2], who used it with cylindrical staggered grids. Furthermore, the bulk velocity is prescribed (and thus the mean pressure gradient adapted) such that the cases share the same Re_b. Unless otherwise indicated, all velocity values are rescaled for comparability with the friction velocity $u_\tau^* = 0.5(u_\tau^h + u_\tau^c)$ averaged over the friction velocities at the heated and cooled wall, respectively.

3 Flow Structures and Heat Transport

3.1 Transport Mechanism

From DNS of isothermal turbulent channel and pipe flows it is well known that the wall-normal transport is organized by sweeps and ejections. Sweeps are carrying high speed fluid towards the wall and ejections carry low speed fluid to the bulk. Close to the wall they form elongated regions of streamwise high and low speed fluid called streaks. In the case of mixed convection considered here, buoyancy accelerates fluid close to a heated channel wall. The result is the suppression of turbulent fluctuations in combination with vortex-stretching leading to thinner streaks with a higher streak spacing in spanwise direction and vice versa on the cooled wall. The aforementioned effects are intensified with increasing Gr, although more so in the aiding flow near the heated wall than in the opposing flow near the cooled wall. This explanation is derived from the description of the self-sustaining process of near-wall turbulence structures described by Kim [5] for isothermal wall-bounded flow and complemented by He et al. [3] for aiding flow in a vertical pipe, who also linked the structure thinning with a lowered apparent friction velocity in the aiding flow. In the present case, the flow alteration due to the body force is generated by the horizontal temperature gradient and additionally involves a change in turbulent heat transport, which is suppressed in the aiding flow and slightly enhanced in the opposing flow. Thus, low-speed streaks

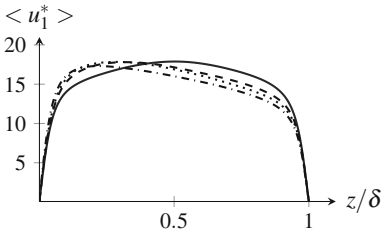

Fig. 2 Profiles of mean streamwise velocity. Solid: $Gr = 0$, dashed: $Gr = 6.4 \cdot 10^5$, dotted: $Gr = 9.6 \cdot 10^5$, dashed-dotted: $Gr = 1.6 \cdot 10^6$

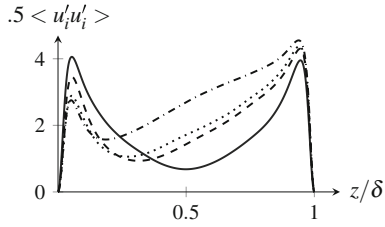

Fig. 3 Profiles of turbulent kinetic energy. Legend cf. Fig. 2

linger longer at the heated/cooled wall than high-speed streaks. As a result, ejections emerging close to the heated/cooled wall carry warm/cold fluid to the bulk.

3.2 Mean Flow Field and Turbulent Kinetic Energy

Figure 2 shows the mean velocity profiles for different Grashof numbers to underline that the fluid is accelerated close to the heated wall and decelerated close to the cooled wall. It is evident that an increase in Grashof number results in a more asymmetric mean velocity profile with a higher peak near the heated wall where the buoyancy is aiding the flow. The turbulent kinetic energy (TKE) profiles presented in Fig. 3 reflect an increase in asymmetry with increasing Gr, where the TKE peak decreases near the heated wall and increases near the cooled wall. This behaviour has been reported before [1, 3, 4] and ultimately results in flow relaminarization near the heated wall. Especially at the higher Grashof numbers, the TKE increases nonlinearly in the channel center due to the mean shear induced by the flow asymmetry. Yet, the integrated TKE increases linearly in the considered Grashof range.

3.3 Reynolds Stress Budgets

In order to further analyse the transport mechanisms discussed above, budgets of the Reynolds stress tensor were evaluated. Figures 4 and 5 show the contributions of the production and pressure strain terms to the streamwise Reynolds stress balance for different Grashof numbers. At the heated wall the peak of the production term

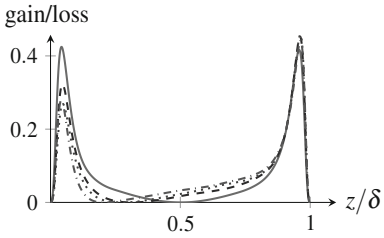

Fig. 4 Production term of the streamwise Reynolds stress. Solid: $Gr = 0$, dashed: $Gr = 6.4 \cdot 10^5$, dotted: $Gr = 9.6 \cdot 10^5$, dashed-dotted: $Gr = 1.6 \cdot 10^6$

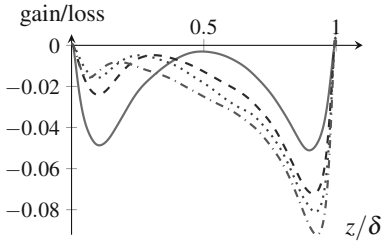

Fig. 5 Pressure strain term of the streamwise Reynolds stress. Legend cf. Fig. 4

decreases with increasing Gr agreeing with the decreasing maxima of the turbulent kinetic energy at the heated wall in Fig. 3. This effect is accompanied by less redistribution of turbulent kinetic energy according to the pressure strain contributions shown in Fig. 5, which eventually leads to laminarization or one-dimensional turbulence as pointed out by He et al. [3]. In contrast, close to the cooled wall, flow turbulence is amplified with larger redistribution according to higher absolute values of the production and pressure strain terms there.

3.4 Quadrant Analysis

In order to confirm that heat is transported in wall-normal direction via sweeps and ejections, a quadrant analysis is conducted. Figure 6 shows the plots of the probability density functions (PDF) obtained by means of the DNS for $Gr = 9.6 \cdot 10^5$. The plots show the correlations at $z^+ = 15$ (top row) near the heated wall and $z^+ = 274$ (bottom row) near the cooled wall. In the first column, PDFs for the Reynolds shear stress (RSS) reflect higher probability densities in quadrant Q2 and Q4 due to ejections and sweeps. The second and third columns are dedicated to the streamwise and wall-normal turbulent heat transport, respectively. In Fig. 6, the leftmost graphs further reveal that the sweeps in the aiding flow are less and weaker than in the opposing flow. This is in agreement with the observation above that the Reynolds shear stresses are lower in the aiding flow. Also, the behaviour of the streamwise turbulent heat transport is different in the aiding and the opposing flow underlining that the low-speed streaks carry fluid whose temperature is adjusted to the temperature at the wall from which they emerge, i.e. the low-speed streaks near the heated wall carry fluid with positive

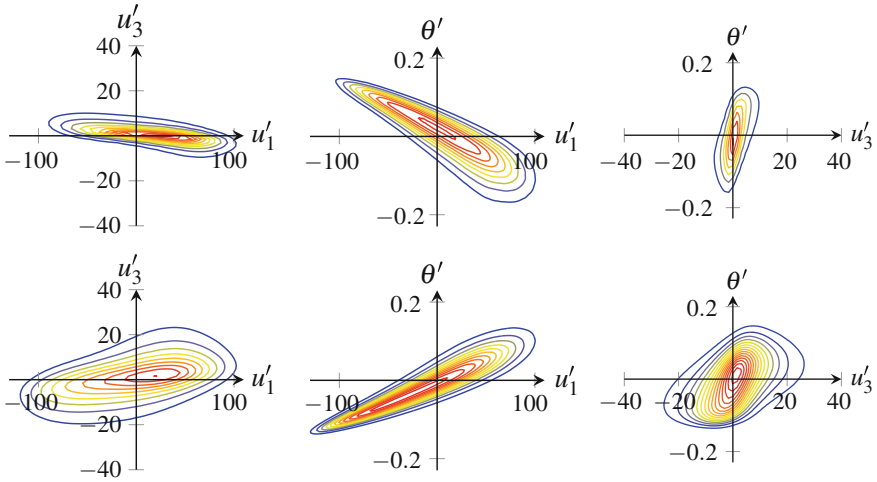

Fig. 6 Probability density plots of fluctuation correlations. Left to right: streamwise velocity and wall-normal velocity, streamwise velocity and temperature, wall-normal velocity and temperature. Top row: $z^+ = 15$ (hot), bottom row: $z^+ = 274$ (cold)

temperature fluctuations and vice versa near the cooled wall. At the same time, the low-speed tails of both PDFs are thinner than their high-speed counterparts, meaning that the low-speed streaks carry a more closely defined temperature. The wall-normal heat transport is almost uninfluenced by the difference in buoyant force. Although the distribution is wider in the opposing flow, the symmetry over the θ'-axis remains and the total heat transport is mainly constant except for the regions very close to the walls.

4 Summary

Results from DNS of mixed convection in an asymmetrically heated vertical channel are presented. It was pointed out that buoyancy accelerates the aiding flow, which leads to thinner coherent flow structures with higher spacing in between them. For increasing Grashof numbers this leads to a decrease of the turbulent kinetic energy and the corresponding production term in the budget of the Reynolds stress in streamwise direction and finally to relaminarization. The Reynolds stress budgets also revealed that with less streamwise velocity fluctuations, there is also less redistribution into the other components, ultimately leading to one-dimensional turbulence. In the subsequent quadrant analysis, it became evident that the sweeps and ejections in the aiding flow are weaker than those in the opposing flow. The major part of the streamwise turbulent heat transport could then be linked to the streaks. The analysis also

reveals that there is only little influence on the wall-normal heat transport, although the wall-normal velocity fluctuations are significantly higher in the opposing flow.

References

1. Bae, J.H., Yoo, J.Y., Choi, H., McEligot, D.M.: Effects of large density variation on strongly heated internal air flows. Phys. Fluids **18**, 1–25 (2006)
2. Feldmann, D., Wagner, C.: Direct numerical simulation of fully developed turbulent and oscillatory pipe flows at $\mathrm{Re}_\tau = 1440$. J. Turb. **13**(32), 1–28 (2012)
3. He, S., He, K., Seddighi, M.: Laminarisation of flow at low Reynolds number due to streamwise body force. JFM **809**, 31–71 (2016)
4. Kasagi, N., Nishimura, M.: Direct numerical simulation of combined forced and natural turbulent convection in a vertical plane channel. Int. J. Heat Fluid Flow **18**, 88–99 (1997)
5. Kim, J.: Physics and control of wall turbulence for drag reduction. Phil. Trans. R. Soc. A **369**, 1396–1411 (2011)
6. Metais, B., Eckert, E.R.G.: Forced, mixed, and free convection regimes. J. Heat Transf. **86**(2), 295–296 (1964)

Buoyancy-Driven Flow Inside An Asymmetrically Heated Cavity

A. D. Demou, D. G. E. Grigoriadis and B. J. Geurts

1 Introduction

Buoyancy-driven flows inside enclosures are in the center of problems related to heat transfer because they can provide a significant insight into the physical mechanisms of heat transfer. Typical examples of such flows include Rayleigh–Bénard convection, differentially heated cavities and partially divided enclosures. In the present study, the buoyancy-driven flow inside an asymmetrically heated closed cavity is investigated and proposed as a benchmark case for future studies to assess the accuracy of simulations and to help in the validation of coarsened turbulence models. Additionally, from an application perspective such a configuration is highly relevant, e.g., in view of its similarity with passive solar systems such as ventilated building facades [1] and Trombe walls [2].

We propose a benchmark study of the flow and heat transfer characteristics inside a closed cuboid cavity with an interior heated wall and a cooled side wall, while all other boundaries are treated as adiabatic. The heated wall is asymmetrically located closer to one side of the cavity, as shown in Fig. 1. Constant temperature boundary conditions are applied on both the heated and cooled walls.

Results are compared for a wide range of Rayleigh numbers, $Ra = 10^5 - 3.2 \times 10^9$, based on the height of the heated wall and its temperature. The effect of Ra on the generated heat transfer as characterised by the Nusselt number Nu as well as the associated flow patterns in the cavity will be presented.

A. D. Demou (✉) · D. G. E. Grigoriadis
University of Cyprus, Nicosia, Cyprus
e-mail: andreas.demou@gmail.com

D. G. E. Grigoriadis
e-mail: dimokratisg@gmail.com

B. J. Geurts
University of Twente, Enschede, The Netherlands
e-mail: b.j.geurts@utwente.nl

M. V. Salvetti et al. (eds.), *Direct and Large-Eddy Simulation XI*,
ERCOFTAC Series 25, https://doi.org/10.1007/978-3-030-04915-7_40

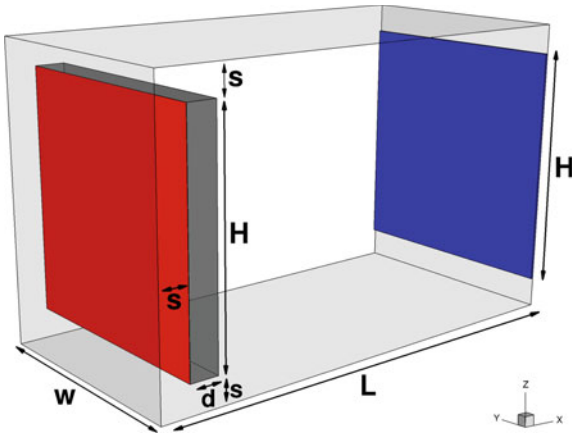

Fig. 1 Geometrical configuration with the heated and cooled surfaces shown with red and blue colour respectively. The figure introduces the characteristic sizes that define the geometry in terms of heights H, L and w as well as thickness d of the hot wall and separation from the walls s

2 Mathematical and Numerical Modeling

2.1 Mathematical Modeling

Assuming that the flow is incompressible and that the Boussinesq approximation is valid, the governing equations for natural convection take the form,

$$\frac{\partial u_j}{\partial x_j} = 0 \tag{1}$$

$$\frac{\partial u_i}{\partial t} + \frac{\partial u_i u_j}{\partial x_j} = -\frac{\partial p}{\partial x_i} + \frac{Pr}{\sqrt{Ra}} \frac{\partial^2 u_i}{\partial x_j \partial x_j} + Pr\Theta\delta_{i3} \tag{2}$$

$$\frac{\partial \Theta}{\partial t} + \frac{\partial \Theta u_j}{\partial x_j} = \frac{1}{\sqrt{Ra}} \frac{\partial^2 \Theta}{\partial x_j \partial x_j} \tag{3}$$

where $i = 1, 2, 3$, represent the x, y and z directions and the respective velocities u_i in each direction are denoted hereafter also as u, v, w. Gravity acts along the z $(= x_3)$ direction and Pr is the Prandtl number. Ra represents the Rayleigh number which can be defined with respect to the wall and ambient temperatures (T_w and T_∞) according to,

$$Ra_{\Delta T} = \frac{g\beta(T_w - T_\infty)H^3}{\nu\alpha}\,, \tag{4}$$

In Eq. 4, β is the coefficient of volumetric expansion, ν the kinematic viscosity, α the thermal diffusivity and k the thermal conductivity of the fluid. Equations 1–3 have been non-dimensionalised using the height of the heated wall H as the characteristic length scale, $V_0 = \alpha\sqrt{Ra}/H$ as a velocity scale, $t_0 = H/V_0$ as a time scale and $P_0 = \rho V_0^2$ as a pressure scale. The non-dimensional temperature is defined as $\Theta = (T -$

$T_\infty)/T_0$ where the characteristic temperature scale T_0 is taken as the temperature difference $(T_w - T_\infty)$.

The Nusselt number is defined for all cases with respect to the wall height as $Nu = h\ H/k$, where h is the convection heat transfer coefficient. Nu is calculated as the average temperature gradient, normal to the heated wall, i.e.

$$Nu = \langle \frac{\partial \Theta}{\partial n} \rangle_w \tag{5}$$

2.2 Numerical Methodology

The numerical method used is based on a second order finite difference method on Cartesian staggered grids utilising a direct pressure solver. Velocities are discretised in space using central differences. For the temperature equation 3, a hybrid linear parabolic approximation (HLPA) scheme was implemented [3]. Time advancement consisted of a fully explicit Adams–Basforth scheme. The presence of obstacles inside the flow is achieved with the use of the Immersed Boundary method [4].

2.3 Computational Parameters

Results will be presented for a cuboid cavity with $L = 2H$ and a wall spacing equal to the wall thickness, i.e., $s = d = H/8$ (Fig. 1). Preliminary simulations revealed independence of the time-averaged isotherms and the two-point correlations when the spanwise length of the domain is larger than H. Therefore, the spanwise extent w of the domain is chosen equal to H so that periodic boundary conditions can be applied without suppressing the contained flow structures. For all cases examined, the Prandtl number is set to $Pr = 0.71$, i.e., the cavity is assumed to be filled with air.

No-slip boundary conditions are used for the velocity field along solid boundaries. The boundary conditions along the heated and cooled walls are specified as constant temperature ($\Theta_w = \pm 1$). All other boundary surfaces are assumed to be adiabatic.

The grid resolution was carefully selected for each case, so that the near-wall dynamics are properly resolved [5, 6]. For the range of Ra numbers considered here, eight to ten points were placed within the thickness of the boundary layers. Table 1 lists the test cases that were studied, along with the resolution used.

Table 1 Test cases in 2D and 3D presented, Ra numbers and million nodes for each numerical grid used

Case	$Ra_{\Delta T}$	Grid	M nodes
T1	1.0×10^5	$56 \times 38(2D)$	0.002
T2	1.0×10^6	$114 \times 82(2D)$	0.009
T3A	1.0×10^7	$206 \times 164(2D)$	0.03
T3B	1.0×10^7	$206 \times 128 \times 164$	4.3
T4A	1.0×10^8	$380 \times 298(2D)$	0.1
T4B	1.0×10^8	$380 \times 128 \times 298$	15
T5A	1.0×10^9	$764 \times 558(2D)$	0.4
T5B	1.0×10^9	$764 \times 128 \times 558$	54.6
T6A	3.2×10^9	$764 \times 558(2D)$	0.4
T6B	3.2×10^9	$764 \times 160 \times 558$	68.2

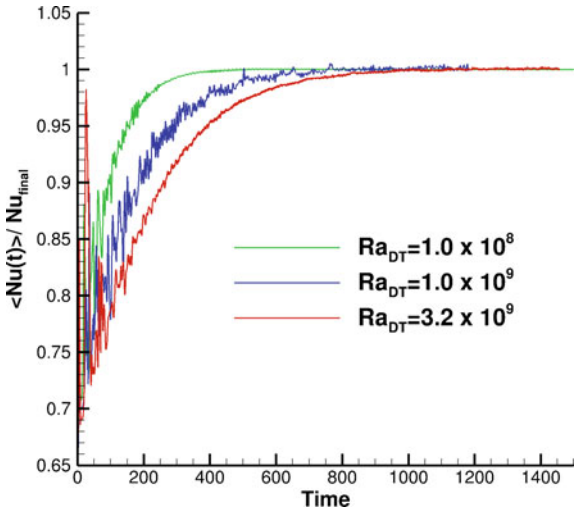

Fig. 2 Normalised average Nusselt number on the heated wall as a function of non-dimensional time. The normalisation is done with respect to the average Nusselt number on the heated wall, after the flow became statistically steady

3 Results

3.1 Statistical Convergence

Initially, the air adjacent to the heated surface warms up, rises due to buoyancy and hits the roof of the cavity, before being ejected further into the cavity. A similar but opposite behaviour is observed in the vicinity of the cooled wall. Figure 2 shows the non-dimensional time interval needed for the average Nusselt number on the heated wall to stabilise statistically. This time scale depends on the Rayleigh number and in all cases is in the order of ∼1000 dimensionless time units.

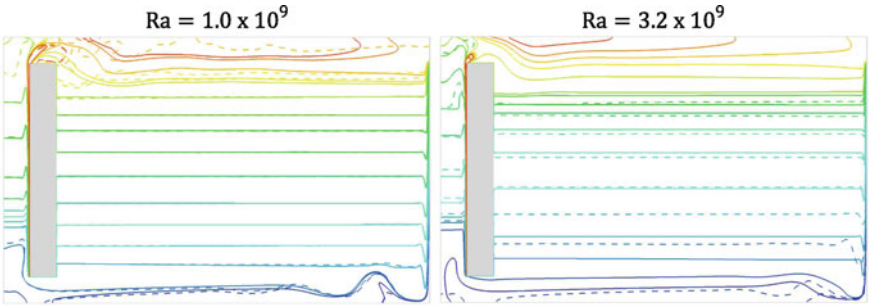

Fig. 3 Comparison of the time-averaged isotherms of $2D$ (dashed) and $3D$ (solid) simulations, for $Ra = 1.0 \times 10^9$ (left) and 3.2×10^9 (right)

3.2 Statistics

After the initial transient stage, the flow becomes statistically steady, with stratified temperature and weak flow at the centre of the cavity, and most of the dynamics contained at the top-left and bottom-right corners of the cavity. This is confirmed by spectral analysis (not presented here), revealing a turbulent flow only at the downstream parts of the boundary layers. Figure 3 shows a comparison of the isotherms inside the cavity obtained with the 2D and 3D simulations for the two highest Rayleigh number considered here. It is clear that for a Rayleigh number of 1.0×10^9 the differences are contained only on the top and bottom of the cavity, while for 3.2×10^9 also in the bulk of the cavity the isotherms no longer overlap. This illustrates the increase of $3D$ turbulent structures inside the cavity as the Rayleigh number increases.

Moreover, as shown in Fig. 4, the $2D$ and $3D$ predictions of the average Nusselt number on the heated wall are very similar in the entire Ra range studied. This is explained by the fact that the highest Nusselt numbers are observed on the bottom of the heated wall, where the flow is laminar, while the contribution of the turbulent flow on the top of the heated wall is much less. A strong evidence for scaling of the Nusselt number with respect to Ra numbers is observed. The calculated correlation $Nu = 0.518 \times Ra^{0.268}$ is also an indication of the similarity between the $2D$ and $3D$ Nusselt predictions, since the exponent 0.268 is much closer to the $1/4$ laminar scaling than the $1/3$ turbulent scaling [7]. Additionally, as shown in Fig. 4, the heat transfer rate of the heated wall is consistently higher than that reported for similar configurations such as differentially heated cavities, vertical heated plates and Trombe walls, illustrating its potential for intensified heat transfer.

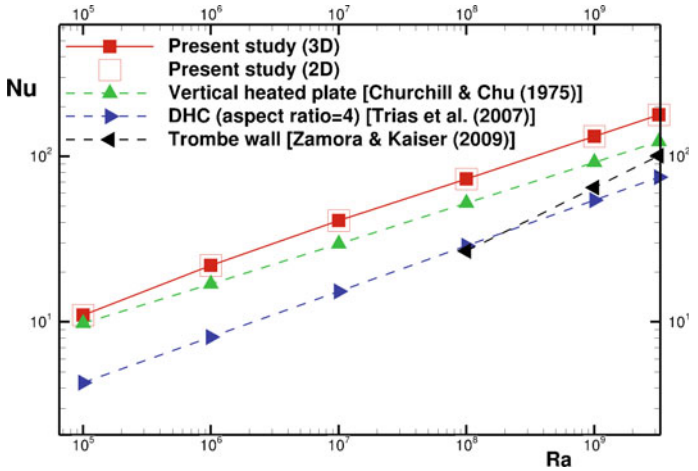

Fig. 4 Predicted Nusselt numbers of the heated wall as a function of Rayleigh numbers compared to similar configurations. For high Ra the results can be well approximated with a scaling law $Nu = 0.518 \times Ra^{0.268}$

4 Conclusions

The study of the flow inside the asymmetrically heated cavity, revealed that ∼1000 non-dimensional time units are needed for the flow to become statistically steady. The differences between $2D$ and $3D$ results become more intense with increasing Rayleigh numbers, but Nusselt numbers as predicted from the 2D and 3D simulations are similar for all Rayleigh numbers studied. Finally the flow exhibits higher Nusselt numbers than other relevant configurations, with a scaling close to the laminar one.

References

1. Puangsombuta, W., Hirunlabha, J., Khedarib, J., Zeghmatic, B., Win, M.M.: Enhancement of natural ventilation rate and attic heat gain reduction of roof solar collector using radiant barrier. J. Fluid Mech. **42**(6), 2218–2226 (2007)
2. Zamora, B., Kaiser, A.S.: Thermal and dynamic optimization of the convective flow in Trombe Wall shaped channels by numerical investigation. Heat Mass Transf. **45**(11), 1393–1407 (2009)
3. Kaloudis, E., Grigoriadis, D.G.E., Papanicolaou, E., Panidis, T.: Large eddy simulations of turbulent mixed convection in the charging of a rectangular thermal storage tank. Int. J. Heat Fluid Flow **44**, 776–791 (2013)
4. Lai, M.C., Peskin, C.S.: An immersed boundary method with formal second-order accuracy and reduced numerical viscosity. J. Comput. Phys. **160**(2), 705–719 (2000)
5. Maystrenko, A., Resagk, c, Thess, A.: Structure of the thermal boundary layer for turbulent Rayleigh-Bnard convection of air in a long rectangular enclosure. Phys. Rev. E-Stat., Nonlinear Soft Matter Phys. **75**(6), 066303 (2007)

6. Shishkina, O., Stevens, R.J.A.M., Grossmann, S., Lohse, D.: Boundary layer structure in turbulent thermal convection and its consequences for the required numerical resolution. New J. Phys. **12**(7), 075022 (2010)
7. Churchill, S.W., Chu, H.H.: Correlating equations for laminar and turbulent free convection from a vertical plate. Int. J. Heat Mass Transf. **18**(11), 1323–1329 (1975)
8. Trias, F.X., Soria, M., Oliva, A., Prez-Segarra, C.D.: Direct numerical simulations of two-and three-dimensional turbulent natural convection flows in a differentially heated cavity of aspect ratio 4. J. Fluid Mech. **586**, 259–293 (2007)

LES of Natural Convection in a Closed Cavity

A. Pilkington and B. Rosic

1 Introduction

Natural convection cavity flows are of interest due to their occurrence in a range of engineering situations, such as in gas and steam turbines during shutdown. These natural convection flows can affect the operation of gas and steam turbines so reliable prediction of these flows is desirable. Accurate prediction of the wall heat transfer is of particular importance to engineers.

Only a limited number of experimental test cases involving high Rayleigh number cavity flows, using air as the working fluid, are available in the literature. One of these cases is a differentially heated tall cavity, investigated by Betts and Bokhari [1].

The tall cavity test case was investigated numerically by the authors using LES simulations, with the results being compared to the available experimental data. The investigation looked at the effect of different subgrid-scale models and the effects of subgrid turbulent Prandtl number on both the mean and rms temperature and velocity.

The aim of this analysis was to quantify the performance of LES in simulating natural convection cavity flows. Of particular interest is accurate prediction of the wall heat transfer, which would allow LES to be used as an engineering analysis tool. It would be also desirable to be able to calculate turbulent statistics, such as the turbulent heat flux ($\overline{u_i' T'}$), as very limited experimental data is available for these.

2 Test Case

The geometry used in this investigation is a differentially heated tall cavity, investigated experimentally by Betts and Bokhari [1]. The rectangular cavity has dimen-

A. Pilkington (✉) · B. Rosic
Osney Thermofluids Laboratory, Unversity of Oxford, Oxford OX2 0ES, UK
e-mail: andrew.pilkington@eng.ox.ac.uk

M. V. Salvetti et al. (eds.), *Direct and Large-Eddy Simulation XI*,
ERCOFTAC Series 25, https://doi.org/10.1007/978-3-030-04915-7_41

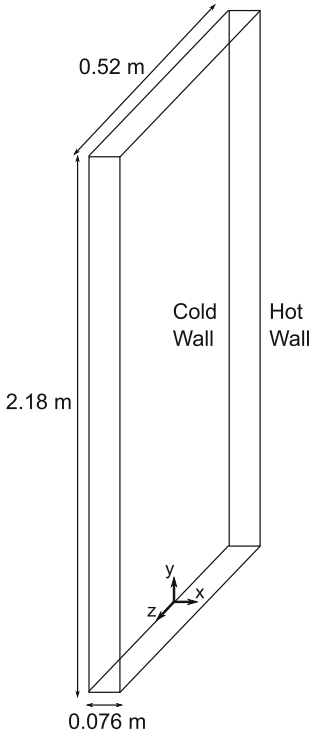

Fig. 1 Tall cavity case, adapted from [1]

sions 2.18 m high by 0.076 m wide by 0.52 m depth, Fig. 1. One sidewall was heated and the other cooled, data is available for temperature differences of 19.6 °C and 39.9 °C. These temperatures differences give Rayleigh numbers of 0.86×10^6 and 1.43×10^6 respectively. Validation data is available for both mean and rms temperature and velocity profiles at several locations in the cavity.

3 Methodology

LES Simulations were conducted on the tall cavity geometry, the computational domain used was the same size as the experimental cavity. The baseline mesh consisted of $150 \times 50 \times 75$ nodes in the cavity height, width and depth respectively, with the cells clustered nearest to the walls. It was found that this mesh density gave a well resolved LES solution, with the bulk of the cells being less than five times the Kolmogorov length scale, as shown in Fig. 2. The wall y^+, defined as $y^+ = \frac{yU_\tau}{\nu}$, was also one or less for the side, top and bottom walls.

The wall temperature boundary conditions for the simulations were taken from the experiment. The hot and cold walls had a constant uniform temperature applied

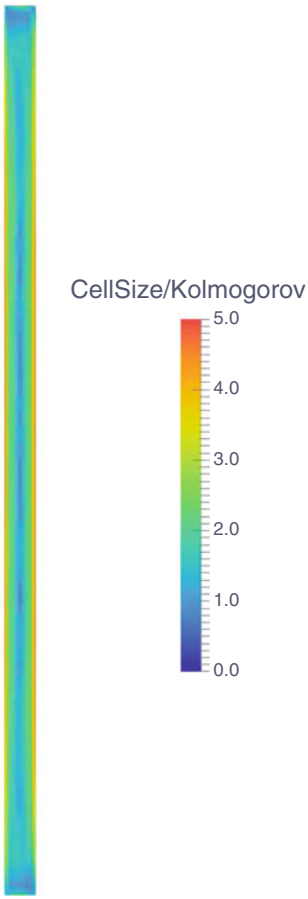

Fig. 2 Ratio of cell size to Kolmogorov scale

and the top and bottom walls had a constant temperature linearly varying between the hot and cold temperatures. The front and back walls had adiabatic boundary conditions applied. All of the wall boundaries had the no slip condition applied.

The solver used for the study was ANSYS Fluent v15.0, using the pressure based solver. A low Mach number approach was used, with the air density being a function of temperature. Bounded central differencing schemes were used used for both the momentum and energy equations with second order implicit time advancement. Different subgrid-scale models were used in this investigation, the baseline model was the dynamic Smagorinsky model [2]. Also investigated was the use of a one equation kinetic energy model [3] and the WALE model [4]. The effect of different turbulent Prandtl numbers (Pr_t), used in the subgrid-scale heat flux model, was also investigated. A dynamically calculated method for Pr_t has been compared to cases with constant specified values of Pr_t of 0.85 and 0.2.

A 20 ms timestep was used for the simulations, this kept the cell Courant number less than one. The simulations were typically ran for 2000 timesteps to overcome the transient period, statistics were then collected over a following 10000 timesteps.

4 Results

Results from the LES simulations have been compared to the experimental results of Betts and Bokhari [1]. Comparisons have been made of both the mean and rms values of temperature and vertical velocity. Results are shown on the cavity mid-plane at 50% height. The temperature has been non-dimensionalised into the T^* parameter using the hot and cold wall temperatures,

$$T^* = \frac{(T - T_{cold})}{(T_{hot} - T_{cold})} \tag{1}$$

Comparing the time averaged temperature profiles, shown in Fig. 3, it can be seen that all three simulations have well predicted the mean temperature profile compared to the experimental data. The effect of the turbulent Prandtl number on the average temperature profile was found to be small, this was also the case at other cavity heights where experimental data is available. An important parameter for engineers to be able to predict accurately is the wall heat transfer. The heat flux was calculated from the near wall temperature gradient using an integral method [5]. It was found that all three cases did an acceptable job in predicting the wall heat flux, giving errors

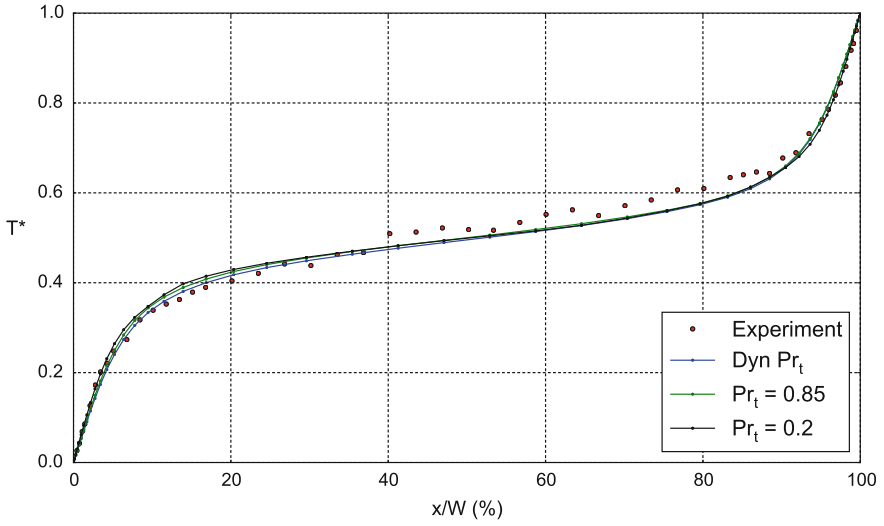

Fig. 3 Time averaged temperature profiles at 50% cavity height

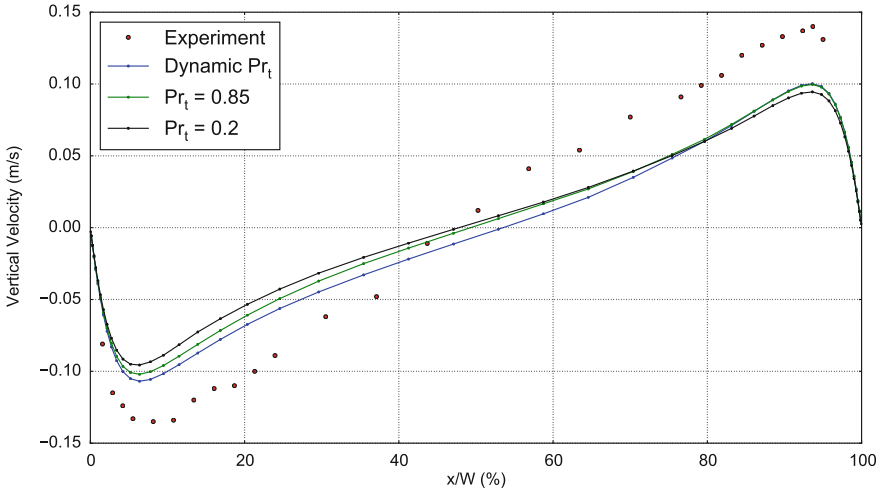

Fig. 4 Time averaged vertical velocity profiles at 50% cavity height

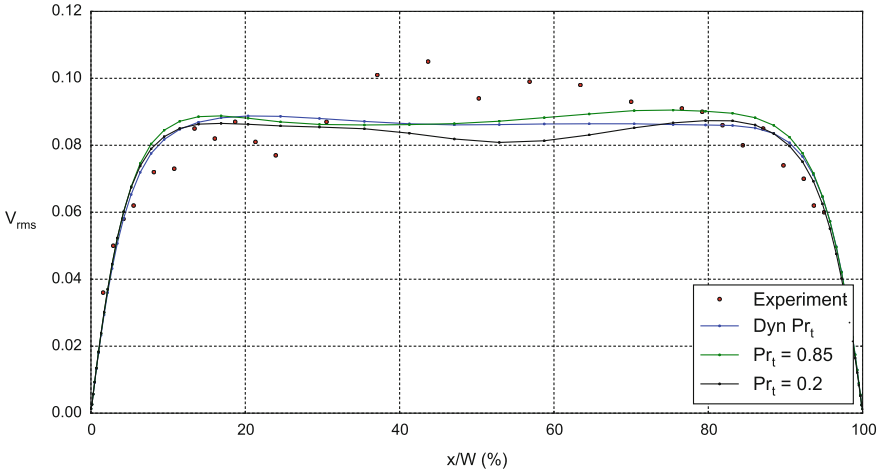

Fig. 5 Rms vertical velocity profiles at 50% cavity height

relative of the experiment of less than 10%. This shows that these simulations are suitable for engineering analysis of wall heat flux.

Looking at the average vertical velocity in the same plane, shown in Fig. 4, also shows a reasonable good agreement between the LES and the experimental values.

The rms vertical velocity fluctuations, again at the mid-plane profile at 50% cavity height, are shown in Fig. 5. It can be seem in all three cases there is good agreement between the LES results and experimentally measured values, with little variation with turbulent Prandtl number.

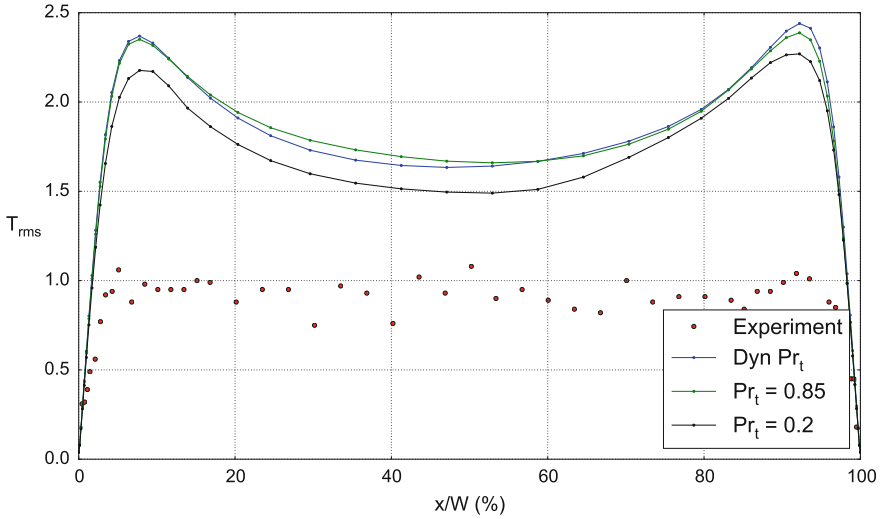

Fig. 6 Rms temperature profiles at 50% cavity height

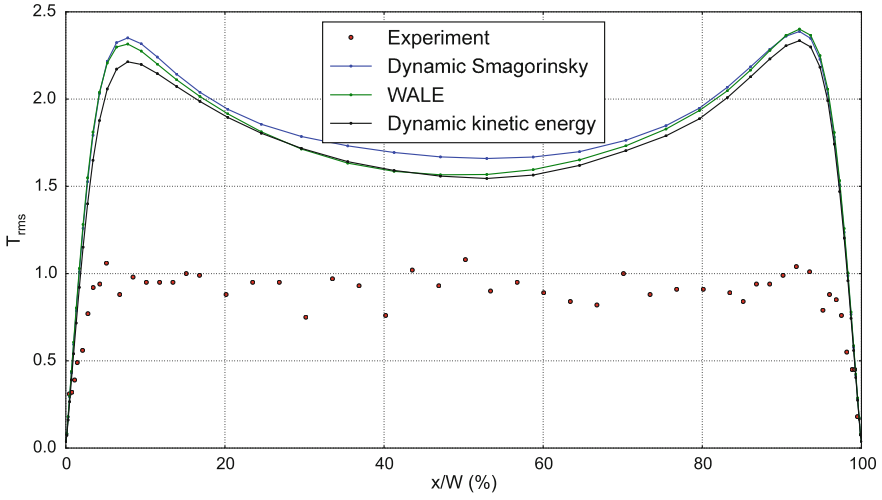

Fig. 7 Rms temperature profiles at 50% cavity height with different subgrid-scale models

Looking at profiles of the rms temperature in Fig. 6 it can be seen that there is some over-prediction of the temperatures by the LES simulations. It was thought that this could be due to the Smagorinsky subgrid-scale model used, so simulations using other subgrid-scale models were conducted. It can be seen in Fig. 7 however that the dynamic Smagorinsky model gave similar results to both the WALE and dynamic kinetic energy models.

The reason for the well predicted velocity fluctuations but over-predicted temperature fluctuations could be due to the subgrid-scale heat flux model used, in this case the scalar diffusivity model. A subgrid heat flux model with an explicit buoyancy term, such as the Eidson model [6], may be required in order to accurately predict the rms temperatures.

Due to the over-prediction of the rms temperatures the simulations are not able to provide reliable predictions of the turbulent heat fluxes ($\overline{u_i' T'}$).

5 Conclusions

LES Simulations were performed of natural convection flow in a closed cavity. The simulations reliably predicted mean temperature and velocity profiles and the wall heat fluxes. The LES also well predicted the rms velocity fluctuations but over predicted the rms temperature fluctuations. It was found that the sub-grid scale model used had little effect on the rms temperature fluctuation. It is likely that a sub-grid heat flux model which includes buoyancy effects would be required to match the rms temperatures. Finally this investigation has shown that LES can be used for engineering analysis of wall heat flux.

References

1. Betts, P.L., Bokhari, I.H.: Experiments on turbulent natural convection in an enclosed tall cavity. Int. J. Heat Fluid Flow **21**, 675–683 (2000)
2. Lilly, D.K.: A proposed modification of the germano subgrid-scale closure model. Phys. Fluids **4**, 633–635 (1992)
3. Kim, S.-E.: Large eddy simulation using unstructured meshes and dynamic subgrid-scale turbulence models. Technical Report AIAA-2004-2548. 34th Fluid Dynamics Conference and Exhibit American Institute of Aeronautics and Astronautics. June 2004
4. Nicoud, F., Ducros, F.: Subgrid-scale stress modelling based on the square of the velocity gradient tensor. Flow Turbul. Combust. **62**(3), 183–200 (1999)
5. Ebadi, A., Mehdi, F., White, C.M.: An exact integral method to evaluate wall heat flux in spatially developing two-dimensional wall-bounded flows. Int. J. Heat Mass Trans. **84**, 856–861 (2015)
6. Numerical simulation of the turbulent Rayleigh-Bénard problem using subgrid modelling, J. Fluid Mech. **158**, 245–268 (1985)

Part VI
Compressible Flows

Polynomial Adaptivity in LES: Application to Compressibility Effects Investigation on Bluff Bodies

M. Tugnoli and A. Abbà

1 Introduction

The use of a Discontinuous Galerkin framework to perform a compressible Large Eddy Simulation is an effective and accurate way to simulate complex turbulent flows. However, since the turbulent scales size is not known a priori, assumptions during the grid generation must be made. With the aim of reducing the influence of such assumptions, lowering the computational effort required to perform the LES and moving towards the adaptive LES postulated by [5], we introduced a polynomial adaptive framework in [7]. In the present work we employ the aforementioned procedure to assess the effects of a varying Mach number in a flow around a square section cylinder, a configuration of interest for example for flame holders in combustors. Since most of the reference data on this kind of flows is obtained by incompressible computations (e.g. [6]) and experiments (e.g. [4]) the aim is to assess what are the effects of slightly higher Mach numbers in such flows, and what is the error involved into comparing compressible simulations results with incompressible reference data.

2 Numerical Results

To simulate a compressible turbulent flow the LES filtered Navier–Stokes equations, in non-dimensional form, were employed. The employed framework of equations, LES filtering and modelling, and numerical discretization are detailed in [1] and

M. Tugnoli (✉) · A. Abbà
Department of Aerospace Science and Technology, Politecnico di Milano,
via La Masa 34, 20156 Milan, Italy
e-mail: matteo.tugnoli@polimi.it

A. Abbà
e-mail: antonella.abba@polimi.it

M. V. Salvetti et al. (eds.), *Direct and Large-Eddy Simulation XI*,
ERCOFTAC Series 25, https://doi.org/10.1007/978-3-030-04915-7_42

here only the essential details will be briefly discussed. The filtered Navier–Stokes were discretized using a discontinuous Galerkin approach on an unstructured grid of tetrahedra. Over each tetrahedron the solution was represented in terms of a hierarchical orthonormal base which is the extension to three dimensional tetrahedra of the Legendre base. A Rusanov flux was employed for inviscid fluxes while centred ones were used for all the other fluxes. No over integration was employed due to the limited polynomial degree and the use of the subgrid model. The viscous terms in the Navier–Stokes equations were dealt with the so called Local Discontinuous Galerkin approach [2]. The projection over the finite dimensional space of the bases on the elements was identified as the LES filtering operation. To model the subgrid terms arising from the filtering of the equations a simple Smagorinsky model was employed.

The main complication in the use of adaptation in LES is the choice of a suitable indicator to obtain an effective distribution of the polynomial degrees. Among the several tested, the more effective was an indicator based on the structure function, which was employed for the computations. The structure function

$$D_{ij} = \left\langle [u_i(\mathbf{x}+\mathbf{r},t) - u_i(\mathbf{x},t)] \left[u_j(\mathbf{x}+\mathbf{r},t) - u_j(\mathbf{x},t)\right] \right\rangle, \tag{1}$$

is calculated between all the couples of vertices of the element K, then the norm is taken as indicator

$$Ind_{SF}(K) = \sqrt{\sum_{ij} \left[D_{ij}(K) - D_{ij}(K)^{iso}\right]^2}, \tag{2}$$

where a correction to take into account the form that the structure function would take in case of homogeneous isotropic turbulence is introduced (details in [7]). The idea is that the structure function calculates how much the velocity is not correlated on the element: if the velocity exhibits a high correlation fewer degrees of freedom are necessary on such element, while if the velocity shows a strong lack of correlation a higher degree base is necessary on the element. The homogeneous isotropic turbulence correction accounts for the fact that such conditions are ideal for the subgrid model and the refinement can be limited allowing for a higher role of the model.

The adaptation was performed in a static way. A preliminary computation was performed, and the results from that previous computation were used to calculate the indicator and then average it in time. The obtained indicator distribution, using suitable thresholds, was then converted into a polynomial degree map, which was used to run the adapted simulation.

Details on the adaptation procedure can be found in [7].

3 Test Case and Validation

The test case selected for the computations is the flow around a square section cylinder at $Re = 22000$, based on the cylinder side. Despite the simple geometry the test case is a representative example of flows past a bluff bodies with fixed separation points. The reference data comes from an incompressible experiment [4].

The domain for the computations is $30H$ long in the streamwise direction, and wide $20H$ in the cross stream direction, while in the spanwise direction is extruded for $4H$. The cylinder of side H is positioned $10H$ downstream the inflow and centred in the cross stream direction. A uniform Dirichlet condition with sponge layers is imposed at the inflow, as well at the outflow, while Neumann conditions are imposed at the upper and lower boundaries, wall adhesion condition are prescribed at the cylinder walls, and periodic conditions are enforced in the spanwise direction. The mesh is composed by 23816 tetrahedra organized in a structured block around the cylinder and fully unstructured in the rest of the domain. The simulations are started from uniform condition, evolved until statistically stationary state is achieved and then the statistics are accumulated for around 16 shedding periods.

Adaptive simulations are started from low (2nd) degree simulations, which are used to calculate the indicator and the polynomial distribution with polynomial degree varying from 2nd to 4th and then re-started with the new polynomial distribution to accumulate statistics. The comparison of statistics from adaptive simulations and increasing uniform degree simulations (at $Ma = 0.3$) is shown in Fig. 1 and show a good agreement of adaptive solution with the highest order solution, with just around a half of the degrees of freedom and around one third of total computational time needed to start from zero the full 4th degree simulation. All details on validation are presented in [7].

In order to investigate the effects of weak compressibility on flows around bluff bodies, the flow around the square section cylinder was calculated with adaptive simulations at Mach numbers equal to $Ma = \{0.15, 0.3, 0.4\}$, which represent respectively a very low value for a compressible simulation, the commonly assumed thresh-

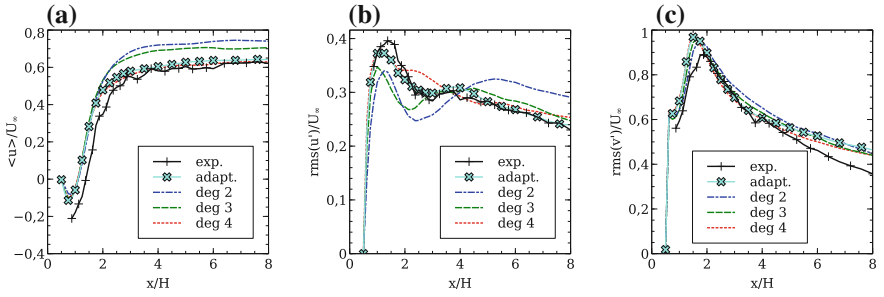

Fig. 1 **a** Average streamwise velocity along the wake, constant degree and adaptive simulations. **b** Streamwise velocity fluctuations along the wake, constant degree and adaptive simulations. **c** Vertical velocity fluctuations along the wake, constant degree and adaptive simulations

Table 1 Global results at different Mach numbers

	St	<Cd>	Rms(Cd')	Rms(Cl')
Experiments	≈0.13	≈2.1	≈0.18	≈1.2
$Ma = 0.15$	0.1372	2.385	0.1838	1.532
$Ma = 0.3$	0.1483	2.390	0.1642	1.338
$Ma = 0.4$	0.1578	2.435	0.1261	1.291

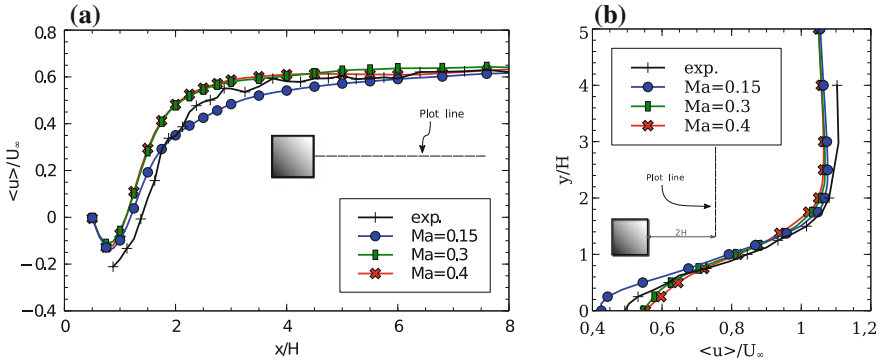

Fig. 2 **a** Average streamwise velocity along the wake. **b** Average streamwise velocity across the wake

old of the regimes which can be considered incompressible and a value slightly higher. Note that significantly higher local Mach numbers are experienced around the cylinder due to strong fluid acceleration, up to $Ma = 0.8$ for the most compressible case.

The global results obtained are presented in Table 1 and several trends can be identified. First, as expected the mean drag coefficient increases with the Mach number. However more interesting are the trends about the fluctuations: with the increase of the Mach number the shedding frequency becomes higher (increasing Strouhal), while the intensity of the fluctuations of the forces coefficients becomes lower.

The average streamwise velocity, plotted along the wake and across the wake two diameters downstream the cylinder, is plotted in Fig. 2, where it is possible to see how increasing Mach the average velocity seems to slightly increase, especially in the near wake. Looking at the fluctuations, the streamwise component is presented in Fig. 3 and it is possible to observe that higher Mach simulations show lower values of fluctuations, especially close to the cylinder. The opposite trend is shown by vertical fluctuations, in Fig. 4, with higher values of the fluctuations at higher Mach numbers. In both cases differences appear until some diameters downstream in the wake, but outside the wake differences become soon negligible.

We also tested if considering the variations of the density due to compressibility changed how the results compared among themselves. For this reason we considered instead of the velocity statistics $< u_i u_j >$ the statistics weighted by the average den-

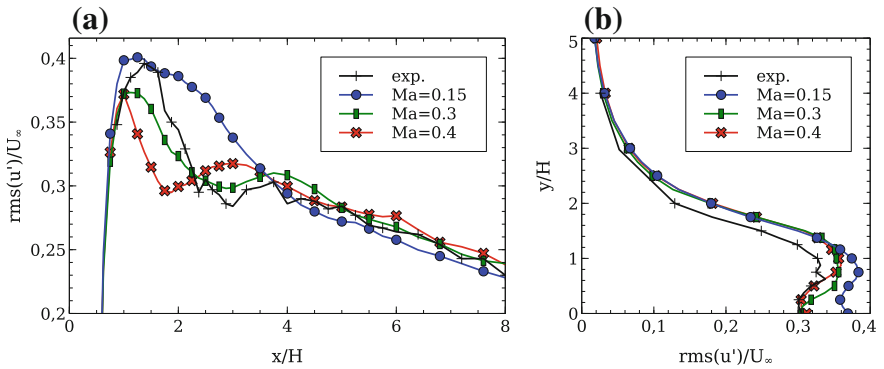

Fig. 3 **a** Rms of total turbulent stresses, streamwise component, along the wake. **b** Rms of total turbulent stresses, streamwise component, across the wake

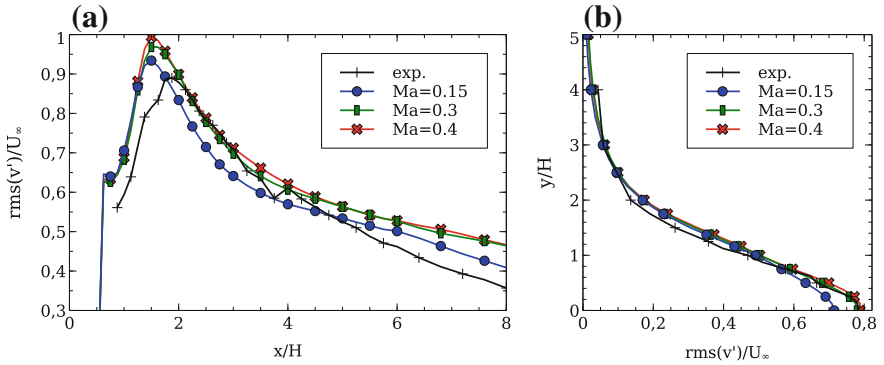

Fig. 4 **a** Rms of total turbulent stresses, vertical component component, along the wake. **b** Rms of total turbulent stresses, streamwise component, across the wake

sity $< \rho > \{u_i u_j\}$ where $\{\cdot\}$ is the Favre average. This is both justified by the fact that this is the turbulent stresses term that arises from Reynolds averaging the compressible Navier–Stokes equations, as $< u_i u_j >$ arises from averaging the incompressible ones, and it is justified by the Morkovin hypothesis that the fluctuations of the density have negligible effects with respect to the mean variations of density, which is true in our case since fluctuations of density are two orders of magnitude lower than average variations.

We observed that even if some statistics appear closer with this weighting, as seen for example in Fig. 5, most of the profiles even if changed a little with the density weighting, still show the same trends as the pure velocity statistics. Differently from the plane channel flow [3], statistics from different Mach numbers do not show a substantial increase of accord employing density weighting.

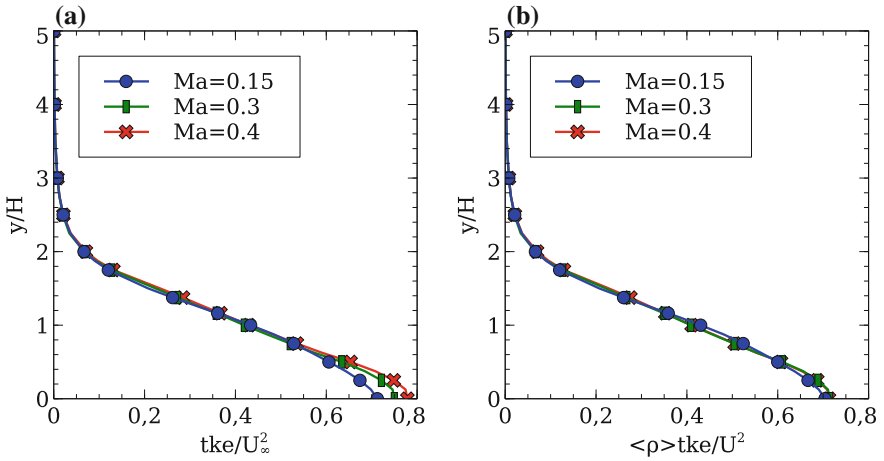

Fig. 5 **a** Total turbulent kinetic energy, across the wake. **b** Total turbulent kinetic energy, across the wake, weighted by average density

4 Conclusions

We used a novel static adaptivity procedure to efficiently compute the flow around the square section cylinder at three increasing Mach numbers, to assess the dependence of statistics on the weak compressibility effects.

The results show a limited variability, which falls within the broad spectrum of the available computational data. However, the trends highlighted are clear and show a progressive increase of the shedding frequency, a decrease of the intensity of the forces fluctuations on the cylinder and a redistribution of velocity fluctuations from streamwise fluctuations to vertical fluctuations. Taking into account the variations of the density does not change the described trends.

References

1. Abbà, A., Bonaventura, L., Nini, M., Restelli, M.: Dynamic models for Large Eddy Simulation of compressible flows with a high order DG method. Comput. Fluids **122**, 209–222 (2015)
2. Cockburn, B., Shu, C.: The local discontinuous Galerkin method for time-dependent convection-diffusion systems. SIAM J. Numer. Anal. **35**, 2440–2463 (1998)
3. Coleman, G.N., Kim, J., Moser, R.D.: A numerical study of turbulent supersonic isothermal-wall channel flow. J. Fluid Mech. **305**, 159–183 (1995)
4. Lyn, D.A., Einav, S., Rodi, W., Park, J.-H.: A laser-doppler velocimetry study of ensemble-averaged characteristics of the turbulent near wake of a square cylinder. J. Fluid Mech. **304**, 285–319 (1995)
5. Pope, S.B.: Ten questions concerning the large-eddy simulation of turbulent flows. New J. Phys. **6**(1), 35 (2004)

6. Rodi, W., Ferziger, J.H., Breuer, M., Pourquie, M.: Status of large Eddy simulation: results of a workshop. J. Fluids Eng. **119**(2), 248–262 (1997)
7. Tugnoli, M., Abbà, A., Bonaventura, L., Restelli, M.: A locally p-adaptive approach for large eddy simulation of compressible flows in a DG framework. J. Comput. Phys. **349**, 33–58 (2017)

Direct Numerical Simulation of Compressible Flows Around Spherical Bodies Using the Immersed Boundary Method

H. Riahi, E. Constant, J. Favier, P. Meliga, E. Serre, M. Meldi and E. Goncalves

1 Introduction

The three-dimensional flow around a sphere is one of the most classical subjects of investigation for fundamental analysis of external aerodynamics. In fact this flow configuration, which is described by a very simple geometrical shape, exhibits the potential for complex multi-physics analysis. Some aspects that can be investigated include turbulence, acoustics and heat transfer, and this test case is particularly favorable for the analysis of coupled problems. In addition, the emergence of a number of different regimes is observed for moderate Reynolds number, which are extremely sensitive to the Mach number Ma investigated. Furthermore, multiple physical systems can be modeled by multi-spherical bodies in motion involving complex interactions. Owing to this large number of aspects which are relevant for industrial applications, this case represents an important benchmark for validation of new numerical/modeling strategies.

In the present work, this test case is analyzed via the Immersed Boundary Method (IBM). The surface of the sphere is not directly embedded in the physical domain, but it is represented by a set of discrete Lagrangian points which are associated with volume forces included in the Navier–Stokes equation. This procedure allows

H. Riahi (✉) · M. Meldi · E. Goncalves
Department of Fluid Flow, Heat Transfer and Combustion, Institut PPRIME,
ENSMA - CNRS - Université de Poitiers, UPR 3346, Poitiers, France
e-mail: hamza.riahi@ensma.fr

M. Meldi
e-mail: marcello.meldi@ensma.fr

E. Goncalves
e-mail: eric.goncalves@ensma.fr

E. Constant · J. Favier · P. Meliga · E. Serre
CNRS, Ecole Centrale Marseille, Laboratoire M2P2 UMR 7340,
Aix-Marseille Université, 13451 Marseille, France

M. V. Salvetti et al. (eds.), *Direct and Large-Eddy Simulation XI*,
ERCOFTAC Series 25, https://doi.org/10.1007/978-3-030-04915-7_43

for flow representation through Cartesian grids, instead of the classical solution of a spherical frame of reference. This analysis aims to produce ground research for future fluid structure interactions analysis, including moving spherical objects in the physical domain. In this scenario, the use of a spherical frame of reference is clearly problematic.

The flow configurations here investigated encompass a large range of Ma numbers, including subsonic, transonic and supersonic flows, for low to moderate Reynolds numbers Re. This very large parametric two dimensional space $[Ma,\ Re] \in [0.3 - 2,\ 50 - 600]$ allows for a robust validation of the proposed IBM methodology, which must achieve a successful representation for numerous physical configurations exhibiting different features.

2 Numerical Ingredients and IBM Development

The starting point of the present work are the compressible Navier–Stokes equations:

$$\frac{\partial \rho}{\partial t} + div(\rho \mathbf{U}) = 0 \tag{1}$$

$$\frac{\partial \rho \mathbf{U}}{\partial t} + \mathbf{div}(\rho \mathbf{U} \otimes \mathbf{U}) = -\mathbf{grad}\, p + \mathbf{div}\overline{\overline{\tau}} + \mathbf{F} \tag{2}$$

$$\frac{\partial \rho E}{\partial t} + div(\rho E \mathbf{U}) = -div(p\mathbf{U}) + div(\overline{\overline{\tau}} \cdot \mathbf{U}) + div(\lambda(T)\mathbf{grad}T) + \mathbf{F} \cdot \mathbf{U} \tag{3}$$

where ρ is the density, p the pressure, T the temperature, λ the thermal conductivity, t the time, $\mathbf{U}$ the velocity, $\overline{\overline{\tau}}$ the tensor of the viscous stresses, E the total energy and $\mathbf{F}$ a prescribed volume force. The IBM exploits this last term to account for the presence of the immersed body, which is not represented via a boundary condition. Among the favorable characteristics of this method we have that mesh elements are not stretched/distorted close to the body surface. In addiction, expensive updates of the mesh are naturally excluded in the analysis of moving bodies.

The present method roots in previous works proposed by Uhlmann [10] and Pinelli et al. [9] which combine strengths of classical continuous forcing methods [8] and discrete forcing methods [6].

The novelty of the approach is represented by:

1. the extension to compressible flow configurations
2. the addition of a component which penalizes deviation from the expected behavior of the pressure gradient. In numerical simulation, the pressure field must comply with a Neumann condition in the wall normal direction.

The forcing is calculated on Lagrangian points representing the discretized shape of the body via *interpolation* of the physical fields available on the Eulerian Cartesian Grid. This step is followed by a consistent *spreading* of this value back to the Eulerian

mesh elements. The resulting forcing term F in Eulerian coordinates, which will be referred to as F_{IB}, is expressed as:

$$\mathbf{F}_{IB} = \frac{1}{\Delta t}\,\rho_{interpol}(\mathbf{U}_{target} - \mathbf{U}_{interpol}) - (\mathbf{grad}\,p_{target} - \mathbf{grad}\,p_{interpol}) \quad (4)$$

here the subscript *interpol* represents the quantities that have been interpolated on the Lagrangian points, while the subscript *target* represents the expected behavior of the flow close to the wall. Δt is the time step of the numerical simulation.

3 Numerical Implementation and Validation

The implementation of the IBM model has been performed in the framework of a specific open source library for numerical simulation, namely OpenFOAM. This code has been identified as the best tester because of the simplicity in implementation as well as the availability of numerous routines already integrated [1]. Owing to the large spectrum of Ma numbers investigated, the IBM has been implemented in two different solvers:

- segregated pressure-based solver with pimple loop for compressible flow with low Mach number ($Ma \leq 0.3$) [2].
- segregated density-based solver with Kurganov and Tadmor divergence scheme for compressible flow with high Mach number ($Ma > 0.3$) [5].

Two 2D test cases have been identified to validate the performance of the compressible IBM solver, namely the flow around a circular cylinder and the flow around a three cylinders configuration. For both test cases, numerical results indicate that the present version of the IBM successfully captures the physical features over the whole parametric space investigated. In addition, the pressure correction term in

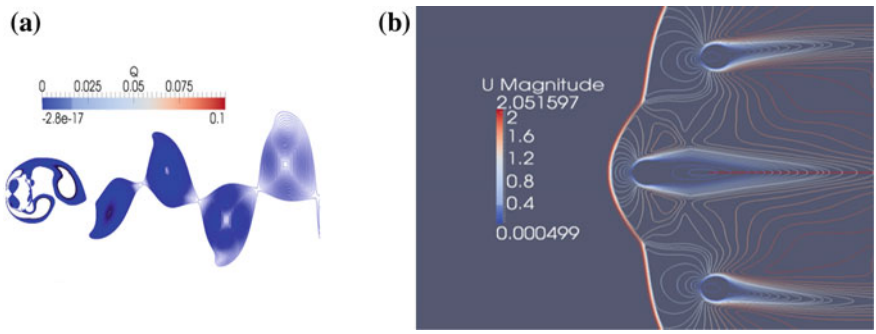

Fig. 1 **a** Q-Criterion for a 2D subsonic flow around a circular cylinder, Ma = 0.3. **b** Mach isocontours for a 2D supersonic flow around a circular cylinders, Ma = 2

Eq. 4 proves to be essential in obtaining an accurate near wall estimation of the flow. Results are shown for reference in Fig. 1a for the unsteady subsonic flow around circular cylinder, where the Karman street is correctly represented, and in Fig. 1b for the supersonic flow around a three cylinder configuration. For this last case, it is observed that the presence of the lateral cylinders decreases the drag coefficient of the central cylinder.

4 DNS of Compressible Flows Around a Sphere

The three-dimensional flow around a sphere has been investigated for different configurations including subsonic, transonic and supersonic flow cases. Present results are compared with classical DNS by Nagata [7] for embedded surfaces using a spherical mesh. The near wall Cartesian mesh resolution has been fixed accordingly with Johnson and Patel formula for direct numerical simulation [3], resulting in cubic elements of resolution 0.0078 D, where D is the sphere diameter. This level of refinement is imposed in a region of size $x \times y \times z = [-1,\ 1] \times [-1,\ 1] \times [-1, 1]$ in D units. The origin is fixed in the center of the sphere. A progressive coarsening ratio is imposed outside this region, resulting in a total of 2×10^7 mesh elements. As discussed in the introduction, this test case exhibits numerous physical configurations which are sensitive to the value of Ma and Re initially imposed. Results for nine configurations are here discussed, as summarized in Table 1. Depending on the choice of the parameters Ma, Re a steady axisymmetric configuration or an unsteady flow configuration is observed.

A very good agreement with results in the literature [4, 7] is observed for all the configurations investigated. In particular, results for the bulk flow quantities (friction coefficient C_D, recirculation bubble Xs, Strouhal number St and shock distance from stagnation point $Dshock$) are presented in Table 2. In the following, a brief discussion is proposed clustering the results with respect to the Mach number.

The subsonic flow configuration for $Ma = 0.3$ clearly exhibits an stationary behavior for $Re = 50$, while unsteady flows are obtained for $Re = 300$ and $Re = 600$ (see Fig. 2a, b). For the unstationary cases, the IBM method allows for a precise estimation of the bulk statistical quantities.

Table 1 Flow regimes

	Subsonic low Mach Ma = 0.3	Transonic flow Ma = 0.95	Supersonic flow Ma = 2
Re = 50	Steady axisymmetric	Steady axisymmetric	Steady axisymmetric
Re = 300	Unsteady	Steady axisymmetric	Steady axisymmetric
Re = 600	Unsteady	Unsteady	Steady axisymmetric

Table 2 Results of a 3D compressible flow around sphere

		Ma = 0.3			Ma = 0.95			Ma = 2		
		C_D	Xs	St	C_D	Xs	St	C_D	Xs	Dshock
Re = 50	IBM results	1.6	0.96	–	2.116	1.15		2.03	0.5	0.73
	Nagata et al. [7]	1.57	0.95	–	–	–		2.25	0.5	0.75
Re = 300	IBM results	0.703	–	0.123	1.03	3.8		1.39	1	0.7
	Nagata et al. [7]	0.68	–	0.128	1	4.1		1.41	1	0.7
Re = 600	IBM results	0.58	–	0.143	0.91	–	0.138	1.27	1.7	0.68
	Krumins [4]	0.54	–	–	0.9	–	–	1.17	–	–

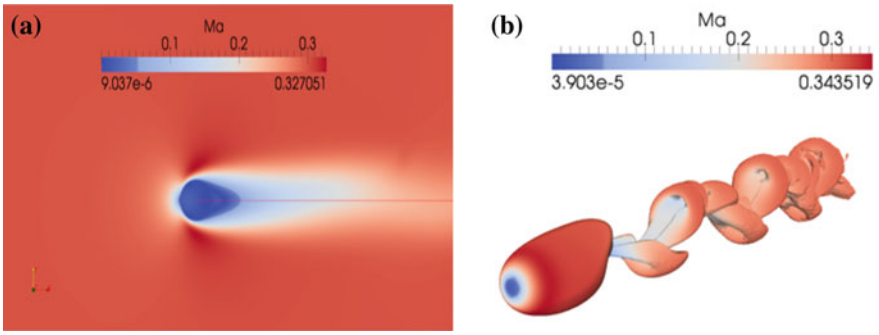

Fig. 2 **a** Mach isocontours for a 3D steady flow around a sphere, Ma = 0.3 Re = 50. **b** Q-Criterion for a 3D unsteady flow around a sphere, Ma = 0.3 Re = 300

The results obtained for the transonic case ($Ma = 0.95$) are shown in Fig. 3a–d. For this case, steady configurations are observed for $Re = 50$ and $Re = 300$, while an unsteady flow is obtained for $Re = 600$. The most interesting aspect for this class of simulations is that an accurate representation of the supersonic zone at the wall is observed, which is usually a challenging point for IBM methods.

At last, the supersonic flow configurations for $Ma = 2$ are considered. In this case compressibility effects are very strong and all the simulations produce steady flows. Again, the analysis of the main bulk flow quantities indicate that all the physical features are accurately captured, when compared with data in the literature [4, 7]. Isocontours are shown in Fig. 4a, b.

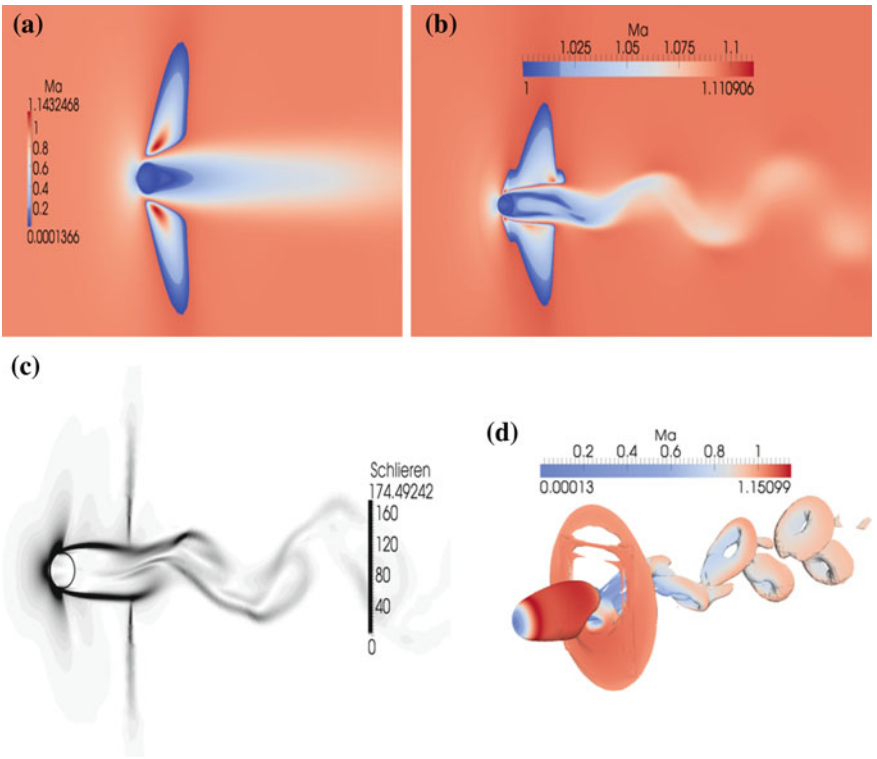

Fig. 3 **a** Mach isocontours for a 3D steady flow around a sphere, Ma = 0.95 Re = 50. **b** Mach isocontours for a 3D unsteady flow around a sphere, Ma = 0.95 Re = 600. **c** Schlieren Criterion of a 3D steady flow around a sphere, Ma = 0.95 Re = 600. **d** Q-Criterion for a 3D unsteady flow around a sphere, Ma = 0.95 Re = 600

5 Conclusion

The flow around a sphere has been analyzed via an IBM for adiabatic compressible flows. The analysis has encompassed a wide range of Re, Ma for which various physical features emerge. The results of the present analysis indicate that the proposed IBM model successfully captures the physical features for the entire spectrum of configurations investigated. An accurate prediction of the main bulk quantities has been obtained and, in particular, the method has proven robustness characteristics in capturing shock features and the supersonic zone on the sphere surface.

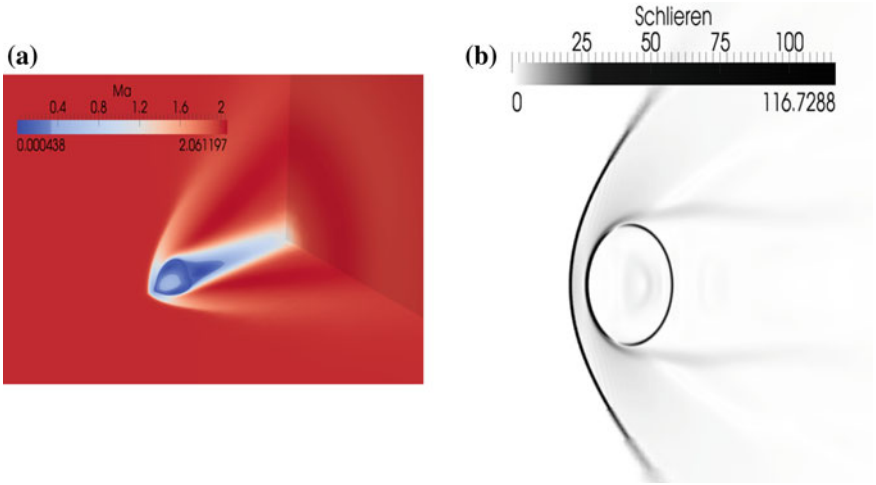

Fig. 4 **a** Mach field of a 3D supersonic flow around a sphere, Ma = 2 Re = 300. **b** Schlieren Criterion of a 3D supersonic flow around a sphere, Ma = 2 Re = 600

Acknowledgements This research work has been developed using computational resources in the framework of the project DARI-GENCI A0012A07590.

References

1. Constant, E., Favier, J., Meldi, M., Meliga, P., Serre, E.: An immersed boundary method in OpenFOAM: verification and validation. Comp. Fluids **157**, 55–72 (2017)
2. Gutirrez Marcantoni, L.F., Tamagno, J.P., Elaskar, S.A.: High speed flow simulation using OpenFOAM. Mecánica Comput. 2939–2959 (2012)
3. Johnson, T.A., Patel, V.C.: Flow past a sphere up to a Reynolds number of 300. J. Fluid Mech. (1999)
4. Krumins, V.: A review of sphere drag coefficients applicable to atmospheric density sensing. Naval Ordance Laboratory (1972)
5. Kurganov, A., Tadmor, E.: New high-resolution central schemes for nonlinear conservation laws and convection-diffusion equations. J. Comp. Phys. **160**, 241–282 (2000)
6. Mohd-Yosuf, J.: Combined immersed boundary/B-spline methods for simulation of flow in complex geometries. Annu. Res. Briefs 317–328 (1997)
7. Nagata, T., Nonomura, T., Takahashi, S., Mizuno, Y., Fukuda, K.: Investigation on subsonic to supersonic flow around a sphere at low Reynolds number of between 50 and 300 by direct numerical simulation. Phys. Fluids **28**, 056101 (2016)
8. Peskin, C.S.: Flow patterns around heart valves: a numerical method. J. Comp. Phys. **10**, 252–271 (1972)
9. Pinelli, A., Naqavi, I.Z., Piomelli, U., Favier, J.: Immersed-boundary methods for general finite-difference and finite-volume Navier-Stokes solvers. J. Comp. Phys. **229**, 9073–9091 (2010)
10. Uhlmann, M.: An immersed boundary method with direct forcing for the simulation of particulate flows. J. Comp. Phys. **209**, 448–476 (2005)

Large Eddy Simulation of Highly Compressible Jets with Tripped Boundary Layers

R. Gojon, C. Bogey and M. Mihaescu

1 Introduction

In high-speed aircraft, supersonic jets used for propulsion can lead to very intense aerodynamically generated acoustic noise. Thus, there is a need to study the aerodynamic and aeroacoustic properties of highly compressible jets. In previous studies [1, 2], several simulations of supersonic jets have been conducted. Unfortunately, the turbulence intensity at the nozzle exit was dependent on the internal geometry of the nozzle and could not be tuned. This is a pity given that, as shown experimentally [3] and numerically [4, 5] for subsonic and supersonic jets, the boundary layer state of the jet affects the jet flow and noise.

In this study, a boundary-layer tripping method permitting to obtain an initially turbulent supersonic jet is studied. The influence of the tripped jet boundary layers on the flow and acoustic fields of the jet is analyzed. The impact of nozzle-exit turbulence levels on the noise radiation and notably on the acoustic components specific to supersonic jets (screech noise, broadband shock-associated noise, mixing noise and Mach wave radiation) is discussed.

R. Gojon (✉) · M. Mihaescu
Department of Mechanics, Royal Institute of Technology (KTH),
Linné FLOW Centre, Stockholm, Sweden
e-mail: gojon@mech.kth.se

M. Mihaescu
e-mail: mihai@mech.kth.se

C. Bogey
Laboratoire de Mécanique des Fluides et d'Acoustique, UMR CNRS 5509,
Ecole Centrale de Lyon, Université de Lyon, Ecully, France
e-mail: christophe.bogey@ec-lyon.fr

M. V. Salvetti et al. (eds.), *Direct and Large-Eddy Simulation XI*,
ERCOFTAC Series 25, https://doi.org/10.1007/978-3-030-04915-7_44

2 Parameters of the Study

The nozzle of the jet in the present study is the one used in an experimental study conducted at the University of Cincinnati [6]. The jet exits from a conical converging-diverging nozzle characterized by a design Nozzle Pressure Ratio $NPR = 4.0$ and an exit diameter $D = 57.53$ mm. At the inlet of the nozzle, a Temperature Ratio of 1.25 and a NPR of 3.5 are imposed, yielding an ideally expanded jet velocity of $U_j = 471$ m.s^{-1}. The jet is thus overexpanded. The jet conditions are chosen in order to match those of Cuppoletti and Gutmark [6]. They are those of the experimental case where the screech noise component is the strongest.

The simulations are performed by using a finite-volume solver [7] of the unsteady compressible Navier–Stokes equations. An explicit standard four-stage Runge–Kutta algorithm is implemented for time integration and a second-order central difference scheme is used for spatial discretization. At the end of each time step, an artificial dissipation [1] is applied in order to remove grid-to-grid oscillations and to avoid Gibbs oscillations near shocks. For free shear flows, adding a subgrid-scale model, like the dynamic Smagorinsky model, leads to a decrease of the effective Reynolds number [8]. Given the importance of this parameter in jet noise, such model has not been used and the artificial dissipation acts as a subgrid-scale model, in a similar way as explicit filtering in other studies [9, 10]. Adiabatic no-slip conditions are imposed at the nozzle walls. Finally, in order to avoid reflections on the boundaries, sponge zones are implemented all around the computational domain and characteristic boundary conditions are applied.

A structured mesh consisting of about 160 millions of nodes is used. It is similar to the one of a previous study [1] on rectangular jets. Near the nozzle exit, mesh sized of $\Delta r^+ \sim 1$ in the wall normal direction and of $\Delta z^+ \sim r\Delta\theta^+ < 10$ in the axial and azimuthal directions are found. In order to preserve numerical accuracy, aspect ratios of the volume cells are kept below 25 and stretching is limited to 8%.

3 Tripping of the Boundary Layer

In order to trigger turbulence in the jet boundary-layer, a geometric step is added in the nozzle, as in the work of Vuillot et al. [11]. The height of the step is 0.4mm and its axial length is 1mm. Two positions of the step are tested, in the straight section and in the converging section of the nozzle, respectively. The two simulations will be referred to as case 1 and case 2. Side views of the meshes are provided in Figs. 1 and 2. A simulation without step is also conducted, and will be referred to as the baseline case. It is worth noting that the step should be placed in the nozzle, in the low Mach number flow region, in order to avoid compressibility effects, like the appearance of a shock at the position of the step.

Fig. 1 Case 1: step in the straight section of the nozzle

Fig. 2 Case 2: step in the converging section of the nozzle

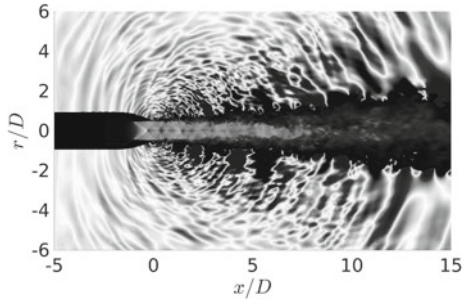

Fig. 3 Baseline case: Mach number distribution and near-field pressure fluctuations. The Mach number ranges from 0.25 to 2.5 and the fluctuating pressure from −1000 to 1000 Pa

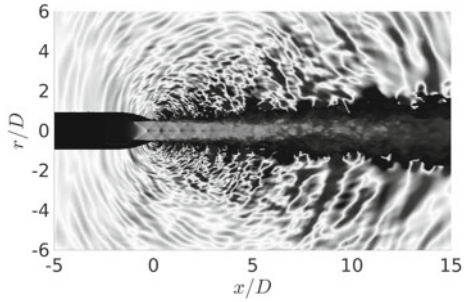

Fig. 4 Case 2: Mach number distribution and near-field pressure fluctuations. The Mach number ranges from 0.25 to 2.5 and the fluctuating pressure from −1000 to 1000 Pa

4 Aerodynamic Results

Figures 3 and 4 display the Mach number distribution and the near-field acoustic waves in a mid-longitudinal plane for the baseline case and for case 2.

The double-diamond pattern of the shock cell structure, observed experimentally [6], is visible in the aerodynamic field in both cases. In the near acoustic field, the classical components of supersonic jet noise can be identified; the broadband shock associated noise, mixing noise, Mach wave radiation and screech noise [1]. Moreover, the acoustic waves near the nozzle, propagating in the upstream direction and corresponding to screech noise, have a higher amplitude for the baseline case than for case 2.

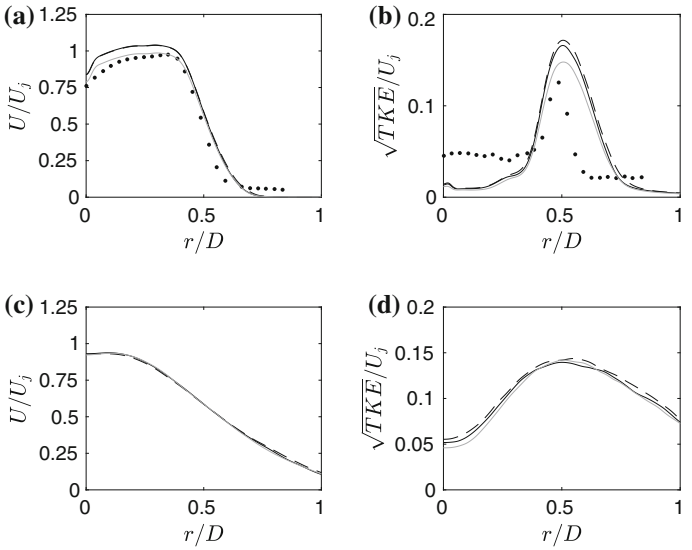

Fig. 5 Radial profile of mean axial velocity (**a**, **c**) and 2-D turbulent kinetic energy (**b**, **d**) at **a**, **b** $x = D$ and **c**, **d** $x = 5D$; experimental data (bullets) [6], baseline case (black line), case 1 (dashed line) and case 2 (grey line)

The mean axial velocity and the turbulent kinetic energy of the simulations are compared with PIV measurements [6] in Fig. 5. As in the experiments, only the two components of velocity in the azimuthal plane considered are used to compute the 2-D turbulent kinetic energy. At $x = D$, the results of case 2 are in much better agreement with the experimental results than the results of the baseline case and of case 1, which overpredict the mean axial velocity and the turbulent kinetic energy. This overprediction is characteristic for the transition from a laminar boundary layer inside the nozzle to a turbulent jet shear layer [4, 5]. At $x = 5D$, the three simulations give similar results.

For the baseline case and for case 2, the 2-D mean turbulent kinetic energy is shown in Fig. 6 in the plane (z, r). Higher amplitudes are found in the shock cell structure in the baseline case than in case 2. This suggests a stronger motion of the shock cells, which is consistent with a stronger screech mechanism. Moreover, the development of the jet shear layer is slower for case 2 than for the baseline case, yielding a shorter potential core in the latter case. This trend is similar to that observed in subsonic jets [4] as the initial turbulence intensity increases.

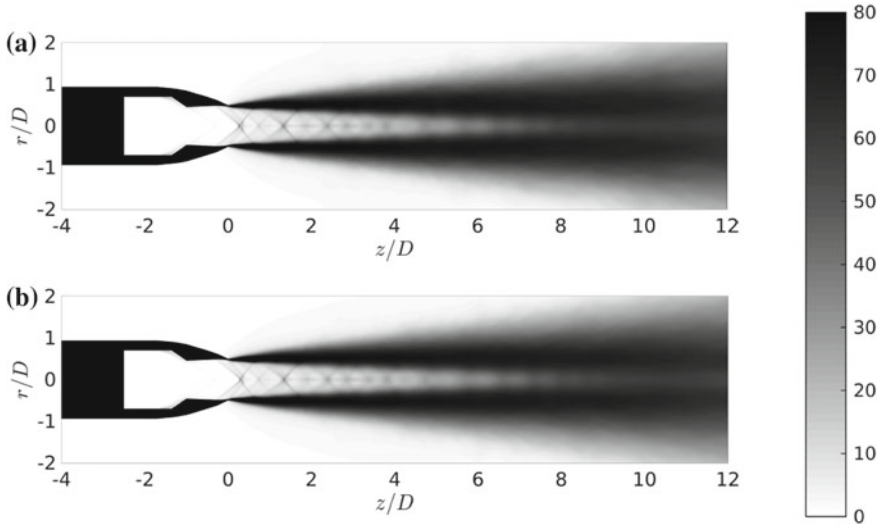

Fig. 6 2-D turbulent kinetic energy for the baseline case (**a**) and case 2 (**b**). The color scale ranges from 0 to 80 m.s^{-1}

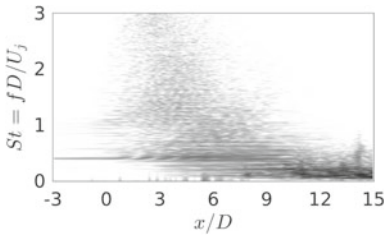

Fig. 7 Baseline case: pressure spectra as function of the axial location of the probe and Strouhal number. The color scale ranges from 140 to 155 dB/St

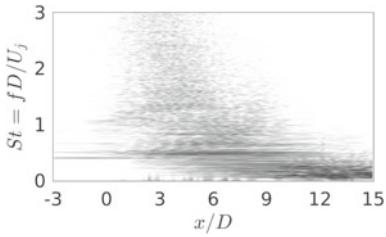

Fig. 8 Case 2: pressure spectra as functions of the axial location of the probe and Strouhal number. The color scale ranges from 140 to 155 dB/St

5 Acoustic Results

The near-acoustic fields are directly studied from the fluctuating pressure given by the LES. The acoustic spectra obtained at $r = 2D$, from $x = -3D$ to $x = 15D$, are plotted in Figs. 7 and 8 for the baseline case and case 2, respectively.

Three acoustic components are well visible; the broadband shock associated noise, mixing noise and screech noise. In the upstream region, the screech frequency is observed at $St = 0.29$, which is in very good agreement with the frequency of $St = 0.30$ found in experiments [6]. Moreover, the screech amplitude is 5 dB higher for the baseline case than for case 2, as qualitatively observed in the snapshots of Figs. 3 and 4. In the downstream direction, for $x > 10D$, the mixing noise is about 3 dB higher for the baseline case than for case 2.

6 Conclusions

Large Eddy Simulations of a round supersonic screeching jet have been performed. In order to reach a turbulent state of the boundary layer at the nozzle exit, a geometrical step is added in the nozzle. With the step in the straight section of the converging-diverging nozzle, no differences with the baseline case are noticed. With the step in the converging section of the nozzle, several differences with respect to the baseline case are observed:

- the development of the jet shear layer is slower
- the overprediction of the turbulent kinetic energy near the nozzle exit is lower
- screech noise is 5 dB lower in the near acoustic field
- mixing noise is 3 dB lower in the near acoustic field.

These observations indicate that the geometrical step, under certain circumstances, allow us to simulate more accurately the aerodynamic and acoustic fields of a turbulent supersonic jet.

Acknowledgements The computations were performed using HPC resources provided by the Swedish National Infrastructure for Computing (SNIC) at the PDC center.

References

1. Gojon, R., Gutmark, E., Baier, F. Mihaescu, M.: Temperature effects on the aerodynamic and acoustic fields of a rectangular supersonic jet. AIAA Paper, no. 2017-0002 (2017). https://doi.org/10.2514/6.2017-0002
2. Gojon, R., Gutmark, E., Mihaescu, M.: On the response of a rectangular supersonic jet to a near-field located parallel flat plate. AIAA Paper, no. 2017-3018 (2017). https://doi.org/10.2514/6.2017-3018
3. Zaman, K.B.M.Q.: Effect of initial boundary-layer state on subsonic jet noise. AIAA J. **50**(8), 1784–1795 (2012). https://doi.org/10.2514/1.J051712
4. Bogey, C., Marsden, O., Bailly, C.: Influence of initial turbulence level on the flow and sound fields of a subsonic jet at a diameter-based Reynolds number of 10^5. J. Fluid Mech. **701**, 352–385 (2012). https://doi.org/10.1017/jfm.2012.162
5. Brés, G.A., Ham, F.E., Nichols, J.W., Lele, S.K.: Nozzle wall modeling in unstructured large eddy simulations for hot supersonic jet predictions, *AIAA paper*, no. 2013-2142 (2013). https://doi.org/10.2514/6.2013-2142

6. Cuppoletti, D.R., Gutmark, E.: Fluidic injection on a supersonic jet at various Mach numbers. AIAA J. **52**(2), 293–306 (2014). https://doi.org/10.2514/1.J010000
7. Eliasson, P.: EDGE: A Navier-Stokes solver for unstructured grids. FOI (2001)
8. Bogey, C., Bailly, C.: Decrease of the effective Reynolds number with eddy-viscosity subgrid-scale modeling. AIAA J. **43**(2), 437–439 (2005). https://doi.org/10.2514/1.10665
9. Bogey, C., Bailly, C.: Large eddy simulations of transitional round jets: influence of the Reynolds number on flow development and energy dissipation. Phys. Fluids **50**(8), 065101 (2006). https://doi.org/10.1063/1.2204060
10. Kremer, F., Bogey, C.: Large-eddy simulation of turbulent channel flow using relaxation filtering: resolution requirement and Reynolds number effects. Comput. Fluids **116**, 17–28 (2015). https://doi.org/10.1016/j.compfluid.2015.03.026
11. Vuillot, F., Lupoglazoff, N., Lorteau, M. Cléro, F.: Large eddy simulation of jet noise from unstructured grids with turbulent nozzle boundary layer. AIAA paper, no. 2016-3046 (2016). https://doi.org/10.2514/6.2016-3046

Analysis of Dense Gas Effects in Compressible Turbulent Channel Flows

L. Sciacovelli, P. Cinnella and X. Gloerfelt

1 Introduction

In this work we investigate the influence of dense gas effects on compressible wall-bounded turbulence. Turbulent flows of dense gases represent a research field of great importance for a wide range of applications in engineering. Dense gases are single-phase fluids with a molecular complexity such that the fundamental derivative of gas dynamics [1] $\Gamma := 1 + \frac{\rho}{c}\left.\frac{\partial c}{\partial \rho}\right|_s$ (where ρ is the density, p the pressure, s the entropy, and c the sound speed), which measures the rate of change of the sound speed in isentropic transformations, is less than one in a range of thermodynamic conditions close to the saturation curve. In such conditions, the speed of sound increases in isentropic expansions and decreases in isentropic compressions, unlike the case of perfect gases. For dense gases, the perfect gas model is no longer valid, and more complex equations of state must be used to account for their peculiar thermodynamic behavior. Moreover, in the dense gas regime, the dynamic viscosity μ and the thermal conductivity λ depend on temperature and pressure through complex relationships. Similarly, the approximation of nearly constant Prandtl number $Pr{=}\mu c_p/\lambda$ is no longer valid. Numerical simulations of turbulent dense gas flows of engineering interest are based on the (Reynolds-Averaged Navier–Stokes) RANS equations, which need to be supplemented by a model for the Reynolds stress tensor and turbulent heat flux. The accuracy of RANS models for dense-gas flows has not been properly assessed up to date, due to the lack of both experimental and numerical

P. Cinnella (✉) · X. Gloerfelt
Laboratoire DynFluid, Arts et Métiers ParisTech, Paris, France
e-mail: paola.cinnella@ensam.eu

X. Gloerfelt
e-mail: xavier.gloerfelt@ensam.eu

L. Sciacovelli
California Institute of Technology, Pasadena, CA, USA
e-mail: lsciacov@caltech.edu

M. V. Salvetti et al. (eds.), *Direct and Large-Eddy Simulation XI*,
ERCOFTAC Series 25, https://doi.org/10.1007/978-3-030-04915-7_45

reference data. DNS databases [2, 3] are then needed to quantify the deficiencies of existing turbulence models and to develop and calibrate improved ones. In this work we first summarize some recent direct numerical simulation (DNS) results [4] for supersonic turbulent channel flows (TCF) of PP11, a heavy fluorocarbon representative of dense gases, at various bulk Mach and Reynolds numbers. The most relevant effects are represented by non-conventional variations of the fluctuating thermodynamic quantities, compared to perfect gases and a strong decoupling between thermal and dynamic effects almost everywhere in the flow, except in the immediate vicinity of the solid wall. Preliminary considerations about the validity of some currently-used models for the turbulent stresses and heat flux are carried out based on a priori comparisons between the exact terms computed from the DNS and their modeled counterparts.

2 Governing Equations and Numerical Method

Dense gas flows are governed by the compressible Navier–Stokes equations, supplemented by suitable thermodynamic and transport-property models. In the present work, the gas behavior is modeled through the Martin–Hou (MAH) thermal equation of state [5], which is reasonably accurate for the fluid of interest and requires a minimum amount of experimental information for setting the gas-dependent coefficients. In addition thermodynamic models relating the dynamic viscosity μ and thermal conductivity κ to the gas temperature and pressure have to be specified. In the present calculations, the transport properties follow the Chung et al. model [6], which incorporates a correction term in the dense-gas region. The working fluid is perfluoro-perhydrophenanthrene (chemical formula $C_{14}F_{24}$), called hereafter with its commercial name PP11, often used in dense-gas studies. DNS were also carried for air, modeled as a polytropic perfect gas. In the latter case, the viscosity is assumed to follow a power law of the temperature and the thermal conductivity is computed according to a constant Prandtl number assumption. The governing equations are approximated in space by means of optimized finite difference schemes, supplemented by an optimized selective sixth-order filter. A low-storage six-step optimized Runge–Kutta is used for time integration.

3 DNS Results

A parametric study was carried out at three bulk Reynolds numbers $Re_B := \frac{\overline{\rho}_B \widetilde{u}_B h}{\overline{\mu}_w}$ (3000, 7000 and 12000) and three bulk Mach numbers $M_B := \frac{\widetilde{u}_B}{\overline{c}_w}$ (1.5, 2.25 and 3.0) [4]. Details about the computational setup and grid resolution can be found in [4]. In the following, the subscripts $(\cdot)_B$, $(\cdot)_w$ and $(\cdot)_{CL}$ denote time and space averaged values over the channel cross-section, at the wall and at the centerline, respectively;

$\overline{(\cdot)}$ indicates Reynolds averaging and $(\cdot)'$ Reynolds fluctuations; similarly, $\widetilde{(\cdot)}$ and $(\cdot)''$ denote Favre averages and fluctuations. Results for the different cases were compared by introducing an empirical semi-local scaling initially proposed by Huang et al. [7] for compressible flows, which corrects the usual wall scaling with centerline quantities. Specifically, $y^* = \frac{\overline{\rho}(y) u_\tau^* y}{\overline{\mu}(y)}$ and $Re_\tau^* = Re_\tau \sqrt{\frac{\overline{\rho}(y)}{\overline{\rho}_w}} \frac{\overline{\mu}_w}{\overline{\mu}(y)}$, with $u_\tau^* := \sqrt{\frac{\overline{\tau}_w}{\overline{\rho}(y)}}$ the semi-local friction velocity. This mixed scaling provided quite satisfactory results in collapsing first- and second-order moments for a wide range of M_B. For PP11, due to the large specific heat of the fluid, the average temperature is almost constant across the channel for any choice of the Mach and Reynolds numbers, and the centerline temperature differs less than 1% from $\widetilde{T}_w$. Decoupling of dynamic and thermal effects in the dense gas also leads to smaller mean density variations across the channel. The normalized viscosity $\overline{\mu}/\overline{\mu}_w$, which follows temperature variations for air, varies instead like the density for PP11 and tends to decrease toward the channel center. As a consequence the friction Reynolds number Re_τ^* increases toward the channel centerline in PP11. Specifically, the dense gas flow exhibits lower values of Re_τ^* near the wall, compared to a perfect gas flow at the same bulk conditions, whereas the centerline value of Re_τ^* is much higher in the dense gas, due to the negligible friction heating in the outer region. On the other hand, the average Prandtl number $\overline{Pr}$ decreases from the wall to the centerline, following essentially the same trend as the average specific heat. Figure 1 displays the distributions of the above-mentioned quantities across the channel, as a function of y^*. Dense gas effects are stronger at higher M_B, since the local thermodynamic states spread over a wider range. Sample results for second-order statistics are reported in Fig. 2, which displays the r.m.s. values of the density, the Reynolds shear stress in semi-local scaling $\overline{\rho u'' v''}^+ = \tau_w^{-1} \overline{\rho u'' v''}$, as well as the ratio of the turbulent kinetic energy production to dissipation. The relative density and pressure fluctuations are of the same order of those observed for air flows (see [4]), whereas temperature fluctuations (not reported) are nearly

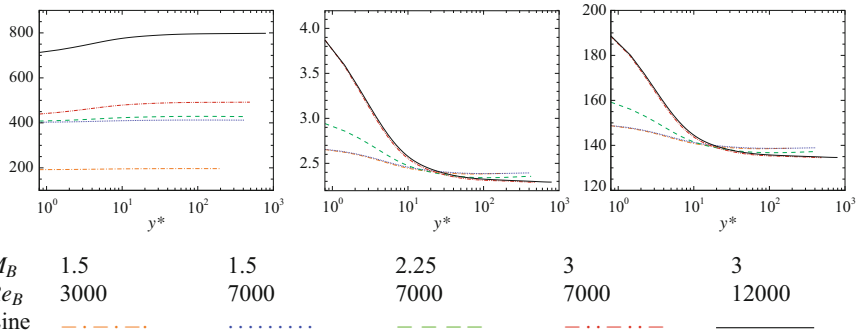

Fig. 1 From left to right: local friction Reynolds number (Re_τ^*), average Prandtl number ($\overline{Pr}$), and average isobaric specific heat normalized with the gas constant ($\overline{c}_p/R$) as a function of y^* for DNS of PP11 TCF at various M_B and Re_B

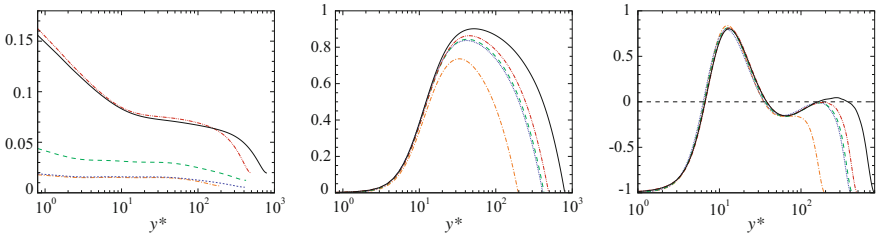

Fig. 2 From left to right: normalized density fluctuations ($\sqrt{\overline{\rho'^2}}/\overline{\rho}$), Reynolds shear stresses ($\overline{\rho u'' v''}^+$), and production-to-dissipation ratio of turbulent kinetic energy ($P_k/\varepsilon_k - 1$) as a function of y^* for DNS of PP11 TCF at various M_B and Re_B. Line legend as in Fig. 1

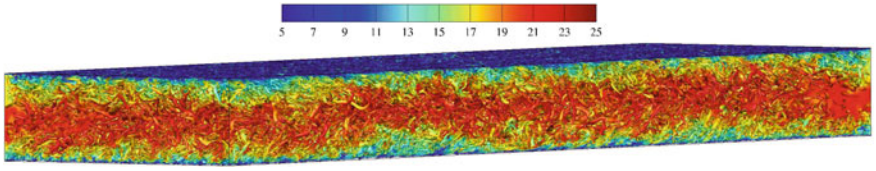

Fig. 3 Isosurface of $Q(h/u_B)^2 = 1$ coloured with streamwise velocity ($M_B = 3$, $Re_B = 7000$)

two orders of magnitude lower. Remarkably, $\overline{\rho'^2}$ decreases monotonically from wall to centerline, contrary to light gases. This is due to the peculiar thermodynamic behavior of PP11 at the considered conditions, as demonstrated in [4] by using the equation of state. In all cases, density fluctuations remain small compared to the mean value, and Morkovin's hypothesis is satisfied even at the highest Mach number. Despite the striking differences in the thermodynamic behavior, Reynolds stress profiles are similar to those observed, e.g., in [8] for low-Mach TCF with temperature-dependent transport properties. The liquid-like behavior of viscosity leads to an increase of the spanwise, wall-normal and Reynolds shear stresses with respect to the corresponding incompressible evolution, whereas the streamwise one decreases. This effect is stronger when increasing Mach number. The last subfigure shows the ratio of production to dissipation term P_k/ε_k of the turbulent kinetic energy budget. The production peak is located as usual at $y^* \approx 12$. For the higher Reynolds number, a second production peak is observed in the outer region, like in high-Re incompressible flow, due to the reduced dissipation close to centerline. A visualization of flow structures for $M_B = 3$, $Re_B = 12000$ is provided in Fig. 3.

4 A Priori Analysis of Turbulence Models

DNS data are used to investigate the validity of some popular models for the RANS equations. More specifically, we focus hereafter on the eddy-viscosity and turbulent Prandtl number assumptions, commonly used to approximate, respectively, the Reynolds stress tensor and the turbulent heat flux. To this end, "exact" eddy viscosity

and turbulent Prandtl number are computed from DNS data as:

$$\mu_t = \overline{\rho u'' v''} \left(\frac{d\overline{u}}{dy} \right)^{-1} ; \quad Pr_t = \overline{c}_p \mu_t / \lambda_t \tag{1}$$

where $\overline{u}$ is the average streamwise velocity and $\lambda_t = \overline{\rho v'' h''} \left(\frac{d\overline{h}}{dy} \right)^{-1}$ is a turbulent thermal conductivity, with $\overline{h}$ the average static enthalpy. Input quantities required by eddy models are also based on DNS. In this study we restrict our attention to two low-Reynolds variants of the $k - \varepsilon$ model, namely, the Launder–Sharma (LS) [9] and Chien (CH) [10] models, which assume that $\mu_t = C_\mu f_\mu \rho k^2/\varepsilon$, with C_μ usually taken equal to 0.09, the damping function f_μ is $\exp(-3.4/(1 + R_t/50)^2)$ ($R_t = \rho k^2/(\mu\varepsilon)$) for LS and $1 - \exp(-0.0115 y^+)$ for CH. Durbin [11] showed that a more appropriate choice for the velocity scale in the inner region is represented by the root-mean square of the wall-normal fluctuating velocity, and reformulated the eddy viscosity as $\mu_t = C\sqrt{\widetilde{v''^2}} k/\varepsilon$ with $C = 0.2$. In Fig. 4 we report the results for the highest Reynolds number, both for air and PP11. In both cases the LS model badly overestimates the turbulent viscosity, especially in the viscous sublayer, as also observed by other authors (e.g. [11, 12]) for incompressible flows. Chien's model captures better the trend of μ_t but also overestimates the turbulent viscosity in the outer region. Durbin's model provides a reasonably accurate approximation of the μ_t profile up to part of the logarithmic region. For air, the model departs from the DNS profile at $y^* \approx 40$ and, unlike the two preceding models, it underestimates μ_t in the outer region. For PP11, the model remains in rather good agreement with DNS up to $y^* \approx 150$ and overestimates μ_t for higher values of y^*.

In Fig. 5 we report the exact turbulent Prandtl number at various M_B and Re_B. For air, Pr_t follows the trends observed by other authors in the literature (e.g. [7]). In particular, for the present relatively low-Re flow, Pr_t exhibits only a small plateau around $y^* \approx 100$ where its value is close to the standard "constant" value of 0.9. In the outer region, Pr_t decreases with y^*, while in the inner region it exhibits a local maximum at about $y^* = 50$ and tends to approximately 1.1 at the wall. For PP11,

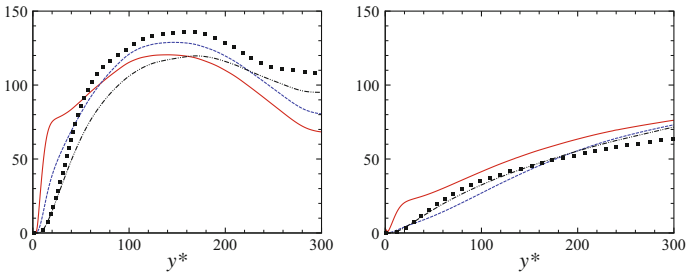

Fig. 4 Exact and modeled eddy viscosity (ν_t/ν_w) for air (left) and PP11 (right) at $M_B = 3$ and $Re_B = 12000$. ———: LS; – – –: CH; – · – · –: Durbin; ■: DNS

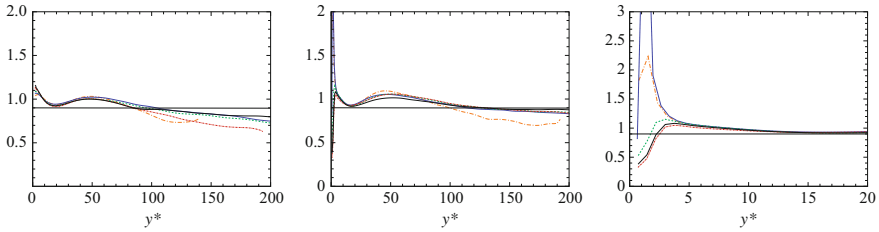

Fig. 5 Exact turbulent Prandtl number (Pr_t) for air (left), PP11 (centre) and close-up view for PP11 (right) at various M_B and Re_B. Legend as in Fig. 1. Horizontal line is set at $Pr_t = 0.9$

the overall behavior is rather close to that of the perfect gas over most of the channel height ($y^* \gtrapprox 5$). However, the solution exhibits a larger '0.9' plateau than the air flow, located at $y^* \approx 120$, most likely because of the higher local Re_τ^*. The local maximum around $y^* \approx 50$ is also observed for the dense gas. A drastically different behavior is observed in the viscous sublayer ($y^* \lessapprox 5$), where the local Prandtl number is much higher and the local Re_τ^* much lower than in air. In this region ($y^* \approx 2$), Pr_t exhibit another local maximum (more or less pronounced according to the flow conditions) and tends to values lower than 1 at the wall (≈ 0.4 at the highest Mach number). Inspection of the DNS data for μ_t and λ_t suggests the following explanation: for air, both μ_t and λ_t decrease approximately at the same rate ($O(y^{*3})$) when $y^* \to 0$. Since in this case $c_p = const$, then Pr_t tends toward a constant nonzero value. For PP11, λ_t decreases at a lower rate than μ_t in the near wall region, due to the smaller enthalpy variation in this high-c_p fluid. As a consequence, their ratio tends to vanish at the wall. However, $\overline{c}_p$ increases abruptly when $y^* \to 0$ (following an approximately exponential trend), hence the local maximum.

5 Conclusions

Direct numerical simulations of plane turbulent channel flows of dense gases have been performed at various bulk Mach and Reynolds numbers. For a dense-gas, the classical y^+ scaling based on the friction velocity fails to collapse thermodynamic profiles and Reynolds stresses at high M_B, and semi-local scaling, which accounts for variations of the flow properties, has to be adopted instead. Due to the high specific heat, coupling between dynamic and thermal effects is found to be very small for the dense fluid. Turbulence structure is shown to be little affected by dense gas effects. For the adopted thermodynamic conditions, transport properties exhibit a liquid-like behavior and the local Reynolds number in the outer region is found to be much higher than in corresponding air flows. A priori analyses of the validity of some common modeling assumptions for the eddy viscosity and turbulent Prandtl number showed that, for a dense gas, turbulence models for eddy viscosity follow the exact trend more closely than in perfect gas (at the present high Mach numbers), due to the

higher local Reynolds number, but eddy viscosity is overestimated. An adjustment of the model constant could help improving the results. A peculiar behavior is observed for the turbulent Prandtl number close to the wall, which peaks more or less abruptly in the viscous sublayer, instead of tending to a constant value. Further investigations of the near wall thermal behavior are planned as future research.

Acknowledgements This work was granted access to the HPC resources of GENCI (Grand Equipement National de Calcul Intensif) under the allocation 7332.

References

1. Thompson, P.A.: A fundamental derivative in gasdynamics. Phys. Fluids **14**, 1843–1849 (1979)
2. Sciacovelli, L., Cinnella, P., Content, C., Grasso, F.: Dense gas effects in inviscid homogeneous isotropic turbulence. J. Fluid Mech. **800**, 140–179 (2016)
3. Sciacovelli, L., Cinnella, P., Grasso, F.: Small-scale dynamics of dense gas compressible homogeneous isotropic turbulence. J. Fluid Mech. (2017). In press
4. Sciacovelli, L., Cinnella, P., Gloerfelt, X.: DNS of supersonic turbulent channel flows of dense gases. J. Fluid Mech. **821**, 153–199 (2017)
5. Martin, J., Hou, Y.: Development of an equation of state for gases. AIChE J. **1**, 142–151 (1955)
6. Chung, T.H., Ajlan, M., Lee, L.L., Starling, K.E.: Applications of kinetic gas theories and multiparameter correlation for prediction of dilute gas viscosity and thermal conductivity. Ind. Eng. Chem. Res. **27**, 671–679 (1988)
7. Huang, P.G., Coleman, G.N., Bradshaw, P.: Compressible turbulent channel flows: DNS results and modeling. J. Fluid Mech. **305**, 185–218 (1995)
8. Patel, A., Peeters, J.W.R., Boersma, B.J., Pecnik, R.: Semi-local scaling and turbulence modulation in variable property turbulent channel flows. Phys. Fluids **27**, 095101 (2015)
9. Launder, B.E., Sharma, B.I.: Application of the energy-dissipation model of turbulence to the calculation of flow near a spinning disc. Lett. Heat Mass Transf. **1**, 131–138 (1971)
10. Chien, K.Y.: Predictions of channel and boundary-layer flow with a low-Reynolds turbulence model. AIAA J. **20**, 33–38 (1982)
11. Durbin, P.A.: Near-Wall turbulence closure modeling without "damping functions". Theoret. Comput. Fluid Dyn. **3**, 1–13 (1991)
12. Shih, T.H.: An improved $k-\varepsilon$ model for near-wall turbulence and comparison with direct numerical simulation. NASA TM 103221 (1990)

Part VII
Airfoils and Wings

Effect of Inflow Turbulence on LES of an Airfoil Flow with Laminar Separation Bubble

M. Breuer and S. Schmidt

1 Introduction

The turbulence intensity of the incoming flow can have a strong impact on the arising flow field around bodies especially when transition to turbulence plays an important role. A classical example is the flow past airfoils at moderate Reynolds numbers (e.g., for micro air vehicles), where laminar separation bubbles are often observed in the boundary layer on the suction side. For such cases experimental investigations carried out in different wind or water tunnels typically show strong variations of the separation, transition and reattachment locations, which to a great extent is caused by different levels of the turbulence intensity of the oncoming flow. Beside these deviations observed due to the natural turbulence level of the facility used, the effect of inflow turbulence becomes even more significant when the turbulence intensity is artificially increased for example by active or passive grids in order to mimic an atmospheric boundary layer. During the last years an increasing interest to simulate these flow phenomena is observed. Eddy-resolving simulations such as LES or hybrid LES-URANS are in principle the right choice for this challenging task. However, the inflow turbulence has to be prescribed in such a manner that it reaches the region of interest. Recently, a source term formulation [9] based on a synthetic turbulence inflow generator (STIG) was suggested. It allows to superimpose turbulent fluctuations in finer resolved flow regions, where the damping of small structures due to an inadequate grid resolution is negligible. This technique is applied here to investigate the flow past a SD7003 airfoil at $\mathrm{Re}_c = 60{,}000$ and an angle of attack $\alpha = 4°$ for a wide range of turbulence intensities of the oncoming flow ($0 \leq TI \leq 11.2\%$). The results of the reference case without inflow turbulence are compared with the predictions with increasing turbulence intensities.

M. Breuer (✉) · S. Schmidt
Professur für Strömungsmechanik, Helmut–Schmidt Universität Hamburg, Hamburg, Germany
e-mail: breuer@hsu-hh.de

M. V. Salvetti et al. (eds.), *Direct and Large-Eddy Simulation XI*,
ERCOFTAC Series 25, https://doi.org/10.1007/978-3-030-04915-7_46

2 Applied Methodology

Three main ingredients are required to carry out these investigations on the effect of the inflow turbulence:

1. *Eddy-resolving simulation methodology (LES)*:
   Here, a classic large-eddy simulation relying on a dynamic Smagorinsky model is used in order to appropriately resolve the transition process. In [7, 9] it was shown that this kind of flows can also be reliably predicted based on a hybrid LES-URANS approach. Nevertheless, in order to concentrate on the physical issues of the flow under investigation, the present study purely relies on LES predictions on a fine grid with about 17.2 million control volumes. The grid is refined near the wall with y^+ values below 1.5 allowing to resolve the viscous sublayer. The spanwise extension of the airfoil is a quarter of the chord length c and resolved by 100 grid points. A classical finite-volume approach for curvilinear body-fitted block-structured grids and a predictor-corrector scheme with an overall second-order accuracy in space and time is applied [1].
2. *Synthetic turbulence inflow generator (STIG)*:
   In the present study the method proposed by Klein et al. [5] is applied to generate artificial turbulent inflow data. It relies on discrete linear digital non-recursive filters which depend on statistical properties. These spatial and temporal correlations and the resulting length and time scales allow a straightforward adjustment on the flow situation of the particular case. Appropriate inflow data are generated by multiplying filter coefficients, which describe the two-point correlations and the autocorrelation of the inflow turbulence, with a series of random numbers. A required three-dimensional correlation between the filter coefficients is achieved by the convolution of three one-dimensional filter coefficients. Moreover, the cross-correlations between all three velocity components and thus the representation of a realistic inflow behavior is guaranteed due the application of the method by Lund et al. [6]. The required time and length scales are based on experimental data of Hain et al. [3] carried out in the empty water tunnel. In dimensionless form these are $T \cdot u_\infty/c = 0.118$ and $L_y/c = L_z/c = 0.118$, i.e., an isotropic flow is assumed. Six different turbulence intensities are studied. First, the case without inflow turbulence ($TI = 0\%$) is studied and taken as reference. Next, the turbulence intensities is set to $TI = 0.7\%$. Finally, the turbulence is doubled step by step ($TI = 1.4\%, 2.8\%, 5.6\%$) ending up at $TI = 11.2\%$.
3. *Source term concept of the STIG*:
   In the usual application (see, e.g., [8]) the resulting velocity fluctuations are superimposed on appropriate mean velocities and applied as inflow conditions at the inlet. However, the inlet region of such configurations often provides only a grid resolution which leads to a strong damping of small flow structures. Thus, a highly damped flow field reaches the airfoil after a certain development length. To overcome this problem, the fluctuations are introduced by a newly developed source term formulation $S_{u_i}^{\mathrm{syn}}$ in the momentum equations [2, 9]. It allows to shift the artificial turbulence generation closer to the airfoil, where a higher resolution

guarantees the correct development of the flow structures. The source term given by Eq. (1) is added to the filtered momentum equations in a small influence area explained below. Its formulation is based on the ratio between the synthetically generated velocity fluctuations $(u_i')^{\mathrm{syn}}$ and the integral time scale T. The latter is already used by the STIG and thus no additional quantity besides the known quantities of the generation procedure is required:

$$S_{u_i}^{\mathrm{syn}} = \int_{\mathrm{V}} \frac{\rho \left(u_i'\right)^{\mathrm{syn}}}{T} \, dV \, . \tag{1}$$

Considering the physical meaning of the integral time scale T within the source term formulation, this quantity can be interpreted as a relaxation time defining a time interval required for a reaction of the system to changes of the undistributed flow field. In order to reduce the required development length of the synthetic turbulence and to avoid discontinuities, the source terms are superimposed in a predefined influence area which in the present case is located about one chord length c upstream of the leading-edge of the airfoil. Based on a Gaussian bell-shaped distribution the source terms are scaled within this influence area. The streamwise extension of this region is defined by twice the integral length scale L_x in main flow direction calculated with the help of the integral time scale and the Taylor hypothesis (more details in [2, 9]). Thus, all required parameters are directly coupled to the synthetic inflow generator and the source term formulation does not demand any additional empirical parameters.

3 Results, Discussion and Conclusions

In Fig. 1 snapshots of the instantaneous flow fields based on the Q-criterion are shown for three different inflow turbulence intensities, i.e., $TI = 0.0\%$, 1.4% and 5.6%. Additionally, for $TI = 0.0\%$ contours of the streamwise velocity in one x-y-slice are depicted. The effect of the oncoming turbulence is obvious. Without any inflow turbulence the flow separates at about 20% of the chord length in the laminar regime close to the leading edge. A strong separated shear layer develops. Due to the Kelvin–Helmholtz instability a roll-up of vortices is observed at about the middle of the suction side, where these flow structures are more or less two-dimensional. Further downstream with the onset of transition these develop into a fully three-dimensional flow field. In the turbulent flow regime the reattachment of the flow is found at about 70% of the chord length. The resulting pressure-induced thin laminar separation bubble can also clearly detected in the contour of the turbulence intensity (not shown here), which has a strong peak in the region where transition takes place.

The situation changes completely for the case with inflow turbulence. For these cases two-dimensional flow structures are no longer visible. In the region, where the time-averaged flow depicts the tiny laminar separation bubble, the developing flow

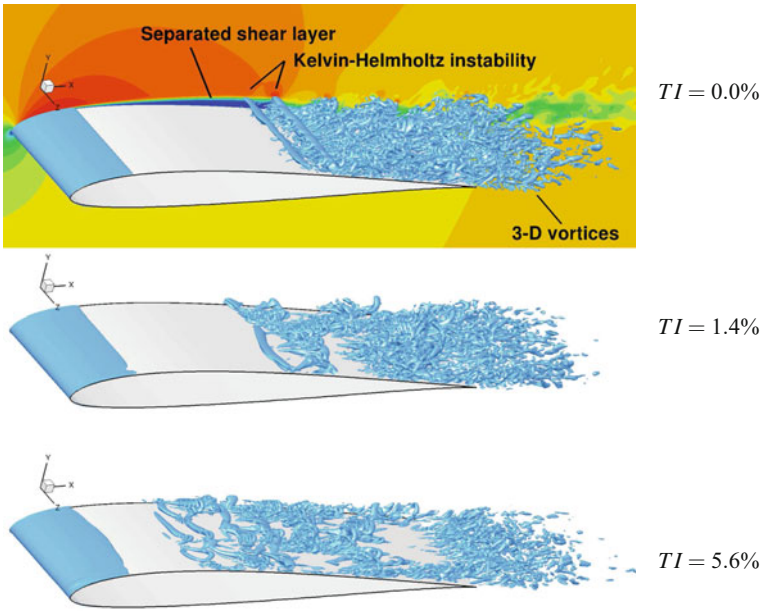

Fig. 1 Instantaneous snapshot of the flow for $TI = 0.0\%$, 1.4% and 5.6% based on the dimensionless Q–criterion (Q = 250). For the reference case without inflow turbulence the contour of the streamwise velocity is included

structures are three-dimensional from the beginning. Furthermore, with increasing inflow turbulence intensities the separation is more and more delayed, whereas the transition onset and the reattachment are moving upstream until finally the laminar separation bubble vanishes completely. These trends can be discussed more clearly based on the averaged flow field (time-averaging $\Delta T > 1300$ and averaging in spanwise direction).

For this purpose, Fig. 2 depicts the results of all six LES predictions of the flow past the SD7003 airfoil with identical setups except for the turbulence intensity of the oncoming flow. A strong influence on the pressure coefficient $c_p = (p - p_\infty)/(0.5\,\rho u_\infty^2)$ and the friction coefficient $c_f = \tau_w/(0.5\,\rho u_\infty^2)$ is obvious. Without any inflow turbulence the situation is as follows: Due to the positive pressure gradient in streamwise direction the laminar boundary layer on the suction side separates quite early ($x_{sep}/c = 0.21$) building up a laminar separation bubble. Transition onset is observed inside the separation bubble leading to the subsequent reattachment of the flow ($x_{rea}/c = 0.68$) and a closed rather thin separation bubble with a pressure plateau inside (Fig. 2, upper). Increasing the level of turbulence of the approaching flow leads to an increased momentum exchange. That results in a delayed separation and further downstream to an earlier transition onset. Subsequently, the reattachment point is found further upstream. The resulting separation locations are $x_{sep}/c = 0.25$, 0.27 and 0.3 for $TI = 0.7\%$, 1.4% and 2.8%,

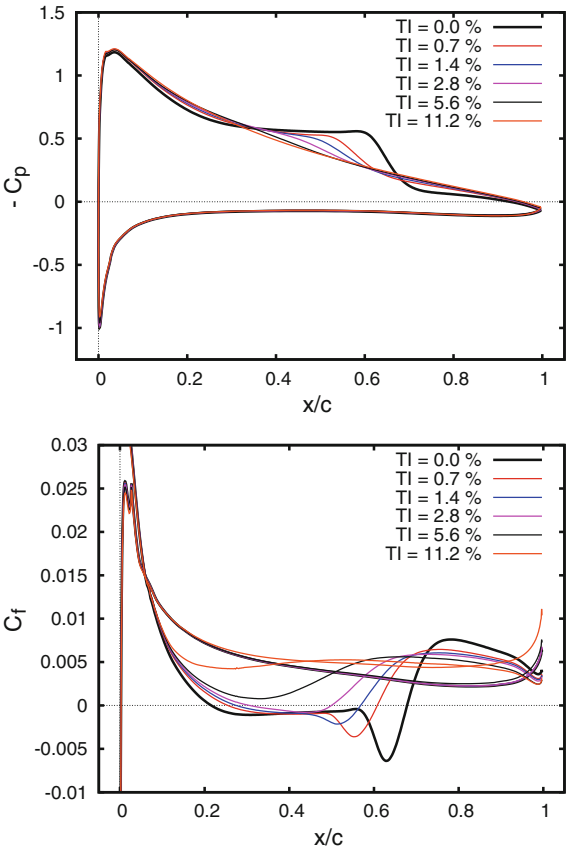

Fig. 2 Distribution of the pressure coefficient c_p and the friction coefficient c_f at $\mathrm{Re}_c = 60{,}000$ and $\alpha = 4°$ based on the averaged flow for six different inflow turbulence intensities

respectively. Accordingly, the reattachment point moves upstream to $x_{\mathrm{rea}}/c = 0.6$, 0.56 and 0.5 for the three inflow turbulence levels mentioned above. At the two highest turbulence intensities ($TI = 5.6\%$ and 11.2%) the laminar separation bubble completely disappears in the averaged flow, which coincides with recent measurements [4] at $TI \approx 10\%$. Contour plots of the turbulent kinetic energy and the Reynolds shear stress (not depicted here for brevity) indicate that the boundary layer is turbulent on the suction side for these cases. The size of the pressure plateau found for $TI = 0.0\%$ reduces significantly already for $TI = 0.7\%$. Then, each doubling of the inflow turbulence intensity further decreases the extension of the plateau until it vanishes completely.

Finally, Fig. 3 depicts the effect of the inflow turbulence on the time-averaged lift and drag of the airfoil. The attenuation of the laminar separation bubble by an increased inflow turbulence level significantly reduces the drag coefficient. A minimum is found at the turbulence intensity at which the laminar separation bubble disappears. At $TI = 5.6\%$ a saturation appears and the drag increases again for higher

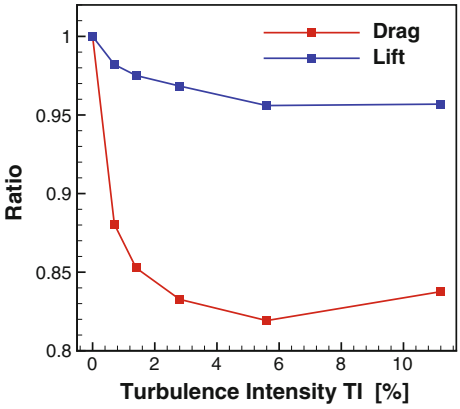

Fig. 3 Ratio of the lift and drag coefficient for different inflow turbulence intensities. All values are scaled by the corresponding lift and drag coefficient of the reference case without inflow turbulence

TI. The lift is affected in a similar manner but the maximal variations are only about 4%, whereas for the drag reductions up to about 18% are observed.

In conclusion, the inflow turbulence strongly influences the flow development, which was successfully predicted based on the proposed methodology. With increasing turbulence intensity the separation is more and more delayed and the transition onset appears earlier. Consequently, also the reattachment shifts upstream until finally the laminar separation bubble disappears. As an outlook other length scales of the incoming turbulence have to be taken into account in the investigations (see [2]). Finally, in the near future these simulations will be compared in detail with corresponding measurements presently carried out by Herbst et al. [4] using passive turbulence-generating grids upstream of the airfoil.

References

1. Breuer, M.: Direkte Numerische Simulation und Large-Eddy Simulation turbulenter Strömungen auf Hochleistungsrechnern. Habilitationsschrift, Universität Erlangen-Nürnberg. Berichte aus der Strömungstechnik. Shaker, Aachen (2002)
2. Breuer, M.: Effect of inflow turbulence on an airfoil flow with laminar separation bubble: An LES study. Flow Turbul. Combust. **101**, 433–456 (2018)
3. Hain, R., Kähler, C.J., Radespiel, R.: Dynamics of laminar separation bubbles at low-Reynolds number aerofoils. J. Fluid Mech. **630**, 129–153 (2009)
4. Herbst, S.L., Kähler, C.J., Hain, R.: SD7003 airfoil in large-scale free stream turbulence. In: 35th AIAA Applied Aerodynamics Conference, AIAA AVIATION Forum, (AIAA 2017-3748) Denver, CO, 5-9 June (2017)
5. Klein, M., Sadiki, A., Janicka, J.: A digital filter based generation of inflow data for spatially-developing direct numerical or large-eddy simulations. J. Comput. Phys. **186**, 652–665 (2003)
6. Lund, T.S., Wu, X., Squires, K.D.: Generating of turbulent inflow inlet data for spatially-developing boundary layer simulations. J. Comput. Phys. **140**, 233–258 (1998)
7. Schmidt, S., Breuer, M.: Hybrid LES-URANS methodology for the prediction of non-equilibrium wall-bounded internal and external flows. Comput. Fluids **96**, 226–252 (2014)

8. Schmidt, S., Breuer, M.: Extended synthetic turbulence inflow generator within a hybrid LES-URANS methodology for the prediction of non-equilibrium wall-bounded flows. Flow Turbul. Combust. **95**, 669–707 (2015)
9. Schmidt, S., Breuer, M.: Source term based synthetic turbulence inflow generator for eddy-resolving predictions of an airfoil flow including a laminar separation bubble. Comput. Fluids **146**, 1–22 (2017)

Flow Around Thick Airfoils at Very High Reynolds Number. Stall and Dynamic Stall Applications

F. Barnaud, P. Bénard, G. Lartigue, V. Moureau and P. Deglaire

1 Introduction

With the increase of the power and rotor diameter of modern wind turbines, blade loads must be predicted with high confidence in order to optimize accurately the complex blade internal structure. Unsteady aerodynamic loadings such as dynamic stall are the main challenges for state-of-the-art numerical tools [5]. Dynamic stall can appear on horizontal-axis wind turbines (HAWT) in several operating conditions: misalignment with the wind direction, free-stream turbulence, fast pitch maneuvers... Wind tunnel experiments and RANS or URANS simulations are the state-of-the-art tools to obtain estimations of aerodynamic forces, specifically in stall and dynamic stall cases. The present work aims at getting a better insight into the dynamics of the flow around thick wind turbines airfoils thanks to Large-Eddy Simulation (LES), which resolves a broader range of turbulent scales. These thick airfoils operate at very high Reynolds number because of the dimensions of the rotor. In order to perform LES with realistic CPU time, a Wall-Modeled LES (WMLES) strategy is considered. Several simulations are carried out at Reynolds number of $1.6 \cdot 10^6$ on the FFA-W3-

F. Barnaud (✉) · P. Bénard · G. Lartigue · V. Moureau
CORIA, CNRS UMR 6614, Normandie Université, INSA and University of Rouen, 76801 Saint-Étienne-du-Rouvray, France
e-mail: felix.barnaud@coria.fr

P. Bénard
e-mail: pierre.benard@coria.fr

G. Lartigue
e-mail: ghislain.lartigue@coria.fr

V. Moureau
e-mail: vincent.moureau@coria.fr

P. Deglaire
Adwen, 60 Avenue du Général de Gaulle, 92800 Puteaux, France
e-mail: paul.deglaire@adwenoffshore.com

M. V. Salvetti et al. (eds.), *Direct and Large-Eddy Simulation XI*,
ERCOFTAC Series 25, https://doi.org/10.1007/978-3-030-04915-7_47

Table 1 Mesh characteristics

Mesh	Control volumes[a]	Spanwise length	Mean Y^+	Mean X^+, Z^+	CPU time[a,b] for 50 s
M1	7.5 M	0.25c - 4c	25	250	0.5 kHrs
M2	17 M	0.25c - 2c	9	100	3 kHrs
M3	55 M	0.25c - 1c	3	40	50 kHrs

[a]For Span = 0.25c
[b]Steady attached cases, Intel Xeon Broadwell 2.30 Ghz cores

241 profile, a 24.1% relative thickness profile. Attached flow is first investigated, then detached flow in steady and oscillating conditions are studied. The impact of spanwise length is considered, in particular for stalled cases.

2 Methodology

Considering the airfoil chord c, the 3D computational domain is modeled as a circle of radius $15c$ extruded in spanwise direction, the airfoil being located at the center. Periodic conditions are applied spanwise. The spanwise length sensitivity is tested in steady conditions with values from $0.25c$ to $4c$ [3]. Spanwise length convergence study reveals that for attached cases, a spanwise length of 0.25c is enough to capture correctly the 3D behavior of small vortices created after transition zone. However, this length is not enough to capture correctly the larger vortices that appear in stalled conditions, creating unrealistically stable 2D vortices which prevent the airfoil to stall correctly. If the span is lower than $1c$ in stalled cases, aerodynamic forces undergo strong variations corresponding to the presence of large 2D vortices. With a span over $1c$, mean aerodynamic forces still appear to evolve slightly up to $2c$. Three unstructured hybrid meshes with different resolutions are defined in Table 1. Prism layers are generated around the airfoil, with an aspect ratio between 10 and 15 on the wall and a growth rate of 1.25. The global growth rate for tetrahedra is 1.10. The minimum tetrahedron size goes from $3 \cdot 10^{-4}c$ (mesh M1) to $3 \cdot 10^{-3}c$ (mesh M3) close to the airfoil whereas the maximum size is around $0.1c$ in the whole domain.

Calculations are performed using the parallel LES YALES2 code [7]. The code solves the incompressible Navier–Stokes equations with central 4th-order finite-volume schemes and specific domain decomposition that allows very good performances on large super-computers. The WALE turbulence model is used [8]. As described in Sect. 3, 4th-order artificial viscosity [1] has been used in stalled cases to compensate the under-resolution of the flow near the wall. A tabulated wall-law model described in [6] is applied to the airfoil for meshes M1 and M2. For mesh M3, a logarithmic law with viscous sublayer behavior is chosen, considering the small Y^+ values obtained with this mesh. The calculations are performed on 128–4096 Intel Xeon Broadwell 2.30 Ghz cores. Considering the non-dimensional distance traveled by airfoil in semi-chords $s = 2Vt/c$, with V the fluid velocity at inlet, and

t the physical time, around 50 s are needed to obtain converged statistics in attached flow cases, and 200 s in stalled cases due to the unsteady nature of the flow. For oscillating cases, the moving frame strategy is chosen in order to model the airfoil motion: velocity source terms are added in the momentum transport equation and boundary conditions are modified during the simulation, keeping fixed connectivity and metrics.

3 Results

Several **steady cases** with constant angle of attack (AoA) are investigated in order to validate the computational methodology. These cases are compared with experimental data measured at the VELUX open jet wind tunnel [2] and with the Rfoil code [9], which has been proven to be accurate for such cases. Attached cases correspond to small AoAs, for which the flow remains attached to the airfoil, with constant aerodynamic forces. Detached flows appear at high angle of attack, creating large vortical structures and unsteady forces on the profile.

When comparing force coefficients in Fig. 1, the Rfoil results show very good agreement with LES, with around 1% difference on the lift coefficient in attached cases. The three meshes with a span length of $0.25c$ are able to obtain correct forces.

However, this methodology is not satisfying for stalled angles, leading to unrealistically high lift values. This issue was overcome by extending the span length to $2c$ and adding artificial viscosity. This artificial viscosity is introduced because in the stalled case, the separated boundary layer may cross the prism/tetrahedron transition, a region where the central finite-volume schemes need stabilization. Two methodologies for attached and stalled cases are thus defined regarding spanwise length and use of artificial viscosity. Less than 10% difference with Rfoil in stalled cases are then obtained. The experimental data have been obtained with an estimated background turbulence intensity of 1%, which can justify the lower measured lift coefficient as no turbulence is injected in the LES simulation. Figure 2 shows very good correlation of the pressure coefficient between experiment, LES results

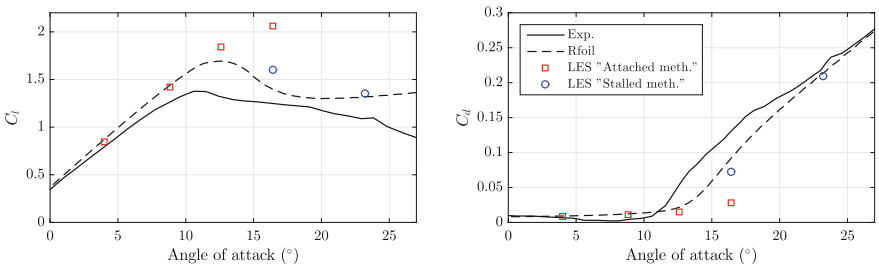

Fig. 1 Aerodynamic forces coefficients comparison - Attached and stalled methodologies

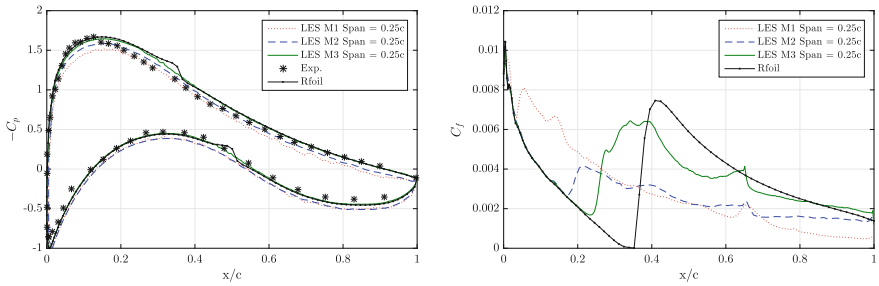

Fig. 2 Pressure and friction coefficients comparison for AoA = 4°

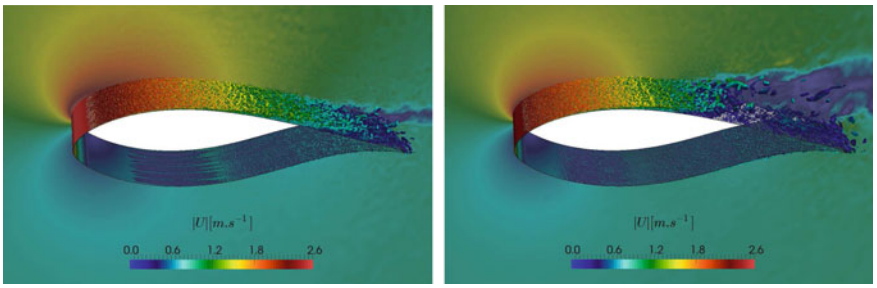

Fig. 3 AoA = 16.4° without (left) and with (right) artificial viscosity - M1 mesh

and Rfoil code [9]. The friction coefficient in attached cases converges toward Rfoil results as the mesh gets finer: the transition is better predicted with finer meshes, without significant consequences on pressure coefficient. For stall angles, Mesh M3 is able to obtain results close to Rfoil with the stalled methodology. Figure 3 show iso-surfaces of Q-criterion colored by the norm of velocity.

Separation is only correctly obtained with artificial viscosity. The flat pressure coefficient after mid-chord in Fig. 4 characterizes the separation, despite friction coefficient prediction is not improved by artificial viscosity. Near stall cases (angle of attacks between 12° and 16°) have proven to be much more complex to obtain than attached and deep stall cases, for which coarse meshes have given satisfying results despite the poor prediction of transition.

Oscillations in the flow close to transition zone are not well captured by the mesh, triggering locally artificial viscosity with the same order of magnitude than physically modeled viscosity, as can be observed in Fig. 5. The sensitivity of separation point prediction to the amount of artificial viscosity introduced is low, raising questions regarding the difficulty to capture it without.

Pitching cases both in attached and detached flows conditions are then studied. Few studies on such configurations have been conducted with LES, most at lower Reynolds number and for thin airfoils [4, 10]. The reduced frequency k is defined as $k = \pi f c/V$, with f the pitching frequency. The center of rotation is located at $x/c = 0.4$, with x the position of the rotation center along the chord. The parameters

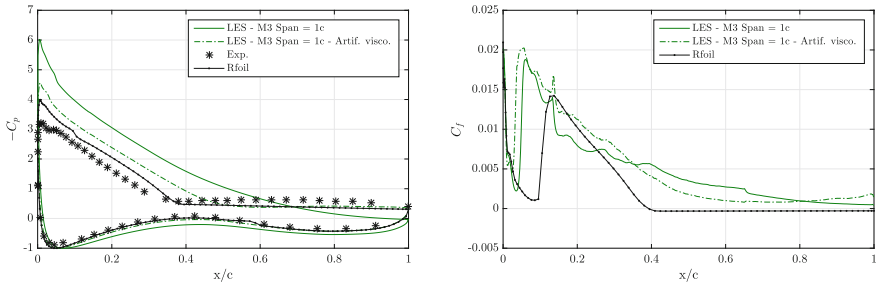

Fig. 4 Pressure and friction coefficients comparison for AoA = 16.4° - M1 mesh

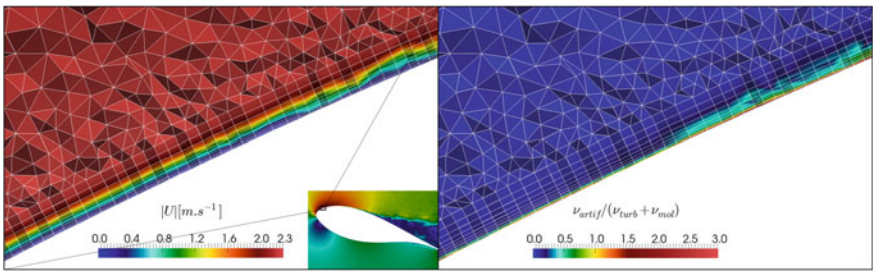

Fig. 5 Velocity and artificial viscosity near transition zone - AoA = 16.4° - M1 mesh

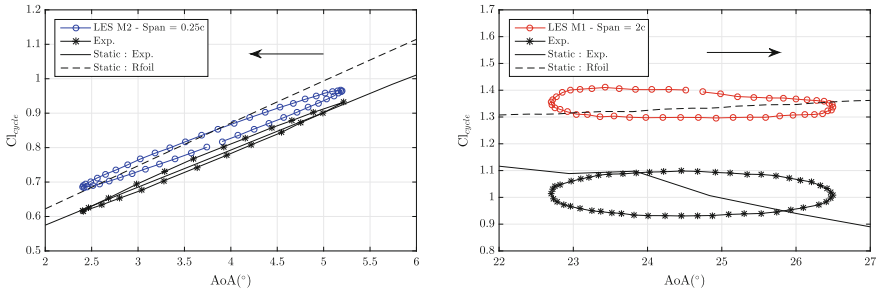

Fig. 6 Average cycle values of lift coefficient - Dynamic attached (left) and detached (right) cases

α_{mean} and α_{amp} are respectively the mean and amplitude values of angle of attacks. Two cases have been studied based on the available experimental data, both with $k = 0.093$: an attached case with $\alpha_{\text{mean}} = 3.8°$ and $\alpha_{\text{amp}} = 1.4°$, and a deep stall case with $\alpha_{\text{mean}} = 24.6°$ and $\alpha_{\text{amp}} = 1.9°$.

Figure 6 compares the experimental results with the current study for both attached and detached cases. The mean cycle values for aerodynamic forces can be obtained with less than 5 cycles in attached cases, which represent around 330 s in the present configuration. To obtain correct cycle average values in stalled case, more than 30 cycles are needed, which leads to prohibitive CPU time even with the coarsest mesh M1. More investigations should be carried on with M2 mesh to verify the behaviour

observed with mesh M1. In both attached and attached cases, the hysteresis loop is correctly captured, but the shift observed in steady cases between experimental and numerical results is still present.

4 Conclusion

Wall-Modeled LES are performed on static cases with success, with correct prediction of aerodynamic force coefficients when compared to state-of-the-art numerical tools. Pressure coefficients have shown very good correlation with both experimental and numerical data. Mesh convergence study has shown that a correct prediction of transition with realistic CPU time still seems a challenge. Stalled cases are more challenging than attached cases, and the separation point prediction was obtained with extended span and artificial viscosity, with a behavior that must be further investigated. These results exhibit larger discrepancies around stall angle, while attached cases and deep stall cases are correctly captured with coarse meshes. Based on these results, dynamic cases have been performed in attached and deep stall conditions with acceptable results. Further validation should then be performed.

Acknowledgements This work was granted access to the HPC resources of IDRIS, CCRT and CRIANN, under the allocations GENCI/x20172b6186 and CRIANN/2008013, respectively. This study is part of the MOQUA project managed by IRT Jules Verne (French Institute in Research and Technology in Advanced Manufacturing Technologies for Composite, Metallic and Hybrid Structures). The authors wish to associate the industrial and academic partners of this project: IRT Jules Verne, Adwen, Loiretech, UBS, Nenuphar, ECN and CNRS.

References

1. Cook, A.W., Cabot, W.H.: A high-wavenumber viscosity for high-resolution numerical methods. J. Comput. Phys. **195**(2), 594–601 (2004)
2. Fuglsang, P.: Wind tunnel tests of the FFA-W3-241, FFA-W3-301 and NACA 63–430 airfoils, Risø-R-1041(EN). Risø National Laboratory, Roskilde (1998)
3. Fukumoto, H., Aono, H., Nonomura, T., Oyama, A., Fujii, K.: Significance of computational spanwise domain length on LES for the flowfield with large vortex structure. In: Proceedings of 54th AIAA Aerospace Sciences Meeting (2016)
4. Kim, Y., Xie, Z.-T.: Modelling the effect of freestream turbulence on dynamic stall of wind turbine blades. Comput. Fluids **129**, 53–66 (2016)
5. Leishman, J.G.: Challenges in modeling the unsteady aerodynamics of wind turbines. In: 21st ASME Wind Energy Symposium, Reno, NV, USA, pp. 85–132 (2002)
6. Maheu, N., Moureau, V., Domingo, P., Duchaine, F., Balarac, G.: Large-eddy simulations of flow and heat transfer around a low-Mach number turbine blade. In: Proceedings of the Summer Program 2012, Center for Turbulence Research (2012)
7. Moureau, V., Domingo, P., Vervisch, L.: Design of a massively parallel CFD code for complex geometries. Comptes Rendus Mécanique **339**(2), 141–148 (2011)
8. Nicoud, F., Ducros, F.: Subgrid-scale stress modelling based on the square of the velocity gradient tensor. Flow, Turbul. Combust. **62**, 183–200 (1999)

9. van Rooij, R.P.J.O.M.: Modification of the boundary layer calculation in RFOIL for improved airfoil stall prediction. In: Report IW-96087R TU-Delft, the Netherlands (1996)
10. You, D., Bromby, W.: Large-eddy simulation of unsteady separation over a pitching airfoil at high Reynolds number. In: Proceedings of ICCFD7, Big Island, Hawaiii (2012)

On the Resolution of Mean Skin Friction by Hybrid RANS/LES Simulations at High Reynolds Numbers

N. Renard and S. Deck

1 Motivation of Hybrid RANS/LES Treatments of Wall-Bounded Turbulence at High Reynolds Number

The incentive to numerically resolve wall-bounded turbulent fluctuations instead of resorting to RANS modelling is given by applications such as unsteady load or aeroacoustic predictions, by limitations of the universality of the RANS approaches and by flow situations dominated by the upstream boundary layer dynamics, such as mild flow separations. At the high Reynolds numbers of aerospace applications, the cost of a DNS of wall-bounded turbulence is however prohibitive, and the reduction provided by Wall-Resolved LES (WRLES) is not substantial because of the near-wall dynamics. Consequently, the only affordable approach is Wall-Modelled LES (WMLES) [4]. Among the possible strategies [13], a near-wall RANS zone may be coupled with the LES of the outer zone in a hybrid RANS/LES context which focuses LES on the zones of interest of the flow, for instance defined by the user in the framework of Zonal Detached Eddy Simulation (ZDES [3], among other popular methods such as [2, 17]). The ZDES technique has been validated for both academic and industrial use and its mode 3 can perform a WMLES [4]. The proper prediction of mean skin friction is crucial for applied aerodynamics, but in a hybrid context comes the question: what are the contributions of the RANS model and of the LES resolved fluctuations? This is especially interesting at high Reynolds number where the logarithmic layer plays a growing role in the boundary layer dynamics, for instance with very large scale motions (or superstructures [8]) which WMLES is expected to resolve. In order to evaluate the RANS and LES contributions to

N. Renard (✉) · S. Deck
ONERA The French Aerospace Lab, Meudon, France
e-mail: nicolas.renard@onera.fr

S. Deck
e-mail: sebastien.deck@onera.fr

M. V. Salvetti et al. (eds.), *Direct and Large-Eddy Simulation XI*,
ERCOFTAC Series 25, https://doi.org/10.1007/978-3-030-04915-7_48

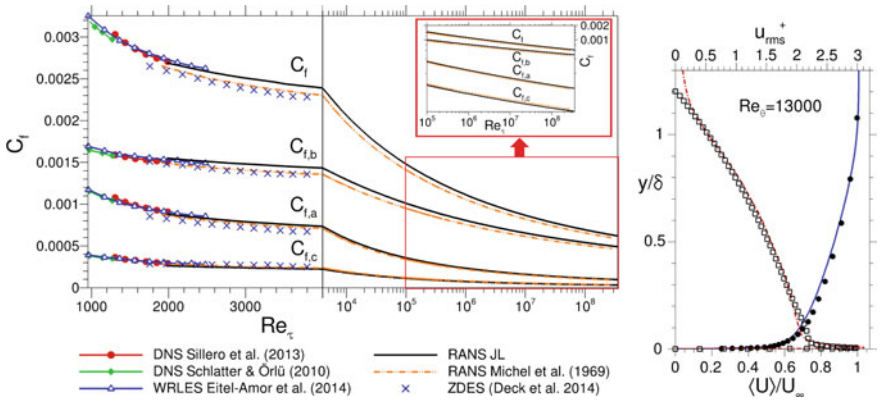

Fig. 1 Evolution of the C_f decomposition (1) with the Reynolds number (left). ZDES WRLES [5] profiles at $Re_\theta = 13\,000$ ($Re_\tau = 3\,600$): mean velocity (solid line) compared with experimental data by [6] (circles), u^+_{rms} (dash-dotted line) compared with the model by [10, 11] (squares) (right)

mean skin friction in Sect. 3, a physical scale decomposition of mean skin friction generation is first presented in the next section.

2 Towards a Physical Scale Decomposition of the Generation of Mean Skin Friction

A decomposition of the generation of mean skin friction into physical phenomena localised within the boundary layer has been derived in [15] based on a mean streamwise kinetic energy budget written in an absolute reference frame bound to the outer fluid undisturbed by the wall, resulting in the following relation for the skin friction coefficient $C_f = \nu\,(\partial\,\langle u\rangle\,/\partial y)(y=0)/\left(1/2\,U_\infty^2\right)$ in a zero-pressure-gradient flat-plate incompressible boundary layer:

$$C_f = \underbrace{\frac{2}{U_\infty^3}\int_0^\infty \nu\left(\frac{\partial\,\langle u\rangle}{\partial y}\right)^2 dy}_{C_{f,a}} + \underbrace{\frac{2}{U_\infty^3}\int_0^\infty -\left\langle u'v'\right\rangle\frac{\partial\,\langle u\rangle}{\partial y}dy}_{C_{f,b}} + \underbrace{\frac{2}{U_\infty^3}\int_0^\infty (\langle u\rangle - U_\infty)\,\frac{\partial}{\partial y}\left(\frac{\tau}{\rho}\right)dy}_{C_{f,c}} \tag{1}$$

with the wall distance y and the total shear stress $\tau/\rho = \nu(\partial\,\langle u\rangle\,/\partial y) - \left\langle u'v'\right\rangle$. This decomposition describes what the mean mechanical energy provided by the wall to the fluid in the absolute reference frame becomes. The first term represents direct dissipation into heat, the second term ($C_{f,b}$) corresponds to the production of turbulent kinetic energy (TKE), whereas the third term stands for the actual gain of mean streamwise kinetic energy by the fluid.

The evaluation of the decomposition in Fig. 1 using DNS and WRLES datasets [7, 16, 18, 19] and RANS simulations (from the ONERA boundary layer code CLICET

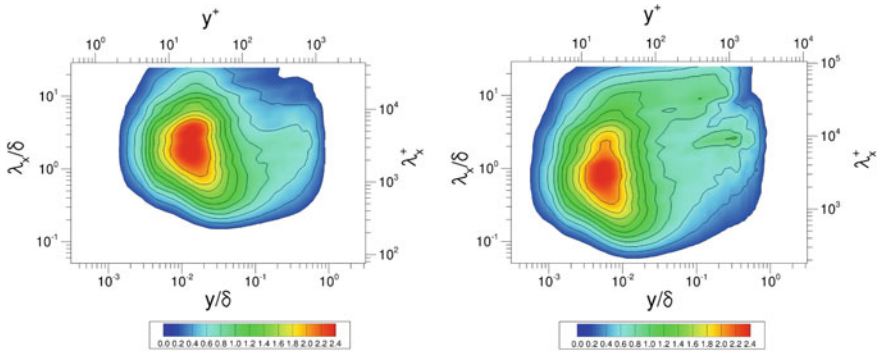

Fig. 2 Reynolds number impact on the streamwise velocity spectra $k_x G_{uu}(k_x)/u_\tau^2$ (left: $Re_\theta = 5\,200$, right: $Re_\theta = 13\,000$, reconstructed from ZDES with a correlation-based convection velocity)

[1] with Jones and Launder [9] $k-\epsilon$ (JL) model and Michel et al. [12] model) shows that the $C_{f,b}$ term is dominating the high-Reynolds-number turbulent behaviour of C_f. As discussed in [15], this is caused by the increasingly important contribution of the logarithmic layer to TKE production at high Reynolds number. For this reason, the following analysis of the contribution of turbulence (modelled and resolved) to mean skin friction at high Reynolds number focuses on the contribution to TKE production (represented by $C_{f,b}$). This term already exhibits the wall-distance distribution of the contribution, and it can be further decomposed into the contributive scales of motion by means of a spectral analysis of the Reynolds shear stress. Assuming that only the large scales are resolved, this decomposition will be used in Sect. 3 to relate the resolved fraction of $C_{f,b}$ to the resolved scales larger than a wall-distance-dependent cut-off. The analysis resorts to a WRLES database obtained with the ZDES technique (see a validation of the outer layer in [5] and an illustration of the profiles and C_f prediction in Fig. 1). The station considered is $Re_\theta = 13\,000$, a rather high value which is necessary for superstructures to be visible in the streamwise velocity spectra (Fig. 2).

The Reynolds shear stress spatial spectra are reconstructed from time signals using a frequency-dependent convection velocity [14], and used to estimate the cumulative resolved contribution to TKE production defined as:

$$\mathscr{C}(y,\lambda_x) = \frac{\int_y^\infty -\left\langle u'v'\right\rangle_{\mathrm{res},[\lambda_x;+\infty[} \frac{\partial\langle u\rangle}{\partial y} dy}{\int_0^\infty -\langle u'v'\rangle \frac{\partial\langle u\rangle}{\partial y} dy} \tag{2}$$

where $\left\langle u'v'\right\rangle_{\mathrm{res},[\lambda_x;+\infty[}$ is the Reynolds shear stress carried by the resolved fluctuations of wavelength greater than λ_x. The result in Fig. 3 shows for instance that the superstructures ($\lambda_x \geq 3\delta$) in the region $y^+ \geq 100$ contribute approximately 0.19 times the total TKE production ($\mathscr{C}(y^+ = 100, \lambda_x = 3\delta) \approx 0.19$).

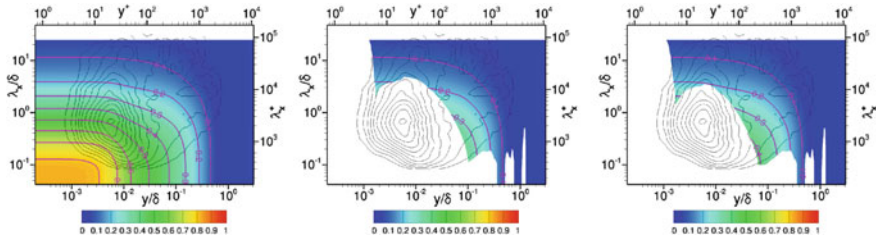

Fig. 3 Cumulative resolved contribution to TKE production $\mathscr{C}(y, \lambda_x)$ (2) at $Re_\theta = 13\,000$ predicted by ZDES in WRLES mode (together with $k_x G_{uu}(k_x)/u_\tau^2$ in black isolines) (left). Expected modelled scales blanked out for ZDES in WMLES mode: interface $y = 0.1\delta$ (middle) and $y^+ = 3.9\sqrt{Re_\tau}$ (right)

3 Assessment of the Fraction of Mean Skin Friction Resolved by Hybrid RANS/LES Methods

The scales that are expected to be modelled when the ZDES method is used as a WMLES are blanked out from the WRLES results in Fig. 3 at $Re_\theta = 13\,000$, assuming that the large scales are fully resolved down to a cut-off wavelength below which all smaller scales are fully modelled. Two different locations of the user-set RANS/LES interface are considered: $y = 0.1\delta$ and $y^+ = 3.9\sqrt{Re_\tau}$. The cut-off wavelength is determined such that the resolved contribution to the Reynolds shear stress matches an assumed resolved fraction given by a function illustrated in Fig. 4. This function grows linearly from 0 at the wall to 1 at the RANS/LES interface, and is constant equal to 1 above the interface. This is a simplified but fair representation of the general behaviour observed for ZDES calculations, as shown in Fig. 4 with two different interface settings and a WMLES mesh (note that the previously introduced WRLES simulation required 26 times as many grid points as these WMLES simulations for the same test case, showing the benefit of the WMLES approach over WRLES). Although the assumptions made are very simple, the scales blanked out in Fig. 3 include quite convincingly the inner spectral site corresponding to the near-wall turbulent cycle, which is to be represented by the wall model instead of being resolved. Conversely, the near-wall footprint of the largest scales is preserved. The lower interface setting ($y^+ = 3.9\sqrt{Re_\tau}$) provides with a wider range of expected resolved scales, without surprise.

The actual resolved fraction of $C_{f,b}$ (1) is directly evaluated in Fig. 5 for the two WMLES cases of ZDES with no assumption (the resolved and modelled Reynolds shear stresses are taken from the statistics of the simulations). The lower interface setting leads to a higher resolved fraction, greater than 50% at $Re_\theta = 13\,000$. The trend at higher Reynolds number is evaluated from RANS simulations with an assumed resolved fraction of Reynolds shear stress given by the function described in Fig. 4. The result suggests that the resolved fraction of $C_{f,b}$ decreases when the interface is set at $y = 0.1\delta$, whereas it tends to a constant value of 50% with the $y^+ = 3.9\sqrt{Re_\tau}$ interface setting at very high Reynolds number. This difference

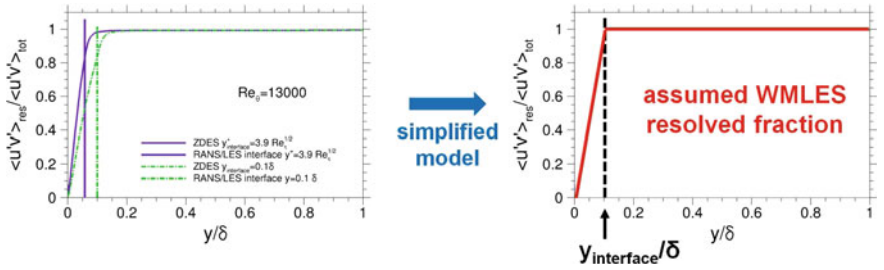

Fig. 4 Resolved fraction of Reynolds shear stress for ZDES in WMLES use

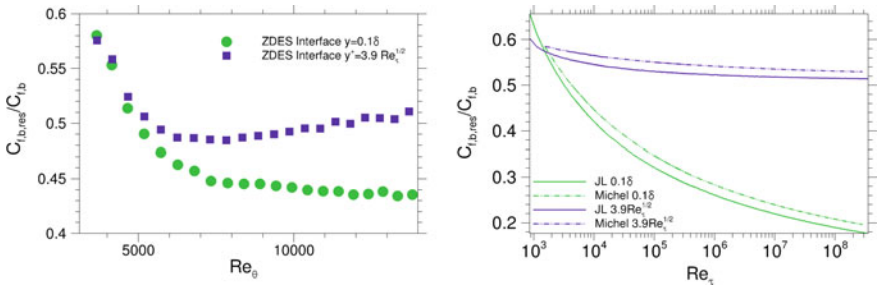

Fig. 5 Resolved fraction of $C_{f,b}$. ZDES WMLES (left) and high-Reynolds number RANS predictions assuming the simplified resolved fraction of Reynolds shear stress illustrated in Fig. 4 (right)

illustrates the dominant role played by the logarithmic layer at very high Reynolds number.

4 Outlook

The contribution of the resolved and modelled turbulence to mean skin friction in a WMLES performed by a zonal hybrid RANS/LES method (the ZDES technique) has been discussed. This involves a physical decomposition of C_f whose second term ($C_{f,b}$, related to the production of TKE) is dominant at very high Reynolds number because of the logarithmic layer contribution. Hence the analysis focuses on $C_{f,b}$. When the RANS/LES interface is set at $y^+ = 3.9\sqrt{Re_\tau}$, approximately 50% of the total TKE production is resolved rather than modelled. A simplified representation of the profile of the resolved fraction of Reynolds shear stress in WMLES ZDES is applied to a WRLES database, suggesting that the unresolved scales include quite convincingly the inner energy site of the spectrum, consistent with the purpose of WMLES. This needs to be confirmed by the spectral analysis of a WMLES, including at higher values of the Reynolds number where new DNS databases would also offer useful insights.

Acknowledgements The authors wish to thank all the people involved in the past and present evolution of the FLU3M code. Romain Laraufie and Pierre-Élie Weiss are warmly acknowledged for very stimulating discussions. The WRLES computation was made thanks to the HPC resources from GENCI-CINES (Project ZDESWALLTURB, Grant 2012-[c2012026817]).

References

1. Aupoix, B.: Couches Limites Bidimensionnelles Compressibles. Descriptif et Mode d'emploi du Code CLICET - Version 2010. Technical Report RT 1/117015 DMAE, Onera, Octobre 2010
2. Choi, J.-I., Edwards, J.R., Baurle, R.A.: Compressible boundary-layer predictions at high Reynolds number using hybrid LES/RANS methods. AIAA J. **47**(9), 2179–2193 (2009)
3. Deck, S.: Recent improvements in the Zonal Detached Eddy Simulation (ZDES) formulation. Theor. Comput. Fluid Dyn. **26**, 523–550 (2012)
4. Deck, S., Renard, N., Laraufie, R., Sagaut, P.: Zonal Detached Eddy Simulation (ZDES) of a spatially developing flat plate turbulent boundary layer over the Reynolds number range $3\,150 \leq Re_\theta \leq 14\,000$. Phys. Fluids **26**, 025116 (2014)
5. Deck, S., Renard, N., Laraufie, R., Weiss, P.-É.: Large scale contribution to mean wall shear stress in high Reynolds number flat plate boundary layers up to $Re_\theta = 13\,650$. J. Fluid Mech. **743**, 202–248 (2014)
6. DeGraaff, D.B., Eaton, J.K.: Reynolds number scaling of the flat plate turbulent boundary layer. J. Fluid Mech. **422**, 319–346 (2000)
7. Eitel-Amor, G., Örlü, R., Schlatter, P.: Simulation and validation of a spatially evolving turbulent boundary layer up to $Re_\theta = 8\,300$. Int. J. Heat Fluid Flow **47**, 57–69 (2014)
8. Hutchins, N., Marusic, I.: Evidence of very long meandering features in the logarithmic region of turbulent boundary layers. J. Fluid Mech. **579**, 1–28 (2007)
9. Jones, W.P., Launder, B.E.: The prediction of laminarization with a two-equation model of turbulence. Int. J. Heat Mass Transf. **15**(2), 301–314 (1972)
10. Marusic, I., Kunkel, G.J.: Streamwise turbulence intensity formulation for flat-plate boundary layers. Phys. Fluids **15**(8), 2461–2464 (2003)
11. Marusic, I., Uddin, A.K.M., Perry, A.E.: Similarity law for the streamwise turbulence intensity in zero-pressure-gradient turbulent boundary layers. Phys. Fluids **9**, 3718–3726 (1997)
12. Michel, R., Quémard, C., Durant, R.: Application d'un schéma de longueur de mélange à l'étude des couches limites turbulentes d'équilibre. Note Technique 154, ONERA (1969)
13. Piomelli, U.: Wall-layer models for large-eddy simulations. Prog. Aerosp. Sci. **44**, 437–446 (2008)
14. Renard, N., Deck, S.: On the scale-dependent turbulent convection velocity in a spatially developing flat plate turbulent boundary layer at Reynolds number $Re_\theta = 13\,000$. J. Fluid Mech. **775**, 105–148 (2015)
15. Renard, N., Deck, S.: A theoretical decomposition of mean skin friction generation into physical phenomena across the boundary layer. J. Fluid Mech. **790**, 339–367 (2016)
16. Schlatter, P., Örlü, R.: Assessment of direct numerical simulation data of turbulent boundary layers. J. Fluid Mech. **659**, 116–126 (2010)
17. Shur, M.L., Spalart, P.R., Strelets, MKh, Travin, A.K.: A hybrid RANS-LES approach with delayed-DES and wall-modelled LES capabilities. Int. J. Heat Fluid Flow **29**, 1638–1649 (2008)
18. Sillero, J.A., Jimenez, J., Moser, R.D.: One-point statistics for turbulent wall-bounded flows at Reynolds numbers up to $\delta^+ \approx 2000$. Phys. Fluids **25**, 105102 (2013)
19. Sillero, J.A., Jimenez, J., Moser, R.D.: Two-point statistics for turbulent boundary layers and channels at Reynolds numbers up to $\delta^+ \approx 2000$. Phys. Fluids **26**, 105109 (2014)

DNS of Separated Low-Re Flow Around a Cambered Aerofoil

M. F. Shahab, M. Omidyeganeh and A. Pinelli

1 Introduction

Nowadays, Unmanned Air Vehicles (UAVs) are widely used in many societal, scientific and military applications. Recent improvements in manufacturing and control technology have led to the introduction of a new class of micro and even nano sized air vehicles (Micro/Nano UAVs) operating in flight conditions characterized by a medium-to-low Reynolds number regime. Their reduced size exposes this class of UAVs to the unsteadiness and vorticity embedded in the background flow. These interactions may lead to critical aerodynamic conditions such as massive separation, dynamic stall and aerodynamic hysteresis causing a drastic degradation of their aerodynamic performances. Aerofoils operating at low Reynolds number and high angle of attack can be classified into two distinct flow regimes according to the topology of the separated region. The latter can be either characterised by a closed separation bubble, or by a completely separated flow without boundary layer reattachment. The effect of low Reynolds number regimes and its impact on boundary layer separation and flow unsteadiness have been the subject of many previous studies. Formation and bursting of laminar separation bubbles (LSB), shedding of coherent vortices downstream of LSBs and development of the reattached turbulent boundary layer have attracted many investigators [1, 2]. Other phenomena like the flapping and the transition of the separated shear layer, or the formation and the shedding of wake vortices, have also received substantial attention in the literature because of their potential influence on the aerodynamic performances of an aerofoil [3, 7]. Although

M. F. Shahab (✉) · M. Omidyeganeh · A. Pinelli
City, University of London, London, UK
e-mail: muhammad.shahab@city.ac.uk

M. Omidyeganeh
e-mail: Omid.Yeganeh@city.ac.uk

A. Pinelli
e-mail: Alfredo.Pinelli.1@city.ac.uk

M. V. Salvetti et al. (eds.), *Direct and Large-Eddy Simulation XI*,
ERCOFTAC Series 25, https://doi.org/10.1007/978-3-030-04915-7_49

a comprehensive knowledge has been matured for the flow regime where the shear layer reattaches in pre-stall condition, detailed information on the dynamics of low Reynolds number fully separated flow regime in off-design conditions (post-stall) is not available in the current literature.

2 Numerical Formulation

Direct numerical simulations have been performed to investigate the main features of the flow around a NACA 65(12)10 cambered aerofoil at a chord based Reynolds number (Re_c) of 20,000. The aerofoil is set to a high angle of attack ($\alpha = 15°$) leading to fully separated conditions where no reattachment takes place on the foil. The present study, has been conducted using an in-house developed 3D incompressible Navier–Stokes solver (SUSA). The solver is second order accurate in time and space using cell centred finite volume approach. Readers interested in the solver and the extensive validation campaign can find further information in [6]. To generate the 3D mesh system around the wing, equally-spaced spanwise copies of a body fitted 2D, C-grid have been assembled. The external surface that bounds the wing contains both the inflow and outflow portions of the boundary. On the outflow region a non-reflective condition is used, while at the inlet Dirichlet values obtained from a companion potential flow solution are enforced. Standard impermeable, no-slip wall boundary conditions are used on the surface of the wing, while the spanwise end-planes are prescribed as periodic boundaries [6]. The simulations, that will be reported share the same chord Reynolds number and the same computational mesh on the 2D plane consisting of $N_\xi = 4321$ and $N_\eta = 1031$ cells along the two coordinate directions. The spanwise direction has been discretised using either $N_\zeta = 97$ or $N_\zeta = 293$ cells, for the spanwise extension $lz = 0.15c$ or $lz = 0.45c$, respectively. The grid spacing in terms of wall units, Δx^+, Δy^+ and Δz^+, in regions of attached boundary layer are kept in the range of 2.2, 0.4 and 1.5, respectively. This wall resolution is well within the resolution requirements of a wall resolved DNS [4]. However, in these massively separated flows, the mesh spacing in the regions accommodating the separated shear layer and the wake must be kept sufficiently small to capture the correct vortex shedding and flapping motion of the shear layer. Using the mentioned mesh, the grid resolution in terms of local Kolmogorov scale (η) in the shear layer region turned out to be $ds/\eta = 1.7$, $dn/\eta = 1.5$ and $dz/\eta = 2.2$, where ds, dn and dz are the grid spacings in streamwise, wall-normal and spanwise directions, respectively. These grids have been selected after having conducted a careful mesh convergence analysis. Figures 1 and 2, clearly highlight the impact of using a smaller lz on the flow topology. In particular, the two figures display the instantaneous isosurfaces of Q-criterion colored with the spanwise vorticity levels. For these type of largely separated flows the spanwise extent of the domain has a substantial influence on the flow structures. In particular, the shorter domain features more organised and spanwise-aligned quasi 2D vortex tubes and streamwise oriented braids. These structures maintain their coherence even in the far wake region. However, the flow field generated in the larger

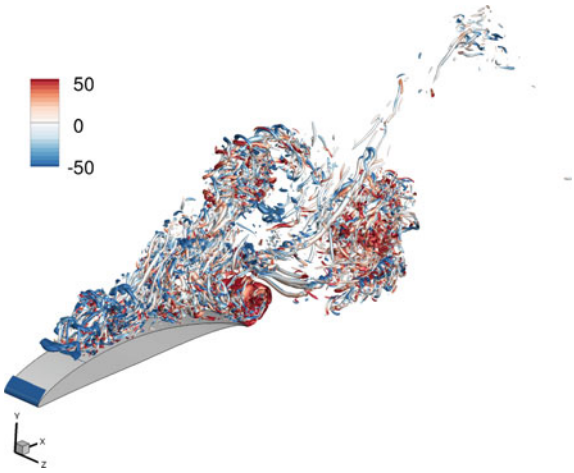

Fig. 1 Instantaneous isosurfaces of Q-criterion colored with the spanwise vorticity levels: Short Spanwise Domain (0.15c)

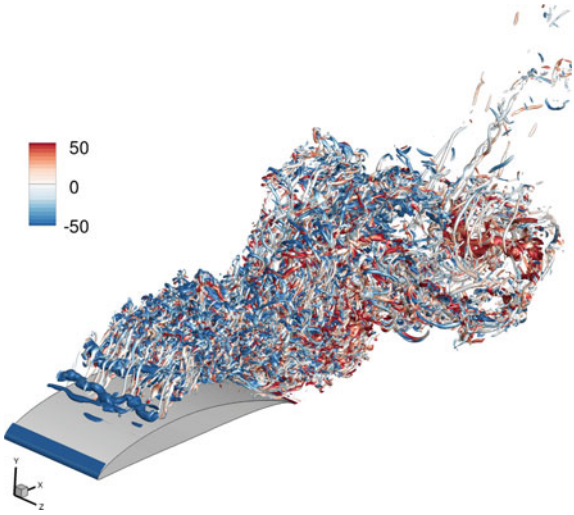

Fig. 2 Instantaneous isosurfaces of Q-criterion colored with the spanwise vorticity levels: Large Spanwise Domain (0.45c)

domain does not present any very large scale coherent motions and the vorticity seems to be of finer grain, probably as a consequence of a larger non-linear activity in the transition region that destabilises the vortex tubes causing them to lose their spanwise coherence leading to a field with a higher degree of three-dimensionality. Changing the spanwise extension of the computational domain has also a dramatic impact on many other flow features that include the shedding frequencies, wake extent, and three-dimensionality of the flow field (e.g., the values of $\overline{w'w'}$). All the results in the next section have been obtained considering the larger computational box.

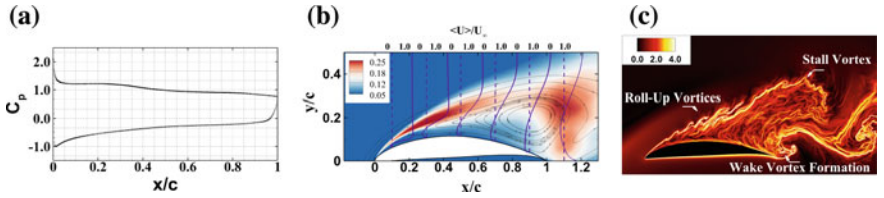

Fig. 3 **a** Variation of pressure coefficient along the surface of NACA 65(12)10 aerofoil at 15°. **b** Isocontours of streamwise Reynolds stresses superposed over the mean velocity profiles. **c** Instantaneous iso-contours plot of the FTLE

3 Results

High-Reynolds number experiments on the selected NACA 65(12)10 aerofoil, have shown that for an incidence of $10° < \alpha < 17°$, the lift coefficient presents a plateau region typical of fully stalled conditions [5]. For our low-Reynolds number simulations, at the selected angle of attack ($\alpha = 15°$), a post-stall condition is achieved in Fig. 3a that displays the distribution of time and spanwise averaged pressure coefficient ($C_p = (p - p_\infty)/(0.5\rho_\infty U_\infty^2)$) along the surface of the aerofoil. Downstream of the initial suction peak at the leading edge, the laminar boundary layer detaches and a nearly constant pressure region follows along the chord length indicating a boundary layer separation without reattachment [1, 7]. Further evidence of a fully separated regime can be evinced from the distribution of the mean velocity profile and the contours of streamwise Reynolds stresses $\overline{u'u'}$ along the foil (Fig. 3b) showing that at this low Re_c and high angle of attack, the flow separates near the leading edge and remains detached along the whole extent of the aerofoil. The separated region is characterised by a massive recirculation region, with velocity profiles having well-defined inflexion points and also exhibiting a thick wake region downstream of the trailing edge. The contours of $\overline{u'u'}$ take on high values in the separated shear layer and in the aerofoil near wake. At $x/c = 1.1$, the maximum turbulence intensity reaches a value of $0.5U_\infty$ and the extracted profile (not shown here) exhibiting a double peak located at $y/c = 0.11$ and 0.25, resembling the experimental study of Yarusevych et al. [8], that are ultimately generated by the cores of the vortices originating from the suction and pressure sides of the aerofoil.

To gain some insights into the structure of the separated shear layer and wake vortex formation, an instantaneous snapshot of the attracting finite-time Lyapunov exponent (FTLE) [6] is shown in Fig. 3c. The FTLE analysis highlights the region of the flow which are more prone to present a clear separation line between flow behaviours being as a space measure of the trend of neighbouring fluid particles to diverge in their trajectory. The qualitative comparison of the results presented here are in agreement with Rosti et al. [6] and Yarusevych et al. [7] that have identified the formation of the roll-up vortices in the shear layer to be associated with a Kelvin–Helmholtz type instability at the leading edge. An examination of the unsteady shedding mechanism reveals that the initial stage of the transition of the

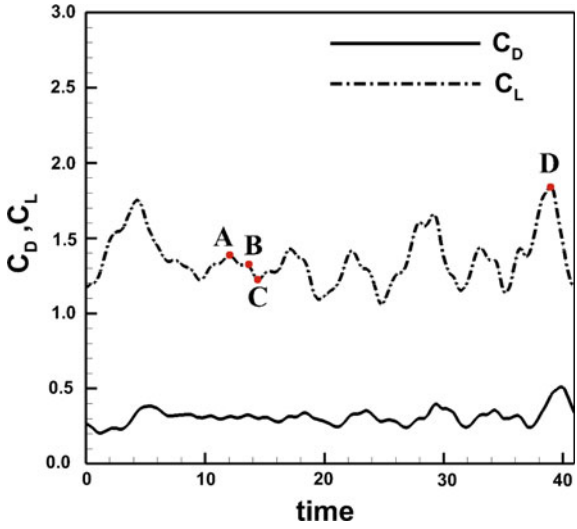

Fig. 4 Lift (C_L) and Drag (C_D) coefficients as a function of time Mean values: $C_L = 1.36$ and $C_D = 0.31$

separated shear layer is dominated by the linear growth of roll-up instability while the later stage is dominated by non-linear interactions of the coherent structures that leads to the formation of a large turbulent stall vortex. On its downstream trajectory, this stall vortex entrains fluid from the outer region towards the wall until a saturated condition is reached and a massive detachment is finally produced. The wake vortex formation also plays a major role in controlling the aerodynamic performance of the aerofoil. At high angle of attack, the formation of the large trailing edge vortex induces an upstream motion of the low momentum flow towards the leading edge. This counter flow is considered to be responsible for the unsteady flapping of the leading edge shear layer. Figures 4 and 5 present the variation of lift and drag coefficients as a function of time and the corresponding spectrum of the lift coefficient. These graphs and the snapshots of corresponding iso-contours of spanwise vorticity (Fig. 6a–d) may help in unravelling key events in the regeneration cycle of the large scale vortices that ultimately govern the fluid behaviour and thus may also provide insights for the development of novel flow control strategies. In particular, the C_L fluctuations characterised by a long time period (e.g., A-B-C) correspond to the flow evolution between states at maximum (e.g., events A and D) and minimum lift conditions (e.g., C). Flow states like the event B are also selected to sample the flow behaviour between these conditions of maximum/minimum lift. Events like A and D, correspond to maximum lift conditions occurring when the separated shear layer is lifted up at its highest position. In this condition, the entrainment of momentum within the stall vortex is maximised together with the associated low suction pressure region on the top of the aerofoil. At the same time, a wake vortex is shed from the trailing edge and following one is under formation. The scenarios depicted in A and D are not identical: the strength of the created stall vortex and also the difference in streamwise distance between the already detached and newly forming

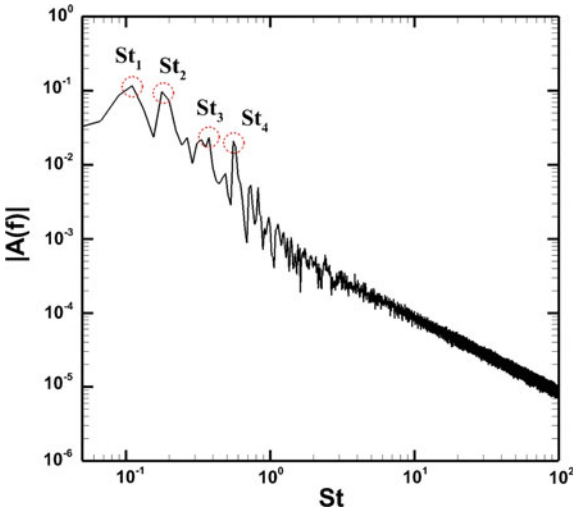

Fig. 5 Single-sided amplitude spectrum of $C_L(t)$

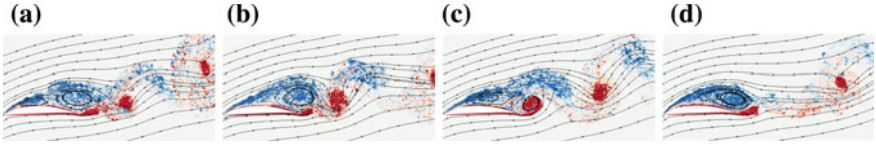

Fig. 6 **a** Event A. **b** Event B. **c** Event C. **d** Event D

vortex lead to a higher value of C_L in event D. Snapshot B takes place during the interaction between the two vortices before a detachment event. In this situation, the shear layer pushes downward the fluid on the top surface inducing a downstream acceleration that eject the trailing edge vortex into the wake. Event C corresponds to a minimum lift condition. The flow attains this configuration when the shear layer reaches its lowest location and the recently formed stall vortex starts entraining outer momentum into the recirculation region. In this condition, the wake vortex reaches its maximum circulation being on the verge of detachment from the trailing edge.

A careful inspection of about 1200 snapshots of spanwise vorticity spanning over a period of 40 time units (tU_∞/c) has been used to estimate the characteristic flapping and vortex shedding periods. This analysis allows to associate with a good degree of confidence the frequency peaks of the C_L spectrum with the salient features of the flow. In the frequency spectrum of C_L given in Fig. 5, the peak $St_2 = 0.18$ corresponds to the low frequency flapping motion of the shear layer while $St_4 = 0.58$ represents the principal vortex shedding frequency. The interaction between those two unsteady phenomena give rise to other clearly identified unsteady modes, the $St_1 = 0.11$ and $St_3 = 0.38$ which are representative of the very low frequency flapping of the shear layer and a time lag in the shedding of vortices. The non-

dimensional value of the wake shedding frequency in terms of Strouhal number defined based on of the projected length of the aerofoil on the cross-stream plane is $St_d = fc\sin\alpha/U_\infty = 0.15$. This value lies within the range 0.12–0.22 as reported by Huang and Lin [3] for a NACA 0025 aerofoil (in supercritical regime).

4 Summary

We have considered a deeply stalled flow over an infinite span, cambered wing at low Reynolds number. The main conclusions have concerned the importance of the domain extension in the spanwise direction and the origin and interactions of the main flow structures. In particular, a too small domain introduces artificial but energetic coherent motions that disappear when the domain size is increased. It has been found that the dynamics of shear layer formed at the leading edge and the trailing edge wake together with their interplay dominate the time behaviour of the flow field inducing the flapping of the shear layer and the delay of vortex shedding in the wake. Of course, it is expected the detailed characteristics of the wake evolution and of the shear layer development depend on the Reynolds number, the angle of attack and the aerofoil geometry. In particular, for a given aerofoil in stalled conditions the number of frequency peaks in the spectrum is expected to grow with the Reynolds number [3, 7]. It is also evident that the irregular high frequency shear layer instabilities are not represented by a single peak in the spectrum but spreads over a continuous range of frequencies as also demonstrated by Huang and Lin [3]. However, as it happens in other *bluff body* flows, we believe that our study even if carried out at low Reynolds number still captures the largest scales of motion and their dominant interactions. Normally, these leading unsteadiness, induced by linear convective instabilities persists in the flow at even much higher Reynolds numbers.

Acknowledgements The authors gratefully acknowledge the support of the Engineering and Physical Sciences Research Council under the project Quiet Aerofoils of the Next Generation (EP/N020413/1) and ARCHER, the UK high-performance computing facility.

References

1. Gaster, M.: The structure and behaviour of laminar separation bubbles, Aerodynamics Division N.P.L., Report and Memoranda No. 3595 (1967)
2. Hain, R., Kahler, C.J., Radespiel, R.: Dynamics of laminar separation bubbles at low-Reynolds-number airfoils. J. Fluid Mech. **630**, 129–153 (2009)
3. Huang, R.F., Lin, C.L.: Vortex shedding and shear-layer instability of wing at low-Reynolds numbers. AIAA J. **33**(8), 1398–403 (1995)
4. Jones, L.E., Sandberg, R.D.: Acoustic and hydrodynamic analysis of the flow around an aerofoil with trailing-edge serrations. J. Fluid Mech. **706**, 295–322 (2012)

5. Liu, X., Jawahar, J.K., Azarpeyvand, M., Theunissen, R.: Aerodynamic and aeroacoustic performance of serrated airfoils. In: 21st AIAA/CEAS Aeroacoustics Conference, AIAA AVIATION Forum. Dallas, Tx (2015)
6. Rosti, M.E., Omidyeganeh, M., Pinelli, A.: Direct numerical simulation of the flow around an aerofoil in ramp-up motion. Phys. Fluids **28**, 025106 (2016)
7. Yarusevych, S., Sullivan, P.E., Kawall, J.G.: On vortex shedding from an airfoil in low-Reynolds-number flows. J. Fluid Mech. **632**, 245–271 (2009)
8. Yarusevych, S., Boutilier, M.S.H.: Vortex shedding of an airfoil at low Reynolds numbers. AIAA J. **49**(10), 2221–27 (2011)

High Reynolds Number Airfoil: From Wall-Resolved to Wall-Modeled LES

A. Frère, K. Hillewaert, P. Chatelain and G. Winckelmans

1 Introduction

Wall-Modeled Large-Eddy Simulation (WMLES) alleviates the near-wall grid requirement by employing a wall-model to reconstruct the wall shear-stress. In this way, WMLES simultaneously reduces the computational cost associated with Wall-Resolved LES (WRLES) and opens the door towards higher Reynolds numbers [1, 2].

Several complications still prevent its application to realistic industrial flow configurations. Firstly, there is no consensus regarding the accuracy and applicability of the many different wall-model approaches, in particular when applied in the presence of adverse pressure gradient (APG), separation and transition. Secondly, there is a lack of validation test cases. On the one hand, numerical databases usually concern Reynolds numbers too low to be relevant for WMLES. On the other hand, experimental measurements are often biased by setup and installation effects, such as the interaction with wind tunnel walls, that cannot be reproduced without incurring a significant computational overhead. The present project therefore aims at performing a WRLES of the widely used NACA4412 airfoil at near-stall condition, illustrated in Fig. 1, to

- provide a clean benchmark for the validation of WMLES or related approaches;

A. Frère (✉) · K. Hillewaert
Cenaero, Gosselies, Belgium
e-mail: ariane.frere@cenaero.be

K. Hillewaert
e-mail: koen.hillewaert@cenaero.be

A. Frère · P. Chatelain · G. Winckelmans
Institute of Mechanics, Materials and Civil Engineering (iMMC), Université catholique de Louvain (UCL), Louvain-la-Neuve, Belgium
e-mail: philippe.chatelain@uclouvain.be

G. Winckelmans
e-mail: gregoire.winckelmans@uclouvain.be

M. V. Salvetti et al. (eds.), *Direct and Large-Eddy Simulation XI*,
ERCOFTAC Series 25, https://doi.org/10.1007/978-3-030-04915-7_50

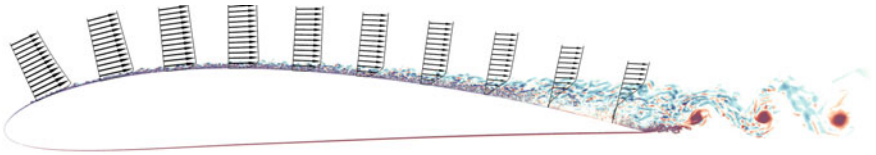

Fig. 1 Mean velocity profiles and instantaneous spanwise vorticity at $\alpha = 12°$ and $Re = 1.64 \times 10^6$

- extract from this database the quantities used as wall-model in- and outputs;
- use these quantities to assess the validity of various existing wall-models.

Instead of comparing the different models a posteriori by analyzing the results of different WMLES computations, the models will be confronted here in a priori manner on the basis of a wall-resolved LES. The focus of the comparison presented in this paper is on evaluating the model capacity to represent APG effects and, more specifically, in answering the following questions:

1. Can an analytical approach based upon Reichardt law-of-the-wall, assuming equilibrium, match velocity profiles stemming from APGs?
2. Does the analytical model of Shih [3], which explicitly includes the pressure gradient, improve Reichardt's law estimate?
3. Can the more advanced and expensive Two-Layer Model [4] be simplified by removing the convective and/or the pressure-gradient terms?

2 CFD Methodology and Computational Setup

The simulations are performed using the Discontinuous Galerkin (DG) method, selected for its accuracy, low dissipation and low dispersion on structured and unstructured meshes. The method is highly scalable and is thus a good candidate for LES of large-scale industrial applications [5]. Argo, the DGM code used in this study, solves the compressible Navier–Stokes equations with an Implicit LES (ILES) approach, in which the subgrid scale dissipation is provided by the numerical scheme. Argo has already been successfully validated and assessed on DNS, WRLES and WMLES of academic and industrial benchmarks such as the Taylor-Green vortex [6], the turbulent channel flow [7] and multiple low Reynolds number airfoils [8, 9].

The NACA4412 airfoil has been chosen as it constitutes a widely used case for the development and the validation of CFD methods. It has been recently used for testing WMLES approaches [10–12]. During this validation, questions remained on the impact of the experimental setup. Therefore it was decided to regenerate a high-resolution numerical reference to remove these uncertainties on the basis of a recent PRACE allocation. The WRLES computation is performed at $\alpha = 12°$ and $Re = 1.64 \times 10^6$, corresponding to Wadcock's experiment [13]. In this paper we present preliminary results obtained on the local Tier-1 cluster installed at Cenaero.

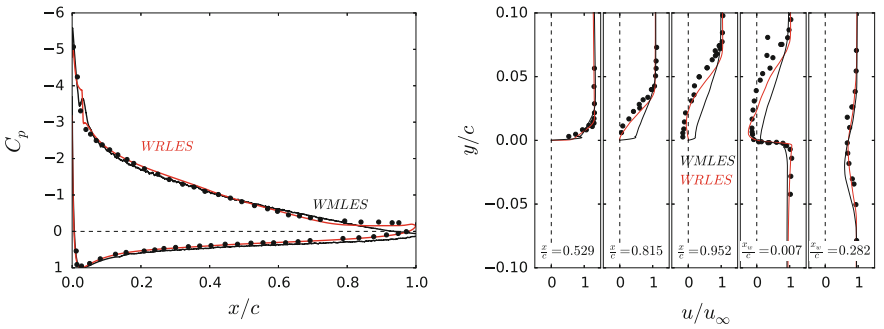

Fig. 2 Comparison of the WM- and WRLES results to the experiment from Wadcock (black circles) [13]. Chordwise pressure coefficient evolutions are on the left. Streamwise velocity profiles above the airfoil and in the wake are on the right

The simulation is performed on a mixed-element mesh, extruded in the spanwise direction. Due to limitations in computational resources, the span extent is restricted to 1% of the chord and the far-field boundary is placed 40 chords away. The very narrow span leads to two-dimensional wake vortices, see Fig. 1. For the purpose of developing and validating WMLES, the two-dimensionality of the near-wake might not be a problem, as the WMLES can be applied to the same geometry. Larger span and far-field extents will be considered in later computations to remove this issue. Cubic polynomials (P3) interpolate the solution within each cell. The effective streamwise, wall-normal and spanwise resolutions are $\Delta x^+ \leq 80$, $\Delta y^+ \leq 1.4$ and $\Delta z^+ \leq 25$, in agreement with the guidelines of Choi and Moin [14].

3 WRLES Results Compared to Experimental Data

According to the experimental observations [13], the flow presents a small laminar region followed by a laminar/turbulent transition, and a trailing-edge separation at $x/c \simeq 85\%$. In the experiment, the transition is forced using boundary layer tripping on both the suction and pressure side. Given modeling ambiguity and the artificial nature of such a device, the tripping is not considered in the computation. Nevertheless, transition occurs on the suction side almost exactly at the same position as in the experiment. Therefore, the computation appears to capture the general flow behavior observed in the experiment, see Fig. 1.

Figure 2 presents the chordwise pressure coefficient evolution and the velocity profiles obtained at three locations on the airfoil suction side and at two locations in the wake. The WRLES results are compared to the experimental results as well as to previously obtained WMLES results [10]. The fact that WMLES did not reproduce the flow at the last 20% of the chord was one of the first motivations for performing a WRLES. It was indeed not clear whether this discrepancy between WMLES and

experimental results was due to an improper wall-model or, more simply, to a different setup. As WRLES results provide a much better match to the experimental results, we conclude that the wall-model was responsible for the discrepancy, reducing somewhat the reservation regarding the experiment. However, even if a perfect match would be obtained, a numerical reference is needed to provide the detailed statistics and instrumentation required for model improvement and assessment.

4 WRLES Results Compared to Wall-Model Estimates

The most basic wall-models are based on analytical laws that provide a direct link between the velocity u at a certain wall-distance y and the wall-shear stress $\tau_w = \rho\, u_\tau^2$. The most widely used law is the Reichardt law-of-the-wall:

$$u^+ = \frac{1}{\kappa} ln\left(1 + \kappa y^+\right) + \left(C - \frac{1}{\kappa} ln\left(\kappa\right)\right)\left(1 - e^{-\frac{y^+}{11}} - \frac{y^+}{11} e^{-\frac{y^+}{3}}\right), \tag{1}$$

with $u^+ = \frac{u}{u_\tau}$ and $y^+ = \frac{y\, u_\tau}{\nu}$. Although this law is dedicated to equilibrium flows, it should be applicable to out-of-equilibrium flows as long as the input position is chosen below the end of the log-layer region. More advanced models include the APG explicitly. An example is the "Generalized law-of-the-wall" of Shih [3]:

$$u = \frac{\tau_w}{|\tau_w|} u_\tau\, f_1(y^+) + \frac{p^+}{|p^+|} u_p\, f_2\left(y^+ \frac{u_p}{u_\tau}\right), \tag{2}$$

with p^+ the pressure gradient in wall units and f_1 and f_2 calibrated fifth-order polynomials. This approach has basically the same cost as the equilibrium model, and produced promising results on a detached aircraft wing [15].

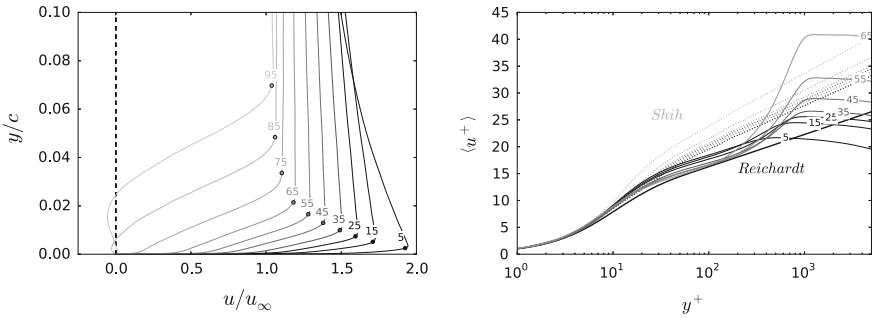

Fig. 3 Tangential velocity profile evolutions along the chord. WRLES results for $5\% \leq x/c \leq 95\%$ are presented on the left. WRLES data for $5\% \leq x/c \leq 65\%$ are confronted on the right to the estimations using Reichard (black line) and Shih's law (dotted line)

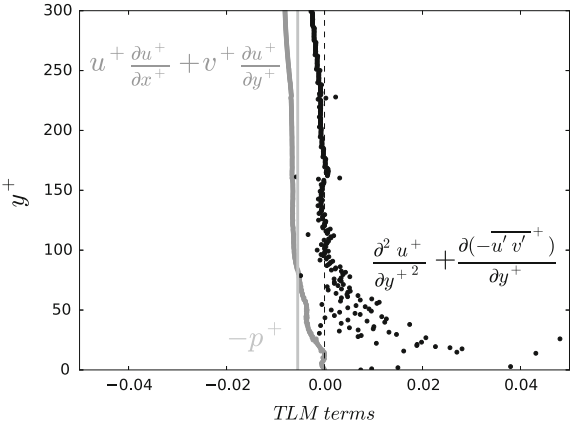

Fig. 4 Balance along the wall-distance of the convective (dark grey circles), pressure gradient (light gray line) and left-hand side terms considered in the TLM equation Eq. (3) (black circles), at $x/c = 35\%$

Both analytical approaches are compared in Fig. 3 that presents the streamwise velocity profiles at the locations indicated in Fig. 1. In physical coordinates, the deceleration and separation induced by the APG are clearly visible. The profiles submitted to a mild APG ranging $0.4\% \leq p^+ \leq 3.0\%$ are then compared in wall-units. All WRLES profiles between $5\% \leq x/c \leq 65\%$ present a quite large log-region and collapse on the Reichardt law-of-the-wall for $y^+ \leq 150$. If the wall-model input is chosen below that threshold, an equilibrium wall-model appears sufficient.

If one wants to use $y^+ \geq 150$, APG effects should be taken up in the model. Shih's law overestimates the impact of p^+ and neglects the log region. It is hence not adapted to the flow physics considered here. The "Two-Layer Model" (TLM) of Balaras et al. [4] couples LES to simplified RANS equations:

$$\frac{\partial^2 u^+}{\partial y^{+2}} + \frac{\partial(-\overline{u'v'}^+)}{\partial y^+} = p^+ + u^+\frac{\partial u^+}{\partial x^+} + v^+\frac{\partial u^+}{\partial y^+}, \tag{3}$$

This model is computationally more expensive, and is therefore often simplified. The main simplification neglects the convective term [16]. However, as mentioned in a recent review by Larsson et al. [2], the convective terms approximately balance the pressure gradient term, such that both should either be considered or neglected together. Figure 4 presents a balance of the TLM terms at $x/c = 35\%$, supporting Larsson et al.'s argument: below a certain distance, here $y^+ \simeq 150$, both terms balance and can be removed. Above, all terms likely need to be retained.

5 Conclusion and Perspectives

In the present work, a wall-resolved LES of the NACA4412 at $Re = 1.64 \times 10^6$ and $\alpha = 12.0°$ was performed in order to increase the understanding about boundary layer

physics and to serve the development of wall-modeled LES. The present WRLES results agree well to the experimental results. The differences observed previously between these experimental data and WMLES results were hence more likely due to an inadequate wall-model rather than a difference in setup.

The WRLES results permitted to shed light on some debates regarding APG modeling. The analysis showed that, on 70% of the chord, a basic wall-model as Reichardt's law-of-the-wall can be sufficient as long as it is used for $y^+ \leq 150$. It appears also that Shih's law, which is supposed to improve the APG capture, is not adapted to the considered flow case. Finally, an analysis of the TLM terms at $x/c = 35\%$ confirmed previous observations that the convective terms are almost balanced by the pressure gradient term in the region above the viscous sublayer and below $y^+ \simeq 150$. Therefore, to simplify the TLM equations, one should remove not only the convective terms but also the pressure gradient term.

In the near future, the study will be enlarged by repeating the presented analysis on the entire chord extent and by comparing other wall-models. A much larger WRLES calculation has also been launched to evaluate the eventual span and domain size impact, as well as to produce an open-database for WMLES validation.

Acknowledgements The author thanks Prof. Piomelli and Prof. Schlatter for their fruitful discussions. This research has been financed by the Walloon Region through the FirstDoCA framework. The study benefited from computational resources made available on the Tier-1 supercomputer of the Fédération Wallonie-Bruxelles (n°1117545).

References

1. Piomelli, U.: Wall-Modeled Large-Eddy Simulations: Present Status and Prospects. Springer, Netherlands (2010)
2. Larsson, J., Kawai, S., Bodart, J., Bermejo-Moreno, I.: Large-Eddy Simulation with modeled wall-stress: recent progress and future directions. Mech. Eng. Rev. **3** (2016)
3. Shih, T.-H.: A generalized wall function. NASA Technical report (1999)
4. Balaras, E., Benocci, C., Piomelli, U.: Two-layer approximate boundary conditions for large-eddy simulations. AIAA J. **34** (1996)
5. Hillewaert, K.: Development of the discontinuous Galerkin Method for high-resolution, large scale CFD and acoustics in industrial geometries. PhD Ecole polytech. de Louvain (2013)
6. Carton de Wiart, C., Hillewaert, K., Duponcheel, M., Winckelmans, G.: Assessment of a discontinuous Galerkin method for the simulation of vortical flows at high Reynolds number. Int. J. Numer. Meth. Fluids **74** (2013)
7. Frère, A., Carton de Wiart, C., Hillewaert, K., Chatelain, P., Winckelmans, G.: Application of wall-models to discontinuous Galerkin LES. Phys. Fluids **29** (2017)
8. Carton de Wiart, C., Hillewaert, K., Bricteux, L., Winckelmans, G.: LES using a DG Method: isotropic turbulence, channel flow and periodic flow. In: Proceedings of DLES 9 (2013)
9. Frère, A., Hillewaert, K., Sarlak, H, Mikkelsen, R.F., Chatelain, P.: Cross-validation of numerical and exp. studies of transitional airfoil performance. In: Proceedings of 33rd AIAA-ASME (2015)
10. Frère, A., Sørensen, N.N., Hillewaert, K., Chatelain, P., Winckelmans, G.: Discontinuous Galerkin methodology for LES of wind turbine airfoils. J. Phys. Conf. Ser. **753** (2016)
11. Park, G.I., Moin, P.: An improved dynamic non-equilibrium wall-model for large eddy simulation. Phys. Fluids **26** (2014)

12. Bose, S.T., Moin, P.: A dynamic slip boundary condition for wall-modeled large-eddy simulation. Phys. Fluids **26** (2014)
13. Wadcock, A.J.: Investigation of low-speed turbulent separated flow around airfoils. NASA Technical report 177450 (1987)
14. Choi, H., Moin, P.: Grid-point requirements for large eddy simulation: Chapman's estimates revisited. Phys. Fluids **24** (2012)
15. Brionnaud, R., Holmann, D.M., Modena, M.C.: Aerodynamic analysis of the 2nd AIAA High Lift Prediction Workshop by a Lattice-Boltzmann Method solver (2014)
16. Duprat, C., Balarac, G., Métais, O., Congedo, P.M., Brugière, O.: A wall-layer model for LES of turbulent flows with/out pressure gradient. Phys. Fluids **23** (2011)

Robust Feedback Control of Two and Three Dimensional Flow Separation Around a NACA0012 Profile Using Plasma Actuators

R. Broglia, D. Durante and L. Pasquale

1 Introduction

Closed-loop flow control is aimed at altering a natural flow state into a more desirable state, which is chosen depending on control objectives. The control input is usually an electric signal, which has to be converted to a physical quantity by means of an actuator. A new and original technology using non-thermal surface plasmas has witnessed a significant growth in interest in recent years, as they: have no moving parts; exhibit an extremely fast time-response; are characterised by low mass and low input power. These surface dielectric barrier discharge (DBD) actuators are used to accelerate the near-wall flow, thus modifying the velocity profile within the boundary layer. In this paper, we focus on the robust feedback control of the flow separation using plasma actuators. Our objective is to solve the problem of directly controlling the unsteady flow separation using real-time velocity measurements, which are available in realistic applications. We propose this flow separation problem as a practical application of the new theoretical results in [4]. The aim of this paper is to show how, despite the high complexity of the system, a simple robust output regulator is sufficient to effectively suppress the flow separation along an aerofoil, using two actuator/sensor pairs. Accurate two-dimensional (laminar flow) and three-dimensional (turbulent flow) numerical simulations of incompressible flows on a NACA0012 at Reynolds $Re = 20{,}000$ are performed in order to illustrate the effectiveness of the proposed approach. In the two-dimensional case a robust, fast flow reattachment is achieved,

R. Broglia (✉) · D. Durante
CNR-INM, Rome, Italy
e-mail: riccardo.broglia@cnr.it

D. Durante
e-mail: danilo.durante@cnr.it

L. Pasquale
University of Nottingham, Nottingham, UK
e-mail: laura.pasquale.3@gmail.com

M. V. Salvetti et al. (eds.), *Direct and Large-Eddy Simulation XI*,
ERCOFTAC Series 25, https://doi.org/10.1007/978-3-030-04915-7_51

along with both stabilisation and increase/reduction of the lift/drag, respectively. The control system shows good dynamic performances, as the angle of attack is varied. For the three-dimensional test, a Large Eddy Simulation (LES) approach has been chosen for the modelling of the turbulence dynamics, whereas the eddy viscosity is calculated according to the well established classical Smagorinsky model.

2 Problem Statement and Objectives

This paper addresses the practical problem of robustly controlling the unsteady flow separation over an aerofoil, using the plasma actuator voltage as the control input and realistically available real-time velocity measurements as the control output. In particular, we aim to formulate and solve the flow separation problem, i.e., to make

$$\partial_{\mathbf{n}} u_\tau(t,\mathbf{x})|_{\Gamma_N} = \big(\tau(\mathbf{x})\cdot\nabla\mathbf{u}(t,\mathbf{x})\cdot\mathbf{n}(\mathbf{x})\big)|_{\Gamma_N} > 0, \tag{1}$$

as a simple output regulation problem, i.e. to make the measured outputs

$$\mathrm{y}(t) = u_\tau(t,\mathbf{x}_{s_i}) = \tau(\mathbf{x}_{s_i})\cdot\mathbf{u}(t,\mathbf{x}_{s_i}) \geq \varepsilon > 0, \tag{2}$$

for $i = 1,\ldots,n_s$. Here: $\mathbf{u}$ is the time-dependent flow velocity vector; $\mathbf{x}$ and $\mathbf{x}_{s_i}$ denote the spatial coordinates and the ith sensor location, respectively; Γ_N represents the aerofoil boundary; $\mathbf{n}$ and τ are the normal and tangent unit vectors to Γ_N, respectively; n_s is the number of sensors.

Our objective is to design a robust output feedback control algorithm, along with suitable reference signals y_i^* for y_i, in order to suppress the flow separation along the aerofoil in unknown scenarios, depending on uncertain parameters, i.e., Reynolds number Re and angle of attack β. To this end, we assume there exist suitable configurations of actuators and sensors, along with suitable references ε_i for the outputs $\mathrm{y}_i(t)$, which guarantee that, given a certain range for both Re and β, the solution of the output regulation problem (2) implies the solution of the flow separation problem (1). This is formalised by the following assumption.

3 Flow Model

Let Ω be an open bounded domain in $\mathscr{R}^d$, where d denotes the dimension of the geometry, and let $T > 0$ denote the final time. The flow of an incompressible viscous Newtonian fluid can be described by the non-dimensionalised Navier–Stokes equations, which are derived from the conservation of mass and momentum, namely,

$$\begin{aligned} \partial_t\mathbf{u} &= -(\mathbf{u}\cdot\nabla)\mathbf{u} - \nabla p + \tfrac{1}{Re}\Delta\mathbf{u} + \mathbf{f} \ \text{ in } \ (0,T]\times\Omega, \\ 0 &= \nabla\cdot\mathbf{u} \qquad\qquad\qquad\qquad\quad \text{in } \ (0,T]\times\Omega, \end{aligned} \tag{3}$$

with suitable initial and boundary conditions. Here: $\mathbf{u}: [0,T]\times\Omega\to\mathscr{R}^d$ is the velocity vector; $p: [0,T]\times\Omega\to\mathscr{R}$ is the pressure; $Re=\rho U_\infty c/\mu$ is the Reynolds number; U_∞ is the free-stream velocity (in m/s); ρ is the fluid density (in kg/m^3); $c=0.1$ m is the chord length; $\mathbf{f}: [0,T]\times\Omega\to\mathscr{R}^d$ is the total body force vector field, which depends the control inputs. The latter can be expressed as $\mathbf{f}(t,\mathbf{x})=c/\rho U_\infty^2(f_x(t,\mathbf{x}),\, f_y(t,\mathbf{x}))=c/\rho U_\infty^2\sum_{j=1,\dots,n_a}\mathbf{f}^{(j)}(t,\mathbf{x})$, where n_a is the number of actuators and f_x, f_y are the streamwise and normal component (in N/m^3). All the above listed functions are assumed to be sufficiently smooth. The wall-tangential velocity $\mathrm{y}_i(t)=u_\tau(t,\mathbf{x}_{s_i}),$, evaluated at the selected sensor location $\mathbf{x}_{s_i}$, where τ denotes the tangent unit vector, is chosen as the measured output. Several models for the DBD actuator force have been proposed; here, we select a modified version of the recent model proposed by [6], which demonstrated good agreement with the experimental data. The model is characterised by an exponential dependence on the spatial coordinates and, in particular, the force is modelled by a Rayleigh distribution.

A Balanced Dynamic Mode Decomposition (BDMD) linear model [2] for given Reynolds number Re and angle of attack β, can be obtained in the following form:

$$\begin{cases}\dot{\xi}=A\xi+B\mathrm{v}, \quad \xi(0)=\xi_0,\\ \mathrm{y}=C\xi,\end{cases} \tag{4}$$

where: $\xi:\mathscr{R}\to\mathscr{R}^r$ is the reduced-order state vector; $A\in\mathscr{R}^{r\times r}$ is a low-order linear operator approximating the nonlinear dynamics, whose eigenvalues belong to the open left half of the complex plane; $B\in\mathscr{R}^{r\times n_a}$ is Let: I_r be the $r\times r$ identity matrix and $P(s)=C(sI-A)^{-1}B$, whose poles have all negative real part, be the open-loop $n_s\times n_a$ transfer function matrix of system (4). The number r of BDMD modes is chosen so that $\sum_{i=1}^{r}\sigma_i=99\%$, where σ_i are the Hankel singular values of the full-order model, thus yielding a linear, stable model of order $r=11$, which is both controllable and observable. The key objective is to design v such that the closed-loop trajectories of system (4) are guaranteed to evolve within some "*safe*" invariant set in different scenarios, depending on uncertain parameters (e.g., the Reynolds number Re and angle of attack β). The initial control objective (2) is then translated into the following: $\mathrm{y}_i(t)\in\Omega_{\varepsilon_i}=[\varepsilon_{m_i},\varepsilon_{M_i}]$, where ε_{m_i} and ε_{M_i} are chosen positive constants. In particular, the lower bound for the output reference can be chosen in order to guarantee any a priori fixed requirement, such as, in the present application, the suppression of the separation bubble over the aerofoil; the upper bound can be chosen in order to limit the power consumption. The resulting control algorithm reads (see [5])

$$\begin{cases}\dot{\hat{\eta}}_i=k_i\ \mathrm{sign}(P_{ii}(0))\tilde{\mathrm{y}}_i, \quad \hat{\eta}_i(0)=\hat{\eta}_{0_i},\\ \mathrm{v}_i=-\hat{\eta}_i,\end{cases} \tag{5}$$

for $i=1,\dots,n_p$, where $n_p=n_a=n_s$ is the number of actuator/sensor pairs and $\tilde{\mathrm{y}}_i=\mathrm{y}_i-\mathrm{y}_i^*$ is the regulation error. The overall control algorithm (5) depends on: the measured outputs y_i; the bounded references

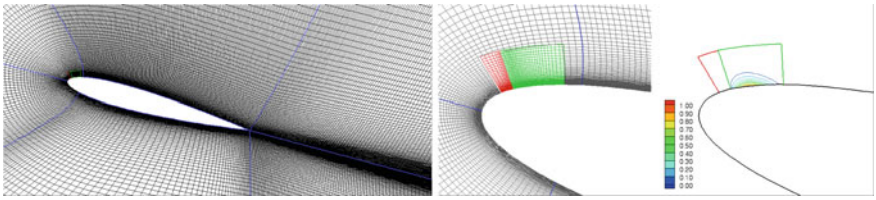

Fig. 1 Left, detailed view of the computational mesh around the profile; middle, detail of the actuator region; right, normalised plasma actuator force

$$\mathrm{y}_i^*(t) = \begin{cases} \varepsilon_{m_i}, & \text{if } \mathrm{y}_i(t) < \varepsilon_{m_i}, \\ \mathrm{y}_i(t), & \text{if } \mathrm{y}_i(t) \in \Omega_{\varepsilon_i}, \\ \varepsilon_{M_i}, & \text{if } \mathrm{y}_i(t) > \varepsilon_{M_i}; \end{cases} \tag{6}$$

the known sign of the diagonal elements $P_{ii}(0)$; the positive design parameters k_i, ε_{m_i}, ε_{M_i}. System (3) is discretised using χnavis, a general-purpose, second order, finite volume, multi-block, unsteady Reynolds averaged Navier–Stokes equations (uRaNSe) based solver, developed at CNR-INM. For the sake of conciseness, details of the numerical solver are not given here, the reader is addressed to [1, 3].

4 Numerical Results

The robustness of the proposed control scheme (5), (6), is tested at $Re = 20{,}000$ in a 2D configuration $\mathscr{C} = \{n_p = 2, \bar{x}_a^{(1)} = 0.02, \bar{x}_a^{(2)} = 0.6, \Delta_s^{(1)} = 0.2, \Delta_s^{(2)} = 0.2, \Omega_{\varepsilon_1} = [0.1, 0.15], \Omega_{\varepsilon_2} = [0.05, 0.1]\}$, where $\Delta_s^{(i)} \doteq |\bar{x}_a^{(i)} - \bar{x}_s^{(i)}|$, $i = 1, \ldots, n_p$. The angle of attack is varied within the range $\mathscr{R}_\beta = [5, 25]$; in particular, we considered two different scenarios: in the first scenario, the initial angle of attack $\beta_0 = 15°$ is, first, smoothly decreased to 5° and, then, increased to β_0 again. In the second scenario, the initial angle is, first, smoothly increased to 25° and, then, decreased to β_0 again.

The computational grid (for the two-dimensional simulations) has $N = 127,872$ total volumes and is divided into extremely fine actuator grids (see Fig. 1 right), a fine C-type inner grid (see Fig. 1 left) and coarser outer grids. The inner region around the profile has 320×96 volumes, in the tangent and normal direction, respectively; the points are clustered towards the wall, where the mesh spacing is equal to 2.1×10^{-4}. The presence of the plasma actuator is taken into account by a system of body forces distributed in the flow field within a block of fixed dimension and position. Both an example of the plasma actuator block and the distribution of the magnitude of its corresponding body force, normalised with respect to its maximum value, are shown in Fig. 1. In Fig. 2 the time histories of the drag and lift coefficients for both scenarios are compared with the corresponding time histories for the simulations with

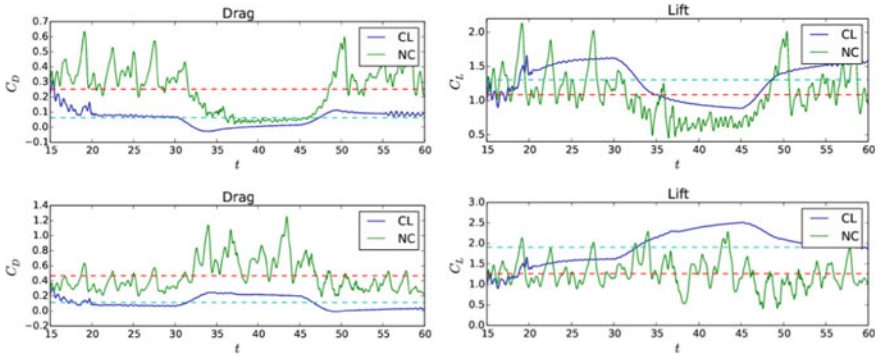

Fig. 2 Simulation results in the scenario $\beta = \beta_1$ (top) and $\beta = \beta_2$ (bottom). CL stands for Closed Loop; NC for Not Controlled

no actuators: about 75% average drag reduction, along with about 50% average lift increase is obtained for both cases.

The vorticity contours (101 non-dimensional vorticity levels uniformly distributed over the range $[-15, 15]$) in the stationary regimes, with angle of attack 5°, 15° and 25°, are shown in Fig. 3 results for both with and without the actuation are reported for comparison purposes. Without the actuation, strong vortex structures are generated as a consequence of both the strong adverse pressure gradients and the boundary layer separation, which occurs on the upper side of the profile; as expected, larger vortices are shed at larger angle of attack. The activation of the control on the NACA profile suppresses the boundary layer separation and avoids the generation of any vortical structure. A detailed view of the streamlines in the region close to the NACA profile is shown in Fig. 4, both cases with and without actuation are reported for comparison. For the three dimensional test case a fixed angle of attack configuration ($\beta = 5°$) is considered, the chord based Reynolds number is $Re = 20{,}000$. For the three dimensional case, the numerical grid has been extended in the span-wise direction using 128 grid volumes uniformly distributed; the span-wise length is 0.2 chord lengths. Figure 5 depicts an example of the solution: coherent structures using the swirl factor are shown for different time instants. In the top left frame the actuator is not activated, the simulations correctly predict the presence of a laminar boundary layer both on the pressure side of the NACA profile and on the first part of the suction side. Due to the adverse pressure gradients, a laminar separation occurs on the suction side. The transition to turbulent follows, with a turbulent reattachment close to the trailing edge. Once the actuator is activated (figures in the top right and in the bottom row) the separation of the boundary layer is progressively suppressed and the transition to turbulence is delayed.

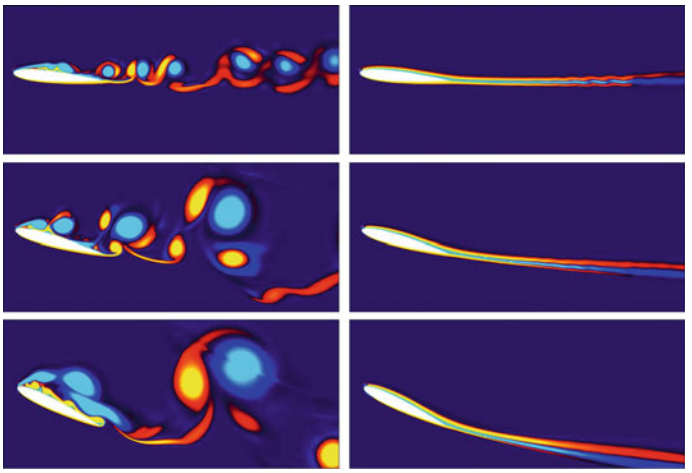

Fig. 3 Vorticity contours without (left) and with (right) closed-loop control for: $\beta = 5°$ (top); $\beta = 15°$ (middle); $\beta = 25°$ (bottom)

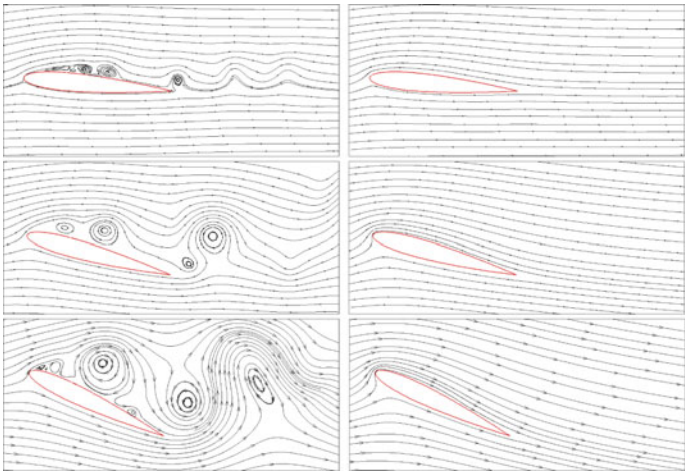

Fig. 4 Streamlines for without (left) and with (right) closed-loop control for: $\beta = 5°$ (top); $\beta = 15°$ (middle); $\beta = 25°$ (bottom)

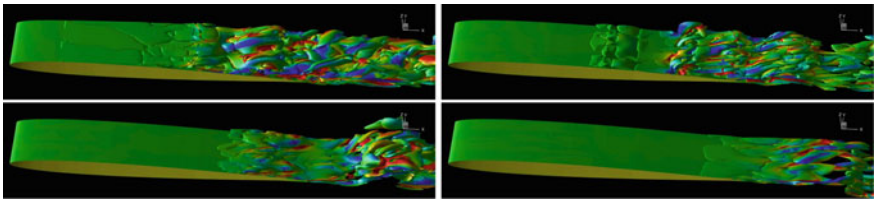

Fig. 5 Instantaneous three dimensional view of the flow field. Top left uncontrolled case; top right and bottom row, three time instants after the controller has been activated

5 Conclusions

We addressed the practical problem of robustly controlling the unsteady flow separation over an aerofoil, using the plasma actuators' voltage as the control inputs and realistically available real-time velocity measurements as the control outputs. The proposed controller guarantees the exponential regulation of the output measurements to some suitable reference sets, when the steady-state gain of the system is non-zero and of known sign. Accurate numerical simulations of flows past a pitching NACA0012 are performed in order to test the control effectiveness and validate the modelling assumptions. Transient performance have been investigated in different scenarios, for time-varying angles of attack. The proposed controller is able to effectively suppress the separation bubble, as well as the shedding vortices, while achieving robust dynamic performances, with respect to the variation of the uncertain angle of incidence. Three dimensional computations have been reported as well, demonstrating the effectiveness of the proposed control algorithm to completely suppress three dimensional separation bubble.

References

1. Broglia, R. Zaghi, S. Muscari, R., Salvadore, F.: Enabling hydrodynamics solver for efficient parallel simulations. In: Proceedings International Conference on High Performance Computing & Simulation (HPCS), pp. 803–810. Bologna, Italy (2014)
2. Broglia, R., Choi, K.-S., Houston, P., Pasquale, L., Zanchetta, P.: Output feedback control of flow separation over an aerofoil using plasma actuators. Int. J. Numer. Anal. Model. **15**(6), 864–883. ISSN 1705–5105 (2018)
3. Di Mascio, A., Broglia, R., Muscari, R.: Prediction of hydrodynamic coefficients of ship hulls by high-order Godunov-type methods. J. Marine Sci. Tech. **14**, 19–29 (2009)
4. Marino, R., Tomei, P.: Output regulation for unknown stable linear systems. Automatica **60**(8), 2213–2218 (2015)
5. Pasquale, L., Broglia, R., Choi, K.-S., Durante, D., Zanchetta, P.: Robust control of flow separation over a pitching aerofoil using plasma actuators. In: IFAC 2017-20th World Congress, Toulouse, France (2017)
6. Yang, Q., Chung, Y.M.: Numerical study of reducing turbulent skin-friction drag using DBD plasma actuators. In: EDRFCM 2015, Cambridge (2015)

Performance Analysis of a Heaving Wing Using DNS and LES

N. De Tullio, Z. Xie, J. Chalke and N. D. Sandham

1 Introduction

The weight and structure of civil transport aircraft are mainly dictated by the loads they experience at the limit of the design envelope (e.g. turbulence, gusts and manoeuvres). During the design process aircraft loading is often predicted using simplified models. However, under extreme operating conditions aircraft experience erratic unsteady loads that are not well understood, and hence difficult to predict using state of the art reduced models. Achieving a more profound understanding of the flow structures dictating the aerodynamic loads under extreme conditions will be crucial for the design of efficient aircraft. An example of such conditions occurs when a wing starts heaving or encounters a gust near its stall angle (e.g. during landing); unsteady flows and transient effects, including flow instabilities and vortex shedding, take place, making the aerodynamic loads highly unpredictable (see for example [1]). These complex physical mechanisms can only be fully captured by experiments and accurate numerical simulations, both of which are currently expensive to be used during the design stages, but can provide useful insight. Direct numerical simulations (DNS), being free from simplified modelling assumptions, have the advantage of including all the relevant flow physics. On the other hand, the large eddy simulation (LES) technique can be used to simulate realistic flow conditions, but its accuracy in predicting complex flow phenomena including flow instability and vortex shedding is not clear. This work focuses on assessing the performance of OpenFoam's

N. De Tullio (✉) · Z. Xie · J. Chalke · N. D. Sandham
Aerodynamics and Flight Mechanics Group, Faculty of Engineering and the Environment, University of Southampton, Southampton SO17 1BJ, UK
e-mail: n.de-tullio@soton.ac.uk

Z. Xie
e-mail: z.xie@soton.ac.uk

N. D. Sandham
e-mail: n.sandham@soton.ac.uk

M. V. Salvetti et al. (eds.), *Direct and Large-Eddy Simulation XI*,
ERCOFTAC Series 25, https://doi.org/10.1007/978-3-030-04915-7_52

LES solver for the prediction of the aerodynamic loads acting on a heaving wing at incidence through comparisons with DNS and experimental results.

2 Numerical Simulations

The DNS have been carried out using the SBLI code; a highly accurate, multi-block, finite-difference solver developed at the University of Southampton. The code solves the compressible Navier–Stokes equations in dimensionless form, using standard fourth-order central differences and a third-order compact Runge–Kutta method. Further details about SBLI's features and validation cases can be found in [2] and references therein. The LES have been performed with the OpenFoam CFD solver, which solves the incompressible Navier–Stokes equations, using the mixed-time-scale model of Inagaki et al. [3] to model the subgrid scale turbulence.

The numerical simulations have been performed for the flow over a NACA-0012 airfoil, modified to include a sharp trailing edge, at a Reynolds number based on the airfoil chord of $Re_c = 2 \times 10^4$. While the LES simulations assume incompressible flow, the DNS simulations are carried out for a compressible flow at a Mach number $M = 0.4$. The Mach number was chosen low enough to limit compressibility effects, while maintaining a reasonable computational effort. Two sets of numerical simulations were carried out for this work: a pre-stall condition with angle of attack $\alpha = 5°$, amplitude $A = 0.1$ and heaving frequency $St = 0.1$, and a post-stall condition with $\alpha = 15°$, $A = 0.25$ and $St = 0.3$. Note that, the amplitude A is made dimensionless using the airfoil chord c and St is the Strouhal number defined using the free-stream velocity and c. The LES where carried out using a dynamic mesh and either an imposed gust or a moving airfoil (using OpenFoam's dynamic mesh solver with body force to include heaving effects [4]) with imposed vertical motion given in dimensionless variables by $y = A \sin(2\pi St \cdot t)$, while the heaving motion was modelled by imposing a sinusoidal vertical velocity gust given by $V_\infty = -A2\pi St \cos[2\pi St(t - x)]$ in the DNS. The airfoil is represented using a no-slip, isothermal boundary condition, with the wall temperature equal to the freestream temperature $T_\infty = 273.15\,\mathrm{K}$. The DNS employ characteristic boundary conditions for the external computational domain boundaries in order to minimise wave reflections, while for the incompressible LES solver Dirichlet conditions are applied at inflow boundaries and zero pressure gradient Neumann conditions at outflow boundaries. The spanwise direction is treated with periodic boundary conditions. The computational grids used for the LES cases were chosen after a grid-convergence study, while the DNS grids are based on previous work performed by Jones [5] for the same airfoil configuration analysed here. The spanwise size of the computational domain is $L_z/c = 0.4$ for the DNS and $L_z/c = 0.25$ for the LES cases.

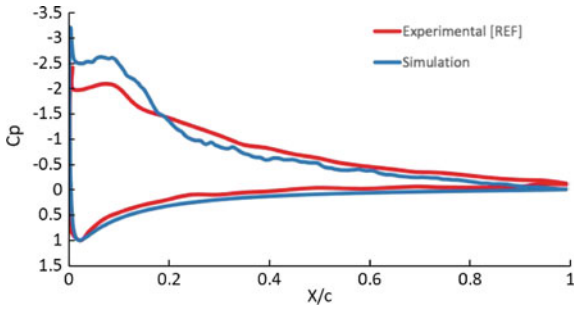

Fig. 1 Chordwise C_p distribution. Comparison between LES results (in blue) and reference experimental data [6] (in red)

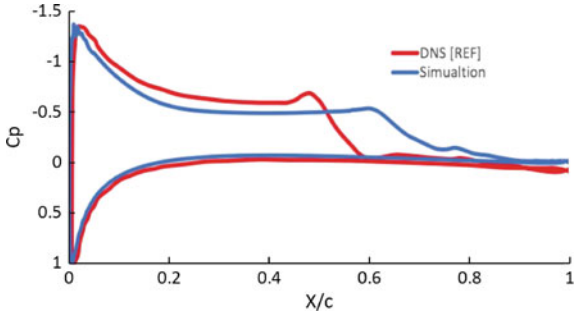

Fig. 2 Chordwise C_p distribution. Comparison between LES results (in blue) and reference DNS data [7] (in red)

3 Validation of the LES Methodology

A validation of the LES methodology for the flow over a static NACA0012 airfoil was performed against experimental [6] and DNS [7] data available in the literature. The experimental data of Tanaka [6] are for a Reynolds number of $Re_c = 1.3 \times 10^6$ and an angle of attack of $\alpha = 11°$. Figure 1 shows a comparison of the chordwise pressure coefficient (C_p) distribution between the experimental and LES results. It can be seen that, despite a somewhat large difference in pressure peak, the LES is able to capture the laminar-turbulent transition downstream of the laminar separation bubble (evidenced by a region of constant C_p near the leading edge). The two C_p distributions are in good agreement in the turbulent part of the suction surface and along the entire extension of the pressure surface.

For the second validation case the Reynolds number was dropped to $Re_c = 5 \times 10^4$ and the angle of attack was set to $\alpha = 5°$, in order to match the DNS data of Jones et al. [7]. Figure 2 gives a comparison of the two chordwise C_p distributions. The LES captures the suction peak accurately, but over-predicts the size of the laminar separation bubble on the airfoil's suction side (indicated by the C_p plateau in Fig. 2) by wrongly predicting the laminar-turbulent transition point. At low Reynolds numbers, the laminar-turbulent transition of the boundary layer developing over the suction surface is highly dependent on the exponential growth of small disturbances in the laminar separation bubble. The dissipative character of the LES methodology tends to under predict the instability growth rate, making the modelling of laminar-turbulent

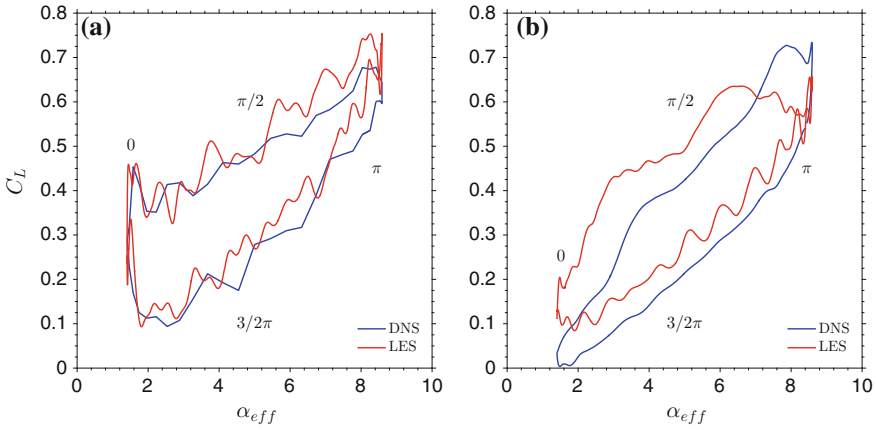

Fig. 3 Phase-averaged C_L distribution as a function α_{eff} for the pre-stall cases. **a** 2D and **b** 3D

transition at low Reynolds numbers difficult. It was initially believed that this problem will be alleviated with the introduction of heaving motion, as in this case the laminar-turbulent transition will be driven by the large structures induced by the motion of the wing.

4 Comparisons with DNS and Experiments

A comparison between the LES (heaving) and the DNS (static wing with imposed gust) results for the pre-stall case is given in Fig. 3, showing the variation of the phase-averaged lift coefficient (C_L) as a function of the effective angle of attack $\alpha_{eff} = \alpha + \arctan(v/U_\infty)$, where v is the vertical velocity of the wing. In this case, the investigation was carried out using both two-dimensional (2D) and three-dimensional (3D) numerical simulations. The 2D LES and 2D DNS results, shown in Fig. 3a, agree very closely over the whole heaving cycle. This suggests that the main flow dynamics for a heaving wing and a wing encountering a sinusoidal gust are very similar for this flow regime. The agreement remains good also for the 3D simulations, as shown in Fig. 3b; both LES and DNS predict an almost linear lift decrease towards the end of the cycle and a more erratic lift increase at the beginning. Both results show a hysteresis in the heaving cycle with a $\Delta C_L \approx 0.2$. However, the 3D LES tends to over-predict the lift coefficient over most of the heaving cycle. Given the agreement of the 2D results, it appears that the difference in C_L in the 3D cases may be again due to the LES not being able to correctly predict the laminar-turbulent transition taking place on suction side of the airfoil. This is also confirmed by inspections of the full 3D LES and DNS flow fields (not shown).

The 3D LES and DNS results obtained for the post-stall conditions are reported in Fig. 4a. The discrepancy between the heaving LES and gust DNS results is large,

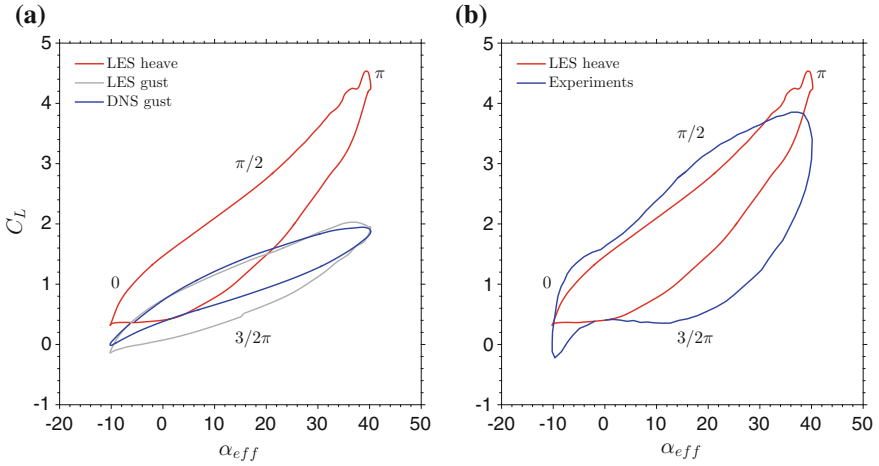

Fig. 4 Phase-averaged C_L distribution as a function α_{eff} for the post-stall cases. **a** Comparisons with DNS and **b** comparisons with experiments

with the heaving case reaching a maximum C_L more than twice that of the case with imposed gust. An additional LES simulation was carried out for a static airfoil encountering a gust equivalent to that imposed in the DNS, the results of which are shown as a grey line in Fig. 4a. The results are in very good agreement with the DNS data, especially for the maximum and minimum lift achieved and during the first part of the cycle, showing that the discrepancies between the heaving LES and gust DNS cases are not due to numerical or modelling issues. In order to shed some light on the causes leading to the big differences in the lift attained in the gust and heaving cases, instantaneous contours of pressure on the midspan plane at a phase of π during the cycle are shown in Fig. 5a, b for the gust and heaving cases, respectively. In both cases, the maximum lift is achieved at π (the point of maximum downward velocity) due to the shedding of a spanwise coherent vortex from the airfoil's leading edge. The vortex is much stronger and induces a larger region of low pressure over the suction side of the airfoil in the heaving case than in the gust case, explaining the large discrepancy in the maximum lift achieved in the two cases. The reasons for such a difference in flow structures, however, are still not fully understood and will require further investigations. Figure 4b gives a comparison between the heaving LES results and the experimental results reported by Chiereghin et al. [8] for the same flow conditions. The experimental results were obtained in a water tunnel with with a static-wing blockage ratio of 3%. The flow was kept quasi-2D with the inclusion of plates at the wing's root and tip. Despite a reasonable agreement in the minimum and maximum lift attained, considerable differences in C_L can be observed throughout the heaving cycle. Potential causes for this discrepancy could be three-dimensional flow and blockage effects in the experiments, as well as spanwise domain size in the LES. Further investigations aimed at clarifying this issues are currently ongoing.

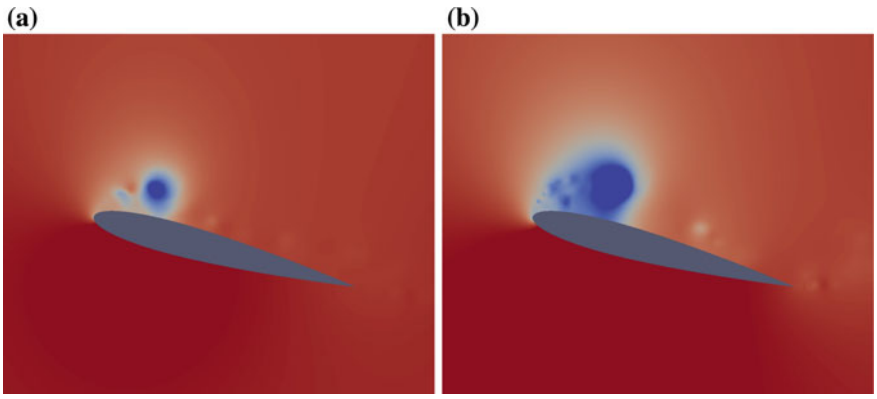

Fig. 5 Instantaneous pressure contours on the midspan plane at phase π. **a** Imposed gust, **b** heaving airfoil

5 Conclusions

An investigation of the capabilities of the LES methodology for the simulation of heaving airfoils was carried out using comparisons with DNS and experiments. The results show that LES is a promising methodology for the accurate simulation of heaving airfoils, where transition is mainly dominated by geometrical and dynamical effects. The study, which was carried out for pre-stall and post-stall conditions, also indicates that flow characteristics and airfoil performance are very similar for a heaving aerofoil and for a static airfoil encountering a gust, provided the heaving motion is weak and the angle of attack small. For strong heaving motion and large angles of attack, the gust and heaving results were found to disagree, with the heaving results being in reasonably good agreement with available experimental results.

References

1. Von Ellenrieder, K.D., Parker, K., Soria, J.: Flow structures behind a heaving and pitching finite-span wing. J. Fluid Mech. **490**, 129–138 (2003)
2. De Tullio, N.: Receptivity and transtion to turbulence of supersonic boundary layers with surface roughness, Ph.D. Thesis, University of Southampton (2013)
3. Inagaki, M., Kondoh, T., Nagano, Y.: A mixed-time-scale SGS model with fixed model-parameters for practical LES. J. Fluids Eng. **127**(1), 1–13 (2005)
4. Kim, Y., Xie, Z.: Modelling the effect of freestream turbulence on dynamic stall of wind turbine blades. Comput. Fluids **129**, 53–66 (2016)
5. Jones, L.E.: Numerical study of the flow around an airfoil at low Reynolds number. Ph.D. Thesis, University of Southampton (2008)
6. Tanaka, H.: Flow visualization and PIV measurements of laminar separation bubble oscillating at low frequency on an airfoil near stall. In: 24th International Congress of the Aeronautical Sciences, pp. 1–13 (2004)

7. Jones, L.E., Sandberg, R.D., Sandham, N.D.: Direct numerical simulations of forced and unforced separation bubbles on an airfoil at incidence. J. Fluid Mech. 602, 175–207 (2008)
8. Chiereghin, N., Cleaver, D., Gursul, I.: Unsteady measurements for a periodically plunging airfoil. AIAA 2017-0996 (2016)

A Numerical Study of Low-Aspect-Ratio Flapping-Wings in Forward Flight

A. Gonzalo, G. Arranz, M. Moriche, O. Flores and M. García-Villalba

1 Introduction

Unsteady aerodynamics at low Reynolds number is receiving an increasing attention from the scientific community due to the recent development of Flapping Micro Air Vehicles (FMAV). These vehicles generate thrust and lift by flapping their wings, like insects or small birds do. The specific unsteady aerodynamic mechanisms involved in the generation of forces in flapping flight have been studied by several authors, as reviewed in [6]. However, our understanding of flapping flight is still limited.

Some of the aforementioned studies focus on the role that fictitious forces (Coriolis and centripetal forces) have in the aerodynamic forces [3]. The intensity of these fictitious forces is influenced mainly by the Rossby number (Ro), which relates linear and angular momentum of the flow. Most of the work found in the literature focus on the effect of Ro on the aerodynamic forces in hover [2], whereas the case of forward flight has received less attention. For hover flight, Ro can be defined as a non-dimensional radius of gyration, in terms of the second moment of area of the wing [2]. In this study, a similar non-dimensional parameter ($R_g = \Delta R/c$) has been used to describe the cases studied.

Here, we present direct numerical simulations (DNS) of low-aspect-ratio (AR) flapping wings in a forward flight configuration, with the aim of increasing our understanding of the effect of R_g on the aerodynamic forces. Several simulations have been carried out with different R_g to describe a smooth transition from flapping ($R_g = 0$) to heaving ($R_g \to \infty$).

Since the aim of this work is to characterize the aerodynamic forces with R_g, we also present a comparison between the forces obtained with DNS and with a 3D unsteady panel method (3DUPM) code. The 3DUPM code used in this study was developed by [1], we refer the reader to their work for a detailed description

A. Gonzalo (✉) · G. Arranz · M. Moriche · O. Flores · M. García-Villalba
Universidad Carlos III de Madrid, Getafe, Spain
e-mail: alejgonz@ing.uc3m.es

M. V. Salvetti et al. (eds.), *Direct and Large-Eddy Simulation XI*,
ERCOFTAC Series 25, https://doi.org/10.1007/978-3-030-04915-7_53

of the code. Potential methods are good candidates to model aerodynamic forces in three-dimensional (3D) flapping wings kinematics [8], with potential to speed-up the design process of FMAV.

2 Computational Setup

We present here several 3D DNS of flapping wings in forward flight. The Reynolds number (Re) of the flow based on the free stream velocity u_∞ and the wing chord c is 500. We use rectangular wings of AR $= 2$ rounded at the inboard and outboard tips. The section of the wings is made of NACA0012 airfoils. The body of the FMAV is not considered, instead, we impose a gap of $c/2$ between the inboard tips of the wings. A sketch of the two wings configuration is shown in Fig. 1a.

The motion of the wings consists of a rotation with respect to an axis parallel to the free stream. The projection of the axis of rotation on a yz plane is represented with a black circle in Fig. 1b, where the rotation of the right wing is outlined. In order to isolate the effect of R_g on the aerodynamic forces, we keep the wings' motion as simple as possible. Thus, no pitching motion was imposed and the wing angle of attack was fixed to zero. We have performed simulations for different distances between the axis of gyration and the inboard wing tip ($R_g = 0$, 2 and ∞).

The kinematics of the wing are completed with the time dependence of the stroke angle

$$\phi = \phi_0 \cos(2\pi f t), \tag{1}$$

where t is the time, f is the frequency of oscillation and ϕ_0 is the amplitude of the motion. The reduced frequency is $k = 2\pi f c/u_\infty = 1$ and the amplitude ϕ_0 is

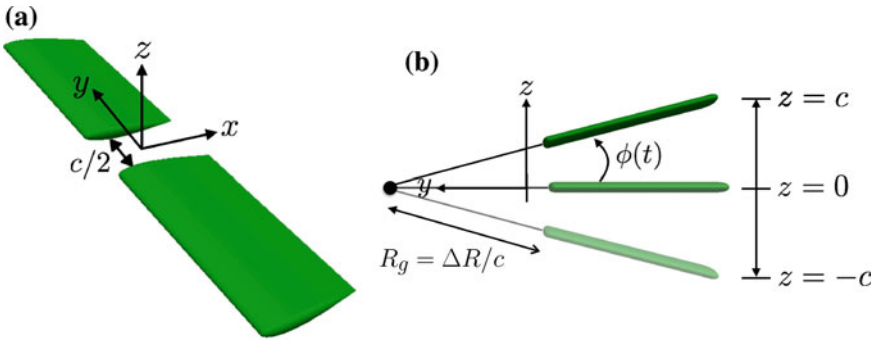

Fig. 1 **a** Sketch of the two wings configuration and **b** outline of the right wing's kinematic. The streamwise direction is x, which is also the direction of the free-stream velocity, y is the spanwise direction, z is the vertical direction and R_g is the distance between the inboard wing tip and the axis of rotation

selected so that the vertical position of the outboard tip oscillates between $[-c, c]$ (see Fig. 1b).

The simulations are performed with TUCAN, an in-house code which solves the Navier–Stokes equations for an incompressible flow. The spatial discretization is done with second-order centered finite-differences on an uniform staggered grid and the time integration is performed with a fractional step method and a low storage semi-implicit Runge–Kutta scheme of three stages. The presence of the wings is modeled with the immersed boundary method proposed by Uhlmann [7]. TUCAN has been extensively validated and used for 2D and 3D flows [4, 5].

The size of the computational domain is $12c \times 5.25c \times 8c$ in the streamwise, spanwise and vertical directions, respectively, discretized with $672 \times 294 \times 448$ points. This yields a resolution of 56 points per c. This resolution has been validated with a grid refinement study for the equivalent 2D configuration. We only simulate one wing by using a symmetric boundary condition in the middle of both wings, saving computational resources. The use of mirror symmetry is justified since Re is low. At the inlet plane (located at $3c$ from the leading edge) we impose the free-stream velocity. A convective boundary condition is used at the outlet and for the top, bottom and side boundaries, we use free-slip boundary conditions.

3 Results

Figure 2 shows the time evolution of lift and drag coefficients. First, the lift generated in the downstroke is counteracted by the (negative) lift of the upstroke and the drag generated in the downstroke is the same as in the upstroke. This is due to the vertical symmetry of the motion. The peaks of lift and thrust (negative drag) grow with increasing R_g.

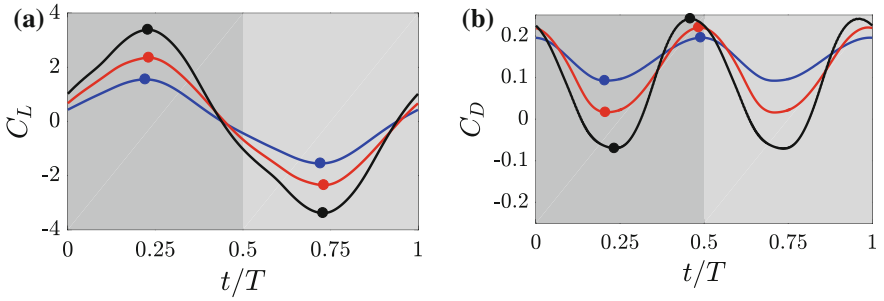

Fig. 2 Time evolution of **a** lift and **b** drag coefficients for different R_g during one period. Blue line $R_g = 0$, red line $R_g = 2$ and black line $R_g \to \infty$. Downstroke motion is coloured in dark grey and upstroke motion in light grey

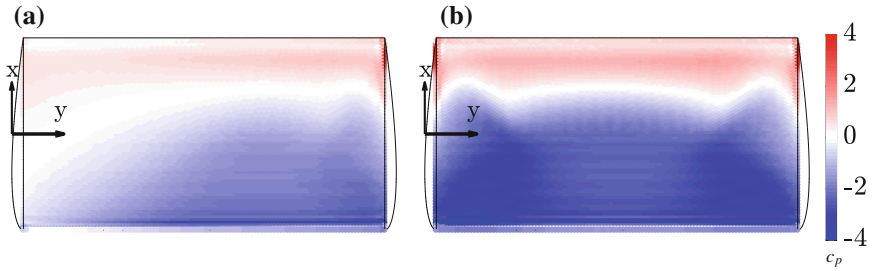

Fig. 3 Contours of pressure coefficient (c_p) at the top surface of the wing for **a** $R_g = 0$ and **b** $R_g \to \infty$ at the middle of the downstroke $t/T = 0.25$

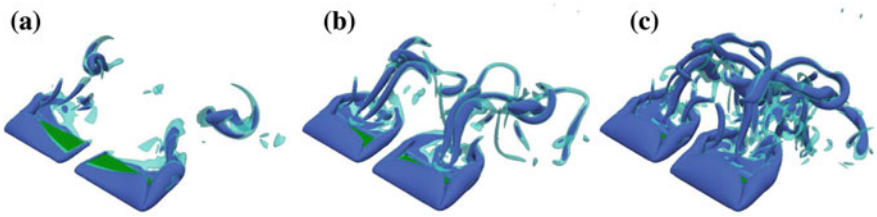

Fig. 4 Flow visualization using the contours of second invariant of the velocity gradient tensor (Q) at the middle of the downstroke. Wings are colored in green. Dark and light blue correspond to different values of Q. **a** $R_g = 0$, **b** $R_g = 2$ and **c** $R_g \to \infty$

All cases generate a mean drag force during the whole period, decreasing with R_g. Note that the case with $R_g \to \infty$ (heaving motion) is able to provide thrust at the middle of the downstroke ($t/T = 0.25$).

In order to characterize the effect of R_g on the force distribution on the upper surface of the wing, Fig. 3 shows the pressure distribution (c_p) at the middle of the downstroke. At this instant, lift and thrust are maximum. In Fig. 3 we can see that the suction area on the top surface of the wing becomes larger as $R_g \to \infty$. Furthermore, (negative) c_p values also become higher. This suction area observed on the top surface of the wing is related with the presence of a Leading Edge Vortex (LEV), which can be seen in Fig. 4 at the middle of the downstroke for cases with different R_g. The LEV of the case with $R_g \to \infty$, shown in Fig. 4c covers a larger region of the top surface of the wing than the other two cases. On the other hand, when R_g is low (Fig. 3a) we can observe that the low pressure area on the top of the wing decreases towards the inboard tip. This fact coincides with the decrease of intensity of the LEV from the outboard to the inboard wing tip seen in Fig. 4a and it is caused by the smaller amplitude of the vertical motion of the inboard wing tip as $R_g \to 0$.

Lift and drag coefficients obtained with DNS and 3DUPM are compared in Fig. 5 for the cases studied. The lift curves predicted using 3DUPM are qualitatively similar to those obtained with DNS. However, 3DUPM fails to predict the forces along the x direction (drag, thrust). In fact, unlike DNS, it predicts thrust for the whole period

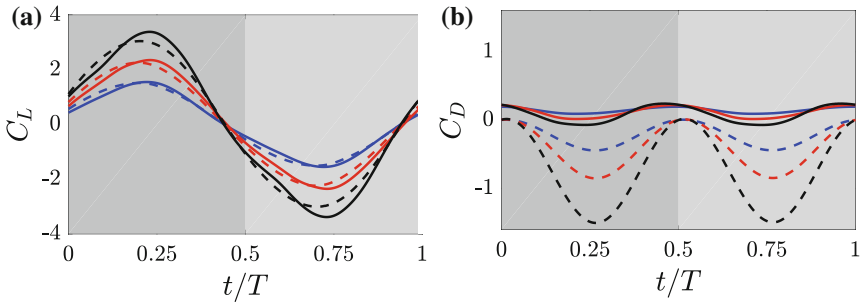

Fig. 5 Time evolution of **a** lift and **b** drag coefficients for different R_g during one period. DNS (3D Unsteady Panel Method) is represented with solid (dashed) lines. Blue line $R_g = 0$, red line $R_g = 2$ and black line $R_g \to \infty$. Downstroke motion is coloured in dark grey and upstroke motion in light grey

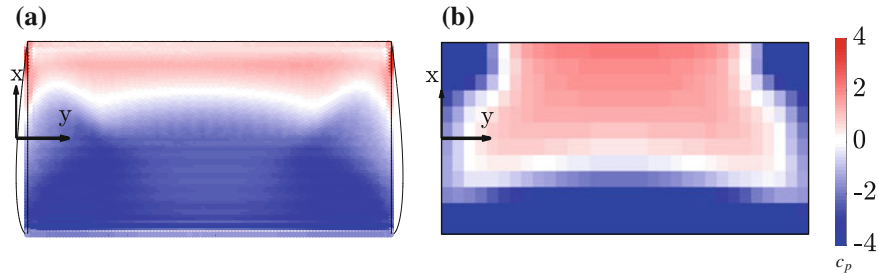

Fig. 6 Contours of pressure coefficient at the top surface of the wing for $R_g \to \infty$ at the middle of the downstroke $t/T = 0.25$. **a** DNS and **b** 3D Unsteady Panel Method

instead of drag. The differences obtained in C_D can be explained due to several factors.

First, the 3DUPM code deals with potential, inviscid flow. Hence, there are no tangential forces, since the boundary condition for the velocity on the surface of the wing is free-slip. Second, the 3DUPM code assumes that the flow is completely attached to the upper surface, and the circulation corresponding to the LEV is absorbed in the bound circulation of the wing (i.e., the circulation of the singularities inside the wing's surface). As a consequence, 3DUPM develops a strong suction at the leading edge, while the leading edge in the DNS simulations has a much lower pressure.

This can be observed in Fig. 6, where the pressure coefficients on the upper surface of the heaving wing are presented for both, DNS and 3DUPM. Similar observations are made for cases with different R_g and at different time instants. Thus, for the sake of clarity, we only show the results of the case with $R_g \to \infty$ at the middle of the downstroke motion.

Even though the net lift is qualitatively similar, as shown in Fig. 5a, pressure distributions on the top surface of the wing are not well predicted by 3DUPM. First of all, the intensity of the suction peak at the leading edge is different between DNS

and 3DUPM, being a factor of 6 larger on the latter. Besides, DNS results show a larger area of negative pressure distribution with a smaller suction force, which seems to be located below the area covered by the LEV. Note also that despite the chordwise pressure distribution is not well predicted, the spanwise pressure distribution shows an acceptable agreement.

4 Conclusions

In this study, we have performed direct numerical simulations of flow around flapping wings in forward flight. We have varied R_g to study its effect on the aerodynamic forces. Furthermore, a 3D unsteady panel method code has been used to model the aerodynamic forces. The comparison of results obtained with 3DUPM and DNS has been also discussed. The lift coefficient peaks increase with R_g, while the mean drag coefficient decreases with R_g. When net lift and drag are maximum, we have observed that the suction area on the top surface of the wing is larger for higher R_g, specially close to the inboard wing tip. Furthermore, the negative c_p values also increase with R_g. The 3DUPM used is able to model the net lift force, but results obtained for drag force and pressure distribution are not well predicted.

Acknowledgements This work was supported by grant TRA2013-41103-P (MINECO/FEDER, UE).

References

1. Arranz, G., Flores, O.: Thrust generation in heaving and flapping wings in forward flight. In: 34th AIAA Applied Aerodynamics Conference, p. 3556 (2016)
2. Lee, Y., Lua, K., Lim, T.: Aspect ratio effects on revolving wings with Rossby number consideration. Bioinspir. Biomim. **11**(5), 056013 (2016)
3. Lentink, D., Dickinson, M.H.: Rotational accelerations stabilize leading edge vortices on revolving fly wings. J. Exp. Biol. **212**(16), 2705–2719 (2009)
4. Moriche, M.: A numerical study on the aerodynamic forces and the wake stability of flapping flight at low Reynolds number. PhD thesis, University of Carlos III Madrid (2017)
5. Moriche, M., Flores, O., García-Villalba, M.: Three dimensional instabilities in the wake of a flapping wing at low Reynolds number. Int. J. Heat Fluid Flow **62**, 44–55 (2016)
6. Shyy, W., Aono, H., Kang, C.-K., Liu, H.: An Introduction to Flapping Wing Aerodynamics. Cambridge University Press, Cambridge (2013)
7. Uhlmann, M.: An immersed boundary method with direct forcing for the simulation of particulate flows. J Comput. Physics **209**(2), 448–476 (2005)
8. Vest, M.S., Katz, J.: Unsteady aerodynamic model of flapping wings. AIAA J. **34**(7), 1435–1440 (1996)

The Influence of the Reynolds Number on the Auto-Rotation of Samaras

G. Arranz, M. Moriche, M. Uhlmann, O. Flores and M. García-Villalba

1 Introduction

As samara seeds fall from trees, they enter into auto-rotation. In this way they maximize dispersal distances [2]. The autorotation of samaras has been studied experimentally by several authors, see for example [1]. The interest in the study of samaras was renewed when it was found that the lift experienced by the seeds is increased by the presence of a stable leading edge vortex (LEV) [3, 4], which is one of the most important unsteady aerodynamic mechanisms employed by birds and insects to increase their lift. Indeed, a proper understanding of the stability of the LEV is required to design efficient flapping-wing micro air vehicles.

In this study, we present direct numerical simulations of the autorotation of a model samara at Reynolds numbers, Re, somewhat smaller than those observed in nature. The aim is to detect the presence of a LEV, if it exists, and to understand how the kinematics of the seed are related to the vortical structures of the flow.

2 Methodology

The simulations are carried out using TUCAN, an in-house code that solves the Navier Stokes equations for an incompressible flow using a fractional step method on a staggered grid. The body is modelled using the immersed boundary method proposed by Uhlmann [8]. TUCAN has been extensively validated [6] and employed for 2D and 3D simulations [5]. For the present study, the Newton–Euler equations

G. Arranz (✉) · M. Moriche · O. Flores · M. García-Villalba
Universidad Carlos III de Madrid, Getafe, Spain
e-mail: garranz@ing.uc3m.es

M. Uhlmann
Karlsruhe Institue of Technology, Karlsruhe, Germany

M. V. Salvetti et al. (eds.), *Direct and Large-Eddy Simulation XI*,
ERCOFTAC Series 25, https://doi.org/10.1007/978-3-030-04915-7_54

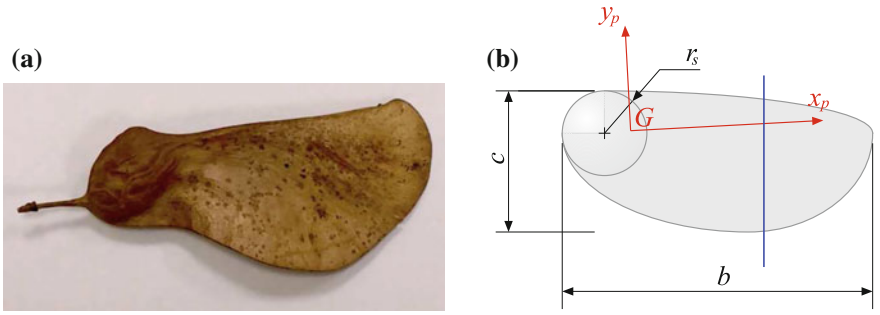

Fig. 1 **a** Real samara *Tipuana Tipu*. **b** Sketch of the model samara, top view, including the position of the centre of mass, G, and the principal axes of inertia. The blue line correspond to the span section $0.65b$

of the rigid body are coupled to the Navier–Stokes equations in TUCAN, extending the methodology developed by Uhlmann [8].

For illustration, a real samara *Tipuana Tipu*, collected by the authors, is shown in Fig. 1a. Inspired by several of these seeds we have developed a simplified model sketched in Fig. 1. The geometrical model consists of a flat wing of maximum chord c and span $b = 2.2c$ and an oblate spheroid of aspect ratio 0.6 and radius $r_s = 0.3c$. The mass of the samara is distributed such that the center of mass, G, is located closer to the leading edge than to the trailing edge, as shown in Fig. 1b. Such mass distribution is based on guidelines from several references [7, 9]. The density ratio between the solid and the fluid, ρ_s/ρ_f, has been set to 300 which is close to the value expected for the *Tipuana Tipu* seed.

The simulations are conducted by fixing the vertical coordinate of the centre of mass, which is located at a distance $6c$ from the inflow plane. The samara is free to translate in the horizontal plane and all three rotations are also possible. The descent speed of the samara is modelled by fixing the speed at the inflow plane, v_d. At the outflow plane a convective condition is imposed and periodic boundary conditions are imposed at the lateral boundaries. To promote entrance into auto-rotation, an initial rotational velocity is given to the seed at the start of the simulation.

The size of the computational domain is $8c \times 8c$ in the cross plane and $16c$ in the vertical direction. The grid consists of $128 \times 128 \times 256$ grid points. This resolution is slightly marginal. However, the results presented in the following sections are qualitatively similar to preliminary results obtained with higher resolution simulations, which are underway at the time of writing.

3 Results

We have performed several simulations varying Re based on v_d and c in the range $[75 - 240]$. We tried to lower further Re but at $Re = 50$ the samara stopped autorotating.

Fig. 2 Flow visualization using the Q criterion for the case $Re = 240$. Light-blue isosurface corresponds to $Q = 3v_d^2/c^2$, dark-blue isosurface corresponds to $Q = 30v_d^2/c^2$

For all cases considered, after an initial transient, the samara auto-rotates at a constant angular velocity, and with a constant attitude (defined by two angles, β and θ, which are explained in detail in the following paragraphs). For illustration, Fig. 2 shows isosurfaces of the Q-criterion. The vortex system is composed of two main structures extending into the wake following helical paths. The first one corresponds to the LEV and tip vortex, and the second one is formed by the wake of the oblate spheroid. The LEV is the the strongest vortical structure on the wing surface, shown in the figure with a darker shade of blue.

The flight characteristics of the samara vary with Re, as one can observe in Fig. 3a, b, which shows the trajectory of the gravity centre and the wing tip of the seed, as well as its attitude at several time instants. Note that the vertical position of the gravity centre is fixed in the simulations, but for illustration purposes, $z = v_d t$ (where t is the time), which is equivalent to a seed falling at a constant speed, v_d.

It is possible to observe in Fig. 3a, b that the rotational velocity increases with Re. The seed performs more revolutions along the same distance z/c as Re increases. The trajectory of the gravity centre also changes with Re. Figure 3a ($Re = 80$) shows that the gravity centre does not displace on the horizontal plane (its position lies at $x/c \approx 0$); whereas in Fig. 3b ($Re = 240$) is observed that the gravity centre has displaced with respect to the origin. In fact, if one plots the horizontal position of the gravity centre (not shown), the gravity centre of the seed is rotating about an axis of rotation which is fixed for $Re = 80$, meanwhile it also displaces on the horizontal plane as Reynolds number is increased.

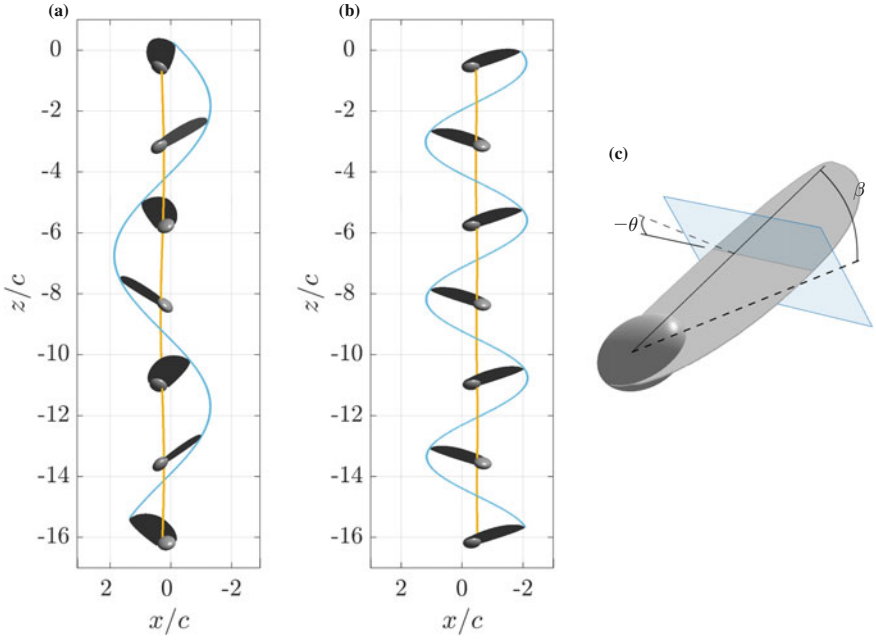

Fig. 3 **a** and **b** Trajectory of the seed after the initial transient for two different Reynolds number, **a** $Re = 80$, and **b** $Re = 240$. Light-blue line is the trajectory of the wing tip, yellow line is the trajectory of the gravity centre, G. **b** Definition of the coning angle, β and the pitch angle, θ

The attitude of the seed also changes with Re (see the samaras depicted in Fig. 3a, b). To quantify this change, three angles are defined. The coning angle β (see Fig. 3c is defined as the elevation of the wing with respect to the horizontal plane. The pitch angle θ (see Fig. 3c) is the angle that the wing chord at any spanwise section makes with the horizontal. One can define it as the geometric angle of attack of the wing. However, this geometric angle of attack does not take into account the effect of the rotational velocity. Therefore, an effective angle of attack α is defined as the angle between the chord at a spanwise section and the velocity of this section. Thus, α is a function of the spanwise location. These three angles are shown in Fig. 4a, where α has been computed at $0.65b$, where b is the total span of the wing (see Fig. 1b). Note that these angles remain constant along the trajectory of the seed for a given Re.

Both the coning angle and the geometric angle of attack increase with decreasing Re. This indicates that the seed's wing tends to be more horizontal as Re is increased, as can be appreciated in Fig. 3. The effective of angle attack seems to be rather constant for the whole range of Re considered. This is an indication that the angular velocity Ω of the samara must increase with increasing Re to keep this angle constant, since the velocity at a given spanwise section is proportional to the angular velocity, $\cos\beta$, and its distance from G. This is indeed the case: Fig. 4b shows the ratio between the rotational velocity of the wing tip ΩR and the descent speed v_d, $\lambda = \Omega R / v_d$,

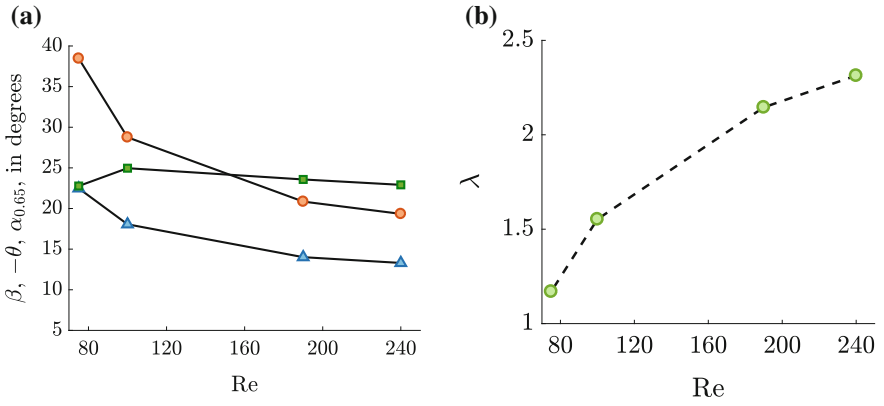

Fig. 4 Attitude of the samara as a function of the Reynolds number. **a** Triangles, coning angle β; circles, (minus) pitch angle, $-\theta$; squares, effective angle of attack at $0.65b$, α. **b** Ratio between the wing tip rotational velocity and the descent speed, λ, as a function of Re

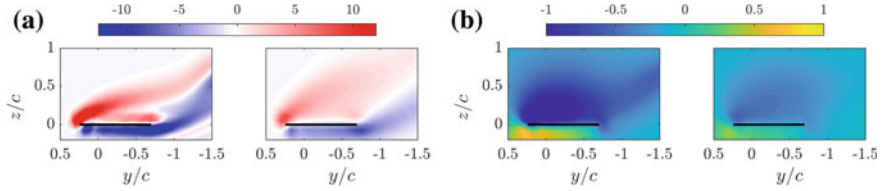

Fig. 5 **a** Relative spanwise vorticity, $\omega_x/(v_d/c)$, at spanwise position $0.65b$. Left $Re = 240$, right $Re = 80$. **b** pressure, $p/(\rho_f v_d^2)$, at spanwise position $0.65b$. Left $Re = 240$, right $Re = 80$

(where R is the distance from G to the tip of the seed) as a function of Re, showing that λ increases with Re.

Reynolds number also affects the flow around the seed. Figure 5 depicts the relative spanwise vorticity and the pressure at a spanwise section of the seed's wing. There is a strong vorticity concentration at the leading edge (Fig. 5a) which decreases in intensity as Re decreases. The effect of decreasing λ with Re is noticed in the shape of the vorticity wake above the chord. Pressure field (Fig. 5b) is qualitatively similar for both Re: a low pressure region above the wing, coincident with the LEV, but with a decreasing intensity as Re decreases. This behaviour entails higher aerodynamic forces normal to the wing for higher Re, which is confirmed by the forces obtained in the DNS (not shown). Both the vorticity field and the pressure field indicates the LEV becomes more intense as Reynolds number increases.

4 Conclusions

The auto-rotation of a samara has been numerically simulated at different Reynolds numbers. In all the cases under study the seed reached an stable auto-rotation after an initial transient, but auto-rotation was inhibited when Re was too low ($Re \leq 50$).

Varying the Reynolds number has an effect both on the kinematics and on the flow field due to the coupling between the equations of motion of the seed and the Navier-Stokes equations. Overall, decreasing the Reynolds number makes the seed auto-rotate at a slower rotational velocity and with higher coning and pitch angles, meanwhile the intensity of the vorticity and pressure fields decreases. Despite that, the presence of an stable LEV is observed for all Re where the seed auto-rotated.

Acknowledgements This work was supported by grant TRA2013-41103-P of the Spanish Ministry of Economy and Competitiveness. This grant includes FEDER funding. MGV was partially supported by a grant of the BBVA Foundation. The code was partially developed during a stay of MM (funded by BBVA) and MGV (funded by the Spanish Ministry of Education through the program José Castillejo) at the Karlsruhe Institute of Technology.

References

1. Azuma, A., Yasuda, K.: Flight performance of rotary seeds. J. Theor. Biol. **138**(1), 23–53 (1989)
2. Green, D.S.: The terminal velocity and dispersal of spinning samaras. Am. J. Bot. **169**(8), 1218–1224 (1998)
3. Lentink, D., Dickson, W.B., van Leeuwen, J.L., Dickinson, M.H.: Leading-edge vortices elevate lift of autorotating plant seeds. Science **324**(5933), 1438–1440 (2009)
4. Limacher, E., Rival, D.E.: On the distribution of leading-edge vortex circulation in samara-like flight. J. Fluid Mech. **776**, 316–333 (2015)
5. Moriche, M., Flores, O.: García-Villalba: three dimensional instabilities in the wake of a flapping wing at low Reynolds number. Int. J. Heat Fluid Flow **62**, 44–55 (2016)
6. Moriche, M.: A Numerical Study on the Aerodynamic Forces and the Wake Stability of Flapping Flight at Low Reynolds Number, Thesis. University of Carlos III Madrid (2017)
7. Norberg, R.: Autorotation, self-stability, and structure of single-winged fruits and seeds (samaras) with comparative remarks on animal flight. Biol. Rev. **48**(4), 561–596 (1973)
8. Uhlmann, M.: An immersed boundary method with direct forcing for the simulation of particulate flows. J. Comput. Phys. **209**(2), 448–476 (2005)
9. Yasuda, K., Azuma, A.: The auto-rotation boundary in the flight of samaras. J. Theor. Biol. **185**, 313–320 (1997)

Part VIII
Bluff-Body and Separated Flows

A Priori Analysis and Benchmarking of the Flow Around a Rectangular Cylinder

A. Cimarelli, A. Leonforte and D. Angeli

1 Introduction

The flow around bluff bodies is recognized to be a rich topic due to its huge number of applications in natural and engineering sciences. Of particular interest is the case of blunt bodies where a reattachment of the separated boundary layer before the definitive separation in the wake occurs. One of the main feature of this type of flows is the combined presence of small scales due to the occurrence of self-sustained turbulent motions and large scales due to classical vortex shedding. The complete understanding of these multiple interacting phenomena would help for a correct prediction and control of relevant features for engineering applications such as wind loads on buildings and vehicles, vibrations and acoustic insulation, heat transfer efficiency and entrainment. Archetypal of these kind of flows is the flow around a rectangular cylinder. Many studies have been carried out in the past. The general aim is the understanding of the main mechanisms behind the two unsteadiness of the flow, the shedding of vortices at the leading-edge shear layer and the low-frequency flapping mode of the separation bubble, see e.g [1–3].

Despite the large interest on separating and reattaching flow, there is still a number of open physical issues that need to be assessed especially in rectangular cylinders with chord-to-thickness range $3 < c/D < 7$. The most relevant one concerns the understanding of the entangling mechanisms between the separated wake and the shear layer instability at the leading edge. From a practical point of view, an additional issue is present and concerns difficulties on obtaining consistent results

A. Cimarelli (✉) · A. Leonforte · D. Angeli
University of Modena and Reggio Emilia, Modena, Italy
e-mail: andrea.cimarelli@unimore.it

A. Leonforte
e-mail: adriano.leonforte@unimore.it

D. Angeli
e-mail: diego.angeli@unimore.it

M. V. Salvetti et al. (eds.), *Direct and Large-Eddy Simulation XI*,
ERCOFTAC Series 25, https://doi.org/10.1007/978-3-030-04915-7_55

between different experiments and CFD (Computational Fluid Dynamics) simulations as highlighted by the BARC project (Benchmark on the Aerodynamics of a Rectangular 5:1 Cylinder) [4]. From an experimental point of view, the reason of the inconsistencies essentially comes from the high sensitivity of the flow on little changes in the boundary conditions and from resolution limits in the measuring techniques. On the other hand, from a CFD point of view, the main reason of inconsistencies comes from the sensitivity of the flow on the turbulence models and mesh resolution adopted. Despite the large interest in such a flow and the above mentioned issues, to the author's knowledge, no Direct Numerical Simulation (DNS) at sufficiently high Reynolds number has been performed. Indeed, the only attempt to face the problem via DNS has been those of [5] but the analysis has been carried out for very low Reynolds numbers, namely $Re = 350 \div 400$, and a fully developed turbulent state has not been achieved. The DNS approach would allow from one side to have access at the multi-dimensional large and small scale features fundamental for the understanding of the self-sustaining mechanisms of the flow. From the other side, a DNS would allow to set the statistical properties of the flow without turbulence modelling and grid resolution inaccuracies as in CFD simulations.

The present work reports for the first time Direct Numerical Simulation data of the flow around a rectangular cylinder with chord-to-thickness ratio $c/D = 5$ and Reynolds number $Re = U_\infty D/\nu = 3000$ where U_∞ is the free-stream velocity and ν the kinematic viscosity of the fluid. The first aim is to provide a reference statistical data base. The second aim is to develop *best practices* for LES techniques, by means of an a priori analysis of the DNS data. Here, we focus on the a priori analysis. In particular, we consider the behaviour of the subgrid dissipation term appearing in the budget for the resolved mean kinetic energy in order to understand the energetic role of the subgrid motion and, hence, the modelling approach to be used.

2 Direct Numerical Simulation

A common practice for the assessment of the subgrid scale behaviour in LES is to analyse filtered DNS data, the so-called *a priori* analysis. The governing equations numerically integrated when performing a DNS of an incompressible flow are

$$\begin{aligned} &\frac{\partial u_i}{\partial x_i} = 0 \\ &\frac{\partial u_i}{\partial t} + \frac{\partial u_i u_j}{\partial x_j} = -\frac{\partial p}{\partial x_i} + \frac{1}{Re}\frac{\partial^2 u_i}{\partial x_j \partial x_j} \end{aligned} \tag{1}$$

where $x = x_1$ ($u = u_1$), $y = x_2$ ($v = u_2$), $z = x_3$ ($w = u_3$) are the streamwise, vertical and spanwise directions (velocities), p is the pressure field, and $Re = U_\infty D/\nu$ is the Reynolds number with ν the kinematic viscosity, U_∞ the free-stream velocity and D the rectangle thickness. Unless specifically stated, all the quantities will be

reported in a dimensionless form by using D and U_∞ for the lengths and velocities, respectively. A cell-centered finite volume method has been chosen to discretize the equations by means of the OpenFOAM® open source code [6]. Time integration is performed by means of a second-order backward Euler implicit scheme while convective and diffusive fluxes at the volume faces are evaluated through a second-order central difference scheme. Finally, a pressure-implicit split-operator (PISO) algorithm is used to numerically solve the pressure-velocity coupling. Given the simple geometry of the problem, a structured Cartesian grid is adopted. A laminar free-stream velocity is imposed at the inlet while free-stream boundary conditions (mixed Dirichlet–Neumann conditions) are imposed at the outlet and upper-lower boundaries. Periodic boundary conditions are imposed in the spanwise direction.

The studied case consists of a flow around a rectangular cylinder whose lengths are $(L_x, L_y, L_z) = (5D, D, 5D)$ at a Reynolds number $Re = 3000$. The extent of the numerical domain is $(\mathscr{D}_x, \mathscr{D}_y, \mathscr{D}_z) = (112D, 50D, 5D)$ and is found to be large enough to not interfere with the flow dynamics. The number of volumes used to discretize the numerical domain is $1.5 \cdot 10^7$. The distribution of volumes is not homogeneous in the streamwise and vertical directions in order to obtain higher resolution levels near the walls of the rectangle and in the leading and trailing edge regions. On the other hand, in the spanwise direction an homogeneous spacing is adopted. The final resolution in the near wall region, averaged in the streamwise direction, is $(\Delta x^+, \Delta y^+, \Delta z^+) = (6.1, 0.31, 5.41)$ where the superscript $+$ implies the customary normalization with friction units. A relatively small time step is used, $\Delta t = 0.0023$, which leads to a CFL number less than unity.

3 The Filtering Procedure

In the present section, we assess the behaviour of the LES approach for solving the flow around a rectangular cylinder by means of an a priori analysis. The DNS data described in the previous section, are filtered by means of a Gaussian filter,

$$\mathscr{G}_i(\mathbf{x}, \mathbf{x}') = \sqrt{\frac{6}{\pi \Delta_i^2}} \exp\left(-\frac{6r_i^2}{\Delta_i^2}\right) \tag{2}$$

where $r_i = x_i - x_i'$ and Δ_i are the filter lengths. Hence, the filtered velocity field is computed as

$$\bar{u}_i(\mathbf{x}, t) = \int \mathscr{G}_i(\mathbf{x}, \mathbf{x}') u_i(\mathbf{x}', t) d\mathbf{x}' \tag{3}$$

and the subgrid stresses as $\tau_{ij}(\mathbf{x}, t) = \overline{u_i u_j} - \bar{u}_i \bar{u}_j$. The filtering is applied only in the horizontal directions. Indeed, the vertical one is commonly recognized to not allow for a significant reduction of the degrees of freedom of the problem when a near-wall resolved LES approach is considered. The adopted filter lengths are chosen

to be four times the streamwise and spanwise spacing of the DNS, thus allowing a reduction of the degrees of freedom of the problem to 6% those of the DNS. Hence, the resulting near-wall resolution of the filtered field expressed in viscous units and averaged along the rectangle length is $(\Delta x^+, \Delta z^+) = (24.4, 21.6)$.

4 Subgrid Dissipation and Modelling Approach

The behaviour of the subgrid stresses is here analysed from an energetic point of view by analysing the so-called subgrid dissipation ε_{sgs}. Indeed, amongst all the possible statistical observables, the subgrid dissipation is recognized to represent the most important feature the subgrid scale models should reproduce accurately [7, 8]. It represents the net statistical energy transfer between large resolved and small subgrid scales as can be shown by considering the balance equation for the resolved kinetic energy $\bar{k} = \bar{u}_i\bar{u}_i/2$. Actually, by decomposing the resolved velocity field in a mean and fluctuating part, $\bar{k} = \bar{Q} + \bar{q}$ with $\bar{Q} = \bar{U}_i\bar{U}_i/2$ and $\bar{q} = \bar{u}'_i\bar{u}'_i/2$, the subgrid dissipation splits in two terms, $\varepsilon_{sgs} = E_{sgs} + \varepsilon'_{sgs}$, corresponding to the net energy transfer of the subgrid motions with the mean and fluctuating resolved fields. The balance equations for the mean and fluctuating resolved energy read

$$\frac{\partial \bar{Q}}{\partial t} + \frac{\partial \bar{Q}\bar{U}_j}{\partial x_j} + \frac{1}{\rho}\frac{\partial \bar{P}\bar{U}_i}{\partial x_i} + \frac{\partial \langle \bar{u}'_i\bar{u}'_j\rangle \bar{U}_i}{\partial x_j} - \nu\frac{\partial^2 \bar{Q}}{\partial x_j \partial x_j} + \frac{\partial \langle \tau_{ij}\rangle \bar{U}_i}{\partial x_j} = \underbrace{\langle \bar{u}'_i\bar{u}'_j\rangle \frac{\partial \bar{U}_i}{\partial x_j}}_{\bar{\Pi}} \underbrace{- \nu\frac{\partial \bar{U}_i}{\partial x_j}\frac{\partial \bar{U}_i}{\partial x_j}}_{\bar{\Phi}} + \underbrace{\langle \tau_{ij}\rangle\langle \bar{S}_{ij}\rangle}_{E_{sgs}} \tag{4}$$

$$\frac{\partial \langle \bar{q}\rangle}{\partial t} + \frac{\partial \langle \bar{q}\bar{u}'_j\rangle}{\partial x_j} + \frac{1}{\rho}\frac{\partial \langle \bar{p}'\bar{u}'_i\rangle}{\partial x_i} + \frac{\partial \langle \bar{q}\rangle \bar{U}_j}{\partial x_j} - \nu\frac{\partial^2 \langle \bar{q}\rangle}{\partial x_j \partial x_j} + \frac{\partial \langle \tau'_{ij}\bar{u}'_i\rangle}{\partial x_j} = \underbrace{- \langle \bar{u}'_i\bar{u}'_j\rangle \frac{\partial \bar{U}_i}{\partial x_j}}_{\bar{\Pi}} \underbrace{- \nu\langle \frac{\partial \bar{u}'_i}{\partial x_j}\frac{\partial \bar{u}'_i}{\partial x_j}\rangle}_{\bar{\varepsilon}} + \underbrace{\langle \tau'_{ij}\bar{S}'_{ij}\rangle}_{\varepsilon'_{sgs}} \tag{5}$$

where $\bar{S}_{ij} = (\partial\bar{u}_i/\partial x_j + \partial\bar{u}_j/\partial x_i)/2$ is the resolved strain rate tensor. Equations (4) and (5) describe how mean and turbulent energy are produced transferred and dissipated. The net energy source/sink terms are reported in the right hand side while the transport terms in the left hand side. Here, we restrict the analysis to the source/sink terms of the mean kinetic energy, i.e. the turbulent production, $\bar{\Pi} = \langle \bar{u}'_i\bar{u}'_j\rangle(\partial\bar{U}_i/\partial x_j)$, the viscous dissipation, $\bar{\Phi} = \nu(\partial\bar{U}_i/\partial x_j)(\partial\bar{U}_i/\partial x_j)$ and the subgrid dissipation $E_{sgs} = \langle \tau_{ij}\rangle\langle \bar{S}_{ij}\rangle$, see the energy boxes in Fig. 1. In the common settings of turbulence, $\bar{\Pi}$, is negative and, hence is a sink for the mean and a source

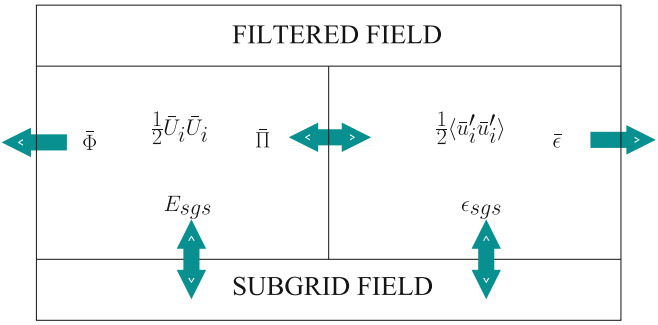

Fig. 1 Sketch of the net energy transfer terms between resolved mean kinetic energy, resolved turbulent kinetic energy and unresolved subgrid kinetic energy

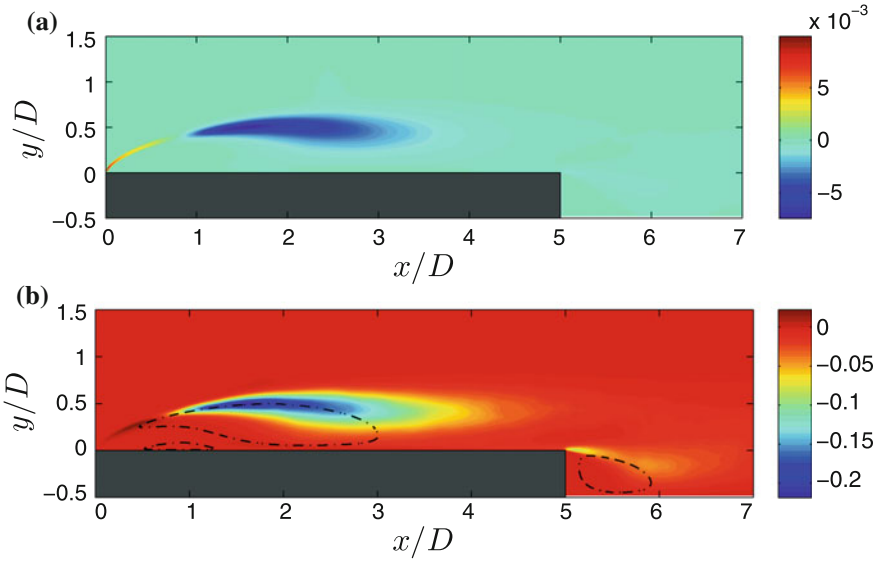

Fig. 2 Iso-contours in the $(x - y)$-plane of **a** the subgrid dissipation of mean kinetic energy E_{sgs} and **b** of the production of turbulence, Π

for the turbulent kinetic energy. On the other hand, the viscous dissipation by mean shear, $\bar{\Phi}$, is positively defined and, hence, is always a sink for the mean kinetic energy. Finally, E_{sgs} describes the energy exchange with the subgrid motions. In particular, E_{sgs} is a measure of the amount of turbulence production occurring at subgrid scale level and, hence, is commonly negative being a sink of mean kinetic energy.

In Fig. 2a, the behaviour of the subgrid dissipation of mean kinetic energy, E_{sgs}, is shown. The largest values of subgrid dissipation are reached in a region of the flow following the development of the leading-edge shear layer. Interestingly, E_{sgs} shows a double feature being both positive and negative in the first transitional and in the

fully developed part of the leading-edge shear layer, respectively. Indeed, contrarily to the common expectation of E_{sgs} as a sink of mean kinetic energy, the transitional region of the flow develops physical phenomena such that the subgrid motion turns out to be a source of mean kinetic energy. Let us try to give an explanation to this pheneomenon. As anticipated, the subgrid dissipation of mean kinetic energy can be understood as a measure of the amount of turbulence production occurring at subgrid scales. Since, in most of the flow cases turbulence production is a sink for mean kinetic energy, $\Pi < 0$, it turns out that also E_{sgs} is a sink. On the contrary, we observe that the subgrid motion is a source of mean kinetic energy, $E_{sgs} > 0$. Accordingly, this behaviour can be explained by positive values of the turbulent production, $\Pi > 0$. As shown in Fig. 2b, this picture is confirmed by the DNS data. Hence, the transitional region of the flow is characterized by a production of mean kinetic energy from the field of fluctuations rather than a production of turbulence from the mean flow.

5 Concluding Discussions

The observed double feature of the subgrid dissipation of mean kinetic energy, E_{sgs}, challenges for LES model which should be able to reproduce simultaneously both a source and sink of mean kinetic energy in the corresponding regions of the flow. In this respect, we can argue that a classical subgrid viscosity approach such as that given by the Smagorinsky model, is not well suited for modelling the subgrid stresses in the flow around a rectangular cylinder. Indeed, its formulation is such that subgrid dissipation is constrained to be negatively defined. Hence, this modelling approach in spite of reproducing a source in the leading-edge shear layer, introduces a strong sink of mean kinetic energy associated with the high levels of shear of this region. On the other hand, it is argued that an improved subgrid viscosity approach [9] or a mixed approach [10] should be better suited for the correct prediction of the main flow features.

References

1. Cherry, N.J., Hillier, R., Latour, M.E.M.: Unsteady measurements in a separated and reattaching flow. J. Fluid Mech. **144**, 13–46 (1984)
2. Kiya, M., Sasaki, K.: Structure of large-scale vortices and unsteady reverse flow in the reattaching zone of a turbulent separation bubble. J. Fluid Mech. **154**, 463–491 (1985)
3. Nakamura, Y., Ohya, Y., Tsuruta, H.: Experiments on vortex shedding from flat plates with square leading and trailing edges. J. Fluid Mech. **222**, 437–447 (1991)
4. Bruno, L., Salvetti, M.V., Ricciardelli, F.: Benchmark on the aerodynamics of a rectangular 5:1 cylinder: an overview after the first four years of activity. J. Wind Eng. Ind. Aerodyn. **126**, 87–106 (2014)
5. Hourigan, K., Thompson, M.C., Tan, B.T.: Self-sustained oscillations in flows around long blunt plates. J. Fluids Struct. **15**, 387–398 (2001)

6. Weller, H.G., Tabor, G., Jasak, H., Fureby, C.: A tensorial approach to computational continuum mechanics using object-oriented techniques. Comp. Phys. **12**, 620–631 (1998)
7. Piomelli, U., Yu, Y., Adrian, R.J.: Subgrid-scale energy transfer and near-wall turbulence structure. Phys. Fluids **8**, 215–224 (1996)
8. Cimarelli, A., De Angelis, E.: The physics of energy transfer toward improved subgrid-scale models. Phys. Fluids **26**, 055103 (2014)
9. Germano, M., Piomelli, U., Moin, P., Cabot, W.H.: A dynamic subgrid-scale eddy viscosity model. Phys. Fluids A **3**, 1760–1765 (1991)
10. Vreman, B., Guerts, B., Kuerten, H.: Large-eddy simulation of the turbulent mixing layer. J. Fluid Mech. **339**, 357–390 (1997)

Benchmark on the Aerodynamics of a 5:1 Rectangular Cylinder: Further Experimental and LES Results

C. Mannini, A. Mariotti, L. Siconolfi and M.V. Salvetti

1 Introduction

The flow around a rectangular cylinder, having chord-to-depth ratio equal to 5, has been the object of a benchmark (BARC) launched in 2008 (http://www.aniv-iawe.org/barc/). The BARC configuration is of practical interest, e.g. in civil engineering, and, in spite of the simple geometry, the related flow dynamics and topology is complex. Indeed, the high-Reynolds-number flow around such a stationary rectangular cylinder is turbulent with flow separation from the upstream corners and unsteady reattachment on the cylinder side. Furthermore, a vortex shedding also occurs from the rear corners and interferes with the leading-edge vortices, according to the mechanism of impinging shear-layer instability [1].

The experimental and numerical results obtained by the benchmark contributors during the first four years of activity were summarized and reviewed in [2]. Good agreement between different results in terms of near-wake flow, base pressure and drag coefficient was found. However, it was observed that some quantities of interest, as the standard deviation of the lift coefficient or the distribution of mean and fluctuating pressure on the cylinder sides, are affected by a significant dispersion, both in experiments and in simulations. Sensitivity analyses carried out by the BARC

C. Mannini (✉)
Dip. Ingegneria Civile e Ambientale, Università di Firenze,
Via S. Marta 3, Firenze 50139, Italia
e-mail: claudio.mannini@unifi.it

A. Mariotti · L. Siconolfi · M. V. Salvetti
Dip. Ingegneria Civile e Industriale, Università di Pisa,
Via G. Caruso 8, Pisa 56122, Italia
e-mail: alessandro.mariotti@for.unipi.it

L. Siconolfi
e-mail: siconolfi.lorenzo@gmail.com

M. V. Salvetti
e-mail: mv.salvetti@ing.unipi.it

M. V. Salvetti et al. (eds.), *Direct and Large-Eddy Simulation XI*,
ERCOFTAC Series 25, https://doi.org/10.1007/978-3-030-04915-7_56

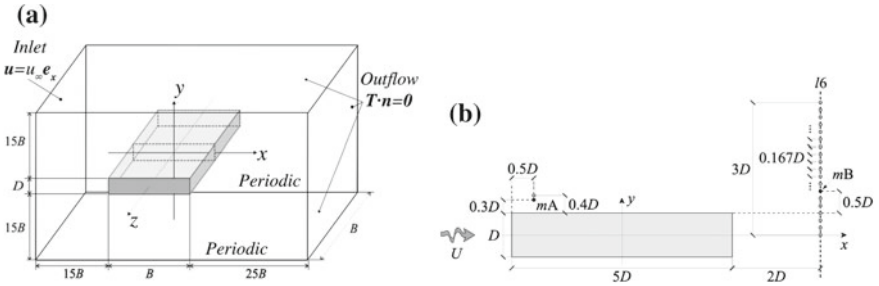

Fig. 1 **a** Sketch of the computational domain; **b** position of anemometry measurement points in the wake of the cylinder ($l6$, mA and mB represent respectively a reference transverse line and two reference points of the benchmark study)

contributors were not conclusive to explain the observed dispersion; rather, in some cases, they led to controversial results. In particular, in a single large-eddy simulation (LES) contribution [3] a strong sensitivity to the grid resolution in the spanwise direction was pointed out, but the results obtained for the finest grid significantly deviated from the ensemble average of those of the experimental and numerical contributions [2].

Recently, a set of LES was carried out in the framework of a stochastic analysis of the sensitivity to grid resolution in the spanwise direction and to the amount of subgrid scale (SGS) dissipation [4], and further wind tunnel measurements were obtained for different angles of attack and different oncoming flow turbulence features (intensity and integral length scale) [5], including unsteady surface pressures, forces and wake flow velocities. Experimental data on the flow velocity in the wake were still completely missing among the BARC contributions.

The aim of the present work is to exploit the new sets of LES and experimental results to give a contribution to highlight the reasons of the dispersion of data evidenced in the synopsis in [2].

2 Simulation and Experiment Set Up

LES simulations are carried out for the incompressible flow around a fixed sharp-edged rectangular cylinder with a chord-to-depth ratio, B/D, equal to 5. The angle of attack is zero. The computational domain is sketched in Fig. 1a. A uniform velocity profile is imposed at the inflow (no turbulence), while no-slip conditions are applied at the solid walls. Periodic conditions are imposed in the spanwise direction, and traction-free boundary conditions are used at the outflow, on the remaining lateral sides of the computational domain. Finally, the Reynolds number based on the free-stream velocity and on the cylinder depth, Re, is equal to 40,000. The sensitivity to the value of Re was observed to be low [2], although not null [5].

The simulations are performed through an open-source code, Nek5000, based on a high-order accurate spectral-element method (http://nek5000.mcs.anl.gov). The order of the Legendre polynomials used as basis functions inside each element is kept herein constant $N = 6$. The grid resolution in the streamwise and lateral directions is $\Delta x = \Delta y = 0.125D$. As for the LES formulation, a simple approach based on the application of a low-pass explicit filter in the modal space, which is characterized by a cut-off k_c, here equal to $N - 3$, and by a weight w, is adopted (see [4] for more details). This modal filter provides a dissipation in the resolved modes that are higher than the cut-off value, and can be interpreted as a SGS dissipation.

The parameters chosen for the sensitivity analysis are the grid resolution in the spanwise direction, defined in terms of the average element size, Δz (in the range $[0.321D, 0.674D]$), and the weight of the explicit filter, w (in the range $[0.01, 0.131]$). The latter has been chosen because it directly controls the amount of SGS dissipation, while the grid resolution in the spanwise direction is investigated because of the high impact of this parameter shown in the LES simulations in [3]. A total of 16 LES simulations were carried out (see [4] for more details).

The wind tunnel tests were conducted in the CRIACIV laboratory at the University of Florence on an aluminum sectional model with a cross section 300×60 mm and a spanwise length of 2.38 m. The model presented very sharp edges, smooth surfaces and high degree of symmetry. For a null angle of attack, the blockage ratio was 3.75%. Unsteady pressure measurements were performed through 61 taps distributed along the midspan section. A single-component hot-wire anemometer allowed the measurement of the fluctuating flow velocities in the wake downstream of the model and in the shear-layer region. The experiments were carried out for Reynolds numbers in the range 12,000 to 110,000, for various angles of attack (up to 10°), in smooth and various grid-induced free-stream turbulent flows (for further details, see [5]).

3 Results and Discussion

Figure 2 shows the distribution over the cylinder side of the pressure coefficient averaged in time, in the spanwise direction and between the upper and lower half perimeters of the cylinder, denoted as $t\text{-}avg(C_p)$, obtained in the 16 LES simulations. As in [2], the local abscissa s/D denotes the distance from the cylinder stagnation point measured along the cylinder side. The considered values of the spanwise spacing of the grid nodes are denoted in the following as Δz_1 to Δz_4 (from the coarsest to the finest), whereas the values of the weight of the explicit filter are indicated as w_1 to w_4 (from the lowest to the highest level of SGS dissipation). It can be seen that most of the calculated C_p distribution are characterized by a recovery occurring upstream compared to the experimental data. As explained in [2], the mean pressure distribution on the body surface is directly related to the curvature of the time-averaged flow streamlines and, in particular, to the shape and length of the main recirculation region on the cylinder sides. Therefore, most parameter combinations lead to a main recirculation region that is significantly shorter than those obtained in most of the BARC contributions. This is consistent with the findings of the most refined LES in

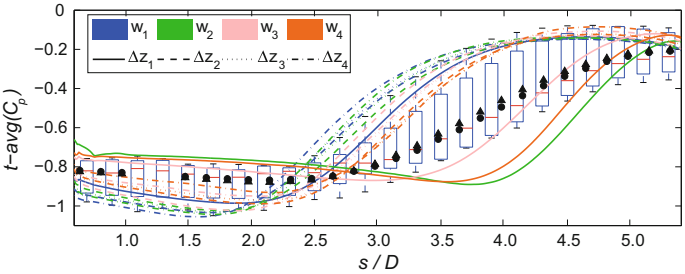

Fig. 2 Mean pressure coefficient on the lateral sides of the prism cross section obtained in the LES analysis. A comparison is provided with the ensemble statistics of the BARC experiments [2] and the experimental data in [5] (circles and triangles refer respectively to $Re = 56{,}700$ and 112,200)

[3]. In particular, increasing the spanwise resolution and decreasing the SGS dissipation, very small vortical structures, which originate from the instability of the shear layers detaching from the upstream corners, are observed in LES (see [4]), and this behavior corresponds to short main recirculation regions. A similar result was also obtained through detached-eddy simulation (DES) in [6] when reducing the artificial viscosity introduced to stabilize the central-difference scheme for the discretization of the convective term in the governing equations. It is worth noting that a grid with a fine spanwise resolution ($\Delta z = 0.078D$) was employed in that case.

The still open question is whether these perturbations have a physical or a numerical origin. Indeed, the mean C_p distribution obtained in the experiments, reported in Fig. 2, shows that, for low turbulence in the oncoming flow, the length of the plateau, and thus that of the main recirculation region, is significantly longer than that obtained in most of the LES computations, which are yet carried out for smooth oncoming flow. Indeed, the level of flow perturbation upstream of the leading edge separation is negligible in all the LES simulations.

In order to investigate how the differences between experiments and simulations are related to the features and dynamics of the separated shear layers and of the downstream wake, a comparison with the flow velocity measurements reported in [5] is carried out.

Figure 3a shows the mean streamwise velocity profile in the shear-layer region at the point mA of Fig. 1b ($x/D = -2$). The mean velocity profile in the calculations exhibits low uncertainty and a very good agreement with the experiments. In contrast, the standard deviation in time of the velocity fluctuations is very different from one simulation to another, and the experimental data fall inside the uncertainty band (Fig. 3b). Nevertheless, a low level of fluctuations at this streamwise position is not necessarily associated with a long recirculation bubble. Indeed, there are solutions characterized by fluctuations in the shear layer significantly lower than or of the same order as in the experiments that correspond to much shorter mean recirculation regions, as demonstrated by the streamlines in Fig. 4b, d. For example, the simulation with w_1, Δz_1, in spite of the very good agreement with the experimental data in terms of flow velocity fluctuations, is characterized by a short bubble. The simula-

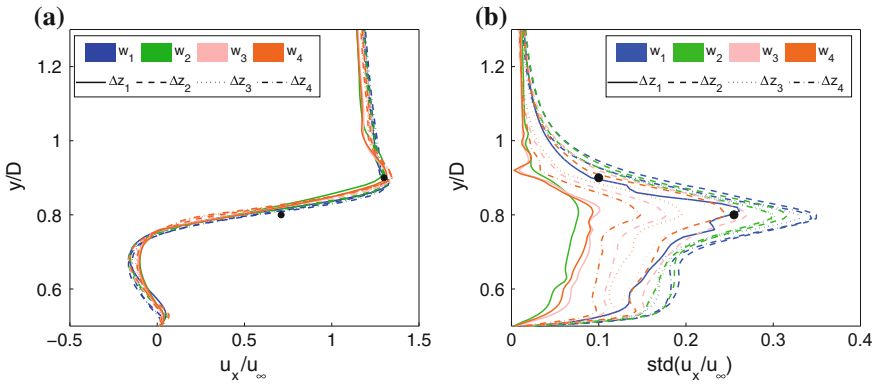

Fig. 3 **a** Mean streamwise velocity profile, and **b** standard deviation of the velocity fluctuations in the x-direction at $x/D = -2$ (see Fig. 1b). The experimental data (black circles) correspond to $Re = 11,800$ [5]

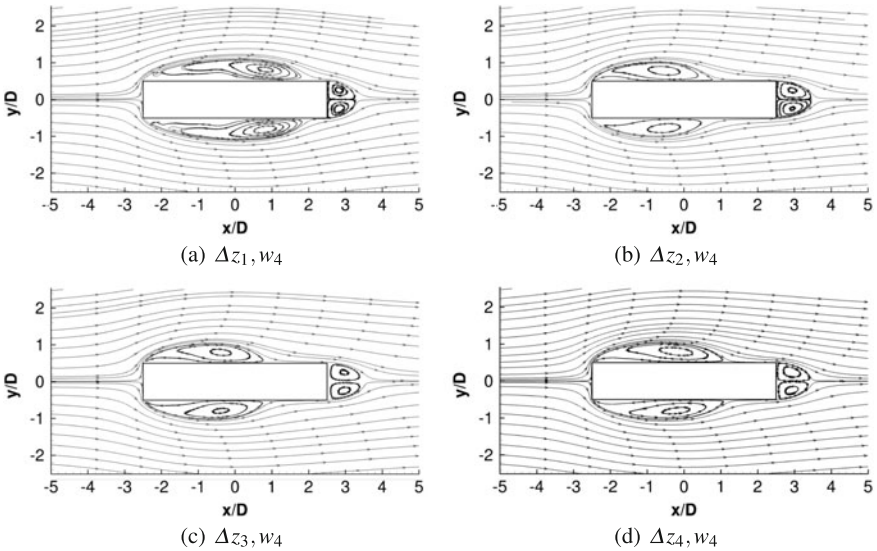

Fig. 4 Mean flow streamlines obtained with LES simulations for four values of the grid spanwise resolution and the same SGS-like dissipation

tions with w_4, Δz_1 and w_4, Δz_4 have a similar level of fluctuations in the shear layer being, nonetheless, characterized by significantly different lengths of the recirculation regions (compare Fig. 4a, d). It is also noteworthy that the behavior of velocity fluctuations in the bubble and shear layer with the mesh resolution is not monotonous (see for instance the results for w_4 in Fig. 3b). In conclusion, the comparison with the available wake measurement data is not yet conclusive, and further analyses are required in the shear layers at more upstream and downstream locations.

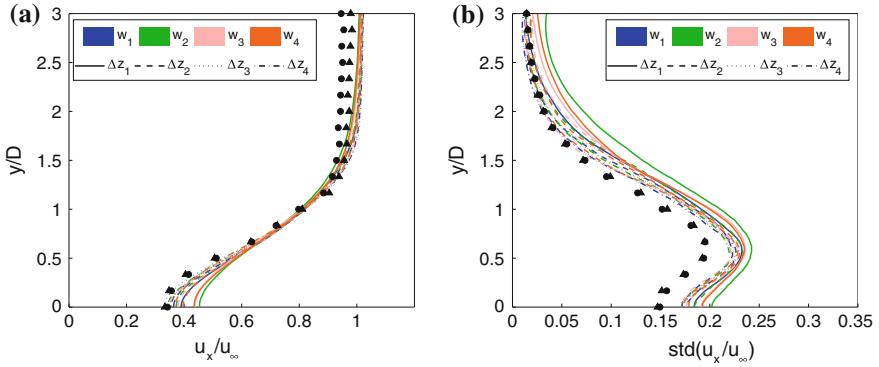

Fig. 5 **a** Mean and **b** standard deviation of the velocity fluctuations in the streamwise x-direction at $x/D = 4.5$ (along line $l6$ in Fig. 1b). Circles and triangles denote the experimental data [5] and refer respectively to $Re = 44{,}900$ and 112,600

Focusing now on the near wake behind the body, Fig. 5 shows the mean velocity profile and the standard deviation of the velocity fluctuations in the streamwise direction along the line $l6$ of Fig. 1b. It is clear that, in spite of the large differences observed in the flow on the cylinder lateral surface, the dispersion of the results in the wake is small and the agreement with the hot-wire anemometry measurements is good, especially for the mean velocity profile. Such a result suggests that the interaction between the wake behind the cylinder and the upstream dynamics near the body is rather weak, and that the mesh resolution and artificial dissipation have a minor influence on the former.

References

1. Nakamura, Y., Ohya, Y., Tsuruta, H.: Experiments on vortex shedding from flat plates with square leading and trailing edges. J. Fluid Mech. **222**, 437–447 (1991)
2. Bruno, L., Salvetti, M.V., Ricciardelli, F.: Benchmark on the aerodynamics of a rectangular 5:1 cylinder: an overview after the first four years of activity. J. Wind Eng. Ind. Aerodyn. **126**, 87–106 (2014)
3. Bruno, L., Coste, N., Fransos, D.: Simulated flow around a rectangular 5:1 cylinder: spanwise discretisation effects and emerging flow features. J. Wind Eng. Ind. Aerodyn. **104–106**, 203–215 (2012)
4. Mariotti, A., Siconolfi, L., Salvetti, M.V.: Stochastic sensitivity analysis of large-eddy simulation predictions of the flow around a 5:1 rectangular cylinder. Eur. J. Mech. B-Fluid **62**, 149–165 (2017)
5. Mannini, C., Marra, A.M., Pigolotti, L., Bartoli, G.: The effects of free-stream turbulence and angle of attack on the aerodynamics of a cylinder with rectangular 5:1 cross section. J. Wind Eng. Ind. Aerodyn. **161**, 42–58 (2017)
6. Mannini, C., Soda, S., Schewe, G.: Numerical investigation on the three-dimensional unsteady flow past a 5:1 rectangular cylinder. J. Wind Eng. Ind. Aerodyn. **99**, 469–482 (2011)

Large-Eddy Simulation of a Sheared Air-Water Flow Around a Cylinder

S. López Castaño and V. Armenio

1 Introduction and Methods

The objective of the present work is to study wake dynamics behind a surface-mounted circular cylinder immersed between two highly stratified fluids in the cross-flow, by performing LES. The focus is to evaluate the degree of interference and interaction caused by the presence of obstacles and of the air-water interface over incoming turbulent boundary layers, while keeping the interface flat.

To achieve this, the incompressible, spatially filtered, Navier–Stokes equations are integrated numerically and the SGS stresses result of the filtering are calculated via the *Dynamic Lagrangian Mixed* model [1]. Subsequent improvements described in [2] allow the study of flows over complex geometries by means of the *Immersed Boundary Method*, or IBM, which in the present work is used to represent the flow around the cylinder. For the coupling, the algorithm of [3] is followed, where the normalized jump conditions for a fluid-fluid interface are expressed as follow:

$$\frac{1}{Re}\left((\overline{\tau}_{liquid} - \overline{\tau}_{gas}) \cdot \mathbf{n}\right) \cdot \mathbf{n} + \overline{p}_{gas} - \overline{p}_{liquid} = 0 \tag{1}$$

$$\overline{\mathbf{u}}_{gas} = \frac{1}{\sqrt{\rho_{liquid}/\rho_{gas}}}\overline{\mathbf{u}}_{liquid} \tag{2}$$

For the inflow, we consider the canonical case of a turbulent Couette boundary layer (located at the liquid side) generated by the traction imposed by a Poiseuille turbulent

S. L. Castaño (✉) · V. Armenio
University of Trieste, Trieste, Italy
e-mail: santilopez01@gmail.com

V. Armenio
e-mail: armenio@dica.units.it

M. V. Salvetti et al. (eds.), *Direct and Large-Eddy Simulation XI*,
ERCOFTAC Series 25, https://doi.org/10.1007/978-3-030-04915-7_57

Table 1 Properties at $T = 320\ K$ for the comprising fluids

	Grid dimensions	Density (m^3/s)	Kinematic viscosity ($\times 10^{-6}$ m^2/s)	Dynamic viscosity ($\times 10^{-6}$ kg/m · s)
Air (Upper)	$128 \times 96 \times 64$	1.08	18.11	19.62
Water (Lower)	$128 \times 96 \times 64$	988.92	0.57	56.60

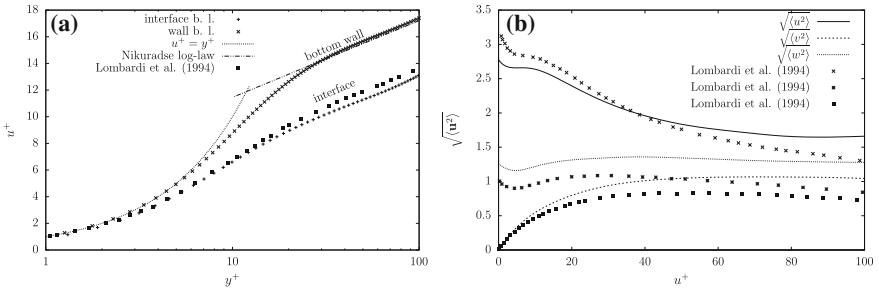

Fig. 1 **a** Velocity profiles on water subdomain. 1b RMS velocity fluctuations close to interface. **b** RMS velocity fluctuations close to interface

boundary (on the gaseous side) layer at the interface between two fluids, as seen in Fig. 2a.

The study will be limited to turbulent boundary layers with the same *Reynolds Number*, $Re_\tau = 171$. For this, if one wants to preserve the same viscous length scale for both domains, i.e. for $l^+ = l\mathbf{u}_*^e/\nu$ to remain invariant, the following condition can be derived from the dynamic condition along interfaces:

$$\frac{\mu_{gas}}{\mu_{liquid}} \sqrt{\frac{\rho_{liquid}}{\rho_{gas}}} = 1 \tag{3}$$

The condition expressed in Eq. 3 imposes certain qualities on the properties of the fluids that, if one is interested to draw a direct comparison with real-life scenarios, are somewhat stringent. Anyway, the fluid properties described in Table 1 for the comprising fluids, namely air and water, have the particularity of being set at a rather high ambient temperature.

Results show three boundary layers formed in this case, which allow for a comparison that elucidates the role of the interface on defining the velocity offset of the boundary layers. Hereinafter, all velocity profiles are normalized respect to U_Γ, the mean interfacial velocity, to facilitate the analysis. Two of these boundaries are contained in the lower sub-domain, where a Couette-type flow is expected but with some differences. One such difference, seen in Fig. 1a, is the velocity reduction of the boundary layers as a consequence of the heightened Reynolds stresses imposed by the air subdomain, as shown in part by Fig. 1b.

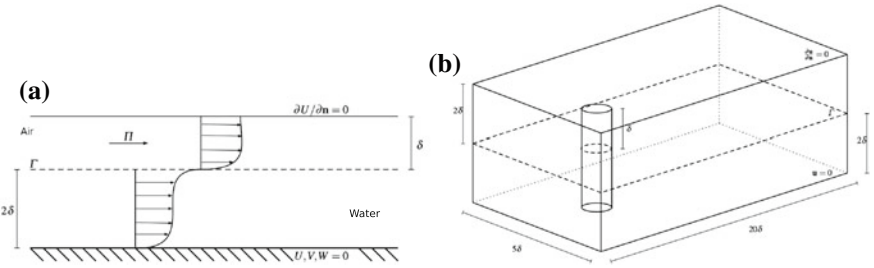

Fig. 2 Domain sketch for: **a** inflow, and **b** cylinder

Also, the velocity RMS profiles show important differences, in fact, the maximum is located on the interface, when comparing Fig. 1b, which goes in contrast with the results on wall-bounded turbulence where the maximum u_{rms} is shown to be located at $\approx$10 viscous units away from the interface. A comparison with the DNS data of [3], show that the interfacial boundary layer is largely influenced by the bottom boundary layer, and viceversa. On the other hand, the mean velocity profile and RMS of velocity fluctuations on the upper sub-domain are similar to wall-bounded flows, as previously noted by [3]. Figure 3b, c are clear in showing that, after making the profile relative to the mean interfacial velocity, U_Γ, the features present in the upper subdomain are similar to wall-bounded turbulence.

2 Cylinder: Results

The geometry of the domain and the location of the cylinder is depicted on Fig. 2, where the lateral boundaries are set periodic. The grid points used for each sub-domain (gas and liquid) were $256 \times 96 \times 96$, and apart from this the settings follow that of the input channel described previously.

On the air side, the streamwise velocity profiles shown in Fig. 3b serve to study the extent of the anomaly caused by the cylinder in the crossflow with the incident turbulent boundary layer. This fully-submerged cylinder, for which its tip is indicated by the vertical dashed line in the aforementioned figures, causes anomalies in the velocity and RMS profiles on the incident flow that extends up to the outlet of the domain; previous studies [4] reported that, for high-Re, the mean streamwise velocity deficit decays at $X/D \approx 8$, although these experiments were for much higher Re thus having the wall-mounted obstacle fully immersed in the inner region. However, similarities in the velocity fluctuations shown in Fig. 3d are present, such as the second u_{rms} peak located below the cylinder tip (around 7/8 of the cylinder height), and that the interaction of the vortices shed from the cylinder with the structures of the incoming flow suppresses the prominence of the former, as it can be seen in Fig. 3a where no dominant shedding frequency is detected after $X/D \approx 11$. The suppression of the shedding is due to the splat-downwash generated by the high-velocity flow

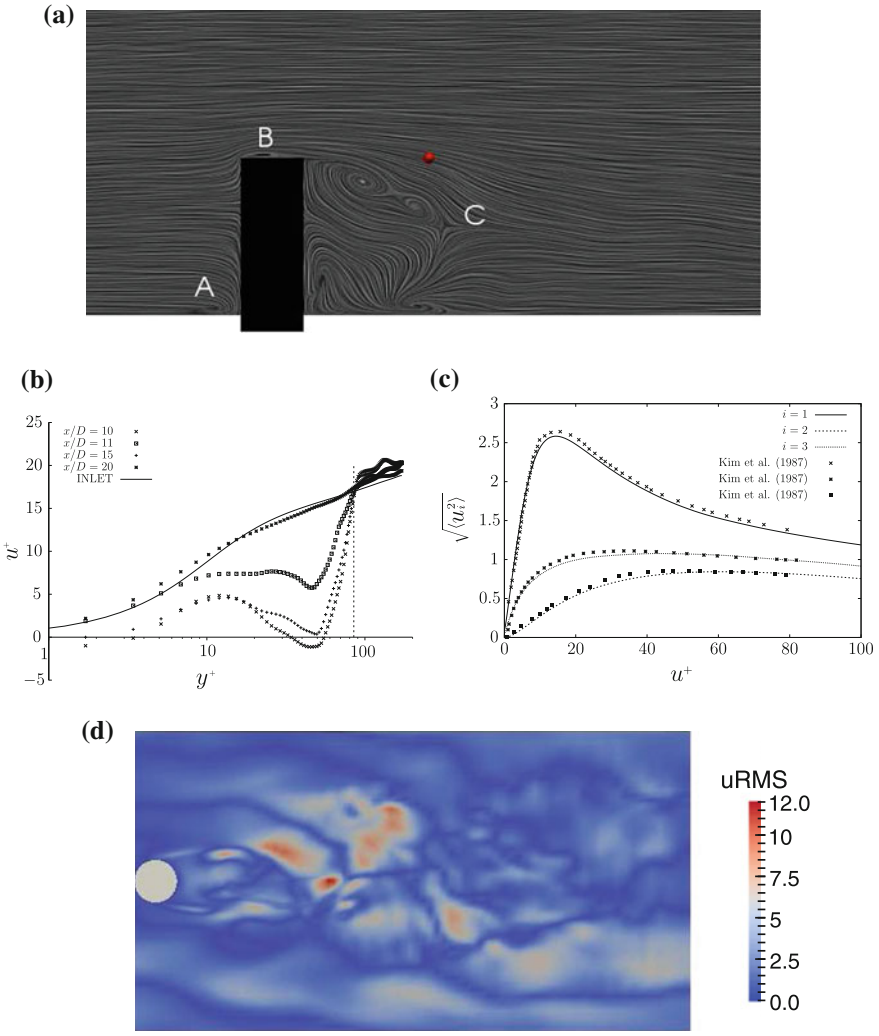

Fig. 3 **a** Vortex eduction via Lagrangian tracers on air side, at midplane. A: separation Vortex, B: Tip Vortex, C: Recirculacion and splat (Saddle), **b** Mean velocity profiles behind the cylinder with zero offset. The solid line is the velocity profile of the incident flow, **c** RMS velocity fluctuations on air side, of the incident flow, **d** Contours of u_{rms} behind the cylinder, on a plane at height $y^+ = 40$

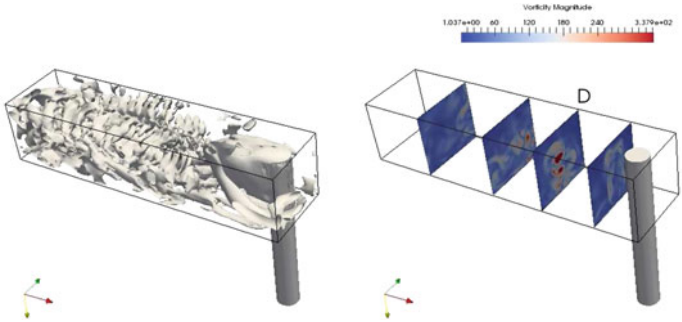

Fig. 4 Left: iso-contours of λ_2 on the air side, right: vorticity contours at different planes

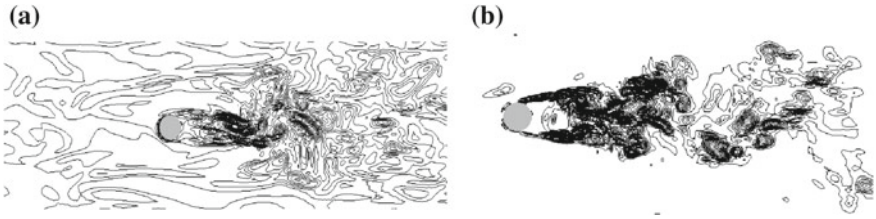

Fig. 5 **a** Vorticity contours in air side at cylinder base close to interface $Y/D = 0.1$ **b** Vorticity contours in water side at cylinder base close to interface $Y/D = 0.9$

passing at the tip of the cylinder, confining the recirculation zone behind it to a length of $X/D = 3.5$ measured from the axis of the cylinder, depicted as region B in Fig. 3a and detectable as the region of highest u_{rms} in Fig. 3d. Finally, the interaction between wakes generated by the spanwise arrangement of finite-height cylinders are detected downstream of the splat, as depicted in Fig. 3d. Such interaction usually is detected [4] farther downstream ($X/D = 11.5$) but on a shorter offset from the midplane ($Z/D = 1.5$). Further work will reveal whether the interference is function of Re and/or U_Γ.

It is typically accepted that for flows around finite cylinders generated by incident near-uniform flows or zero-pressure boundary layers, height-to-diameter ratios larger than 2.5, three vortex structures are generated: Kàrmàn streets, tip vortex, and horseshoe vortex; focus will be given to the horseshoe vortex. In Fig. 5a, mean vorticity magnitude contours close to the interface show no distinguishable shedding behavior in the region upstream of the splat, and Fig. 4 on the left show the formation of the horseshoe vortex in front of the cylinder while on the right the mean vorticity contours show (plate D) the vortex pairing of the horseshoe's legs. Note that the legs of the horseshoe vortex lift well into the mid-channel depth. On the other hand, Fig. 5b show that where the interaction with the incident structures is not as strong as it is the case close to the interface in the water side, the horseshoe vortex and vortex shedding are clearly present. In fact, although the flow velocities are much higher close to the interface that to the wall in the shallow-water case the vortex system

near the interface is more free to develop laterally compared to the obstacle-interface junction in the air side or at the wall.

3 Conclusions

A LES around a wall-mounted circular array cylinder in a shallow water channel driven by interface interaction with a pressure-driven boundary layer in the air is presented. In the air side, the cylinder is immersed well within the outer region of the boundary layer which modulates (by shortening) the incoming coherent structures and at the same time the latter interrupt the shedding process of the wake generated by cylinder. Such anomaly extends up to $X/D = 11.5$ and $Z/D = 1.5$. The recirculation region on the air side is bounded by three types of vortices: (1) the horseshoe vortex emanated at the intersect between the interface and the cylinder bounds the region from the sides; (2) the tip vortex that bounds and deflects the high speed flows towards the interior of the wake, generating splats; and (3) a reduced separation vortex at the front of the cylinder. In uniform incoming flows, the splat generated by the deflected flow is not present.

On the water side, shedding behavior behind the cylinder is detected on horizontal planes close to the interface. The coupled interaction between air and water causes a higher degree of mixing and reduces shear which, in turn, reduces the coherence of motions present in the near-interface region on the water side. This, and the increased convective speed of the interface allows for a more coherent shedding behind the cylinder.

References

1. Armenio, V., Piomelli, U.: A lagrangian mixed subgrid-scale model in generalized coordinates. Flow Turbul. Conbustion **65**, 51–81 (2000)
2. Roman, F., Napoli, E., Milici, B., Armenio, V.: An improved immersed boundary method for curvilinear grids. Comput. fluids **38**, 1510–1527 (2009)
3. Lombardi, P., De Angelis, V., Banerjee, S.: Direct numerical simulation of near-interface turbulence in coupled gas-liquid flow. Phys. Fluids **8**(6), 1643–1665 (1994)
4. Tomkins, C.D.: The structure of turbulence over smooth and rough walls. Ph.D. thesis, University of Illinois at Urbana-Champaign, Urbana, IL, p. 375 (2001)

Scaling Laws in the Axisymmetric Wake of a Sphere

K. Chongsiripinyo, A. Pal and S. Sarkar

1 Introduction

An axisymmetric turbulent wake is often assumed to be self-similar when the streamwise location x is sufficiently far from the wake generator. Thus, profiles of the single-point statistics have the local wake width, $\delta(x)$, and the centerline streamwise mean defect velocity, $U_0(x)$, as the characteristic length and velocity scales. Under self-similarity, the evolution of the scaling parameters, U_0 and δ, is described by power laws: $U_0/U_\infty \sim x^m$ and $\delta/D \sim x^n$ where D is a characteristic length scale of the body. The power-law coefficients m and n were found theoretically [1] to be $(m_L, n_L) = (-1, 1/2)$ and $(m_H, n_H) = (-2/3, 1/3)$ for low-Re and high-Re regimes, respectively. According to [2], the high-Re regime should apply only after the initial transient has decayed so that u'/U_0 becomes constant and only as long as the *local* Reynolds number is sufficiently large, $Re_l = U_0\delta/\nu > 500$. The decrease in *local* Reynolds number as one travels downstream distinguishes the turbulent axisymmetric wake from other free shear flow. There may be a transition from the high to low-Re scaling at large x where Re_l is sufficiently small. It is worth noting that the dissipation is taken to scale as $\varepsilon \propto U_0^3/\delta$ at high Re while $\varepsilon \propto \nu U_0^2/\delta^2$ at low Re. Recently, [3] have found that the axisymmetric wakes of high-drag, irregularly shaped plates exhibit $(m, n) = (-1, 1/2)$ while flow past a regular circular disk and a square plate leads to a wake with the classical high-Re scaling of $(m, n) = (-2/3, 1/3)$. The Reynolds number was not small in the experiments of [3] and, different from [1], a nonequilibrium (NEQ) dissipation law is proposed by [3] to explain their finding of the anomalous $(m, n) = (-1, 1/2)$ scaling.

K. Chongsiripinyo · A. Pal · S. Sarkar (✉)
Department of Mechanical and Aerospace Engineering, University of California, San Diego, USA
e-mail: sarkar@ucsd.edu

K. Chongsiripinyo
e-mail: kchongsi@eng.ucsd.edu

M. V. Salvetti et al. (eds.), *Direct and Large-Eddy Simulation XI*,
ERCOFTAC Series 25, https://doi.org/10.1007/978-3-030-04915-7_58

Table 1 Computational domains. L_x^- and L_x^+ refer to domain upstream and downstream lengths. N is number of grid points

Re	L_r/D	L_θ	L_x^-	L_x^+	N_r	N_θ	N_x	$N_{total}(\cdot 10^6)$
3700 (DNS)	16	2π	23	80	632	128	4608	372.77
10^4 (LES)	59	2π	40	80	918	128	6144	721.94

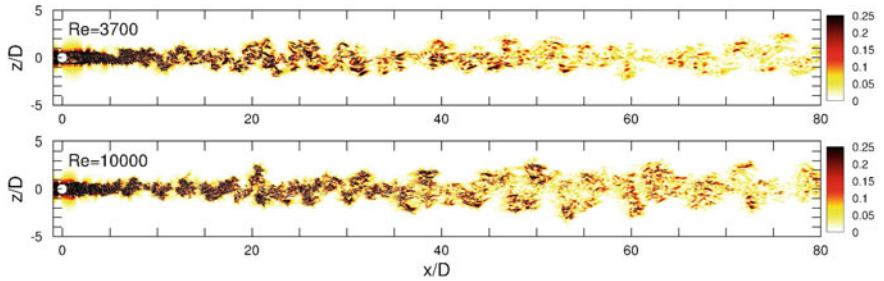

Fig. 1 Contours of azimuthal vorticity magnitude. z/D is cross-stream direction normalized by sphere diameter

In the present work, we consider another canonical wake generator, a sphere, that gives rise to an axisymmetric wake. Numerical simulations are conducted with the objective of characterizing the power laws and discussed in the context of the previous work on this topic.

2 Numerical Approach

The incompressible Navier–Stokes equations along with the continuity equation are numerically solved in a cylindrical coordinate system. The sphere is represented by the immersed boundary method [4, 5]. The equations are marched using a combination of explicit (third-order Runge–Kutta) and implicit (Crank–Nicolson) schemes. Periodicity allows Fourier transformation of the Poisson equation in the azimuthal direction and the resulting equation for the Fourier modes is solved using a direct solver. Velocity boundary conditions (BCs) are Dirichlet, convective outflow, and free-stream at the inlet, outlet and outer radial directions, respectively. The dynamic eddy viscosity model is utilized for the $Re = 10^4$ (LES) case. Table 1 lists the computational parameters. The values of C_p and C_f at the body have been validated previously for both $Re = 3700$ [11] and $Re = 10000$ [12] (Fig. 1).

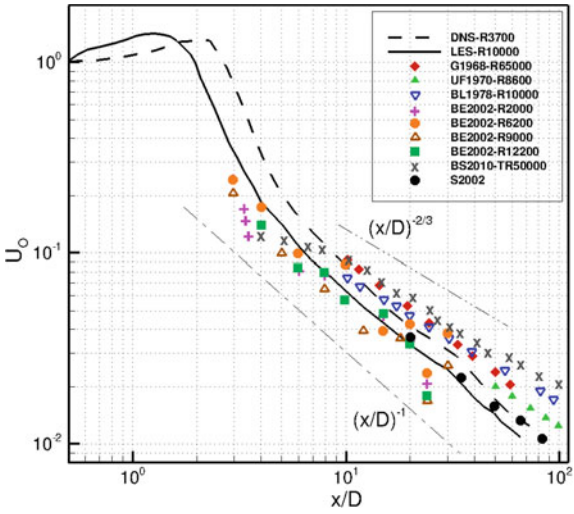

Fig. 2 Centerline streamwise mean defect velocity. The dashed-dotted line is $U_O \sim (x/D)^{-1}$ and the dashed-dotted-dotted line is $U_O \sim (x/D)^{-2/3}$. Legends are as follows: G1968[9]; UF1970 [13]; BL1978 [10]; BE2002 [14]; BS2010 [6]; S2002 [15]

3 Decay of Turbulent Wake

Figures 2 and 3 show the present simulation results of $U_0(x)$ and $\delta(x)$, respectively, along with previous results of the sphere wake. At $Re = 10,000$, the recirculation region is shorter than at $Re = 3700$. Further downstream, both cases exhibit a power law close to $U_0 \propto x^{-1}$. The literature shows different combinations of power-law exponents. At $Re = 50,000$, the temporally evolving model of [6] exhibits $(m, n) = (-2/3, 1/3)$. Note that the temporal model uses synthetic initial turbulence that does not contain the large scale helical structures that arise from shedding of the sphere boundary layer [7, 8]. A laboratory experiment at similar $Re = 65,000$ [9] in Fig. 2 exhibits a power-law decay of U_0 at least during $10 < x/D < 60$. This decay rate is, however, neither $m = -1$ nor $m = -2/3$. Let us turn to sphere wakes at lower Re. The laboratory experiment of [10] at $Re = 10,000$ exhibits $(m, n) = (-2/3, 1/3)$. In contrast, the wakes spanning $Re = 2000 - 12,000$ studied by [14] show behavior closer to $(m, n) = (-1, 1/2)$.

The evolution of local $Re_l = U_0\delta/\nu(x)$ is shown in Fig. 4. If the criterion [2] of $Re_l = U_O\delta/\nu > 500$ for the high-Re regime is true, it can be inferred from Fig. 4 that the present simulations at $Re = 3700$ and $10,000$ do not fall into the high-Re regime and, therefore, $m = -2/3$ and $n = 1/3$ would not be expected. Note that the experiment of [10] contradicts the criterion of [2] since their $Re = 10,000$ wake exhibits $(m, n) = (-2/3, 1/3)$ despite that fact that $Re_l < 500$.

The evolution of centerline t.k.e (K) is shown in Fig. 5. The $x^{-3/2}$ power law of K translates to a $u' \propto x^{-3/4}$ scaling for the turbulence velocity scale of $u' = \sqrt{K}$. The streamwise velocity fluctuation (not shown) also shows a $-3/4$ decay exponent. It is worth noting that u' does not vary at the same rate as U_0.

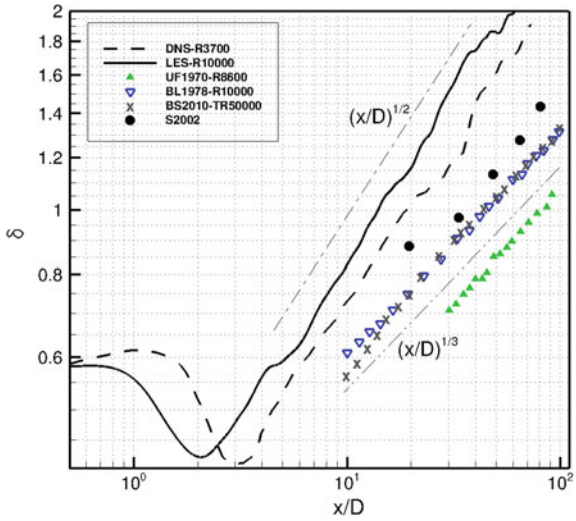

Fig. 3 Wake half width, L_v (or δ). The dashed-dotted line is $\delta \sim (x/D)^{1/2}$ and the dashed-dotted-dotted line is $\delta \sim (x/D)^{1/3}$. The legend is the same as Fig. 2

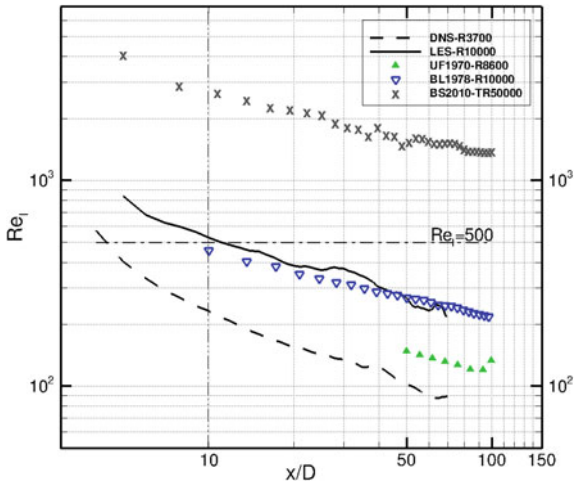

Fig. 4 Local Reynolds number, $Re_l = U_O \delta / \nu$

The turbulent dissipation (Fig. 5) follows $x^{-5/2}$. The classical high-Re scaling of $\varepsilon \propto U_0^3/\delta$ leads to an exponent of $-7/2$ while the low-Re scaling of $\varepsilon \propto \nu U_0^2/\delta^2$ introduced by [1] leads to an exponent of -3. Both of these scaling laws lead to steeper decay of ε than the $-5/2$ behavior found in the simulations. We can alternatively use u' as the velocity scale instead of U_0 in the dissipation estimate. The low-Re scaling of $\varepsilon \propto \nu u'^2/\delta^2$ leads to $\varepsilon \propto -5/2$ which is in agreement with the LES result. Thus, one explanation of the behavior of ε in the simulations is low-Re.

The energy spectrum in the LES at $Re = 10,000$ has a decade of broad-band fluctuations (not $k^{-5/3}$ but similarly steep) in the intermediate wake where the wake power laws with $(m, n) = (-1, 1/2)$ are already established. We, therefore, explore the

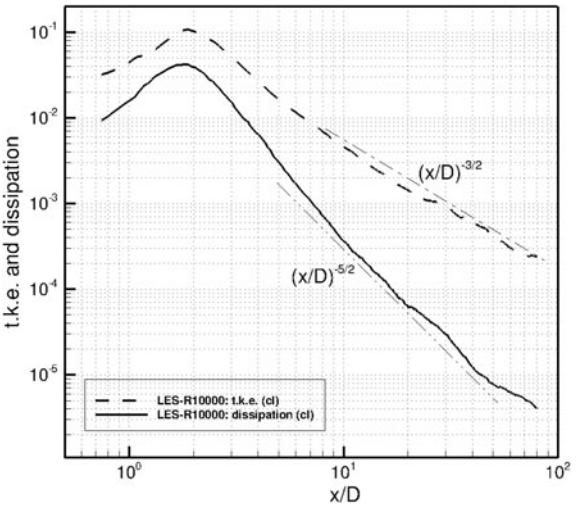

Fig. 5 Turbulent kinetic energy, t.k.e (or K) and dissipation, ε, at the centerline for the $Re = 10,000$ LES. The dashed-dotted line is $K \sim (x/D)^{-3/2}$ and the dashed-dotted-dotted line is $\varepsilon \sim (x/D)^{-5/2}$

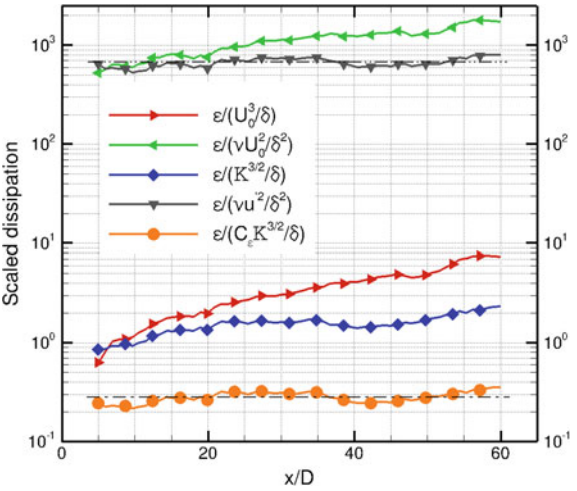

Fig. 6 Scalings of dissipation for the $Re = 10,000$ case. The classical high-Re scaling: $\varepsilon \propto U_0^3/\delta$; the classical low-$Re$ scaling: $\varepsilon \propto \nu U_0^2/\delta^2$; the classical inviscid estimate: $\varepsilon \propto K^{3/2}/\delta$; the modified low-$Re$ scaling: $\varepsilon \propto \nu u'^2/\delta^2$; and the NEQ scaling: $\varepsilon = C_\varepsilon K^{3/2}/\delta$ with $C_\varepsilon = (Re_G/Re_l)^{1/2}$

implications of the high-Re NEQ dissipation *ansatz* [3, 16] and find that NEQ dissipation provides an alternate explanation for the ε power law found in the simulations. According to the NEQ dissipation formulation, the coefficient C_ε in $\varepsilon = C_\varepsilon K^{3/2}/\delta$ is no longer a universal constant but takes the form $C_\varepsilon = Re_G^m/Re_l^n$. Here Re_G is a global Reynolds number characteristic of the inflow and is taken to be $Re_G = UD/\nu$, the sphere Reynolds number.

By taking the decay rates of centerline dissipation and t.k.e., shown in Fig. 5, along with the growth rate of wake dimensions in Fig. 3, it follows that $C_\varepsilon = \varepsilon K^{-3/2}\delta$ varies as $x^{1/4}$ which contradicts the classical Kolmogorov theory of constant C_ε. However, the decay of defect velocity as in Fig. 2 along with the growth rate in Fig. 3 gives $C_\varepsilon = Re_G^m/Re_l^n \sim x^{1/4}$ if we choose $m = n = 0.5$. This is in agreement with the

simulation result of $\varepsilon K^{-3/2}\delta$. Note, [17] reports m=n=0.5 to be effective at $55 < x/L_b < 100$, where L_b is their equivalent wake generator length scale. Thus, the new non-equilibrium dissipation law in which C_ε as in $\varepsilon = C_\varepsilon K^{3/2}/\delta$ is not a constant but takes the value $C_\varepsilon = (Re_G/Re_l)^{1/2}$ provides an alternative explanation. Figure 6 shows the evolution of centerline ε normalized according to different theoretical scaling laws. It can be seen that both the modified low-Re and the NEQ dissipation theory are successful in explaining the power law for ε found in the $Re = 10,000$ simulation.

Acknowledgements We are grateful to acknowledge the support of ONR Grant No. N00014-15-1-2718. Computational resources were provided by the Department of Defense High Performance Computing Modernization Program.

References

1. George, W.K.: The self-preservation of turbulent flows and its relation to initial conditions and coherent structures. Advances in Turbulence, pp. 39–73 (1989)
2. Johansson, P.B.V., George, W.K., Gourlay, M.J.: Equilibrium similarity, effects of initial conditions and local Reynolds number on the axisymmetric wake. Phys. Fluids **15**, 603–617 (2003)
3. Nedic, J., Vassilicos, J.C., Ganapathisubramani, B.: Axisymmetric turbulent wakes with new nonequilibrium similarity scalings. Phys. Rev. Lett. **111**(14), 144503 (2013)
4. Balaras, E.: Modeling complex boundaries using an external force field on fixed Cartesian grids in large-eddy simulations. Comput. Fluids **33**(3), 375–404 (2004)
5. Yang, J., Balaras, E.: An embedded-boundary formulation for large-eddy simulation of turbulent flows interacting with moving boundaries. J. Comput. Phys. **215**(1), 12–40 (2006)
6. Brucker, K.A., Sarkar, S.: A comparative study of self-propelled and towed wakes in a stratified fluid. J. Fluid Mech. **652**, 373–404 (2010)
7. Yun, G., Kim, D., Choi, H.: Vortical structures behind a sphere at subcritical Reynolds numbers. Phys. Fluids **18**(1), 015102 (2006)
8. Chongsiripinyo, K., Pal, A., Sarkar, S.: On the vortex dynamics of flow past a sphere at Re= 3700 in a uniformly stratified fluid. Phys. Fluids **29**(2), 020704 (2017)
9. Chen, C.C., Gibson, C.H., Lin, S.C.: Measurements of turbulent velocity and temperature fluctuations in the wake of a sphere. AIAA J. **6**(4), 642–649 (1968)
10. Bevilaqua, P.M., Lykoudis, P.S.: Turbulence memory in self-preserving wakes. J. Fluid Mech. **89**(3), 589–606 (1978)
11. Pal, A., Sarkar, S., Posa, A., Balaras, E.: Direct numerical simulation of stratified flow past a sphere at a subcritical Reynolds number of 3700 and moderate Froude number. J. Fluid Mech. **826**, 5–31 (2017)
12. Chongsiripinyo, K., Sarkar, S.: Effect of stratification on the turbulent wake behind a sphere at Re=10,000. In: 10th International Symposium on Turbulence and Shear Flow Phenomena (TSFP10), Chicago, USA (2017)
13. Uberoi, M.S., Freymuth, P.: Turbulent energy balance and spectra of the axisymmetric wake. Phys. Fluids **13**(9), 2205–2210 (1970)
14. Bonnier, M., Eiff, O.: Experimental investigation of the collapse of a turbulent wake in a stably stratified fluid. Phys. Fluids **14**(2), 791–801 (2002)
15. Spedding, G.R.: Vertical structure in stratified wakes with high initial Froude number. J. Fluid Mech. **454**, 71–112 (2002)
16. Vassilicos, J.C.: Dissipation in turbulent flows. Ann. Rev. Fluid Mech. **47**, 95–114 (2015)
17. Dairay, T., Obligado, M., Vassilicos, J.C.: Non-equilibrium scaling laws in axisymmetric turbulent wakes. J. Fluid Mech. **781**, 166–195 (2015)

Hybrid Versus Pure-LES Models Comparison for Subcritical Cylinder Flows

E. Itam, S. Wornom, B. Koobus and A. Dervieux

1 Introduction

In Computational Fluid Dynamics applications, there is a need for turbulence models which deliver good predictions for flows involving both laminar and turbulent boundary layers, without knowing in advance the regions where turbulence occurs, and then without changing their parameters according to such an a priori knowledge of the flow characteristics. In this work, which extends the study [7], we are interested in the assessment of hybrid models for the computation of subcritical flows with laminar boundary layers and in the improvement of the wake behavior prediction in a hybrid RANS/LES model [6, 7, 10]. The performances of a DDES model are compared with a dynamic variational multi-scale (DVMS) large eddy simulation model. The reasons why DDES computations give less good predictions are many. We concentrate in this study on the treatment of the wake. We define RANS/DVMS and DDES/DVMS hybrid models, and compare their predictions with those provided by a DDES model. Three subcritical flows past a circular cylinder are considered,

E. Itam (✉) · B. Koobus
Institut Montpellierain Alexander Grothendieck (IMAG), Universite de Montpellier, Montpellier, France
e-mail: emmanuelle.itam@umontpellier.fr

B. Koobus
e-mail: Bruno.Koobus@umontpellier.fr

S. Wornom
Societe technologique LEMMA, 2000 route des Lucioles, Sophia-Antipolis, France
e-mail: stephen.wornom@inria.fr

A. Dervieux
Institut National de Recherche en Informatique et en Automatique (INRIA), 2004 Route des lucioles, F-06902 Sophia-Antipolis, France
e-mail: alain.dervieux@inria.fr

M. V. Salvetti et al. (eds.), *Direct and Large-Eddy Simulation XI*,
ERCOFTAC Series 25, https://doi.org/10.1007/978-3-030-04915-7_59

Table 1 Bulk quantities for Re = 3900 flow around a cylinder. $\overline{C}_d$ holds for the mean drag coefficient, $\overline{C}_{p_b}$ for the mean pressure coefficient at cylinder basis, C_L^{rms} for the root mean square of lift time fluctuations, L_r is the recirculation length, S_t the Strouhal number

	$\overline{C}_d$	$-\overline{C}_{p_b}$	C_L^{rms}	L_r	S_t
Experiments					
Norberg [12] min.	0.94	0.83	–	–	–
Norberg [12] max.	1.04	0.93	–	–	–
Parnaudeau [14]	–	–	–	1.51	0.210
Present simulations					
No model	0.87	0.73	0.04	2.11	
RANS $k-\varepsilon$-Menter	0.86	0.72	0.03	2.18	0.216
DDES $k-\varepsilon$-Menter	0.98	0.83	0.10	1.70	0.215
DVMS	1.03	0.86	0.19	1.50	0.216
DDES/DVMS	0.99	0.79	0.12	1.67	0.216
Other simulations					
D'Alessandro SA-IDDES [1]	0.98	0.83	0.109	1.67	0.214
D'Alessandro $\bar{v}^2-f$ DES [1]	1.02	0.87	0.14	1.42	0.222

Table 2 Bulk flow parameters for Re = 20000 flow around a cylinder. Θ_{sep} is the separation angle. The other symbols are the same as in Table 1

	$\overline{C_d}$	$-\overline{Cp_b}$	C_L^{rms}	Θ_{sep}	L_r	S_t
Experiments						
Norberg [13]	1.16	1.16	0.47	78	1.03	0.194
Present simulations						
No model	1.27	1.35	0.61	82	0.96	
RANS $k-\varepsilon$-Menter	1.31	1.49	0.75	85	0.50	0.212
DDES $k-\varepsilon$-Menter	1.25	1.21	0.58	86	0.90	0.194
DVMS	1.18	1.20	0.46	81	0.96	0.196
DDES/DVMS	1.17	1.13	0.46	82	1.05	0.200
Other simulations						
Salvatici LES [15] min.	0.94	0.83	0.17	–	0.7	–
Salvatici LES [15] max.	1.28	1.38	0.65	–	1.4	–

namely at Reynolds numbers 3900, 20000 and 140000 (see Tables 1, 2 and 3). Computations are also compared with other LES and hybrid computations in the literature and with experimental data.

Table 3 Bulk quantities for Re = 140000 flow around a cylinder. Same symbols as in Table 2

	$\overline{C}_d$	$-\overline{C}_{p_b}$	C_L^{rms}	L_r	S_t	Θ_{sep}
Experiments						
Cantwell–Coles [3]	1.24	1.21	–	0.5	0.179	77
Szepessy–Bearman [17]	–	–	0.39	–	–	–
Present simulations						
No model	0.43	0.40	0.14	0.63	0.142	
RANS $k-\varepsilon$-Menter	0.77	0.87	0.31	1.05	0.218	98
DDES $k-\varepsilon$-Menter	0.97	1.01	0.30	0.96	0.217	85
DVMS	1.25	1.33	0.64	0.88	0.217	76
DDES/DVMS	1.04	1.12	0.41	0.91	0.214	85
Other simulations						
Froehlich (LES Smago.) [4]	1.16	1.33	–	0.41	0.217	94
Breuer (LES Smago. Dyn) [2]	1.24	1.40	–	0.57	0.204	96

2 Numerical Model

The spatial discretization is based on a mixed Finite-Element / Finite-Volume formulation on unstructured grids, with degrees of freedom located at vertices i of the tetrahedrization. The finite volume part is integrated on a dual mesh built from medians in 2D and median plans in 3D. The space-discretized unsteady Navier–Stokes equations can be written as follows:

$$\left(\frac{\partial W}{\partial t}, \phi_i\right) + (\nabla \cdot F(W), \phi_i) = 0$$

where W is the set of conservatives variables, ϕ_i the test function related to vertex i, and $F(W)$ denotes the convective and diffusive fluxes. The diffusive terms are evaluated by a Finite-Element method, whereas a Finite-volume method is used for the convective fluxes. The numerical approximation of the convective fluxes at the interface of neighboring cells is based on the Roe Scheme. In order to obtain second-order accuracy in space, a particular MUSCL-like method is used. The numerical (spatial) dissipation provided by this scheme is made of sixth-order space derivatives and is concentrated on a narrow-band of the highest resolved frequencies. This dissipation behaves as $O(\Delta x^5)$ (on uniform 1D meshes). This is expected to limit dissipation on the large scales. Lastly, a parameter γ_S directly controls the amount of introduced viscosity and can be explicitly tuned in order to control the influence of numerical dissipation and, when necessary, reduce it to the minimal amount needed to stabilize the simulation. Typically, γ_S is set to a value which gives a 10 times smaller dissipation than the fully-upwind fifth-order scheme. Time integration is performed by a

second-order implicit second-order backward difference scheme allowing to address flows at various Mach numbers. In the present paper, the Mach number is chosen equal to 0.1.

3 Turbulence Modeling

In the VMS approach [8] used herein, the subgrid-scale (SGS) stress term is acting only on small scales and is computed from the small scale component of the flow field by applying either a Smagorinsky or a WALE SGS model. Further, the constants of these models can be evaluated by a Germano-Lilly dynamic procedure [11]. This results in our *DVMS model*, the semi-discretization of which writes:

$$\Big(\frac{\partial W}{\partial t}, \phi_i\Big) + (\nabla \cdot F(W), \phi_i) = -\big(\tau^{DVMS}(W'), \phi_i'\big).$$

where W' holds for the small resolved scales. In order to define our hybrid model, we choose a RANS modelling. It is based on the k-ε Goldberg model [5] combined with the Menter correction [9]. We denote it in the sequel as *RANS* $k-\varepsilon$*-Menter* and write it in short:

$$\Big(\frac{\partial W}{\partial t}, \phi_i\Big) + (\nabla \cdot F(W), \phi_i) = -\big(\tau^{RANS}(W), \phi_i\big).$$

Let us define the hybrid *RANS/DVMS* model based on the above DVMS and RANS models:

$$\Big(\frac{\partial W}{\partial t}, \phi_i\Big) + (\nabla \cdot F(W), \phi_i) = -\theta\big(\tau^{RANS}(W), \phi_i\big) - (1-\theta)\big(\tau^{DVMS}(W'), \phi_i'\big).$$

The symbol $\theta \in [0, 1]$ holds for the blending function and is defined as following: $\theta = 1 - tanh(\xi^2) f_d$, where $\xi = \Delta / l_{RANS}$ with Δ the local mesh size and l_{RANS} the RANS characteristic length, or $\xi = \mu_{SGS}/\mu_{RANS}$ with μ_{SGS} the SGS viscosity and μ_{RANS} the RANS viscosity. The shielding function f_d is defined as in DDES [16], and therefore $f_d \approx 0$ in the boundary layer, and $f_d \approx 1$ outside the boundary layer.

For comparison purpose, we introduce the *DDES* $k-\varepsilon$*-Menter*, written

$$\Big(\frac{\partial W}{\partial t}, \phi_i\Big) + (\nabla \cdot F(W), \phi_i) = -\big(\tau^{DDES}(W), \phi_i\big),$$

in which the above RANS model is introduced in a DDES formulation by replacing in the RHS of the k equations the $D_k^{RANS} = \rho\varepsilon$ dissipation term by $D_k^{DDES} = \rho k^{\frac{3}{2}}/l_{DDES}$ with $l_{DDES} = k^{\frac{3}{2}}/\varepsilon - f_d max\big(0, k^{\frac{3}{2}}/\varepsilon - C_{DDES}\Delta\big)$ where $C_{DDES} = 0.65$ and Δ is a measure of the local mesh size. We have checked in [7] that this model gives predictions close to other DDES approach based on the $k-\omega$ SST model.

Lastly, we define the *DDES/DVMS* model. This version has the same switching as the previous hybrid one, but combines DVMS with the DDES model:

$$\left(\frac{\partial W}{\partial t}, \phi_i\right) + (\nabla \cdot F(W), \phi_i) = -\theta\left(\tau^{DDES}(W), \phi_i\right) - (1-\theta)\left(\tau^{DVMS}(W'), \phi_i'\right).$$

Compared to the RANS/DVMS model, and outside the boundary layer where the RANS approach applies, this hybrid model still behaves as DVMS if the grid resolution is sufficient, but it switches to DDES instead of RANS in coarser grid locations. It may also be noted that the LES component (DVMS) of our hybrid models allows a priori a better prediction of the wake than the simpler LES model invoked by DDES.

4 Results and Comments

We reconsider here the two first test cases of [7], with several updates and new computations involving other models. A third test case which concerns a high subcritical Reynolds number, is also presented for the assessment of the different turbulence models introduced in this work. Among our hybrid models, it turned out that DDES/DVMS performs slightly better, and only its results are reported in the following tables.

For low and medium subcritical Reynolds numbers (Re = 3900 and Re = 20000), the computations performed with the turbulent models mentioned above compare rather well with experimental data and numerical results in the litterature. Several remarks can however be made. First, although theoretically not adapted (the laminar boundary layer is computed by a RANS model), the DDES and our hybrid approach provide a reasonably good prediction of main outputs. As noticed in [1], the eddy viscosity introduced in the attached boundary layer is small enough so that its effect may be small if not negligible. We compare in Table 1 our results with the DES results obtained by D'Alessandro and co-workers, and we observe that these results and the one obtained with our DDES are close to each other, which tend to show that our DDES behaves in a reasonable way. Second, for Reynolds number 3900, the DDES and our hybrid model predictions are essentially less accurate than those obtained with DVMS.

For $Re = 3900$, the recirculation length predicted by the DDES and hybrid model are much too large, while the DVMS is in accordance with the Parnaudeau measurement. This may result from the boundary layer RANS treatment.

Comparing our hybrid approach with DDES, we observe that an overall improvement is obtained for Reynolds number 20000 when a better LES component is locally imposed (through the use of DVMS in the wake region) and this results in a prediction according as well with measurements as for the DVMS.

For a higher subcritical Reynolds number (Re = 140000), while DVMS behaves correctly, the RANS, DDES and our hybrid turbulence models automatically apply a RANS model in the boundary layer with a turbulent viscosity ν_t which, for this

Reynolds number can be much higher than the laminar viscosity. Now we know from experiments that the physical boundary layer is laminar. Applying $\nu + \nu_t$ instead of ν may result in inaccuracies. The DDES/DVMS model shows an intermediate prediction quality with a reasonable improvement with respect to DDES. However, still only LES-type simulations provide bulk quantities prediction inside a 10% interval. DDES results and our hybrid model predictions are in a 20% interval, with a slight improvement for our hybrid approach. These models still need further improvements for properly tackling such subcritical flows.

Acknowledgements This work has been supported by French National Research Agency (ANR) through project MAIDESC n^o ANR-13-MONU-0010. This work was granted access to the HPC resources of CINES under the allocations 2017-A0022A05067 and 2017-A0022A06386 made by GENCI (Grand Equipement National de Calcul Intensif).

References

1. D'Alessandro, V., Montelpare, S., Ricci, R.: Detached eddy simulations of the flow over a cylinder at Re = 3900 using Open- FOAM a low-diffusion MUSCL scheme for LES on unstructured grids. Comput. Fluids **136**, 152169 (2016)
2. Breuer, M.: A challenging test case for large eddy simulation, high Reynolds number circular cylinder flow. Int. J. Heat Fluid Flow **21**, 648–654 (2000)
3. Cantwell, B., Coles, D.: An experimental study of entrainment and transport in the turbulent near wake of a circular cylinder. J. Fluid Mech. **136**, 321–374 (1983)
4. Froehlich, J., Rodi, W., Bertoglio, J.P., Bieder, U., Touil, H.: Large eddy simulation of flow around circular cylinders on structured and unstructured grids I. In: Hirschel, E.H. (ed.) Numerical Flow Simulation II, vol. 75, pp. 231–249. Vieweg (2001)
5. Goldberg, U., Peroomian, O., Chakravarthy, S.: A wall-distance-free $k-\varepsilon$ model with enhanced near-wall treatment. J. Fluids Eng. **120**, 457–462 (1998)
6. Itam, E., Wornom, S., Koobus, B., Dervieux, A.: Application of a hybrid variational multiscale model to massively separated flows. 3AF, Toulouse, France (2015)
7. Itam, E., Wornom, S., Koobus, B., Dervieux, A.: Hybrid simulation of high-Reynolds number flows relying on a variational multiscale model. In: 6th Symposium on Hybrid RANS-LES Methods, Strasbourg, France, 26–28 September 2016
8. Koobus, B., Farhat, C.: A variational multiscale method for the large eddy simulation of compressible turbulent flows on unstructured meshes-application to vortex shedding. Comput. Methods Appl. Mech. Eng. **193**, 13671383 (2004)
9. Menter, F.R.: Zonal two-equation $k-\omega$ turbulence models for aerodynamic flows. AIAA Paper 93-2906 (1993)
10. Moussaed, C., Salvetti, M.V., Wornom, S., Koobus, B., Dervieux, A.: Simulation of the flow past a circular cylinder in the supercritical regime by blending RANS and variational-multiscale LES models. J. Fluids Struct. **47**, 114123 (2014)
11. Moussaed, C., Wornom, S., Salvetti, M.V., Koobus, B., Dervieux, A.: Impact of dynamic subgrid-scale modeling in variational multiscale large-eddy simulation of bluff body flows. Acta Mech. **12**, 33093323 (2014)
12. Norberg, C.: Effects of Reynolds number and low-intensity freestream turbulence on the flow around a circular cylinder. Publ. No.87/2, Department of Applied Thermosc. and Fluid Mech., Chalmer University of Technology, Sweden (1987)
13. Norberg, C.: Fluctuating lift on a circular cylinder: review and new measurements. J. Fluids Struct. **17**, 5796 (2003)

14. Parnaudeau, P., Carlier, J., Heitz, D., Lamballais, E.: Experimental and numerical studies of the flow over a circular cylinder at Reynolds number 3900. Phys. Fluids **20**, 085101 (2008)
15. Salvatici, E., Salvetti, M.V.: Large eddy simulations of the flow around a circular cylinder: effects of grid resolution and subgrid scale modeling. Wind Struct. **6**(6), 419–436 (2003)
16. Spalart, P.R., Deck, S., Strelets, M., Shur, M.L., Travin, A., Squires, K.D.: A new version of detached-eddy simulation, resistant to ambiguous grid densities. Theor. Comput. Fluid Dyn. **20**, 181–195 (2006)
17. Szepessy, S., Bearman, P.W.: Aspect ratio and end plate effects on vortex shedding from a circular cylinder. J. Fluid Mech. **234**, 191217 (1992)

Modeling of Wind Gusts for Large-Eddy Simulations Related to Fluid-Structure Interactions

G. De Nayer, M. Breuer, P. Perali and K. Grollmann

1 Introduction

The dimensioning of lightweight structures under wind loads strongly depends on realistic flow conditions. Two different setups have to be distinguished. For a long-term analysis such as dynamic fatigue, temporally and spatially correlated velocity distributions are required as inflow conditions for a large-eddy simulation (LES) to mimic a realistic physical setup [9]. To generate these inflow data different synthetic turbulence inflow generators (STIG) such as the digital filter method of Klein et al. [5] are in use for a variety of test cases, e.g., [7–9]. For a short-term analysis aiming at the peak loads acting on a structure under wind load, extreme events in form of wind gusts have to be taken into account.

The development of an advanced methodology to investigate extreme events within a fluid-structure interaction (FSI) framework based on large-eddy simulation developed and validated at the institute [2–4] is the topic of the present contribution. The synthetic turbulence inflow generator based on the digital filter method is extended to generate distinctive wind gusts of different shapes and amplitudes based on either deterministic (Gaussian, 1-cosine, Mexican hat shape) or stochastic methods [1]. The injection of these wind gusts into the flow domain implies a short but brutal change of the total mass inflow, which has to be corrected so that the incompressible solver does not diverge. In order to evaluate the method in the FSI context, a test case based on a rigid structure is considered in a first phase, while

G. De Nayer · M. Breuer (✉) · K. Grollmann
Helmut-Schmidt University, Hamburg, Germany
e-mail: breuer@hsu-hh.de

G. De Nayer
e-mail: denayer@hsu-hh.de

P. Perali
Ecole Centrale de Nantes, Nantes, France
e-mail: paolo.perali@ec-nantes.fr

M. V. Salvetti et al. (eds.), *Direct and Large-Eddy Simulation XI*,
ERCOFTAC Series 25, https://doi.org/10.1007/978-3-030-04915-7_60

simulations with flexible structures will be carried out later. The flow around the wall-mounted cube of Martinuzzi [6] is selected and slightly modified. The effects of different forms and amplitudes of wind gusts on the resulting fluid forces acting on the rigid structure are investigated.

2 Wind Gust Modeling for LES

The first method is deterministic. The gust is generated by a superposition of a velocity signal related to the extreme event $u_{\text{gust}}(t, y, z)$ to the original synthetic velocity components $u_{\text{stig}}(t, y, z)$ generated by the STIG [5] as depicted in Fig. 1.

In order to easily control the form, the duration, the amplitude and the position of the gust entering the flow domain at the y–z plane, the gust-related velocity distribution is expressed as:

$$u_{\text{gust}}(t, y, z) = A_{\text{g}}(y, z) \;\; f_{\text{t}}(t) \;\; f_{\text{y}}(y) \;\; f_{\text{z}}(z) \;, \tag{1}$$

where $f_{\text{t}}(t)$, $f_{\text{y}}(y)$ and $f_{\text{z}}(z)$ are the shape factors of the gust in time, y- and z-direction, respectively. $A_{\text{g}}(y, z)$ is the gust amplitude factor depending on the location.

The definition of the shape factors $f_{\phi}(\phi)$ ($\phi \in \{t, y, z\}$) depending on a given length scale L_{g}^{ϕ} and on a fixed central value ϕ_{g} of the variable ϕ are expressed by analytic functions of the forms:

- A **Gaussian distribution** (similar to the distribution used in the digital filter method applied to generate the original synthetic velocity components u_{stig}):

$$f_{\phi}(\phi) = \exp\left(-18\left(\left(\phi - \phi_{\text{g}}\right)/L_{\text{g}}^{\phi}\right)^2\right) \tag{2}$$

- An **adapted "1-cosine" shape** (*extreme coherent gust* from the 61400–IEC standards for wind turbines):

$$f_{\phi}(\phi) = \frac{1}{2}\left(1 + \cos\left(2\pi\left(\phi - \phi_{\text{g}}\right)/L_{\text{g}}^{\phi}\right)\right) \tag{3}$$

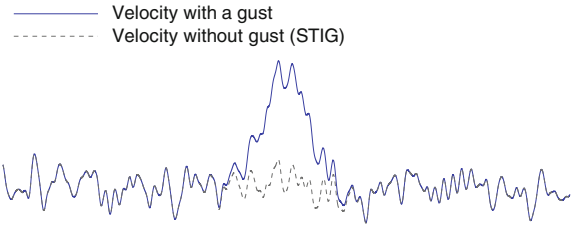

Fig. 1 A sudden wind gust in a turbulent time signal generated by the deterministic method based on the Gaussian shape of the wind gust according to Eq. (2)

- An **adapted "Mexican hat" shape** (*extreme operating gust* from the 61400–IEC standards for wind turbines):

$$f_\phi(\phi) = 0.37 \cos\left(3\pi \left(\phi - \phi_g\right)/L_g^\phi\right)\left(1 + \cos\left(2\pi \left(\phi - \phi_g\right)/L_g^\phi\right)\right) \quad (4)$$

The deterministic method is fast and allows a perfect control of the parameters of the gust. However, per definition, the form of the generated gust is not correlated in time and space, which is not mimicking the reality. A second technique developed by Bierbooms [1] generates a wind gust in a stochastic manner by determining the most probabilistic gust shape based on a given stochastic Gaussian distribution and a set of constraints. The present study is restricted to the deterministic method.

When a gust is introduced into the computational domain, the raise of the mean velocity at the inlet of the domain induces a distortion of the total mass flow. Since the fluid is incompressible, the global mass conservation is no longer satisfied, which often leads to the divergence of the flow solver. To resolve this problem, a velocity correction $u_{\text{corr}}(t, y, z)$ is introduced so that the total mass flow at the inlet remains constant even during the gust injection. This correction is applied at the inlet patches far away from the area of interest, so that the gust is not altered:

$$u_{\text{corr}}(t, y, z) = \frac{\dot{m}_0 - \dot{m}(t)}{\dot{m}_0} \; \overline{u}_i(y, z) \; g(y) \quad (5)$$

with $\dot{m}_0$ the nominal total mass flow, $\dot{m}(t)$ the current total mass flow, $\overline{u}_i(y, z)$ the mean velocity (without gust) in the direction of the gust and the function g:

$$g(y) = \text{erf}\left(4\pi \frac{y - y_{min}}{y_{max} - y_{min}} - \pi\right) - 1 \qquad \text{for} \quad y < \frac{y_{min} + y_{max}}{2}$$

$$g(y) = -\text{erf}\left(2\pi \frac{2y - y_{min} - y_{max}}{y_{max} - y_{min}} - \pi\right) - 1 \qquad \text{else}$$

where erf is the error function and y_{min} and y_{max} the bounding values of the domain in spanwise direction. The correction can also be carried out in vertical direction by replacing $g(y)$ with $g(z)$. The procedure leads to the final inlet velocity: $u_{\text{inlet}} = u_{\text{stig}} + u_{\text{gust}} + u_{\text{corr}}$.

3 Applications

First verification tests were concerned with wind gusts injected into a turbulent boundary layer evolving on a plate and into a turbulent channel flow. The simulations showed the expected locomotion and decay behavior in streamwise direction. The present application related to fluid-structure interaction is a gust within a turbulent boundary layer which approaches and splashes on a wall-mounted rigid cube derived

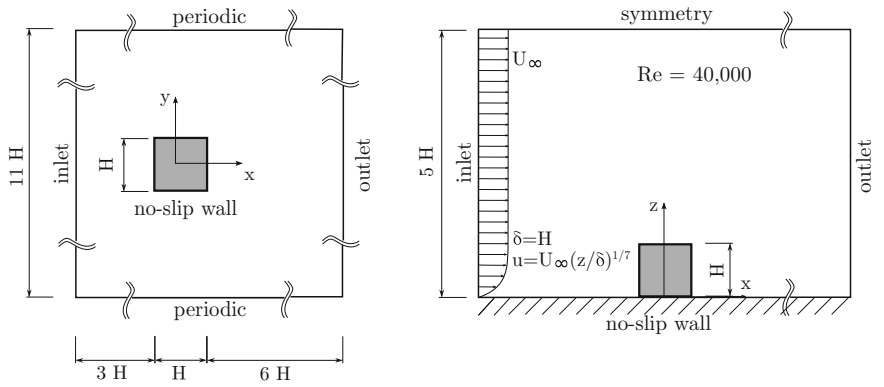

Fig. 2 Description of the test case: Geometry and boundary conditions

from the well-known benchmark of Martinuzzi [6]. The geometry and boundary conditions are depicted in Fig. 2.

The turbulent inflow data are synthetically generated by the STIG based on the 1/7 power law combined with turbulence intensities and integral length scales used by Wood et al. [9]. A moderate Reynolds number Re = 40,000 based on the free-stream velocity is chosen. A block-structured Cartesian grid involving 19 millions control volumes and 264 blocks is applied. A wall-resolved LES is conducted with the in-house fluid solver FASTEST-3D [2, 9]. An explicit time-marching involving a low-storage 3-steps Runge-Kutta scheme is employed. The subgrid-scale model is the Smagorinsky model with $C_s = 0.1$ and Van Driest damping near solid walls.

In a first series of simulations, a gust is superimposed to the original STIG data based on Gaussian distributions in space and time. The width, the height and the duration of the gust is set to $L_g^y = 1$ m, $L_g^z = 1$ m and $L_g^t = 1$ s, respectively. The center of the gust $\left(y_g, z_g\right)$ is positioned at $(0, H/2)$ at the inlet patch.

Figure 3 depicts the important phases of the gust approaching and splashing on the bluff body. The gust is visualized by iso-surfaces of the three velocity components, i.e., for each Cartesian velocity component separate iso-surfaces ($u = 0.75$ m/s, $|v| = |w| = 0.33$ m/s) are generated but uniformly colored. Note that classical criteria such as Q- or λ_2-criterion were found to be inappropriate for visualizing the wind gust. On the left image the gust enters the domain and is convected downstream. Then it splashes on the wall-mounted cube, while the momentum is redirected in the wall-normal and spanwise directions (middle image). The impact of the gust results in a short-term strengthening of the horseshoe vortex and in the detachment of a large symmetrical vortical structure from the front of the cube visible on the right image.

In order get a first impression of the effect of gusts within FSI applications of flexible structures, the streamwise fluid force acting on the cube is investigated for different combinations of gust parameters. In the simulations discussed below the spatial shapes f_y and f_z, the width, the height, the duration and the position of the gust remain the same as before. Only the temporal shape f_t and the amplitude of

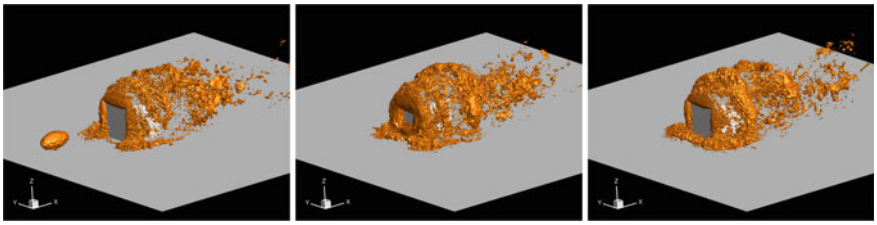

Fig. 3 A gust approaches (left image), splashes on a wall-mounted cube (middle image) and leads to an augmentation of the horseshoe vortex and a large symmetrical vortical structure (right image) (visualization by iso-surfaces of the velocity components)

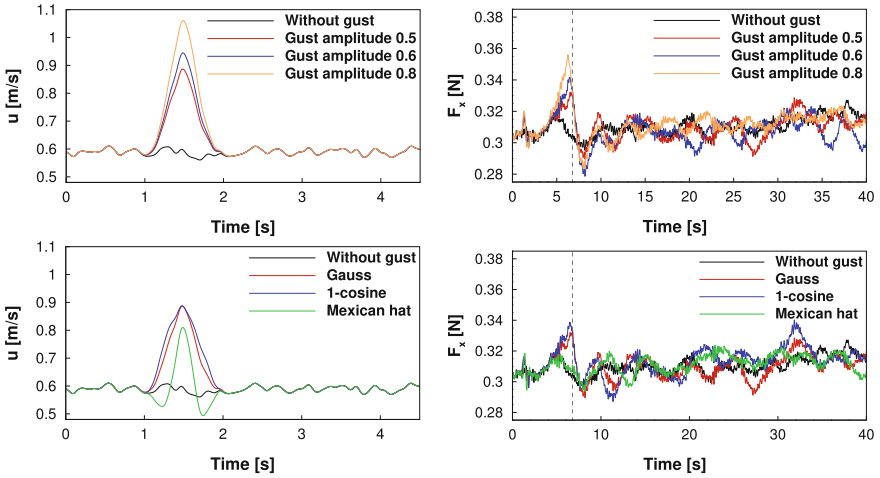

Fig. 4 Influence of the gust amplitude A_g for a given shape (Gauss) (**top**) and influence of the gust shape f_t for a given gust amplitude $A_g = 0.5$ (**bottom**). Evolution of the streamwise velocity at the inlet (**left**); Streamwise fluid force acting on the wall-mounted cube (**right**)

the gust A_g are varied. In the upper row of Fig. 4 the influence of the increase of the gust amplitude on the streamwise fluid force F_x for a given temporal gust shape (Gauss distribution) is shown. In the lower row of Fig. 4 the time history of F_x achieved by three different temporal shapes (Gauss, 1-cosine and Mexican hat) for a constant amplitude of $A_g = 0.5$ is depicted. On each graph the time evolution of the streamwise velocity and streamwise force resulting without a wind gust is plotted as reference. In all simulations the splash of the gust on the bluff body leads to a short-term but strong peak in the force F_x. Immediately after the splash a limited number of damped oscillations are present. In the different tests the pattern of the peak in F_x remains similar. However, the height and position of its maximum vary.

The strength of the peak (width and height of the peak) in F_x directly depends on the initial parameters of the gust. With a higher amplitude of the gust the height of the peak increases. Moreover, as the 1-cosine shape is slightly larger than the Gauss

shape (as noticeable in Fig. 4), the strength of the splash is consequently greater. The Mexican hat shape leads to a weaker peak in F_x due to the specific shape with two local velocity minima at the beginning and at the end of the distribution. From these observations it can be concluded that the integral in time of the initial shape of the gust directly affects the strength of the gust splashing on the bluff body.

The position of the maximum also depends on the initial parameters of the gust: A greater gust amplitude leads to a larger streamwise velocity at the inlet. It implies that the gust is convected faster downstream and reaches the bluff body earlier.

4 Conclusions

In order to reliably dimension flexible structures under wind loads, multi-physics simulations offer an interesting technique to determine the loads on the structure. Numerical predictions for fluid-structure interactions relying on large-eddy simulations have turned out to be reliable and efficient [2–4]. Synthetic turbulence data injected at inlet patches assure realistic results. In order to take extreme events like wind gusts into account, the framework was extended using either deterministic or stochastic methods. Due to the brutal change of the velocity implied by the gust, an additional procedure is necessary to control the global mass flow and guarantee the convergence of the simulation. To evaluate the method in the context of fluid-structure interactions, the flow around a rigid wall-mounted cube originally suggested by Martinuzzi [6] is selected and slightly adapted. Gusts of different forms and amplitudes are injected. At first, the changes in the flow are highlighted based on iso-surfaces of the velocity. Then, the streamwise fluid force acting on the bluff body is analyzed. As expected, a change in the amplitude of the original wind gust has a direct impact on the intensity of the gust splashing on the bluff body. For a given temporal shape the gust pattern visible in the streamwise fluid force remains identical, but the amplitude and the time instant of appearance of the maximum vary.

References

1. Bierbooms, W.A.A.M.: Constrained stochastic simulation of wind gusts for wind turbine design. Ph.D. thesis, Delft University of Technology, Delft, The Netherlands (2009)
2. Breuer, M., De Nayer, G., Münsch, M., Gallinger, T., Wüchner, R.: Fluid-structure interaction using a partitioned coupled predictor-corrector scheme for the application of large-eddy simulation. J. Fluids Struct. **29**, 107–130 (2012)
3. De Nayer, G., Breuer, M.: Numerical FSI investigation based on LES: flow past a cylinder with a flexible splitter plate involving large deformations (FSI-PfS-2a). Int. J. Heat Fluid Flow **50**, 300–315 (2014)
4. De Nayer, G., Kalmbach, A., Breuer, M., Sicklinger, S., Wüchner, R.: Flow past a cylinder with a flexible splitter plate: a complementary experimental-numerical investigation and a new FSI test case (FSI-PfS-1a). Comput. Fluids **99**, 18–43 (2014)

5. Klein, M., Sadiki, A., Janicka, J.: A digital filter based generation of inflow data for spatially-developing direct numerical or large-eddy simulations. J. Comput. Phys. **186**, 652–665 (2003)
6. Martinuzzi, R.: Experimentelle Untersuchung der Umströmung wandgebundener rechteckiger, prismatischer Hindernisse. Ph.D. thesis, Universität Erlangen-Nürnberg, Germany (1992)
7. Schmidt, S., Breuer, M.: Extended synthetic turbulence inflow generator within a hybrid LES-URANS methodology for the prediction of non-equilibrium wall-bounded flows. Flow Turbul. Combust. **95**(4), 669–707 (2015)
8. Schmidt, S., Breuer, M.: Source term based synthetic turbulence inflow generator for eddy-resolving predictions of an airfoil flow including a laminar separation bubble. Comput. Fluids **146**, 1–22 (2017)
9. Wood, J.N., De Nayer, G., Schmidt, S., Breuer, M.: Experimental investigation and large-eddy simulation of the turbulent flow past a smooth and rigid hemisphere. Flow Turbul. Combust. **97**(1), 79–119 (2016)

Dissipation in Front of a Wall-Mounted Bluff Body

W. Schanderl and M. Manhart

1 Introduction

The dissipation rate is required to assess the Kolmogorov scales, the smallest scales of motion in turbulent flow. A priori knowledge about these scales is needed to design both experiments and numerical simulations. However, an explicit evaluation of the dissipation is difficult. Direct Numerical Simulation (DNS) without turbulence model is still rare for practical flow problems. In Reynolds-averaged simulation and Large-Eddy simulation (LES), the dissipation can be biased by the turbulence model. Also, it is almost impossible to gain the dissipation from laser based experiments, as it is highly sensitive to noise in the measured data [1].

We investigated the dissipation of turbulent kinetic energy in front of a wall-mounted cylinder at three moderate Reynolds numbers by highly resolved LES. To achieve reliable results, we ensured that the grid of the LES was fine enough to resolve most of the scales. A perceptible fraction of the total dissipation was modelled. However, this fraction—about one third—was small enough so that the total dissipation suffered only marginally from possible shortcomings of the turbulence model. Single contributors to the dissipation rate and their Reynolds number scaling were investigated and compared among each other. Furthermore, an a priori approximation of the Kolmogorov scale was evaluated and verified by the LES results.

W. Schanderl (✉) · M. Manhart
Technical University of Munich, Arcisstr. 21, 80333 Munich, Germany
e-mail: wolfgang.schanderl@tum.de

M. Manhart
e-mail: michael.manhart@tum.de

M. V. Salvetti et al. (eds.), *Direct and Large-Eddy Simulation XI*,
ERCOFTAC Series 25, https://doi.org/10.1007/978-3-030-04915-7_61

Table 1 Grid parameters for all three Reynolds numbers. The grid spacing refers to the finest locally embedded grid around the cylinder. η_K is based on the maximum total dissipation in the core of the main vortex in front of the cylinder. Also included are the friction Reynolds numbers

Re_D	Re_τ	Grid cells	Cells per diameter horizontal; vertical	Kolmogorov lengths $\Delta x/\eta_K = \Delta y/\eta_K$; $\Delta z/\eta_K$
20000	1520	$166 \cdot 10^6$	148; 571	8.0; 2.0
39000	2770	$400 \cdot 10^6$	250; 1000	6.4; 1.6
78000	4750	$1.6 \cdot 10^9$	440; 1778	6.8; 1.7

2 Computational Configuration

We simulated the flow around a circular cylinder at the Reynolds numbers $Re_D = 20000$, $Re_D = 39000$ and $Re_D = 78000$ based on the cylinder diameter D and the velocity averaged over the whole cross section of the approach flow. The cylinder was placed in the center of an open channel with a flow depth of $H = 1.5D$ and a length of $L = 25D$. The width of the open channel was $W = 11.7D$ at the low and the medium Reynolds number and $W = 7.8D$ at the high Reynolds number. A separate precursor grid was applied to provide a fully-developed, turbulent open-channel flow as inflow condition [2]. The free surface was modelled by a slip boundary condition (which corresponds to an infinitesimal Froude number).

The LES was processed with our in-house Finite Volume-code MGLET. Central differences were applied for spatial approximation. Time-integration was done by a third order Runge-Kutta scheme. Since the grid was Cartesian, the curved surface of the cylinder was represented by a conservative second order Immersed Boundary Method [3]. The grid was refined by locally embedded grids around the cylinder [4]. This way the resolution was fine enough to resolve the viscous sublayer [2, 5]. Parameters of the resulting grids are listed in Table 1.

Being aware of the sensitivity of the dissipation, the results were carefully validated. A grid study indicates the first order statistics to be converged over grid refinement [2]. Comparing statistics of up to the third order to the ones gained from a companion experiment of the same setup showed good accordance [6]. An evaluation of modelled [7] and resolved stresses implied the modelled ones to be small compared to the resolved ones [5]. In addition, all terms of the budget of turbulent kinetic energy [8] were evaluated. The amplitude of the overall residual of the budget was small compared to other contributors like the production or the diffusion term [6]. The numerical dissipation of the applied setup was marginal [6].

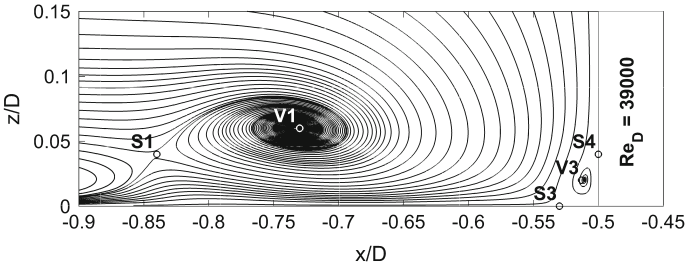

Fig. 1 Time-averaged streamlines in the symmetry plane in front of the cylinder at $Re_D = 39000$

3 Flow Topology

A boundary layer approaching a bluff body induces a vertical pressure gradient in the body front. The resulting down-flow is deflected by the bottom wall and forms a so-called horseshoe vortex system [9]. Figure 1 illustrates the time-averaged flow pattern in the symmetry plane in the cylinder front close to the bottom at $Re_D = 39000$. Most of the down-flow was deflected in upstream direction and accelerated along the bottom wall. Parts of this fluid were entrained by the main vortex V1, while other parts formed a jet along the wall underneath. Since the fluid had to bypass the bluff body, V1 bent around the cylinder wherefore it is called horseshoe vortex. Upstream of the main vortex V1 a stagnation point S1 was observed.

The data presented in Fig. 1 was taken from the simulation at $Re_D = 39000$. In the investigated range of Reynolds numbers, V1 was slightly shifted upstream with increasing Reynolds number, however, the changes were small in general. Thus, the flow topologies at $Re_D = 20000$ and $Re_D = 78000$ are not presented here.

4 Dissipation Rate and a Priori Approximations

In an eddy-viscosity LES, the dissipation is obtained by [8]

$$\varepsilon = 2\nu\langle s_{ij}s_{ij}\rangle + 2\langle \nu_t s_{ij}s_{ij}\rangle \quad . \tag{1}$$

ε is based on the fluctuation of the strain rate tensor $s_{ij} = 1/2(\partial u_i'/\partial x_j + \partial u_j'/\partial x_i)$. The direct dissipation due to the time-averaged strain rate tensor S_{ij} is not included in the presented data. The first summand in Eq. (1) is the resolved dissipation, the second summand the modelled one. The distribution of the modelled dissipation was similar to the one of the total dissipation, its amplitude was approximately one third of the total one [10].

ε at $Re_D = 39000$ normalized by the macro scale estimation of the dissipation u_b^3/D [8] is shown in Fig. 2, where u_b was the depth averaged bulk velocity in the

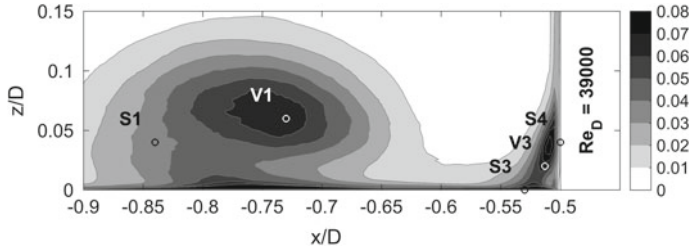

Fig. 2 Total dissipation $\varepsilon D/u_b^3$ in the symmetry plane in front of the cylinder at $Re_D = 39000$

symmetry plane of the approach flow. The distribution of ε beared three features: (i) a broad peak in the area covered by vortex V1; (ii) a tail of large ε along the cylinder, leading into a peak at the junction of cylinder and bottom wall; (iii) a thin stripe of large dissipation where the wall jet moves along the bottom wall under vortex V1. With increasing Reynolds number, the overall amplitude was slightly enhanced and the peak at the wall under V1 was more pronounced. These changes are discussed in the following by means of the pseudo dissipation.

The pseudo dissipation ε_p, defined as [11]

$$\varepsilon_p = \nu \langle \left(\partial u_i' / \partial x_j \right)^2 \rangle \quad , \tag{2}$$

facilitates a decomposition of the dissipation into its contributors. Between ε and ε_p we found small differences only. In the following individual terms of $\varepsilon_{p,ij}$ as given by Eq. (2) without summation over the indices are evaluated.

Figure 3 shows the pseudo dissipation due to the spanwise gradient of the fluctuations of the streamwise velocity $\varepsilon_{p,12} = \nu \langle \left(\partial u' / \partial y \right)^2 \rangle$ for all three Reynolds numbers. In addition, Fig. 4 shows the pseudo dissipation due to the vertical gradient of the fluctuations of the streamwise velocity $\varepsilon_{p,13} = \nu \langle \left(\partial u' / \partial x \right)^2 \rangle$. In both figures the pseudo dissipation was normalized by u_b^3/D and plotted with the same colorbar. These two terms were chosen because they illustrate the pseudo dissipation was not isotropic. $\varepsilon_{p,12}$ peaked in the upstream half of the main vortex between the core of V1 and stagnation point S1. The amplitude of $\varepsilon_{p,12}$ was rather small, especially at $Re_D = 20000$. The amplitude of $\varepsilon_{p,13}$ was significantly larger. Furthermore, $\varepsilon_{p,13}$ held two peaks: one in the region of the vortex core of V1, the other one underneath V1 at the bottom plate. In fact, in the region of the wall jet all components of the pseudo dissipation tensor were small except $\varepsilon_{p,13}$. One can conclude that this peak was not caused by isotropic small scale turbulence. Instead, it hints at a vertical flapping of the wall jet over the whole length of the jet. Evaluating all terms of $\varepsilon_{p,ij}$ indicated that there were terms of relative large amplitude ($\varepsilon_{p,31}$, $\varepsilon_{p,13}$, $\varepsilon_{p,23}$) in the region of the horseshoe vortex system, while the others terms were relatively small. The latter was especially true for the terms of the trace of the tensor $\varepsilon_{p,ii}$.

Another interesting feature was revealed by investigating the single terms with increasing Reynolds number. The distribution and the amplitude of the "large terms"

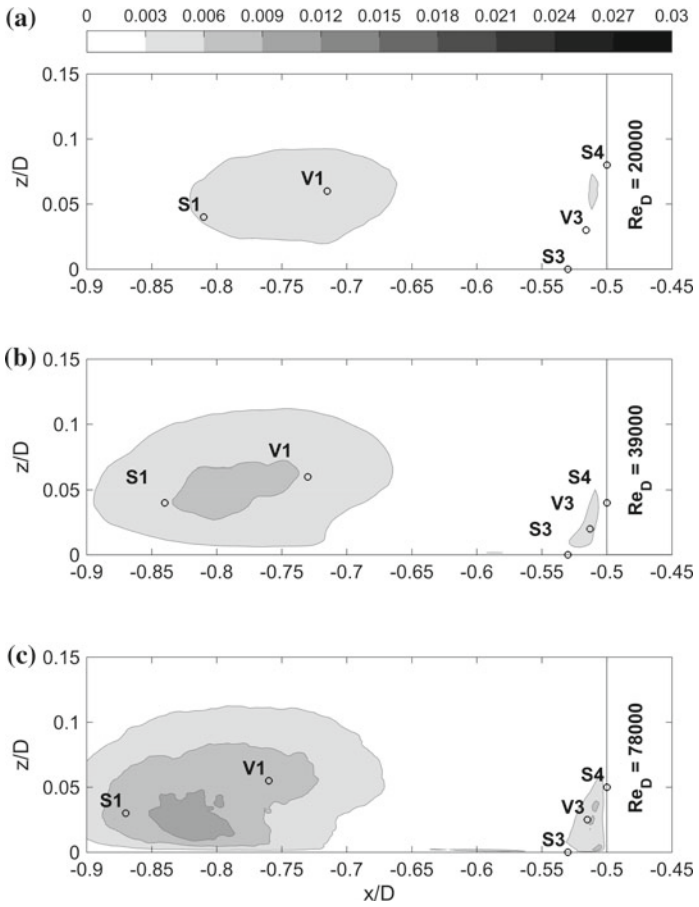

Fig. 3 **a** Pseudo dissipation based on the spanwise gradient of fluctuations of the streamwise velocity $\varepsilon_{p,12} D/u_b^3$ at $Re_D = 20000$, **b** at $Re_D = 39000$ and **c** and at $Re_D = 78000$ in the symmetry plane in front of the cylinder

did not change, see $\varepsilon_{p,13}$ in Fig. 4. However, the amplitude of the "small terms" increased significantly, see $\varepsilon_{p,12}$ in Fig. 3. With increasing Reynolds number, the small terms catched up to the large terms and the dissipation became more isotropic. This was true for all small terms except the terms of the trace of the tensor $\varepsilon_{p,ii}$, which remained small compared to the other terms. The behavior of the small terms can be explained by the energy cascade. The energy cascade became longer with increasing Reynolds number. Thus, the small scale structures had more time to develop to an isotropic state. The increasing amplitude of the small terms cause the slight increase with Reynolds number of the amplitude of the total dissipation.

The presented distributions of dissipation and pseudo dissipation were normalized by u_b^3/D, which can serve as an a priori approximation of the dissipation based

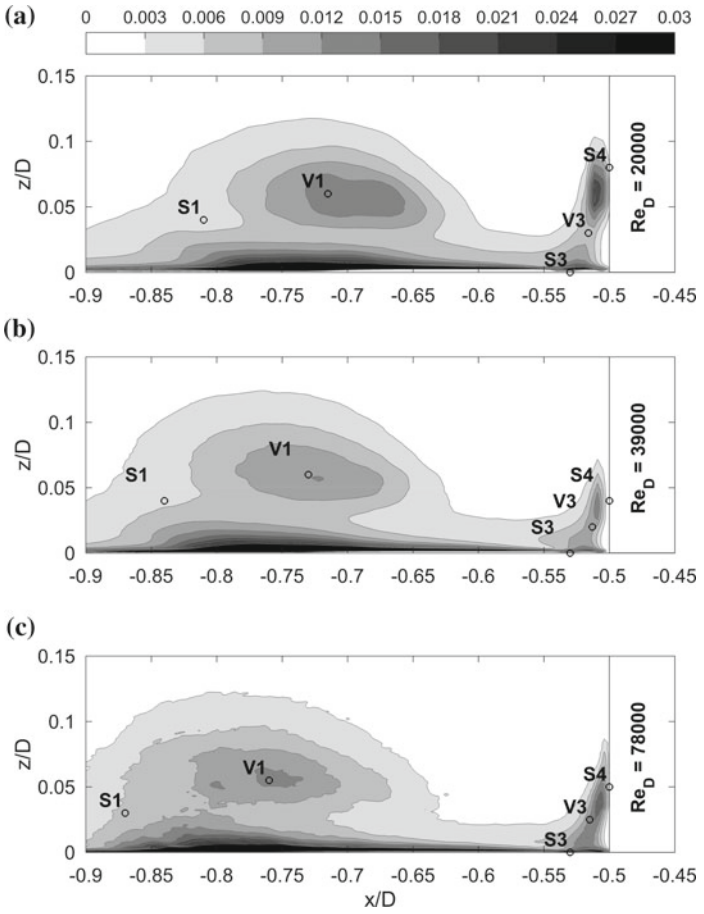

Fig. 4 **a** Pseudo dissipation based on the vertical gradient of fluctuations of the streamwise velocity $\varepsilon_{p,13} D/u_b^3$ at $Re_D = 20000$, **b** at $Re_D = 39000$ and **c** and at $Re_D = 78000$ in the symmetry plane in front of the cylinder

on macro scales [8]. The corresponding approximation of the Kolmogorov length scale is $\eta_{K,macro} = (\nu^3/(u_b^3/D))^{1/4}$. For all three investigated Reynolds numbers, the dissipation computed from the LES was $\varepsilon \approx 0.08 u_b^3/D$ in the core of the main vortex V1. The corresponding Kolmogorov length scale was $\eta_K = 1.88\eta_{K,macro}$.

The Kolmogorov length scale is assumed to scale with $1/Re^{3/4}$. Based on this assumption and the Kolmogorov length scale $\eta_{K,20k}$ computed from the LES at $Re_D = 20000$, the Kolmogorov length scales at $Re_D = 39000$ and $Re_D = 78000$ was estimated as $\eta_{K,39k} = 0.61\eta_{K,20k}$ and $\eta_{K,78k} = 0.36\eta_{K,20k}$ respectively. An a posteriori evaluation of the LES results gave $\eta_{K,39k} = 0.70\eta_{K,20k}$ and $\eta_{K,78k} = 0.38\eta_{K,20k}$, which indicates that the Reynolds scaling can be applied to the Kolmogorov length scale around the horseshoe vortex.

5 Conclusions

We conducted LES of the flow around a wall-mounted cylinder at three moderate Reynolds numbers. A brief overview over the dissipation of turbulent kinetic energy was given and single terms of the pseudo dissipation were discussed. It was observed that the pseudo dissipation in the considered flow was not isotropic. However, with increasing Reynolds number, the pseudo dissipation became more isotropic, as the energy cascade became longer and the small scale structures were more likely to develop to an isotropic state. Our data indicated that the magnitude of the Kolmogorov length scale can be reasonably predicted by a macro scale estimation.

The presented results are discussed in more detail by Schanderl and Manhart [10].

References

1. Adrian, R.J., Westerweel, J.: Particle Image Velocimetry. Cambridge University Press (2011)
2. Schanderl, W., Manhart, M.: Reliability of wall shear stress estimations of the flow around a wall-mounted cylinder. Comput. Fluids **128**, 16–29 (2016)
3. Peller, N., Duc, A.Le, Tremblay, F., Manhart, M.: High-order stable interpolations for immersed boundary methods. Int. J. Numer, Methods Fluids (2006)
4. Manhart, M.: A zonal grid algorithm for DNS of turbulent boundary layers. Comput. Fluids **33** (2004)
5. Schanderl, W., Jenssen, U., Manhart, M.: Near-wall stress balance in front of a wall-mounted cylinder. Flow Turbul. Combust. **99**, 665 (2017)
6. Schanderl, W., Jenssen, U., Strobl, C., Manhart, M.: The structure and budget of turbulent kinetic energy in front of a wall-mounted cylinder. J. Fluid Mech. **827**, 285–321 (2017)
7. Nicoud, F., Ducros, F.: Subgrid-scale stress modeling based on the square of the velocity gradient tensor. Flow Turbul. Combust. **62** (1999)
8. Pope, S.B.: Turbulent Flows. Cambridge University Press (2011)
9. Devenport, W.J., Simpson, R.L.: Time-dependent and time-averaged turbulence structure near the nose of a wing-body junction. J. Fluid Mech. **210**, 23–55 (1990)
10. Schanderl, W., Manhart, M.: Dissipation of turbulent kinetic energy in non-equilibrium flow. Flow Turbul. Combust. **101**, 499(2018)
11. Schlichting, H., Gersten, K.: Boundary Layer Theory. Springer (2006)

Dynamic Unified RANS-LES Simulations of Periodic Hill Flow

R. Mokhtarpoor, S. Heinz and M. K. Stoellinger

1 Introduction

The hybrid RANS-LES methodology intends to combine the most favorable aspects of Reynolds-averaged Navier–Stokes (RANS) and large eddy simulation (LES) to take advantage of both the computational efficiency of RANS and ability of LES to resolve instantaneous large scale flow structures. In this paper we present a new hybrid RANS-LES model which benefits from two important properties. First, it is based on a realizable stochastic velocity model [1–4], which is very beneficial regarding the hybridization of RANS and LES equations. Second, it utilizes a formulation of the dynamic LES model coefficient calculation that is consistent with the derivation of LES equations. The new hybrid RANS-LES model, which will be referred to below as dynamic linear unified model (DLUM), will be applied to high Reynolds number separated flows that were already used for several turbulence model studies of separated turbulent flow. The particular focus will be on the performance difference between the new hybrid RANS-LES model and pure dynamic LES, and on the computational cost of these methods as a function of the Reynolds number.

The paper is organized in the following way. First, the governing equations for the new hybrid RANS-LES model are introduced. Then, the flows considered for

R. Mokhtarpoor · S. Heinz (✉)
Department of Mathematics, University of Wyoming, 1000 E. Univ. Ave.,
Laramie, WY 82071, USA
e-mail: heinz@uwyo.edu

R. Mokhtarpoor
e-mail: rmokhtar@uwyo.edu

M. K. Stoellinger
Department of Mechanical Engineering, University of Wyoming,
1000 E. Univ. Ave., Laramie, WY 82071, USA
e-mail: mstoell@uwyo.edu

M. V. Salvetti et al. (eds.), *Direct and Large-Eddy Simulation XI*,
ERCOFTAC Series 25, https://doi.org/10.1007/978-3-030-04915-7_62

testing our model are described. The performance of pure dynamic LES and the DLUM model are compared, and the DLUM-to-LES cost gain is calculated. Finally, the conclusions are presented.

2 The Dynamic Linear Unified Model

The unified RANS-LES model is based on a realizable stochastic model for turbulent velocities [1–3]. The governing equations for the unified RANS-LES model applied here can be found elsewhere [5]. The conservation of mass and momentum equations read

$$\frac{\partial \bar{U}_i}{\partial x_i} = 0, \tag{1}$$

$$\frac{\bar{D}U_i}{\bar{D}t} = -\frac{1}{\rho}\frac{\partial P}{\partial x_i} + 2\frac{\partial(\nu + \nu_t)\bar{S}_{ij}}{\partial x_j}. \tag{2}$$

Here, the overbar refers to ensemble-averaged (RANS) or space-averaged (LES) variables. $\bar{D}/\bar{D}t$ denotes the filtered Lagrangian time derivative, U_i denotes components of the velocity vector, $P = (\bar{p}/\rho + 2k/3)$ is the modified pressure, ρ is the constant fluid density, ν is the constant kinematic viscosity, and S_{ij} is the rate-of-strain tensor. Equation (2) was obtained by using a linear model $\tau_{ij} = 2/3k\delta_{ij} - 2\nu_t\bar{S}_{ij}$ for the sub-grid scale (SGS) stress τ_{ij} [2], where the turbulent viscosity is given by $\nu_t = 2(1 - c_0)k\tau/3$. Here, τ is the dissipation time scale of turbulence, and c_0 is a model constant that is specified below. The transport equation for SGS kinetic energy k is derived as [1]

$$\frac{\bar{D}k}{\bar{D}t} = \frac{\partial}{\partial x_j}\left[(\nu + \nu_t)\frac{\partial k}{\partial x_j}\right] + \nu_t|\bar{S}|^2 - \frac{k}{\tau}, \tag{3}$$

where $|\bar{S}| = (2\bar{S}_{ij}\bar{S}_{ji})^{1/2}$ refers to the magnitude of the resolved rate-of-strain tensor. Equations (2) and (3) are unclosed as long as the time scale τ is not defined. Usually applied RANS and LES equations can be recovered by using $\tau = \tau^{RANS}$ with $\tau^{RANS} = 1/\omega$ for the RANS case, and $\tau = \tau^{LES}$ with $\tau^{LES} = \Delta k^{-1/2}$ for the LES case, respectively. Here, Δ refers to the filter width, which is defined to be the large side filter, $\Delta = \Delta_{max} = \max(\Delta_x, \Delta_y, \Delta_z)$, and ω is the characteristic turbulence frequency. To provide ω we solve a transport equation for the turbulent frequency [6]. The unification of RANS and LES models is accomplished by introducing the unified time scale by the relation $\tau = min(\tau^{RANS}, \tau^{LES})$.

To clearly distinguish between parameter settings in RANS and LES regimes we introduce new parameters for $2(1 - c_0)/3$ in RANS and LES modes,

$$\nu_t = \begin{cases} C_\mu k\tau^{RANS} & \text{RANS region} \\ C_d k\tau^{LES} & \text{LES region} \end{cases} \tag{4}$$

We can compute C_d dynamically if the equations are in LES mode. There is a variety of dynamic LES methods. In the present work, the dynamic method proposed by Heinz [3, 4] is adopted. The advantage of the approach used here is that the dynamic LES coefficient can be calculated fully consistently with the LES model applied. The implied dynamic coefficient C_d is

$$C_d = -\frac{L_{ij}^d M_{ji}}{M_{kl} M_{lk}}. \tag{5}$$

Here, L_{ij}^d refers to the deviatoric component of the Leonard stress $L_{ij} = \widehat{\bar{U}_i \bar{U}_j} - \hat{\bar{u}}_i \hat{\bar{u}}_j$ (the hat refers to the test filtering), and M_{ij} is given by $M_{ij} = 2\Delta^T \sqrt{k^T} \hat{\bar{S}}_{ij}$, which involves the test-filter turbulent kinetic energy $k^T = L_{nn}/2$ and filter width $\Delta^T = 2\Delta$ on the test-filter level. In RANS mode, the use of a constant value for C_μ does not account for the damping effect of walls. We have used a new C_μ blending method for treating wall effects [5].

3 Periodic Hill Flow

We have considered the separated flow over a periodic hill: see the geometry in Fig. 1. Experimental studies of this flow at a Reynolds number of $Re = 37{,}000$ have been carried out by Rapp and Manhart [7]. Numerical simulations of this flow at $Re = 37,000$ have been performed by Chaouat and Scheistel [8]. They applied their PITM hybrid model on grids ranging from 240×10^3 to 960×10^6 grid points. PITM simulation results were compared with RANS Reynolds stress model (RSM) results. The authors observed that in contrast to the PITM simulations, the RSM computations showed important weaknesses regarding the prediction of this flow because of the lack of large unsteady eddies.

The size of the computational domain is $L_x = 9h$, $L_y = 3.035h$, and $L_z = 4.5h$ in the streamwise, wall normal, and spanwise directions, respectively, where h is the height of the hill. The Reynolds number of the flow is based on hill height and bulk velocity above the hill crest. At the bottom and top, the channel is constrained by solid walls. No-slip and impermeability boundary conditions are used at these walls. Periodic boundary conditions are employed in the streamwise and spanwise directions.

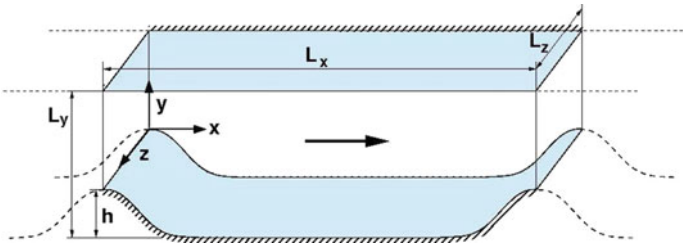

Fig. 1 The geometry of two-dimensional periodic hill flows [9]

Table 1 Location of separation and reattachment points obtained by DLUM and LES simulations on different grids

Simulation	N_{cell}	$(x/h)_{sep}$	$(x/h)_{reatt}$	$(\varepsilon)_{reatt}$ (%)
LES 20 M grid	20 M	0.23	3.65	3
LES 5M grid	5 M	0.24	3.5	7
LES 500 K grid	500 K	0.3	3.5	7
DLUM 500 K grid	500 K	0.35	3.8	1

4 DLUM Versus LES: Performance

We present a comparison of the performance of DLUM versus LES models: LES were performed on 20 M, 5 M, 500 K grids, DLUM simulations were performed on a 500 K grid. First, we consider main flow characteristics by comparing streamlines and reattachment and separation points.

Table 1 summarizes the separation, reattachment points and percentage ϵ_{reatt} of discrepancy with the experimental data with respect to LES and DLUM simulations. The comparison between DLUM and 20 M LES results shows that the reattachment and separation points are approximately the same. The difference is that the reattachment point provided by the DLUM is closer to the experimental result [7] than the 20 M LES reattachment point. There is a difference between fine and coarser LES results regarding the reattachment and separation points: the coarser LES provide this distance 6.4% shorter than the fine grid LES. This indicates shortcomings of coarser LES to accurately simulate the recirculating bubble. Overall, we conclude that the DLUM performance is better than the performance of the fine grid LES considered.

The mean streamwise velocities $\langle U \rangle / U_b$ obtained by the DLUM simulation are compared with available experimental data and the three LES simulations considered (see Fig. 2). It is found that the DLUM shows an impressive ability to reflect the most important flow feature, the mean streamwise velocity. The comparisons with experimental data reveal an almost perfect performance of the DLUM in contrast to (coarse) LES.

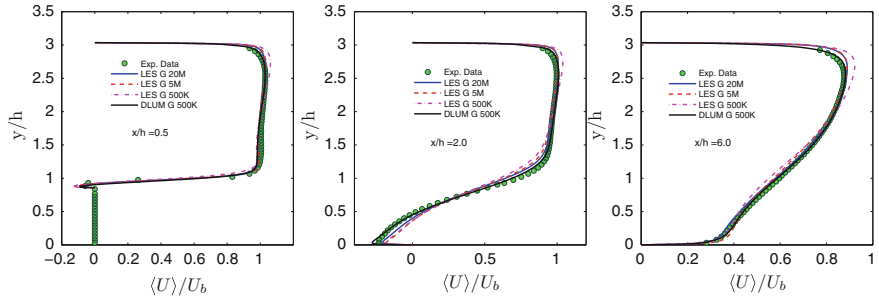

Fig. 2 DLUM versus dynamic LES on different grids and experimental results: profiles of the streamwise velocity $\langle U \rangle / U_b$ are shown at different axial positions x/h

5 DLUM Versus LES: Cost

The LES-to-DLUM computational cost ratio is denoted by G, which is the gain factor of performing hybrid RANS-LES simulations. It is calculated by

$$G = \frac{N_{LES}}{N_{DLUM}} \frac{n_{LES}}{n_{DLUM}} \frac{t^*_{LES}}{t^*_{DLUM}} = \frac{N_{LES}}{N_{DLUM}} \frac{\Delta t_{DLUM}}{\Delta t_{LES}} \frac{t^*_{LES}}{t^*_{DLUM}}. \tag{6}$$

Here, N is the number of cells, n is the number of iterations performed, and t^* is the computer time per iteration. The number n of iterations is inversely related to the time step Δt applied in computations. The number of cells N and the simulation time steps are functions of the Reynolds number, but the ratio t^*_{LES}/t^*_{DLUM} in Eq. (6) is independent of the Reynolds number, it only depends on the number of equations involved and the computational time needed for the numerical integration of equations. We found that the LES to DLUM ratio of computer cost per iteration is $t^*_{LES}/t^*_{DLUM} \approx 0.96$ [5].

To calculate the other cost factors in Eq. (6), simulations have been performed using DLUM and pure LES for three different Reynolds numbers (10,600, 19,000 and 37,000). For each Reynolds number, the criterion for choosing the LES grid was a grid that has a maximum y^+ less than one. Regarding the DLUM grid, we used the criterion that the averaged y^+ at the bottom wall has to be about 2. On this basis, the corresponding LES grids have 5, 10, and 20 million cells, and the DLUM grids have 0.25, 0.35, and 0.5 million cells for Reynolds numbers 10,600, 19,000 and 37,000, respectively. The criterion for choosing the time step was that the maximum CFL number should not exceed 0.5. Based on this criterion, we applied corresponding time steps. Figure 3 shows the dependence of the number N of grid cells and time steps Δt for LES and DLUM simulations depending on the Reynolds number. It can be observed that $ln(N)$ and $ln(\Delta t)$ are basically linear functions of $ln(Re)$. Therefore, the number of grid cells N and time steps Δt can be written as power law functions of Re ($N = aRe^b$ and $\Delta t = cRe^d$). The model parameters a, b, c, and d can be obtained

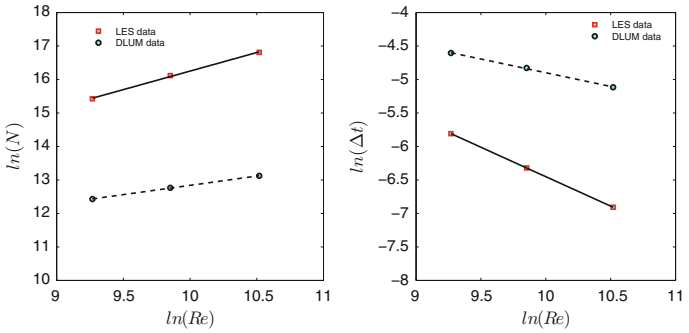

Fig. 3 The dependence of the number of N and Δt on the Reynolds number. Solid and dashed lines show the linear least squares fits to computational results

by linear regression of data points in Fig. 3. Accordingly, the power functions for N and Δt for the LES and DLUM simulations are given by

$$N_{LES} = 177Re^{1.11}, \quad N_{DLUM} = 1478Re^{0.554}, \tag{7}$$

$$\Delta t_{LES} = 10.36Re^{-0.879}, \quad \Delta t_{DLUM} = 0.45Re^{-0.409}. \tag{8}$$

The resulting total gain factor of DLUM versus LES simulation then reads

$$G = \frac{N_{LES}}{N_{DLUM}} \frac{\Delta t_{DLUM}}{\Delta t_{LES}} \frac{t^*_{LES}}{t^*_{DLUM}} = 0.00495Re^{1.026} \approx Re/200. \tag{9}$$

6 Conclusions

A new theoretically well-based hybrid RANS-LES method is presented by combining a hybrid RANS-LES method with dynamic LES. The hybrid RANS-LES model presented here is much more efficient for very high Reynolds number flow simulations compared to LES, it is much more accurate than RANS [5], and more accurate than under-resolved LES. From a more general view point, the DLUM is more reliable than LES for high Reynolds number flows, which often faces the non-trivial question of how well resolving the LES actually is [5]. DLUM velocity fields are hardly affected by using coarser grids, whereas LES velocity fields reveal significant shortcomings. Based on our simulation results, we also concluded that our DLUM does not suffer from the gray area problem [5], which is usually considered to represent the biggest challenge of hybrid RANS-LES methods.

We found that the cost gain of our hybrid RANS-LES method compared to LES scales with Re/200. For instance, in a realistic flow with a Reynolds number of 10^6,

the DLUM cost gain is about 7000. This huge cost gain facilitates accurate and feasible simulations of realistic high Reynolds number flows.

Acknowledgements The authors would like to acknowledge support through NASA's NRA research opportunities in aeronautics program (Grant No. NNX12AJ71A) and support from the National Science Foundation (DMS-CDS&E-MSS, Grant No. 1622488). We are very thankful for computational resources provided by the Wyoming Advanced Research Computing Center [10] and the Wyoming-NCAR Alliance [11].

References

1. Gopalan, H., Heinz, S., Stoellinger, M.: A unified RANS-LES model: computational development, accuracy and cost. J. Comput. Phys. **249**, 249–274 (2013)
2. Heinz, S.: Unified turbulence models for LES and RANS, FDF and PDF simulations. Theor. Comput. Fluid Dyn. **21**, 99–118 (2007)
3. Heinz, S.: Realizability of dynamic subgrid-scale stress models via stochastic analysis. Monte Carlo Methods Appl. **14**, 311–329 (2008)
4. Heinz, S., Gopalan, H.: Realizable versus non-realizable dynamic subgrid-scale stress models. Phys. Fluids **24**, 115105 (2012)
5. Mokhtarpoor, R., Heinz, S., Stoellinger, M.: Dynamic unified RANS-LES simulations of high Reynolds number separated flows. Phys. Fluids **28**, 095101 (2016)
6. Bredberg, J., Peng, S.H., Davidson, L.: An improved k-ω turbulence model applied to recirculating flows. Int. J. Heat Fluid Flow **23**, 731–743 (2002)
7. Rapp, C., Manhart, M.: Flow over periodic hills - an experimental study. Exp. Fluids **51**, 247–269 (2011)
8. Chaouat, B., Schiestel, R.: Hybrid RANS/LES simulations of the turbulent flow over periodic hills at high Reynolds number using the PITM method. Comput. Fluids **84**, 279–300 (2013)
9. ERCOFTAC. Retrieved from http://qnet-ercoftac.cfms.org.uk/w/index.php/UFR_3-30_Test_CaseforErcoftac, 25 June 2017
10. Advanced Research Computing Center. Mount Moran: IBM System X cluster. University of Wyoming, Laramie, WY. Retrieved from http://n2t.net/ark:/85786/m4159c, 25 June 2017
11. Computational and Information Systems Laboratory. Yellowstone: IBM iDataPlex System (Wyoming-NCAR Alliance). Boulder, CO: National Center for Atmospheric Research. Retrieved from http://n2t.net/ark:/85065/d7wd3xhc, 25 June 2017

DNS of Separated Flow: Scale-by-Scale Analysis

J.-P. Mollicone, F. Battista, P. Gualtieri and C. M. Casciola

1 Introduction

The Direct Numerical Simulation (DNS) of a turbulent channel containing a bump is carried out to study the turbulence dynamics in the separated region. Our study is intended to fill the gap among the idealised conditions, e.g. plane channel flows typically addressed in literature and the actual flow geometries where the effects of wall curvature and the presence of bluff bodies immediately generate a substantial separated flow region in the bulk of the flow and produce turbulent wakes behind the bluff body. Such configuration allows retaining, with the minimum level of complexity, all the basic features of separated wall-bounded flows such as the presence of the recirculating region that acts as the main energy source for the turbulent velocity fluctuations in the bulk of the flow and in the wake behind the bump.

2 The Generalised Kolmogorov Equation

The tools usually employed for the statistical analysis of turbulence, i.e. the single point turbulent kinetic energy budget and Reynolds stresses budgets, are extended our geometry. The novelty is in the use, in anisotropic and non-homogeneous conditions, of a powerful tool that characterises the scale-by-scale dynamics of the turbulent flow. We adopt a generalised form of the Kolmogorov equation [1]. The Generalised Kolmogorov Equation follows directly from the equations of motion and characterises all the dynamical effects occurring at each scale in the turbulent flow [2, 3]. The equation successfully accounts for non-homogeneous effects, i.e. spatial energy fluxes which arise due to the presence of the bump. It allows to study the

J.-P. Mollicone (✉) · F. Battista · P. Gualtieri · C. M. Casciola
Department of Mechanical and Aerospace Engineering, Sapienza, University of Rome, via Eudossiana 18, 00184 Rome, Italy
e-mail: jp.mollicone@uniroma1.it

M. V. Salvetti et al. (eds.), *Direct and Large-Eddy Simulation XI*,
ERCOFTAC Series 25, https://doi.org/10.1007/978-3-030-04915-7_63

mechanisms of turbulent kinetic energy production at each scale, the energy transfer and the spatial energy fluxes that, at each scale, arise in the different flow regions i.e. at different positions within the recirculating bubble or along the wake behind the separated flow. This analysis has been used to address homogeneous turbulent flows since this equation appeared in its simplest form [4]. This analysis has been applied in plane turbulent channels [5, 6] and recently to more complex geometries [7] in presence of one or more non-homogenous directions.

3 Simulation Setup

The computational domain is sketched in Fig. 1 and has dimensions $(L_x \times L_y \times L_z) = (26 \times 2 \times 2\pi) \times h_0$ where x, y, and z directions are the stream-wise, wall-normal and span-wise directions respectively and h_0 is half the channel height. Flow is from left to right in the x direction with periodic boundary conditions in both the streamwise, x, and spanwise, z, directions. No slip boundary conditions are enforced at the top and bottom walls. A pressure gradient is applied in the streamwise direction to maintain a constant flow rate. The grid is uniform in the streamwise and spanwise directions, and stretched in the wall normal direction to cluster grid nodes toward the walls. The spatial resolution in the streamwise, spanwise and wall-normal directions, made dimensionless with the average wall-unit, is $\Delta x^+ = 2.8$, $\Delta z^+ = 2.8$ and $\Delta y^+{}_{max/min} = 3.7/0.5$ respectively. The resolution is found to be adequate in all the domain when the local grid spacing is compared with the local Kolmogorov scale, as explained in more detail in [8].

The simulation has a bulk Reynolds number equal to $Re = 2500$ and the maximum friction Reynolds number equal to $Re_\tau = u_\tau h_0/\nu = 300$ where u_τ is the friction velocity. $Re = h_0 U_b/\nu$, where U_b is the bulk velocity and ν is the kinematic viscosity. The incompressible Navier–Stokes equations are solved using direct numerical simulations. The simulations are carried out using Nek5000 [9], an open-source code that can simulate unsteady incompressible fluid flow and has shown strong scaling to over one million processes. Nek5000 employs the Spectral Element Method (SEM) [10] that is similar to the Finite Element Method (FEM) but uses high order polynomials in each element. The SEM approach combines the high accuracy, typical of a spectral method, and the flexibility in terms of geometrical configuration typical of

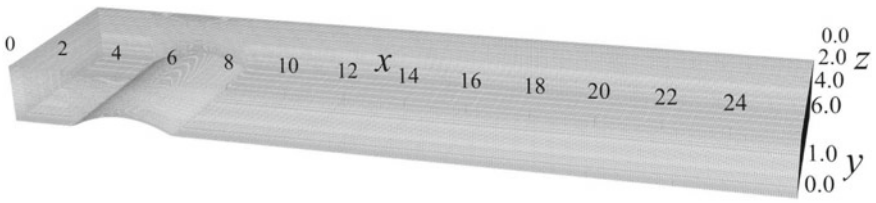

Fig. 1 Sketch of the geometry of the channel with the curved lower wall

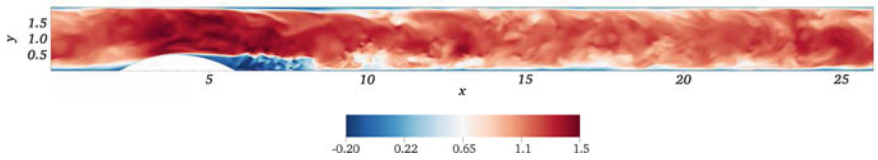

Fig. 2 Instantaneous streamwise velocity in an $x - y$ plane for all the domain

the finite element approaches. The polynomial order used in the present simulation is $N = 9$. Figure 2 shows a two-dimensional snapshot of the instantaneous streamwise velocity in an $x - y$ plane for all the domain. The flow separation is evident, with an intense recirculation bubble behind the bump. An intense shear layer is formed between this bubble and the domain centre and is the main feature of interest for the study. An extensive study on such flow and its dependence on geometry and Reynolds number, with the related one-point statistics, can be found in [8].

4 Results

The following extract of the results concerns the two-dimensional sub-space (y, r_z) at fixed streamwise stations with $r_x = r_y = 0$. $\mathbf{r}$ is the separation vector between two points in the x, y or z direction. Figure 3 reports the energy fluxes, Φ_r and Φ_c, as vectors and $-4\,\varepsilon^* - (\Pi_r + \Pi_c)$ as background contour plots. The wall-normal component of the spatial flux is

$$\Phi_{c,y} = \langle \delta u^2 u_y^* \rangle + \langle \delta u^2 U_y^* \rangle + \frac{\nu}{2} \partial \langle \delta u^2 \rangle / \partial X_{cy} + \frac{2}{\rho} \partial \langle \delta p \delta u_y \rangle / \partial X_{cy}, \tag{1}$$

and the r_z-component of the flux is

$$\Phi_{r,r_z} = \langle \delta u^2 \delta u_z \rangle + 2\nu \partial \langle \delta u^2 \rangle / \partial r_z. \tag{2}$$

The term ε is the turbulent kinetic energy dissipation and Π_r and Π_c are the energy production terms in the separation and physical spaces respectively where

$$\Pi_r = 2\langle \delta u_i \delta u_j \rangle \frac{\partial \delta U_i}{\partial r_j} \quad \Pi_c = 2\langle u_j^* \delta u_i \rangle \frac{\partial \delta U_i}{\partial X_{cj}}. \tag{3}$$

The velocity fluctuation is denoted by u whilst δu denotes the difference in u at two points separated by $\mathbf{r}$. $\mathbf{X}_c$ denotes the mid-point between such two points in the x, y and z directions.

The top panel of the figure represents a fixed x position right after the bump, where the interaction of the main bulk flow and the recirculation bubble produces an intense

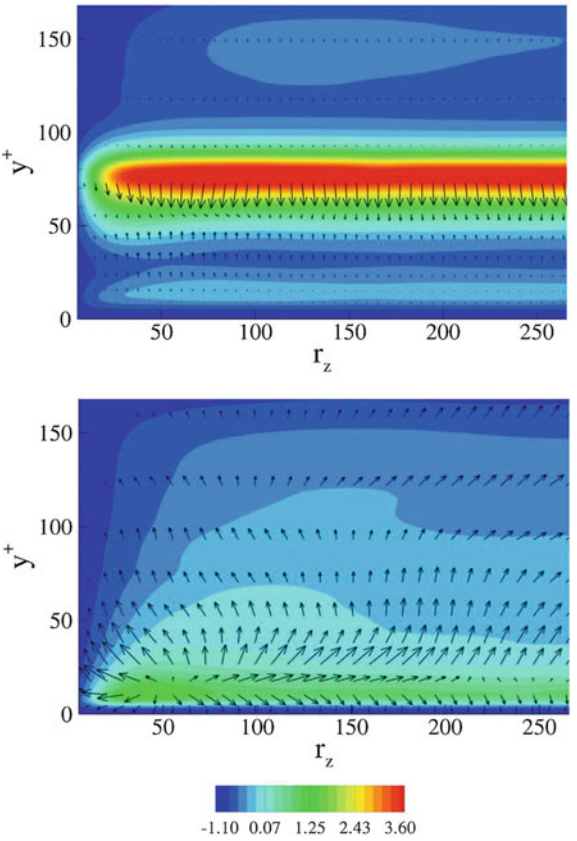

Fig. 3 Contour plots of $(\Pi - 4\varepsilon^*)/(4\varepsilon^*)$ with vectors representing Φ in the reduced space (y, r_z), i.e. in the plane $r_x = r_y = 0$, $x = const$. Top panel represents a fixed x position just behind the bump whilst the bottom panel represents a fixed x position far downstream, at the end of the channel

shear layer. Energy production is intense over a large range of scale separations, for $r_z^+ > 20$, and is spatially located at $y^+ \simeq 75$ which corresponds to the position of the shear layer away from the wall. A second local peak (light blue) with smaller intensity can be observed close to the bottom wall deep inside the recirculating region. These two regions of production feed energy to the recirculating region. The absence of a significant r_z-component of the flux suggests that the fluid structures do not change their spanwise size. The bottom panel shows the energy behaviour at a fixed x location far downstream, at the end of the domain, and agrees with results for a turbulent planar channel flow [6]. The downstream evolution shows the significant difference between fluxes directed into the recirculation bubble and fluxes directed towards the channel center downstream of the bubble.

5 Conclusions

The generalised Kolmogorov equation (GKE) has been used to analyse the turbulent kinetic energy production at different scales and the related energy transfer to different physical regions and separation scales. The flow configuration produces an intense shear layer which is of particular interest since it is the location of maximum production. The GKE has been applied for the first time to such inhomogeneous and anisotropic flow since it has only been used to deal with simpler configurations where no separation occurs. Production, transfer and dissipation of energy is seen to be non-uniform throughout both physical and separation spaces, especially downstream of the bump concerning the spanwise structures discussed here. The analysis indicates that the GKE can be extended to cover all the five components of scale and spatial fluxes and their relationships with production and dissipation in turbulent flow separation.

Acknowledgements The research leading to these results has received funding from the European Research Council under the ERC Grant Agreement no. 339446. PRACE, under grant no. 2014112647, has awarded access to resource FERMI based in Bologna, Italy.

References

1. Hill, R.J.: Exact second-order structure-function relationships. J. Fluid Mech. **468**, 317–326 (2002)
2. Thiesset, F., Danaila, L., Antonia, R.A.: A look at the turbulent wake using scale-by-scale energy budgets. Fluid-Struct.-Sound Interact. Control (2014)
3. Cambon, C., Gréa, B.-J.: The role of directionality on the structure and dynamics of strongly anisotropic turbulent flows. J. Turbul. **14**, 50–71 (2013)
4. Casciola, C.M., Gualtieri, P., Benzi, R., Piva, R.: Scale-by-scale budget and similarity laws for shear turbulence. J. Fluid Mech. **476**, 105–114 (2003)
5. Marati, N., Casciola, C.M., Piva, R.: Energy cascade and spatial fluxes in wall turbulence. J. Fluid Mech. **521**, 191–215 (2004)
6. Cimarelli, A., Angelis, E.D., Casciola, C.M.: Paths of energy in turbulent channel flows. J. Fluid Mech. **715**, 436–451 (2013)
7. Mollicone, J.-P., Battista, F., Gualtieri, P., Casciola, C.: Energy fluxes in turbulent separated flows. J. Phys.: Conf. Ser. (IOP Publishing) **759**, 012003 (2016)
8. Mollicone, J.-P., Battista, F., Gualtieri, P., Casciola, C.: Effect of geometry and Reynolds number on the turbulent separated flow behind a bulge in a channel. J. Fluid Mech. **823**, 100–133 (2017)
9. Fischer, P., Lottes, J.W., Kerkemeier, S.G.: Nek5000 - open source spectral element CFD solver. Argonne National Laboratory, Mathematics and Computer Science Division, Argonne, IL (2008). http://nek5000.mcs.anl.gov
10. Patera, A.T.: A spectral element method for fluid dynamics. J. Comput. Phys. **54**, 468–488 (1984)

Investigation of Turbulent Flow Over Two Wall-Mounted Cubes Using LBM

M. Teng and D. J. Bergstrom

1 Introduction

Large eddy simulation (LES) of a turbulent flow over two cubic prisms is performed based on the Lattice Boltzmann Method (LBM). Two wall-mounted cubic prisms are arranged in tandem on the bottom wall of a fully developed turbulent channel flow for a Reynolds number of $Re_H = 4000$ (based on the centerline velocity, U_c, and the prism height, H). One major objective of the present study is to investigate the typical flow patterns around the cubic prisms and vortex structures in the wake region. Although the flow geometry is symmetric, the wake interaction introduces asymmetric behavior into the instantaneous flow. Meinders and Hanjalic [1] experimentally explored this type of flow for different Re_H using several gap distances. The typical flow features and mean flow patterns are well documented in their study. The current simulation reproduces one of these experiments for a low Reynolds number flow. Although LBM is being increasingly used for simulation of fluid flow, it has not yet been widely applied to complex wake flows. Therefore, this study also intends to explore the capability of LBM in predicting the coherent structures in a complex flow.

2 Lattice Boltzmann Method

A Multiple Relaxation Time (MRT) LBM using the D3Q19 lattice model was employed in the current study. The evolution equation for MRT LBM is given as [2]:

$$f(\vec{x} + \vec{e}\delta t, t + \delta t) - f(\vec{x}, t) = -M^{-1} \times \widehat{S} \times [m - m^{\mathrm{eq}}] \,, \tag{1}$$

M. Teng (✉) · D. J. Bergstrom
University of Saskatchewan, Saskatchewan, Canada
e-mail: mit738@mail.usask.ca

M. V. Salvetti et al. (eds.), *Direct and Large-Eddy Simulation XI*,
ERCOFTAC Series 25, https://doi.org/10.1007/978-3-030-04915-7_64

where $f(\vec{x}, t)$ denotes the density distribution function, M is a 19×19 matrix that linearly transforms the distribution functions into velocity moments and $\widehat{S}$ is the diagonal matrix of the relaxation rates. The LHS of Eq. (1) corresponds to the streaming process where particles move from $\overrightarrow{x}$ to $\overrightarrow{x} + \overrightarrow{e}\,\delta t$ at a speed of $\overrightarrow{e}$ in the specified direction for each time step, δt, whereas the RHS represents the cumulative effect of the collision process [3]. More details pertaining to the parameters and additional background information of LBM are given in reference [2].

The molecular viscosity of the flow is obtained from:

$$\upsilon = \upsilon_1 c^2 \delta t \ , \tag{2}$$

where c = $\delta x/\delta t = 1$, δx denotes the grid space set as 0.001m, δt represents the time step set as 0.001s, and

$$\upsilon_1 = \frac{1}{3}\left(\frac{1}{s_9} - \frac{1}{2}\right) = \frac{1}{3}\left(\frac{1}{s_{13}} - \frac{1}{2}\right) \ , \tag{3}$$

with s_9 and s_{13} denoting two relaxation rates in the diagonal matrix.

3 Smagorinsky SGS Model

A Smagorinsky SGS model is used in the current LES. The eddy viscosity associated with the unresolved-scaled motions is given by [2]:

$$\upsilon_{SGS} = (C_s \Delta)^2 \overline{S} \ , \tag{4}$$

where $C_s = 0.1$, Δ is the reference length scale given by $\Delta = \delta$x, and $\overline{S} = \sqrt{2 S_{ij} S_{ij}}$. The strain rate tensor, S_{ij}, is calculated using the local velocity field based on finite difference relations. The total viscosity is then the summation of the SGS viscosity and molecular viscosity.

In the near-wall regions, the van Driest damping function serves to account for the reduction in the turbulence length scale [3], i.e.

$$\Delta = \delta x \left[1 - exp\left(-\frac{z^+}{A}\right)\right] \ , \tag{5}$$

where z^+ is the normalized distance from the wall given by $z^+ = z u_\tau / \nu$, u_τ is the local friction velocity and A is a constant given as 25.

4 Computational Specifications

The computational domain of the current study was discretized uniformly using a grid of 325×112×182 in the streamwise (x), spanwise (y) and wall-normal (z) directions, respectively. Two cubic prisms were mounted on the bottom wall of the channel with a gap distance of S/H = 1. Each of the prisms is represented by a set of 36 × 36 × 36 gridpoints. The height of the prism in wall units is z^+ = 175, which locates in the overlap region. When normalized using the prism height, the computational domain is 9 H × 3.2 H ×5H in the streamwise, spanwise and wall-normal directions, respectively. The upstream cube is located a distance of 1.5 H away from the inlet plane. A Reynolds number of $Re_H = 4000$ is realized in the current simulation. The inlet boundary condition is implemented using a pre-cursor turbulent channel inflow of 3.5 H × 3.2 H × 5 H. An external force representing the effect of pressure gradient serves to drive the flow, the details of which are provided in reference [3]. At each time step, the velocity profile from the turbulent channel flow is extracted and prescribed as an inlet velocity for the flow over the cubic prisms [4]. At the outlet, a constant pressure is specified. A halfway bounce-back scheme is utilized to achieve the no-slip boundary conditions at the solid walls and a periodic boundary condition is applied in the spanwise direction.

5 Mean Flow Patterns

Figure 1 presents the mean flow pattern in a horizontal plane located at the mid-height of the cubes. A symmetric pattern is observed. Reattachment regions are identified along the lateral sides of the upstream cube, and recirculation is present both in the gap and behind the downstream cube. The corresponding locations of their centers, summarised in Table 1, match reasonably well with those observed by Meinders and Hanjalic [1] for Re_H = 3900. Note that measurement is performed with origin set at the intersection point of the leading edge of the upstream cube and centerline of the channel.

In the vertical mid-plane (X-Z) shown in Fig. 2, a horseshoe vortex and a reattachment region are identified in front of and on the top surface of the upstream cube, respectively. The flow splits at the leading edge of the downstream cube, forming a boundary layer along its top surface and a strong recirculation region in the gap. Recirculation is also evident behind the downstream cube.

6 Instantaneous Flow Features

Figure 3 below illustrates the instantaneous Y vortices in the vertical mid-plane of the channel, and Z vorticities in the horizontal mid-plane of the cubes. In the vertical

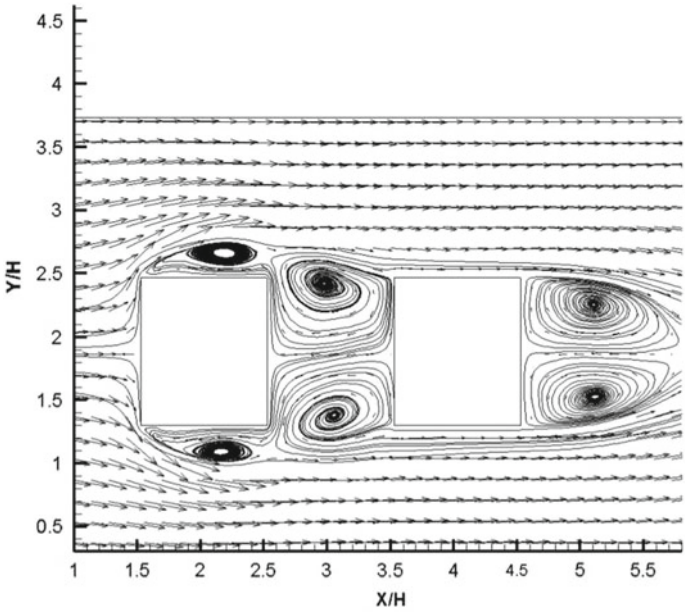

Fig. 1 Streamline and vectors of mean velocity in X-Y plane (z/H = 0.5)

Table 1 Locations of vortex centers

	x/H, y/H (Present study)	x/H, y/H (Ref. [1])
Reattachment vortex	0.58, 0.63	0.57, 0.63
Recirculation in the gap	1.43, 0.42	1.41, 0.43
Recirculation downstream	3.61, 0.31	3.55, 0.30

plane, a horseshoe vortex is observed in front of the upstream cube. Separated shear flow from the leading edge of the upstream cube reattaches back onto the top surface. The impinging flow splits at the front edge of the downstream cube. Part of the flow forms a recirculation region in the gap and the remainder develops into a boundary layer along the top surface of downstream cube. In the wake region, the separated shear layers interact with one another intensely, forming complex vortices extending far down stream. These instantaneous features are also reflected in the horizontal plane, although the vorticity magnitude is different.

Figure 4 presents the instantaneous vortex structures using the Q criteria. The vortex structures around the cubes present a high degree of intensity and complexity. The separated shear layers from the cubes extend far downstream while interacting with one another, and with the surrounding shear flow. A closer look at the vortex structures reveals two horseshoe vortices in front of the upstream cube; the one closer to the cube is more persistent and intrudes into the gap region, thus resulting in instantaneous asymmetric flow patterns. Separated shear layers from the leading

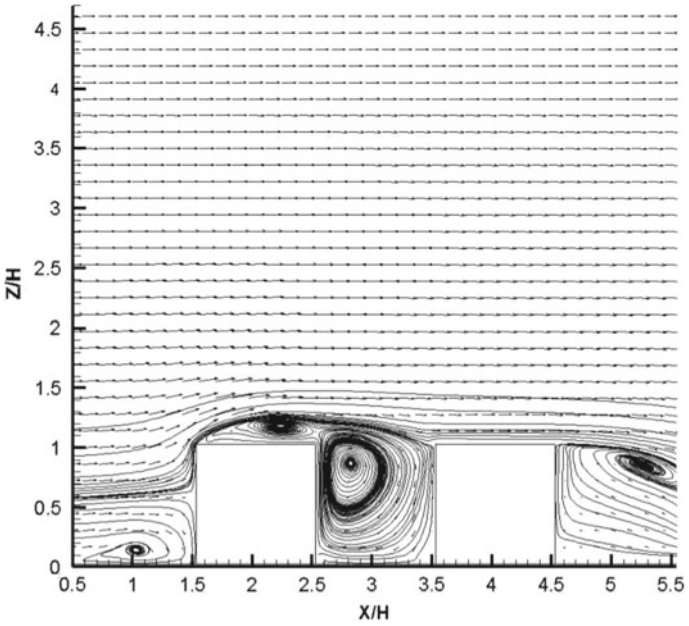

Fig. 2 Streamline and vectors of mean velocity in the middle of X-Z plane

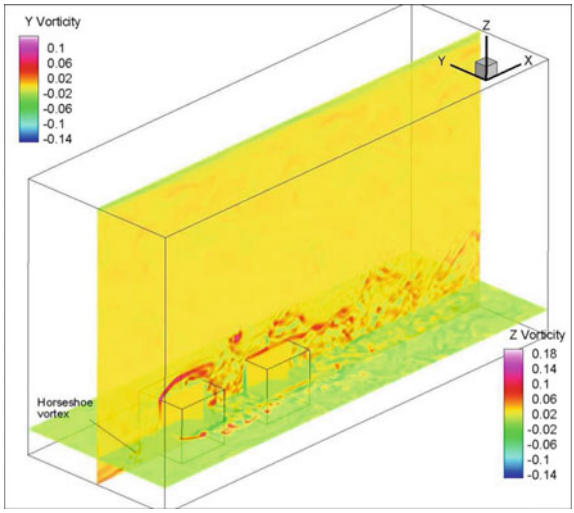

Fig. 3 Instantaneous vorticity

edges of the upstream cube triggers the development of the vortex. Some vortex structures around the cubes appear to resemble proto-typical hairpin structures.

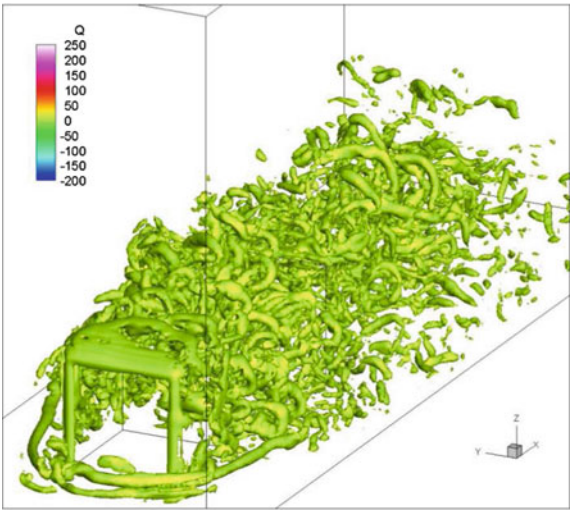

Fig. 4 Vortex visualization using Q criteria (Q = 5)

7 Conclusion

An investigation of a turbulent flow over two wall-mounted cubes is performed based on a LBM LES. The results demonstrate that the LBM is able to capture the mean flow patterns and the instantaneous coherent flow structures. A complex system of vortex structures with different scales develops around the prisms, interacting intensely with one other and extending far downstream. Some of these vortices resemble typical hairpin structures. Further improvements to the simulation will include local grid refinement along with a dynamic subgrid scale model.

References

1. Meinders, E.R., Hanjalic, K.: Experimental study of the convective heat transfer from in-line and staggered configurations of two wall-mounted cubes. Int. J. Heat Mass Transf. **45**, 465–482 (2002)
2. Yu, H.: Lattice Boltzmann Equation simulations of turbulence, mixing, and combustion. Ph.D. thesis, Texas A M University, Department of Aerospace Engineering (2004)
3. Premnath, K.N., Pattison, M.J., Banerjee, S.: Generalized lattice Boltzmann equation with forcing term for computation of wall-bounded turbulent flows. Phys. Rev. E **79**, 1–19 (2009)
4. Koda, Y.: Lattice Boltzmann Method for simulating of turbulent flow. M.Sc. thesis, Univeristy of Waterloo, Department of Mechanical Engineering (2013)

Drag Reduction of Boat-Tailed Bluff Bodies Through Transverse Grooves

A. Mariotti, G. Buresti and M. V. Salvetti

1 Introduction

The present work describes a strategy for the aerodynamic drag reduction of elongated axisymmetric bluff bodies, which can be viewed as simplified models of road vehicles. One well-known method to reduce the drag of this type of body is a geometrical modification denoted as boat-tailing, which consists in a gradual reduction of the body cross-section before a sharp-edged base [1–3]. We combine herein boat-tailing with properly contoured transverse grooves to further delay boundary-layer separation and to reduce drag. In our previous works [4–6] contoured cavities were shown to reduce flow separation and to increase the efficiency of diffusers both in laminar and in turbulent flow regimes. Now we apply the same flow control strategy to an external flow, introducing one transverse groove, i.e. a small cavity, in a boat-tailed axisymmetric body. The axisymmetric body without the boat-tail has already been investigated experimentally and numerically in [7, 8].

The effectiveness of this strategy is assessed through a synergic use of experiments and simulations. In the present work, the results of Variational MultiScale (VMS) LES are presented, discussed and compared to those of the experiments. Indeed, numerical simulations give supplementary information compared to the experiments (e.g. the complete flow dynamics) useful for a better comprehension of the physical mechanisms leading to drag variations on the considered body. The VMS-LES approach adopted in the present work has been successfully applied to the simulation

A. Mariotti (✉) · G. Buresti · M. V. Salvetti
Dipartimento di Ingegneria Civile e Industriale, Università di Pisa,
Via G. Caruso 8, 56122 Pisa, Italy
e-mail: alessandro.mariotti@for.unipi.it

G. Buresti
e-mail: g.buresti@ing.unipi.it

M. V. Salvetti
e-mail: mv.salvetti@ing.unipi.it

M. V. Salvetti et al. (eds.), *Direct and Large-Eddy Simulation XI*,
ERCOFTAC Series 25, https://doi.org/10.1007/978-3-030-04915-7_65

of bluff-body flows in the past (see e.g. [9, 10]), and here it is employed with the same settings and methodology already used for the body without boat tail (see [8]).

2 Geometry Definition, Simulation Set-Up and Numerical Method

The considered geometry consists in an axisymmetric body, having an elliptical forebody and a cylindrical main body followed by a circular-arc boat-tail (see Fig. 1a). The ratio between the main body diameter, D, and the overall length, L, is $D/L = 0.175$. The Reynolds number is $Re = D \cdot U/\nu = 9.6 \times 10^4$ and simulations are carried out for laminar freestream conditions. The freestream Mach number is equal to 0.1. Two boat-tail geometries have been selected, which imply separated flow without the groove. The ratios between the diameter of the base of the boat tail, d, and the main body diameter, D, are equal to $d/D = 0.791$ and $d/D = 0.866$, while the length is kept constant to $D/2$. One suitably contoured transverse groove is introduced in the boat-tail lateral wall. The groove starts with a sharp edge, has an upstream part with a semi-elliptical shape and ends with a spline tangential to the boat tail lateral surface (see, e.g., Fig. 1b for the boat tail having $d/D = 0.791$). The initial sharp edge is introduced to fix the start of a local recirculation region embedded in the lower part of the boundary layer. The location and dimensions are obtained through preliminary RANS analyses. The groove depth is chosen to be equal or lower than one-third of the incoming boundary layer thickness, in order to promote the formation of a steady recirculation region and to avoid the appearance of phenomena of cavity oscillations.

VMS-LES of the considered configuration have been carried out through AERO, a numerical code based on a mixed finite-volume/finite-element method, applicable to unstructured grids for space discretization, and on linearized implicit time advancing. The code has been extremely validated and used for the simulation of bluff body flows (see e.g. [9, 10]). The accuracy of the numerical method is second order both in space and time. The Smagorinsky model is used as subgrid scale model in order to close the VMS-LES equations. The computational domain is cylindrical and has a diameter of $15D$ and a length of $50D$ ($30D$ being the distance between the body base and the outflow); it is discretized through an unstructured grid having approximately 2.4×10^6 nodes. The grid is particularly refined near the body surface and in the near wake (the wall y^+ is lower than 1). Characteristic-based boundary conditions [9] are used at the inflow, outflow and lateral surfaces of the computational domain, while no slip is imposed at the body surface.

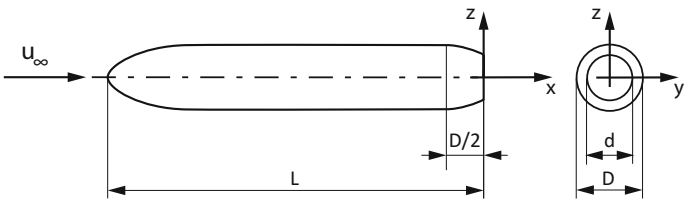

(a) Boat-tailed body

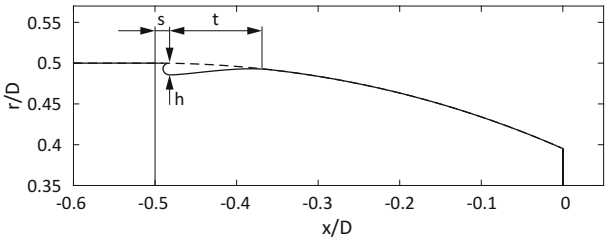

(b) Detail of the boat-tail with the groove

Fig. 1 Sketch of the body geometry ($d/D = 0.791$)

Table 1 Total drag coefficient, $C_{D,tot}$, pressure and viscous contributions to the total drag coefficient, $C_{D,p}$ and $C_{D,v}$. Pressure contributions to the drag coefficient: forebody, $C_{D,p}^{fore}$, boat-tail lateral surface, $C_{D,p}^{bt}$, and base, $C_{D,p}^{base}$

	$C_{D,tot}$	$C_{D,p}$	$C_{D,v}$	$C_{D,p}^{fore}$	$C_{D,p}^{bt}$	$C_{D,p}^{base}$
Boat-tail $d/D = 0.791$	0.1272	0.0960	0.0312	0.0050	0.0404	0.0506
Boat-tail with groove $d/D = 0.791$	0.1040	0.0706	0.0334	0.0050	0.0424	0.0232
Boat-tail $d/D = 0.866$	0.1249	0.0950	0.0299	0.0050	0.0382	0.0518
Boat-tail with groove $d/D = 0.866$	0.1122	0.0810	0.0312	0.0050	0.0381	0.0379

3 Results and Discussion

For both the considered boat-tail geometries, the introduction of the groove leads to a significant drag reduction, through a decrease of the pressure drag (see Table 1). Reductions of the total drag of the order of 18.2 and 10.2% are found for $d/D = 0.791$ and $d/D = 0.866$, respectively. The pressure drag is largely reduced on the base while it slightly increases on the boat-tail lateral surface, as shown by the single contributions to the pressure drag in Table 1 and the pressure coefficient distributions averaged in time for the case $d/D = 0.791$ in Fig. 2.

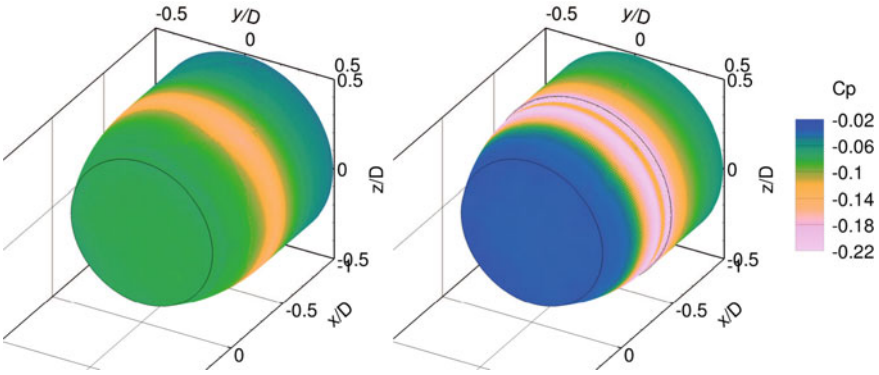

(a) Boat tail (b) Boat-tail with groove

Fig. 2 Time-averaged pressure coefficient ($d/D = 0.791$)

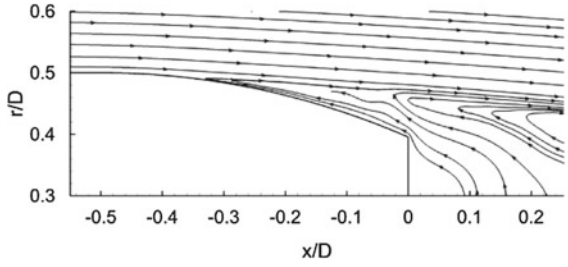

(a) Reference boat-tail

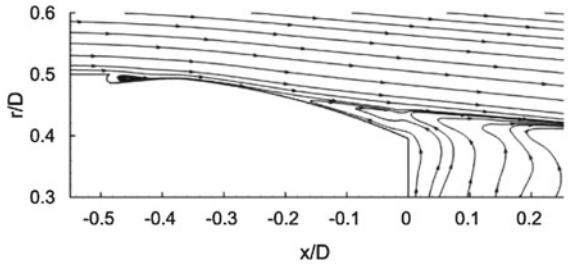

(b) Boat-tail with groove

Fig. 3 Detail of the velocity field averaged in time and in the azimuthal direction ($d/D = 0.791$)

The larger pressures on the body base are due to a delay of flow separation caused by the transverse groove. The separation point for $d/D = 0.791$ is moved from $x/d = -0.347$ in the boat-tailed body without groove to $x/d = -0.192$ in the boat-tail with groove (see Fig. 3) and from $x/d = -0.264$ to $x/d = -0.122$ for the case $d/D = 0.866$.

The success of the proposed flow control strategy is due to the relaxation of the no-slip condition along the outer boundary of the small recirculation region inside the groove, which reduces the momentum losses near the wall and thus delays boundary

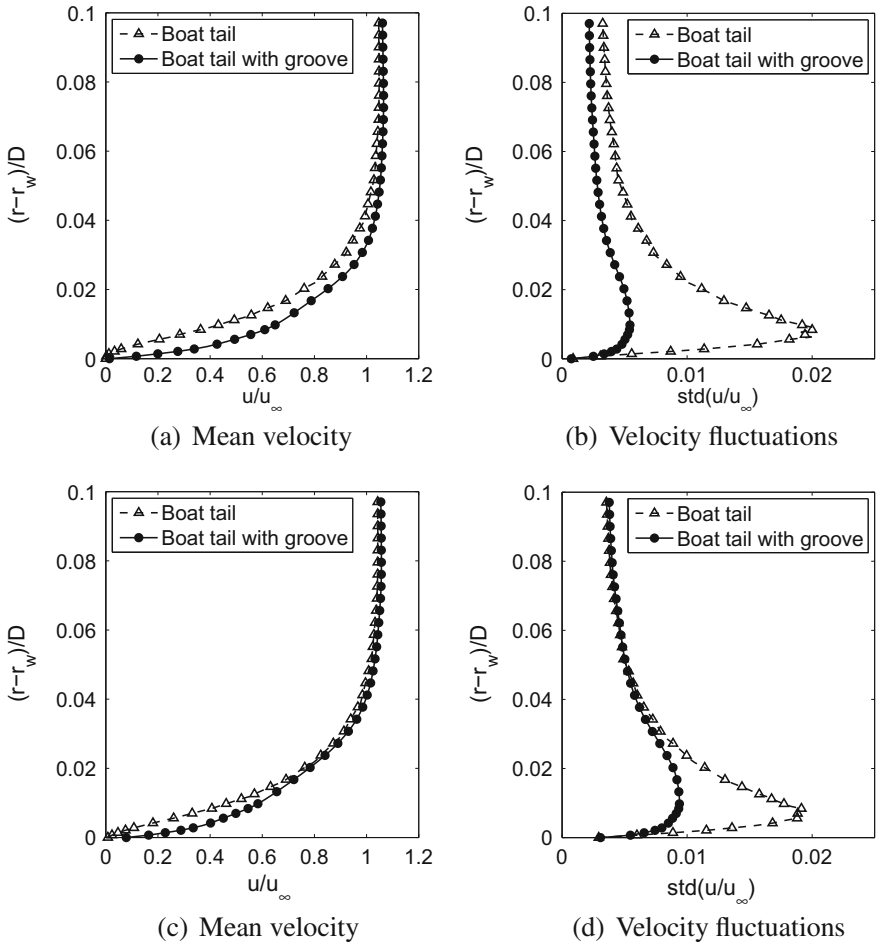

Fig. 4 Non-dimensional boundary-layer profiles evaluated downstream of the groove at the section $x/D = -0.35$ for $d/D = 0.791$ (**a**, **b**) and at $x/D = -0.31$ for $d/D = 0.866$ (**c**, **d**)

layer separation. Indeed, a steady local flow recirculation is present inside the groove (see Fig. 3b) and downstream its reattachment the boundary layer is thinner and has higher-momentum than in the case with no groove, allowing thus separation to be delayed. This can be clearly appreciated from Fig. 4a, c, where the boundary layers corresponding to positions immediately downstream of the grooves are compared to the corresponding ones for the cases without groove. The effect of the groove introduction is to produce a decrease of the thickness and displacement thickness of the boundary layer, with a reduction of the shape factor and a consequent increase of the distance from the separation condition. A reduction of the velocity fluctuations within the boundary layer is also found for the boat tails with groove (see Fig. 4b, d). Particularly remarkable is the decrease of the near-wall turbulence intensity after

Table 2 Sensitivity analysis to the groove position and depth

	s/D	h/D	$C_{D,tot}$	$C_{D,p}$	$C_{D,v}$	$C_{D,p}^{fore}$	$C_{D,p}^{bt}$	$C_{D,p}^{base}$
Reference groove	0.015	0.0143	0.1040	0.0706	0.0334	0.0050	0.0424	0.0232
Effect of s	0.057	0.0143	0.1065	0.0733	0.0332	0.0050	0.0475	0.0208
	0.155	0.0143	0.1104	0.0774	0.0330	0.0050	0.0519	0.0205
Effect of h	0.015	0.0071	0.1249	0.0935	0.0314	0.0050	0.0457	0.0428
	0.015	0.0215	0.0998	0.0663	0.0335	0.0050	0.0592	0.0021

the groove, but a reduction of the fluctuations is present also at the upper edge of the boundary layer. This can represent an additional indication of the steadiness of the recirculation region inside the groove, thus substantiating that the separation-delay action of the groove is not due to an increase of the fluctuations in the downstream boundary layer but rather to the effective relaxation of the no-slip boundary condition for the flow passing over the groove.

Finally, the sensitivity of the separation-delay performance of contoured transverse grooves to the variation of their geometrical parameters was assessed through a few additional simulations for the case $d/D = 0.791$. The effects of the variation of the distance from the start of the boat tail, s, and of the depth of the groove, h, were analysed by carrying out simulations with two additional values of each parameter and keeping the length parameter t/D constant to the reference value 0.129 (see Table 2). The drag-reducing performance does not significantly change with small variations of s/D, provided the flow is able to reattach downstream of the groove. On the other hand, the increase of the groove depth h/D causes a further downstream movement of the separation point. Thus, a progressively stronger pressure recovery on the boat-tail base is obtained and, consequently, a larger base drag reduction. However, the pressure drag contribution of the lateral boat-tail surface increases, so that the reduction of the total drag is more limited. Furthermore, an excessive depth of the groove might imply the appearance of phenomena of self-sustained cavity oscillations (see e.g. [11, 12]), which should be avoided to assure an adequate operation of the groove as an effectively passive flow-control device.

References

1. Maull, D.J., Hoole, B.J.: The effect of boat-tailing on the flow round a two-dimensional blunt-based aerofoil at zero incidence. J. R. Aeronaut. Soc. **71**, 854–858 (1967)
2. Mair, W.A.: Reduction of base drag by boat-tailed afterbodies in low-speed flow. Aeronaut. Q. **20**, 307–320 (1969)
3. Wong, D.-M, Mair, W.A.: Boat-tailed afterbodies of square section as drag-reduction devices. J. Wind. Eng. Ind. Aerodyn. **12**, 229–235 (1983)
4. Mariotti, A., Grozescu, A.N., Buresti, G., Salvetti, M.V.: Separation control and efficiency improvement in a 2D diffuser by means of contoured cavities. Eur. J. Mech. B-Fluid **41**, 138–149 (2013)

5. Mariotti, A., Buresti, G., Salvetti, M.V.: Control of the turbulent flow in a plane diffuser through optimized contoured cavities. Eur. J. Mech. B-Fluid **48**, 254–265 (2014)
6. Mariotti, A., Buresti, G., Salvetti, M.V.: Use of multiple local recirculations to increase the efficiency in diffusers. Eur. J. Mech. B-Fluid **50**, 27–37 (2015)
7. Mariotti, A., Buresti, G.: Experimental investigation on the influence of boundary layer thickness on the base pressure and near-wake flow features of an axisymmetric blunt-based body. Exp. Fluids **54**, 1612 (2013)
8. Mariotti, A., Buresti, G., Salvetti, M.V.: Connection between base drag, separating boundary layer characteristics and wake mean recirculation length of an axisymmetric blunt-based body. J. Fluid Struct. **55**, 191–203 (2015)
9. Camarri, S., Salvetti, M.V., Koobus, B., Dervieux, A.: A low-diffusion MUSCL scheme for LES on unstructured grids. Comput. Fluids **33**, 1101–1129 (2004)
10. Ouvrard, H., Koobus, B., Dervieux, A., Salvetti, M.V.: Classical and variational multiscale LES of the flow around a circular cylinder on unstructured grids. Comput. Fluids **39**, 1083–1094 (2010)
11. Rossiter, J.E.: Wind-tunnel experiments on the flow over rectangular cavities at subsonic and transonic speeds. Aeronautical Research Council. Reports Memoranda No. 3438 (1964)
12. Rockwell, D., Naudascher, E.: Review – self-sustaining oscillations of flow past cavities. J. Fluid Eng. - T. ASME **100**, 152–165 (1978)

Flow Over a Realistic Car Model: WMLES Assessment and Turbulent Structures

D. E. Aljure, J. Calafell, A. Báez and A. Oliva

1 Introduction

Most CFD research on automotive external aerodynamics has been carried out using very simplified models such as the Ahmed car [1]. To reduce the gap between the production cars and models used for academic purposes, the DrivAer car model was introduced in 2012. References [2, 3] performed experimental observations on this geometry. Their results suggested that the Reynolds number dependency of the force coefficients decreased as Re increased. Two values have been reported for Re number independence, $Re = 2 \times 10^6$ [3] and $Re = 4.87 \times 10^6$ [2]. Several numerical works have also been carried out, particularly RANS simulations [4–7] and hybrid approaches such as DES [4, 6] or PANS [7], among others. Most papers show a good agreement of the pressure profiles with those obtained experimentally, however some deviations are found, specially in the vehicle's top. The present work aims to advance in the understanding of the physics governing the flow over the drivAer geometry, in particular the unsteady effects inherent in automotive aerodynamics. Furthermore, we aim to evaluate the behavior of wall models in conjunction with LES for automotive aerodynamic type flows.

D. E. Aljure · J. Calafell · A. Báez · A. Oliva (✉)
Heat and Mass Transfer Technological Center (CTTC), Universitat Politècnica de Catalunya-BarcelonaTech (UPC). ESEIAAT, Colom 11, 08222 Terrassa, Barcelona, Spain
e-mail: oliva@cttc.upc.edu

D. E. Aljure
e-mail: davidal@cttc.upc.edu

J. Calafell
e-mail: joancs@cttc.upc.edu

A. Báez
e-mail: aleix@cttc.upc.edu

M. V. Salvetti et al. (eds.), *Direct and Large-Eddy Simulation XI*,
ERCOFTAC Series 25, https://doi.org/10.1007/978-3-030-04915-7_66

2 Mathematical and Numerical Model

Filtered incompressible Navier–Stokes equations are discretized using finite volume techniques on collocated unstructured meshes. Spatial and temporal discretization is carried out using a symmetry preserving scheme and a self adaptive scheme, respectively [8]. Velocity pressure coupling is resolved by means of the fractional step algorithm and a backward euler scheme is used for the pressure gradient term. Turbulence modeling is done using the SIGMA and VMS models (see [1]). Additionally, the Werner and Wengle wall wall model (WM) is implemented [9]. The present numerical approach has shown good results in cases involving flows with massive separations [1, 10, 11]. The results reported in this work have been performed with the TermoFluids Computational Fluid Dynamics (CFD) software package (www.termofluids.com) and are computed on the in-house JFF cluster (www.cttc.upc.edu) and FinisTerrae II supercomputer at CESGA (www.cesga.es).

3 Case Definition

The car geometry (see [2]) is placed inside a 3/4 virtual wind tunnel of dimensions $8.8L_{ref} \times 1.75L_{ref} \times 1.3L_{ref}$, where L_{ref} corresponds to the longitude of the car (4.6 m). This work uses the fastback drivAer model, with mirrors, simplified underbody and simplified rotating wheels for ground simulation. In order to reduce computational requirements, Reynolds number is set at $Re = u_{ref} L_{ref}/\nu = 2.43 \times 10^6$, lower than the more typical $Re = 4.87 \times 10^6$.

Four different meshes were built, however only the finest, containing approximately 53 M (Mesh 3) and 79 M (Mesh 4) elements, are presented here. Mesh resolution was assessed by analyzing the result convergence and non-dimensional wall normal distance. Average y^+ for the meshes here presented are as follows: $y^+ = 11.8$

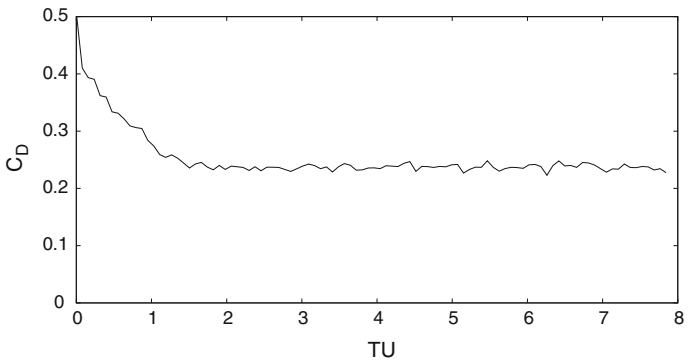

Fig. 1 Drag coefficient time evolution

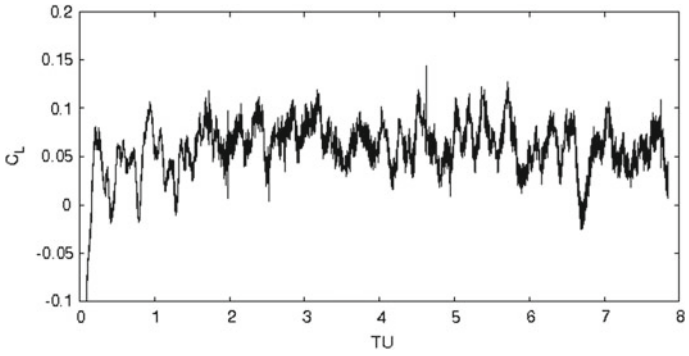

Fig. 2 Lift coefficient time evolution

and $y^+ = 4.3$ for the meshes 3 and 4, respectively. Simulations are then advanced in time until the initial transient behavior has been washed out. Afterwards, instantaneous data is integrated to obtain converged statistics. Several parameters are studied to asses the temporal evolution of the flow such as the time evolution of the force coefficients (Figs. 1 and 2) or autocorrelation functions of the pressure coefficient at selected locations.

4 Results

Table 1 shows the relevant set-ups studied and the resulting force coefficients. The use of the wall model in mesh 3 reduces the difference present in the force coefficients between Mesh 3 and Mesh 4, for both SGS models, indicating a positive effect of the WM. Drag coefficient converges towards 0.25, whereas lift converges towards 0.06. Reported data for the lift coefficient does not include the forces exerted by the wheels, this is shown in Table 1 as C'_L. It should be noted that there is a large difference in this quantity between experiments and simulations. This could be attributed to the differences in experimental set up and CFD i.e. the roof stinger, which may influence the force and pressure distribution around the car.

Figure 3 shows the pressure profiles in the mid plane along the top of the car. Cases M3_S_NW and M3_S_WM are compared to the solutions obtained when not using turbulence modeling (case M3_N_NW) and using the finer mesh (case M4_S_NW). When using WM almost no changes are observable for most of the cars length, except for two zones which are affected: the bonnet-wind shield junction (BW-J) and the fastback (FB).

The BW-J has a small corner that greatly affects the flow configuration as the flow separates and creates a recirculation region. As observed in Fig. 3, the influence of the wall model in this area affects the results negatively. Results in the FB area behave differently. At around $x/L_{ref} \approx 0.8$, flow detaches again and the wall model does

Table 1 Force coefficients for the different numerical configurations and experimental results. *: Extracted from [5]

Case	Mesh	SGS	WM	C_D	C_L	C'_L	C_{LRMS}
M3_S_NW	3	SIGMA	NO	0.246	0.083	0.018	0.024
M3_S_WM	3	SIGMA	YES	**0.251**	0.056	−0.008	0.024
M3_V_NW	3	VMS	NO	0.250	0.063	0.038	0.020
M3_V_WM	3	VMS	YES	**0.251**	0.062	−0.003	0.023
M4_S_NW	4	SIGMA	NO	**0.251**	0.065	−0.003	0.021
M4_V_NW	4	VMS	NO	**0.251**	0.061	−0.006	0.021
Exp. [2]				0.243	–	−0.06*	–

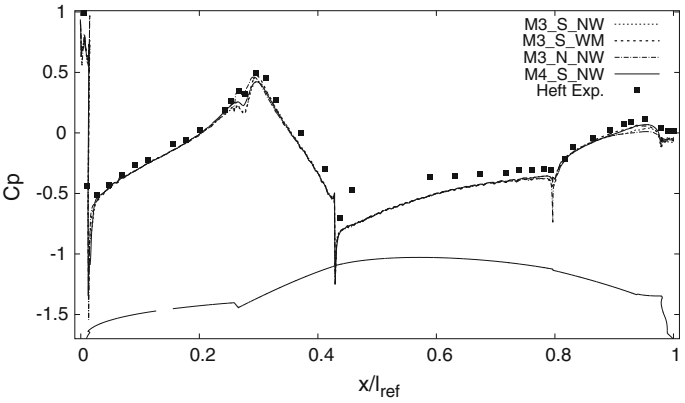

Fig. 3 Average pressure coefficient profile at the midplane over the top of the car geometry

not improve the results. Further downstream, between $0.75 \leq x/L_{ref} \leq 1$, a gradual change in the geometry causes the flow to separate and reattach several times. These small separation areas do not induce a large pressure drop. On the contrary, there is a pressure recuperation over this area. For this zone, results from case M3_S_WM are closer to those of case M4_S_NW than the others, indicating a positive effect of using the wall model in this area.

One of the main concerns when using LES simulations in industry applications is the large computational expense required. As meshes become finer, a higher computational expense is required. Table 2 shows the non-dimensional time step, iteration time, number of iterations and total CPU time required for the simulations of cases M3_S_WM and M4_S_NW. As can be seen in Table 2, there is a nearly 60% reduction in the time step size when changing from Mesh 3 to Mesh 4 due to the smaller control volumes around the car's surface. This time step decrease causes an increase of 130% in the number of iterations required to simulate the time span required in the present case. Using the WM considerably reduces the computational requirements needed for the present simulations, CPU time is reduced in approximately 70%.

Table 2 Average time step dt, iteration time t_{iter}, number of iterations and overall time t_{cpu} required for the different numerical configurations

Case	dt (TU)	iter	t_{iter}(s)	t_{cpu} (CPU hours)
M3_S_WM	2.03×10^{-5}	3.86×10^{5}	0.7 s	8.23×10^{4}
M4_S_NW	8.83×10^{-6}	8.88×10^{5}	1.1 s	2.78×10^{5}

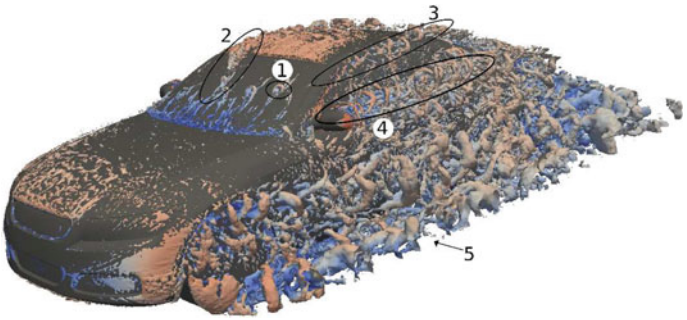

Fig. 4 Front view

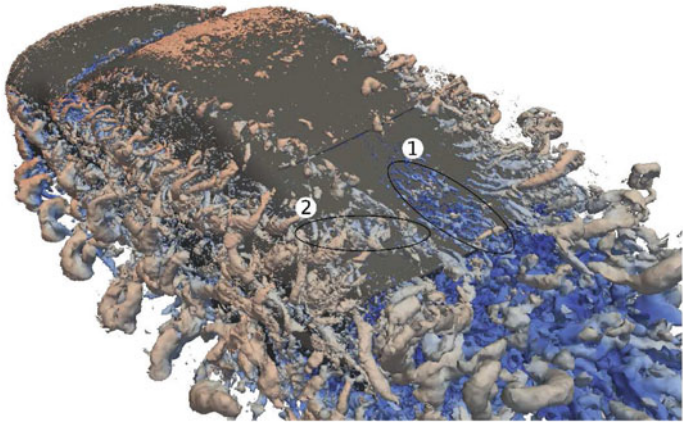

Fig. 5 Back view

Flow around the drivAer model is quite complex, where plenty of vortices are formed around the geometry. Instantaneous turbulent structures around the car are analyzed using the non-dimensional Q criterion. Figures 4 and 5 show the $Q^* = 1$ iso surfaces colored by velocity magnitude. Several locations around the car present flow separation and recirculating regions, resulting in a very complex flow around the car.

When observed from the front, several regions stand out (Fig. 4). The flow crashes into the front of the car creating a stagnation region around the front bumper. Flow

then travels upwards towards the bonnet and side wards towards the wheel well area. As the flow reaches the BW-J, the geometrical discontinuity present there causes the flow to separate again. As a consequence, the flow detaches from the edge, generating small horseshoe-like vortices that travel up the wind shield (see region 1 in Fig. 4). In the junction of the windshield with the roof of the car, a secondary shedding region can be observed. When the horseshoe vortices reach this area, they combine and generate large structures that shed towards the wake, marked as region 2 in Fig. 4. This process takes place at different span wise locations feeding instability to the flow downstream.

Flow along the side of the windshield moves over the A-pillar, where the A-pillar vortex is created (see region 3 in Fig. 4). Furthermore, as the flow passes along the mirrors a large unsteady wake is created. This mirror-wake travels alongside the car and joins the main wake at the rear (see region 4 in Fig. 4). Both these large scale structures are noise sources in external car aerodynamics. Finally, the front and rear wheels interact heavily with the oncoming flow and create the largest structures around the car (region 5 in Fig. 4).

When viewed from behind several structures stand out. Small scale structures form as the flow travels down the FB region. These structures travel downwind and detach from the back of the car (region 1 in Fig. 5). Finally, the C-pillar vortices are also visible in Fig. 5, marked as region 2.

5 Conclusions

In this work LES and WMLES simulations of the flow around the fastback drivAer car model have been carried out using smooth under body, mirrors, simplified wheels and moving ground. The present simulations were ran using $Re = 2.43 \times 10^6$, and some differences between literature results and present ones is expected. Furthermore, the Werner and Wengle wall model was implemented on Mesh 3, in conjunction with two SGS models: SIGMA and VMS, and results compared to those yielded by the finer mesh.

Force coefficient and pressure profiles are well within the range of previous authors' results. A Drag coefficient of $C_D = 0.251$ and a lift coefficient of $C_L = 0.07$ are obtained in the present simulations. Lift and drag values show improvement when using the WM. Small differences are observed in the pressure profiles, and using the WM gives mixed results. Improvement is observed in zones with adverse pressure gradient and smooth geometrical changes. Results obtained in zones where the geometry triggers flow separation and recirculation do not show improvement. Overall analysis of the models leads to the conclusion that, from a practical viewpoint, the WMLES using the Werner and Wengle wall model improves the obtained results with very low computational cost. Additionally, the improvement of the results using the WM allows simulations to be ran in smaller meshes, allowing a larger time step, and thus, a lower number of iterations. In the present case, CPU time required for Mesh 3 with the wall model is around 70% lower than that required for mesh 4.

One of the strongest features of LES is the ability to study flow structures and unsteady effects around the car. This is a very useful tool as it can better predict large scale structures that directly affect aerodynamic behavior, as well as, unsteady effects which can have an important impact on ride stability and noise generation. The most important structures observed are the mirror induced vortices and those created by the rotating wheels. Secondary structures include the A-pillar and C-pillar vortices. Finally, plenty of small scale structures have been observed, such as vortices detaching of off the wind shield-roof junction, small structures detaching of the BW-J area and those forming in the FB area.

Acknowledgements This work has been partially financially supported by the "Ministerio de Economía y Competitividad, Secretaría de Estado de Investigación, Desarrollo e Innovación", Spain (Project reference ENE2010-17801), by the collaboration project between "Universitat Politècnica de Catalunya" and Termo Fluids S. L. and the "Departamento Administrativo de Ciencia, Tecnología e Innovación - Colciencias" through their doctoral training program "Francisco Jose de Caldas". We also acknowledge the access to the FinisTerrae II supercomputer granted by the "Red Espaola de Supercomputación" (RES).

References

1. Aljure, D.E., Lehmkuhl, O., Rodríguez, I., Oliva, A.: Flow and turbulent structures around simplified car models. Comput. Fluids **96**, 122–135 (2014)
2. Heft, A.I., Indinger, T., Adams, N.A.: Introduction of a new realistic generic car model for aerodynamic investigations. SAE Tech. Pap. No. 2012-01-0168 (2012)
3. Strangfeld, C., Wieser, D., Schmidt, J.-J., Woszidlo, R., Nateri, C., Paschereit, C.: Experimental study of baseline flow characteristics for the realistic car model drivaer. SAE Tech. Pap. No. 2013-01-1251 (2013)
4. Guilmineau, E.: Numerical simulations of flow around a realistic generic car model. SAE Tech. Pap. No. 2014-01-0607 (2014)
5. Guilmineau, E.: Numerical simulations of ground simulation for a realistic generic car model. In: Proceedings of the ASME 2014 Joint US-European Fluids Engineering Division Summer. Chicago, Illinois, USA, 3–7 Aug (2014)
6. Ashton, N., West, A., Lardeau, S., Revell, A.: Assesment of RANS and DES methods for realistic automotive models. Comput. Fluids **128**, 1–15 (2016)
7. Jakirlic, S., Kutej, L., Hanssmann, D., Basara, B., Schütz, T., Tropea, C.: Rear-end shape influence on the aerodynamic properties of a realistic car model: a RANS and hybrid LES/RANS study. New Results Numer. Exp. Fluid Mech. X **132**, 397–407 (2016)
8. Trias, F.X., Lehmkuhl, O., Oliva, A., Pérez-Segarra, C.D., Verstappen, R.W.C.P.: Symmetry-preserving discretization of Navier-Stokes equations on collocated unstructured grids. J. Comput. Phys. **258**, 246–267 (2014)
9. Werner, H., Wengle, H.: Large-eddy simulation of turbulent flow over and around a cube in a plate channel. In: 8th Symposium on Turbulent Shear Flows, pp. 155–168. Munich, Germany (1991)
10. Rodríguez, I., Borrell, R., Lehmkuhl, O., Pérez-Segarra, C.D., Oliva, A.: Direct numerical simulation of the flow over a sphere at $Re = 3700$. J. Fluid Mech. **679**, 263–287 (2011)
11. Lehmkuhl, O., Park, G.I., Moin, P.: LES of flow over the NASA common research model with near-wall modeling. In: Proceedings of the Summer Program 2016, Center for Turbulence Research, pp. 335–341. Standford (2016)

Numerical Study of the Flow Around 25° Ahmed Bodies with Hybrid Turbulence Models

F. Delassaux, I. Mortazavi, V. Herbert and C. Ribes

1 Introduction

The aim of this work is to explore the efficiency of different improved Reynolds-Averaged Navier-Stokes (RANS) and hybrid RANS/LES approaches to study the external aerodynamics related to ground vehicles. These computational techniques should be able to build a bridge between accuracy and robustness in order to compute complex high Reynolds number bluff-body flows like ground vehicle flows. Bluff body flows are characterized by separated regions, containing wide spectra of turbulent scales. These regions, especially in the wake behind the body, are responsible for the main part of the drag forces. An accurate computation of these areas is a difficult task. Recently, different hybrid/modified models as Scale-Adaptive Simulation (SAS) [7], Delayed Detached Eddy Simulation (DDES) [10] and Stress-Blended Eddy Simulation (SBES) [2] have been developed to take advantage from the RANS low computational time without totally loosing the accuracy of Large Eddy Simulation (LES) models [9]. In order to get the best setup, the grid design is as critical as the model influence. In this work SAS, DDES and SBES models with unstructured meshes are used to simulate the flow around 25° Ahmed bodies. Two geometries are considered in this work : a sharp and a rounded edges 25° Ahmed bodies. Comparing these two geometries is very interesting as, on one hand, they represent a complex flow detachment on the rear slant for the sharp edges case and on the other hand, this complexity can be sensibly smoothed by rounding appropriate edges of the same body. Moreover, the rounded edges on the sides of the body delay the onset of the longitudinal vortices compared to sharp edges, making more challenging the flow prediction in this area. Ashton et al. [3] and Guilmineau et al. [5] works show the

F. Delassaux (✉) · I. Mortazavi
Equipe M2N, CNAM Paris, 292 rue Saint-Martin, 75003 Paris, France
e-mail: francois.delassaux@ext.mpsa.com

V. Herbert · C. Ribes
Groupe PSA, Route de Gisy, 78943 Velizy-Villacoublay, France

M. V. Salvetti et al. (eds.), *Direct and Large-Eddy Simulation XI*,
ERCOFTAC Series 25, https://doi.org/10.1007/978-3-030-04915-7_67

superiority of hybrid methods over RANS models for the separation/reattachment prediction on the rear slant surface of the body. First, the numerical setup is validated on the very common sharp edges Ahmed body. Then, the flow topology of the rounded case is investigated. The rounded edges allow us to get closer to a real vehicle shape with smooth rounded edges at the back. Numerical results are compared with experimental data from La Ferte Vidame (LFV) wind tunnel carried out by Rossitto et al. [8].

2 Ahmed Bodies, Grid and Setup Description

2.1 Ahmed Bodies Description

Two different shape of Ahmed bodies are studied: a sharp one [1] and a rounded one [8]. These bluff bodies are illustrated in Fig. 1, on the left the Ahmed body with sharp edges and on the right, the Ahmed body with rounded edges at the roof junction and side edges (in blue). The radius of curvature of the afterbody is expressed as a percentage of the reference length and is equal to 10% [8]. Consequently, sharp and rounded edges case are respectively named R_0S_0 and $R_{10}S_{10}$ thereafter.

2.2 Grids and Computational Setup

The computational domain is respectively $5L_B$ long upstream and $10L_B$ long downstream of the Ahmed body, with $L_B = 1.044\,\text{m}$, the length of the body. The cross section of domain is equal to $4.2L_B$ and its height is set to $5L_B$, giving a blockage ratio of 0.5%. The inlet boundary condition is defined as velocity inlet with $V_\infty = 40\,\text{m/s}$, yielding a Reynolds number based on the length of the model of 2.6×10^6. A pressure outlet condition is applied to the exit surface, with gauge pressure equal to 0 Pa. All the Ahmed body geometries are covered by no slip wall boundary condition.

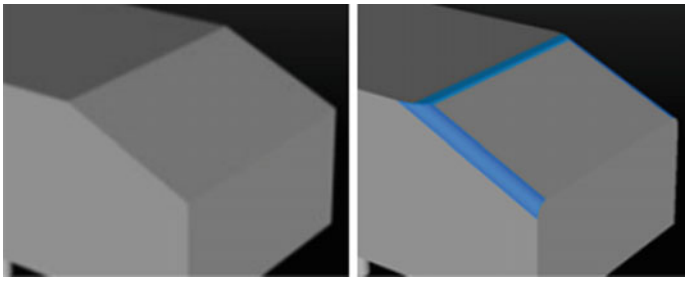

Fig. 1 Ahmed body with sharp edges on the left and Ahmed body with rounded edges on the right

The ground of the computational domain is divided into two parts: from the inlet to $X/L_B = 3$, a slip wall condition is applied. For the remainder part of the ground, a no-slip wall condition is used to allow the build up of the boundary layer. The demarcation between these two parts allows to reproduce the experimental boundary layer thickness [8].

The near-wall regions are meshed with prisms. The others regions of the domain are fitted by tetrahedrons cells with box refinement in strategic locations of the flow (forebody, underbody and rear slant surface) to capture the separation/attachment phenomenon. The grids contain respectively, 22 and 19 million cells for sharp and rounded cases. The wall normal resolution is $y+ < 0.7$. In the streamwise and spanwise directions, the mesh is refined as $30 < \Delta s^+ = \Delta l^+ < 250$ for the rear slant, with a mean value as $\Delta s^+ = \Delta l^+ \approx 120$. More details on the grids can be found in [4]. Besides, the time step is fixed as $\Delta t = 5 \cdot 10^5$s, ensuring a CFL number around 1 in critical areas of the flow. The computations were run for a total of 115 convective transit times defined as $T.V_\infty/L_B$, with $T = 3$ s of physical time. The time-averaging process was started after 77 transit times, to be sure of the relevance of the averaged quantities.

For all turbulence methods, RANS underlying model is the SST k-w [6]. The RANS $k - \omega$ SST is known to be one of the most accurate RANS model for the flow separation prediction. The SAS is an improved RANS formulation, which allows the resolution of a part of the turbulent spectrum in unstable flow conditions. DDES and SBES are called hybrid RANS/LES methods. In these approaches, the unsteady RANS models are employed in the attached boundary layers, while the LES treatment is applied to the separated regions. These models differ from the shielding function used for the switch between RANS and LES [2], to protect the boundary layer from LES intrusion. Furthermore, with SBES, LES model is not embedded in RANS model, and any combination of RANS and LES models could be used.

3 Results and Discussions

3.1 25° Sharp Edges Ahmed Body - Method Validation

On the sharp case, SAS, DDES and SBES approaches show relevant results for both drag and lift coefficients, as seen in Table 1. With an appropriate grid refinement, the DDES approach presents the best results compared to experiments and demonstrates the importance of capturing the shear layer due to separation on the backlight. Both drag and lift coefficient show a very good agreement with experiments, with an estimate error respectively of −2.5 and 3.8%.

One of the main feature of the flow around the 25° sharp edges Ahmed body is the closed recirculation bubble on the rear slant surface. The Fig. 2a illustrates the zero-velocity contours of the longitudinal velocity $\overline{U_x} = 0$ for the three turbulence models studied. The length of the mean recirculation bubble from experiments L_R is equal

Table 1 Comparisons of drag and lift coefficients between experiments and numerical results on sharp edges Ahmed body

Models	C_d	ΔC_d (%)	C_l	ΔC_l (%)
Experiments	0.356	–	0.311	–
SAS	0.355	−0.3	0.298	−4.0
DDES	0.347	−2.5	0.323	3.8
SBES	0.341	−4.2	0.328	5.4

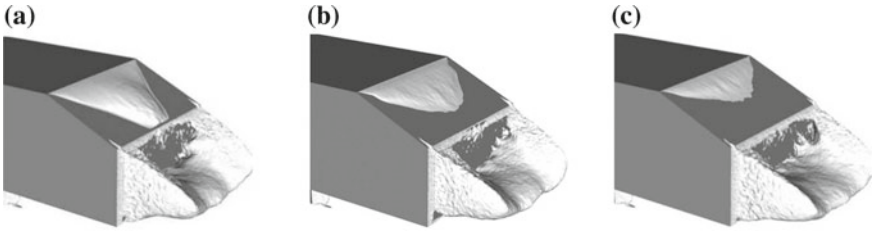

Fig. 2 **a** SAS $L_R = 100\%$, **b** DDES $L_R = 75\%$, **c** SBES $L_R = 53\%$

to 78% of the rear window length. The DDES model shows the best prediction for the mean recirculation bubble length, equal to 75%. SBES leads to a smaller closed recirculation bubble, with a recirculation length equal to 53%. On the contrary, SAS shows a reattachment at the end of the rear slant surface, so that L_R is equal to 100% due to high modeled turbulent kinetic energy in the separation area. More results can be found in [4].

3.2 25° Rounded Edges Ahmed Body

Considering the rounded case, aerodynamical coefficients are drastically reduced as shown by experiments [8]. Drag and lift reductions, respectively of 16 and 18%, are observed. The Table 2 shows the very good prediction of the three turbulence models for aerodynamic coefficients. The Fig. 3 shows the Cp evolution along two different planes: the symmetry plane $Y/H = 0$ and $Y/H = 0.5$ with H the height of the body. The dashed line corresponds to the demarcation between the rear slant surface and the vertical base. It is clearly observable that the three turbulence models give very close results for both planes. For $0.9 < S^* < 1$, the flow acceleration due to the rounded edges lead to lower Cp values compared to sharp edges case. As the bubble recirculation is suppressed, it results in pressure recovery over the slanted surface. This flow topology modification is directly responsible of drag reduction. Figure 4 illustrates Cp values in different cross-section planes from the top of the rear slant surface and the close wake. The left part of the figure is the sharp edges case and the rounded edges case is on the right. We can clearly observe the topology

Table 2 Comparisons of drag and lift coefficients between experiments and numerical results on rounded edges Ahmed body

Models	C_d	ΔC_d (%)	C_l	ΔC_l (%)
Experiments	0.298	–	0.254	–
SAS	0.301	0.9	0.244	−4.0
DDES	0.299	0.4	0.251	−1.1
SBES	0.306	2.8	0.245	−3.7

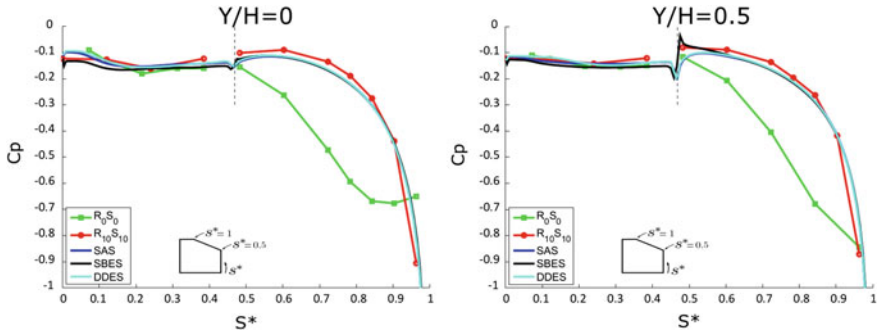

Fig. 3 Pressure coefficient comparison between SAS, DDES and SBES models over the back of the body

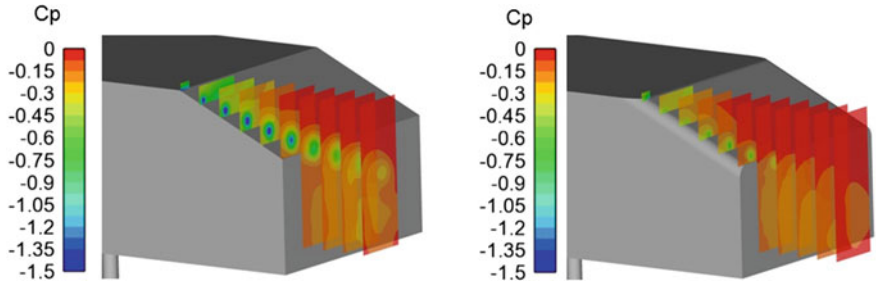

Fig. 4 DDES evolution of pressure coefficient between sharp case (left) and rounded case (right) over cross-section planes

modification of the longitudinal vortices. Indeed, for the sharp case, the strength of the vortices is significantly higher (lower Cp values) compared to the rounded case. Moreover, the onset of the longitudinal vortices is delayed leading to drag and lift forces reduction in this area of the flow.

4 Conclusions

The flow topology around sharped edges and rounded edges Ahmed bodies has been investigated. For the sharp case, DDES model globally shows the best prediction for drag and lift coefficients with respectively errors around −2.5 and 3.8%. The size of the recirculation bubble, equal to 75% compared to 78% experimentally, is also very well predicted with DDES model. SAS seems to suffer in the vicinity of separation zone and acts like RANS models in this area. The higher level of turbulent kinetic energy (not shown here) explains the shorter recirculation bubble obtained with SBES method. For the rounded case, the DDES model shows again the best prediction for both drag and lift coefficient. The Cp values along two planes over the back of the body state that the three turbulence model give very good agreement with experiments. The Cp plots explain the flow topology modification between the two cases. Due to rounded edges at the transition between the roof and the rear slant surface, the flow separation disappears leading to pressure recovery all along the rear surface. The rounded edges on the sides of the body delay the onset of the longitudinal vortices and reduce their intensity. These two major modifications in the flow topology lead to drag and lift reduction. Globally, the main flow structures for both cases have been recovered using Hybrid RANS/LES methods.

References

1. Ahmed, S.R., Ramm, R., Faltin, G.: Some salient features of the time-averaged ground vehicle wake. SAE Tech. Pap. Ser. No. 840300. Detroit (1984)
2. ANSYS Fluent Theory Guide, Release 17.0 (2016)
3. Ashton, N., West, A., Lardeau, S., Revell, A.: Assessment of RANS and DES methods for realistic automotive models. Comput. Fluids **128**, 1–15 (2016)
4. Delassaux, F., Mortazavi, I., Herbert, V., Ribes, C.: Comparison of three hybrid turbulence models for the flow around a 25 Ahmed body. In: Proceedings of the Symposium on 6th Hybrid RANS-LES Methods. Strasbourg, France (2017). (Will be published)
5. Guilmineau, E., Deng, G.B., Leroyer, A., Queutey, P., Visonneau, M., Wackers, J.: Assessment of hybrid RANS-LES formulations for flow simulation around the Ahmed body. Comput. Fluids (2017). (Article in Press)
6. Menter, F.R.: Zonal two equation k-ε turbulence models for aerodynamic flows. AIAA Pap. **2906** (1993)
7. Menter, F.R., Egorov, Y.: The scale-adaptive simulation method for unsteady turbulent flow predictions. Part 1: theory and model description. Flow Turbul. Combust. **85**(1), 113–138 (2010)
8. Rossitto, G., Sicot, C., Ferrand, V., Bore, J., Harambat, F.: Influence of afterbody rounding on the pressure distribution over a fastback vehicle. Exp. Fluids **57**(43) (2016)
9. Sagaut, P.: Large Eddy Simulation for Incompressible Flows: An Introduction. Springer Science & Business Media, Berlin (2006)
10. Spalart, P.R., Deck, S., Shur, M., Squires, K.D., Strelets, M., Travin, A.: A new version of detached-eddy simulation, resistant to ambiguous grid densities. Theor. Comput. Fluid Dyn. **20**, 181–195 (2006)

Part IX
Internal Flows and Wall Turbulence

Large Eddy Simulation of a Compressor Blade Passage Operating at Low Reynolds Number

O.Wilsby, S. Rolfo, A. Agarwal, P. Harley and C. Moulinec

1 Introduction

This paper presents the preliminary results from the numerical study of an axial compressor operating at low maximum Reynolds number of 5×10^4, flow coefficient $\phi = 0.32$ and head coefficient of $\psi = 0.28$. The overall goal is to use high fidelity simulations to accurately calculate the acoustic sources responsible for noise generation in the compressor. However, this is a challenging task and the first step is to gain confidence in the accuracy of the LES with respect to mesh resolution and sub-grid scale modelling. The objective of this study is therefore to assess the effect of mesh resolution and subgrid scale models on the flow field. The main points of interest are to accurately resolve the unsteady wall pressure spectrum at the blade trailing edge, as well as turbulent length scales and intensities in the wake. These results can be used as direct inputs to analytical noise propagation theories to predict the generated noise in the far-field.

O. Wilsby (✉)
University of Melburne, Melburne, Australia
e-mail: ow222@cam.ac.uk

S. Rolfo · C. Moulinec
STFC Daresbury Laboratory, Scientific Computing Department,
Warrington, UK
e-mail: stefano.rolfo@stfc.ac.uk

C. Moulinec
e-mail: charles.moulinec@stfc.ac.uk

A. Agarwal
Cambridge University, Cambridge, UK
e-mail: aa406@cam.ac.uk

P. Harley
Aeroacoustics Group, Dyson Limited, Malmesbury, UK
e-mail: peter.harley@dyson.com

M. V. Salvetti et al. (eds.), *Direct and Large-Eddy Simulation XI*,
ERCOFTAC Series 25, https://doi.org/10.1007/978-3-030-04915-7_68

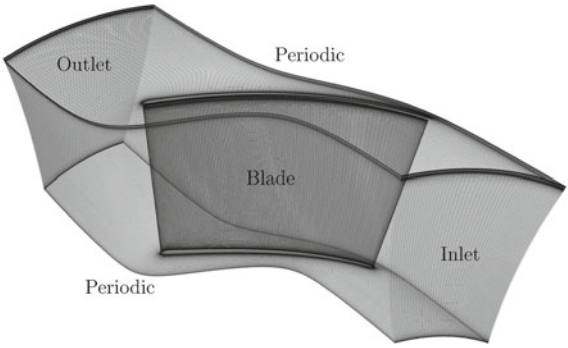

Fig. 1 Computational domain with blade geometry and underlying mesh topology. Periodic boundaries are enforced in the circumferential directions. Tip gap is visible at the shroud location of the mesh

Table 1 Mesh resolution parameters for different refinement levels used in the study

Size (million)	Spanwise cells	Max Δy^+	Max expansion rate	Min orthogonality (deg)
2	150	1.5	1.15	70
5	200	1.0	1.15	70
10	**300**	**0.9**	**1.15**	**70**
20	400	0.8	1.15	70
40	500	0.6	1.15	70

2 Methodology

The simulations were performed using the open source finite volume based code *Code Saturne*, which is developed and maintained by EDF R&D. The code is second order accurate in space and time and the velocity-pressure coupling is ensured through a prediction/correction method based on a SIMPLEC algorithm and Rhie and Chow interpolation. For a general description of the code see [1, 3]. For the results discussed herein, a single rotor blade with tip gap was meshed with 10 million block structured mesh with resolution in the wall normal, streamwise, and spanwise direction would respectively achieve: $\Delta y^+ \leq 1$, $\Delta x^+ \leq 50$, $\Delta z^+ \leq 15$, see Fig. 1. In order to gain confidence in the mesh resolution, further meshes were simulated between 2 and 40 M, see Table 1. The simulations utilised the assumption of periodicity between blade rows valid for machines of reasonably high solidity. The simulation is conducted in the relative frame (Frozen frame), such that the physics of rotation are accounted for by introduction of Coriolis source terms in the governing equations of fluid motion, rather than through mesh motion. The filtered, incompressible Navier Stokes equations are resolved and the sub grid terms are modelled using both a Smagorinky model [6] and its dynamic counterpart [4]. At the inlet a synthetic eddy

method [5] is used to efficiently generate artificial turbulence which is based on the hydraulic diameter of the intake duct and a turbulence intensity of 2%, consistent with the experimental apparatus which will be used to validate the simulations.

3 Results

The quality index proposed by Celik [2] reads $Q_\nu = \frac{1}{1+\alpha_\nu\left(\frac{\overline{\nu}_T}{\nu}\right)^n}$ where $\alpha_\nu = 0.05$, $n = 0.53$, and $\overline{\nu}_T$ is the time averaged turbulent viscosity. It is a quality metric used to evaluate the mesh resolution by comparing the significance of the SGS viscosity relative to the molecular viscosity. Figures 2 and 3 show contours of the quality metric on different axial slices. The light portions show evidence of higher s.g.s. viscosity and hence possible regions of greater modelling error. In this case those regions correspond to the hub-corner separation region on the suction side (SS), as well as the tip gap vortex region. Both these areas are sources of turbulence and require fine, high quality cells to accurately model the effect on the mean flow and local unsteadiness. The wall streamlines also show evidence of significant span-wise flow. This has important implications for the boundary layer development as the flow does not follow the curvature of the blade profile, allowing the boundary layer to stay attached for longer. Figures 4, 5 and 6 show the development of the average wake profile at a fixed radius. It is notable that the 2 M mesh departs significantly from the rest, suggesting it is too coarse. The results for the finer meshes suggest we approach grid independence. The spectral content of probes are plotted from Figs. 7 to 10. Again the 2 M mesh is a clear outlier due to mesh coarseness. However there are still notable differences in spectral levels for higher frequencies for the finer meshes in the hub separation region, showing that this region requires fine cells to capture the turbulence accurately. It also shows that mesh requirements are indeed higher when examining data based on instantaneous variables rather than averages. Less variability across mesh refinements are seen in Figs. 8 and 9 since the mesh is good enough to properly resolve the boundary layer.

3.1 Subgrid Scale Model

For the 5 M mesh refinement, different s.g.s. models were tested comprising of the classic Smagorinksy, Dynamic and no model (implicit LES). Results showed little variation between the models when comparing mean statistics such as C_p and C_f however there were exceptions, as Figs. 11 and 12, for the regions near the tip show. This can be attributed to the tip clearance vortex formation, which is sensitive to the turbulence model used. It is interesting to note that the Smagorinsky and implicit models agree well with the Dynamic model for a normalized chord distance from leading edge of $s/C > 0.6$ for only the SS (and vice versa for the pressure side

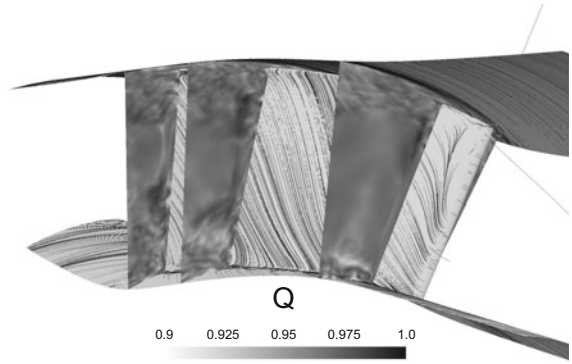

Fig. 2 SS streamlines and contours of Q_v for the 5 M mesh refinement

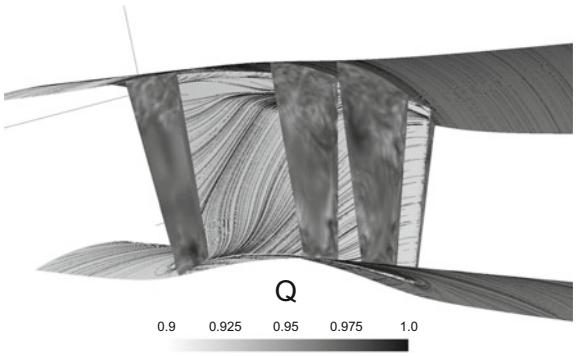

Fig. 3 PS streamlines and contours of Q_v for the 5 M mesh refinement

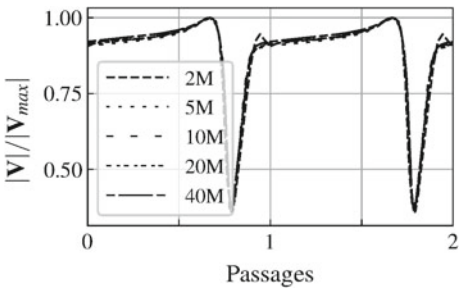

Fig. 4 Midspan wake, 0^+ mm from TE

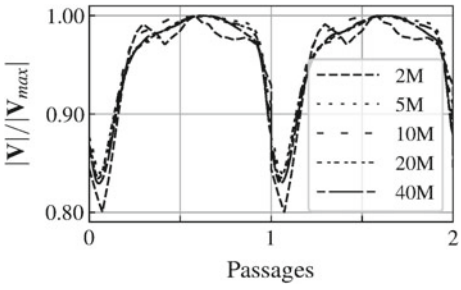

Fig. 5 Midspan wake, 4.5 mm from TE

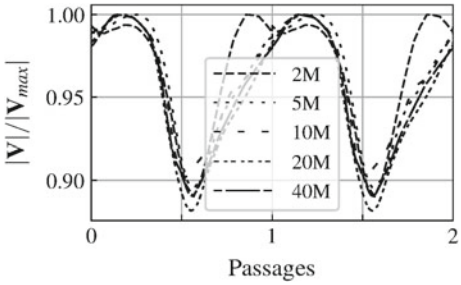

Fig. 6 Midspan wake, 11.5 mm from TE

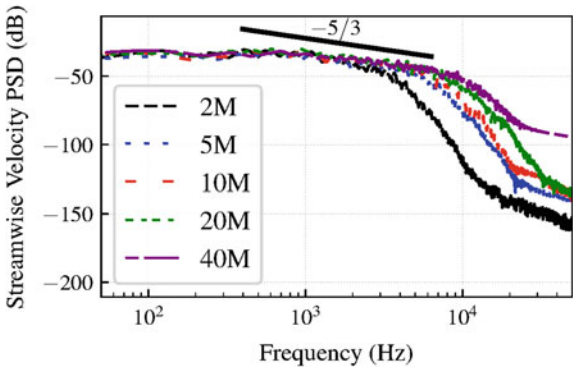

Fig. 7 Separation region on the PS near hub

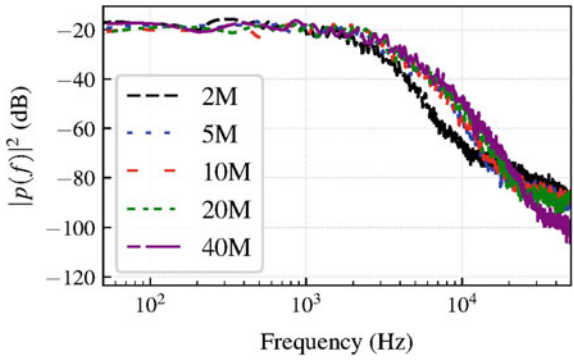

Fig. 8 Midspan blade SS trailing edge

(PS).) Variations, particularly for second order statistics may be due to inadequate averaging of the solution. Since no spatial averaging of the solution makes sense, the only resort is to run for a very large times, which can become highly expensive (Figs. 13 and 14).

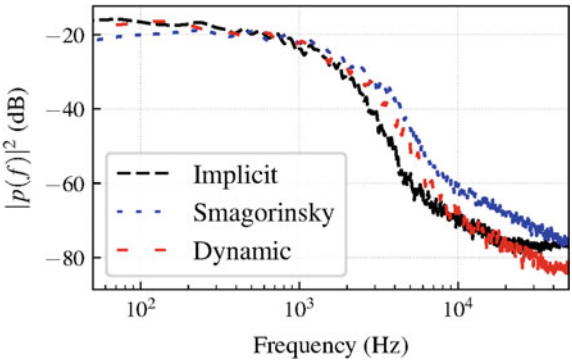

Fig. 9 Hub wake region

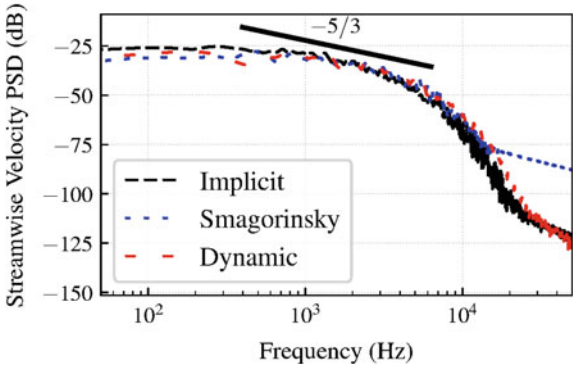

Fig. 10 Midspan wake region

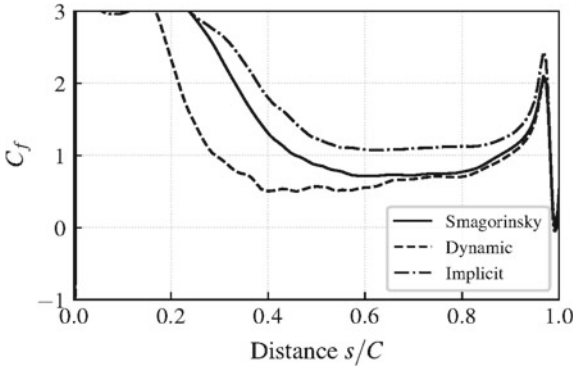

Fig. 11 Wall friction tip pressure side

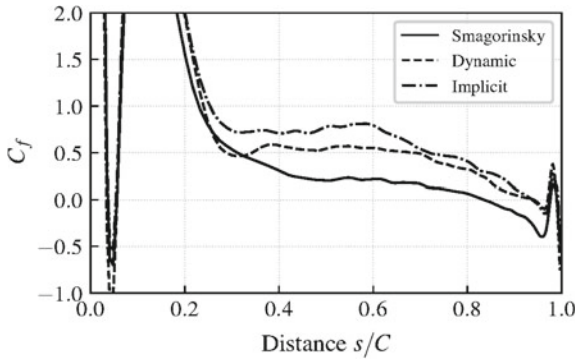

Fig. 12 Wall friction tip suction side

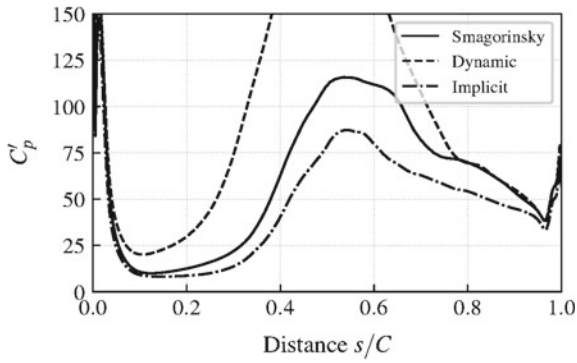

Fig. 13 Pressure variance near tip region on PS

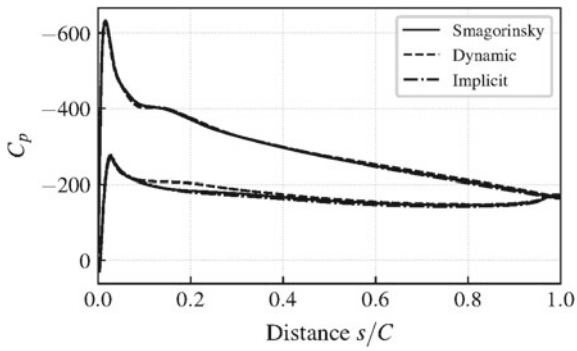

Fig. 14 Pressure coefficient near tip region

3.2 Boundary Layers

Figures 15, 16, 17, 18, 19 and 20 show the boundary layer profiles at different chordwise distances on the blade. The boundary layer is turbulent on both sides as it reaches the trailing edge, as is evidenced by the good fit of the classic turbulent log-wake law: $u^+ = \frac{1}{\kappa}\ln(y^+) + C + \frac{\Pi}{\kappa}2\sin^2\left(\frac{\pi y}{2\delta}\right)$ with $u^+ = u/u_\tau$ and $y^+ = yu_\tau/\nu$ for $y^+ > 30$.

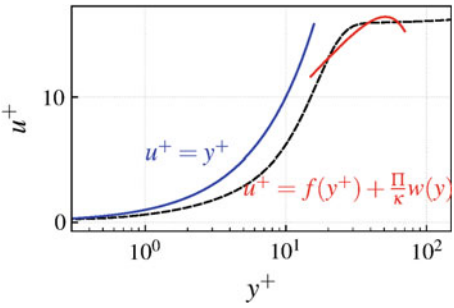

Fig. 15 Midspan pressure side 20% chord

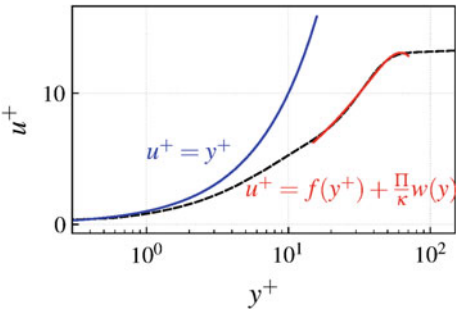

Fig. 16 Midspan pressure side 60% chord

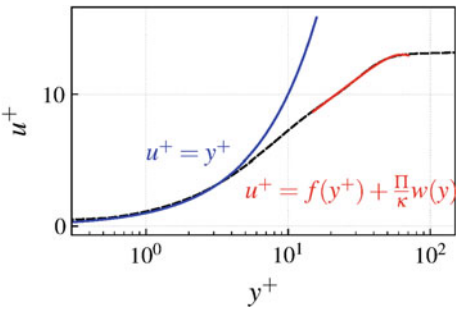

Fig. 17 Midspan pressure side 90% chord

Note that we have found a combination of κ, Π, C, δ that minimize the rms error between the model and the measured boundary layer in the log law region as a way of fitting the boundary layer laws to the data. However the commonly reported von Karman constant $\kappa = 0.41$ and Reynolds dependent constant $C = 5.0$ do not apply here, with κ varying in the range 0.38–0.7 for the boundary layers shown.

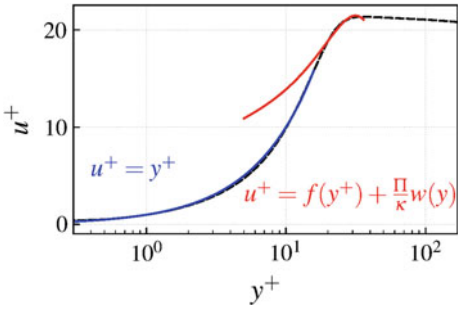

Fig. 18 Midspan suction side 20% chord

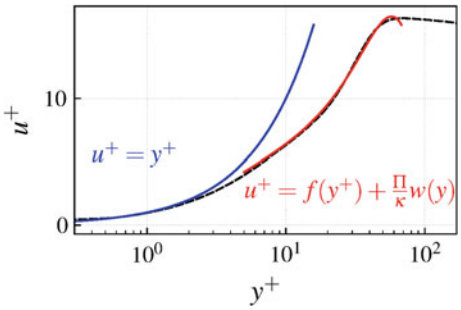

Fig. 19 Midspan suction side 60% chord

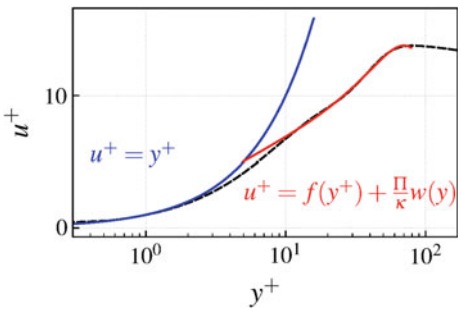

Fig. 20 Midspan suction side 90% chord

4 Conclusions

Large eddy simulations of a single rotor passage have been carried out with the aim of understanding the mesh refinement needed for making predictions of the blade wall pressure spectrum and wake turbulent statistics, which are ultimately of interest for noise predictions. For resolving power spectra up to a maximum desired frequency of 20 kHz it was seen that the 40 M refinement or higher is required in order to resolve the flow in regions off the blade surface, such as the hub-corner separation region. However on the blade surface where the mesh is relatively fine, even the 5 M mesh agrees reasonably well with the higher refinements. The 2 M mesh was notably unsuitable in almost all regards. For estimating accurate parameters from

the blade boundary layer, a 10 M mesh is deemed a reasonable trade off between solution accuracy and computational expense.

References

1. Archambeau, F., Mechitoua, N., Sakiz, M.: Code_Saturne: a finite volume code for the computation of turbulent incompressible flows - industrial applications. Int. J. Finite Vol. **1** (2004)
2. Celik, I.B., Klein, M., Janicka, J.: Assessment measures for engineering LES applications. J. Fluids Eng. **131**(3) (2009)
3. Fournier, Y., Bonelle, J., Moulinec, C., Shang, Z., Sunderland, A., Uribe, J.: Optimizing Code_Saturne computations on petascale systems. Comput. Fluids **45**, 103–108 (2011)
4. Germano, M., Piomelli, U., Moin, P., Cabot, W.H.: A dynamic subgrid-scale eddy viscosity model. Phys. Fluids A-Fluid **3**, 1760–1765 (1991)
5. Jarrin, N., Benhamadouche, S., Laurence, D., Prosser, R.: A synthetic-eddy-method for generating inflow conditions for large-eddy simulations. Int. J. Heat Fluid Flow **27**(4) (2006)
6. Smagorinsky, J.: General circulation experiments with the primitive equations: I. The basic experiment. Mon. Weather Rev. **91**, 99–164 (1963)

Eddy Resolving Simulations of Intake Under Crosswinds

N. R. Vadlamani and P. G. Tucker

1 Introduction

Modern aircraft engine designs are trending towards higher bypass ratio (BPR) and lower fan pressure ratio (FPR). This architectural change has been demonstrated to offer significant fuel burn benefits of upto 25% [1]. With an increase in the BPR, the engine diameter and the associated surface area increases. However, it is crucial to compensate for the additional increase in the drag and also limit the weight of the powerplant. This implies relatively shorter intakes, and nacelles with much more severe restrictions on the external diameter.

An optimal intake design is intended to provide a uniform flow to the downstream components in an engine with minimum total pressure loss over a wide range of operating conditions. However, shorter intakes suffer from a reduced incidence tolerance and the flow is more prone to separation specifically under the off-design conditions like high incidence and crosswinds [2]. The flow also experiences severe acceleration around the intake lip, relaminarization, flow separation and transition to turbulence. The current study aims to capture the flow over the intake-lip under crosswinds and further explore the effects of the Reynolds number.

2 Computational Details

Figure 1 shows the computational domain which is generally motivated from the low-speed experimental setup of Wakelam [3]. An intake lip of length, L, is subjected

N. R. Vadlamani (✉) · P. G. Tucker
Deparment of Engineering, Trumington Street, Cambridge CB2 1PZ, UK
e-mail: nrv24@cam.ac.uk

P. G. Tucker
e-mail: pgt23@cam.ac.uk

M. V. Salvetti et al. (eds.), *Direct and Large-Eddy Simulation XI*,
ERCOFTAC Series 25, https://doi.org/10.1007/978-3-030-04915-7_69

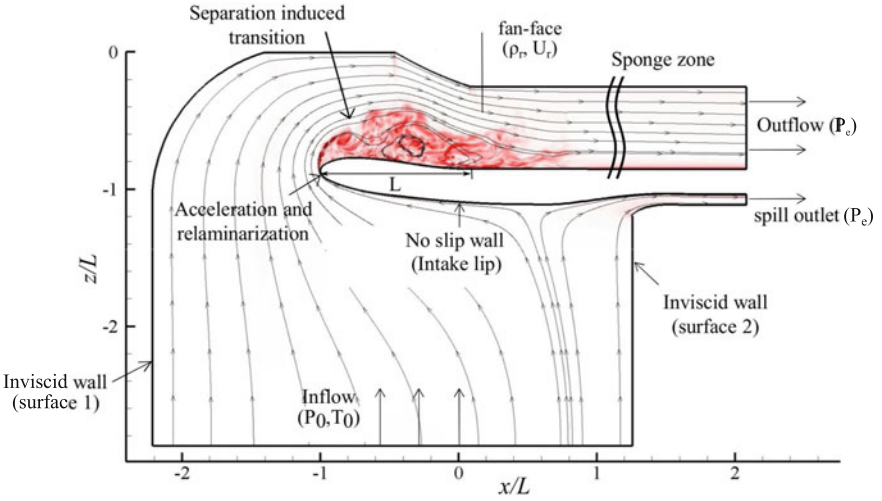

Fig. 1 Computational domain and boundary conditions (contour of vorticity magnitude and streamlines are shown to highlight the separated region around the intake lip)

to crosswind. The aggressive shape of the intake lip is in accordance with the mid-section of the 3D-sector considered in the measurements. The flow approaching from the inlet is guided by means of contoured walls to undergo a 90° turn over the intake. A fraction of the inlet flow (≈10%) is allowed to escape through the spill. Due to the mainstream flow, a new boundary layer develops on the windward side of the intake beyond the stagnation point. In the current simulations, the intake is extruded in the spanwise direction and hence the additional 3D streamtube contraction experienced on a 3D intake is ignored. Also, surfaces 1 and 2 are set to be inviscid and are solely meant to impose a pressure distribution over the intake; thereby minimizing the grid requirements in these regions.

Stagnation conditions ($P_0 = 102\,\text{kPa}$, $T_0 = 288\,\text{K}$) are specified at the inlet and static pressure is imposed at both the outlets ($P_e = 96\,\text{kPa}$). A non-reflective boundary condition based on Riemann invariants is imposed at the inflow as described in Matsuura and Kato [4]. A fringe zone is applied at the exit to damp out the vortical disturbances exiting, and the acoustic waves reflected from the domain exit. Spanwise width of around 0.2 L is chosen with periodicity imposed in the spanwise direction.

In the manuscript, all the length and velocity scales are non-dimensionalized by the lip length, L, and fan-face velocity, U_r. Pressure is normalized by $\rho_r U_r^2$; ρ_r being the density at the fan-face. The Reynolds number is defined on the basis of fan-face velocity and the length of the intake lip which is relevant to the flow separating over intake lip under crosswind. Simulations are carried out at two different Reynolds numbers: 10^4 and 10^5 and the Mach number at the fan-face is ≈0.3. For both the cases, around 55 M nodes are used with 192 nodes to resolve the span. The grid

resolution is chosen after performing a grid-sensitivity study for the $Re = 10^5$ case. The mesh is fine enough to capture the dissipation range (see Fig. 5e, f) and hence no additional sub-grid scale model is employed in the current simulations.

Simulations are performed using an in-house high-order structured code, COMPSQUARE. Three dimensional compressible Navier-Stokes equations are solved in the generalized curvilinear coordinate system. Sixth order compact finite-difference schemes are used to spatially discretize the inviscid, viscous fluxes and the metric terms. Time integration is carried out using an explicit four-stage fourth order Runge–Kutta (RK) scheme. The numerical instabilities arising due to the non-dissipative nature of the high-order compact central difference approximation are eliminated by filtering the conservative variables. For this purpose, 10th order low pass Pade-type non-dispersive spatial filter is employed at each RK stage. Filtering is sequentially applied in each of the three computational directions [5]. The code utilizes MPI message passing system for parallelization on distributed memory platforms. The numerical framework has been validated on a number of canonical test cases: Taylor green vortex, inviscid vortex convection, turbulent channel flows and boundary layers. It has also been used to investigate the distributed roughness effects on transitional and turbulent boundary layers [6].

3 Results

As illustrated in Fig. 1, the incoming flow stagnates on the outer surface of the windward lip; part of which spills through the outlet. Rest of the flow encounters a severe acceleration as it turns around the leading edge of the lip. Typical value of acceleration parameter, $K = \nu/U^2 dU/ds$ is around 3×10^{-5} which is an order of magnitude larger than the threshold for relaminarization. Subsequently, the flow encounters an adverse pressure gradient and the boundary layer separates over the leading edge.

The coherent structures post-separation are shown in Fig. 2a for $Re = 10^5$ using iso-surfaces of Q. The growth of secondary instabilities on the two-dimensional Kelvin-Helmholtz type rollers drives transition to turbulence. Additional acceleration due to the converging section of the spinner wall promotes the flow reattachment. In order to demonstrate that the computational domain is large enough in the spanwise direction, Fig. 2b plots the two point correlations of velocities (R_{uu}, R_{vv}, R_{ww}) along the span at three different wall normal locations. The correlations decay to zero between 0.04 L and 0.05 L assuring that the spanwise extent is sufficient enough to accommodate all the dominant flow features formed during the flow transitioning to turbulence.

In a quest to examine the effect of different operating conditions on the intake aerodynamics, a range of Mach numbers and Reynolds numbers have been simulated. For brevity, the results for $Re = 10^4$ and 10^5 will be presented in this paper. Figure 3a, b shows the instantaneous snapshots of the vorticity field. The effect of Reynolds number on the flow structures is clearly evident from this figure. As expected, with

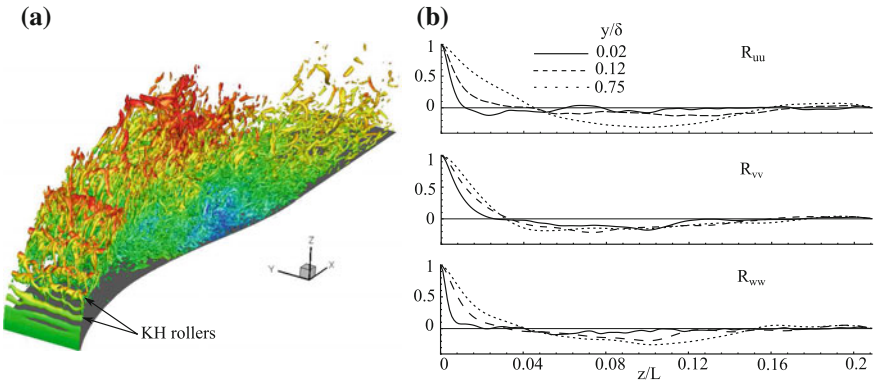

Fig. 2 **a** Coherent structures represented using iso-surfaces of $Q(= 500)$ contoured with streamwise velocity. **b** Spanwise two point correlations R_{uu}, R_{uu} and R_{uu} extracted at three different wall-normal locations for case $Re = 10^5$

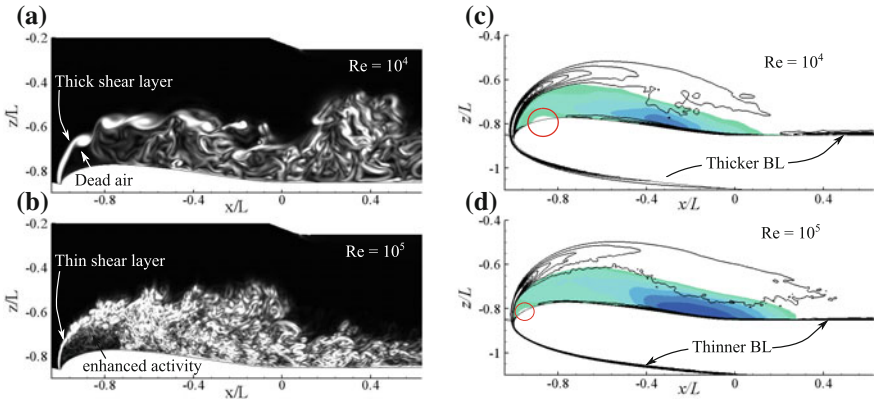

Fig. 3 Instantaneous snapshots of vorticity field: **a** $Re = 10^4$ **b** $Re = 10^5$. Time-averaged contours of vorticity field (lines) and reverse flow (contours): **c** $Re = 10^4$ **d** $Re = 10^5$

increasing Re the energy cascades down to much more finer scales due to an increase in the inertial force of the flow. The thickness of the shear layer and the subsequent size of the KH-rollers shed from the shear layer are also remarkably smaller at higher Re. Small-scale structures in the reverse flow are convected back to the 'dead-air' region and an enhanced turbulent activity is notable. Indeed these structures are also found to further destabilize the shear layer promoting early transition.

Figure 3c, d show the contours of the time-averaged vorticity field (lines) and reverse flow velocity (contours). It is interesting to note that increasing Re had a marginal effect on both the height and extent of the primary separation bubble. On the other hand, the secondary separation bubble typically formed due to the reverse flow has progressively decreased with increasing Re. The observation is further substantiated in Fig. 4a by comparing the axial variation of the skin-friction coefficient,

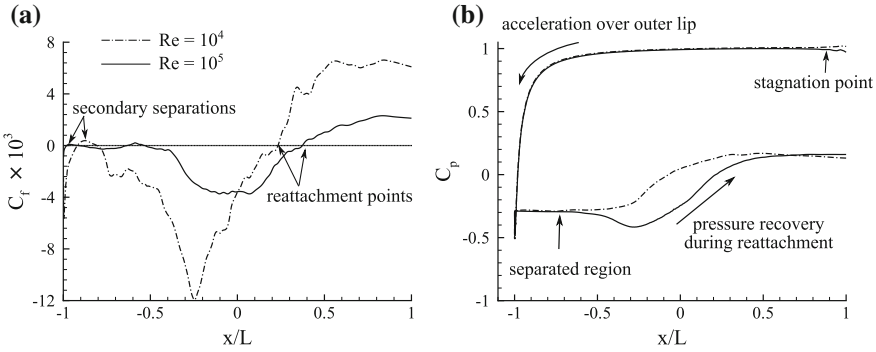

Fig. 4 **a** Skin-friction coefficient, C_f, and **b** Pressure coefficient, C_p, along the intake lip

C_f. The zero-crossings of C_f indicate the points of separation and reattachment. A marginal increase in the primary separation is notable at higher Re. In the context of flow separating behind a sharp leading edge, Crompton and Barret [7] also observed that increasing the Reynolds number had a minimal impact on the size of the primary separation bubble while the secondary separation has subsided.

Figure 4b compares the non-dimensional pressure distribution, $C_p = (p - p_e)/(p_0 - p_e)$, over the intake lip. Here p is the static pressure over the intake, p_0 is the inlet stagnation pressure and p_e is the static pressure at the exit. Three regions of interest are marked in the figure: (a) rapid acceleration around the intake lip (b) plateau of constant pressure indicating separation and (c) pressure recovery due to the flow reattachment. For both the Reynolds numbers, the location of the stagnation point and the separation point at the leading edge had marginally changed. However, the pressure recovery is much more rapid at lower Re. This is attributed to the greater spreading rate of the shear layer (see Fig. 3a, b) which also finds support from the LDA (laser doppler anemometry) measurements of Crompton and Barret [7]. They demonstrated that at low Re, the influence of the shear layer reaches the surface at a shorter distance due to its larger spreading rate promoting earlier reattachment. The reattachment length however remains constant with a further increase in the Reynolds number to 4×10^5 (not shown here).

Figure 5a shows the contours of turbulent kinetic energy, k. It clearly demonstrates the early destabilization of the shear layer at high Re and a larger spreading rate at low Re. Figure 5b further compares the streamwise variation of $\sqrt{k_{max}}$ on a semi-log plot. Soon after the separation, the disturbances grow exponentially indicating transition to turbulence. For both the cases, non-linearity sets in once the disturbance amplitude reaches $\approx 0.28\, U_r$. Carpet plots of time-averaged streamwise velocity, U_m and Reynolds stresses, $u'u'$, are shown in Fig. 5c, d. Of the two distinct peaks evident in the profiles of $u'u'$, the near wall peak corresponds to the reverse flow and the outer peak to the inflectional instability within the shear layer. At high Re, both the reverse flow component of the mean velocity and the near wall peak of $u'u'$ are stronger. Due to early transition of shear layer at high Re, the initial growth of the

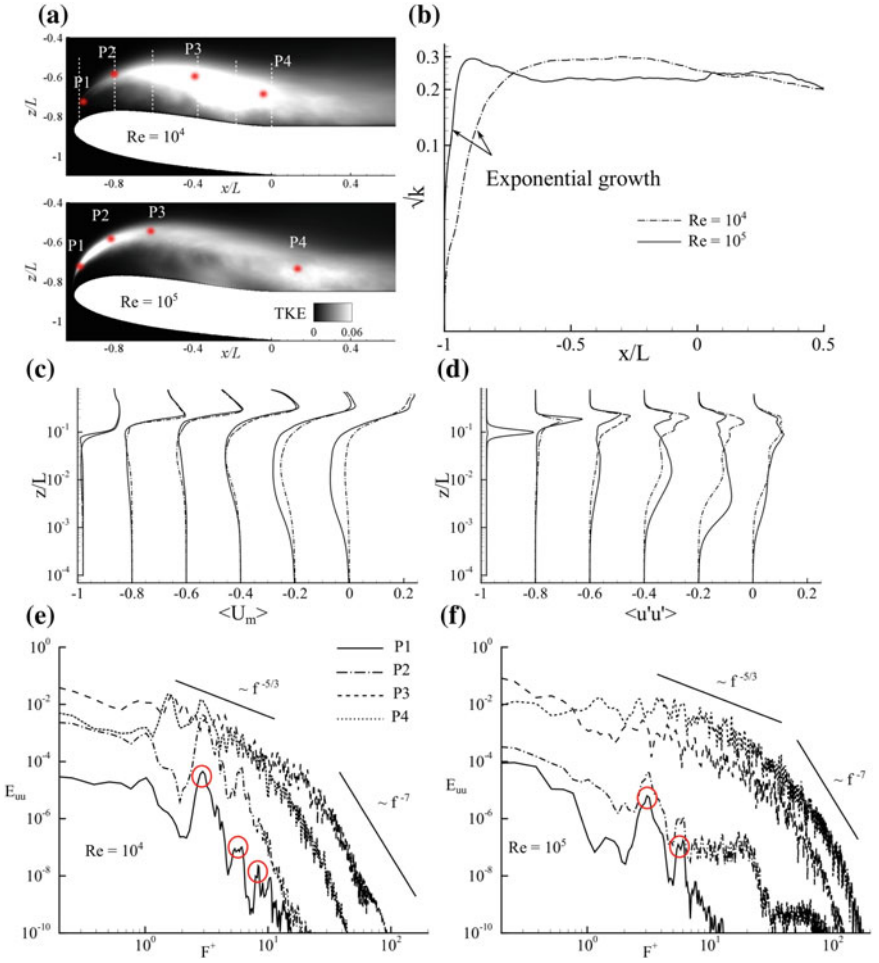

Fig. 5 **a** Contours of TKE, **b** Streamwise variation of $k_{max}^{0.5}$. Carpet plot showing profiles of **c** mean velocity, U_m and **d** streamwise Reynolds stress, $u'u'$ at locations marked by vertical lines in Fig. 5a. Spectra extracted at probes P1–P4 shown in Fig. 5a for **e** $Re = 10^4$ and **f** $Re = 10^5$. Open circles show the fundamental modes and its higher harmonics

outer peak is also more pronounced for $x/L < -0.7$. However, the trend reverses beyond $x/L > -0.7$ when transition initiates in the low Re case.

The dynamic behaviour of the separated shear layer is assessed by collecting the time-series data at P1–P4 (marked in Fig. 5a). Figure 5e, f provide the normalized energy spectra of axial velocity, estimated using Welch's method. For probes P1 and P2, distinct peaks in the spectra are observed at $F^+(= fL/U_r) = 2.9$ for $Re = 10^4$ and $F^+ = 3.1$ for $Re = 10^5$ respectively. Higher harmonics due to non-linear interactions are also notable. At probes P3 and P4, the well-known $-5/3$ slope in the

inertial sub-range is captured; the range being more prominent for case with high Re. The dissipation range is also well captured in the current simulations further demonstrating the reliability of the numerical setup and the mesh resolution.

4 Conclusions

High-fidelity direct numerical simulations are carried out to investigate the flow separating over an intake lip under crosswinds, albeit at low Reynolds numbers. The mean and turbulent characteristics are extracted at $Re = 10^4$ and 10^5. An increase in Re is shown to (a) promote early transition of the shear layer, (b) increase the reverse flow velocity within the primary separation bubble, (c) suppress the secondary separation and (d) marginally increase the length of the primary separation. The spreading rate of the shear layer is found to be more prominent at low Re. For both the Reynolds numbers, the non-linear breakdown to turbulence is initiated when the disturbance amplitude reaches $\approx 0.28\, U_r$. The dynamics of the shear layer and reattaching flow is examined using spectra of streamwise velocity. Distinct peaks corresponding to shear layer shedding, a notable $-5/3$ range and dissipation range are captured.

Acknowledgements This project was funded by Innovate UK. Additional support from St. Catharine's college, Cambridge through the Bowring research fellowship is gratefully acknowledged. Simulations are performed on UK Supercomputer ARCHER, to which access was granted through UK Turbulence consortium (EP/L000261/1) and via the EPSRC RAP call of spring 2017.

References

1. Peters, A., Spakovszky, Z.S., Lord, W.K., Rose, B.: Ultrashort nacelles for low fan pressure ratio propulsors. J. Turbomach. **137**(2), 021001 (2015)
2. Cao, T., Vadlamani, N.R., Tucker, P.G., Smith, A.R., Slaby, M., Sheaf, C.T.: Fan-intake interaction under high incidence. J. Eng. Gas Turbines Power **139**(4), 041204 (2017)
3. Wakelam, C.T., Hynes, T.P., Hodson, H.P., Evans, S.W., Chanez, P.: Separation control for aeroengine intakes, part 1: low-speed investigation of control strategies. J. Propuls. Power **28**(4), 758–765 (2012)
4. Matsuura, K., Kato, C.: Large-eddy simulation of compressible transitional flows in a low-pressure turbine cascade. AIAA J. **45**(2), 442–457 (2007)
5. Rizzetta, D.P., Visbal, M.R., Morgan, P.E.: A high-order compact finite-difference scheme for large-eddy simulation of active flow control. Prog. Aerosp. Sci. **44**(6), 397–426 (2008)
6. Vadlamani, N.R., Tucker, P.G., Durbin, P.: Distributed roughness effects on transitional and turbulent boundary layers. Flow Turbul. Combust. **100**(3), 627–649 (2018)
7. Crompton, M.J., Barrett, R.V.: Investigation of the separation bubble formed behind the sharp leading edge of a flat plate at incidence. Proc. Inst. Mech. Eng. Part G: J. Aerosp. Eng. **214**(3), 157–176 (2000)

On Stability and Transition in Bent Pipes

J. Canton, R. Örlü and P. Schlatter

1 Introduction

This work is concerned with the investigation of the instability and transition to turbulence of the viscous, incompressible flow inside curved pipes. For the first time, the impact of the curvature is analysed over the whole range, presenting new results for both the steady flow and the instabilities encountered by this flow.

Flow through pipe bends has been extensively studied during the past decades, but several phenomena still miss an exhaustive characterisation and explanation (see, e.g., the recent review by Kalpakli Vester et al. [1]). Curved pipes are fundamental components in several industrial devices where they are part of, for example, engines, heat exchangers, nuclear reactors and other machines (for an extensive review see Vashisth et al. [2]). A second fundamental area of research where bent pipes are relevant is the medical field. Curved pipes are, in fact, an integral part of vascular and respiratory systems. Understanding the behaviour of the flow in this case can aid the prevention of several cardiovascular diseases (see, for instance, Refs. [3, 4]).

In the present work we focus on a canonical problem represented by the flow inside of a toroidal pipe, depicted in Fig. 1. This flow is characterised by a single geometrical parameter, the curvature, and constitutes the common asymptotic limit of two 'real' flow cases: the curved (spatially developing) pipe and the helical pipe. The curvature is defined as the ratio between the radius of the pipe and that of the torus, i.e. $\delta = R_p/R_t$; this and the Reynolds number Re (based on pipe diameter and bulk velocity) are the only two parameters defining this flow. The advantage of investigating a flow governed only by these two parameters is that it allows us to isolate the effect of the curvature on the flow properties and on the instability and transition dynamics. It will therefore be possible, when studying helical or differently

J. Canton (✉) · R. Örlü · P. Schlatter
Linné FLOW Centre, KTH Mechanics, Royal Institute of Technology,
SE-100 44 Stockholm, Sweden
e-mail: jcanton@mech.kth.se

M. V. Salvetti et al. (eds.), *Direct and Large-Eddy Simulation XI*,
ERCOFTAC Series 25, https://doi.org/10.1007/978-3-030-04915-7_70

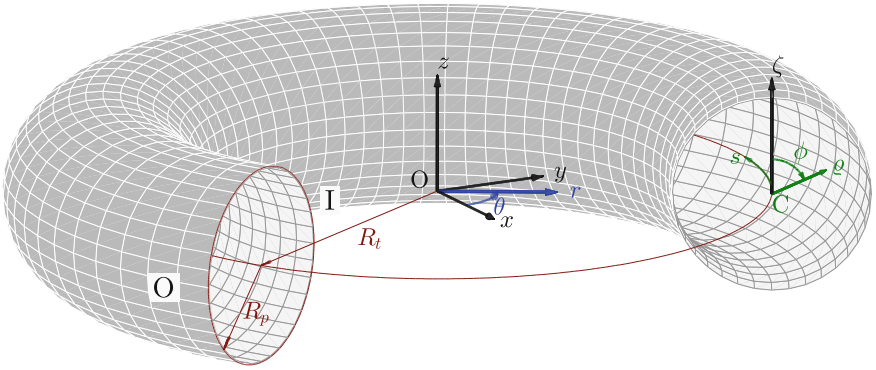

Fig. 1 Sketch of a toroidal pipe with curvature $\delta = R_p/R_t = 0.3$. The 'equatorial' plane of the torus corresponds to the x–y plane

bent pipes, to discern the flow features induced by the curvature from those produced by the torsion of the helix, possible development length effects, or other parameters.

2 Numerical Methods

The fluid is considered as viscous and incompressible, and therefore satisfies the incompressible Navier–Stokes equations. The steady states and the linear stability analysis are computed with `PaStA`, a Fortran 90 code based on the finite element method (for the validation and further details, see Ref. [5]). Nonlinear direct numerical simulations (DNS) are employed to verify the relevance of the linear results and to analyse the subcritical transition; these computations are performed with the spectral element code `Nek5000` [6]. The differences between the results of the two codes are kept below the imposed numerical tolerances by using highly resolved meshes, this allows us to have an uncertainty on the transitional Reynolds numbers below $\Delta Re = \pm 10^{-6}$.

3 Steady (Base) Flow

Following the experimental investigations by Boussinesq [7] and Eustice [8, 9], Dean [10, 11] investigated the flow in a toroidal pipe analytically. In both of his papers he assumed that the curvature of the pipe was small, which allowed him to neglect nonlinear terms in the equations. By means of this and successive approximations, Dean was able to derive a solution to the Navier–Stokes equations depending on a single parameter, later called Dean number in his honour, and defined as $De = Re\sqrt{\delta}$. Despite Dean's own estimates on the validity of his solution, several successive

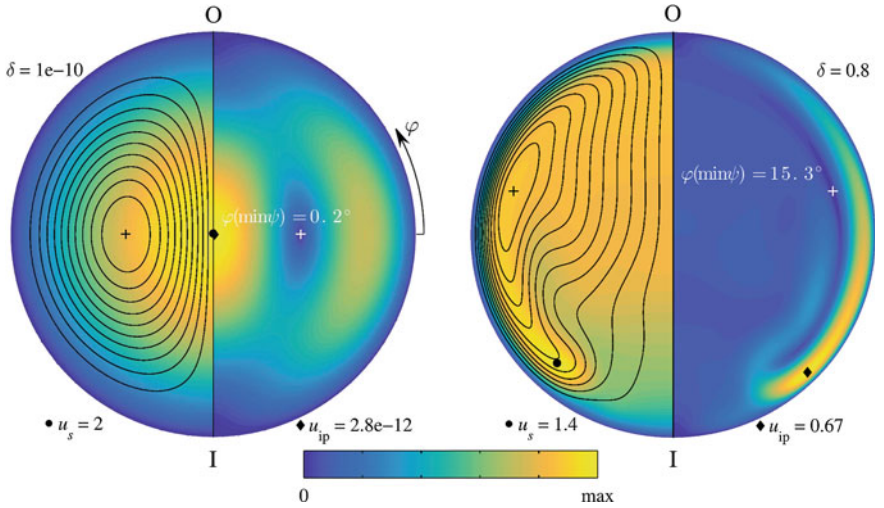

Fig. 2 Steady solutions for $\delta = 10^{-10}$, $Re = 1$ (left) and $\delta = 0.8$, $Re = 1\,000$ (right). Additional flow fields are reported in Ref. [14]. The colours show streamwise (left half) and in-plane (right half) velocity magnitudes, with values between zero and the maxima reported next to the respective markers. Contours of the streamfunction ψ are shown with black lines, and the centres of the Dean vortices are highlighted by plus symbols. Reprinted from Ref. [14], with permission from Elsevier

studies employed the Dean number as a unique scaling parameter, even for relevant quantities such as the friction factor f, with more or less satisfying results (see, e.g., Refs. [12, 13]).

In an in-depth analysis on some of the most relevant flow characteristics [14] we documented and discussed a number of previously unknown phenomena such as, most prominently, a shift in position of the maximum streamwise velocity, and the splitting of the vortex cores (Fig. 2). In addition, we demonstrate that a Dean number-based analysis is valid only below very low bounds on curvature and Dean number: $\delta < 10^{-6}$ and $De < 10$. These bounds are shown to be strict even for quantities that were believed to scale with the Dean number up to much higher values of δ and De, such as the aforementioned friction factor. In our analysis on the laminar flow we quantified that computing f based on the knowledge of the Dean number alone results in an uncertainty comprised between 17 and 340%.

4 Instability and Transition

The stability and transition of this flow has received a considerable amount of interest in the past decades, not only because of its connection to other kinds of bent pipes but also because, for low curvatures, it represents the smallest departure from the canonical straight pipe flow. As can be seen in Fig. 3, there is a number of works

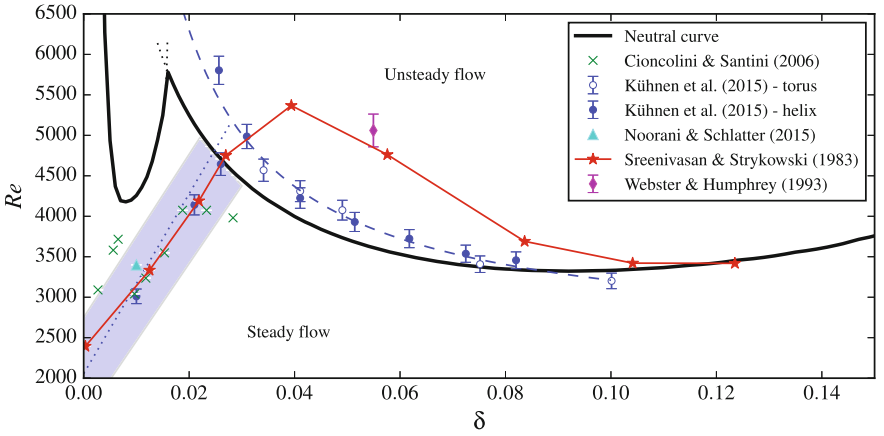

Fig. 3 Supercritical stability boundary, identified by the numerically computed neutral curve (solid, [16]) and by the experiments by Kühnen et al. (dashed, [17]), and subcritical stability boundary, in the shaded (blue) area. Reprinted from Ref. [16], with permission from Cambridge University Press

in the literature that identified, more or less precisely, the boundary between steady and unsteady flow. In fact, determining the mechanisms at the core of the transition to turbulence in this flow can greatly aid both in answering fundamental questions about transition to turbulence, and in understanding more complex phenomena such as swirl-switching in bent pipes (a low-frequency oscillatory motion that received considerable attention in recent years [1, 15]).

The recent works by Canton et al. [16], employing linear stability analysis and continuation algorithms, and Kühnen et al. [17], consisting of experiments in toroidal and helical pipes, determined that the flow is linearly unstable and undergoes a Hopf bifurcation for any curvature greater than zero and for $Re \approx 4000$. Several eigenmodes, in the shape of travelling waves, contribute to the 'irregular' neutral curve for the flow, depicted with a continuous (black) line in Fig. 3. This behaviour is in contrast to the flow in a straight pipe which, despite being linearly stable for any Reynolds number, displays unsteadiness for Re greater than about 2000 [18].

The mechanism that leads to transition appears to be different for low curvatures: while for $\delta \geq 0.028$ DNS confirm the presence of a Hopf bifurcation, with the flow jumping from a steady to a periodic regime, for $\delta < 0.028$ no clear boundary has been observed, different authors have even employed different criteria to determine the transition threshold for this range of curvatures (see, e.g., Refs. [17, 19]). It would appear, in fact, that for low curvatures a toroidal pipe behaves similarly to a straight pipe: the flow undergoes transition to turbulence despite being linearly stable to infinitesimal perturbations. The comparison, in terms of transition scenario, is actually closer to the Poiseuille flow inside of a channel: the flow is actually linearly unstable but for a Reynolds number which is much higher than the one were

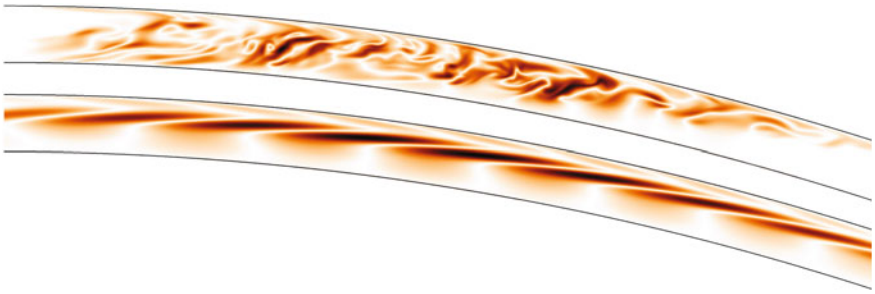

Fig. 4 Two snapshots of the flow in a toroidal pipe for $\delta = 0.01$ and $Re = 2900$, visualised in an $\approx$15 D section of the 100 D periodic pipe employed for the simulations. The *top* snapshot shows the formation of a "slug", while the *bottom* snapshot displays the structure of the eigenmode which is critical for this curvature, but for a higher Reynolds number $Re = 4257$. Both snapshots are visualised by pseudocolours of azimutal velocity magnitude, i.e. $|u_\phi|$

transition is observed in practice (the critical Reynolds number for channel flow is 5772, but turbulent flow is observed for Re as low as 3000).

We investigate this complex behaviour by means of nonlinear direct numerical simulations and, in order to isolate the dominant structures in the flow, we analyse the flow fields by three-dimensional proper orthogonal decomposition (POD) performed on the full domain using the snapshot method. Moreover, we also measure the 'degree of turbulence' in the flow via a more canonical statistical approach aimed at quantifying the level of intermittency and by measuring the lifespan of turbulent events. Preliminary results indicate that, indeed, the flow does not abruptly transition from the steady to the unsteady regime, for this range of curvatures. Instead, transition occurs over a range of curvatures and Reynolds numbers displaying an intermittent behaviour, as shown by the shaded area in Fig. 3, and by the results presented in Refs. [17, 19, 20]. This shows that, indeed, the flow in a low curvature pipe does bear some similarities to the flow inside a straight pipe, at least until the curvature is lower than 0.028; the limit after which the flow undergoes a more 'ordered' transition process.

Figure 4 illustrates this different transition scenario for $\delta = 0.01$ and $Re = 2900$, by means of pseudocolors of azimutal velocity magnitude. The two panels of the figure depict two snapshots of the flow field, captured at different times, in an approximately 15 diameters long section of the 100 D pipe used in the simulations. The top snapshot clearly shows the presence of a turbulent "slug" surrounded by laminar, undisturbed flow, while the bottom snapshots illustrates the presence of a travelling wave, caused by the vicinity (in terms of ΔRe) of the linearly unstable mode (see Ref. [16]). The travelling wave displays the same spatial structure of the eigenmode which is critical for this curvature and, in accordance with the negative growth rate of the mode for this Re, has an amplitude which decays exponentially with time. The wave can be obtained via Newton's method but it can also be naturally observed in

a simple DNS, as is the case for Fig. 4, since the corresponding eigenmode is only very weakly damped.

Acknowledgements This work is funded by The Swedish Research Council Grant No. 621-2013-5788. Computer time was provided by the Swedish National Infrastructure for Computing (SNIC). We acknowledge PRACE for awarding us access to resource Sisu based in Finland at CSC.

References

1. Kalpakli Vester, A., Örlü, R., Alfredsson, P.H.: Turbulent flows in curved pipes: recent advances in experiments and simulations. Appl. Mech. Rev. **68**, 050802 (2016)
2. Vashisth, S., Kumar, V., Nigam, K.D.P.: A review on the potential applications of curved geometries in process industry. Ind. Eng. Chem. Res. **47**, 3291–3337 (2008)
3. Berger, S.A., Talbot, L., Yao, L.-S.: Flow in curved pipes. Annu. Rev. Fluid Mech. **15**, 461–512 (1983)
4. Bulusu, K.V., Hussain, S., Plesniak, M.W.: Determination of secondary flow morphologies by wavelet analysis in a curved artery model with physiological inflow. Exp. Fluids **55**, 1832 (2014)
5. Canton, J.: Global linear stability of axisymmetric coaxial jets. Master's thesis, Politecnico di Milano, Italy (2013)
6. Fischer, P.F., Lottes, J.W., Kerkemeier, S.G.: Nek5000 Web page (2008)
7. Boussinesq, M.J.: Mémoire sur l'influence des frottements dans les mouvements réguliers des fluides. J. Math. Pure Appl. **13**, 377–424 (1868)
8. Eustice, J.: Flow of water in curved pipes. Proc. R. Soc. Lond. Ser. A **84**, 107–118 (1910)
9. Eustice, J.: Experiments on stream-line motion in curved pipes. Proc. R. Soc. A Math. Phys. Eng. Sci. **85**, 119–131 (1911)
10. Dean, W.R.: XVI. Note on the motion of fluid in a curved pipe. Lond. Edinb. Dublin Philos. Mag. J. Sci. **4**, 208–223 (1927)
11. Dean, W.R.: The streamline motion of fluid in a curved pipe. Phil. Mag. **5**, 673–693 (1928)
12. Ito, H.: Friction factors for turbulent flow in curved pipes. J. Basic Eng. **81**, 123–134 (1959)
13. Cieślicki, K., Piechna, A.: Can the Dean number alone characterize flow similarity in differently bent tubes? J. Fluids Eng. **134**(5), 051205 (2012)
14. Canton, J., Örlü, R., Schlatter, P.: Characterisation of the steady, laminar incompressible flow in toroidal pipes covering the entire curvature range. Int. J. Heat Fluid Flow **66**, 95–107 (2017)
15. Noorani, A., Schlatter, P.: Swirl-switching phenomenon in turbulent flow through toroidal pipes. Int. J. Heat Fluid Flow **61**, 108–116 (2016)
16. Canton, J., Schlatter, P., Örlü, R.: Modal instability of the flow in a toroidal pipe. J. Fluid Mech. **792**, 894–909 (2016)
17. Kühnen, J., Braunshier, P., Schwegel, M., Kuhlmann, H.C., Hof, B.: Subcritical versus supercritical transition to turbulence in curved pipes. J. Fluid Mech. **770**, R3 (2015)
18. Avila, K., Moxey, D., de Lozar, A., Avila, M., Barkley, D., Hof, B.: The onset of turbulence in pipe flow. Science **333**, 192–196 (2011)
19. Sreenivasan, K.R., Strykowski, P.J.: Stabilization effects in flow through helically coiled pipes. Exp. Fluids **1**, 31–36 (1983)
20. Noorani, A., Schlatter, P.: Evidence of sublaminar drag naturally occurring in a curved pipe. Phys. Fluids **27**, 035105 (2015)

Scaling of High-Order Statistics in Turbulent Pipe Flow

C. Bauer and C. Wagner

1 Introduction and Numerical Methodology

Turbulent pipe flows have been extensively studied over the last decades by means of both experiments and numerical simulations. However, in terms of turbulent high-order statistics a lack of sufficiently converged data remains. The scatter of the wall-normal flatness value obtained from experiments and different DNS, in particular, is related to the appearance of spatially and temporally rare local wall-normal velocity fluctuations, so called velocity spikes [13]. Furthermore, the Reynolds number dependency of the streamwise Reynolds stress peak has been discussed for turbulent plane channel flow by Hoyas and Jiménez [6] amongst others. The aim of the current work is to investigate the Reynolds number dependency of high-order statistical moments in turbulent pipe flow, namely streamwise Reynolds stresses, streamwise skewness and wall-normal flatness. Therefore, four different simulations for friction Reynolds numbers of Re_τ=180,360,720,1500 have been carried out. All statistical quantities in this work are integrated over sufficiently large spatio-temporal intervals in order to obtain fully converged values, see Bauer et al.[1].

The governing equations in case of a pressure-driven incompressible flow of a Newtonian fluid in a smooth pipe are the incompressible Navier–Stokes equations in the following dimensionless form

$$\frac{\partial \mathbf{u}}{\partial t} + \mathbf{u} \cdot \nabla \mathbf{u} + \nabla p = \frac{1}{Re_\tau} \nabla^2 \mathbf{u}, \tag{1}$$

$$\nabla \cdot \mathbf{u} = 0, \tag{2}$$

C. Bauer (✉) · C. Wagner
German Aerospace Center, Institute of Aerodynamics and Flow Technology,
Bunsenstr. 10, 37073 Gottingen, Germany
e-mail: christian.bauer@dlr.de

C. Bauer · C. Wagner
Institute of Thermodynamics and Fluid Mechanics, Technische Universität Ilmenau,
Helmholtzring 1, 98693 Ilmenau, Germany

M. V. Salvetti et al. (eds.), *Direct and Large-Eddy Simulation XI*,
ERCOFTAC Series 25, https://doi.org/10.1007/978-3-030-04915-7_71

Table 1 Turbulent pipe flow simulation cases. N_z, N_φ and N_r are the number of grid points with respect to the axial, azimuthal and radial direction, respectively. Δz^+, streamwise grid spacing; $R^+\Delta\varphi$, azimuthal grid spacing at the wall; Δr^+_{min} and Δr^+_{max}, minimal and maximal radial grid spacing, respectively, all grid spacings normalised by wall units. Δt, averaging interval for statistics; $\Delta t_b = \Delta t u_b/R$, in bulk time units; $\Delta t^+ = \Delta t u_\tau^2/\nu$, in viscous time units; $\Delta\tau^+ = \Delta t^+ L^+ 2\pi r^+$, averaging coordinate in viscous units. Pipe length for all cases: $L/R = 42$

Case	Re_τ	$N_z \times N_\varphi \times Nr$	Δz^+	$R^+\Delta\varphi$	Δr^+_{min}	Δr^+_{max}	Δt_b	Δt^+	$\Delta\tau^+$
$P180C$	180	$1536 \times 256 \times 84$	4.9	4.4	0.31	4.4	5891	72540	$6.2 \cdot 10^{11}$
$P360$	360	$3072 \times 512 \times 160$	4.9	4.4	0.39	4.4	1791	39808	$1.4 \cdot 10^{12}$
$P720$	720	$4608 \times 1024 \times 222$	6.6	4.4	0.49	6.6	333	13291	$1.8 \cdot 10^{12}$
$P1500$	1500	$8192 \times 2048 \times 408$	7.7	4.6	0.49	7.8	42	3120	$1.9 \cdot 10^{12}$

where $Re_\tau = u_\tau R/\nu$ is the friction Reynolds number based on friction velocity, pipe radius and kinematic viscosity. Equation (2) is integrated in time using a leapfrog-Euler scheme after being discretised by means of a fourth-order finite volume method [5]. The scheme is based on a projection method [3] and consists of three basic steps. First, an auxiliary velocity field is computed from the momentum equation (2) neglecting the pressure term. Then, a Poisson equation is solved in order to fulfill the divergence-free condition, before the actual velocity and pressure fields are updated from the auxiliary field and the solution of the Poisson equation. The flow geometry, which is an annular smooth pipe with length L and radius R, is discretised via staggered grid in a cylindrical coordinate system. In the vicinity of the cylindrical axis a semi-implicit scheme, as proposed by Kim et al. [7], is applied in the region of interest, where flow variables are treated implicitly with respect to the azimuthal direction. Table 1 shows the current simulation setups used within this study. The grid resolution in wall units satisfies commonly accepted values of $\Delta z^+ < 8$, $R^+\Delta\varphi < 5$, $\Delta r^+_{max} < 8$ and $\Delta r^+_{min} < 0.5$ for all simulations.

Statistics are computed by taking advantage of the flow homogeneity with respect to both streamwise and azimuthal directions, see Bauer et al.[1]. Henceforth, the angle brackets indicate an average in space and time as follows:

$$\langle u\rangle(r) = \frac{1}{L}\frac{1}{2\pi r}\frac{1}{\Delta t}\int_{t=t_0}^{t_0+\Delta t}\int_{z=0}^{L}\int_{\varphi=0}^{2\pi} u(z,\varphi,r,t)\,r\,d\varphi\,dz\,dt, \tag{3}$$

where Δt is the averaging interval in time. Since this work focusses on near-wall statistics, averaging intervals both in space and time are normalised by viscous length scales and viscous time units, respectively. In order to obtain comparable results for different Reynolds numbers and domain lengths, we assume the following averaging

coordinate, taking both temporal and spatial averaging intervals in wall units into account:

$$\Delta\tau^+ = \Delta t^+ L^+ 2\pi r^+, \tag{4}$$

where $\Delta t^+ = \Delta t \tau^2/\nu$ is the time interval normalised in viscous time units and L^+ as well as $2\pi r^+$ are the spatial intervals normalised by the viscous length scale $\delta_\nu = \nu/\tau$. High-order statistical moments, defined as follows

$$S(u_i) = \frac{\langle u_i' u_i' u_i' \rangle}{\langle u_i' u_i' \rangle^{3/2}}, \tag{5}$$

$$F(u_i) = \frac{\langle u_i' u_i' u_i' u_i' \rangle}{\langle u_i' u_i' \rangle^2}, \quad i \in \{z, \varphi, r\}, \tag{6}$$

are denoted as skewness (5) and flatness (6) of a velocity component u_i. The prime superscript is used to denote the velocity fluctuation of a component with respect to its mean ($u_i' = u_i - \langle u_i \rangle$), also referred to as the Reynolds decomposition. The variance of a velocity component $\langle u_i' u_i' \rangle$ is denoted as normal Reynolds stress.

2 Scaling of High-Order Statistical Moments

High-order moments of the velocity distribution in turbulent pipe flow were investigated with respect to their dependence on the Reynolds number. Since the streamwise Reynolds stress component, the streamwise skewness and the wall-normal flatness exhibited a strong Reynolds number dependency when normalised in wall units, the behaviour of these quantities will be discussed hereinafter. Note, that the discussion of the components not mentioned above exceeds the scope of this work and will be published somewhere else. Streamwise Reynolds stresses for the four different simulation cases are shown in Fig. 1 in the vicinity of the wall. In agreement with observations from plane channel flow [6, 8] the streamwise Reynolds stress peak at $(R - r)^+ = 15$ shifts towards larger values with increasing Reynolds numbers (Fig. 1a). Applying a scale decomposition on the streamwise scales reveals that the growth of the peak value is related to large-scale outer flow motions that penetrate the near-wall region. However, unlike its channel counterpart the peak value obtained from turbulent pipe flow can not be fitted with a logarithmic scaling law over the full range of Reynolds numbers. For $Re_\tau > 360$ the dependence of the $\langle u_z' u_z' \rangle^+$ peak on Re_τ is fitted by the logarithmic expression

$$\langle u_z' u_z' \rangle^+_{max} = 0.67 \log(Re_\tau) + 3.324, \quad Re_\tau > 360, \tag{7}$$

indicated by the dashed line in Fig. 1b, similar to the expression $\langle u'u' \rangle^+_{max} = 0.642 \log(Re_\tau) + 3.66$ Lee and Moser [8] derived for plane channel flow. For low Reynolds numbers, on the contrary, the linear scaling law

$$\langle u_z' u_z' \rangle^+_{max} = 1/940 Re_\tau + 6.96, \quad Re_\tau < 1000, \tag{8}$$

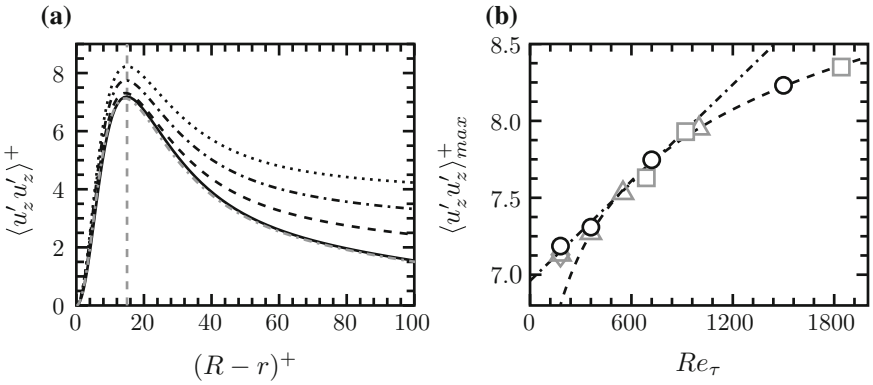

Fig. 1 **a** Streamwise Reynolds stresses $\langle u_z' u_z' \rangle$ for different Reynolds number simulations. Solid lines, $Re_\tau = 180$; dashed lines, $Re_\tau = 360$; dashdotted lines, $Re_\tau = 720$; dotted line, $Re_\tau = 1500$. Grey dashed-dotted line shows highly-resolved channel flow data [12]. Vertical grey dotted line indicates peak position at $(R-r)^+ = 15$. **b** Streamwise Reynolds stress peak values obtained from the current DNS (circles) compared to DNS data of Boersma [2] (box symbols), El Khoury et al. [4] (triangles) and Vreman and Kuerten [12] (diamond). The dashed line corresponds to the logarithmic expression in Eq. (7), the dashdotted line to the linear on in Eq. (8)

indicated by the dashdotted line in Fig. 1b, matches the peak values better. An explanation for the discrepancy between plane channel and pipe flow for low Reynolds numbers is the influence of the pipe curvature on the near-wall structures. For low Re_τ the structures are larger in outer flow units and "see" the curvature of the pipe, whereas for higher Reynolds numbers their size becomes much smaller than the pipe radius and the wall appears flat as in plane channel flow.

In terms of the streamwise skewness, the profiles for the different Reynolds numbers in the vicinity of the wall are shown in Fig. 2a. The dependence on the Reynolds number is clearly visible in the near-wall region and investigated at two prominent locations of the profiles, namely the maximum of the streamwise skewness very close to the wall ($(R-r)^+ \approx 0.5$) and the local minimum at a wall distance of approximately $(R-r)^+ \approx 33$. At both locations the skewness value shifts towards larger skewness values leading to a larger positively skewed streamwise velocity distribution at the wall and a less negatively skewed one at $(R-r)^+ \approx 33$ for higher Reynolds numbers. The Reynolds number dependence of the latter values are fitted by the logarithmic expressions

$$S(u_z)|_{(R-r)^+ \approx 0.5} = 0.082 \log(Re_\tau) + 0.548, \tag{9}$$

$$S(u_z)|_{(R-r)^+ \approx 33} = 0.156 \log(Re_\tau) - 1.343, \tag{10}$$

where the last logarithmic law is plotted in Fig. 2b together with the corresponding skewness values. With the aid of scale decomposition Mathis et al. [11] showed for experimental turbulent boundary layer data that a small-scale/large-scale correlation

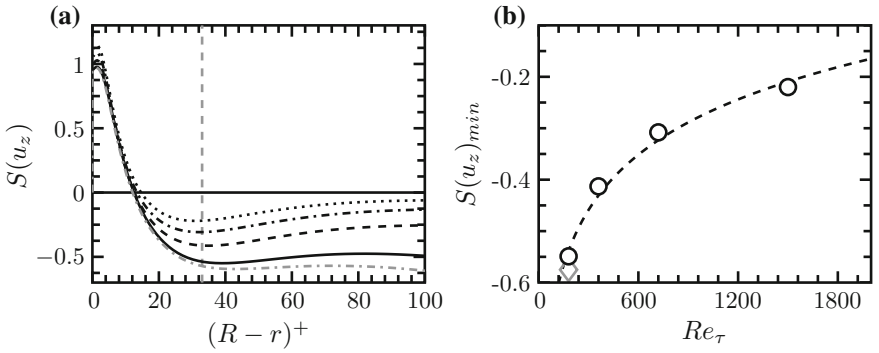

Fig. 2 **a** Streamwise skewness $S(u_z)$ for different Reynolds number simulations, lines as in Fig. 1. Vertical grey dotted line indicates local minimum at $(R-r)^+ = 33$. **b** Local minimum of streamwise skewness at $(R-r)^+ \approx 33$. The dashed line corresponds to the logarithmic expression in Eq. (10). Symbols as in Fig. 1

term, which is related to the amplitude modulation term[10], is responsible for the Reynolds number dependence of streamwise skewness. Reconstructing the streamwise skewness without this correlation term led to a collapse of the different Re_τ skewness profiles. Since the scales are not sufficiently separated in the Reynolds number regime of the current work, a reconstruction of the skewness, involving a decomposition based on the spanwise scales, leads to a collapse only in the very vicinity of the wall ($(R-r)^+ < 15$), where the scales are sufficiently separated.

The profiles of the wall-normal flatness component in the very vicinity of the wall, as they are shown in Fig. 3a, exhibit again a dependence on the Reynolds number. While the flatness values at $(R-r)^+ = 0.5$ for $Re_\tau \geq 360$ can be fitted by the logarithmic expression

$$4.18 \log(Re_\tau) + 8.30, \quad Re_\tau \geq 360, \tag{11}$$

indicated by the dashed line in Fig. 3b, the value for $Re_\tau = 180$ does not match the logarithmic law. Furthermore, the discrepancy between the kurtosis value at the wall obtained from turbulent pipe and plane channel flow is largest for the lowest Reynolds number. While the pipe flow at $Re_\tau = 180$ exhibits a wall-normal flatness value of $F(u_r) \approx 34$ at $(R-r)^+ = 0.5$ the corresponding channel flow simulation from Lenaers et al.[9], indicated by triangles in Fig. 3b, exhibits values of $F(v) \approx 25$ at the same distance from the wall. This discrepancy is related to the above mentioned difference in the Reynolds stress peak value between channel and pipe flow. Xu et al.[13] showed that the large kurtosis value at the wall is caused by velocity spikes, which are related to strong sweeps. The redistribution of streamwise wall-layer streaks by large-scale outer flow motion for high Reynolds number flow implicitly results in a redistribution of the wall-normal velocity spikes, since they are predominantly coinciding with high-speed streaks.

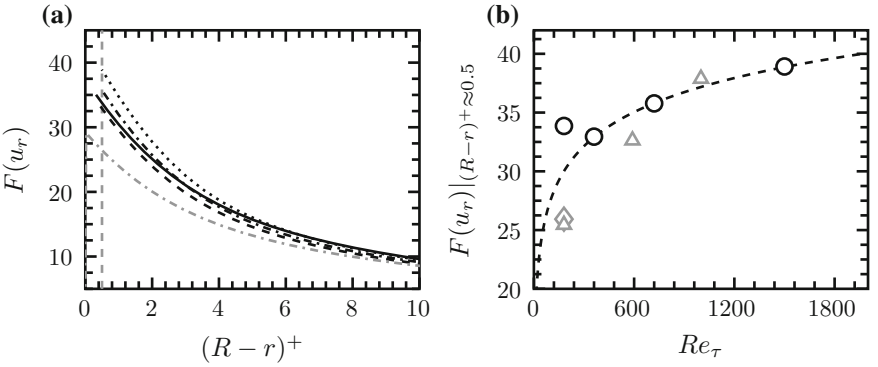

Fig. 3 **a** Wall-normal flatness $F(u_r)$ for different Reynolds number simulations, lines as in Fig. 1. Vertical grey dotted line indicates $(R-r)^+ = 0.5$. **b** Wall-normal flatness at $(R-r)^+ = 0.5$ (circles) compared to turbulent plane channel flow data from Lenaers et al.[9] (triangles, $Re_\tau = 180, 590, 1000$) and Vreman and Kuerten [12] (diamond, $Re_\tau = 180$). The dashed line corresponds to the logarithmic expression in Eq. (11)

3 Conclusion

The Reynolds number dependency of turbulent high-order statistics in turbulent pipe flow was investigated by means of DNS. Logarithmic dependencies on Re_τ were found for the streamwise Reynolds stress, where $Re_\tau \geq 360$, the streamwise skewness and the wall-normal flatness for $Re_\tau \geq 360$. The scaling failure of the latter quantities is related to large-scale outer flow motions that become important at high Reynolds number flow and penetrate into the near-wall region. For the lowest Reynolds number ($Re_\tau = 180$), a discrepancy between the wall-normal flatness at the wall in pipe flow and the one in channel flow was reported.

References

1. Bauer, C., Feldmann, D., Wagner, C.: Revisiting the higher-order statistical moments in turbulent pipe flow using direct numerical simulations. In: Notes on Numerical Fluid Mechanics and Multidisciplinary Design, vol. 136, pp. 75–84. Springer (2018)
2. Boersma, B.J.: Direct numerical simulation of turbulent pipe at high Reynolds numbers, velocity statistics and large scale motions. In: TSFP Digital Library Online. Begell House Inc (2013)
3. Chorin, A.J.: Numerical solution of the Navier-Stokes equations. Math. Comput. **22**, 745–762 (1968)
4. El Khoury, G.K., Schlatter, P., Noorani, A., Fischer, P.F., Brethouwer, G., Johansson, A.V.: Direct numerical simulation of turbulent pipe flow at moderately high Reynolds numbers. Flow Turbul. Combust. **91**(3), 475–495 (2013)
5. Feldmann, D., Wager, C.: Direct numerical simulation of fully developed turbulent and oscillatory pipe flows at Re$\tau = 1440$. J. Turbul. **13**(32), 1–28 (2012)

6. Hoyas, S., Jiménez, J.: Scaling of the velocity fluctuations in turbulent channels up to Reτ = 2003. Phys. Fluids **18**(1), 11702 (2006)
7. Kim, J., Moin, P.: Application of a fractional-step method to incompressible Navier-Stokes equations. J. Comput. Phys. **59**(2), 308–323 (1985)
8. Lee, M., Moser, R.D.: Direct numerical simulation of turbulent channel flow up to $Re_\tau \approx 5200$. J. Fluid Mech. **774**, 395–415 (2015)
9. Lenaers, P., Li, Q., Brethouwer, G., Schlatter, P., Örlü, R.: Rare backflow and extreme wall-normal velocity fluctuations in near-wall turbulence. Phys. Fluids **24**(3), 035110 (2012)
10. Mathis, R., Hutchins, N., Marusic, I.: Large-scale amplitude modulation of the small-scale structures in turbulent boundary layers. J. Fluid Mech. **628**, 311–337 (2009)
11. Mathis, R., Marusic, I., Hutchins, N., Sreenivasan, K.R.: The relationship between the velocity skewness and the amplitude modulation of the small scale by the large scale in turbulent boundary layers. Phys. Fluids **23**(12), 121702 (2011)
12. Vreman, A.W., Kuerten, J.G.M.: Comparison of direct numerical simulation databases of turbulent channel flow at Reτ = 180. Phys. Fluids **26**(1), 015102 (2014)
13. Xu, C., Zhang, Z., den Toonder, J.M.J., Nieuwstadt, F.T.M.: Origin of high kurtosis levels in the viscous sublayer. Direct numerical simulation and experiment. Phys. Fluids **8**(7), 1938–1944 (1996)

Turbulent-Drag Reduction by Oblique Wavy Wall Undulations

S. Ghebali, S. I. Chernyshenko and M. A. Leschziner

1 Introduction

Reducing the turbulent skin-friction drag over civilian aircraft is a potentially high-reward target, as this drag component accounts for about half of the total drag in cruise conditions. Thus, even modest reductions convert into material savings, resulting in significant cuts in costs. Active-control techniques can be remarkably effective at suppressing turbulence and drag, but pose major engineering challenges in terms of actuation, efficient operation, reliability and maintainability. In contrast, passive techniques based on riblets are easier to implement, but face important durability and maintenance limitations related to the extremely small spacing of the grooves. The alternative passive-control method that is the subject of the present paper was first proposed in [1]. The key characteristic of the method is that it involves wavy surface undulations directed obliquely to the mean flow and having wave lengths two orders of magnitude larger than riblets, and would thus be much more practical to manufacture and maintain.

In [1], it is suggested that the oblique-wave topography can be exploited to passively emulate an *active* spatial Stokes layer (SSL) – consisting of streamwise-varying, spanwise in-plane, wall motions of the form $W_w = A\,\sin(2\pi x/\lambda_x)$, as described in [4]. The geometry is configured so as to provoke a transverse shear layer whose properties are as close as possible to those of an equivalent SSL. The rationale is that such an emulation would result in a similar disruption of the near-wall

S. Ghebali (✉) · S. I. Chernyshenko · M. A. Leschziner
Imperial College London, South Kensington Campus, London SW7 2AZ, UK
e-mail: s.ghebali14@imperial.ac.uk

S. I. Chernyshenko
e-mail: s.chernyshenko@imperial.ac.uk

M. A. Leschziner
e-mail: mike.leschziner@imperial.ac.uk

M. V. Salvetti et al. (eds.), *Direct and Large-Eddy Simulation XI*,
ERCOFTAC Series 25, https://doi.org/10.1007/978-3-030-04915-7_72

turbulence, responsible for most of the turbulent skin-friction drag at high Reynolds numbers.

The present study consists of DNS of fully-developed turbulent channel flows with oblique solid wall undulations. The resulting changes in drag with respect to a flat wall are quantified for a range of flow angles and sinusoidal wave shapes.

2 Direct Numerical Simulations

The incompressible Navier–Stokes equations are discretised using a second-order finite-volume scheme, in conjunction with a fractional-step method, and are explicitly integrated in time by means of a third-order gear-like scheme. The pressure–Poisson equation is solved by successive over-relaxation with multigrid acceleration, and velocity–pressure coupling is ensured by use of the Rhie-and-Chow interpolation. A more detailed description of the method can be found in [2].

The present flow configuration, consisting of a skewed wavy wall, can be defined using the three parameters given in Fig. 1. The three-dimensional parameter space is explored by DNS of a fully-developed turbulent channel with both walls wavy. The vertical location of the solid undulations takes the form $y_w = \pm h + h_w$, where h is the channel half-height and $h_w(x, z)$ is the local height of the undulation relative to the mean wall location. The flow makes an angle θ with the wave, as illustrated in Fig. 1, so that an angle $\theta = 0$ corresponds to the crests being perpendicular to the main flow direction.

Owing to the homogeneity along the direction of the crests, time-averaged statistics are invariant by translation in that direction. The discretisation strategy utilises this property by aligning the non-orthogonal mesh planes at 90° to the crests so that it becomes numerically trivial to perform a statistical averaging along the crest direction. Consequently, the flow is driven at an angle to the mesh, as shown in Fig. 2, by adjusting two pressure gradients – implemented as body forces in the momentum

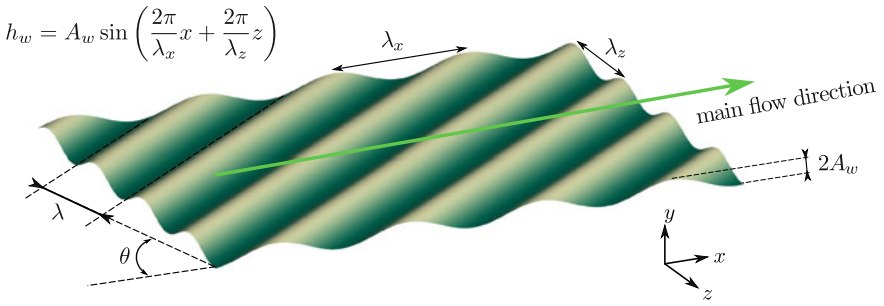

Fig. 1 Sketch of the wavy-channel configuration. A flow configuration is described by three parameters: the wave height A_w, wavelength λ, and angle of the main flow direction θ. The flow direction shown is at $\theta = 70°$, and the wave slope was augmented to show the wall undulations

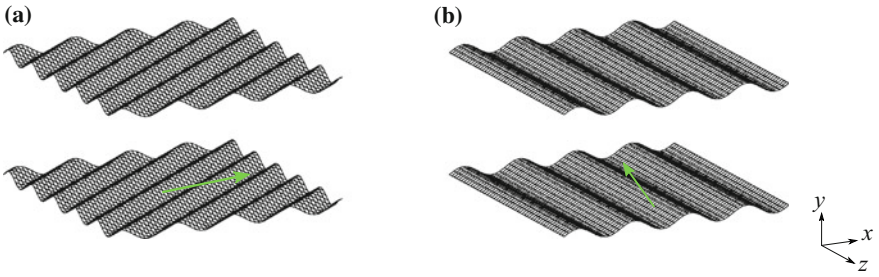

Fig. 2 Implementation of the flow skewness. **a** Physical domain, **b** numerical domain. The green/light-grey arrow indicates the flow direction

Table 1 Flow configurations studied at $Re_\tau \approx 360$, for wave heights ranging from $A_w^+ = 11$, up to 33. Wall units are calculated based on $h^+ = 360$, and the full computational domain comprises approximately 700 million cells

θ	λ^+	λ_x^+	A_w^+	$\Delta x \times \Delta y_{min}^+ - \Delta y_{max}^+ \times \Delta z^+$	L_x^+	L_z^+	Symbol
70°	918	2684	11, 18, 22, 32	$1.7 \times 0.6 - 4.4 \times 1.7$	1836	3672	◇
75°	695	2685	11, 22, 32	$1.9 \times 0.6 - 4.4 \times 1.6$	2084	3600	○
80°	468	2695	11, 22, 32	$1.7 \times 0.6 - 4.4 \times 1.9$	1872	4320	▼

equations – in order to approximately satisfy a unit bulk velocity in the direction of the flow. The bulk Reynolds number is then fixed by imposing the corresponding viscosity to give $Re_b = U_b h/\nu = 6200$, which yields a friction Reynolds number for the baseline case of $Re_\tau \approx 360$.

The flow configurations presented herein, a selection of many investigated, are listed in Table 1. The selected simulations span various angles, wave heights and wavelengths, but all feature a similar streamwise wavelength $\lambda_x^+ \approx 2700$. The reason for choosing to keep λ_x constant is to fix the characteristic length relevant to the spanwise forcing, so as to quantify the influence on the drag of the spanwise-projected wavelength.

Unlike in the case of a plane channel, where the drag is only frictional, the wavy channel gives rise to an additional contribution in the form of pressure drag. Thus, the total drag coefficient (D_t) is formed of a skin-friction contribution (D_f) plus a pressure-drag coefficient (D_p): $D_t = D_f + D_p$.

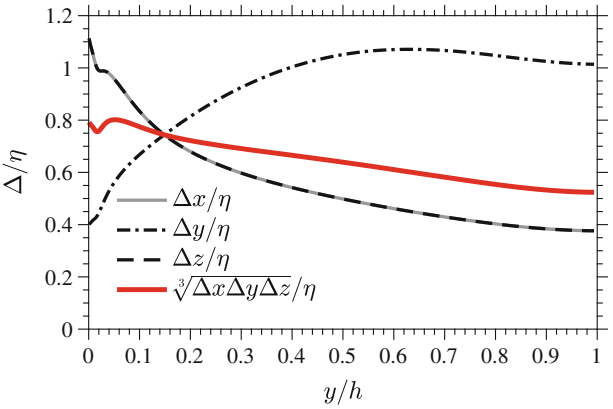

Fig. 3 Grid spacing relative to the Kolmogorov length scale for the baseline (plane-channel) simulation. The flow-to-mesh angle of the latter is $\theta = 70°$

3 Assessment of Accuracy

As will transpire below, the skin-friction is reduced so that D_f decreases with respect to the baseline value, but this reduction is counteracted by a substantial increase in pressure drag D_p so that the variation from the baseline level of the total drag D_t comes as a subtle trade-off between the latter two. Consequently, the accuracy requirements of such simulations are considerably increased relative to commonly-adopted DNS resolutions, as shown in Fig. 3 where the cell dimension is shown to be smaller than the Kolmogorov length scale.

In order to satisfy the stability constraints of the numerical scheme employed, the time-stepping interval is extremely low $\Delta t^+ < 0.02$, which requires a larger number of iterations to obtain statistical convergence. The standard deviation of the time-averaging error (equivalent to the sampling error) is estimated using the method of batch means and batch correlations [3] applied to the time history of the total drag, evaluated from the value of the driving pressure gradient at each time instant. Thus, both the baseline and the wavy-channel drag levels are affected by a different sampling uncertainty. The two are assumed to be independent, so that the standard deviation of the total-drag variation is calculated from that of each drag level as

$$\sigma_{\mathrm{DR}} = \frac{D_{t,\mathrm{wavy}}}{D_{t,\mathrm{plane}}} \sqrt{\left(\frac{\sigma_{D_t}}{D_t}\right)^2_{\mathrm{plane}} + \left(\frac{\sigma_{D_t}}{D_t}\right)^2_{\mathrm{wavy}}}. \tag{1}$$

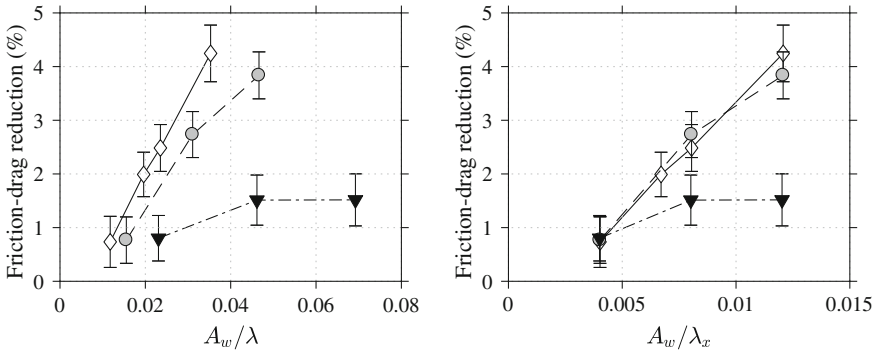

Fig. 4 Reduction in skin-friction drag relative to the baseline drag level versus wave slope (left) or projected slope (right). Symbols are defined in Table 1, error bars quantify the 95% confidence interval for the time-averaging error of the total-drag level

4 Results and Discussion

The relative variations of the contributions to the drag are presented in Figs. 4, 5 and 6. The error bars shown represent the time-averaging uncertainty of the total-drag reduction, which is a conservative choice for comparing differences in friction levels. However, the uncertainty associated with the spatial discretisation is not included in the error bars. Further investigation on the latter can be found in [2].

First, the influence of the wave height is considered. In view of the rationale behind the use of a skewed wavy wall for drag reduction – namely, the emulation of in-plane spanwise wall oscillations – a link between the level of skin-friction reduction and a measure of the intensity of the forcing generated by the spanwise pressure gradient arising from the wavy geometry may be expected. In Fig. 4, it is observed that the friction-reduction curves at $\theta = 70°$ and $\theta = 75°$ almost collapse when scaled with the streamwise wave slope A_w/λ_x, whereas the $\theta = 80°$ case displays a different behaviour. As all simulations feature the same streamwise wavelength λ_x, the present results suggest that the spanwise wavelength has a material effect on the skin-friction-reduction level.

Second, it is shown in Fig. 5 that the pressure drag increases quadratically with the wave slope. Also, for the same streamwise wave slope, larger values of θ exhibit less pressure drag.

Third, the net change in drag, arising from the opposite actions of the skin-friction reduction and the pressure drag, is quantified in Fig. 6. For small wave slopes, the friction reduction slightly surpasses the pressure-drag increase, leading to small amounts of drag reduction. The most effective configuration at reducing the total drag is that at $\theta = 75°$, yielding a net drag reduction of 1%. The slight improvement from the configuration at $\theta = 70°$ arises from a combination of a lower pressure-drag level, a benefit of the greater angle, and a small improvement of the friction reduction. Although the decrease in the pressure-drag penalty with increasing angle is clear, as

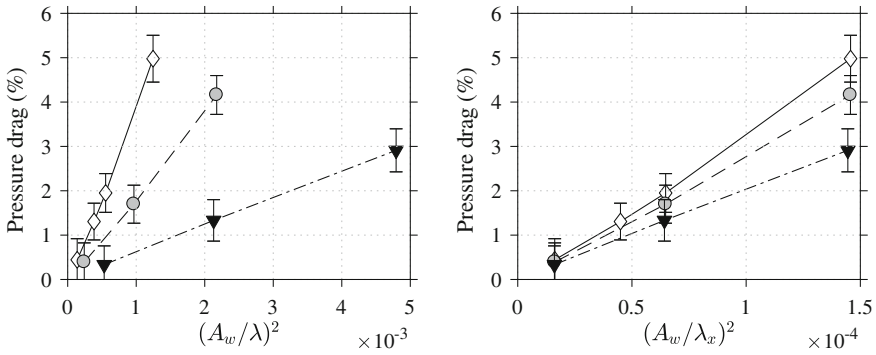

Fig. 5 Pressure-drag penalty relative to the baseline drag level. Same legend as Fig. 4

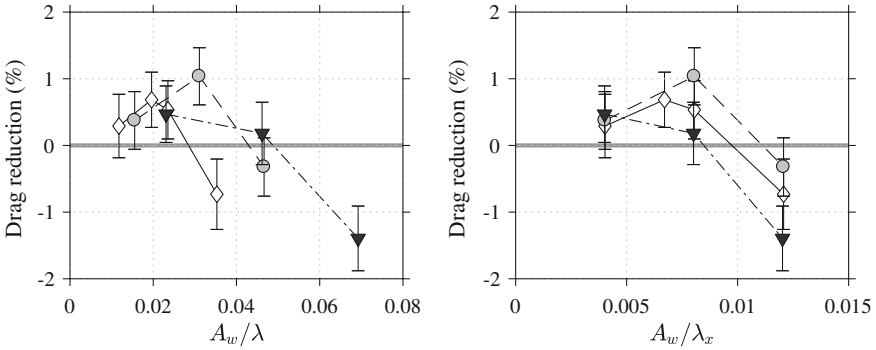

Fig. 6 Net drag reduction relative to the baseline drag level. Same legend as Fig. 4

evidenced in Fig. 5, the improvement of the friction reduction is relatively small and may be the consequence of other sources of error.

5 Conclusions

A parametric study of the drag experienced by skewed large-scale wavy walls at $Re_\tau \approx 360$ was undertaken for a streamwise wavelength of $\lambda_x^+ \approx 2700$, flow angles ranging from $\theta = 70°$ to $80°$, and wave heights up to $A_w^+ \approx 30$. All cases simulated present a reduction of the skin-friction drag. This reduction increases as the wave height is increased. However, the pressure-drag penalty rapidly overcomes the skin-friction reduction, thus leading to drag increase. Among the flow configurations tested, a maximum net-drag reduction of 1% is found at an angle of $\theta = 75°$, with a standard deviation of the time-averaging error of 0.2% of the baseline drag level.

Acknowledgements The project was funded by Innovate UK (Technology Strategy Board), as part of the ALFET project, project reference 113022. The authors are grateful to the UK Turbulence Consortium (UKTC) for providing computational resources on the national supercomputing facility ARCHER under the EPSRC grant EP/L000261/1. Access to Imperial College High Performance Computing Service, doi: 10.14469/hpc/2232 is also acknowledged.

References

1. Chernyshenko, S.: Drag reduction by a solid wavy wall emulating spanwise oscillations. Part 1. [physics.flu-dyn](arXiv:1304.4638) (2013)
2. Ghebali, S., Chernyshenko, S.I., Leschziner, M.A.: Can large-scale oblique undulations on a solid wall reduce the turbulent drag? Phys. Fluids **29**, 105102 (2017)
3. Russo, S., Luchini, P.: A fast algorithm for the estimation of statistical error in DNS (or experimental) time averages. J. Comput. Phys. **347**, 328–340 (2017)
4. Viotti, C., Quadrio, M., Luchini, P.: Streamwise oscillation of spanwise velocity at the wall of a channel for turbulent drag reduction. Phys. Fluids **21**, 115109 (2009)

Estimation of the Roughness Function in Turbulent Flows Using the Slope of the Roughness

M. De Marchis, B. Milici and E. Napoli

1 Introduction

In the last decades, important efforts have been made to better understand the effects of surface roughness on the mean flow. These studies have been performed investigating turbulent channel flows, turbulent boundary layers or pipe flows. The most evident effect of the roughness is the increase of the overall resistance, corresponding to a decrease of the mean streamwise velocity profile in the logarithmic region. This reduction is known as roughness function ΔU^+ (the symbol $^+$ represents quantities made non dimensional using the friction velocity u_τ, or the viscous length scale ν/u_τ). The best known law to predict the roughness function is perhaps the logarithmic law in function of the equivalent sand grain roughness height k_s, given by:

$$\Delta U^+ = \frac{1}{\kappa} ln(k_s^+) + B - C \tag{1}$$

Unfortunately, as pointed out by [1], k_s itself is not a physical length of the roughness and its value can be estimated only once the mean velocity profile is known. Several researches (see among others [2–4] and literature cited therein) analysed the roughness function in light of statistical moments of the roughness geometry, as the averaged absolute deviation k, the rms of wall oscillations k_{rms}, the skewness s_k or the kurtosis k_u have been investigated. Unfortunately, the above coefficients

M. De Marchis (✉) · B. Milici
Faculty of Engineering and Architecture, University of Enna "Kore", Enna, Italy
e-mail: mauro.demarchis@unikore.it

B. Milici
e-mail: barbara.milici@unikore.it

E. Napoli
Department of Civil, Environmental, Aerospace, Materials Engineering,
University of Palermo, Palermo, Italy
e-mail: enrico.napoli@unipa.it

M. V. Salvetti et al. (eds.), *Direct and Large-Eddy Simulation XI*,
ERCOFTAC Series 25, https://doi.org/10.1007/978-3-030-04915-7_73

are representative of a single feature of the roughness: the height, the asymmetry or the randomness. According to the analysis performed by [5], who introduced a geometrical parameter in function of the roughness slope, called *effective slope* (ES), other researchers [2, 3, 6, 7] carried out numerical as well as laboratory experiments over regular and irregular rough walls, confirming that the effective slope seems to be well correlated with the effects on the turbulence. The effective slope for rough surfaces is calculated according to the relation:

$$ES = \frac{1}{L_{x_1} L_{x_2}} \int_{L_{x_1}} \int_{L_{x_2}} \left| \frac{\partial k(x_1, x_2)}{\partial x_1} \right| dx_1 \tag{2}$$

where $k(x_1, x_2)$ is the roughness height, whereas x_1 and x_2 are the streamwise and spanwise direction, respectively, with L_{x_2} and L_{x_3} the corresponding extent of the domain. w In the present study, ES is correlated with the roughness function ΔU^+, so that it can be considered a geometric parameter able to predict the mean flow reduction. The current study is aimed at finding a law able to predict the roughness function produced by regular or irregular roughness, using LES techniques.

2 Numerical Simulations

The turbulent channel flow is resolved using the LES approach, based on the numerical solution of the filtered mass and momentum conservation. The momentum and continuity equations are resolved using the finite-volume numerical code PANORMUS, which is second-order accurate both in time and space (www.panormus3d.org).

In order to investigate both regular and irregular rough surfaces, turbulent channel flows with triangular and randomly variable walls have been investigated. Here, triangular shape has been chosen to tune the roughness slope. Specifically, the otherwise flat wall has been corrugated with triangular bars of sawtooth-like shape (Fig. 1). Two sets of simulations have been carried out. In the first one the roughness has been simulated using eight triangular bars (8T series), whereas in the second geometry 16 triangles were considered (16T series). Several triangle heights were investigated to vary the roughness slope and investigate a wide range of values for ES.

The computational domain is $4\pi\delta$ long (streamwise direction x_1), $\pi\ \delta$ wide (spanwise direction x_2) and 2δ high (wall-normal direction x_3). To ensure a high level of resolution, a relatively fine computational grid was used. In the streamwise and spanwise directions, due to the imposed periodic boundary conditions, an uniform resolution was applied ($\Delta x^+ \approx 20$). As customary, in the wall-normal direction a non-uniform mesh spacing was used. Specifically, the distance of the first grid point from the wall is below one wall unit, while the grid spacing increases toward the channel mid-plane up to 30 wall units. At the walls the no-slip condition was enforced.

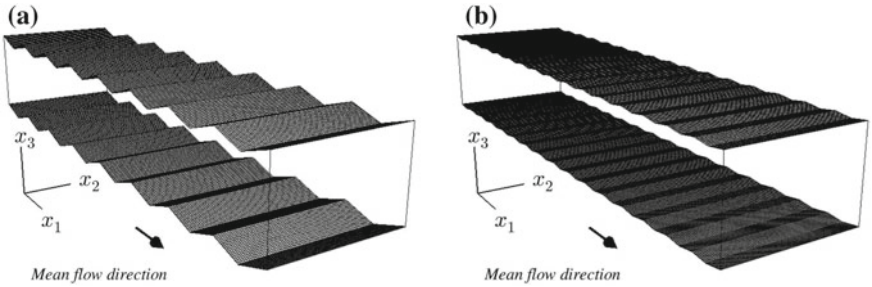

Fig. 1 **a**: 3D plot of the computational domain for the case $8T_3$. **b**: 3D plot of the computational domain for the case $16T_3$

Table 1 Details on the roughness type and the related geometric parameters. k_s^+: equivalent sand grain roughness. k^+: mean roughness height. k_{max}^+: highest roughness peak. k_{rms}^+: root mean squares of the wall roughness. $u_{3,rms}^+$ root mean squares of the wall-normal fluctuation at the mean wall plane. ES effective slope, as defined in [5]. 8T set: eight triangles, Fig. 1a. 16T set: sixteen triangles, Fig. 1b

Case	Roughness type	k_s^+	k^+	k_{max}^+	k_{rms}^+	$u_{3,rms}^+$	ES	ΔU^+
$8T_1$	2D triangle	13.00	9.87	19.75	11.45	0.180	0.064	1.64
$8T_2$	2D triangle	31.20	19.75	39.50	22.51	0.520	0.127	4.84
$8T_3$	2D triangle	102.00	31.60	63.20	36.34	0.760	0.204	8.39
$8T_4$	2D triangle	260.00	47.40	94.80	54.51	0.820	0.306	10.78
$16T_1$	2D triangle	12.25	5.92	11.85	6.71	0.100	0.076	1.60
$16T_2$	2D triangle	22.51	9.87	19.75	11.45	0.150	0.127	3.66
$16T_3$	2D triangle	49.37	15.80	31.60	18.17	0.380	0.204	6.46
$16T_4$	2D triangle	116.50	23.70	47.40	27.65	0.870	0.306	8.70

The simulations were carried out at $Re_\tau = 180, 395, 590$. The above resolutions, in light of the computational domain, give rise to the resulting number of grid cells equal to $128 \times 32 \times 64$ in the streamwise, spanwise and wall-normal direction, respectively for $Re_\tau = 180$. For $Re_\tau = 395$ the number of cell is $256 \times 64 \times 64$ in the streamwise, spanwise and wall-normal directions, respectively, and increased to $256 \times 128 \times 256$ for $Re_\tau = 590$. Figure 1 shows 3D representation of the computational domain of the regular rough channels, whereas for the irregular random roughness the reader can refer to [8].

In Table 1 details on the regular roughness type and on the geometric parameters, of the numerical simulations are reported.

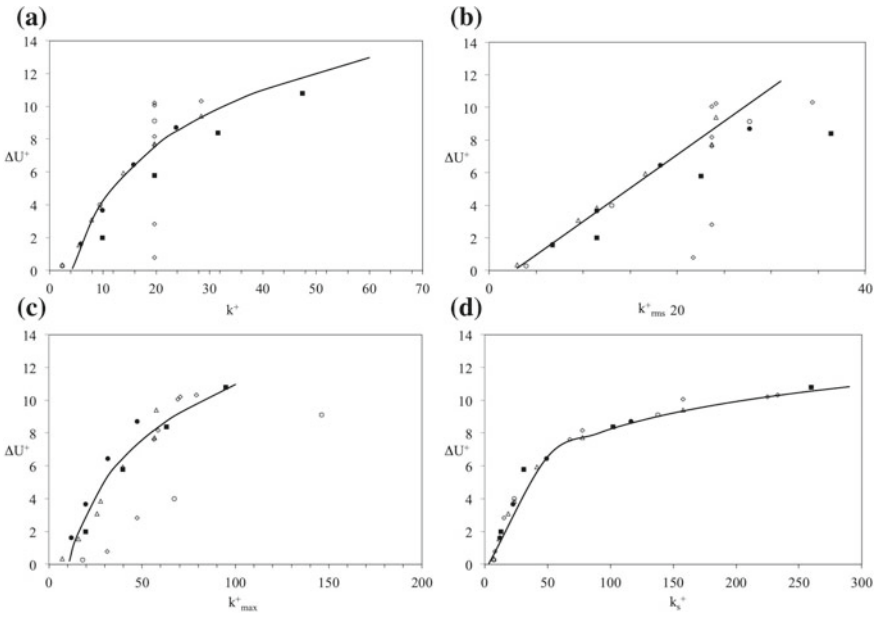

Fig. 2 Dependence of the roughness function ΔU^+ on geometrical parameters. **a** mean roughness height k^+; **b** r.m.s of the roughness height k^+_{rms}; **c** maximum roughness peak k^+_{max}; **d** equivalent sand grain roughness k^+_s Open symbols, irregular roughness; filled symbols, regular roughness. Bold line for visual aid only

3 Results

In the present analysis the attention is focused to find a correlation between a geometric parameter, representative of the roughness surface (regular or irregular), and the roughness function. Several studies have been carried out to achieve this aim, see among others the recent findings of [2] and literature therein cited, nevertheless the question is still open and worth of further investigations.

Figure 2 shows the dependence of the roughness function on geometrical parameters, specifically the mean roughness height k^+ in Fig. 2a. The picture clearly shows that the roughness Reynolds number, cannot be considered a key parameter fully representative of the roughness effect. In fact, regular or irregular roughness having the same k^+ give rise to very different ΔU^+.

Similar considerations can be made looking at the Fig. 2b, where the dependence of ΔU^+ on k^+_{rms} is plotted. In this case, a scatter of the data is visible both for regular and irregular rough walls. Specifically, even though some data seems to be aligned with the linear law, depicted as bold line in the graph, other geometries follow a different pattern, suggesting that also the k^+_{rms} is not a key parameter in the roughness function estimation.

Figure 2c shows the correlation between the roughness function and the maximum peak of the roughness height k^+_{max}. Most of the data seem to follow the same non-linear trend, represented by the bold line in the in the semi-log plot. Thus, the maximum roughness peak could be considered a more representative candidate to find the roughness function, once the roughness geometry is known. Nevertheless, 3D rough surfaces must have higher peaks than 2D roughness to achieve the same ΔU^+. This behavior can be attributed to the meandering shape of the turbulence structures among 3D hills, moreover in 3D roughness there are many positions with the same lower roughness height. The above analysis puts in light the difficult to find a geometric parameter able to be representative of regular as well as irregular rough surfaces. According to literature findings, a parameter able to predict the roughness function independently of the roughness texture, at least in the fully rough region, is the equivalent sand grain roughness.

In Fig. 2d the dependence of the roughness function on k^+_s is depicted. The values of k^+_s have been calculated equating, in the log-region, the mean streamwise velocity profile with the wall law for the mean velocity in a rough-wall turbulent boundary layer.

Even though, k_s is a key parameter to estimate the effect of energy loss induced by the roughness, its value can be obtained once the mean velocity profile is calculated, thus only once the roughness function is known. Recently, [1] observed that k_s is not a physical measure of the surface roughness rather a parameter able to measure the effect of the roughness. The equivalent sand grain roughness k_s can be correlated with roughness physical parameters (see among others [2]).

In Fig. 3 the roughness function versus ES is plotted. According to literature findings, the region has been divided in three regions: waviness region, achieved for $ES < 0.15$; transition region for $0.15 <$ES< 0.35 [3]; roughness regime for $ES > 0.35$ [6]. Following the log-law proposed by Hama (1954), (see Eq. 1), in Fig. 3 a logarithmic interpolating law is proposed to fit the data, given by the equation:

$$\Delta U^+ = \frac{1}{\kappa} ln(ES^2) - B - C \tag{3}$$

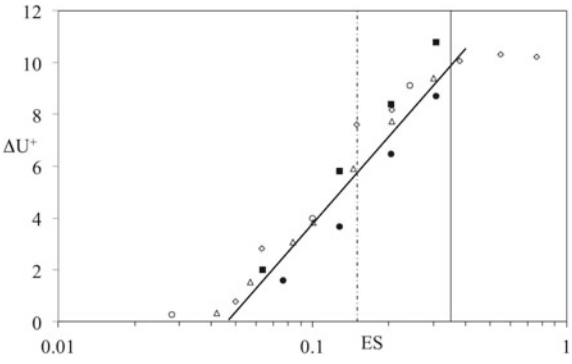

Fig. 3 Dependence of the roughness function ΔU^+ on the effective slope ES. Open symbols, irregular roughness; filled symbols, regular roughness. Bold line: interpolating log-law. Dot dashed line: ES = 0.15. Thin vertical line: ES = 0.35

where κ is the von K*á*rm*á*n constant, B and C are equal to 6.5 and 8.5, respectively. Comparing the trend of the data plotted in the Figs. 2 and 3 it can be argued that the effective slope is the more suitable candidate to estimate the roughness effect on the mean velocity profile.

4 Conclusions

On the basis of several LES, carried out over regular as well as irregular rough walls, here the dependence of the roughness function with geometric parameters, representative of the roughness topography, was investigated. The analysis has been carried out also taking into account a lot of data reported in literature. In this way, a wide range of roughness shapes and textures was covered. The downward shift of the velocity profile has been observed in light of k_s^+ the equivalent sand grain roughness, k^+ the mean roughness height, k_{max}^+, the highest roughness peak, k_{rms}^+ the root mean squares of the wall roughness, $u_{3,rms}^+$ the root mean squares of the wall-normal fluctuation at the mean wall plane and ES the effective slope. The analysis pointed out that the roughness function cannot be properly estimated with a single geometry feature of the roughness, as the mean roughness height or the maximum peak. Conversely, ΔU^+ can be estimated considering both the height and shape of the roughness. The parameter ES seems, in fact, to have a good correlation with roughness function. The trend of the correlation between ES and ΔU^+ suggests the existence of a logarithmic dependence between roughness slope and mean velocity reduction.

References

1. Flack, K.A., Schultz, M.P.: Roughness effects on wall-bounded turbulent flows. Phys. Fluids **26**(103105), 1–17 (2014)
2. Yuan, J., Piomelli, U.: Estimation and prediction of the roughness function on realistic surfaces. J. Turbul. **15**(6), 350–365 (2014)
3. Mejia-Alvarez, R., Christensen, K.T.: Wall-parallel stereo particle-image velocimetry measurements in the roughness sublayer of turbulent flow overlying highly irregular roughness. Phys. Fluids **25**, 115109 (2013)
4. Rao, V.N., Jefferson-Loveday, R., Tucker, P.G., Lardeau, S.: Large eddy simulations in turbines: influence of roughness and free-stream turbulence. Flow Turbul. Combust. **92**(1–2), 543–561 (2014)
5. Napoli, E., Armenio, V., De Marchis, M.: The effect of the slope of irregularly distributed roughness elements on turbulent wall-bounded flows. J. Fluid Mech. **613**, 385–394 (2008)
6. Schultz, M.P., Flack, K.A.: Turbulent boundary layers on a systematically varied rough wall. Phys. Fluids **21**(015104), 1–9 (2009)
7. De Marchis, M.: Large eddy simulations of roughened channel flows: estimation of the energy losses using the slope of the roughness. Comput. Fluids **140**, 148–157 (2016)

8. De Marchis, M., Milici, B., Napoli, E.: Numerical observations of turbulence structure modification in channel flow over 2D and 3D rough walls. Int. J. Heat Fluid Flow **56**, 108–123 (2015)

Part X
Complex Applications

Large-Eddy Simulation of Reactive Plume Dispersion Over Hypothetical Urban Areas

C. H. Liu, Z. Wu and Y. K. Ho

1 Introduction

Air pollution poses major threat to premature mortality [8] but its levels over 80% of cities are unhealthy [15]. Although large-scale computational fluid dynamics (CFD) models are the common research solutions to detailed air quality studies [12], analytical models offer quick screening tools that are surrogates for prohibitively expensive sensitivity tests in practice [9]. The Gaussian models, which are analytical tools developed based on open terrain and chemically inert pollutants, have been well received in the industry for decades [11]. Their results for chemically reactive pollutants over urban areas must be interpreted cautiously. In attempt to refine the functionality of Gaussian models, this study is conceived, using large-eddy simulation (LES), to examine the reactive plume dispersion over hypothetical urban areas.

2 Methodology

LES of the open-source CFD code Open-FOAM 4.1 [10] is used in this paper. The flows are assumed to be isothermal and incompressible. The subgrid-scale (SGS) properties are modeled by the Smagorinsky model [14] and the one-equation SGS turbulence kinetic energy (TKE) conservation [13]. Irreversible ozone (O_3) titration

C. H. Liu (✉) · Z. Wu · Y. K. Ho
Department of Mechanical Engineering, The University of Hong Kong, Hong Kong, China
e-mail: liuchunho@graduate.hku.hk

Z. Wu
e-mail: wzqmec@gmail.com

Y. K. Ho
e-mail: mea09ykh@connect.hku.hk

M. V. Salvetti et al. (eds.), *Direct and Large-Eddy Simulation XI*,
ERCOFTAC Series 25, https://doi.org/10.1007/978-3-030-04915-7_74

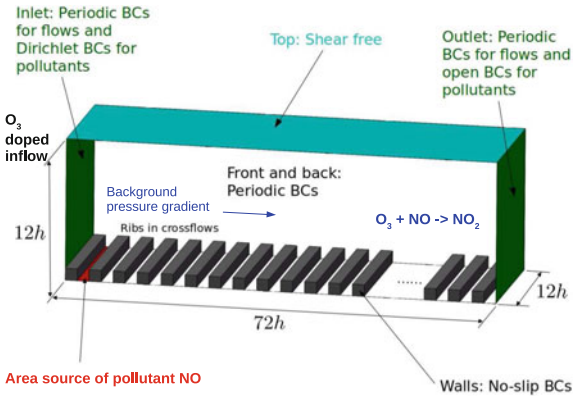

Fig. 1 Computational domain and BCs of the LES for flows and reactive plume dispersion over hypothetical urban areas

$$\mathrm{NO} + \mathrm{O_3} \longrightarrow \mathrm{NO_2} + \mathrm{O_2} \ , \tag{1}$$

where NO is nitric oxide, NO_2 nitrogen dioxide and O_2 oxygen molecule, is handled as a source term in the mass conservation equations in this paper.

Spatial domain, whose size is $72\,h$ (length) $\times$ $12\,h$ (width) $\times$ $12\,h$ (height), consists of 36 identical street canyons (of size h) of unity building-height-to-street-width (aspect) ratio (Fig. 1). The flows are driven by the background pressure gradient normal to the street axes. Periodic flows are assumed in the horizontal extent while periodic boundary conditions (BCs) of pollutants are only assumed in the spanwise (homogeneous) direction. The upstream inflows are doped with constant background O_3 concentration $[O_3]_0$. A ground-surface NO area source with constant concentration $[NO]_0$ is placed in the first street canyon. Open BCs of pollutants ($\partial \overline{c}_\phi/\partial t + \overline{u}\partial \overline{c}_\phi/\partial x = 0$) are prescribed at the outflow to remove all the pollutants from the spatial domain. Wall and shear-free, open-channel ($\partial \overline{u}/\partial z = \partial \overline{v}/\partial z = \overline{w} = 0$) BCs are applied on the solid boundaries and the domain top, respectively. Over 4.6×10^6 hexahedra are used to discretized the spatial domain.

Finite volume method (FVM) is adopted to solve the governing equations. Second-order-accurate backward differencing is used to integrate the momentum and mass conservation in time. The gradient, divergence and Laplacian terms are calculated by the second-order-accurate Gaussian FVM based on the summation on cell faces. The pressure-velocity coupling in incompressible flows is handled by the pressure-implicit with splitting of operators (PISO). The symmetric and asymmetric equation systems are solved by the pre-conditioned conjugate gradient (PCG) and the pre-conditioned bi-conjugate gradient (PBiCG) methods, respectively. The residual of the Krylov iterative solvers is less than 10^{-8} for converged solution.

3 Results and Discussion

In this paper, overbar $\overline{\psi}$ and angle brackets $\langle\psi\rangle$ represent the LES-resolved scales and the ensemble average in the homogeneous direction, respectively. Double prime is the deviation of the LES-resolved scale from its ensemble average $\psi'' = \overline{\psi} - \langle\overline{\psi}\rangle$.

3.1 Flow Structure

The ensemble averaged wind speed $\langle\overline{u}\rangle$ increases with increasing wall-normal distance z that converges to the prevailing wind speed u_∞ at the domain top (Fig. 2a). It agrees with our previous wind tunnel result [6] but overpredicts slightly compared with that available in literature [16]. The sharp near-wall velocity gradient signifies the locally elevated dimensionless streamwise $\langle u''u''\rangle^{1/2}/u_\tau$ (Fig. 2b) and vertical $\langle w''w''\rangle^{1/2}/u_\tau$ (Fig. 2c) fluctuating velocities. A good agreement between the current LES and the wind tunnel measurements [2, 6, 7], especially in the lower domain, is observed. Minor differences, such as the higher LES-calculated $\langle u''u''\rangle^{1/2}$ compared with that of direct numerical simulation (DNS) [3] and the lower LES-calculated $\langle w''w''\rangle^{1/2}$ compared with that of wind tunnel measurements [5], are found. The LES-calculated vertical momentum flux $\langle u''w''\rangle$ is linearly decreasing similar to that of theoretical open-channel flows (Fig. 2d). The discrepancies mentioned above are mainly attributed to the different (roughness) Reynolds number Re_τ (= $u_\tau h/\nu$; where u_τ is the friction velocity and ν the kinematic viscosity) which was 60 in [16], was over 600 in [6] and is 470 in this study. Nonetheless, the current LES output is reliable, facilitating the analyses of plume dispersion.

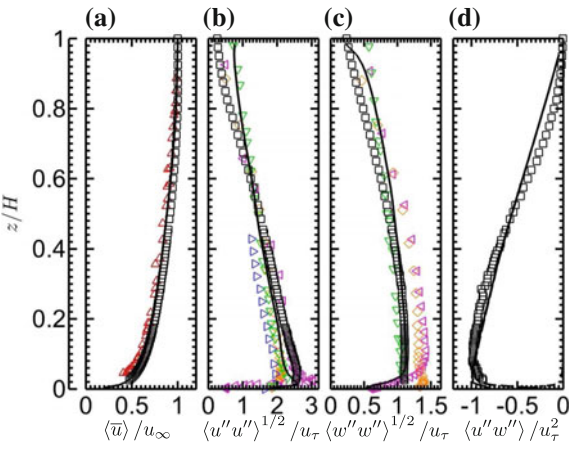

Fig. 2 Dimensionless flow properties **a** mean wind speed $\langle\overline{u}\rangle/u_\infty$, **b** streamwise fluctuating velocity $\langle u''u''\rangle^{1/2}/u_\tau$, **c** vertical fluctuating velocity $\langle w''w''\rangle^{1/2}/u_\tau$ and **d** vertical momentum flux $\langle u''w''\rangle/u_\tau^2$ expressed in dimensionless wall-normal direction z/H. Here H is the domain height. Also shown are the measurement results of [16]: Δ, [5]: $\lhd$, [7]: $\diamond$, [2]: ∇ and [6]: $\square$ together with the DNS results of [3]: $\triangleright$

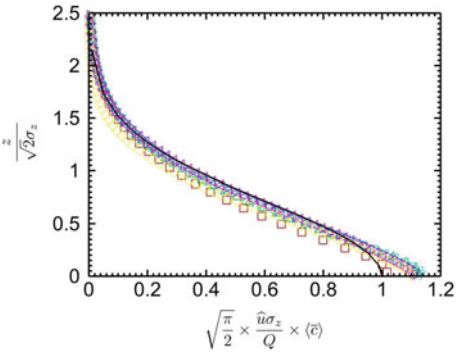

Fig. 3 Dimensionless tracer plume concentrations $(\pi/2)^{1/2} \times \widehat{u}\sigma_z/Q \times \langle\overline{c}\rangle$ in streamwise direction x/h = 15.5: □, 25.5: Δ, 35.5: ∇, 45.5: ▷, 55.5: ◁ and 65.5: ◇ expressed in dimensionless wall-normal distance $z/2^{1/2}\sigma_z$. Here Q is the tracer source strength. Also shown is the Gaussian model: solid line

3.2 Tracer Plume

The LES-calculated tracer plume concentrations $\langle\overline{c}\rangle$ agree well with those of theoretical Gaussian model (Fig. 3). In view of the rapidly changing near-wall mean wind speed $\langle\overline{u}\rangle$, the average mean wind speed across 95% of plume $\hat{u}$ is used instead in the calculation of vertical dispersion coefficient σ_z. The concentrations measured in another wind tunnel experiment [4] followed the theoretical Gaussian form only in $z \geq \sigma_z$. On the contrary, the current LES-calculated tracer concentrations exhibit the Gaussian form across the entire plume except in the vicinity to the roughness elements. The dissimilar tracer behavior could be caused by the sharp velocity gradient in the near-wall region that violates the assumption of uniform flows and eddy diffusivity in Gaussian models. Besides, the different geometric configurations (cubes in [4] and ribs in the current LES) could result in the dissimilarity mentioned above.

3.3 Reactive Plume

Unlike the tracer, rise of reactive plume trajectory is clearly observed (Fig. 4). O_3 titration is more significant in the near-wall region so the NO peaks are elevated. The LES-calculated plume rise z_r increases with increasing chemical reaction rate, i.e. background O_3 concentration $[O_3]_0$, varying from $z_r = 0.1 \times 2^{1/2}\sigma_z$ at $[O_3]_0 =$ 1 ppb to $z_r = 0.6 \times 2^{1/2}\sigma_z$ at $[O_3]_0 = 500$ ppb. Hence, the conventional Gaussian models have to be applied cautiously for urban setting because excluding the plume rise would over-estimate the ground-level concentrations of reactive pollutant (as large as 5 times in this paper), degrading the modeling accuracy substantially.

The dimensionless NO concentrations $(\pi/2)^{1/2} \times \widehat{u}\sigma_z/Q \times \langle\overline{c}_{NO}\rangle$ in the streamwise direction also clearly exhibit self-similarity after including chemical reaction. The source depletion Gaussian model [1] is adopted to handle the O_3 titration (Eq. 1),

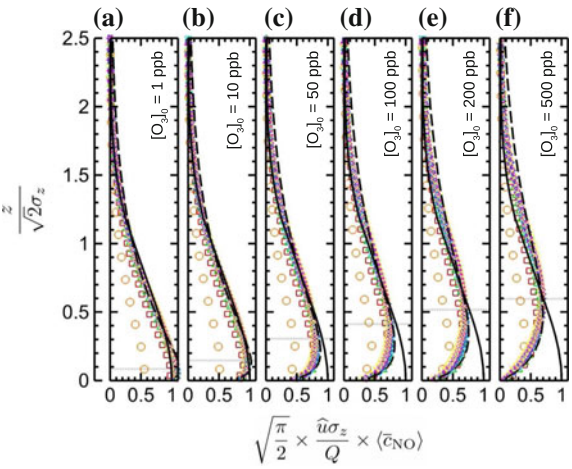

Fig. 4 Dimensionless reactive pollutant concentrations $(\pi/2)^{1/2} \times \widehat{u}\sigma_z/Q \times \langle \overline{c}_{\mathrm{NO}} \rangle$ in streamwise direction x/h = 15.5: □, 25.5: Δ, 35.5: ∇, 45.5: ▷, 55.5: ◁ and 65.5: ◇ expressed in dimensionless wall-normal distance $z/2^{1/2}\sigma_z$ for $[\mathrm{O_3}]_0$ = **a** 1 ppb; **b** 10 ppb; **c** 50 ppb; **d** 100 ppb; **e** 200 ppb and **f** 500 ppb. Also shown are the plume rise z_r: dotted lines, source depletion Gaussian model: sold lines and γ-distribution: dashed lines

which, however, does not work because of the fast chemistry in response to the slower near-wall wind speed right over the roughness elements. Generally, the source depletion Gaussian model is able to calculate the reactive pollutant concentrations over the plume rise. The discrepancy in the near-wall region widens with increasing chemical reaction rate because of the implicit limitation of source depletion Gaussian model. There is thus a need for an innovative formulation describing reactive pollutant dispersion over urban areas.

Additional effort is sought to test the regression of the γ-distribution

$$\sqrt{\frac{\pi}{2}} \times \frac{\hat{u}\sigma_z}{Q} \times \langle \overline{c}_{\mathrm{NO}} \rangle = \frac{\left(z/\sqrt{2}\sigma_z\right)^{\alpha-1}}{\beta^{\alpha}\,\Gamma\,(\alpha)} \times exp\left(-\frac{z/\sqrt{2}\sigma_z}{\beta}\right) \tag{2}$$

in term of the Gamma function $\Gamma\,(\alpha)$ to refine the reactive plume parameterization. Here, α and β are the parameters that are determined by the mean ($\mu = \alpha\beta$) and variance ($\sigma_z^2 = \alpha\beta^2$) of the source depletion Gaussian model. It is able to handle the pollution physics/chemistry coupling that predicts well the NO concentrations throughout the entire reactive plume (Fig. 4). In particular, the fast pollution chemistry in slow turbulent flows in the near-wall region agrees well with the current LES results, outperforming the source depletion Gaussian model. The improvement is more notable in higher background O_3 concentrations. The newly proposed γ-distribution is more accurate that the source depletion Gaussian model except for $[\mathrm{O_3}]_0 = 10$ ppb (Table 1). Nonetheless, its performance is remarkable.

Table 1 Root-mean-square (RMS) error comparing the source depletion Gaussian model and γ-distribution with the current LES results in different background ozone concentrations $[O_3]_0$

$[O_3]_0$ (ppb)	Source depletion Gaussian model	γ-distribution
1	0.00975	0.00176
10	0.000654	0.00217
50	0.00805	0.00267
100	0.0158	0.00297
200	0.0298	0.00361
500	0.0587	0.00432

4 Conclusions

A series of LES of flows and tracer/reactive plume dispersion over hypothetical urban areas is performed to improve the functionality of Gaussian models. The results suggest that reactive plume is no longer Gaussian. Instead, γ-distribution would be another candidate for dispersion coefficient. Future work will focus on strengthening the theoretical foundation and more comprehensive verification.

Acknowledgements The second and last authors thank the Hong Kong Research Grant Council (RGC) for financially supporting their study through the Hong Kong PhD Fellowship (HKPF) Scheme. This research is conducted in part using the research computing facilities and/or advisory services offered by Information Technology Services (ITS), The University of Hong Kong (HKU). Technical support from Ms. Lilian Y. L. Chan, Mr. W. K. Kwan and Mr. Bill H. T. Yau is appreciated. This project is partly supported by the General Research Fund (GRF) of RGC 17205314.

References

1. Arya, S.P.S.: Air Pollution Meteorology and Dispersion. Oxford University Press, Oxford (1998)
2. Burattini, P., Leonardi, S., Orlandi, P., Antonia, R.A.: Comparison between experiment and direct numerical simulations in a channel flow with roughness on one wall. J. Fluid Mech. **600**, 403–426 (2008)
3. Coceal, O., Thomas, T.G., Belcher, S.E.: Spatial variability of flow statistics within regular building arrays urban-like cubical obstacles. Bound. Layer Meteorol. **125**, 537–552 (2007)
4. Davidson, M.J., Snyder, W.H., Lawson Jr., R.E., Hunt, J.C.R.: Wind tunnel simulations of plume dispersion through groups of obstacles. Atmos. Environ. **30**, 3715–3731 (1996)
5. Djenidi, L., Elavarasan, R., Antonia, R.A.: The turbulent boundary layer over transverse square cavities. J. Fluid Mech. **395**, 271–294 (1999)
6. Ho, Y.K., Liu, C.-H.: A wind tunnel study of flows over idealised urban surfaces with roughness sublayer correction. Theor. Appl. Climatol. **130**, 305–320 (2017)
7. Krogstad, P.A., Antonia, R.A.: Surface roughness effects in turbulent boundary layers. Exp. Fluids **27**, 450–460 (1999)
8. Lelieveld, J., Evans, J.S., Fnais, M., Giannadaki, D., Pozzer, A.: The contribution of outdoor air pollution sources to premature mortality on a global scale. Nature **525**, 367–371 (2015)

9. Moonen, P., Allegrini, J.: Employing statistical model emulation as a surrogate for CFD. Environ. Model. Softw. **72**, 77–91 (2015)
10. OpenFOAM 4.1: The OpenFOAM Foundation (2017). https://openfoam.org (Cited 1 July 2017)
11. Roberts, O.F.T.: The theoretical scattering of smoke in a turbulent atmosphere. Proc. Roy. Soc. Lond. A **104**, 640–654 (1923)
12. Russell, A.: Regional photochemical air quality modeling: model formulations, history, and state of the science. Annu. Rev. Energy Environ. **22**, 537–588 (1997)
13. Schumann, U.: Subgrid scale model for finite difference simulations of turbulent flows in plane channels and annuli. J. Comput. Phys. **18**, 376–404 (1975)
14. Smagorinsky, J.: General circulation experiments with the primative equations I: the basic experiment. Mon. Weather Rev. **91**, 99–165 (1963)
15. WHO: WHOs urban ambient air pollution database - update 2016. In: World Health Organization (2016). www.who.int/phe (Cited 1 July 2017)
16. Wood, D.H., Antonia, R.A.: Measurements in a turbulent boundary layer over a d-type surface roughness. J. Appl. Mech. **42**, 591–597 (1975)

Large-Eddy Simulation of an Open Channel Flow with Submerged Rigid Vegetation

A. Monti, M. Omidyeganeh and A. Pinelli

1 Introduction

Flexible slender structures embedded in fluid flows are everywhere. Hairy surfaces are abundant in nature and perform multiple functions: e.g. thermal regulation, water harvesting, flow sensing, transport of species. While a great deal is known about the interplay between individual fibres and fluid flows, considerably less work has been done on flows interacting with ensembles of fibres, such as fur, hair, feathers or vegetation canopies. The particular case of vegetative canopies in river flows represents a paradigmatic example of the wide range of possible interactions between flows and ensembles of slender elements and how nature or human intervention can exploit this interplay to either mitigate disruptive events or to enhance the efficiency of a number of transport processes highlighting the importance of canopy-flow interactions on societal and environmental issues and the advantages that can be achieved by properly managing their reciprocal action. One of the first examples of research on vegetative canopy flows is the pioneering study of Ree and Palmer [10] where, for the first time, a methodology able to determine an estimate of the drag induced by the vegetation in an open channel (thus allowing to predict the actual discharge capacity) was put forward. Other relevant contributions on the characterisation of the effects of vegetative canopies in waterways were defined much more recently by Nepf and co-workers [7]. One of the more important contribution of these works concerns the introduction of a classification of canopy flows which is exclusively based on geometrical considerations. Specifically, the proposed categorisation is based on two geometrical

A. Monti (✉) · M. Omidyeganeh · A. Pinelli
University of London, London, UK
e-mail: alessandro.monti@city.ac.uk

M. Omidyeganeh
e-mail: omid.yeganeh@city.ac.uk

A. Pinelli
e-mail: alfredo.pinelli.1@city.ac.uk

M. V. Salvetti et al. (eds.), *Direct and Large-Eddy Simulation XI*,
ERCOFTAC Series 25, https://doi.org/10.1007/978-3-030-04915-7_75

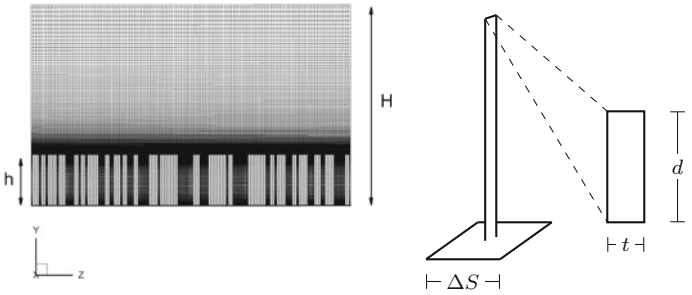

Fig. 1 Geometrical parameters governing a canopy flow according to Nepf [7]. In our simulation, the filaments are randomly distributed on the canopy bed, each one occupying an average area ΔS^2

ratios. The first one involves the flow depth H and the canopy height h (see Fig. 1). If $H/h = 1$, the flow is termed as emergent, otherwise if $1 < H/h < 5$ it is called shallow submerged or deeply submerged when $H/h > 10$. The second geometric parameter introduces a further classification for submerged canopy flows identifying two limiting behaviours, that are approached as the canopy density varies. If the ratio between the frontal area and the bed area, defined as $\lambda = ah$, where $a = d/\Delta s^2$ (see Fig. 1), is less than a threshold value (i.e., $\lambda \ll 0.1$) then the fluid velocity within and above the canopy shows a behaviour comparable to the one observed in a turbulent boundary-layer over a rough wall. This *sparse regime* is also characterized by the dominance of bed drag over the actual canopy drag. For large values of λ (i.e., $\lambda \gg 0.1$), the canopy drag is larger than the one offered by the bed. Under this condition, termed as *dense regime*, the drag distribution features a discontinuity at the top of the canopy that, in turns, determines the appearance of an inflection point in the velocity profile near the canopy edge. Within the given categorisation, the present contribution makes use of a large-eddy simulation (LES) to characterize the behaviour of the flow over a submerged, mildly dense ($\lambda > 0.1$) rigid canopy. In particular, the aim of the work is to explore and unravel the mechanisms of the interaction between the fluid flow and the dense rigid canopy by identifying the physical parameters that govern the mixing mechanisms within the different flow layers and by exploring the impact of the sweep/ejection events at the canopy edge.

2 Methodology

For the present study, the turbulent flow field has been simulated using an in-house developed incompressible Navier–Stokes solver (SUSA). The solver tackles the governing LES equations using a second order accurate, cell centred finite volume approach and a second order time accurate pressure correction scheme. Readers interested in the solver and on the extensive validation campaign can find detailed information in [8]. Further information on the ILSA model used for the subgrid

stress closure can be found in [11]. Differently from other approaches, we resolve the canopy directly introducing a set of rigid and solid filaments of finite cross-section which are placed perpendicularly to the horizontal wall. To impose the boundary conditions that each rigid filament exerts on the fluid (i.e., zero velocity) we have used a particular immersed boundary (IB) method that, as many other IB methods, deals with immersed bodies using a set of Lagrangian nodes that, in general, do not conform with the underlying Cartesian grid used to discretize the LES equations. Further information on the implementation of the IB method can be found in [3]. Concerning the computational domain, we have considered a box periodic in stream- (x) and spanwise (z) directions. The size of the box is $L_x = 4\pi h$, $L_y = 4h$ and $L_z = 2\pi h$ (a size similar to [1]). At the bottom wall, a no-slip boundary condition is imposed while a free-slip condition is set at the top surface. The bulk Reynolds number is set to $Re_b = U_b H/\nu = 6000$, close to the one used in the experiments [4]. The domain is discretized with a Cartesian grid system with a number of nodes (equispaced in stream- and spanwise directions) that yield a resolution in wall units ($\Delta l^+ = \Delta l u_*/\nu$, with $u_* = \sqrt{\tau_{\max}/\rho}$) of $\Delta x^+ \approx 12$, $\Delta y_h^+ \approx 0.3$ and $\Delta z^+ \approx 12$, in the stream-, wall-normal and spanwise directions respectively.

3 Results

To qualitatively compare our results, we have considered the work of Bailey and Stoll [2] that have numerically simulated a similar canopy flow configuration using LES and mimicking the presence of the filamentous layer with distributed volume forces. Despite the differences in the approach chosen to model the presence of the canopy, the agreement between the present results and the ones reported in the aforementioned work [2] is quite good. From the mean velocity profile given in Fig. 2 we can clearly identify at least two separate regions. The outermost one (from

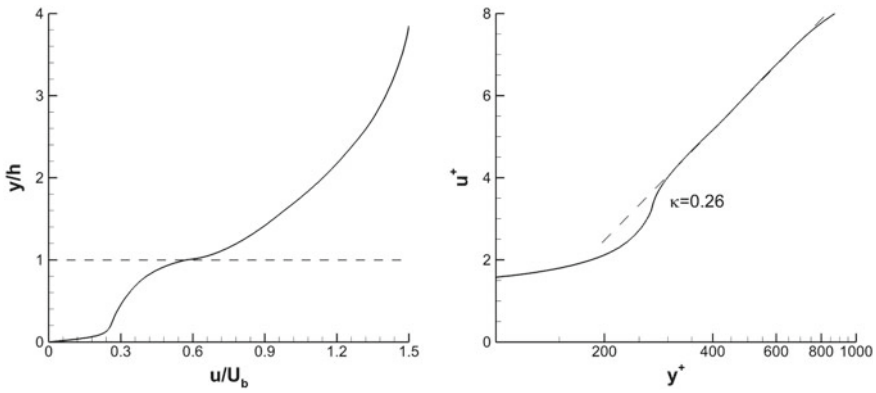

Fig. 2 Mean velocity profile normalized with U_b (left) and u_* (right)

$250^+ - 300^+$ above the canopy) is characterized by a mean velocity shape that reminds the one of turbulent boundary-layer featuring a logarithmic region with a slope that does not match the canonical one (see Fig. 2). Closer to the canopy edge, the mean velocity profile exhibits an inflection point typical of the transitional/dense canopies regimes (note that following the classification in [7], our $\lambda = 0.35$). To better characterize the actual regime, we next focus on the distribution of the off-diagonal Reynolds stresses. According to Nepf [7], when the $\langle u'v' \rangle$ distribution reaches an almost zero value within the canopy, the portion of the layer underneath is shielded and cannot interfere with the outer flow. When this location approaches the bottom wall, the canopy flow regime moves towards a sparse configuration. Figure 3, on the left, shows that indeed our chosen configuration corresponds to a transitional regime (i.e., neither dense nor sparse). The distribution of the total shear stress (given in the same figure) reveals that the viscous contribution plays a role only in the region close to the canopy bed, therefore, the outer layer of the canopy behaves as a virtual porous wall for the external flow. Concerning the Reynolds diagonal stresses (Fig. 3, right), the ones in the streamwise direction shows the presence of a second peak in the outermost region reminiscent of the one produced by large scales motions in turbulent boundary layers (TBL) [5]. A suggestive hypothesis explaining the similarity between these two flows could be based on the common presence of two separated (in the wavenumber/distance from the wall space) but co-existing turbulent flows: in the TBL, the close-to-the wall structures and the outer very large scales; in the present canopy flow, an outer boundary layer conditioned by the presence of large coherent structures present on the edge of the filamentous layer. The presence of the large scale structures by the layer tip is clearly visible from the isosurfaces of the streamwise velocity fluctuations, shown in Fig. 4, revealing two large scale streaks that span the whole extension of the domain. The distance between the two streaks (a high and a low speed one) and their dimension is of $\sim 2 - 3\,\mathrm{h}$. The same figure shows that these streaks are tilted in the streamwise direction in a fashion that recalls the upwash and downwash effects on velocity streaks over porous walls due to the passage of large Kelvin–Helmholtz rollers induced by the inflection point instability [6]. The presence of the Kelvin–Helmholtz vortices can be better detected by looking at the instantaneous velocity fluctuations contours (obtained by averaging in the spanwise direction, i.e. $\langle u' \rangle_z$) given in Fig. 4 in the right panel. The two-point correlations shown in Fig. 5 on the left confirm that the structures in the outer flow are very elongated and tilted in the $x - y$ plane. The effect of those structures is felt also within the canopy as typical of a transitional regime (see Fig. 5, bottom-left). On the right panel of the same figure the correlations in wall-normal and spanwise directions show that the structures have a large size that spans almost half-size of the domain length L_z. These results also show that we are in a *minimal box unit* condition and that larger domains must be considered in the future. To investigate the possible similarity of the outer flow with a TBL in Fig. 6 we provide the joint probability density function of u' and v' (see Ong and Wallace [9] for the same analysis in a TBL). Contrarily to what happens in a TBL, in a canopy flow the region by the tip exhibits a prevalence of ejection events with less frequent energetic sweeps. This trend reverts moving away into the core flow away from the filamentous layer.

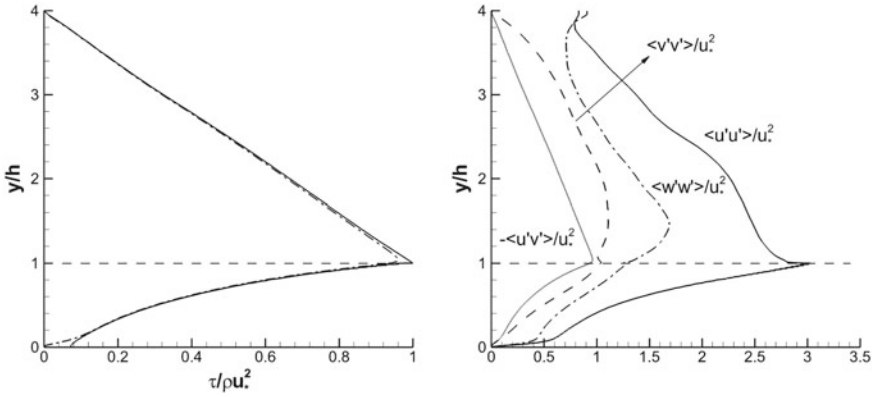

Fig. 3 Left: total (solid) and Reynolds (dash-dotted) shear stresses. Right: Reynolds normal and shear stresses

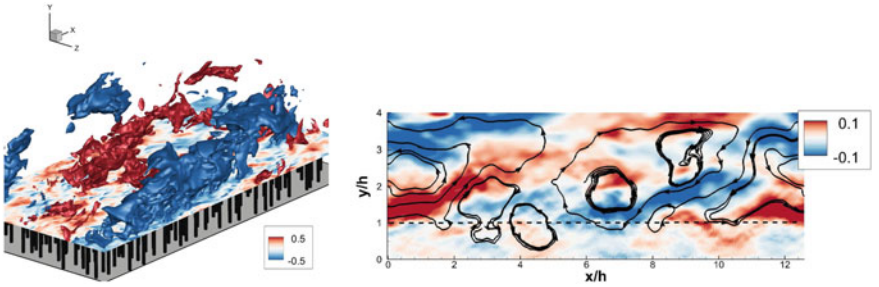

Fig. 4 Streamwise velocity fluctuations u'/U_b isosurfaces (left) and contours averaged in z direction $\langle u' \rangle_z / U_b$ (right). The streamlines represent the averaged in z velocity fluctuations components

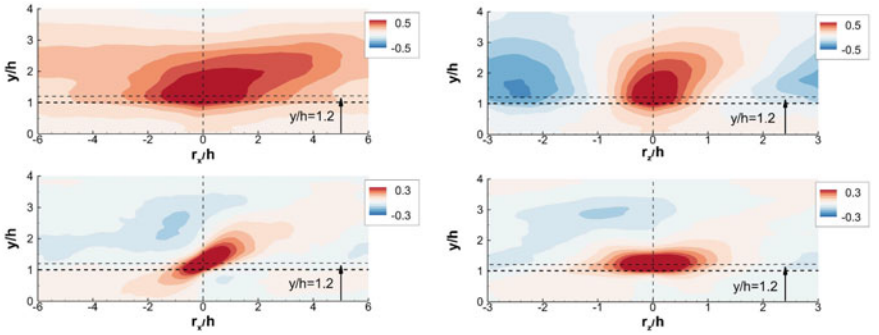

Fig. 5 Two-points correlation of the streamwise (top) and spanwise (bottom) velocity fluctuations in streamwise and wall-normal directions, $R_{u'u'}(r_x, \widehat{y} + r_y)$ and $R_{w'w'}(r_x, \widehat{y} + r_y)$ (left) and in spanwise and wall-normal directions, $R_{u'u'}(r_z, \widehat{y} + r_y)$ and $R_{w'w'}(r_z, \widehat{y} + r_y)$ (right)

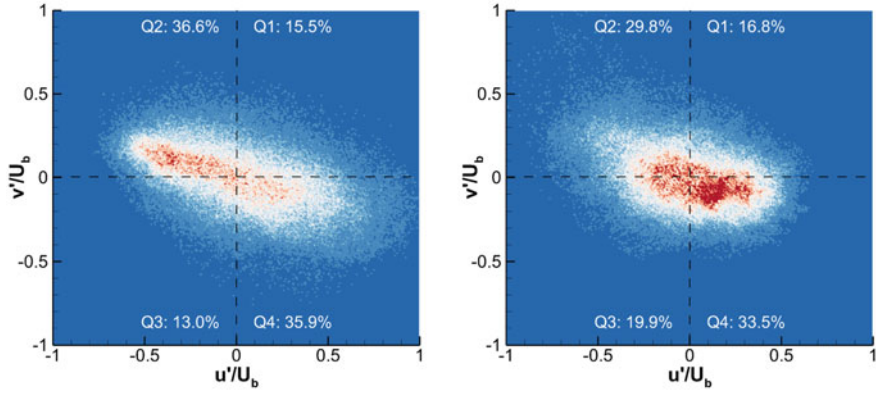

Fig. 6 Joint probability density function of the streamwise and wall-normal velocity fluctuations at $y/h = 1.2$ (left) and $y/h = 2.6$ (right)

4 Conclusion

To the authors knowledge, the present work is the first attempt to produce a high fidelity simulation of a canopy flow in transitional regime. Many interesting features have been found as summarized in the results section. However, further analysis is required to prove that the flow structure that has been described is not largely affected by the size of the computational box that marginally fits the largest scales of motion.

References

1. Bailey, B.N., Stoll, R.: Turbulence in sparse, organized vegetative canopies: a large-eddy simulation study. Bound Layer Meteorol. **147**(3), 369–400 (2013)
2. Bailey, B.N., Stoll, R.: The creation and evolution of coherent structures in plant canopy flows and their role in turbulent transport. J. Fluid Mech. **789**, 425–460 (2016)
3. Favier, J., Revell, A., Pinelli, A.: A Lattice Boltzmann-Immersed Boundary method to simulate the fluid interaction with moving and slender flexible objects. J. Comput. Phys. **261**, 145–161 (2014)
4. Ghisalberti, M., Nepf, H.M.: The limited growth of vegetated shear layers. Water Resour. Res. **40**(7) (2004)
5. Hutchins, N., Marusic, I.: Evidence of very long meandering features in the logarithmic region of turbulent boundary layers. J. Fluid Mech. **579**, 1–28 (2007)
6. Jiménez, J., Uhlmann, M., Pinelli, A., Kawahara, G.: Turbulent shear flow over active and passive porous surfaces. J. Fluid Mech. **442**, 89–117 (2001)
7. Nepf, H.M.: Flow and transport in regions with aquatic vegetation. Annu. Rev. Fluid Mech. **44**, 123–142 (2012)
8. Omidyeganeh, M., Piomelli, U.: Large-eddy simulation of three-dimensional dunes in a steady, unidirectional flow II. Flow structures. J. Fluid Mech. **734**, 509–534 (2013)
9. Ong, L., Wallace, J.M.: Joint probability density analysis of the structure and dynamics of the vorticity field of a turbulent boundary layer. J. Fluid Mech. **367**, 291–328 (1998)

10. Ree, W.O., Palmer, V.J.: Flow of water in channels protected by vegetative linings (No. 967). United States Department of Agriculture (1949)
11. Rouhi, A., Piomelli, U., Geurts, B.J.: Dynamic subfilter-scale stress model for large-eddy simulations. Phys. Rev. Fluids. **1**(4), 044401 (2016)

Detached Eddy Simulations of the Flow Around the Japan Bulk Carrier (JBC)

E. Guilmineau, G. B. Deng, P. Queutey, M. Visonneau and J. Wackers

1 Introduction

The accurate prediction of the velocity field in the wake of a ship is a challenge of crucial importance since it affects the optimal design of the propeller rotating in a non-uniform velocity field. This non-uniformity causes temporal variations of the propeller thrust and torque and, consequently, possible vibrations and fatigue of the propulsive system.

Numerical simulation of the wake of a three-dimensional body has been a subject of study for a long time. Most of the computations at high Reynolds number are based on the URANS (unsteady Reynolds averaged Navier-Stokes) formulation which can provide a reasonably good unsteady solution when the unsteadiness is controlled by large scales and related to unsteady boundary conditions. However, this approach is unable to capture the intrinsic flow unsteadiness of the flow field, which might be necessary to predict to evaluate, for instance, the right level of the turbulent kinetic energy when local flow detachment influences the mean flow field. When such a situation occurs at the stern of a ship, the use of Large Eddy Simulation appears necessary. But a pure LES computation is hardly possible at this Reynolds number even at model scale because of the high computational resources needed, see Nishikawa [6] who uses a mesh with 38×10^9 cells to simulate the flow around the JBC for the Tokyo 2015 workshop. In such a case, hybrid RANS-LES approaches seem to be the only pragmatic alternative to try while keeping at a reasonable level the resource consumption. The objective of this paper will be to compare an explicit anisotropic statistical turbulence closure (EARSM) and a Detached Eddy Simulation (DES) with local flow experiments performed by NMRI [3] in order to assess their

E. Guilmineau (✉) · G. B. Deng · P. Queutey · M. Visonneau · J. Wackers
LHEEA, CNRS UMR 6598, Ecole Centrale de Nantes, BP 92101,
Nantes Cedex 3, 44321 Nantes, France
e-mail: emmanuel.guilmineau@ec-nantes.fr

M. V. Salvetti et al. (eds.), *Direct and Large-Eddy Simulation XI*,
ERCOFTAC Series 25, https://doi.org/10.1007/978-3-030-04915-7_76

Fig. 1 Side view of the Japan Bulk Carrier

respective merits in the simulation of the flow field characteristics in the core of the averaged bilge vortices generated at the stern of the ship and interacting with the rotating propeller (Fig. 1).

2 Test Case

The Japan Bulk Carrier (JBC) [4] is a Capesize bulk carrier. Its length between perpendiculars at full scale is $L_{PP} = 280\,\text{m}$ and its service speed is 14.5 knots, leading to a Froude number $Fn = 0.142$. The depth is 25 m and the draft is 16.5 m. This geometry is investigated at model scale. The scale factor is 40, and then its length is $L_{PP} = 7\,\text{m}$ and the model scale Reynolds number is $Re = 7.46 \times 10^6$, based on the length L_{PP} and the hull velocity $U = 1.179\,\text{m/s}$.

3 Flow Solver

ISIS-CFD, developed by Centrale Nantes and CNRS and available as a part of the FINE/Marine computing suite, is an incompressible unsteady Reynolds-averaged Navier-Stokes (URANS) method. The solver is based on the finite volume method. The unstructured discretization is face-based, which means that cells with an arbitrary number of arbitrarily shaped faces are accepted. The method features many sophisticated RANSE turbulence models: apart from the classical two-equation k-ε and k-ω models, the anisotropic two-equation Explicit Algebraic Reynolds Stress Model (EARSM) is available [1] and will be used here since it is known to perform better for longitudinal vortices because of the turbulence anisotropy. Recently, several variants of Detached Eddy Simulation (DES) closures have been implemented [2]. All these turbulence models are based on the $k - \omega$ model of Menter.

4 Numerical Simulation Set-Up

The computational domain starts $2L_{PP}$ in front of the model and extends up to $5\,L_{PP}$ behind the hull. The width is $4\,L_{PP}$ and the height is $2.06\,L_{PP}$. In this study for the sake of simplicity, the free-surface effects are not taken into account and thus the free-surface is replaced by a symmetry plane leading to a so-called double-body configuration. This mesh is generated by Hexpress™, after which a single step of

the ISIS-CFD adaptive grid refinement is used to make all cells twice smaller. The final mesh contains 90.6 million cells For the URANS simulations, the time step is $\Delta t = 5 \times 10^{-2}$ s and the averaging time, t $\times U/L_{PP}$, is 15.3. For the DES, two time steps are used. The first is $\Delta t1 = 5 \times 10^{-3}$ s and the non-dimensional averaging time, $t \times U/Lpp$ is 24.2 while the second time step is $\Delta t2 = 5 \times 10^{-4}$ s and the non-dimensional averaging time is 11.

5 Results

Figure 2 presents the vortex structures by using a dimensionless iso-surface of the second invariant of the averaged flow field, Q, obtained with the DES model. This figure shows the vortical structures for the mean flow at the stern of the ship and in the wake. A massive vortex is observed in the wake of the hull. A similar topology is obtained with the EARSM turbulence model.

Figure 3 presents the axial velocity component normalized by the ship model velocity at the cross section S4, located at $X/L_{PP} = 0.9843$. The main difference between all simulations and experiments is the prediction of the bilge vortex. The results obtained with the DES model and the large time step, $\Delta t1$, are not in agreement with the measurements as the flow is not sufficiently accelerated and the area of low velocity is much larger than the one measured experimentally. With the DES model and the smaller time step, $\Delta t2$, the level of low velocity is in satisfactory agreement with the experiments but the low velocity area is too large compared to the one measured experimentally. With the EARSM model, the area size of low velocity region corresponds with experiments although the minimum velocity is too low in the numerical simulations.

A local vortex core analysis is then performed only on the main averaged vortex. The main vortex center is defined as the local maximum value of the longitudinal vorticity Ω_X in order to remain consistent with the experimental choice. The transversal evolutions along horizontal and vertical lines across the vortex center are computed for the cross-section S4. The coordinates of the mean vortex center in this plane are called Y_{V1} and Z_{V1}.

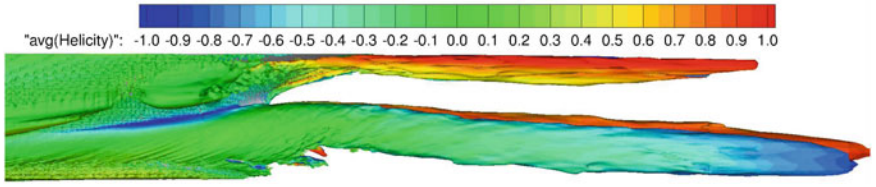

Fig. 2 Side view of the vortical structures visualized by iso-surface of dimensionless second invariant ($Q = 25$)

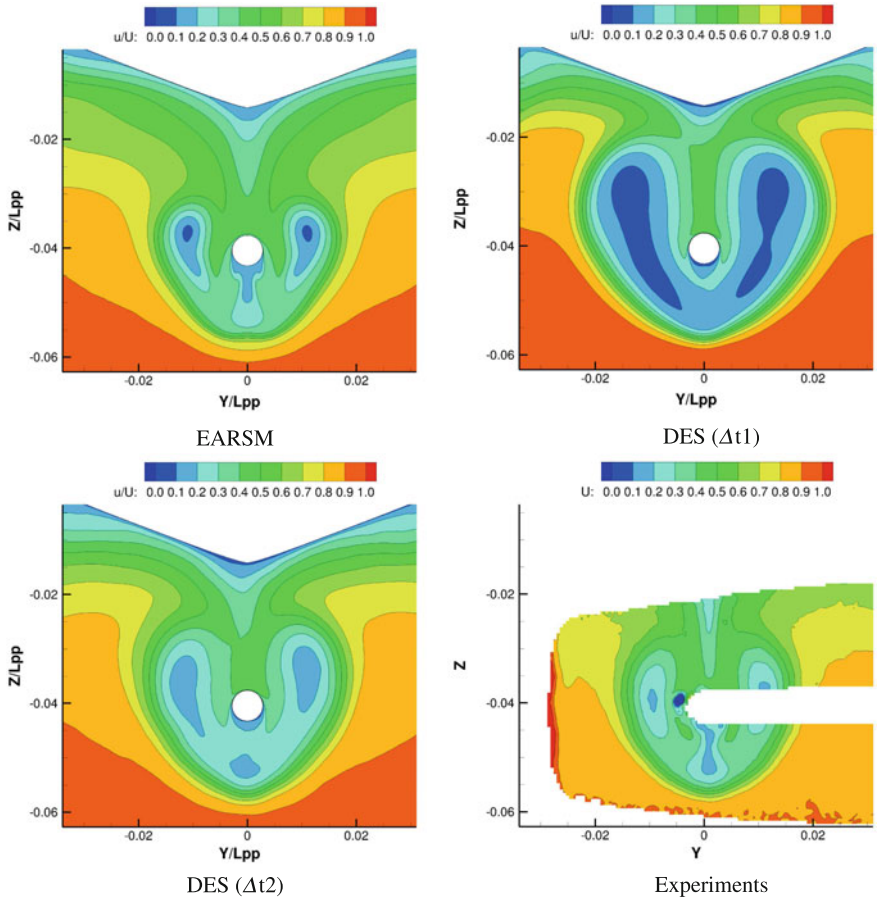

Fig. 3 Non-dimensional axial velocity component, u/U, at the cross section S4

Figures 4 and 5 show the comparison of the longitudinal component of the velocity, U, and the turbulent kinetic energy, TKE, respectively, between the numerical results and the experimental data. A satisfactory agreement is observed for the mean streamwise velocity component, except for the DES computations performed with a larger time step Δt1. For TKE, a large difference between the experimental data and the RANS results obtained is noticed. During the Tokyo 2015 workshop [7], this trend was observed by all the participants using RANS turbulence models.

With the DES formulation, the level of TKE is in very good agreement with measurements, being three to five times higher than what is simulated by the anisotropic RANS turbulence model. Moreover, the high values of TKE obtained with the DES closure are independently confirmed by the results obtained by Kornev's team [5] using a RANS-LES turbulence model, which reinforces the role played by the turbulence models in the simulation of the right level of TKE in the core of the main

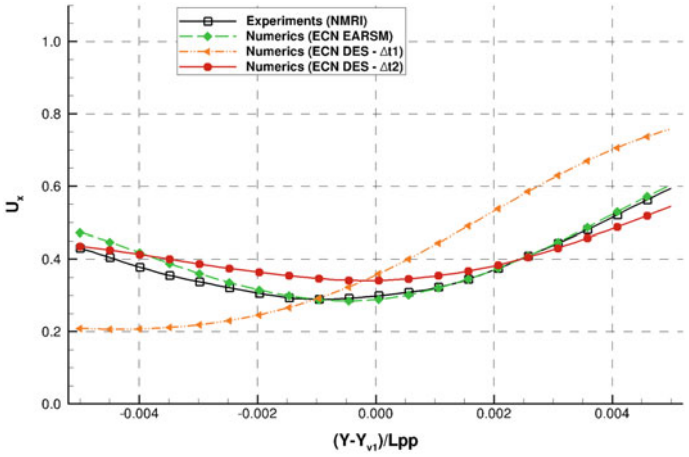

Fig. 4 Horizontal evolution of the streamwise velocity component around the vortex center

vortex. However, it is important to recall that, from a RANS point of view, the co-existence of high levels of TKE and large levels of longitudinal vorticity in the core of a vortex is somewhat contradictory, since high levels of TKE mean even higher levels of turbulence viscosity which contribute to the dissipation of the vortex and consequently reduce its vorticity. A relaminarisation of the flow in the core of vortex would be rather expected as it is observed in the core of tip vortices, for instance. But, such an analysis is valid only if one is in presence of a unique isolated vortex. Here, the unsteady DES computations reveal that there is not an instantaneous isolated bilge vortex in the wake of the JBC, which means that the existence of a well defined isolated bilge vortex is actually a kind of intellectual reconstruction which does not reflect the physical reality.

Actually, what is revealed by the unsteady DES computations is that the averaged bilge vortex results from a superposition of intense and strongly unsteady smaller but coherent vortical structures. Figure 6 provides two instantaneous views of the longitudinal vorticity, obtained by DES with Δt2, at section S4 separated by 120 time steps, i.e. 0.05 s. The cross in the figure shows the position of the core. These figures explain the co-existence of large levels of averaged TKE and longitudinal vorticity: the unsteady meandering of the smaller scale vortical structures contributes to a high level of TKE due to relatively low frequency fluctuations. An instantaneous view of the iso-surface of the second invariant Q, not presented in this paper, shows a succession of ring vortices which are created after the onset of an open separation linked with the initial thickening of the boundary layer illustrated by the convergence of the averaged friction lines. The design of JBC with a large value of the block coefficient $C_B = 0.858$ explains such a large-scale unsteadiness of the flow which is not found for ships with lower block coefficients. The rapid longitudinal reduction of the hull sections at the stern creates the condition of open separation followed by a flow reversal and a strong unsteadiness revealed by the shedding of ring vortices.

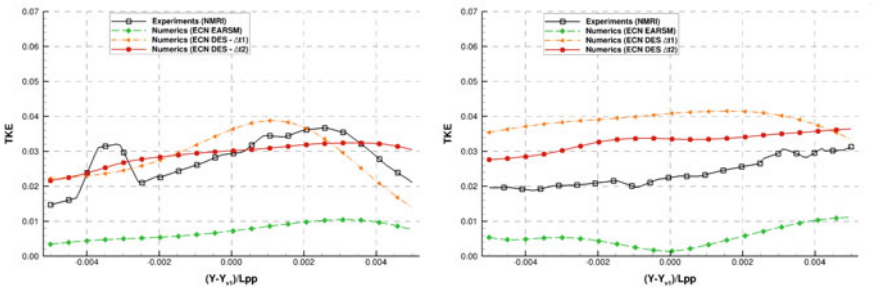

Horizontal evolution Vertical evolution

Fig. 5 Evolution of the turbulent kinetic energy around the vortex center

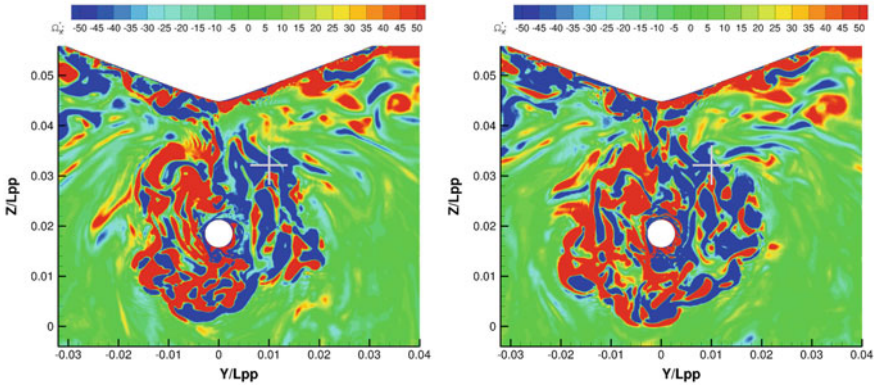

Time t = 525.8220 s Time t = 525.8815 s

Fig. 6 Instantaneous views of the non-dimensional longitudinal vorticity at the cross section S4

6 Conclusions

This paper presents the numerical results for the prediction of the flow around a ship, the Japan Bulk Carrier, with the flow solver ISIS-CFD. Two turbulence modelisations are used, a non-linear EARSM turbulence model and a DES approach. The DES computations reveal the existence of an unsteady separation zone characterized by a wake of coherent ring-vortices periodically shed at the stern of the ship. These numerical simulations provide a new interpretation of the averaged stern flow and explain why one may find simultaneously high levels of vorticity and turbulent kinetic energy in the core of an averaged longitudinal vortex.

Acknowledgements This work was granted access to the HPC resources of CINES/IDRIS under the allocation A0022A00129 made by GENCI.

References

1. Deng, G.B., Visonneau, M.: Comparison of explicit algebraic stress models and second-order turbulence closures for steady flow around ships. In: 7th Symposium on Numerical Ship Hydrodynamics, pp. 4.4-1–4.4-15. Nantes, France (1999)
2. Guilmineau, E., Deng, G.B., Leroyer, A., Queutey, P., Visonneau, M., Wackers, J.: Assessment of hybrid RANS-LES formulations for flow simulation around the Ahmed body. Comput. Fluids (2017). https://doi.org/10.1016/j.compfluid.2017.01.005
3. Hirata, J.: JBC test data in NMRI. In: Tokyo 2015 Workshop on CFD in Ship Hydrodynamics (2015)
4. Japan Bulk Carrier (JBC). http://www.t2015.nmri.go.jp/jbc.html
5. Kornev, N., Taranov, A., Shchukin, E., Kleinsorge, L.: Development of hybrid URANS-LES methods for flow simulation in the ship stern area. Ocean Eng. **38**, 1831–1838 (2011)
6. Nishikawa, N.: Application of fully resolved large eddy simulation to Japan bulk carrier with an energy saving device. In: Tokyo 2015 Workshop on CFD in Ship Hydrodynamics. Tokyo, Japan (2015)
7. Visonneau, M.: JBC local flow analysis. In: Tokyo 2015 Workshop on CFD in Ship Hydrodynamics (2015)

Large Eddy Simulation of a Tornado Flow Around a Train

K. Obara, S. Krajnovic, G. Minelli, B. Basara, N. Okura and M. Suzuki

1 Introduction

A tornado is a destructive rotating column of air extending from a cloud to the ground. It may kill people and damage property. Also there are possibilities of derailment of trains. Some train-turnover accidents are suspected to have been caused by tornadoes in Japan. For instance, a train of the JR Uestu line was overturned by a gust in 2005. According to the accident analysis, a tornado or downburst probably generated the gust [1]. In 2006, a train of the JR Nippo line was overturned by a tornado [2].

A large number of experiments and simulations about aerodynamic effects acting on a train under a crosswind have been studied [3]. However there are almost no studies about the aerodynamic effects on a vehicle by a tornado. Thus, we have examined the aerodynamic forces acting on a train by a tornado experimentally [4]. In this paper, a method simulating the experiment was developed to investigate how a tornado flow acts on a train.

K. Obara (✉) · N. Okura · M. Suzuki
Department of Vehicle and Mechanical Engineering,
Meijo University, Nagoya, Japan
e-mail: 153436007@ccalumni.meijo-u.ac.jp

S. Krajnovic · G. Minelli
Divison of Fluid Dynamic, Department of Applied Mechanics,
Chalmers University of Technology, 41296 Gothenburg, Sweden
e-mail: sinisa@chalmers.se

G. Minelli
e-mail: guglielmo.minelli@chalmers.se

B. Basara
Advanced Simulation Technologies, AVL List GmbH,
Hans-List-Platz 1, 8020 Graz, Austria
e-mail: branislav.basara@avl.com

M. V. Salvetti et al. (eds.), *Direct and Large-Eddy Simulation XI*,
ERCOFTAC Series 25, https://doi.org/10.1007/978-3-030-04915-7_77

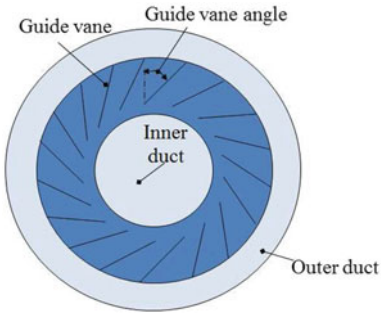

Fig. 1 Top view of the tornado generator

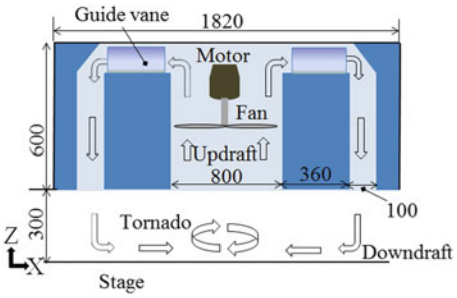

Fig. 2 Cross section of the tornado generator [mm]

2 Referential Experiment

Before explaining our simulation, we describe our referential experiment briefly. A tornado generator and a 1/40th scaled bluff model train were used. The model train was set at the center of the tornado generator, the pressure on the model train were measured. The tornado generator was developed based on the Iowa State University's tornado generator (Figs. 1 and 2) [5]. This tornado generator is shaped like cylinder and consists of a fan, inner duct, outer duct and guide vanes. The fan generates the updraft at the center. The updraft goes through the equally placed guide vanes. Since the guide vanes are attached with an angle, the flow is affected by a rotational component and then proceed down. This cycle creates a tornado on the stage. The guide vanes angle is changeable between 10° and 70°. In this paper, the angle was set to 50°. The model train was made based on a 1/40th scale of the Japanese local train (Fig. 3). The model train contains pressure sensors to measure unsteady surface pressure. There are 72 pressure ports on the model train surface. The tangential velocity was measured to specify the performance of the tornado generator (Fig. 4). The maximum tangential velocity is about 8 m/s and the core radius, at which the tangential velocity occurs is about 100 mm. The Reynolds number based on the maximum tangential velocity and the height of the train is 3.8×10^4.

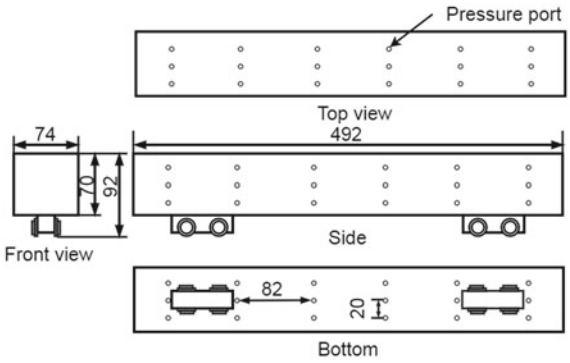

Fig. 3 Model train [mm]

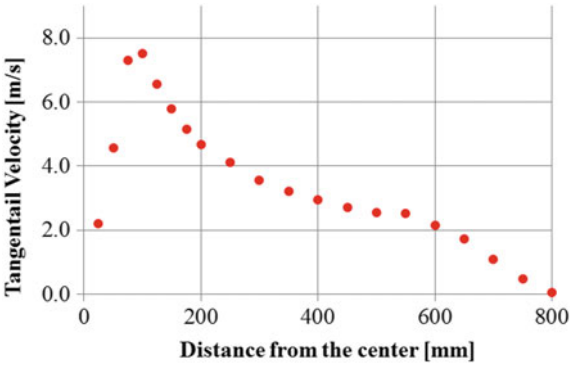

Fig. 4 Velocity distribution

3 Numerical Simulation

3.1 LES Equations

The governing LES equations are the incompressible Navier–Stokes and continuity equations. They are filtered with the implicit spatial filter by the characteristic width which is the computational cell size in the three coordinate directions.

$$\frac{\partial \overline{u}_i}{\partial t} + \overline{u}_j \frac{\partial \overline{u}_i}{\partial x_j} = -\frac{1}{\rho}\frac{\partial \overline{p}}{\partial x_i} + \nu \frac{\partial^2 \overline{u}_i}{\partial x_j \partial x_j} - \frac{\partial \tau_{ij}}{\partial x_j} \tag{1}$$

$$\frac{\partial \overline{u}_i}{\partial x_i} = 0 \tag{2}$$

Here, $\overline{u}$ and $\overline{p}$ are the resolved velocity and pressure respectively. $\tau_{ij} = \overline{u_i u_j} - \overline{u}_i \overline{u}_j$ is a sub grid scale stress tensor which contains the influence of the small scales. The algebraic eddy viscosity model proposed by Smagorinsky with the van Driest damping function is used [6].

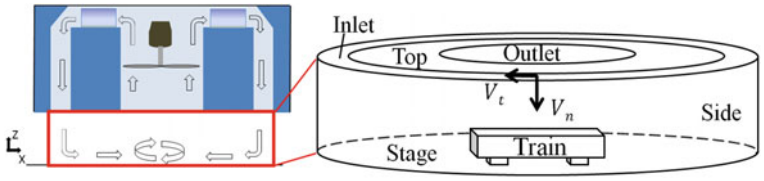

Fig. 5 The computational domain

Fig. 6 Computational grid

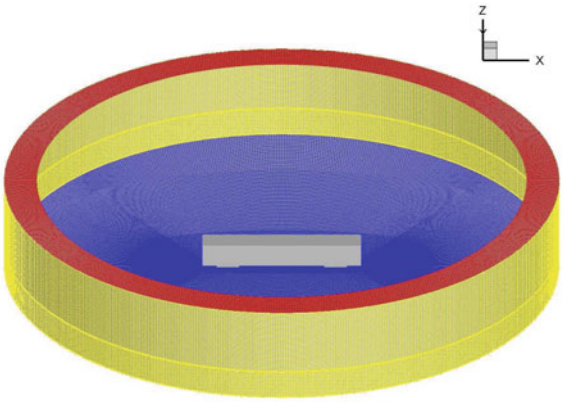

3.2 Numerical Setups

Simulations were performed on two computational grids. One is 9 million nodes and the other is 4 million nodes. They were created by using the commercial software package ICEM-CFD. The computational meshes were created resembling the experimental setup. The meshes represent the area between the stage and the tornado generator (Fig. 5). One plane near the train body of fine mesh is displayed in Fig. 7. To simulate the tornado flow, the tangential velocity V_t and the normal velocity V_n were set for the Inlet boundary. For the outlet and side boundaries a homogeneous Neumann boundary condition was applied. For the top, stage and train boundaries, the no-slip wall boundary condition was set (Fig. 6).

4 Results

4.1 Comparison with Experimental Results

The surface pressure distributions obtained by the experiment and LES are compared in Fig. 8. The agreement between the experiment and LES is relatively good near the central part of the train (B, C, D,and E section). However, there is discrepancy near

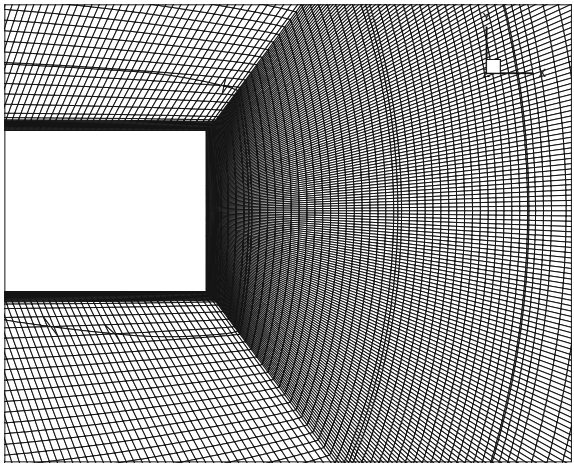

Fig. 7 Top view of a mesh around a train

the edge of the train (A and F section). These differences between experiment and LES are considered to be caused by the difference of the experimental and numerical setups. Especially on the outlet, in the experiment the fan forces to circulate the flow. On the other hand there is no forced flow in the simulation. We consider that these differences near the outlet may cause the differences in the flow field

4.2 Flow Structure

Figures 9 and 10 show iso-surfaces of the second invariant of velocity gradient, $Q = 20000$, colored by the average velocity. The flow separates on the edge of the train and a swirling flow that wraps the model is clearly observed. The smaller flow structures were captured only by the fine mesh.

5 Concluding Remarks

Large eddy simulation for tornado flow around a train was performed and the results were compared to experimental data. The results show a relatively good agreement between measurements and simulations, being promising for further investigations. The main discrepancy found in the comparison was probably due to slightly different setup of the experiments, but the overall trend of the flow is well predicted by the simulation. This was the first step toward a realistic simulation that reproduces the effect of a tornado on a running train. In fact, a simulation that reproduces a train passing through the tornado is currently under investigation.

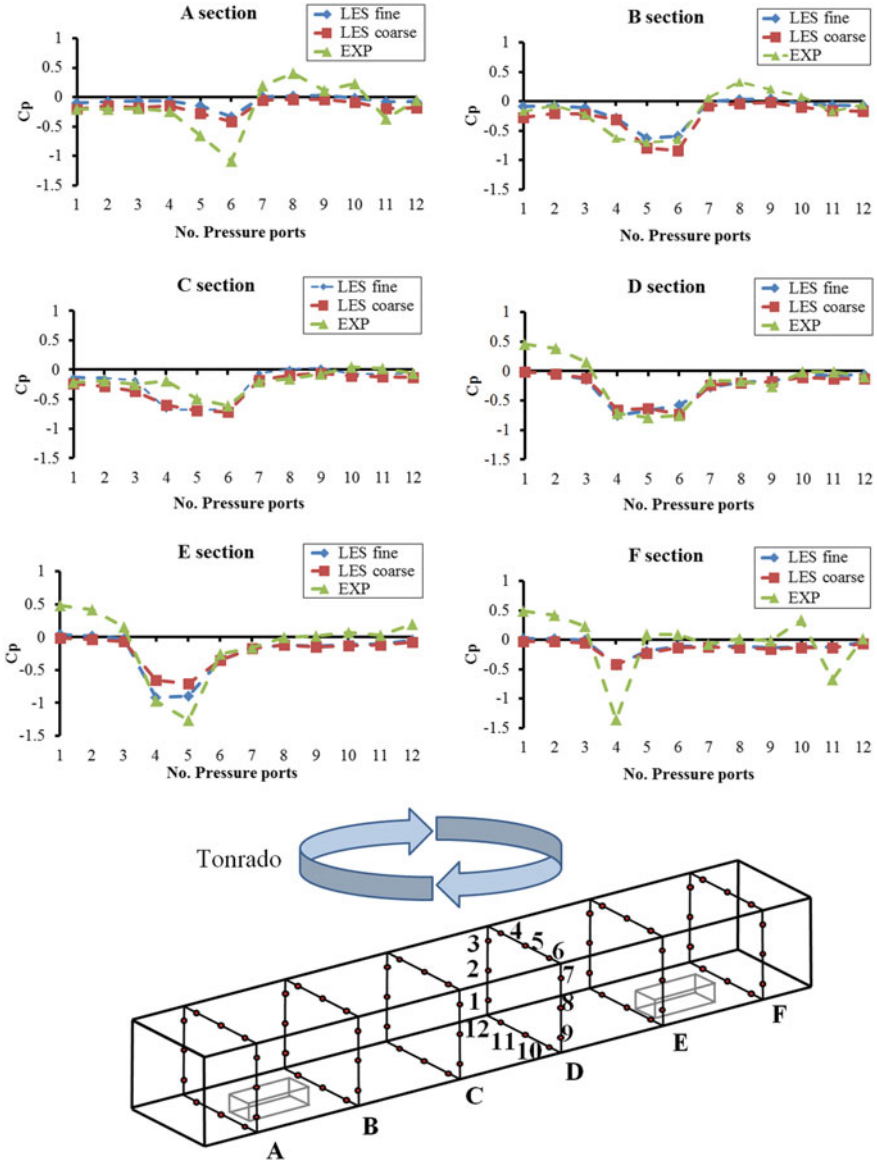

Fig. 8 Comparison of the pressure coefficient C_p between LES and experiment

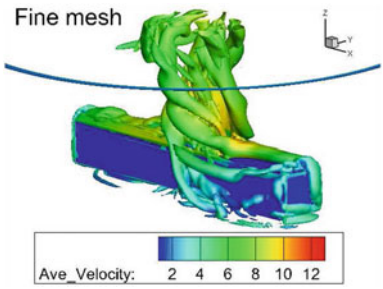

Fig. 9 Fine mesh

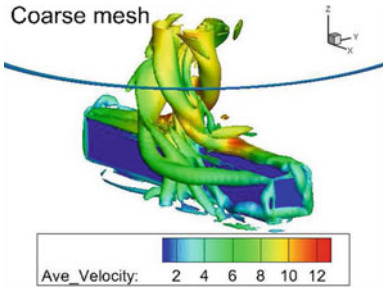

Fig. 10 Coarse mesh

Acknowledgements This work was partly supported by JSPS KAKEN Grant Number 26350491. Software licenses were provided by AVL List GMBH. Computations were performed at SNIC (Swedish National Infrastructure for Computing) at the Center for Scientific Computing at Chalmers (C3SE) and the National Supercomputer Center (NSC) at LiU.

References

1. Aircraft and railway accidents investigation commission: railway accident analysis report RA2008 -4 (2008). (in Japanese)
2. Aircraft and railway accidents investigation commission: railway accident analysis report RA2008 -6 (2008). (in Japanese)
3. Krajnovic, S., Ringqvist, P., Nakade, K., Basara, B.: Large eddy simulation of the flow around a simplified train moving through a crosswind flow. J. Wind Eng. Ind. Aerodyn. **110**, 86–99 (2012)
4. Suzuki, M., Okura, N.: Study of aerodynamic forces acting on a train using a tornado simulator. Mech. Eng. Lett. **2**, 16-00505 (2016)
5. Haan Jr., F.L., Sarkar, P.P., Gallus, W.A.: Design construction and performance of a large tornado simulator for wind engineering applications. Eng. Struct. **30**(4), 1146–1159 (2008)
6. Smagorinsky, J.: General circulation experiments with the primitive equations. Mon. Weather Rev. **91**(3), 99–165 (1963)

Large Eddy Simulation of a Wind Farm Experiment

B. Rocchio, U. Ciri, M. V. Salvetti and S. Leonardi

1 Introduction

The growing interest in renewable resources [1] is encouraging research on wind turbines. The present work is focused on the turbine wake because it plays a key role in the power production of the entire wind farm. The wake is strongly turbulent and it persists more than fifteen rotor diameters (D) downstream [2], while the distance between two "in line" turbines is much less than this length. Therefore, the downstream turbines are impinged by a velocity that is completely different from the undisturbed one and the turbine operates off-design. A good representation of the evolution and decay of the turbine wake is needed to accurately predict the turbine performance.

This is addressed in the present paper by discussing LES results of the turbulent flow over an array of turbines. The geometrical set up reproduces the experiment performed at the Portland State University [3] on 4×3 array of wind turbines impinged by turbulent inlet in the wind tunnel. The turbulence is obtained by using three different devices: a uniform grid, strakes and chains on the floor.

We wish to investigate how the inlet turbulence influences the features of the flow field seen by each turbine and the turbine performance.

B. Rocchio (✉) · M. V. Salvetti
University of Pisa, Pisa, Italy
e-mail: benedetto.rocchio@ing.unipi.it

M. V. Salvetti
e-mail: mvsalvetti@ing.unipi.it

U. Ciri · S. Leonardi
University of Texas at Dallas, Richardson, TX, USA
e-mail: Umberto.Ciri@utdallas.edu

S. Leonardi
e-mail: stefano.leonardi@utdallas.edu

M. V. Salvetti et al. (eds.), *Direct and Large-Eddy Simulation XI*,
ERCOFTAC Series 25, https://doi.org/10.1007/978-3-030-04915-7_78

2 Numerical Methodology and Computational Set Up

The filtered non-dimensional Navier–Stokes equations in incompressible flow are considered here. Filtering is implicit, i.e. the numerical discretization is assumed to act as a filter, and the subgrid-scale stress tensor is modeled by using the Smagorinsky closure [4].

The turbine blades are not explicitly simulated but they are replaced by the forces that they apply to the flow-field. These forces are considered in the LES equations as a source term, F_i. Two different methods can be employed. In the *Actuator Line Model* (ALM; [5, 6]) the blade is modeled as a rotating line, whose length is equal to the blade length, and it is divided into finite segments. For each segment, the lift and drag forces are evaluated (**F**). This method consists of the projection of **F** along the computational axes and in its distribution among the nearest grid-points within a cylinder with axis parallel to the actuator line according to a Gaussian regularization kernel. The second method is Rotating Actuator Disk Model (RADM). The total aerodynamic force **F** is now spread on the whole rotor area and on several grid-points in the stream-wise direction. The advantage in the use of the RADM is that the force field is smoother than in the ALM approach and the time step can be larger, so that the simulations are faster. On the other hand, the use of the ALM allows to have a closer representation of the wake and its turbulence. Towers and nacelles are numerically modeled by using the Immersed Boundary (IB) Method [7].

The numerical discretization of the LES equations is described in details in [8]. A centered second-order finite-difference approximation on a staggered Cartesian grid is employed to discretize the terms. Time-advancement is performed by means of a hybrid low-storage third-order Runge–Kutta scheme combined with a fractional step method. The viscous terms are treated implicitly and convective terms explicitly. The pressure at the previous step is used. The obtained field is non-solenoidal; it is then projected onto a solenoidal field by means of a scalar quantity ϕ.

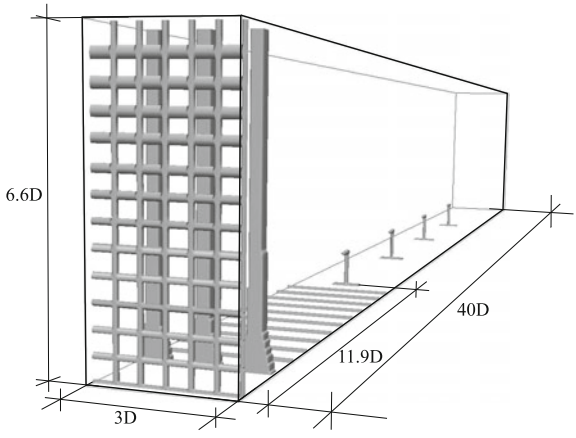

Fig. 1 Wind tunnel reproduction with the immersed boundary method

Table 1 Mesh details. The streamwise, wallnormal and spanwise directions are respectively x, y and z

Axis	Range	N_{points}	Δ_{min}/c	Δ_{max}/c
x	$[0:40D]$	2048	0.0195	0.0195
y	$[0:6.6D]$	256	0.0129	0.0682
z	$[0:3D]$	192	0.0156	0.0156

The turbulent inlet in the wind tunnel is obtained by using three different devices: a uniform grid, strakes and chains on the floor. All these elements are numerically modeled by using the Immersed Boundary Method (see Fig. 1). To reduce the computational cost of the simulation, only the central column of the turbine array present in the experiments has been considered with periodic boundary conditions in the spanwise direction. The inlet velocity at the rotor height is $U_{hub} = 4.53$ m/s and the Reynolds number, based on $D = 0.12$ m and U_{hub}, is $Re = 32700$. In Table 1 the computational domain and the number of nodes for each direction are shown.

3 LES of the Empty Wind Tunnel

A preliminary analysis is performed to verify if our representation of the wind tunnel well reproduces the incoming velocity profile. A first LES is thus carried out just by taking into account the main elements of the wind tunnel without the turbines. The time-averaged Turbulent Kinetic Energy (TKE) is shown (see Fig. 2) in the middle plane of the wind tunnel. The turbulence fluctuations generated by grid, strakes and chains can be observed. The streamwise velocity profile, averaged in time and along the spanwise direction, taken at $x = 11.65D$ is shown in Fig. 3. The profile shows a very good matching with the reference experimental velocity starting from the hub height, $y/D = 1$, while below the hub the evolution of the boundary layer is not perfectly reproduced due to the fact that, since the real geometry of the chains and strakes was not available, some assumptions were made in our simulations, which probably do not completely match the actual geometry. The same considerations can be made for the Reynolds stresses (Figures 4 and 5).

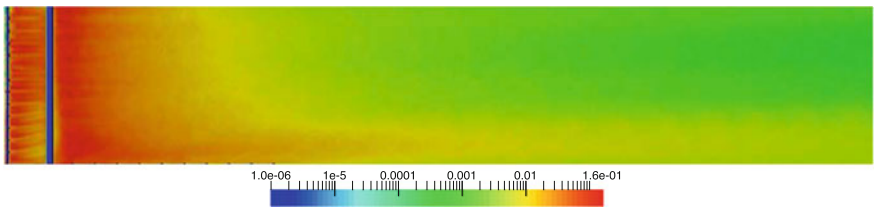

Fig. 2 Time-averaged turbulent kinetic energy (wind-tunnel middle plane)

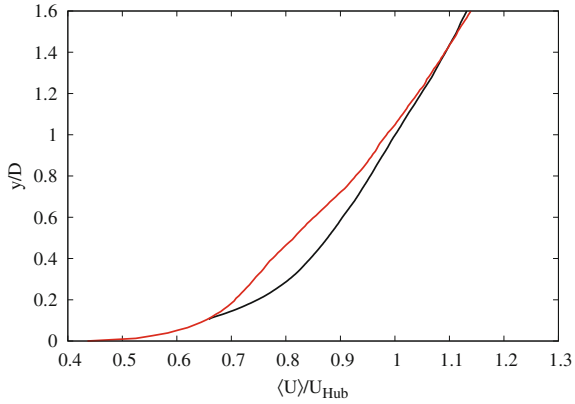

Fig. 3 Mean streamwise velocity profile. Red line: LES; black line: experiments

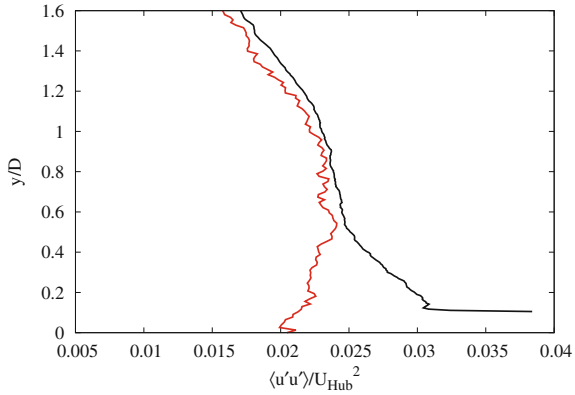

Fig. 4 Time-averaged stream-wise stress profile. Red line: LES; black line: experiments

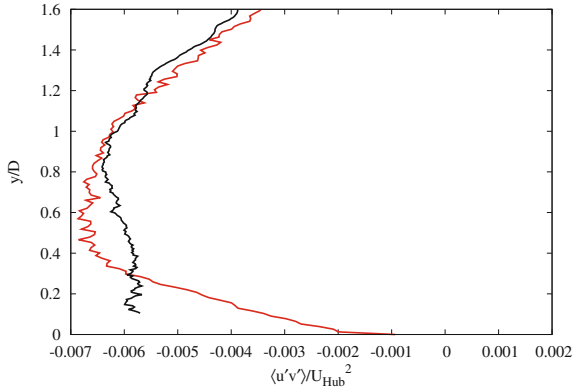

Fig. 5 Time-averaged shear stress profile. Red line: LES; black line: experiments

4 LES of a Turbine Array

Now the central column of the array is considered and the towers and nacelles are numerically represented by using the Immersed Boundary Method. The rotor blades have a flat plate as cross-section and they are modeled herein by means of the RADM. The remaining computational set up is the same as that of the empty wind tunnel simulation.

The incoming velocity, seen by the turbines, changes in time due to the turbulent inlet of the wind tunnel. Thus, the angular speed is updated with the angular momentum balance Eq. 1:

$$I\dot{\omega} = T_{aero} - M_{gen} \tag{1}$$

where I is the rotor inertia, ω is the angular speed of the turbine, T_{aero} is the torque produced by the aerodynamic forces. $M_{gen} =$ is the generator torque given by the following control law:

$$M_{gen} = k\omega^2 \tag{2}$$

where k is the torque gain.

Figures 6 and 7 show the time-averaged streamwise velocity (U/U_{hub}) and the time-averaged Turbulent Kinetic Energy obtained in the simulation. The most important qualitative features can be observed. The productions of turbulence by the inlet devices, viz. grid, chains and strakes, is evident, and it appears that the first turbine is the most affected by the inlet turbulence, while the downstream turbines are immersed in the wake of the upstream ones that dominates its behavior. The effects of towers and nacelles are also visible especially if the TKE is considered. Figures 8 and 9 show the aerodynamic torque for the first and second turbine. Before that the turbulence from the inlet reaches the first turbine, or the wake of the first turbine reaches the second one, the flow in front of each turbine is uniform. Thus, the aerodynamic torque shows just the disturbance that the tower makes on the blades, when each blade passes in front of it. When the velocity starts to change in time, due to the turbulence, the total force that acts on the turbine blades changes deeply. Turbulent fluctuations are significant and large changes on the angle of attack are observed. Depending on the turbulent structures advected from the inlet, the blade may stall especially due to the geometry of the blades cross section. This phenomenon is predominant for the first turbine (Fig. 9), because the velocity fluctuations from the inlet are larger compared to the ones in the turbine wake (Fig. 7). When the blade stalls the aerodynamic torque is negative and the rotational speed decreases until a new equilibrium is found. In fact, by reducing the angular speed, the generator torque decreases and the aerodynamics torque improves because of a change in the angle of attack of the blade (see Eq. 1). This results suggest importance of unsteadiness of incoming flow conditions on at least the first turbine.

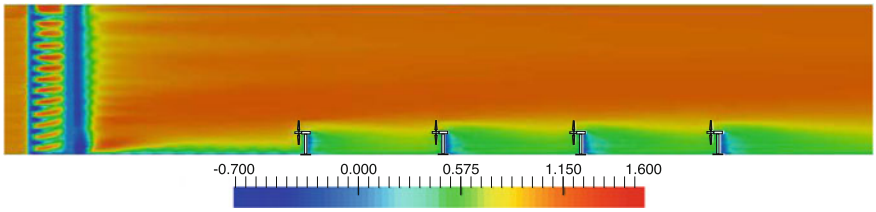

Fig. 6 Time-averaged stream-wise velocity

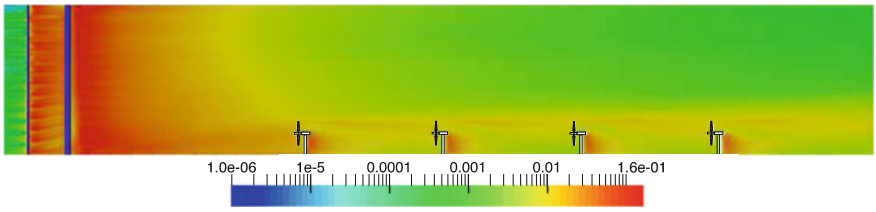

Fig. 7 Time-averaged turbulent kinetic energy

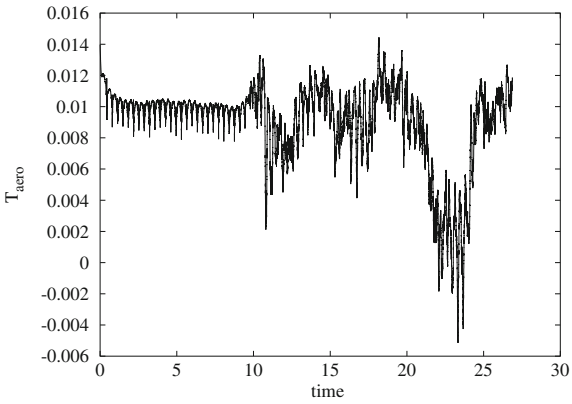

Fig. 8 Normalized aerodynamic torque for the first turbine

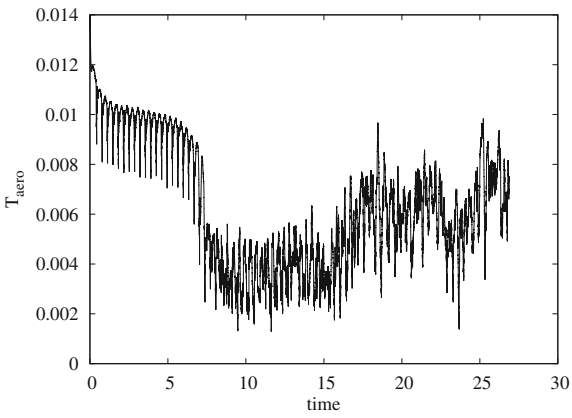

Fig. 9 Normalized aerodynamic torque for the second turbine

References

1. Global Wind Energy Council. Global Wind Report Annual Market Update 2014. Technical report, February (2015)
2. Chamorro, L.P., PortéAgel, F.: A wind-tunnel investigation of wind-turbine wakes: boundary-layer turbulence effects. Boundary Layer Meteorol. **132**(1), 129–149 (2009)
3. Camp, E.H., Cal, R.B.: Mean kinetic energy transport and event classification in a model wind turbine array versus an array of porous disks: energy budget and octant analysis. Phys. Rev. Fluids **1**(4), 044404 (2016)
4. Smagoringsky, J.: General circulation experiments with the primitive equations, I: the basic experiment. Mon. Weather Rev. **91**, 99–164 (1963)
5. Sørensen, J.N., Shen, W.Z.: Computation of wind turbine wakes using combined Navier-Stoke/actuator-line Methodology. In: Proceedings of the European Wind Energy Conference and Exhibition. Nice, France, 1–5 March (1999)
6. Martìnez-Tossas, L.A., Churchfield, M.J., Leonardi, S.: Large eddy simulations of the flow past wind turbines: actuator line and disk modeling. Wind Energy **18**, 1047–1060 (2015)
7. Orlandi, P., Leonardi, S.: DNS of turbulent channel flow with two- and three-dimensional roughness. J. Turbul. **7** (2006)
8. Orlandi, P.: Fluid Flow Phenomena: A Numerical Toolkit. Kluwer Academic Publisher (2000)

On Direct Aeroacoustics Calculations of the Vocal Tract

L. Schickhofer, A. Dahlkild and M. Mihaescu

1 Introduction

Voice production and the verbal expression through speech are crucial components of human communication. The human voice is not just conveying information directly through words, but also indirectly as paralinguistic information such as the speaker's emotional state through tonality [7]. As such, voice is generated through a two-part process: First, a source signal is produced by the vocal folds that are pulsating the lung pressure and volumetric flow rate in a particular frequency through periodic opening and closing. Second, the vocal tract causes an attenuation or amplification of this source signal at certain frequencies depending on its specific shape. The voice generation process can therefore be described by a source-filter model with the vocal folds acting as the source and the vocal tract as an acoustic filter [6]. Thus, we are able to produce different vowels and sounds as we manipulate the vocal tract during phonation. However, the ability to speak can be compromised due to clinical conditions affecting the opening between the vocal folds (i.e. *glottis*) or the vocal tract. Certain voice disorders such as partial or total vocal fold paralysis and laryngeal cancer are known to affect the source signal and its waveform considerably [2]. Nevertheless, the actual cause-effect relations between physiological changes in the vocal tract and the acoustic pressure in the far field are unclear. In acoustics, the far field is defined as the region away from the source, where sound pressure levels follow the inverse square law and show a decrease of approximately 6 dB for each doubling of the distance from the source.

An additional factor in voice production is the shedding of intraglottal vortical structures [3]. The sound output generated by vortices becomes important in cases of incomplete glottal closure or paralysed vocal folds. In this study, the acoustic signal

L. Schickhofer (✉) · A. Dahlkild · M. Mihaescu
Department of Mechanics, Linné FLOW Centre, BioMEx Competence Centre,
KTH Royal Institute of Technology, Stockholm, Sweden
e-mail: schic@mech.kth.se

M. V. Salvetti et al. (eds.), *Direct and Large-Eddy Simulation XI*,
ERCOFTAC Series 25, https://doi.org/10.1007/978-3-030-04915-7_79

generated through speech is computed directly as pressure fluctuations resulting from unsteady large eddy simulations, applied to magnetic resonance imaging (MRI) data. Thus, a time-resolved solution for the acoustic pressure in the upper airways is achieved, contributing to the knowledge of cause-effect relations in phonation and opening up new therapeutic options for vocal tract and airway disorders by the use of computational fluid dynamics [4].

2 Method

The investigated geometry is extracted from MRI scans of a healthy, 30-year-old male subject vocalising particular Finnish vowels [1]. The model for vowel [a] is shown in Fig. 1. It includes the upper respiratory tract and extends from the vocal folds to the mouth region. The compressible flow governing equations were discretised using a finite volume approach over a numerical grid counting $3.4 \cdot 10^6$ mesh volumes. The solution of the compressible Navier–Stokes equations is obtained with a time step of $\Delta t \approx 2 \cdot 10^{-5}$ s and an implicit temporal discretisation scheme of second order. For the spatial discretisation a second order scheme is applied with the convection term being solved by bounded central differencing. The Dirichlet boundary condition for the fluid velocity, $u_i = 0$, ensuring the no-slip condition, is imposed at the vocal tract walls, while atmospheric free stream boundary conditions are applied at the mouth outlet.

The dynamic non-linear behaviour of the vocal folds, which leads to an intermittent pressure signal in the upper airways, is modelled by the Rosenberg waveform of volume velocity [5]. It gives the glottal pulse as a function f_p for the opening period (i.e. positive slope) and f_n for the closing period (i.e. negative slope):

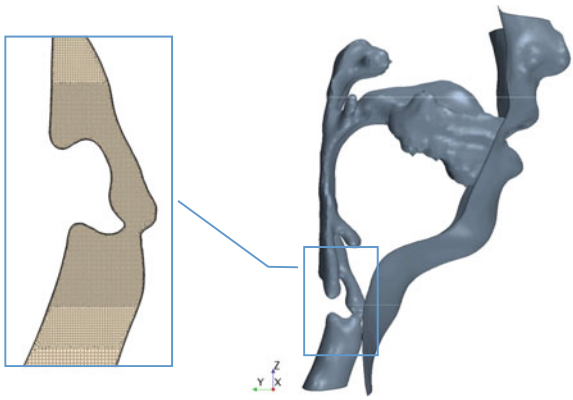

Fig. 1 Surface geometry of the dataset for vowel [a] with a magnified plane section of the mesh in the glottal region

$$f_p(t) = \frac{A_0}{2}\left[1 - cos\left(\frac{t}{T_p}\pi\right)\right] \qquad 0 \le t \le T_p, \tag{1}$$

$$f_n(t) = A_0 cos\left(\frac{t - T_p}{T_n}\frac{\pi}{2}\right) \qquad T_p \le t \le T_p + T_n. \tag{2}$$

The acoustics are computed by propagating the pressure fluctuations into the far-field region connected to the mouth outlet. For sufficient resolution of the sound emitted from the airways, the grid entails more than 40 cells per wavelength for the highest targeted frequencies of approximately 10 kHz. By computing the Fourier transform of the signal, the spectral envelope with the dominant, energy-containing frequencies can be obtained. Furthermore, sound amplitudes in terms of the power spectral density of the acoustic pressure at discrete frequencies are calculated using Hanning filtering.

3 Results

The flow instabilities occurring in the intraglottal region are giving rise to a trail of coherent structures that is convected downstream, as shown for the vocal tract of vowel [a] in Fig. 2. The vortex production reaches its peak as the glottal pulse

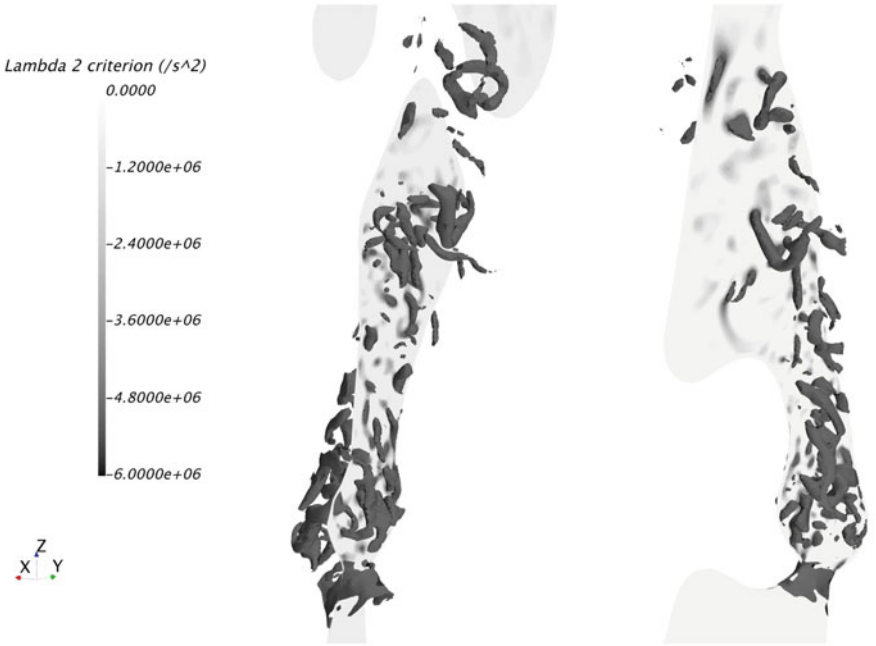

Fig. 2 Vortical structures in the supraglottal region visualised by λ_2-isosurfaces of value $-5 \cdot 10^6\,\mathrm{s}^{-2}$ and by sections through the coronal (*left*) and sagittal plane (*right*)

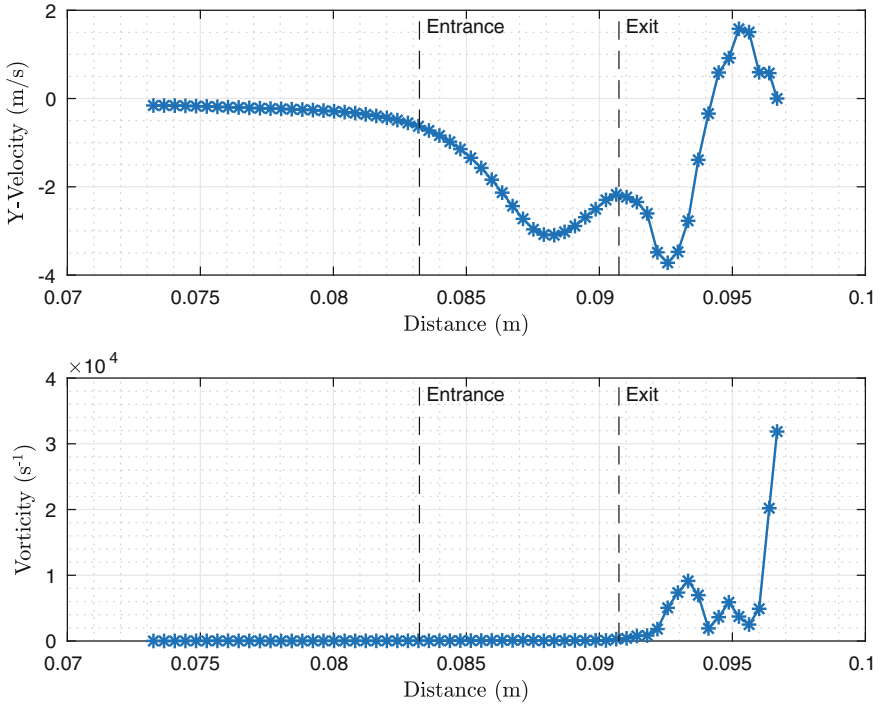

Fig. 3 Y-velocity perpendicular to the mean flow direction (*top*) and vorticity along the centreline through the glottis (*bottom*). Glottal entrance and exit are marked

passes its amplitude of volume velocity. The vortices are impinging on the walls of the airway, where they lead to fluctuating pressure and increasing wall shear stress.

The magnitude of vorticity undergoes a sharp rise at the glottal exit. This coincides with a local maximum of y-velocity, which is the velocity component perpendicular to flow direction and coronal plane, respectively. It indicates secondary flow motion of the fluid (cf. Fig. 3). The sound induced by the vortical structures shed at the glottis is mainly of broadband in nature and occurs at frequencies of 2 kHz and above. This is typically above the harmonic frequencies resolved by lower-order acoustic models. For the validation of the method, the dominant frequencies in the far-field spectrum of the acoustic pressure (i.e. *formants*) are compared with the Helmholtz eigenfrequencies of the domain obtained by solving the eigenvalue problem of the three-dimensional wave equation. Figure 4 shows the result for the vowels [a] and [u].

Additionally to the far field, the Fourier transform is computed for the surface pressure fluctuations at the inner vocal tract walls. Thus, it is possible to identify the regions of amplification for the different formants. Figure 5 shows the resulting maps of power spectral density at the surfaces for the most important frequencies F_1 and F_2 of the vowel [a]. While the *laryngopharynx* as the lower part of the airways

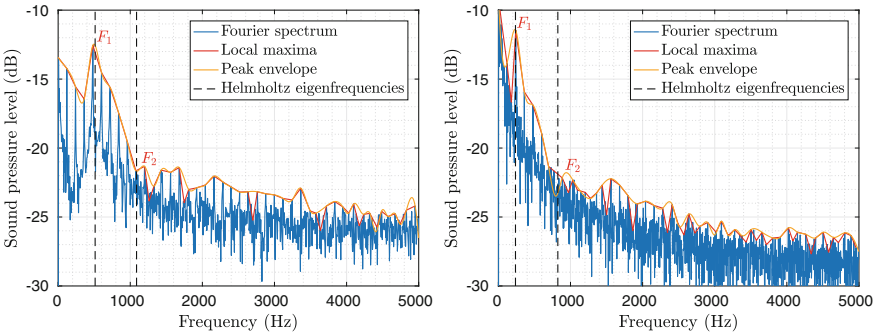

Fig. 4 Fourier spectrum of the pressure fluctuations in the far field for the vowels [a] (*left*) and [u] (*right*). The formants F_1 and F_2 are shown alongside the Helmholtz eigenfrequencies of the domain

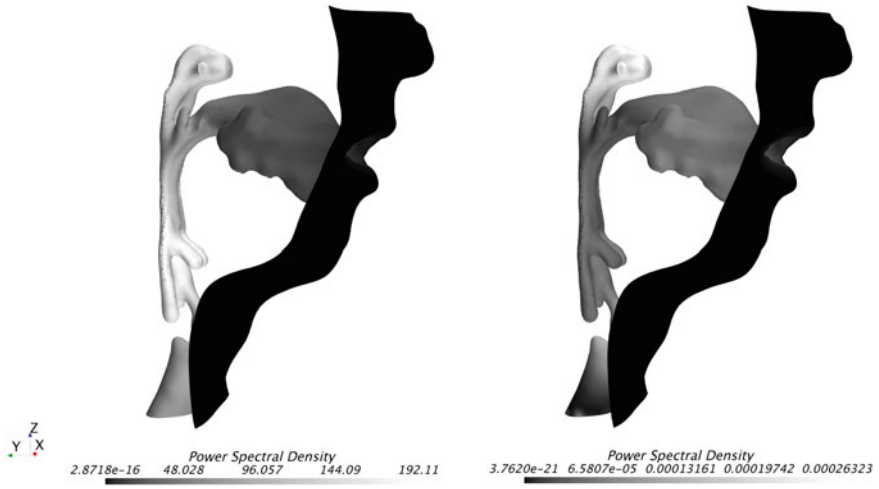

Fig. 5 Surface pressure amplitudes at the vocal tract walls for the pronounciation of the vowel [a] for the formants $F_1 = 480\,\text{Hz}$ (*left*) and $F_2 = 1166\,\text{Hz}$ (*right*)

seems to be the crucial resonating area at low frequencies around $F_1 = 480\,\text{Hz}$, the *nasopharynx* and nasal cavity are most relevant for the amplification of acoustic frequencies of about $F_2 = 1166\,\text{Hz}$.

4 Conclusion

By using the presented approach, the flow field inside the upper airways is computed alongside the acoustic spectra in the far field that match well with previous lower-

order models of speech acoustics. For the investigated Finnish vowels [a] and [u], the dominant frequencies are predicted accurately. Vortex shedding is observed at the level of the vocal folds, introducing a sharp rise of the amplitude of pressure fluctuations in the upper airways downstream of the glottal constriction. Furthermore, amplitudes of the formant frequencies inside the vocal tract are obtained through Fourier analysis of the time-resolved fluctuating pressure. This gives a strong indication of the critical areas of acoustic amplification inside the upper airways. For the vowel [a], the resonating parts happen to be the laryngopharynx at formant F_1 and the nasal cavity at formant F_2 in the higher frequency range of the acoustic spectrum. The results gained through this study can contribute to a better understanding of the voice generation process and to improved strategies for the treatment of vocal disorders.

Acknowledgements This work is supported by the Swedish Research Council (Vetenskapsrådet) through the grant VR 621-2012-4256. The MRI scans and Helmholtz eigenfrequencies in Fig. 4 were obtained by the Speech Modelling Group from the Department of Mathematics and Systems Analysis at Aalto University, Finland (http://speech.math.aalto.fi). The Swedish National Infrastructure for Computing (SNIC) is acknowledged for the computational resources used for the simulations.

References

1. Aalto, D., Aaltonen, O., Happonen, R.-P., Jsaari, P., Kivel, A., Kuortti, J., Luukinen, J.-M., Malinen, J., Murtola, T., Parkkola, R.: Large scale data acquisition of simultaneous MRI and speech. Appl. Acoust. **83**, 64–75 (2014)
2. Mathieson, L.: Greene and Mathieson's the Voice and Its Disorders. Wiley, New York (2013)
3. Mihaescu, M., Khosla, S.M., Murugappan, S., Gutmark, E.J.: Unsteady laryngeal airflow simulations of the intra-glottal vortical structures. J. Acoust. Soc. Am. **127**, 435–444 (2010)
4. Mylavarapu, G., Mihaescu, M., Fuchs, L., Papatziamos, G., Gutmark, E.J.: Planning human upper airway surgery using computational fluid dynamics. J. Biomech. **46**, 1979–1986 (2013)
5. Rosenberg, A.E.: Effect of glottal pulse shape on the quality of natural vowels. J. Acoust. Soc. Am. **49**, 583–590 (1971)
6. Titze, I.R., Alipour, F.: The Myoelastic Aerodynamic Theory of Phonation. National Center for Voice and Speech (2006)
7. Zhang, Z.: Mechanics of human voice production and control. J. Acoust. Soc. Am. **140**(4), 2614–2635 (2016)